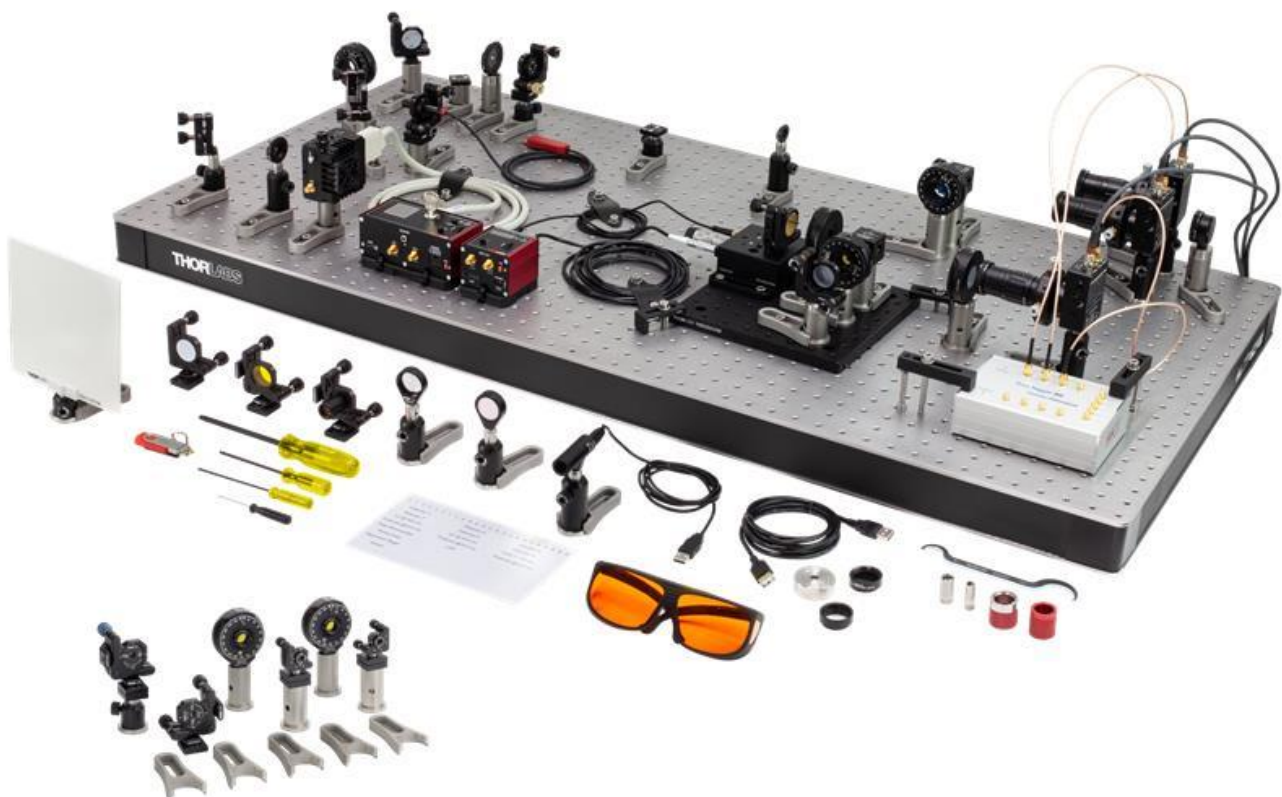




# EDU-QOP1(/M) and EDU-QOPA1(/M) Quantum Optics Kit and Polarization-Entanglement Extension Kit User Guides



## **Table of Contents**

**EDU-QOP1(/M)**

**Quantum Optics Kit**

**EDU-QOPA1(/M)**

**Polarization-Entanglement Extension Kit**

Click on the Links Above to be Taken to the First Page





# EDU-QOP1(/M) Quantum Optics Kit

## User Guide





# Table of Contents

<b>Chapter 1</b>	<b>Intended Use and Safety Warnings .....</b>	1
1.1	<b>Intended Use.....</b>	1
1.2	<b>Warning Symbol Definitions.....</b>	1
1.3	<b>Laser Radiation Warning .....</b>	1
1.4	<b>Piezo Controller Warnings.....</b>	1
<b>Chapter 2</b>	<b>Product Description.....</b>	2
<b>Chapter 3</b>	<b>Principles of Quantum Optics .....</b>	4
3.1	<b>Classical Description of Light.....</b>	4
3.1.1	Behavior at a Beamsplitter .....	4
3.1.2	Interference .....	5
3.1.3	Polarization .....	6
3.2	<b>Mathematical Formalism of Quantum Mechanics .....</b>	8
3.2.1	Dirac Notation .....	8
3.2.2	General Case .....	8
3.2.3	Application in Quantum Mechanics and Quantum Optics .....	8
3.2.4	Linear Operators .....	9
3.2.5	Eigenstates and Eigenvalues .....	9
3.2.6	Commutator Relations .....	10
3.2.7	Bases of the Hilbert Space.....	10
3.2.8	Observables.....	10
3.2.9	Measurements and Superposition of Quantum States .....	11
3.2.10	Expectation Values .....	11
3.2.11	Mixed States.....	12
3.2.12	Combination of Quantum Systems .....	12
3.3	<b>Quantum Description of Light .....</b>	12
3.3.1	Fock States .....	13
3.3.2	Coherent States.....	14
3.3.3	Thermal States .....	14
3.4	<b>Proof of Quantized Light - Theory .....</b>	15
3.4.1	Second-Order Correlation Function .....	15
3.4.2	Quantum Mechanical Treatment of a Beamsplitter.....	17
3.4.3	Quantum Fields .....	17
3.5	<b>Proof of Quantized Light - Experiment .....</b>	19
3.5.1	Hanbury-Brown-Twiss Experiment.....	19
3.5.2	Correlation Function for Single Photon Detectors .....	20
3.5.3	Grangier-Roger-Aspect Experiment .....	21
3.5.4	Triple Coincidence Detection Scheme.....	22
3.5.5	Triple Coincidence Detection Scheme: Explanation 1 .....	23
3.5.6	Triple Coincidence Detection Scheme: Explanation 2 .....	23
3.5.7	Accidental Coincidences.....	24
3.6	<b>Single Photon Interference.....</b>	25
3.6.1	Theoretical Description .....	25
3.6.2	Experimental Realization.....	27
3.7	<b>Quantum Treatment of Polarization.....</b>	28
3.7.1	Theoretical Description .....	28
3.7.2	Experimental Realization.....	29
3.8	<b>The Quantum Eraser .....</b>	30
3.8.1	Theoretical Description .....	30
3.8.2	Experimental Realization.....	31

---

3.9	Spontaneous Parametric Down-Conversion .....	32
<b>Chapter 4</b>	<b>Experimental Concepts .....</b>	<b>36</b>
4.1	Single Photon Detectors .....	36
4.2	Time Tagging .....	37
4.2.1	Time Tagging vs. Coincidence Electronics .....	37
4.2.2	Jitter and Coincidence Window .....	37
4.2.3	Delay Compensation .....	38
<b>Chapter 5</b>	<b>Kit Components .....</b>	<b>40</b>
5.1	Pump and Alignment Laser .....	40
5.2	Crystal and Adjustment Aids .....	41
5.3	Optics .....	42
5.4	Detectors .....	44
5.5	Michelson Interferometer .....	45
5.6	Time Tagger and Software .....	46
5.7	Quantum Eraser .....	46
5.8	Mounting and Tools .....	47
5.9	Included Hardware .....	48
5.9.1	Imperial Kit .....	48
5.9.2	Metric Kit .....	48
<b>Chapter 6</b>	<b>Quick Setup .....</b>	<b>50</b>
<b>Chapter 7</b>	<b>Setup and Adjustment .....</b>	<b>53</b>
7.1	Assembly of Components .....	53
7.1.1	Pump Laser .....	53
7.1.2	Alignment Laser .....	55
7.1.3	Mirrors .....	55
7.1.4	Iris Apertures .....	57
7.1.5	Half-Wave Plates .....	57
7.1.6	Crystal, Aicon, and Filter .....	58
7.1.7	Beamsplitter .....	60
7.1.8	Detectors .....	61
7.1.9	Detector Optics .....	61
7.1.10	Beam Trap .....	63
7.1.11	Alignment Target .....	63
7.1.12	Economy Beamsplitter .....	64
7.1.13	Screen .....	64
7.1.14	Mirrors for Michelson Interferometer .....	64
7.1.15	Lens .....	66
7.1.16	Mounting the LED .....	66
7.1.17	Polarizers for Quantum Eraser .....	67
7.1.18	Labelling the Time Tagger .....	68
7.2	Preliminary Alignment .....	69
7.2.1	Software Installation .....	69
7.2.2	Collimating the Pump Laser .....	69
7.2.3	Calibrating the Polarizer .....	72
7.3	Setting Up the HBT Experiment with the Alignment Laser .....	74
7.4	Setting Up the Photon Pair Source .....	78
7.4.1	Setting up the Pump Laser Beam Path .....	78
7.4.2	Aligning Both Pump and Alignment Laser on the Same Path .....	81
7.4.3	Detector Positioning .....	84

---

---

7.4.4	Detector Fine Adjustment (Colored Glass Filter).....	87
7.4.5	Crystal Angle Adjustment.....	88
<b>7.5</b>	<b>Setting Up the Grangier-Roger-Aspect Experiment.....</b>	<b>90</b>
7.5.1	Beamsplitter Positioning .....	91
7.5.2	Third Detector Positioning .....	92
7.5.3	Third Detector Fine Adjustment.....	92
7.5.4	Test Measurement .....	93
<b>7.6</b>	<b>Setting Up the Michelson Interferometer .....</b>	<b>94</b>
7.6.1	Additional Alignment Path .....	95
7.6.2	Interferometer Adjustment.....	96
7.6.3	Detector Positioning.....	103
7.6.4	Detector Fine Adjustment .....	104
7.6.5	Single Photon Interference Adjustment.....	105
7.6.6	Michelson Interferometer Test Measurement.....	105
<b>7.7</b>	<b>Setting Up the Quantum Eraser .....</b>	<b>107</b>
<b>Chapter 8</b>	<b>Learning Goals and Misconceptions .....</b>	<b>110</b>
<b>Chapter 9</b>	<b>Experiments.....</b>	<b>112</b>
9.1	<b>HBT-Experiment with Attenuated Laser .....</b>	<b>112</b>
9.2	<b>Photon Pair Source .....</b>	<b>113</b>
9.3	<b>HBT Experiment with one Arm of the Pair Source .....</b>	<b>114</b>
9.4	<b>Grangier-Roger-Aspect Experiment .....</b>	<b>114</b>
9.5	<b>GRA Experiment with Classical Light.....</b>	<b>116</b>
9.6	<b>Malus' Law for Single Photons .....</b>	<b>117</b>
9.7	<b>Single Photon Michelson Interferometer .....</b>	<b>118</b>
9.8	<b>Quantum Eraser .....</b>	<b>121</b>
<b>Chapter 10</b>	<b>Additional Experiments.....</b>	<b>124</b>
10.1	<b>Coherence Length .....</b>	<b>124</b>
10.2	<b>Single Photon Double Slit Experiment .....</b>	<b>126</b>
10.2.1	Overview .....	126
10.2.2	Theory .....	127
10.2.3	Setup .....	129
10.2.4	Measurement.....	134
10.3	<b>The Three-Polarizer-Paradox.....</b>	<b>136</b>
10.4	<b>Imaging the SPDC Cone with a Camera.....</b>	<b>137</b>
10.5	<b>Spatial Correlation of the Photon Pairs .....</b>	<b>137</b>
10.6	<b>Experiments with Different Crystal Thicknesses .....</b>	<b>138</b>
10.7	<b>Bomb Tester - Interaction Free Measurement .....</b>	<b>139</b>
10.8	<b>Quantum Computing .....</b>	<b>139</b>
10.8.1	Qubits and Gates.....	139
10.8.2	Deutsch-Jozsa Algorithm .....	141
10.8.3	Optical Implementation .....	142
10.8.4	Experimental Realization.....	143
10.8.5	Sample Measurements .....	147
10.8.6	Discussion of Error Sources .....	148
10.8.7	Further Algorithm Ideas .....	149
10.9	<b>Direct Event Pulse Observation.....</b>	<b>149</b>

---

<b>Chapter 11 Software</b>	152
<b>11.1 Software Installation</b>	152
<b>11.2 General Remarks</b>	152
<b>11.3 Saving Results</b>	152
<b>11.4 Connection Window</b>	153
<b>11.5 Alignment Tab</b>	154
<b>11.6 Delay Adjust Tab</b>	155
<b>11.7 HBT and GRA Tabs</b>	156
<b>11.8 Malus' Law Tab</b>	157
<b>11.9 Michelson Interferometer Tab</b>	159
<b>11.10 Configuration Tab</b>	160
<b>11.11 KDC Stage Tab</b>	161
<b>11.12 Hidden Settings</b>	162
<b>11.13 Operating Labview Graphs</b>	162
<b>Chapter 12 Technical Notes</b>	165
<b>12.1 Matrix Notation of Quantum States and Operators</b>	165
<b>12.2 Different Detection Schemes</b>	167
12.2.1 Standard Triple Coincidences	167
12.2.2 Gated Detection Scheme	168
12.2.3 Changing the Detection Scheme in the Software	169
<b>12.3 Environmental Conditions</b>	170
<b>12.4 Avoiding Fluctuations in the Michelson Interferometer</b>	170
<b>12.5 Accidental Coincidences</b>	172
<b>12.6 Time-Dependent Second-Order Correlation Function</b>	174
<b>12.7 Maximizing the Count Rate</b>	175
<b>12.8 Choice of Polarizers</b>	175
<b>12.9 Polarizers vs. Quarter-Wave Plates</b>	175
<b>12.10 Aicon Design</b>	176
<b>12.11 Temperature Dependence of Pump Laser Wavelength</b>	177
<b>12.12 Adjustable Count Rate Ratio</b>	177
<b>12.13 Movable Michelson Interferometer</b>	177
<b>12.14 Polarization In the SPDC Process</b>	178
<b>12.15 Improving Laser Safety</b>	179
<b>Chapter 13 Troubleshooting</b>	181
<b>13.1 Pump Laser not Working</b>	181
<b>13.2 Collimation of Pump Laser not Working</b>	181
<b>13.3 Detectors not Working</b>	182

---

<b>13.4 Low Count Rates with Filter .....</b>	182
<b>13.5 Low Count Rates with BBO crystal .....</b>	182
<b>13.6 Low Coincidence Count Rates .....</b>	183
<b>13.7 Malus' Law Measurement is Asymmetric.....</b>	183
<b>13.8 Michelson Interferometer Problems .....</b>	183
<b>13.9 Quantum Eraser Problems .....</b>	184
<b>13.10 Software not Working .....</b>	184
<b>Chapter 14    Laser Safety Calculation .....</b>	186
<b>14.1 Laser System .....</b>	186
<b>14.2 Laser Class Calculation.....</b>	186
<b>14.3 Laser Safety Glasses Calculation .....</b>	186
<b>Chapter 15    Acknowledgements.....</b>	188
<b>Chapter 16    Disposal, Warranty, and RMA Information.....</b>	189
<b>16.1 Return of Devices.....</b>	189
<b>Chapter 17    Thorlabs Worldwide Contacts .....</b>	190



Scan Here For  
More Information



## Chapter 1 Intended Use and Safety Warnings

### 1.1 Intended Use

This kit is intended to be used as teaching aid for the set of experiments outlined in Chapter 9 and similar concepts for physics and optics courses at high-school to university level.

### 1.2 Warning Symbol Definitions

Below is a list of warning symbols you may encounter in this manual or on your device



Warning: Laser Radiation



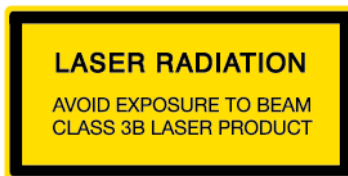
General Warning

### 1.3 Laser Radiation Warning



#### Warning

The class 3B laser diode used in this kit can emit more than 35 mW of optical power, which can cause damage to the eyes if viewed directly. The laser driver is equipped with a key switch and safety interlock, which should be used appropriately to avoid injury. Additionally, we recommend wearing appropriate laser safety glasses when using this kit.



### 1.4 Piezo Controller Warnings



#### General Warnings

If this equipment is used in a manner not specified by the manufacturer, the protection provided by the equipment may be impaired. In particular, excessive moisture may impair operation.

This product generates, uses, and outputs high voltages from the SMC connector (HV Output) that are hazardous and can cause serious injury. In any installation that uses the KPC101 piezo controller, it is the user's responsibility to ensure adequate insulation and precautions are taken to avoid shock risk. Cables for HV Out must be rated for 250 V RMS.

Spillage of fluid, such as sample solutions, should be avoided. If spillage does occur, clean up immediately using absorbent tissue. Do not allow spilled fluid to enter the internal mechanism.

## Chapter 2 Product Description

The field of quantum physics evolves quickly: quantum computers, quantum cryptography networks, and quantum-based sensing are all nearing introduction into real world applications. Highlighting this, the 2022 Nobel Prize in Physics was awarded to Alain Aspect, John F. Clauser, and Anton Zeilinger for their groundbreaking work in quantum optics. In turn, teaching quantum concepts is becoming ever more important. Our Quantum Optics Educational Kit allows students to investigate the quantum properties of light first-hand in an open and accessible environment.

One particularly important aspect of the kit is to educate people about what constitutes a non-classical light source, e.g., students can measure that an attenuated laser does not constitute a single photon source. The source that is set up and analyzed in this kit is called a photon pair source; pairs of 810 nm photons are generated inside a nonlinear, type-I BBO crystal from the output of a 405 nm pump laser. The photons in the pair are correlated in time and energy (though not polarization-entangled). Since the detection of one of the photons of the pair signals the presence of the other, on which single-photon experiments can be performed, this type of non-classical light source is also called a heralded single-photon source. The use of nonlinear crystals is widespread in the quantum optics community because of their ease of alignment and their high count rates.

A look at this educational system, as displayed in Figure 1, reveals the open design that allows students to investigate each component's properties and function. Moreover, we do not utilize optical fibers which are often used to guide light from the table to detectors housed somewhere else. Instead, we use free space optics and very small single photon detectors which allow us to place the detectors in the system and perform the measurement in that spot. This is even more important since the discussion of when and where a measurement occurs is fundamental in quantum mechanics. The open setup requires a darkened room; see Section 12.3 for more details.

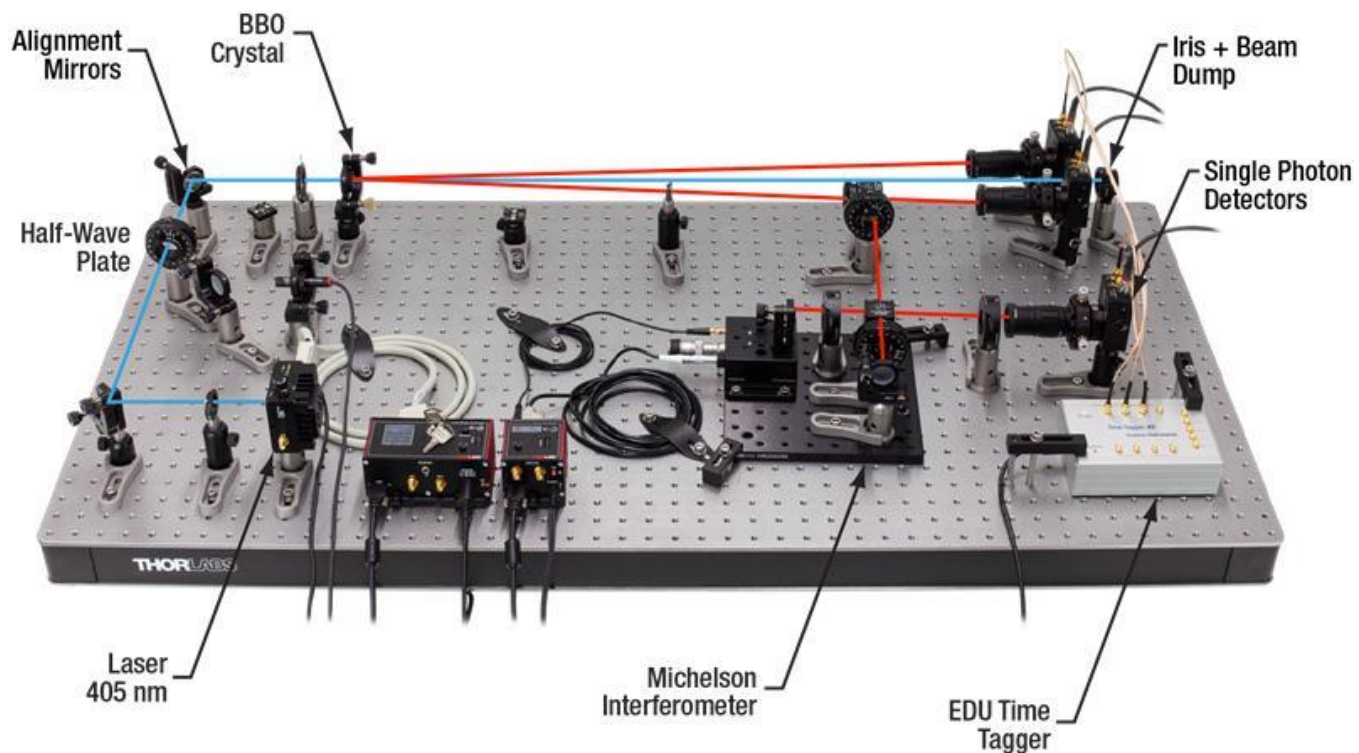


**Figure 1**      *Overview of the Quantum Optics Setup (Breadboard not included: We recommend the B2448FX (B60120AX) optical breadboard with the AV5(/M) damping feet.)*

To analyze and correlate the signals coming from the three single photon detectors, modern time-tagging electronics is employed. There are several experiments that students can set up and measure themselves:

- The pair source itself
- The experimental proof of a non-classical light source (Grangier-Roger-Aspect experiment)
- Experimental falsification of the misconception that attenuated lasers are single photon sources
- Behavior of single photons at a linear polarizer
- Single photon interference in a Michelson interferometer
- Quantum eraser experiment

All these experiments are described in detail in this manual and are made experimentally accessible by clear alignment procedures and experimental alignment tools that greatly help in reliably finding the signals of interest.

## Chapter 3 Principles of Quantum Optics

### 3.1 Classical Description of Light

In this section, a summary of the classical description of light is given, focused on the properties that play a role in the experiments in this kit. It is often useful to compare the quantum mechanical results derived in later sections to the classical results of this section.

Classically, light is described as an electromagnetic field governed by the Maxwell equations.

$$\nabla \cdot \vec{E} = \frac{\rho}{\epsilon_0} \quad (1)$$

$$\nabla \cdot \vec{B} = 0 \quad (2)$$

$$\nabla \times \vec{E} = -\frac{\partial \vec{B}}{\partial t} \quad (3)$$

$$\nabla \times \vec{B} = \mu_0 \left( \vec{J} + \epsilon_0 \frac{\partial \vec{E}}{\partial t} \right) \quad (4)$$

Here,  $\vec{E}$  and  $\vec{B}$  are the electric and magnetic fields,  $\rho$  is the charge density,  $\vec{J}$  is the electric current density,  $\epsilon_0$  is the vacuum permittivity constant, and  $\mu_0$  is the vacuum permeability constant.

By combining the Maxwell equations, the electromagnetic wave in vacuum can be described by a single equation:

$$\left( \nabla^2 - \frac{1}{c^2} \frac{\partial^2}{\partial t^2} \right) \vec{E}(\vec{r}, t) = 0 \quad (5)$$

One solution of this equation is a plane wave with:

$$\vec{E}(\vec{r}, t) = \vec{E}_0 \cdot e^{i(\vec{k}\vec{r} - \omega t)} \quad (6)$$

Here,  $\vec{k}$  is the wave vector and  $\omega$  is the angular frequency.

A Cartesian coordinate system can be chosen in such a way that the propagation of the wave is along the z-direction, i.e., the wave vector is  $\vec{k} = k \cdot \vec{u}_z$ , with  $\vec{u}_z$  being the unit vector in the z-direction. The following equation therefore applies:

$$k = \frac{2\pi}{\lambda} = \frac{2\pi f}{c} = \frac{\omega}{c} \quad (7)$$

Here,  $\lambda$  is the wavelength,  $f$  is the frequency, and  $c$  is the speed of light.

The electric field emitted by a collimated laser can be approximated as a plane wave and the intensity is the square of the electric field  $I = |\vec{E}_0|^2$ .

#### 3.1.1 Behavior at a Beamsplitter

If a plane wave with an amplitude  $\vec{E}_i$  is incident on the input port of a beamsplitter with a transmission coefficient  $t$  and a reflection coefficient  $r$ , the output fields are still plane waves with amplitudes of  $\vec{E}_t = t \cdot \vec{E}_i$  and  $\vec{E}_r = r \cdot \vec{E}_i$ , respectively. The output intensities are then:

$$I_t = t^2 \cdot |\vec{E}_i|^2 = t^2 \cdot I_i \quad (8)$$

$$I_r = r^2 \cdot |\vec{E}_i|^2 = r^2 \cdot I_i \quad (9)$$

Under the assumption of an ideal lossless beamsplitter, the squares of the coefficients add up to 1:

$$t^2 + r^2 = 1 \quad (10)$$

### 3.1.2 Interference

Consider the experimental setup<sup>1</sup> shown in Figure 2. An incoming light wave,  $\vec{E}_i$  (green arrow), is split at a beamsplitter. The light from each output port,  $\vec{E}_\alpha$  and  $\vec{E}_\beta$  (blue dashed arrows), then hits a mirror at normal incidence and is reflected backwards into the beamsplitter. The waves from the two arms recombine at the beamsplitter and leave in the direction of the detector,  $\vec{E}_d$  (such as a screen, camera, or eye) as well as back towards the light source,  $\vec{E}_s$  (red dashed arrows). At the beamsplitter, the phase of the light is shifted. The exact nature of this shift depends on the beamsplitter, with the following restriction: When combining two beams at a beamsplitter, energy conservation dictates that in one of the outgoing beams, the incoming beams are phase-shifted by an additional  $\pi$  to each other<sup>2</sup>. For the calculation here, we assume a beamsplitter as shown in Figure 2, with no phase shift occurring on all transmissions and on reflection on the lower left surface of the beamsplitter and a phase shift of  $180^\circ$  (or  $\pi$ ) upon reflection on the upper right surface.

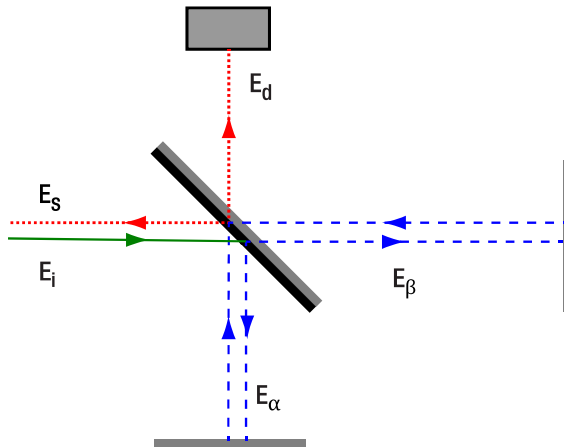


**Figure 2** Schematic of a Michelson interferometer. A phase shift of  $180^\circ$  occurs only upon reflection on one surface of the beamsplitter (marked grey).

If the input field has an amplitude  $E_i$  and the beamsplitter ratio is 50:50, then the amplitudes  $E_\alpha$  and  $E_\beta$  in the arms are:

$$E_\alpha = E_\beta = \frac{1}{\sqrt{2}} \cdot E_i \quad (11)$$

Due to the path length difference  $\Delta l$  of arms  $\alpha$  and  $\beta$ , the fields in the arms become out of phase with a phase difference  $\phi$ :

$$\phi = \frac{2\pi\Delta l}{\lambda} \quad (12)$$

Being aware of the additional  $180^\circ$  phase shift upon the reflection at the other side of the beamsplitter, the amplitude of the field  $E_d$  at the output port is then:

$$E_d = \frac{1}{\sqrt{2}}(E_\alpha + E_\beta \cdot e^{i(\phi+\pi)}) = \frac{1}{\sqrt{2}} \cdot \left( \frac{1}{\sqrt{2}} \cdot E_i + \frac{1}{\sqrt{2}} \cdot E_i \cdot e^{i(\phi+\pi)} \right) = \frac{1}{2} \cdot E_i \cdot (1 + e^{i(\phi+\pi)}) \quad (13)$$

The intensity  $I_d$  measured at the detector on the output path is then:

$$\begin{aligned} I_d &= |E_d|^2 = \frac{|E_i|^2}{4} \cdot (1 + e^{i(\phi+\pi)}) \cdot (1 + e^{-i(\phi+\pi)}) = \frac{I_i}{4} (2 + 2 \cos(\phi + \pi)) = \frac{I_i}{2} (1 + \cos(\phi + \pi)) \\ &= \frac{I_i}{2} (1 - \cos(\phi)) \end{aligned} \quad (14)$$

Where  $I_i$  is the intensity of the initial input. Hence, depending on the path length difference, the output intensity can reach from 0 (destructive interference) to  $I_i$  (constructive interference).

<sup>1</sup> Thorlabs offers the EDU-MINT2/(M) Educational Kit for Classical Interferometry. The manual is freely available on the product webpage and introduces the Michelson interferometer in more detail.

<sup>2</sup> M. Fox, Quantum Optics: An Introduction. (Oxford University Press, Oxford, 2006).

The field  $E_s$  and intensity  $I_s$  in this path can be calculated the same way (be aware that on this side of the beamsplitter no additional phase shift occurs between the two arms):

$$E_s = \frac{1}{\sqrt{2}}(E_\alpha + E_\beta \cdot e^{i\phi}) = \frac{1}{2} \cdot E_i \cdot (1 + e^{i\phi}) \quad (15)$$

$$I_s = |E_s|^2 = \frac{|E_i|^2}{4} \cdot (1 + e^{i\phi}) \cdot (1 + e^{-i\phi}) = \frac{I_i}{4} (2 + 2 \cos(\phi)) = \frac{I_i}{2} (1 + \cos \phi) \quad (16)$$

It is apparent that the sum of the intensities in the two output arms is always equal to the input intensity  $I_i$ , meaning that the energy is conserved.

### 3.1.3 Polarization

The Maxwell equations show that the electromagnetic field of a plane wave in a vacuum is a transverse field, i.e., the field vectors are perpendicular to the propagation direction<sup>2</sup>. Figure 3 shows an example of such a wave.

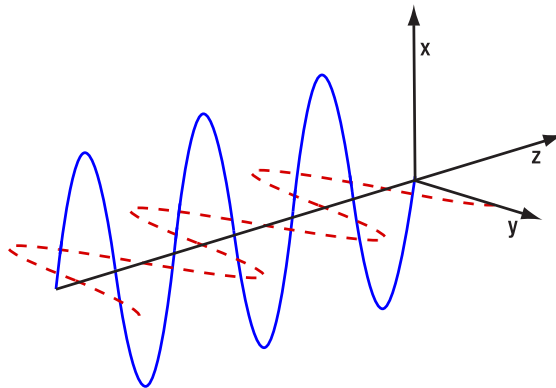


**Figure 3** An electromagnetic wave propagating along the z-direction. The electric field is marked as a solid blue line, and the magnetic field is marked as a red dashed line.

The polarization is defined by the direction of the electric field; hence the magnetic field is omitted in the following equations. For a plane wave propagating in the z-direction, the electric field vector is in the xy-plane and can be described as:

$$\vec{E} = E_x \cdot \vec{u}_x + E_y \cdot \vec{u}_y \quad (17)$$

For this plane wave, the following equations apply:

$$E_x = E_{0x} \cdot \cos(kz - \omega t) \quad (18)$$

$$E_y = E_{0y} \cdot \cos(kz - \omega t + \phi) \quad (19)$$

Here,  $E_{0x}$  and  $E_{0y}$  are the amplitudes of the fields in x- and y-direction, respectively, and  $\phi$  is the phase factor, describing the fact that the field can oscillate in separate phases in the x- and y-direction. The overall amplitude of the electric field  $E_0$  is then:

$$E_0 = \sqrt{E_{0x}^2 + E_{0y}^2} \quad (20)$$

The polarization vector  $\vec{\varepsilon}$  describes the direction of the electric field oscillation and is defined as:

$$\vec{\varepsilon} = \frac{E_{0x}}{E_0} \cdot \vec{u}_x + \frac{E_{0y}}{E_0} \cdot e^{i\phi} \cdot \vec{u}_y \quad (21)$$

and the electric field  $\vec{E}$  can be described in terms of the polarization vector (see the literature<sup>3</sup> for a more detailed derivation) as:

<sup>3</sup> M. Beck, *Quantum Mechanics, Theory and Experiment*. (Oxford University Press, Oxford, 2012).

$$\vec{E} = E_0 \cdot e^{i(kz - \omega t)} \cdot \vec{\varepsilon} \quad (22)$$

To understand the meaning of the polarization vector, it is helpful to investigate several special cases.

### Linear Polarization

If  $\phi = 0$ , i.e., the x- and y-components of the electric field are oscillating in phase, then  $\vec{\varepsilon}$  is a real vector, describing a line which is offset by an angle  $\theta$  from the x-axis:

$$\theta = \tan^{-1} \left( \frac{E_{0y}}{E_{0x}} \right) \quad (23)$$

The electric field oscillates along this line, and the light is called linearly polarized. Figure 4 displays an example of a linearly polarized electric field.

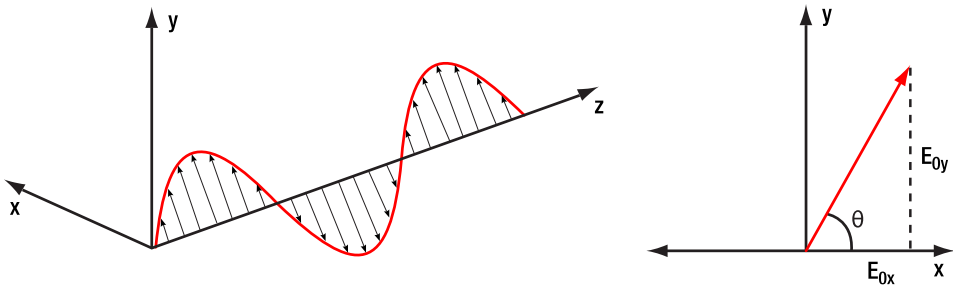


**Figure 4** Electric field of a linearly polarized wave. The perspective in the right graph is along the negative z-direction (towards the source).

### Circular Polarization

If  $\phi = \frac{\pi}{2}$  and  $E_{0x} = E_{0y}$ , the polarization vector becomes  $\vec{\varepsilon}_L = \frac{1}{\sqrt{2}} \cdot (\vec{u}_x + i\vec{u}_y)$ . The subscript L denotes left-circular polarization. Calculating the electric fields in this case and setting  $z = 0$  to only view the oscillation in time at a fixed point, one obtains:

$$E_x = \frac{E_0}{\sqrt{2}} \cdot \cos(\omega t) \quad (24)$$

$$E_y = \frac{E_0}{\sqrt{2}} \cdot \sin(\omega t) \quad (25)$$

This means that the direction of the electric field is constantly changing and tracing a circle in the x-y-plane, hence the name circular polarization. The rotation is counterclockwise (when looking towards the source) and called left-circularly polarized.

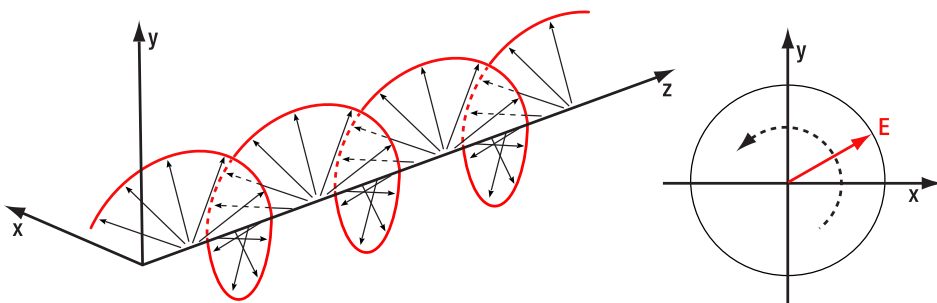


**Figure 5** Electric field of a left-circularly polarized wave. The perspective in the right graph is along the negative z-direction (towards the source).

A phase difference of  $\phi = -\frac{\pi}{2}$  results in clockwise rotation (again, when looking towards the source) and the light is then called right-circularly polarized. In this case, the polarization vector becomes:

$$\vec{\varepsilon}_R = \frac{1}{\sqrt{2}} \cdot (\vec{u}_x - i\vec{u}_y) \quad (26)$$

## Elliptical Polarization

Elliptical polarization is the general case when none of the special cases above apply. The phase shift and the ratio of the amplitudes in the x- and y-directions determine the orientation and eccentricity of the ellipse.

## Linear Polarizers

Linear polarizers are optical elements that only transmit the component of incoming light that is linearly polarized along the polarizer axis. The light after the polarizer is then linearly polarized along this axis.

The polarization of linearly polarized light passing a linear polarizer will be projected onto the polarizer axis, and the intensity will be attenuated according to Malus' Law:

$$I_{out} = I_{in} \cdot \cos^2(\theta_{in} - \theta_{pol}) \quad (27)$$

Here,  $I_{in}$  and  $I_{out}$  are the intensities before and after the polarizer, respectively.  $\theta_{in}$  is the angle between the polarization of the incoming light and the x-axis, while  $\theta_{pol}$  is the angle between the polarizer axis and the x-axis.

The intensity of circularly polarized light will always be attenuated by a factor of  $\frac{1}{2}$  when passing through a linear polarizer, irrespective of the polarizer axis.

## 3.2 Mathematical Formalism of Quantum Mechanics

Before the quantum mechanical treatment of the electromagnetic field is introduced in the next section, a very brief introduction to quantum mechanics is given in this section, only as far as will be required for the calculations in the remainder of the chapter. A more comprehensive introduction can be found in the literature<sup>4,5</sup>.

### 3.2.1 Dirac Notation

In this chapter, the Bra-Ket notation introduced by Dirac will be used. In the following subsection, a brief overview of the components and their mathematical and physical meanings are given.

### 3.2.2 General Case

A ket is written in the form  $|w\rangle$ . Mathematically it is a vector in a vector space  $V$ .

A bra is written in the form  $\langle f|$ . Mathematically it is a linear form  $f: V \rightarrow \mathbb{C}$ , mapping a vector into the plane of complex numbers.

Letting the linear form  $\langle f|$  act on a ket  $|w\rangle$  is denoted as  $\langle f|w\rangle$ . The result of this operation is a complex number.

### 3.2.3 Application in Quantum Mechanics and Quantum Optics

In quantum physics, quantum states can be represented by vectors in a complex Hilbert space (the exact nature of that space depends on the problem at hand), which facilitates calculation in most cases. These vectors are denoted by kets. The symbol(s) inside the ket are a label denoting the state, they are not a mathematical entity on which operations can be performed. For example, in general  $|1\rangle + |2\rangle \neq |3\rangle$  and  $\frac{1}{2}|2\rangle \neq |1\rangle$ .

As an inner product  $(\cdot, \cdot)$  is defined in every Hilbert space (the " $\cdot$ " being a placeholder for any possible element of the Hilbert space), the bra  $\langle v|$  can be understood as positioning the vector  $v \equiv |v\rangle$  in the first position of this inner product  $(v, \cdot) \equiv \langle v|$ . A bra  $\langle v|$  acting on a ket  $|w\rangle$  is then understood as the inner product  $(v, w) \equiv \langle v|w\rangle$ . This is typically interpreted as a projection of state  $|w\rangle$  onto the state  $|v\rangle$ , i.e., the probability amplitude for the state  $|w\rangle$  to collapse into the state  $|v\rangle$ . The inner product is antilinear, i.e., exchanging the components gives the complex conjugate:

$$\langle v|w\rangle = \langle w|v\rangle^* \quad (28)$$

<sup>4</sup> M. Beck, *Quantum Mechanics, Theory and Experiment*. (Oxford University Press, Oxford, 2012).

<sup>5</sup> R. Loudon, *The Quantum Theory of Light*. (Oxford University Press, Oxford, 1965).

### 3.2.4 Linear Operators

Linear operators are denoted  $\hat{A}$  and when acting on a ket, output a ket, e.g.,  $\hat{A}|w\rangle = |x\rangle$ . A typical way to construct linear operators is the outer product. If  $|w\rangle$  is a ket and  $\langle v|$  is a bra, then the outer product is defined as  $|w\rangle\langle v|$  and acts on a ket  $|x\rangle$  in the following way:

$$|w\rangle\langle v|(|x\rangle) \equiv |w\rangle\langle v|x\rangle = \langle v|x\rangle \cdot |w\rangle \quad (29)$$

Linear operators are distributive, i.e.:

$$(\hat{A} + \hat{B})|w\rangle = \hat{A}|w\rangle + \hat{B}|w\rangle \quad (30)$$

$$\hat{A}(|w_1\rangle + |w_2\rangle) = \hat{A}|w_1\rangle + \hat{A}|w_2\rangle \quad (31)$$

In the following, we will list some special types of operators which are of importance later.

#### Adjoint Operator

For every linear operator  $\hat{A}$  there exists an operator  $\hat{A}^\dagger$ , for which the following holds true:

$$\text{If } \hat{A}|w\rangle = |x\rangle, \text{ then } \langle w|\hat{A}^\dagger = \langle x| \text{ for all } |w\rangle \text{ and } |x\rangle \quad (32)$$

The operator  $\hat{A}^\dagger$  (pronounced “A-dagger”) is called the adjoint operator to  $\hat{A}$ .

#### Identity Operator

The identity operator  $\hat{1}$  has no effect on any state, i.e.:

$$\hat{1}|w\rangle = |w\rangle \text{ for all } |w\rangle \quad (33)$$

#### Inverse Operator

The inverse operator to  $\hat{A}$  is denoted as  $\hat{A}^{-1}$  and defined as:

$$\hat{A}\hat{A}^{-1} = \hat{A}^{-1}\hat{A} = \hat{1} \quad (34)$$

#### Unitary Operators

A unitary operator is an operator for which the following equation holds true:

$$\hat{U}\hat{U}^\dagger = \hat{U}^\dagger\hat{U} = \hat{1} \quad (35)$$

#### Projection Operators

An operator of the form  $\hat{P}_w = |w\rangle\langle w|$  is called a projection operator because it projects any state in the Hilbert space onto the state  $|w\rangle$ . Projection operators are idempotent, i.e.:

$$\hat{P}_w^2 = \hat{P}_w \quad (36)$$

After projecting once onto the state  $|w\rangle$  any subsequent projection onto the same state does not change the result.

#### Hermitian Operators

An operator is called Hermitian or self-adjoint, if it is identical to its own adjoint operator, i.e.:

$$\hat{\theta} = \hat{\theta}^\dagger \quad (37)$$

Hermitian operators play a key role in quantum mechanics as they represent measurable physical quantities, such as energy or momentum.

### 3.2.5 Eigenstates and Eigenvalues

For a linear operator  $\hat{A}$ , if there exist one or more state vectors  $|A_i\rangle$  for which:

$$\hat{A}|A_i\rangle = A_i|A_i\rangle \quad (38)$$

then these vectors are called eigenstates of  $\hat{A}$  and the  $A_i$  (in general complex numbers) are called eigenvalues.

If  $|A_i\rangle$  is an eigenstate of  $\hat{A}$ , then the following relation applies to the corresponding bra vector  $\langle A_i|$  and the adjoint operator  $\hat{A}^\dagger$ :

$$\langle A_i| \hat{A}^\dagger = A_i^* \cdot \langle A_i| \quad (39)$$

Here,  $A_i^*$  is the complex conjugate value of  $A_i$ .

### 3.2.6 Commutator Relations

In general, operators are not commutative, i.e.:  $\hat{A}\hat{B} \neq \hat{B}\hat{A}$ . The commutator of two operators is defined as:

$$[\hat{A}, \hat{B}] \equiv \hat{A}\hat{B} - \hat{B}\hat{A} \quad (40)$$

If  $[\hat{A}, \hat{B}] = 0$ , the operators are said to be commuting.

### 3.2.7 Bases of the Hilbert Space

In any Hilbert space, there exists at least one orthonormal basis, i.e., a set of vectors  $|b_i\rangle$  for which the following relation holds:

$$\langle b_i | b_j \rangle = \delta_{ij} \quad (41)$$

With  $\delta_{ij}$  being the Kronecker delta function defined as:

$$\delta_{ij} = \begin{cases} 1 & \text{for } i = j \\ 0 & \text{for } i \neq j \end{cases} \quad (42)$$

An orthonormal basis contains exactly as many elements as the dimension of the Hilbert space and a linear combination of these basis vectors can be used to describe any vector in the Hilbert space. Let  $|b_i\rangle$  be the basis vectors in an N-dimensional Hilbert space, then any normalized vector  $|w\rangle$  (meaning  $|\langle w|w \rangle|^2 = 1$ ) can be expressed as:

$$|w\rangle = \sum_i c_i \cdot |b_i\rangle \quad i = 1, 2, \dots, N \quad (43)$$

Here, the  $c_i$  are complex coefficients for which the following holds:

$$\sum_i |c_i|^2 = 1 \quad i = 1, 2, \dots, N \quad (44)$$

If a ket  $|w\rangle$  is expressed via a basis of the Hilbert space, the corresponding bra is:

$$\langle w| = \sum_i c_i^* \cdot \langle b_i| \quad (45)$$

Here, the basis vectors are replaced by their corresponding bra and the coefficients are the complex conjugates of the ones used to express the ket.

Additionally, for an orthonormal basis, the following relation applies:

$$\hat{1} = \sum_i \hat{P}_{b_i} = \sum_i |b_i\rangle\langle b_i| \quad i = 1, 2, \dots, N \quad (46)$$

Here,  $\hat{P}_{b_i} = |b_i\rangle\langle b_i|$  is called a projection operator as explained in Section 3.2.4. The eigenstates of a Hermitian operator in a finite dimensional Hilbert space always form an orthonormal basis, and the eigenvalues are real numbers.

### 3.2.8 Observables

An observable is any physically measurable quantity, such as momentum, energy, polarization, and many more. Every observable corresponds to a Hermitian operator, and the possible results of a measurement of the observable are the eigenvalues of the corresponding operator.

For a system in any normalized state  $|\psi\rangle$ , the probability of measuring the value  $\lambda$  is:

$$P(\lambda \parallel \psi) = |\langle \lambda | \psi \rangle|^2 \quad (47)$$

Here,  $\lambda$  is the eigenvalue corresponding to the eigenstate  $|\lambda\rangle$ .

Using Equation (46) and the fact that the eigenvectors of a Hermitian operator form a basis of the Hilbert space, we can rewrite any Hermitian operator  $\hat{O}$  with the eigenvectors  $|\lambda_i\rangle$  as

$$\hat{O} = \hat{O}\hat{1} = \sum_i \hat{O}|\lambda_i\rangle\langle\lambda_i| = \sum_i \lambda_i \cdot |\lambda_i\rangle\langle\lambda_i| \quad (48)$$

### 3.2.9 Measurements and Superposition of Quantum States

Hidden in the prior subsection is an important property of quantum physics, the superposition of states. As stated previously, measuring an observable  $O$  of a particle in the state  $|\psi\rangle$  can in general result in any eigenvalue  $\lambda_i$  of the operator  $\hat{O}$ . This is because, prior to the measurement, the particle is in a superposition of all states  $|\lambda_i\rangle$ .

$$|\psi\rangle = \sum_i c_i \cdot |\lambda_i\rangle$$

The result of the measurement is not defined beforehand! The squared absolute value of the superposition coefficients  $c_i$  give the probabilities of different measurement results (and define the state  $|\psi\rangle$ ).

When considering multiple measurements, there are two cases to distinguish:

#### Multiple measurements on the same particle:

After a measurement that yielded  $\lambda_i$  as a result, the state is changed to  $|\lambda_i\rangle$ . This means that every consecutive measurement of the same observable will yield  $\lambda_i$  with 100% probability (unless the state was changed in the meantime, e.g., by measuring a different observable). This process of changing the state due to a measurement is often called a collapse of the state (superposition of states), as in: "The measurement resulted in  $\lambda_i$  so the state collapsed to  $|\lambda_i\rangle$ ."

#### Multiple measurements on identical particles:

Here, a critical difference between classical and quantum physics becomes visible: in classical physics, a quantity like momentum is always well defined (even if unknown). When performing measurements of this quantity on an ensemble of identical particles in the same state, one will always get the same result. This is not the case in quantum physics: measurements on an ensemble of particles in the identical state can have different results. Before performing the measurement, the result is often not only unknown, but unknowable!

### 3.2.10 Expectation Values

If many measurements of an observable  $O$  are performed on a state  $|\psi\rangle$  (not on the same system, but on an ensemble of systems in the identical state), then the expected average of the measurement results is called the expectation value  $\langle \hat{O} \rangle$  of the measurement. It is calculated as follows:

$$\langle \hat{O} \rangle = \langle \psi | \hat{O} | \psi \rangle \quad (49)$$

The probability of measuring a specific eigenvalue  $\lambda$  of  $\hat{O}$  is:

$$P(\lambda \parallel \psi) = |\langle \lambda | \psi \rangle|^2 = \langle \lambda | \psi \rangle^* \cdot \langle \lambda | \psi \rangle = \langle \psi | \lambda \rangle \cdot \langle \lambda | \psi \rangle = \langle \psi | \hat{P}_\lambda | \psi \rangle = \langle \hat{P}_\lambda \rangle \quad (50)$$

For the third equality we used the antilinear property of the inner product; see Equation (28). We can see that the probability of measuring an eigenvalue is the expectation value of the projection operator  $\hat{P}_\lambda$  onto the corresponding eigenstate  $|\lambda\rangle$ .

The variance of the measurement is:

$$\Delta O^2 = \langle \hat{O}^2 \rangle - \langle \hat{O} \rangle^2 \quad (51)$$

### 3.2.11 Mixed States

States that can be expressed by a single ket vector are called pure states. However, there are states of the electromagnetic field that cannot be represented by a pure state. Instead, they are statistical mixtures of pure states, i.e., one can only give the probabilities for the system to behave as being in one of two or more pure states. These states are called mixed states<sup>6</sup> and are expressed by the so-called density operator:

$$\hat{\rho} = \sum_{n=1}^N P_n |n\rangle\langle n| \quad \text{with} \quad 0 < P_n \leq 1 \quad \text{and} \quad \sum_{n=1}^N P_n = 1 \quad (52)$$

The  $P_n$  are the weights for the pure state and can be interpreted as the probabilities of the mixed state to behave as if being in the corresponding pure state when an observable is being measured. Note that they are not the probability of the mixed state being the pure state. The number N here can be any number.

### 3.2.12 Combination of Quantum Systems

Assume you have two quantum systems (such as particles), called A and B. Each system has a corresponding Hilbert space,  $H_A$  and  $H_B$ , and a set of orthonormal basis vectors  $|A_i\rangle$  and  $|B_j\rangle$ . If the two quantum systems interact, then the state of the combined system is an element of the enlarged Hilbert space  $H_{AB} = H_A \otimes H_B$ . The symbol  $\otimes$  denotes the tensor product. The dimension of  $H_{AB}$  is the product of the dimensions of  $H_A$  and  $H_B$  and  $|A_i\rangle \otimes |B_j\rangle$  is an orthonormal basis of  $H_{AB}$ .

Let  $|\psi_A\rangle_A$  be a normalized vector in  $H_A$  and  $|\psi_B\rangle_B$  be a normalized vector in  $H_B$ . Then  $|\psi_A\rangle_A \otimes |\psi_B\rangle_B$  is also normalized and an element of  $H_{AB}$ . To simplify the notation, we define:

$$|\psi_A\rangle_A \otimes |\psi_B\rangle_B \equiv |\psi_A, \psi_B\rangle \equiv |\psi_A\rangle_A |\psi_B\rangle_B \quad (53)$$

Expressed in the orthonormal basis  $|A_i\rangle \otimes |B_j\rangle$ , the state is:

$$|\psi_A, \psi_B\rangle = \sum_{i,j} c_{ij} |A_i\rangle |B_j\rangle \quad \text{with} \quad \sum_{i,j} |c_{ij}|^2 = 1 \quad (54)$$

The inner product between two vectors  $|\psi_A, \psi_B\rangle$  and  $|\phi_A, \phi_B\rangle$  in  $H_{AB}$  is defined as:

$$\langle \psi_A, \psi_B | \phi_A, \phi_B \rangle \equiv \langle \psi_A | \phi_A \rangle \cdot \langle \psi_B | \phi_B \rangle \quad (55)$$

An observable of a subsystem is still represented by an operator. Let  $O_A$  be an observable in subsystem A. Then the operator is  $\hat{O}_A \hat{1}_B$ , acting only on the part of the combined state that describes subsystem A and leaving subsystem B unchanged. Often, this is only written as  $\hat{O}_A$ .

The expectation value of  $O_A$  for a combined state  $|\psi_A, \psi_B\rangle$  is:

$$\langle \hat{O}_A \rangle = \langle \psi_A, \psi_B | \hat{O}_A | \psi_A, \psi_B \rangle \quad (56)$$

## 3.3 Quantum Description of Light

In this section, we will give a brief overview of the quantum description of light, focusing on the light states that are most important for the experiments in this kit. A more comprehensive introduction can be found in the literature<sup>7</sup>.

To treat the electromagnetic field quantum mechanically, it is assumed that every mode of the field corresponds to a harmonic oscillator<sup>8</sup>. The Hamiltonian of a mode of the electromagnetic field can then be written as:

$$\hat{H} = \hbar\omega \left( \hat{n} + \frac{1}{2} \right) \quad (57)$$

<sup>6</sup> R. Loudon, *The Quantum Theory of Light*. (Oxford University Press, Oxford, 1965).

<sup>7</sup> R. Loudon, *The Quantum Theory of Light*. (Oxford University Press, Oxford, 1965).

<sup>8</sup> M. Beck, *Quantum Mechanics, Theory and Experiment*. (Oxford University Press, Oxford, 2012).

Here,  $\hbar = \frac{h}{2\pi}$  with  $h$  being the Planck constant,  $\omega$  is the resonance angular frequency, and  $\hat{n}$  is the number operator. The number operator can be expressed in terms of the annihilation operator  $\hat{a}$  and the creation operator  $\hat{a}^\dagger$ :

$$\hat{n} = \hat{a}^\dagger \hat{a} \quad (58)$$

Quantum mechanics thus treats the electromagnetic field as a quantized excitation in energy packages of  $\hbar\omega$ , called photons. This means that for a known  $\omega$ , measuring energy and measuring the photon number is equivalent, as the two quantities are proportional. Therefore, when expectation values and variance of photon numbers are discussed in the following, this is equivalent to the expectation value and variance of an energy measurement.

### 3.3.1 Fock States

A single photon is the fundamental excitation quantum of the electromagnetic field, i.e., the smallest possible excitation of the field. It is described by the so-called Fock state  $|1\rangle$ . Fock states in general describe the fundamental excitations of the electromagnetic field. They are the eigenstates  $|n\rangle$  of the Hamiltonian and of the number operator:

$$\hat{n}|n\rangle = n|n\rangle \quad n = 0, 1, 2, \dots \quad (59)$$

The following equations hold for Fock states:

$$\hat{a}|n\rangle = \sqrt{n} \cdot |n-1\rangle \quad (60)$$

$$\hat{a}^\dagger|n\rangle = \sqrt{n+1} \cdot |n+1\rangle \quad (61)$$

Here, the names of the operators  $\hat{a}$  and  $\hat{a}^\dagger$  becomes clear. The annihilation operator acting on a Fock state results in a Fock state with one less photon, while the creation operator acting on a Fock state results in Fock state with one additional photon. The ground state of the electromagnetic field is  $|0\rangle$  and is called the vacuum state. It describes the complete absence of photons.

The operators  $\hat{a}$  and  $\hat{a}^\dagger$  do not commute. We can calculate the commutator by letting it act on a state  $|n\rangle$  and apply the definitions above:

$$\begin{aligned} [\hat{a}, \hat{a}^\dagger]|n\rangle &= \hat{a}\hat{a}^\dagger|n\rangle - \hat{a}^\dagger\hat{a}|n\rangle = \sqrt{n+1} \cdot \hat{a}|n+1\rangle - \sqrt{n} \cdot \hat{a}^\dagger|n-1\rangle \\ &= \sqrt{n+1}\sqrt{n+1} \cdot |n\rangle - \sqrt{n}\sqrt{n} \cdot |n\rangle = (n+1-n)|n\rangle = 1 \cdot |n\rangle \end{aligned} \quad (62)$$

As this holds for any state  $|n\rangle$ , we obtained:

$$[\hat{a}, \hat{a}^\dagger] = 1 \quad (63)$$

The expectation value and the variance of the photon number in a Fock state are:

$$\langle n|\hat{n}|n\rangle = n \cdot \langle n|n\rangle = n \quad (64)$$

$$\Delta n^2 = \langle n|\hat{n}^2|n\rangle - \langle n|\hat{n}|n\rangle^2 = n^2 - n^2 = 0 \quad (65)$$

This means that a field mode in a Fock state contains exactly  $n$  photons; see the left graph in Figure 6. An energy measurement of light in a Fock state would yield  $n\hbar\omega$  with unity probability. Generating Fock states experimentally has long been a challenge. Nowadays, reliable methods exist to prepare light in the state  $n = 1$ , but Fock states with higher numbers require increasingly complex techniques. Fock states are not the only possible states of the light field. As they form an orthonormal basis of the Hilbert space, a general state  $|\phi\rangle$  can be expressed as a linear combination of Fock states, i.e.:

$$|\phi\rangle = \sum_{n=0}^{\infty} c_n \cdot |n\rangle$$

Here, the  $c_n$  are complex numbers with  $\sum_{n=0}^{\infty} |c_n|^2 = 1$ . When an energy measurement is performed on a field in this state, the result will be  $n\hbar\omega$  with a probability of the corresponding  $|c_n|^2$ . This does not mean that the state **is** in the state  $|n\rangle$  with that probability but that it is **measured as if it had been** in that state. Without a measurement, it is in a superposition of all states  $|n\rangle$  for which  $c_n \neq 0$ .

This also means that in general, it is misleading to describe light in a purely particle-based picture. In this picture, photons always have a defined position in space and time, which is misleading because there is no defined number of photons at any given point and time, only a probability distribution of possible results of an energy measurement.

### 3.3.2 Coherent States

One might think that a plane electromagnetic wave with constant amplitude, such as one emitted by a (strongly attenuated) laser, is described by a Fock state with a number of photons that matches the energy contained in the wave. This is **not** the case. Instead, such a plane wave is described by a coherent state.

A coherent state can be expressed as a linear combination of Fock states as described above. The coherent state  $|\alpha\rangle$  is:

$$|\alpha\rangle = e^{-\frac{|\alpha|^2}{2}} \cdot \sum_{n=0}^{\infty} \left( \frac{\alpha^n}{\sqrt{n!}} \cdot |n\rangle \right) \quad (66)$$

Coherent states are the eigenstates of the annihilation operator  $\hat{a}$ , i.e.,  $\hat{a}|\alpha\rangle = \alpha \cdot |\alpha\rangle$ . The annihilation operator is not Hermitian, so in general, the eigenvalues  $\alpha$  are complex numbers. Coherent states are the closest quantum mechanical analog to classical oscillators.

The mean photon number (expectation value of the number operator) of a coherent state is:

$$\langle n \rangle = \langle \alpha | \hat{n} | \alpha \rangle = \langle \alpha | \hat{a}^\dagger \hat{a} | \alpha \rangle = \alpha^* \cdot \alpha \cdot \langle \alpha | \alpha \rangle = |\alpha|^2 \quad (67)$$

The variance of such a state is:

$$\begin{aligned} \Delta n^2 &= \langle \alpha | \hat{n}^2 | \alpha \rangle - \langle \alpha | \hat{n} | \alpha \rangle^2 = \langle \alpha | \hat{a}^\dagger \hat{a} \hat{a}^\dagger \hat{a} | \alpha \rangle - |\alpha|^4 = \alpha^* \cdot \alpha \cdot \langle \alpha | \hat{a} \hat{a}^\dagger | \alpha \rangle - |\alpha|^4 \\ &= |\alpha|^2 \cdot \langle \alpha | 1 + \hat{a}^\dagger \hat{a} | \alpha \rangle - |\alpha|^4 = |\alpha|^2 \cdot (1 + |\alpha|^2) - |\alpha|^4 = |\alpha|^2 \end{aligned} \quad (68)$$

Here, we used the commutator relation of the annihilation and creation operators:  $\hat{a}\hat{a}^\dagger = 1 + \hat{a}^\dagger \hat{a}$  (see Section 3.3.1). The variance is equal to the expectation value, which hints at a Poisson distribution of the photon numbers. Indeed, it can be proven that the probabilities of a coherent state measured to be in different Fock states is Poissonian<sup>9</sup>, as depicted in the center graph of Figure 6.

### 3.3.3 Thermal States

Besides Fock states and coherent states, there are other, more chaotic states of light such as thermal radiation emitted by a black body, fluorescent light sources, and LEDs. Chaotic light cannot be described by a pure quantum state. Instead, it is a statistical mixture of pure states; for more information, see Section 3.2.11.

All the chaotic light sources above share the same photon number distribution for a fixed mean photon number  $\langle n \rangle$ :

$$P(n) = \frac{\langle n \rangle^n}{(1 + \langle n \rangle)^{1+n}} \quad (69)$$

It can be shown that the variance for the probability distribution in Equation (69) is always:

$$\Delta n^2 = \langle n^2 \rangle - \langle n \rangle^2 = \langle n \rangle^2 + \langle n \rangle \quad (70)$$

As a black body is the most prominent example of this kind of light source, all states with this probability distribution are called thermal states in the following, even if the explicit density matrix depends on the exact type of the source. For example, the state of a black body with a temperature  $T$  can be expressed by the following density matrix<sup>10</sup>:

<sup>9</sup> M. Fox, *Quantum Optics: An Introduction*. (Oxford University Press, Oxford, 2006).

<sup>10</sup> R. Loudon, *The Quantum Theory of Light*. (Oxford University Press, Oxford, 1965).

$$\hat{\rho} = \left(1 - e^{\left(\frac{-\hbar\omega}{k_B T}\right)}\right) \cdot e^{\left(\frac{-\hbar\omega\hat{n}}{k_B T}\right)} \quad (71)$$

Here,  $\omega$  is the angular frequency,  $k_B$  is the Boltzmann constant, and the exponential of the number operator is defined by a power series expansion. One can see from Equation (70) that the photon number variance of thermal states is always larger than for a Poissonian statistic such as displayed by coherent states. Figure 6 shows a graph of the photon number probabilities for a Fock state, a coherent state, and a thermal state with the same mean photon number 5. For all three of these states the average of multiple energy measurements would be  $5\hbar\omega$ . However, for the Fock state, every single measurement would result in exactly that value, while the measurement results would stray for the coherent and thermal states according to the distributions below.

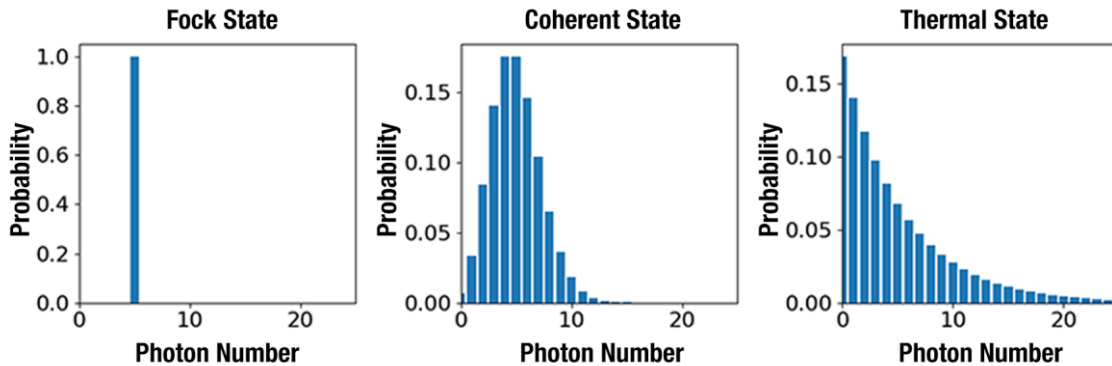


**Figure 6** Photon number probabilities for a Fock state (left), a coherent state (center), and a thermal state (right), all with the same mean photon number  $\langle n \rangle = 5$ . Be aware that the scaling for the first plot is different than for the second and third to provide better visibility.<sup>11</sup>

### 3.4 Proof of Quantized Light - Theory

In educational literature, the quantization of light is often motivated by the photoelectric effect<sup>12</sup>. However, this phenomenon can be completely described by semiclassical theories that do not require a quantization of the electromagnetic field. Only the energy levels of the atoms in the matter are quantized in these theories<sup>13</sup>, while the light field is still defined by the classical Maxwell's equations. Therefore, different experiments are required to test the quantum nature of light.

#### 3.4.1 Second-Order Correlation Function

A conceptually simple test is to send a light beam with extremely low intensity through a beamsplitter with two detectors at the two possible outputs of the splitter. If light is indeed quantized, then it should be impossible for the two detectors to detect light at the exact same time (in coincidence), because a single quantum of light can only be detected in one of the detectors. A sketch of such a setup, often called an intensity interferometer as introduced by Hanbury Brown and Twiss (HBT)<sup>14</sup>, is shown in Figure 7.

<sup>11</sup> The figure was composed with the Qutip Quantum Toolbox for Python.

<sup>12</sup> B. J. Pearson and D. P. Jackson, American Journal of Physics, **78**(5), 471 (2010).

<sup>13</sup> R. Loudon, *The Quantum Theory of Light*. (Oxford University Press, Oxford, 1965).

<sup>14</sup> R. H. Brown and R. Q. Twiss, Nature, **177**, 27 (1956).

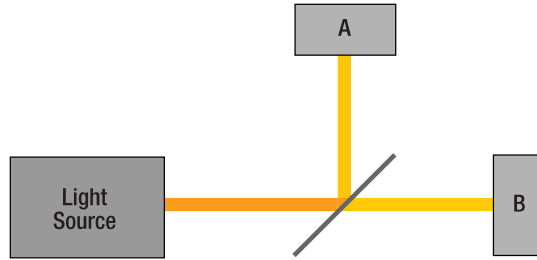


**Figure 7      Schematic of an Intensity Interferometer**

Here, we will focus on the definition of important quantities, while the experiment is described in Section 3.5.1. The measured quantity in this setup is the second-order correlation function. For the classical electromagnetic field and two detectors A and B, this function is defined as follows:

$$g_{AB}^{(2)}(\tau) = \frac{\langle I_A(t + \tau) \cdot I_B(t) \rangle}{\langle I_A(t + \tau) \rangle \cdot \langle I_B(t) \rangle} \quad (72)$$

Here,  $I_A(t + \tau)$  and  $I_B(t)$  are the intensities at detector A at the time  $t + \tau$  and at detector B at the time  $t$ , respectively. The angle brackets denote a time average. This function is called “second order” because it describes the correlation of intensities. A first-order correlation function indicates correlations between amplitudes.

Second-order correlations give insight into the nature of the light entering the setup. The most important aspect is the correlation of the detector signals at the same time, i.e., at  $\tau = 0$ .

$$g_{AB}^{(2)}(0) = \frac{\langle I_A \cdot I_B \rangle}{\langle I_A \rangle \cdot \langle I_B \rangle} \quad (73)$$

If  $g_{AB}^{(2)}(0)$  takes a value of 1, this means that the detector signals are completely uncorrelated. A value larger than 1 means correlation of the detector signals, i.e., if one detector measures a large (small) signal, the other detector is more likely to also measure a large (small) signal than expected for complete randomness.  $g_{AB}^{(2)}(0) < 1$ , on the other hand, indicates anti-correlation of the signals, i.e., a high (low) signal on one detector is more likely to coincide with a small (large) signal on the other one.

Using Equations (8) and (9) in Section 3.1.1, we can rewrite Equation (73) in terms of the input intensity  $I_i$  for the setup displayed in Figure 7 (irrespective of the transmission and reflection coefficients of the beamsplitter):

$$g_{HBT}^{(2)}(0) = \frac{\langle I_i^2 \rangle}{\langle I_i \rangle^2} \quad (74)$$

The subscript HBT indicates that the equation is valid for an intensity interferometer as introduced by HBT and shown in Figure 7. Using the Cauchy-Schwarz inequality, it can be proven that<sup>15</sup>:

$$g_{HBT}^{(2)}(0) = \frac{\langle I_i^2 \rangle}{\langle I_i \rangle^2} \geq 1 \quad (\text{classical fields}) \quad (75)$$

This means that for classical fields, the second-order correlation function is always larger than or equal to 1 and there can be no anti-correlation of the detector signals. This is intuitive, as the beamsplitter always splits the wave into two parts with a constant ratio. The signals at the detectors can then either be uncorrelated (amplitude constant in time) or correlated (amplitude varies in time, both detectors “see” the same increase and decrease of the signal) and there is no way that the signal on one detector increases while the signal on the other decreases. In the case of a constant amplitude and hence uncorrelated detector signals, we expect  $g_{HBT}^{(2)}(0) = 1$ .

This means that any experiment showing anti-correlation in an HBT setup violates the classical description of light.

<sup>15</sup> The validity of this equation can be motivated by noting that the variance of the intensity has to be a positive number and can be written as  $\Delta I^2 = \langle I_i^2 \rangle - \langle I_i \rangle^2$ , hence  $\langle I_i^2 \rangle \geq \langle I_i \rangle^2$ .

### 3.4.2 Quantum Mechanical Treatment of a Beamsplitter

To calculate the quantum mechanical expectation for the HBT experiment, it is important to understand how a beamsplitter is treated in quantum mechanics. Assume a lossless beamsplitter with the geometry shown in Figure 8, with  $\hat{a}_1$  and  $\hat{a}_2$  being the annihilation operators of the input ports and  $\hat{a}_3$  and  $\hat{a}_4$  being the annihilation operators of the output ports.

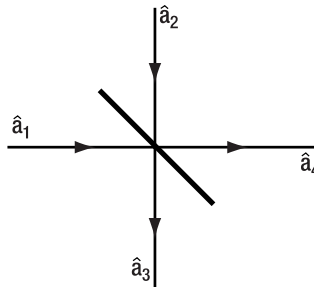


**Figure 8**      **Geometry of Beamsplitter**

With the transmission and reflection coefficients of the beamsplitter being  $t$  and  $r$ , it can be shown<sup>16</sup> that the following relations hold for the annihilation and creation operators of the ports:

$$\hat{a}_1 = r \cdot \hat{a}_3 + t \cdot \hat{a}_4 \quad (76)$$

$$\hat{a}_2 = t \cdot \hat{a}_3 - r \cdot \hat{a}_4 \quad (77)$$

$$\hat{a}_1^\dagger = r \cdot \hat{a}_3^\dagger + t \cdot \hat{a}_4^\dagger \quad (78)$$

$$\hat{a}_2^\dagger = t \cdot \hat{a}_3^\dagger - r \cdot \hat{a}_4^\dagger \quad (79)$$

These operator relations can then be used to transform the input states to the beamsplitter to the output states. As an important example, take the input mode  $|1\rangle_1|0\rangle_2$ , i.e., a Fock state with a photon number of 1 at input port 1 and the vacuum state at input port 2 (a single photon incident on the beamsplitter at port 1). This transforms to:

$$|1\rangle_1|0\rangle_2 = \hat{a}_1^\dagger|0\rangle = (r \cdot \hat{a}_3^\dagger + t \cdot \hat{a}_4^\dagger)|0\rangle = r \cdot |1\rangle_3|0\rangle_4 + t \cdot |0\rangle_3|1\rangle_4 \quad (80)$$

The single photon at input port 1 transforms to a superposition state of the photon being in the output ports 3 or 4. Calculating the expectation value of the photon number at output port 3 yields:

$$\begin{aligned} \langle n_3 \rangle &= (r \cdot \langle 1|_3\langle 0|_4 + t \cdot \langle 0|_3\langle 1|_4) \hat{n}_3 (r \cdot |1\rangle_3|0\rangle_4 + t \cdot |0\rangle_3|1\rangle_4) \\ &= (r \cdot \langle 1|_3\langle 0|_4 + t \cdot \langle 0|_3\langle 1|_4)(1 \cdot r \cdot |1\rangle_3|0\rangle_4 + 0 \cdot t \cdot |0\rangle_3|1\rangle_4) \\ &= (r \cdot \langle 1|_3\langle 0|_4 + t \cdot \langle 0|_3\langle 1|_4)(r \cdot |1\rangle_3|0\rangle_4) \\ &= r^2 \cdot 1 + r \cdot t \cdot 0 = r^2 \end{aligned} \quad (81)$$

As long as there is no measurement, the photon is in a superposition state of both outputs; see Section 3.2.9. The probability of the photon being measured at one of the outputs is distributed the same as the intensity in the classical description. Measuring a single photon is a statistical process: only the probabilities are known, and the result cannot be predicted with certainty. However, the distribution of the photons will approach the classical result for large numbers of photons.

### 3.4.3 Quantum Fields

Classically,  $g^{(2)}(0)$  in an intensity interferometer cannot be smaller than 1, as shown in Section 3.4.1. In this section, the limits and expected values of  $g^{(2)}(0)$  are derived depending on the characteristics of the incoming light.

The quantum mechanical second-order correlation function is defined as<sup>17</sup>:

<sup>16</sup> M. Beck, *Quantum Mechanics, Theory and Experiment*. (Oxford University Press, Oxford, 2012).

<sup>17</sup> J. J. Thorn et al., *American Journal of Physics*, **72**(9), 1210 (2004).

$$g^{(2)}(0) = \frac{\langle : \hat{I}_A \hat{I}_B : \rangle}{\langle \hat{I}_A \rangle \cdot \langle \hat{I}_B \rangle} \quad (82)$$

Here,  $\hat{I}_A$  and  $\hat{I}_B$  are the intensity operators at detector A and B and the colons denote normal ordering, meaning all creation operators appear to the left of all annihilation operators. This function has the same properties as its classical counterpart<sup>18</sup>.

The intensity operator is proportional to the photon number operator<sup>19</sup>, so that we can write:

$$g^{(2)}(0) = \frac{\langle : \hat{n}_A \hat{n}_B : \rangle}{\langle \hat{n}_A \rangle \cdot \langle \hat{n}_B \rangle} \quad (83)$$

Expressing the number operators via creation and annihilation operators and taking care of the normal ordering, this can be written as:

$$g^{(2)}(0) = \frac{\langle : \hat{a}_B^\dagger \hat{a}_A^\dagger \hat{a}_A \hat{a}_B : \rangle}{\langle \hat{a}_A^\dagger \hat{a}_A \rangle \cdot \langle \hat{a}_B^\dagger \hat{a}_B \rangle} = \frac{\langle \hat{a}_B^\dagger \hat{a}_A^\dagger \hat{a}_A \hat{a}_B \rangle}{\langle \hat{a}_A^\dagger \hat{a}_A \rangle \cdot \langle \hat{a}_B^\dagger \hat{a}_B \rangle} \quad (84)$$

Now assume an intensity interferometer as described in Section 3.4.1. The field at port 1 is in an arbitrary state  $|\psi\rangle$  and the field at port 2 is in the vacuum state  $|0\rangle$ . The annihilation and creation operators after the beamsplitter can then be expressed via the corresponding operators of the incoming field via Equations (76) - (79) (with  $\hat{a}_A = \hat{a}_3$  and  $\hat{a}_B = \hat{a}_4$ ) so that the numerator becomes:

$$\begin{aligned} \langle \hat{a}_B^\dagger \hat{a}_A^\dagger \hat{a}_A \hat{a}_B \rangle &= \langle (t\hat{a}_1^\dagger - r\hat{a}_2^\dagger)(r\hat{a}_1^\dagger + t\hat{a}_2^\dagger)(r\hat{a}_1 + t\hat{a}_2)(t\hat{a}_1 - r\hat{a}_2) \rangle \\ &= \langle \psi |_1 \langle 0 |_2 (t\hat{a}_1^\dagger - r\hat{a}_2^\dagger)(r\hat{a}_1^\dagger + t\hat{a}_2^\dagger)(r\hat{a}_1 + t\hat{a}_2)(t\hat{a}_1 - r\hat{a}_2) |\psi \rangle_1 |0 \rangle_2 \\ &= \langle \psi |_1 (t\hat{a}_1^\dagger)(r\hat{a}_1^\dagger)(r\hat{a}_1)(t\hat{a}_1) |\psi \rangle_1 = r^2 t^2 \cdot \langle \psi | \hat{a}_1^\dagger \hat{a}_1^\dagger \hat{a}_1 \hat{a}_1 |\psi \rangle_1 \end{aligned} \quad (85)$$

The expectation values in the denominator can be similarly written as:

$$\langle \hat{a}_A^\dagger \hat{a}_A \rangle = r^2 \cdot \langle \psi |_1 \hat{a}_1^\dagger \hat{a}_1 |\psi \rangle_1 \quad (86)$$

$$\langle \hat{a}_B^\dagger \hat{a}_B \rangle = t^2 \cdot \langle \psi |_1 \hat{a}_1^\dagger \hat{a}_1 |\psi \rangle_1 \quad (87)$$

Combining these results leads to the following expression of the second order correlation function of the intensity interferometer:

$$g_{HBT}^{(2)}(0) = \frac{\langle \hat{a}_B^\dagger \hat{a}_A^\dagger \hat{a}_A \hat{a}_B \rangle}{\langle \hat{a}_A^\dagger \hat{a}_A \rangle \cdot \langle \hat{a}_B^\dagger \hat{a}_B \rangle} = \frac{\langle \hat{a}_1^\dagger \hat{a}_1^\dagger \hat{a}_1 \hat{a}_1 \rangle}{\langle \hat{a}_1^\dagger \hat{a}_1 \rangle^2} \quad (88)$$

With the help of this equation, the expected values of  $g_{HBT}^{(2)}(0)$  can be determined for different states of the incoming light.

### Single Photons

The first example is  $|1\rangle$ , the Fock state with the photon number 1, called a single photon.

$$g_{HBT}^{(2)}(0) = \frac{\langle 1 | \hat{a}_1^\dagger \hat{a}_1^\dagger \hat{a}_1 \hat{a}_1 | 1 \rangle}{\langle 1 | \hat{a}_1^\dagger \hat{a}_1 | 1 \rangle^2} = \langle 1 | \hat{a}_1^\dagger \hat{a}_1^\dagger \hat{a}_1 \hat{a}_1 | 1 \rangle = \langle 1 | \hat{a}_1^\dagger \hat{a}_1^\dagger \hat{a}_1 \hat{a}_1 | 0 \rangle = 0 \quad (89)$$

The expected value for the second order correlation function with a single photon incident on the beamsplitter is zero. This describes complete anti-correlation, i.e., if the photon is detected at one output of the beamsplitter it can never be detected at the other output. This agrees with intuition: as the photon is the smallest possible excitation of the electromagnetic field, it cannot be split further. This can be experimentally confirmed in this kit; see Section 9.4.

### Laser Light

<sup>18</sup> R. Loudon, *The Quantum Theory of Light*. (Oxford University Press, Oxford, 1965).

<sup>19</sup> M. Beck, *Quantum Mechanics, Theory and Experiment*. (Oxford University Press, Oxford, 2012).

What about a strongly attenuated laser? This would be represented quantum-mechanically by a coherent state  $|\alpha\rangle$ , as seen in Section 3.3.2.

$$g_{HBT}^{(2)}(0) = \frac{\langle\alpha|\hat{a}_1^\dagger\hat{a}_1^\dagger\hat{a}_1\hat{a}_1|\alpha\rangle}{\langle\alpha|\hat{a}_1^\dagger\hat{a}_1|\alpha\rangle^2} = \frac{|\alpha|^4}{(|\alpha|^2)^2} = 1 \quad (90)$$

The second order correlation function for coherent states is 1 irrespective of the mean photon number  $\langle n \rangle = |\alpha|^2$  of the state, i.e., the detector signal in the intensity interferometer will be completely uncorrelated. This means that even a very strongly attenuated laser is not a suitable source to perform quantum optics experiments. The experimental confirmation of this is part of this kit, as seen in Section 9.1.

### Thermal Light

To obtain the expected value for the second order correlation of thermal light, it helps to express  $g_{AB}^{(2)}(0)$  in terms of the expectation value and the variance of the photon number:

$$\begin{aligned} g_{HBT}^{(2)}(0) &= \frac{\langle\hat{a}_1^\dagger\hat{a}_1^\dagger\hat{a}_1\hat{a}_1\rangle}{\langle\hat{a}_1^\dagger\hat{a}_1\rangle^2} = \frac{\langle\hat{a}_1^\dagger(\hat{a}_1\hat{a}_1^\dagger - 1)\hat{a}_1\rangle}{\langle\hat{a}_1^\dagger\hat{a}_1\rangle^2} = \frac{\langle\hat{a}_1^\dagger\hat{a}_1\hat{a}_1^\dagger\hat{a}_1 - \hat{a}_1^\dagger\hat{a}_1\rangle}{\langle\hat{a}_1^\dagger\hat{a}_1\rangle^2} = \frac{\langle\hat{n}^2 - \hat{n}\rangle}{\langle\hat{n}\rangle^2} = \frac{\langle\hat{n}^2\rangle - \langle\hat{n}\rangle}{\langle\hat{n}\rangle^2} \\ &= \frac{(\Delta n)^2 + \langle\hat{n}\rangle^2 - \langle\hat{n}\rangle}{\langle\hat{n}\rangle^2} = \frac{\langle\hat{n}\rangle^2 + \langle\hat{n}\rangle + \langle\hat{n}\rangle^2 - \langle\hat{n}\rangle}{\langle\hat{n}\rangle^2} = 2 \end{aligned} \quad (91)$$

For the first equality, the commutator relation between  $\hat{a}_1^\dagger$  and  $\hat{a}_1$  is used. For the penultimate equality we used a variance  $(\Delta n)^2 = \langle\hat{n}\rangle^2 + \langle\hat{n}\rangle$ , as derived in Section 3.3.3.

As a result, the second order correlation for thermal light is 2, i.e., the detector signals in the intensity interferometer are correlated. Descriptively formulated, the source emits no photons most of the time, but when it does, it tends to emit multiple at the same time, which are split evenly at the beamsplitter. The correlated/dense bursts of photons increase  $g_{HBT}^{(2)}(0)$  above 1.

## 3.5 Proof of Quantized Light - Experiment

### 3.5.1 Hanbury-Brown-Twiss Experiment

The concept of the intensity interferometer (see Section 3.4.1) was first introduced by Hanbury Brown and Twiss (HBT) in 1956<sup>20</sup> when they were looking for a method to measure the angular size of stars. This was a purely classical experiment.

However, when simulating their experiment in the laboratory and using a strongly attenuated spectral line from a mercury vapor lamp as the light source, they found that the signals at the two detectors were positively correlated, i.e.,  $g_{HBT}^{(2)}(0) > 1$ .

Following the publication of these results, there was a dispute about the interpretation, which was resolved by Hanbury Brown and Twiss showing that the result  $g_{HBT}^{(2)}(0) > 1$  is consistent with semi-classical theories, as seen in Section 3.4.1. The reason that no anti-correlation is detected, even though the light consists of photons, lies in the state of the incoming light. The mercury vapor lamp is a thermal source, so the light will be in a thermal mixture of states, as defined in Section 3.3.3. The second order correlation function for this case is calculated in Equation (91):

$$g_{HBT}^{(2)}(0) = 2 \quad (\text{Thermal Light}) \quad (92)$$

Please note that this value can only be measured in the limit of idealized detectors with perfect time resolution. The time resolution of real detectors will reduce the measured value of  $g_{HBT}^{(2)}(0)$  towards the limit of 1, as seen in Section 3.5.2.

<sup>20</sup> R. H. Brown and R. Q. Twiss, *Nature*, **177**, 27 (1956).

### 3.5.2 Correlation Function for Single Photon Detectors

To detect the extremely low intensities that are common in quantum optics, single photon detectors are used. These detectors do not output a continuous signal, but single output pulses (called counts or clicks). It is important to be clear that the clicks of such a detector do not in themselves prove the quantization of the light field. In semi-classical theories, only the quantization of the energy levels in the detector is required to explain the detector behavior. The pulse generation is a random process, and the pulse rate is proportional to the intensity of the light hitting the detector<sup>21</sup>.

$$P_i = \eta_i \cdot \langle I_i(t) \rangle \cdot \Delta t \quad (93)$$

Here,  $P_i$  is the probability of a detection event at detector  $i$  in the short time window  $\Delta t$ ,  $\eta_i$  is the detection efficiency of detector  $i$ , and  $I_i(t)$  is the intensity of the light hitting detector  $i$ .

To calculate the correlation function for single photon detectors, Equation (72) can be modified to incorporate count rates instead of intensities.

The probability of a detection event at detector  $i$  in a short time window  $\Delta t$  followed by a detection event at detector  $j$  (also in a short time window  $\Delta t$ ) after a time  $\tau$  is:

$$P_{ij}(\tau) = \eta_i \cdot \eta_j \cdot \langle I_i(t + \tau) \cdot I_j(t) \rangle \cdot \Delta t^2 \quad (94)$$

Substituting Equations (93) and (94) (for  $i = A$  and  $j = B$ ) into Equation (72) yields:

$$g^{(2)}(\tau) = \frac{P_{AB}(\tau)}{P_A \cdot P_B} \quad (95)$$

The probabilities are just the average count rates  $R_A$  and  $R_B$  of the detectors A and B, respectively, and the average count rate of coincidences  $R_{AB}$  multiplied by the time window  $\Delta t$ .

$$P_A = R_A \cdot \Delta t \quad P_B = R_B \cdot \Delta t \quad P_{AB}(\tau) = R_{AB}(\tau) \cdot \Delta t \quad (96)$$

Substituting this in Equation (95) yields:

$$g^{(2)}(\tau) = \frac{R_{AB}(\tau)}{R_A \cdot R_B \cdot \Delta t} \quad (97)$$

For  $\tau = 0$ , this is written as:

$$g^{(2)}(0) = \frac{R_{AB}(0)}{R_A \cdot R_B \cdot \Delta t} = \frac{R_{AB}}{R_A \cdot R_B \cdot \Delta t} \quad (98)$$

This two-detector correlation function is used in two distinct ways in this kit:

- 1.) As a characterization of the photon pair source: Here, the photon pairs generated in a BBO crystal (see Section 3.9) are directly sent to the two detectors. In this case, one measures significantly more coincidences than expected for uncorrelated light, thus  $g_{PS}^{(2)}(0) \gg 1$ . The subscript PS stands for “Pair Source.” The quantity  $g_{PS}^{(2)}(0)$  is used as an indicator for the quality of the pair source (the larger, the better) and is measured at about 100 in the setup in this kit.
- 2.) As a measurement for the correlation of light in an HBT experiment: This is the quantity  $g_{HBT}^{(2)}(0)$  as described in Section 3.5.1. Here, a value lower than 1 would indicate non-classical light.

Strictly speaking, what is called  $g_{HBT}^{(2)}(0)$  here is not the value at the point  $\tau = 0$  anymore<sup>22</sup>, but an integration of  $g_{HBT}^{(2)}(\tau)$  over the time window  $\Delta t$  centered at  $\tau = 0$ . As long as  $g_{HBT}^{(2)}(\tau)$  is not rapidly changing over  $\Delta t$ , there is no difference between the two. Most importantly, the inequalities that include the  $g_{HBT}^{(2)}(0)$  term always remain valid.

<sup>21</sup> M. Beck, *Quantum Mechanics, Theory and Experiment*. (Oxford University Press, Oxford, 2012).

<sup>22</sup> R. W. Boyd, S. G. Lukishova, and V. N. Zadkov, *Quantum Photonics: Pioneering Advances and Emerging Applications*. (Springer, New York City, 2019), p. 3.

For thermal sources (see Section 3.3.3), the time-dependent correlation function drops from 2 at  $\tau = 0$  to 1 for  $\tau \gg \tau_c$ , with  $\tau_c$  being the coherence time of the light<sup>23</sup>, as seen in Figure 9. The coherence time of a light source is a measure of the duration over which the phase of the light emitted by the source remains stable.

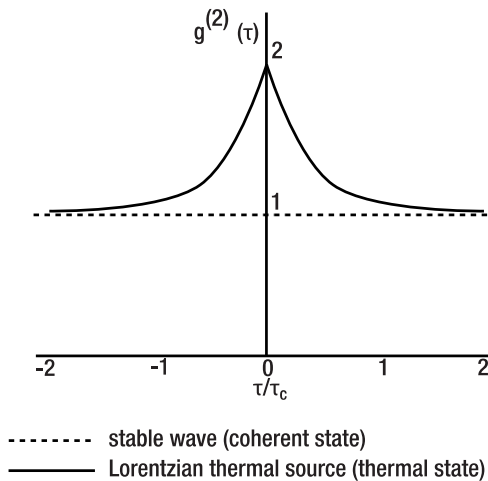


**Figure 9      Time Dependent Second-Order Correlation Function**

Even for spectrally filtered thermal sources,  $\tau_c$  is on the order of femtoseconds<sup>24</sup>, while typical values of  $\Delta t$  are in the order of 1 ns. Thus,  $g_{HBT}^{(2)}(\tau)$  is 1 for the vast majority of the window, resulting in measured values of  $g_{HBT}^{(2)}(0) \approx 1$  for the time-integrated correlation.

This is confirmed experimentally in this kit; see Section 9.3 for more details. Only with extremely fast detectors and electronics could one measure  $g_{HBT}^{(2)}(0) = 2$  for thermal sources.

In the literature, there are several approaches to constructing a pseudo-thermal light source that shows the same statistics as thermal light but with fluctuations on a much longer time scale. Prominent examples are moving laser speckles induced by a rotating diffusor<sup>25</sup> or an LED programmed to output randomized intensity<sup>26,27</sup>. With such sources,  $g_{HBT}^{(2)}(0) \approx 2$  may be measurable with the setup in this kit.

### 3.5.3 Grangier-Roger-Aspect Experiment

In the 1970s, several experiments<sup>28,29,30</sup> were performed with various kinds of single photon sources that experimentally proved effects that could only be explained by the quantization of the light field.

An experimental concept that forms the basis of the experiments in this kit, was introduced by Grangier, Roger, and Aspect (GRA) in 1986<sup>31</sup>. They used an atomic cascade that produced pairs of photons, with the two photons leaving the source in different directions (see Figure 10). One of these photons was used as a trigger (when detected at detector T) to “announce” the presence of the other one, with which a correlation experiment analog to the Hanbury-Brown-Twiss intensity interferometer (detectors A and B) was performed.

<sup>23</sup> R. Loudon, *The Quantum Theory of Light*. (Oxford University Press, Oxford, 1965).

<sup>24</sup> M. Beck, *Quantum Mechanics, Theory and Experiment*. (Oxford University Press, Oxford, 2012), p. 461.

<sup>25</sup> F. T. Arecchi, *Physical Review Letters*, **15**(24), 912 (1965).

<sup>26</sup> R. Scholz et al., *European Journal of Physics*, **37**(5), 055302 (2016).

<sup>27</sup> R. Scholz, K.-A. Weber, *Statistische Optik - Messung von Lichtfluktuationen mit einer programmierbaren LED*, Nordmeier, V. & Grötzebach, H. (Hrsg.), *PhyDid B, Didaktik der Physik, Beiträge zur DPG-Frühjahrstagung Würzburg 2018*. Berlin, 455 (2018)

<sup>28</sup> D. C. Burnham and D. L. Weinberg, *Physical Review Letters*, **25**(2), 84 (1970).

<sup>29</sup> J. F. Clauser, *Physical Review D*, **9**(4), 853 (1974).

<sup>30</sup> H. J. Kimble et al., *Physical Review Letters*, **39**(11), 912 (1974).

<sup>31</sup> P. Grangier et al., *Europhysics Letters*, **1**(4), 173 (1986).

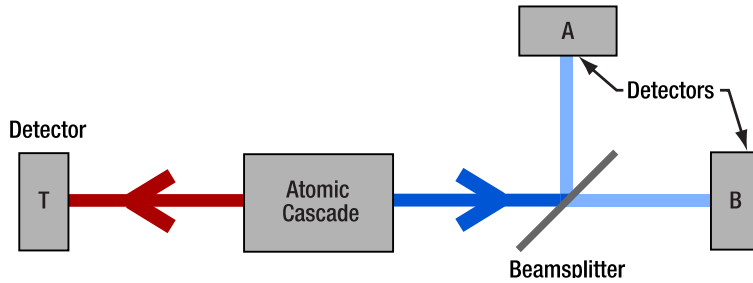


**Figure 10 Schematic of the Grangier-Roger-Aspect Experiment**

Using this approach, they obtained  $g_{GRA}^{(2)}(0) = 0.18$ , a result that can only be explained by the quantization of the electromagnetic field (the subscript GRA indicates the change in setup compared to an HBT intensity interferometer). Later advantages in photon pair sources and detectors have allowed experiments that show even more significant violations of  $g_{GRA}^{(2)}(0) \geq 1$ . The mathematical treatment of the GRA setup is explained in the following section.

It is important to note the meaning of smaller values of  $g_{GRA}^{(2)}(0)$  here. If the value of the correlation function is below 1, the quantum nature of light is proven. In principle, it does not matter by how much the inequality is violated,  $g_{GRA}^{(2)}(0) = 0.9$  and  $g_{GRA}^{(2)}(0) = 0.001$  both prove the quantum character of light. However, errors have to be taken into account, and thus often the number of standard deviations by which the inequality is violated is given along with the absolute value of  $g_{GRA}^{(2)}(0)$ . A larger value of  $g_{GRA}^{(2)}(0)$  (provided that it is below 1) with a small measurement error can provide a higher level of certainty that the violation occurred than a smaller value with a larger error.

A big advantage of the GRA setup is that if one does experiments with the photons in one arm after the beamsplitter, such as the Michelson interferometry described in Section 3.6, a test of the non-classical nature of the light can be run in parallel, validating the single photon nature of the main experiment.

### 3.5.4 Triple Coincidence Detection Scheme

In the GRA experiment, one photon of the pair reaches detector T directly, while the other one passes a beamsplitter with detectors A and B at the output ports. As the source produces pairs of photons, one could assume that the light in each arm consists of single photons. However, this is **not** the case. An HBT experiment while disregarding detector T would lead to the result  $g_{HBT}^{(2)}(0) = 1$  (to within the error of the measurement), showing that the photon statistics in a single arm are of classical character.

To show the quantization of the light field, the information about the photon distribution at detector T must be used. The two photons of a pair are emitted at the same time. Measuring a photon at detector T yields the information that at this exact point of time, there must be another photon in the A-B arm. At this point of time, the quantum state in the A-B arm is then not thermal anymore but becomes the single photon Fock state. The thermal state is said to collapse into the Fock state. Counting only such heralded events at detectors A and B will yield the non-classical result  $g_{HBT}^{(2)}(0) < 1$ . This is why a photon pair source is also called a heralded single photon source. This process is called a triple coincidence detection scheme and is described in more detail in the remainder of this subsection.

Each count on A or B is only counted when in coincidence with a count on T. The coincidence window is  $\Delta t$ . If an event is registered at detector A in coincidence with T, this contributes to the count rate  $R_{TA}$ . The count rate  $R_{TB}$  is obtained in the same fashion. Detection events at A and B that are not in coincidence with events at T are discarded. A coincidence count between A and B is only registered when both detector A and B register an event in coincidence with the **same** event at detector T, resulting in the triple coincidence count rate  $R_{TAB}$ . The definition for the second order correlation function remains (see Section 3.5.2):

$$g_{GRA}^{(2)}(0) = \frac{P_{TAB}}{P_{TA} \cdot P_{TB}} \quad (99)$$

Here, the subscript GRA indicates that the correlation function is measured with the detection scheme of the original GRA experiment.

The probabilities in the triple coincidence case can be normalized to the count rate of the trigger detector T, as this is the maximum rate of counts at the other detectors<sup>32</sup>. Thus:

$$P_{TA} = \frac{R_{TA}}{R_T}, \quad P_{TB} = \frac{R_{TB}}{R_T}, \quad P_{TAB} = \frac{R_{TAB}}{R_T} \quad (100)$$

Substituting this into Equation (99), the result is:

$$g_{GRA}^{(2)}(0) = \frac{R_{TAB} \cdot R_T}{R_{TA} \cdot R_{TB}} \quad (101)$$

### 3.5.5 Triple Coincidence Detection Scheme: Explanation 1

Why does this process enable measuring  $g_{GRA}^{(2)}(0) < 1$  when the simpler HBT experiment with one arm of the pair source does not? There are multiple ways to answer this question. Here, we will give a quantum mechanical answer, while the next section offers a more intuitive explanation.

There are different techniques to produce photon pairs that are entangled in time. One example is the Spontaneous Parametric Down-Conversion (SPDC) process used in this kit (see Section 3.9). If one photon of the time-entangled photon pair is measured at a time  $t$  at one detector, the second photon is guaranteed to be detected at nearly exactly the same time at the second detector (if it is placed the same distance from the pair source and the detector is perfect). The uncertainty of the arrival time of the second photon is much smaller than the typical time resolution of the experiment. Therefore, one can approximate the system in the second arm to be in a Fock state  $|1\rangle$  whenever a photon is measured in the first arm and  $|0\rangle$  at all other times. The triple coincidence detection scheme ensures that we are only looking at the system in the state  $|1\rangle$  (when the counts are in coincidence with the trigger detector T), instead of the thermal state as in the simpler two-detector HBT setup.

### 3.5.6 Triple Coincidence Detection Scheme: Explanation 2

A second, maybe more intuitive, explanation goes as follows:

First, assume a completely randomly distributed stream of photons with 10 000 photons per second as the input to the HBT experiment using detectors with 100% efficiency.

When performing the HBT experiment with a 50:50 beamsplitter, the single detector count rates will be  $R_A = R_B = 5000$  Hz because half of the photons go to each detector. We set the coincidence window to  $\Delta t = 1 \mu\text{s}$ <sup>33</sup>, i.e., a coincidence is defined as detector B registering a count within a  $1 \mu\text{s}$  window around detector A.

We do the experiment and measure a coincidence count rate  $R_{AB} = 25$  Hz. We then calculate  $g_{HBT}^{(2)}(0)$  from Equation (98) to be:

$$g_{HBT}^{(2)}(0) = \frac{R_{AB}}{R_A \cdot R_B \cdot \Delta t} = \frac{25 \text{ Hz}}{5 \text{ kHz} \cdot 5 \text{ kHz} \cdot 1 \mu\text{s}} = 1 \quad (102)$$

So far, everything is as expected. But now we have a second photon stream that is identical to the first one (as the photons are generated in pairs). We can use the second stream of photons to limit the time we are watching our experiment. We place detector T at the same distance from the pair source and send the second photon stream

<sup>32</sup> Technically, this is only true if the count rates are low enough that it is very improbable that multiple events are registered at a detector during a gate window. However, as the detectors normally exhibit dead times much larger than the window, see Section 4.1, this is automatically the case.

<sup>33</sup> The window length must be much lower than the average time between two counts, which is the case here. The exact length is chosen to facilitate the calculation, and any window length fulfilling the constraint above would work.

to detector T. We only watch our experiment for a 1  $\mu\text{s}$  window around counts at detector T. This means that if the experiment is running for a time  $T$ , we watch it only for a time  $T_c$ :

$$T_c = R_T \cdot \Delta t \cdot T = 10\,000 \text{ Hz} \cdot 1 \mu\text{s} \cdot T = 0.01 \cdot T \quad (103)$$

so only 1/100th of the time. However, we get the same number of counts, because all the events at detectors A and B happen within the 1  $\mu\text{s}$  window around events at T.

If we write Equation (101) with counts instead of rates, we immediately see the influence of the shortened measurement time at constant counts:

$$g_{GRA}^{(2)}(0) = \frac{R_{TAB} \cdot R_T}{R_{TA} \cdot R_{TB}} = \frac{N_{TAB} \cdot T \cdot 0.01}{N_{TA} \cdot N_{TB} \cdot \Delta t} = 0.01 \cdot g_{HBT}^{(2)}(0) = 0.01 \quad (104)$$

Here, we used the relation  $R_T = \frac{0.01}{\Delta t}$ , which can be derived from Equation (103), and the fact that the rates are the numbers divided by the measurement time, e.g.  $R_{TA} = \frac{N_{TA}}{T}$ . The gating process allowed us to measure  $g_{GRA}^{(2)}(0) = 0.01$  because we were able to shorten the effective measurement time by the factor  $R_T \cdot \Delta t$  without losing any counts due to the time correlation between the photons in the two arms.

### 3.5.7 Accidental Coincidences

As shown in Section 3.4.3, the expectation is  $g_{HBT}^{(2)}(0) = 0$  for a single photon Fock state in an HBT experiment. When using the GRA setup and the triple coincidence detection scheme, one still expects  $g_{GRA}^{(2)}(0) = 0$ . However, in the experiment several factors can lead to measurement results higher than that. In the case of the GRA experiment, the main factor is accidental triple coincidences.

There are two types of accidental triple coincidences:

- **Purely accidental triple coincidence:** A photon from photon pair 1 hits detector T, and during the coincidence window detectors A and B register counts due to uncorrelated events (such as other pairs generated during the gate window, background light, or detector dark counts). The rate  $R_{acc}^{(3)}$  of such purely accidental triple coincidences<sup>34</sup> is:

$$R_{acc}^{(3)} = R_T \cdot R_A \cdot R_B \cdot \Delta t^2 \quad (105)$$

Here,  $\Delta t$  is the width of the coincidence window.

- **Normal double coincidence with accidental third count:** In this case, two photons of a pair generate a coincidence event at either T&B or T&A and an uncorrelated event leads to a count at the third detector during the coincidence window. The rate  $R_{acc}^{(2+1)}$  for this type of accidental triple coincidence is:

$$R_{acc}^{(2+1)} = (R_{TA} \cdot R_B + R_{TB} \cdot R_A) \cdot \Delta t \quad (106)$$

An example calculation using the values typical for this kit of  $R_T = 200 \text{ kHz}$ ,  $R_A = R_B = 100 \text{ kHz}$ ,  $R_{TA} = R_{TB} = 10 \text{ kHz}$ , and  $\Delta t = 5 \text{ ns}$  yields:

$$R_{acc}^{(3)} = R_T \cdot R_A \cdot R_B \cdot \Delta t^2 = 2 \cdot 10^{15} \text{ Hz} \cdot 25 \cdot 10^{-18} \text{ s} = 0.05 \text{ Hz} \quad (107)$$

$$R_{acc}^{(2+1)} = (R_{TA} \cdot R_B + R_{TB} \cdot R_A) \cdot \Delta t = 2 \cdot 10^9 \text{ Hz} \cdot 5 \cdot 10^{-9} \text{ s} = 10 \text{ Hz} \quad (108)$$

It is apparent that the second type of accidental triple coincidences dominates. Inserted into Equation (101), these accidental coincidences result in an expectation for  $g_{GRA}^{(2)}(0)$  with the example values above of

$$g_{GRA}^{(2)}(0) = \frac{R_{acc}^{(2+1)} \cdot R_T}{R_{TA} \cdot R_{TB}} = \frac{10 \text{ Hz} \cdot 200 \text{ kHz}}{10 \text{ kHz} \cdot 10 \text{ kHz}} = 0.02 \quad (109)$$

<sup>34</sup> B. J. Pearson and D. P. Jackson, American Journal of Physics, 78(5), 471 (2010).

All single detector count rates are proportional to the pair generation rate  $R_{pp}$  (the absolute rate of generated photon pairs, whether detected or not) and independent of  $\Delta t$ . The twofold coincidence count rates are also proportional to  $R_{pp}$  (with a different proportionality factor) and independent of  $\Delta t$ . Substituting this in Equation (108) yields that  $R_{acc}^{(2+1)}$  is proportional to  $R_{pp} \cdot \Delta t$ . Thus:

$$g_{GRA}^{(2)}(0) \propto \frac{R_{pp}^2 \cdot R_{pp} \cdot \Delta t}{R_{pp} \cdot R_{pp}} = R_{pp} \cdot \Delta t \quad (110)$$

This agrees with intuition. Both a larger rate of photons and a wider coincidence window increase the probability of two uncorrelated events being registered as if they were correlated, increasing  $g_{GRA}^{(2)}(0)$ . As a result, there are two ways to limit accidental triple coincidences and move  $g_{GRA}^{(2)}(0)$  closer to 0:

- Shorten the coincidence window. This is limited by the time resolution of the detectors and electronics. In the case of this kit, the jitter of the EDU Time Tagger is 720 ps (see Section 4.2.2), so coincidence windows shorter than 1 ns do not improve the result.
- Lower the rate of photon pairs. This is most easily achieved by lowering the power of the pump laser. The drawback is of course a reduction of the count rates, which means that longer measurements are required to avoid larger error bars. For details, see Section 12.5.

The standard values for the coincidence window and laser power given in this manual are optimized for satisfactory results and comfortable measurement times.

## 3.6 Single Photon Interference

### 3.6.1 Theoretical Description

Here, the experimental case of a Michelson Interferometer, explained in Section 3.1.2 and shown in Figure 2, is treated quantum mechanically. We label the ports “i” for input, “d” for detector, and “α” and “β” for the two arms of the interferometer.

If the state  $|1\rangle_i \otimes |0\rangle_d$  is incident on the beamsplitter, describing a single photon at the input port and vacuum at the detector port (see Section 3.2.12 for the explanation of combined states), the state after the beamsplitter is (according to Equation (80) in Section 3.4.2):

$$\frac{1}{\sqrt{2}}(|1\rangle_\alpha|0\rangle_\beta + |0\rangle_\alpha|1\rangle_\beta) \quad (111)$$

If the two arms are the same length. A difference in the lengths of the interferometer arms  $\Delta l$  induces a relative phase shift  $\phi = \frac{2\pi\Delta l}{\lambda}$ . This phase shift can be represented by a phase shift of the creation operator in one of the arms<sup>35</sup> (here β):  $\hat{a}_\beta^\dagger \rightarrow e^{i\phi} \cdot \hat{a}_\beta^\dagger$ , so that the state before recombination at the beamsplitter becomes:

$$\frac{1}{\sqrt{2}}(|1\rangle_\alpha|0\rangle_\beta + e^{i\phi}|0\rangle_\alpha|1\rangle_\beta) \quad (112)$$

The recombination at the beamsplitter is described by the same equations as the splitting process. However, instead of  $|1\rangle$  and  $|0\rangle$ , the input is now the split state of Equation (112). Adding and subtracting equations (78) and (79) and setting  $t = r = \frac{1}{\sqrt{2}}$  (to account for the 50:50 beamsplitter) results in the following equations:

$$\hat{a}_\alpha^\dagger = \frac{1}{\sqrt{2}} \cdot (\hat{a}_d^\dagger + \hat{a}_i^\dagger) \quad (113)$$

$$\hat{a}_\beta^\dagger = \frac{1}{\sqrt{2}} \cdot (\hat{a}_i^\dagger - \hat{a}_d^\dagger) \quad (114)$$

<sup>35</sup> M. Beck, *Quantum Mechanics, Theory and Experiment*. (Oxford University Press, Oxford, 2012).

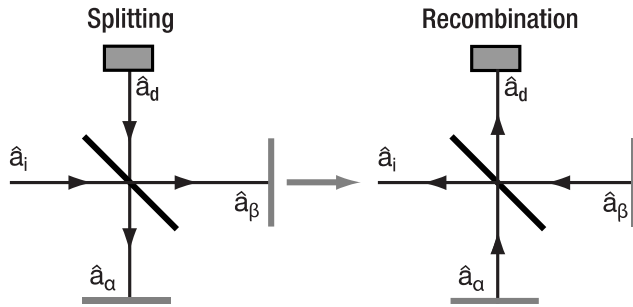


**Figure 11**      **Geometry of Michelson Interferometer. Left: Splitting, Right: Recombination**

The state after recombination is then:

$$\begin{aligned}
 |\psi_{rec}\rangle &= \frac{1}{\sqrt{2}}(|1\rangle_\alpha|0\rangle_\beta + e^{i\phi}|0\rangle_\alpha|1\rangle_\beta) \\
 &= \frac{1}{\sqrt{2}}(\hat{a}_\alpha^\dagger|0\rangle + e^{i\phi}\hat{a}_\beta^\dagger|0\rangle) = \frac{1}{\sqrt{2}}\left(\frac{1}{\sqrt{2}}(\hat{a}_d^\dagger|0\rangle + \hat{a}_i^\dagger|0\rangle) + \frac{1}{\sqrt{2}}e^{i\phi} \cdot (\hat{a}_i^\dagger|0\rangle - \hat{a}_d^\dagger|0\rangle)\right) \\
 &= \frac{1}{\sqrt{2}}\left(\frac{1}{\sqrt{2}}(|0\rangle_i|1\rangle_d + |1\rangle_i|0\rangle_d) + \frac{1}{\sqrt{2}}e^{i\phi} \cdot (|1\rangle_i|0\rangle_d - |0\rangle_i|1\rangle_d)\right) \\
 &= \frac{1}{2}\left((1 + e^{i\phi})|1\rangle_i|0\rangle_d + (1 - e^{i\phi})|0\rangle_i|1\rangle_d\right)
 \end{aligned} \tag{115}$$

The quantity of interest is the probability of the photon leaving the interferometer through the detection port d, which we denote  $P(1_d)$ . The respective projection operator is  $\hat{P}_{n_d=1} = \hat{I}_i \otimes |1\rangle_d \langle 1|$  (with  $\hat{I}_i$  being the identity operator in the i-basis, meaning that the combined operator only acts on the d-basis and leaves the i-component of all vectors unchanged) and the probability can be calculated as:

$$P(1_d) = \langle \psi_{rec} | \hat{P}_{n_d=1} | \psi_{rec} \rangle \tag{116}$$

Combining equations (115) and (116) yields:

$$\begin{aligned}
 P(1_d) &= \frac{1}{4} \left( (1 + e^{-i\phi}) (1|_i 0|_d + (1 - e^{-i\phi}) (0|_i 1|_d) \hat{I}_i \right. \\
 &\quad \left. \otimes |1\rangle_d \langle 1| \left( (1 + e^{i\phi}) |1\rangle_i |0\rangle_d + (1 - e^{i\phi}) |0\rangle_i |1\rangle_d \right) \right) \\
 &= \frac{1}{4} (1 - e^{-i\phi}) (0|_i (1 - e^{i\phi}) |0\rangle_i \\
 &= \frac{1}{4} (1 + 1 - e^{-i\phi} - e^{i\phi}) (0|_i 0|_i) \\
 &= \frac{1}{2} \cdot (1 - \cos(\phi))
 \end{aligned} \tag{117}$$

Please note that all  $e^{i\phi}$  in  $|\psi_{rec}\rangle$  transform to  $e^{-i\phi}$  in  $\langle\psi_{rec}|$  by standard Dirac notation (see Section 3.2.7). The last transformation uses the relation  $\cos(\phi) = \frac{e^{i\phi} + e^{-i\phi}}{2}$ .

This result is analogous to the classic one; see Section 3.1.2. The probability of the photon leaving the interferometer through the detection port depends on the arm length difference and can reach from 0 to 1. The probability of the photon leaving through the input port can be analogously calculated as:

$$P(1_i) = \frac{1}{2} \cdot (1 + \cos \phi) \tag{118}$$

The sum  $P(1_d) + P(1_i) = 1$  for all phase differences  $\phi$ , hence the energy is conserved.

### 3.6.2 Experimental Realization

In the experiment in this kit, which follows the original setup by GRA, as well as others after<sup>36</sup>, a Michelson interferometer is placed between the beamsplitter and detector B. The basic setup geometry is displayed in Figure 12.

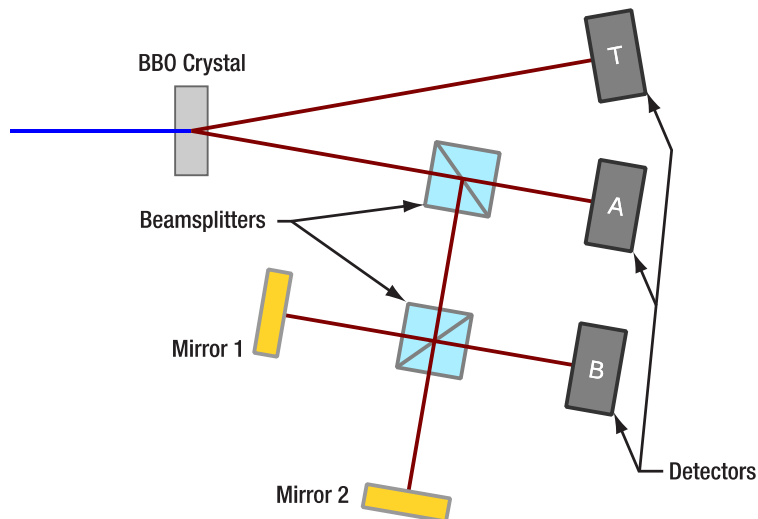


**Figure 12** Setup Geometry of Michelson Interferometer Coupled with GRA Experiment

Mirror 1 is positioned on a movable stage. In the experiment, the stage position and therefore the path length difference  $\Delta l$  is varied and the coincidence count rate  $R_{TB}$  is plotted. The expected count rate is then a function of the arm length difference:

$$R_{TB} = R_{TB}^{\max} \cdot \frac{1}{2} \left( 1 + \cos \left( \frac{2\pi \Delta l}{\lambda} \right) \right) \tag{119}$$

<sup>36</sup> E. J. Galvez et al., American Journal of Physics, 73(2), 127 (2005).

with  $\lambda \approx 810$  nm being the wavelength of the single photons and  $R_{TB}^{max}$  an experimentally obtained maximum count rate. Parallel to this interferogram, the second-order correlation function  $g_{GRA}^{(2)}(0)$  is recorded as described in Equation (101) to continuously verify the single photon character of the light in the experiment.

By moving the mirror over a length  $l$  and counting the number  $N$  of maxima during this movement, the wavelength of the photons can be determined via:

$$\lambda = 2 \cdot \frac{l}{N} \quad (120)$$

## 3.7 Quantum Treatment of Polarization

### 3.7.1 Theoretical Description

Single photons have a polarization. As polarization is associated with spin angular momentum<sup>37</sup>, photons are usually described to have either left-circular or right-circular polarization (for the classical definition, see Section 3.1.3) or a superposition of the two. The state of a single photon (Fock state with  $n = 1$ ) with left-circular polarization (spin 1) is denoted as  $|L\rangle$  and with right-handed polarization (spin -1) as  $|R\rangle$ . The spin state 0 is not possible as photons are massless and always move at the speed of light.

Those two states are orthogonal, i.e.,  $\langle L|R \rangle = 0$ . They also form a basis in the Hilbert space of polarization states, meaning that every polarization state can be described by a linear combination of  $|L\rangle$  and  $|R\rangle$ . As an example, the photon state  $|H\rangle$  corresponding to linear polarization along the x-axis in the coordinate system introduced in Section 3.1.3 is described as follows:

$$|H\rangle = \frac{1}{\sqrt{2}} \cdot (|L\rangle + |R\rangle) \quad (121)$$

This polarization is called horizontal. The vertical polarization state  $|V\rangle$  (linear polarization along the y-axis) is:

$$|V\rangle = \frac{1}{i\sqrt{2}} \cdot (|L\rangle - |R\rangle) \quad (122)$$

$|H\rangle$  and  $|V\rangle$  also form an orthonormal basis of the Hilbert space and as such can be used to describe every polarization state. For example, the circular polarization states written as linear combinations of  $|H\rangle$  and  $|V\rangle$  are:

$$|L\rangle = \frac{1}{\sqrt{2}} \cdot (|H\rangle + i|V\rangle) \quad (123)$$

$$|R\rangle = \frac{1}{\sqrt{2}} \cdot (|H\rangle - i|V\rangle) \quad (124)$$

A linear polarization state along a line with an angle  $\theta$  to the x-axis is denoted  $|\theta\rangle$  and calculated as:

$$|\theta\rangle = \cos(\theta) \cdot |H\rangle + \sin \theta \cdot |V\rangle \quad (125)$$

If a photon passes through a linear polarizer with a polarizer axis that forms an angle  $\theta$  with the x-axis, it is either completely transmitted or completely absorbed. If it is transmitted, it is then linearly polarized in the direction of the polarizer axis, i.e., its state is transformed to  $|\theta\rangle$ . This constitutes a measurement of the polarization; see Section 3.2.9. The measured observable is the polarization along the  $\theta$ -axis, the corresponding Hermitian operator is called  $\hat{\rho}_\theta$ , and its eigenvectors are  $|\theta\rangle$  and  $|\theta + \frac{\pi}{2}\rangle$  with the eigenvalues 1 and -1, respectively. A photon in an arbitrary polarization state  $|\psi\rangle$  being transmitted by the polarizer is equivalent to measuring the photon to be in the state  $|\theta\rangle$ . As such, the probability of transmission is given as the conditional probability<sup>38</sup> (see Section 3.2.10):

<sup>37</sup> L. He et al., *Science Advances*, 2(9), (2016).

<sup>38</sup>  $P(A|B)$  is defined here as the conditional probability of A given B.

$$P(\theta \parallel \psi) = |\langle \theta | \psi \rangle|^2 \quad (126)$$

It is instructive to look at the special case of the incoming photon being linearly polarized with an angle  $\phi$ , i.e., in the state  $|\phi\rangle$ . Combining Equations (125) and (126) yields:

$$\begin{aligned} P(\theta \parallel \phi) &= |\langle \theta | \phi \rangle|^2 = |(\cos(\theta) \cdot \langle H \rangle + \sin \theta \cdot \langle V \rangle)(\cos(\phi) \cdot |H\rangle + \sin \phi \cdot |V\rangle)|^2 \\ &= |\cos \theta \cos \phi + \sin \theta \sin \phi|^2 = |\cos(\theta - \phi)|^2 = \cos^2(\theta - \phi) \end{aligned} \quad (127)$$

For a large numbers of photons, this result is the same as the classical Malus' Law (see Equation (27) in Section 3.1.3), as the expectation value of the transmitted photon number is proportional to the classical intensity. The experimental validation of this result is part of the kit; see Section 9.6.

In the classical description, polarizers act on the intensities of the beam. The quantum mechanical formalism, however, describes the probability of each single photon to propagate through optical elements and/or be measured in a certain state (here the polarization angle). The fact that the polarizer not only determines the transmission probability of the photon but also alters its state can be shown with a three-polarizer experiment<sup>39</sup>, as will be explained in Section 10.2.

If very few events are measured, we cannot tell the underlying probability distribution from the measurement. For a large number of measurements of photons prepared in the same state, the probabilistic result converges towards the classical expectation.

### 3.7.2 Experimental Realization

In the experiment in this kit, a linear polarizer is placed in front of detector B in a GRA setup geometry as displayed in Figure 13.

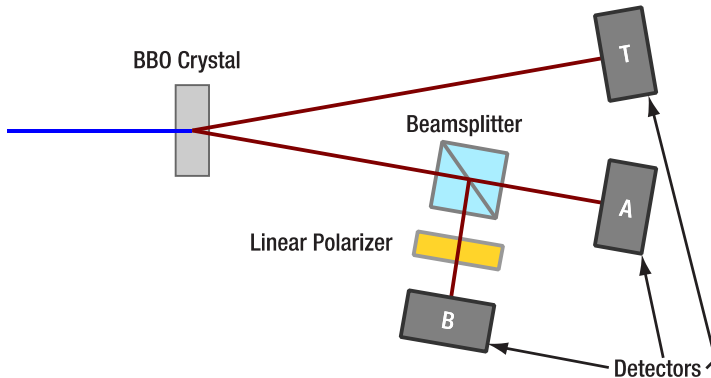


**Figure 13 Schematic of a Setup for Measuring Malus' Law for Single Photons**

This polarizer is then rotated and the coincidence count rate  $R_{TB}$  is recorded with respect to the polarizer angle  $\theta$ . According to the theory above, the expected result is:

$$R_{TB} = R_{TB}^{max} \cdot \cos^2(\theta - \phi) \quad (128)$$

with  $\phi$  being the polarization angle of the single photons and  $R_{TB}^{max}$  being the maximum coincidence count rate (reached when the polarization axes of the polarizer and the photons are identical). This measurement can then additionally be used to determine  $\phi$ . At the same time,  $g_{GRA}^{(2)}(0)$  is calculated according to Equation (101) to verify the single photon character of the light in the experiment for every data point.

Due to the process of generating the photon pairs (described in detail in Section 3.9), the polarization in both arms of the pair photon source is expected to be parallel. This can be verified by positioning the polarizer in front of detector T instead of B and repeating the experiment.

<sup>39</sup> J. M. Brom and F. Rioux, *The Chemical Educator*, 7, 200 (2002).

## 3.8 The Quantum Eraser

### 3.8.1 Theoretical Description

In Section 3.6, we discussed the Michelson interferometer. What happens when we insert polarizers into the interferometer? This will link polarization with the information about the interferometer arms. To demonstrate that, we will use combined states of the form<sup>40</sup>  $|n_\alpha, n_\beta, p\rangle$  and  $|n_i, n_d, p\rangle$  with  $n_x$  being the photon number at the  $x$ -port of the beamsplitter and  $p$  being the polarization as described in Section 3.7.

We start with the state  $|1_i, 0_d, 45^\circ\rangle$  at the beamsplitter. The beamsplitter itself does not affect the polarization, so we can use Equation (80) to calculate the state after the beamsplitter as:

$$\frac{1}{\sqrt{2}}(|1_\alpha, 0_\beta, 45^\circ\rangle + |0_\alpha, 1_\beta, 45^\circ\rangle) \quad (129)$$

Now we insert a linear polarizer with a polarization axis along  $0^\circ$  in the  $\alpha$ -arm and a second linear polarizer with a polarization axis along  $90^\circ$  in the  $\beta$ -arm. The polarizers act only on the third part of the combined states in the same way as described in Section 3.7. Thus, the states in the arms are transformed by the polarizers in the following way<sup>41</sup>:

$$|1_\alpha, 0_\beta, 45^\circ\rangle \rightarrow \frac{1}{\sqrt{2}}|1_\alpha, 0_\beta, H\rangle \quad (130)$$

$$|0_\alpha, 1_\beta, 45^\circ\rangle \rightarrow \frac{1}{\sqrt{2}}|0_\alpha, 1_\beta, V\rangle \quad (131)$$

Additionally, the path length difference induces a phase difference, just as explained in Section 3.6:

$$\frac{1}{\sqrt{2}}|0_\alpha, 1_\beta, V\rangle \rightarrow \frac{e^{i\phi}}{\sqrt{2}}|0_\alpha, 1_\beta, V\rangle \quad (132)$$

Recombination at the beamsplitter is handled analogously to Section 3.6. The creation operators pick up subscripts denoting the polarization of the created photon but Equations (113) and (114) remain unchanged in their structure:

$$\begin{aligned} |\psi_{rec}\rangle &= \frac{1}{2}(|1_\alpha, 0_\beta, H\rangle + e^{i\phi}|0_\alpha, 1_\beta, V\rangle) = \frac{1}{2}(\hat{a}_{\alpha,H}^\dagger|0\rangle + e^{i\phi}\hat{a}_{\beta,V}^\dagger|0\rangle) \\ &= \frac{1}{2}\left(\frac{1}{\sqrt{2}}(|0_i, 1_d, H\rangle - |1_i, 0_d, H\rangle) + \frac{e^{i\phi}}{\sqrt{2}}(|1_i, 0_d, V\rangle + |0_i, 1_d, V\rangle)\right) \\ &= \frac{1}{2\sqrt{2}}(|0_i, 1_d, H\rangle - |1_i, 0_d, H\rangle + e^{i\phi}|1_i, 0_d, V\rangle + e^{i\phi}|0_i, 1_d, V\rangle) \end{aligned} \quad (133)$$

We want to know the probability of the photon leaving the interferometer through the detection port. Analog to Section 3.6, this is the probability  $P(1_d)$  which is the expectation value of the projection operator  $\hat{P}_{n_d=1} = \hat{l}_i \otimes |1\rangle_d \langle 1| \otimes \hat{l}_p$ . The calculation is similar to that in Section 3.6 with the addition of the polarization base:

$$\begin{aligned} P(1_d) &= \langle \psi_{rec} | \hat{l}_i \otimes |1\rangle_d \langle 1| \otimes \hat{l}_p | \psi_{rec} \rangle = \frac{1}{(2\sqrt{2})^2} (\langle 0_i, H | + e^{-i\phi} \langle 0_i, V |)(\langle 0_i, H | + e^{i\phi} \langle 0_i, V |) \\ &= \frac{1}{(2\sqrt{2})^2} \langle 0_i, H | 0_i, H \rangle + \frac{e^{-i\phi} \cdot e^{i\phi}}{(2\sqrt{2})^2} \langle 0_i, V | 0_i, V \rangle = \frac{1}{8} + \frac{1}{8} = \frac{1}{4} \end{aligned} \quad (134)$$

<sup>40</sup> Please note that we use a different but equivalent notation for the combined states from here on for brevity. As specified in Equation (53):

$$|n_\alpha, n_\beta, p\rangle \equiv |n_\alpha\rangle_\alpha \otimes |n_\beta\rangle_\beta \otimes |p\rangle_p$$

<sup>41</sup> Please note that the states in Equations (130) and (131) are not normalized, which could lead to errors in the calculation of probabilities if one is not careful. The vacuum terms  $\frac{1}{\sqrt{2}}|0_\alpha, 0_\beta, V\rangle$  and  $\frac{1}{\sqrt{2}}|0_\alpha, 0_\beta, H\rangle$  (representing the probability of the photon being absorbed at the polarizer) could be added to the right side of Equations (130) and (131), respectively, in order to preserve normalization. However, this would make the following calculation very bulky without changing the result, as those vacuum states don't contribute to any detection probability. Thus, we proceed with the non-normalized states.

The probability is now independent of the phase difference  $\phi$ , meaning that there is no interference pattern when changing the length difference of the interferometer arms<sup>42</sup>. This can be interpreted as follows:

The polarizers in the interferometer arms provide “which-way” (WW) information. By measuring the polarization of a photon after the interferometer output, one can tell which path it took. Horizontally polarized photons went through the  $\alpha$ -arm and vertically polarized photons went through the  $\beta$ -arm. Interference of a photon with itself is only possible if the paths are indistinguishable, so there can be no interference pattern when WW information is available. The polarization measurement does not need to be performed; its mere possibility is sufficient to make the photons distinguishable.

However, it is possible to remove the WW information. In our case, this can be done by placing a third linear polarizer in front of the detector in the interferometer output and setting its polarization axis to  $45^\circ$ . In this case we measure the probability  $P(0,1,45^\circ)$  that the photon is in state  $|0_i, 1_d, 45^\circ\rangle = \frac{1}{\sqrt{2}}(|0_i, 1_d, H\rangle + |0_i, 1_d, V\rangle)$ :

$$\begin{aligned} P(0,1,45^\circ) &= |\langle 0_i, 1_d, 45^\circ | \psi_{rec} \rangle|^2 = \frac{1}{2} |\langle 0_i, 1_d, H | \psi_{rec} \rangle + \langle 0_i, 1_d, V | \psi_{rec} \rangle|^2 = \frac{1}{16} |1 + e^{i\phi}|^2 \\ &= \frac{1}{8} (1 + \cos \phi) \end{aligned} \quad (135)$$

This is the same result as for the interferometer without any polarizers! The probability of a detected photon is again dependent on the arm length difference of the paths, meaning that the interference pattern is recovered. The only difference is a factor of  $\frac{1}{4}$ , which represents that twice in the experiment, half of the photons are absorbed (first at the polarizers in the interferometer and again at the polarizer in front of the detector). This is interpreted as follows:

By inserting the third polarizer, the WW information is erased (the probability of a photon to be measured as  $45^\circ$ -polarized is the same for photons going through arms  $\alpha$  and  $\beta$ ). After the polarizer, the arms are again indistinguishable, allowing interference to occur.

Interestingly, it is also possible to change the recovered interference pattern. If the axis of the third polarizer is chosen to be  $-45^\circ$ , then the above calculation yields:

$$P(0,1,-45^\circ) = \frac{1}{8} (1 - \cos \phi) \quad (136)$$

In this case, the minima and maxima of the interference pattern are switched compared to the  $45^\circ$  polarizer.

The phenomenon of the Quantum Eraser<sup>43</sup> can also be understood without the use of WW information by regarding the “erasing” process more as an “editing” process, where a different subset of photons is probed<sup>44</sup> or by explaining it in the framework of projecting the beams from the arms to a different polarization basis.

### 3.8.2 Experimental Realization

The setup geometry is the same as in Section 3.6.2. The coincidence count rate  $R_{TB}$  is plotted over the stage position  $\Delta l$ .

The experiment consists of three measurements with the following expected results:

- 1.) Both polarizers at  $0^\circ$ , no eraser:  $R_{TB} = R_{TB}^{\max} \cdot \frac{1}{2} \left(1 + \cos\left(\frac{2\pi\Delta l}{\lambda}\right)\right)$
- 2.) Polarizers at  $0^\circ/90^\circ$ , no eraser:  $R_{TB} = R_{TB}^{\max} \cdot \frac{1}{2}$
- 3.) Polarizers at  $0^\circ/90^\circ$ , eraser polarizer at  $45^\circ$ :  $R_{TB} = R_{TB}^{\max} \cdot \frac{1}{4} \left(1 + \cos\left(\frac{2\pi\Delta l}{\lambda}\right)\right)$

<sup>42</sup> Note, the probability is only  $\frac{1}{4}$  instead of  $\frac{1}{2}$  as one may expect. The reason is that half of the photons get absorbed by the polarizers in each of the interferometer arms.

<sup>43</sup> Thorlabs offers the EDU-QE1/(M) Quantum Eraser Analogy Kit. The manual is freely available on the product webpage and introduces the quantum eraser experiment in more detail.

<sup>44</sup> P. G. Kwiat et al., AIP Conference Proceedings, **461**(1), 69 (1999).

With  $\lambda = 810 \text{ nm}$  being the wavelength of the single photons and  $R_{TB}^{max}$  the maximum coincidence count rate of experiment 1. Parallel to the interferograms, the second-order correlation function  $g_{GRA}^{(2)}(0)$  is recorded as described in Equation (101) to continuously verify the single photon character of the light in the experiment.

### 3.9 Spontaneous Parametric Down-Conversion

The atomic cascade that Grangier, Roger, and Aspect used to obtain photon pairs is a very inefficient and complicated source. Nowadays, most experiments use a process called Spontaneous Parametric Down-Conversion (SPDC) to generate photon pairs. In SPDC, pairs of photons are generated inside a nonlinear crystal from pump light, typically the output of a pump laser. These photons are created virtually simultaneously, so that one of the photons can be used to signal the existence of the other, making it possible to perform measurements on single photons. That is why the photons of the pair are historically called the “idler” and “signal” photon. A schematic drawing of the SPDC process is shown in Figure 14.

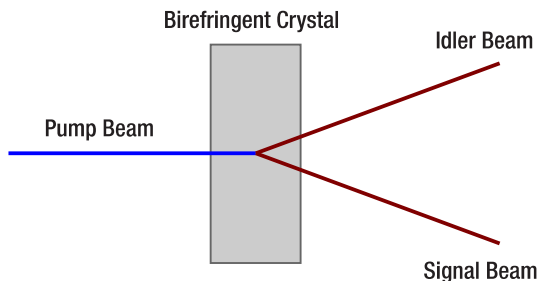


**Figure 14 Schematic Drawing of the SPDC Process (Top View)**

The process<sup>45</sup> is called spontaneous (as opposed to stimulated) because the photon pair is created without the presence of an external electromagnetic field at the target wavelength. It is called parametric because it has a relation to the parametric oscillator model. The term down-conversion is used because the photons of the pair have a lower energy than the incoming photon.

SPDC is the reverse process to Second Harmonic Generation (SHG), a process used very commonly in optics labs for multiple applications, such as creating 532 nm wavelength lasers. Unlike SHG, however, it cannot be explained by classical fields. Classical theories only allow for the generation of an idler and signal beam if a weak signal beam already exists, a process called parametric amplification. Therefore, the existence of the SPDC process can only be explained quantum-mechanically.

For the complete derivation, we refer to the literature<sup>46</sup>, but we will highlight some of the important properties of the process in the following.

Energy and momentum need to be conserved by the SPDC process. This means:

$$\omega_p = \omega_s + \omega_i \quad (137)$$

$$\vec{k}_p = \vec{k}_s + \vec{k}_i \quad (138)$$

Here,  $\omega$  is the angular frequency of the photon and  $\vec{k}$  is the wave vector. The indices p, i, and s stand for pump, idler, and signal, respectively. The frequencies and wave vectors are not independent but linked via the dispersion relation. As all three indices would have the same representative equation, the pump photon is given as an example below:

$$k_p = \frac{n_p \cdot \omega_p}{c} \quad (139)$$

<sup>45</sup> M. Beck, *Quantum Mechanics, Theory and Experiment*. (Oxford University Press, Oxford, 2012).

<sup>46</sup> C. Couteau, *Contemporary Physics*, 59(3), 291 (2018).

Here,  $n_p$  is the index of refraction of the crystal at the pump frequency  $\omega_p$ , and  $c$  is the speed of light in vacuum. The index of refraction depends on the frequency of the light. For most materials it increases with increasing frequency in the optical regime, the so-called normal dispersion.

For SPDC, however, if we assume the wavelengths of the signal and idler photons to be similar, we need the same index of refraction for both pump and signal/idler photons. That is the reason birefringent crystals are used for SPDC. Those crystals have different indices of refraction for different polarizations. In Type-I crystals, such as the barium borate (BBO) crystal used in this kit, the polarization of the signal and idler photons is perpendicular to the plane spanned by the optical axis of the crystal and the propagation direction of the pump laser, see Figure 15. If the pump is polarized orthogonally to the signal and idler polarization, a different dispersion relation applies for the pump compared to the photons of the pair. This makes it possible to find orientations of the crystal (in relation to  $\vec{k}_p$  and the pump polarization), that satisfy both equations (137) and (138).

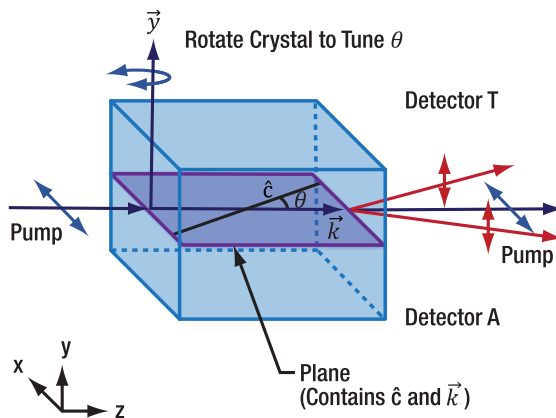


**Figure 15**      **Polarization During the SPDC Process for a Type-1 BBO Crystal ( $\hat{c}$  is the Optical Axis of the Crystal and  $\vec{k}$  is the Wave Vector of the Pump)**

The refractive index as a function of the wavelength for BBO is shown in Figure 16. The red solid curve marks the refractive index for the ordinary beam ( $n_o$ ). The black dashed curve is the refractive index for the extraordinary beam ( $n_e$ ) if the input beam is orthogonal to the crystal plane. By rotating the crystal axes, the refractive index curve can be moved until  $n_e(405 \text{ nm}) = n_o(810 \text{ nm})$ . This is called phase matching and allows efficient SPDC from pump photons at 405 nm to signal/idler photon pairs at about 810 nm each. The BBO crystal in this kit is cut at an angle of  $29.2^\circ$  to ensure optimal phase matching for a pump beam under normal incidence and a half-opening angle of  $3^\circ$  for the photon pair emission. Section 12.14 provides more details about the crystal angle and polarization.

Another factor in the experiment is the thickness of the crystal. Thicker crystals provide a higher pair generation rate per pump power as there is more volume for the light to interact with the crystal. However, increasing thickness also blurs the wavelength-position correlation of the SPDC photons, as pairs created at different spots in the crystal have a different point of origin for the cone on which they are emitted.

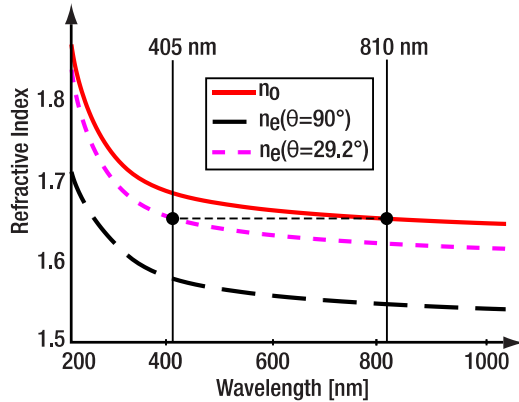


**Figure 16 Refractive Indices for the Ordinary Beam ( $n_o$ , Red Curve), the Extraordinary Beam ( $n_e$ ) at  $90^\circ$  (Black Curve), and  $29.2^\circ$  (Pink Curve) Crystal Orientation**

Depending on the exact phase matching parameters, the signal and idler pairs either leave the crystal collinearly or on a cone with a small opening angle. The k-vectors of the photons in this case are schematically shown in Figure 17. For this kit, the half opening angle of the cone is  $3^\circ$ .

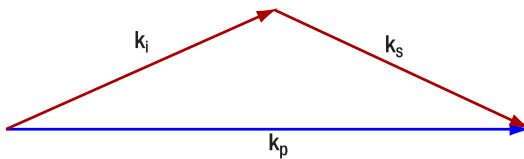


**Figure 17 Schematic of the k-vectors of the Pump (p), Idler (i) and Signal (s) Photons in a SPDC process with Non-Collinear Emission**

It is important to note that for a pump wavelength of 405 nm, the wavelength of the signal and idler photons will not always be 810 nm. Equation (137) also allows for pairs of different wavelengths, such as 812 nm / 808 nm<sup>47</sup>. In those cases, the photon with the longer wavelength makes a slightly larger angle with the pump beam and vice versa. This wavelength deviation is limited by how well the phase matching is fulfilled at the different wavelengths, as the efficiency of the SPDC process will drop sharply with non-optimal phase matching. In the configuration of this kit, the photon pairs are emitted under a range of wavelengths of up to several 10s of nm and angles up to several degrees<sup>48,49</sup>. Figure 18 shows a theoretically calculated plot for the normalized signal intensity depending on the signal wavelength for a pump wavelength of 405 nm and crystal parameters matching the crystal in the kit. The broad signal spectrum also means that the photons generated by the SPDC process are distributed over a rather large angle. When measuring with two detectors in coincidence, one must be careful that the detectors are positioned in such a way that they are able to detect photons from the same pair. Furthermore, when measuring wavelength-dependent quantities, such as the coherence length of the SPDC generated photons, one must consider that the wavelengths are spatially separated, which makes it likely that not all generated wavelengths are detected.

<sup>47</sup> Be aware that the wavelength of the pairs is calculated by  $\frac{1}{\lambda_p} = \frac{1}{\lambda_s} + \frac{1}{\lambda_i}$ , not by  $\lambda_p = \frac{\lambda_s + \lambda_i}{4}$ . The example above would therefore be 812.00 nm / 808.01 nm when given with more precision.

<sup>48</sup> M. Beck, *Quantum Mechanics, Theory and Experiment*. (Oxford University Press, Oxford, 2012).

<sup>49</sup> N. Beouf et al., *Optical Engineering*, 39(4), (2000).

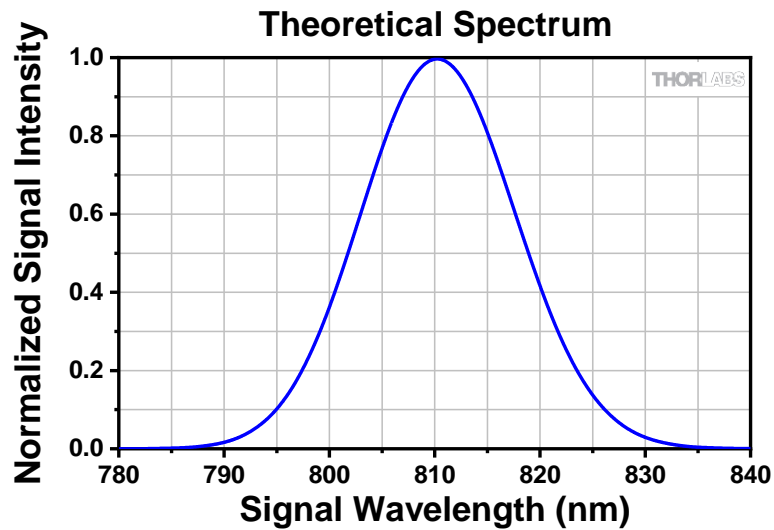


**Figure 18**      *Theoretical Spectrum of Signal Intensity as a Function of Signal Wavelength (Calculation via [spdcalc.org](http://spdcalc.org))*

## Chapter 4 Experimental Concepts

### 4.1 Single Photon Detectors

Single Photon Detectors are based on the Avalanche Photodiode (APD) design. An incoming photon creates an electron-hole pair in the semiconductor material of the APD (silicon for the detectors in this kit). A strong reverse voltage is applied to the semiconductor, accelerating the electron to the point that it creates additional free electrons via impact ionization, which in turn create even more electrons. This effect generates a large internal gain factor, resulting in a measurable voltage pulse even with a single photon as the original signal. In that sense the functional principle is remarkably close to a Geiger-Müller counter (the detectors are said to be operated in Geiger mode) but it works at much lower photon energies. This output pulse is often shaped by internal electronics of the detector to match an international standard, such as TTL. A typical output pulse of Thorlabs' SPDMA Single Photon Detection Module, included in this kit, is displayed on the left graph of Figure 19.

After an avalanche event, the detector is unresponsive to additional photons for a small amount of time, called the dead time (<35 ns for the SPDMA detectors). The dead time is the main contribution to the maximum count rate the detector can detect (20 MHz for the SPDMA detectors).

The photon detection efficiency (i.e., the percentage of incoming photons that result in a signal pulse) of such a detector depends on the detector material and the wavelength of the photons. The SPDMA detectors used in this kit provide a maximum efficiency of 65% at about 600 nm. At the design wavelength of this kit (810 nm), they still detect about 45% of all incoming photons, as seen in the graph on the right side of Figure 19.

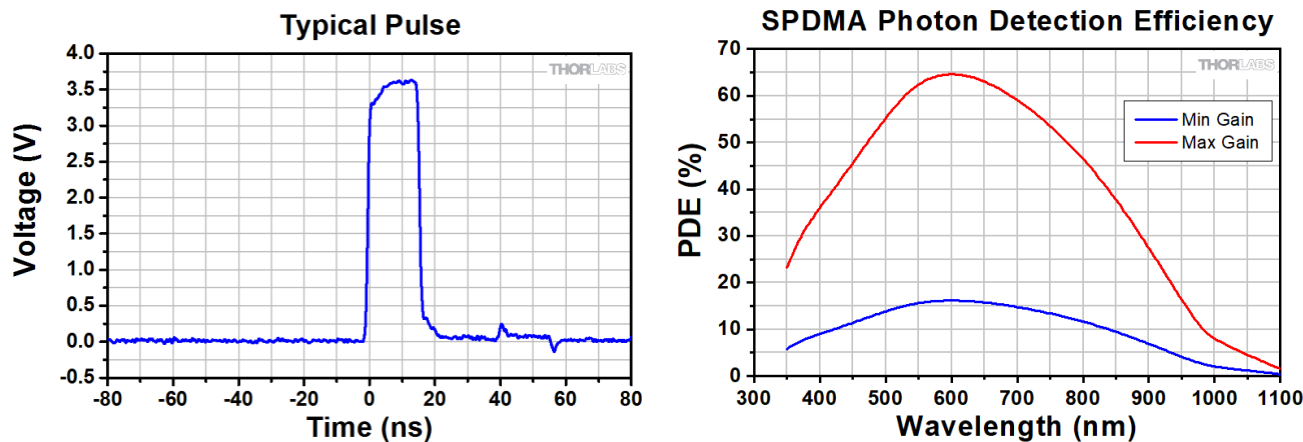


**Figure 19**      **Typical Output Pulse (Left) and Spectral Photon Detection Efficiency (Right) for the SPDMA Detectors Used in this Kit**

Sometimes, an avalanche event occurs without an external photon hitting the detector. Such an event is called a “dark count.” Dark counts are undesirable, as they cause errors in the measurement, especially at low signal count rates. The typical dark count rate of the SPDMA detectors is <300 Hz. As the signal count rates in the experiments described here are typically several 10s or even 100s of kHz, the negative impact of the dark counts on the results is negligible. Furthermore, the coincidence counting method, described in Section 4.2, further reduces the impact of dark counts.

The SPDMA detectors offer the option of reducing the reverse voltage (gain) at the diode, decreasing the dark count rate but at the same time reducing the photon detection efficiency. As described above, dark counts are not a problem in the experiments of this kit, so the detectors should be operated at maximum gain all the time (see Section 7.1.8).

Sometimes, a detection event does not generate a single output pulse from the detector but two or more pulses. This unwanted effect is called afterpulsing. There are several mechanisms that contribute to this effect. For our detectors, the probability of afterpulsing rises with increasing gain, but is low even at maximum gain. In the

experiments described in this manual, afterpulsing results in a slight overestimation of all detector count rates but does not meaningfully change any of the results.

## 4.2 Time Tagging

### 4.2.1 Time Tagging vs. Coincidence Electronics

A fundamental part of doing quantum optic experiments with a photon pair source is counting the coincidence events. There are two main technical implementations to determine whether two events are temporally close enough to be counted as a coincidence:

- 1.) Coincidence Electronics: By constructing a gated circuit with serial logic elements or on a field programmable gate array (FPGA), one can count events in which the pulses of two detectors arrive in a given coincidence window in real time.
- 2.) Time Tagging: A time tagging device associates every detector event with a very precise timestamp. The number of coincidences can then be calculated from the time differences derived from the timestamps.

Coincidence electronics can be designed in the price range of a few hundred dollars, while time tagging devices with the precision required for quantum optics are more expensive. However, time tagging also offers several advantages over coincidence electronics, most importantly flexibility. While coincidence electronics are often limited in their parameters (e.g., by the rate of the processor clock) and must be designed for the specific experiment, time tagging is only limited by the precision of the timestamps and different experiments can easily be accounted for by changing the calculation parameters. Additionally, time tagging electronics allows for more versatile post-processing: different input channels can be compared after the measurements were performed. In this kit, we use a time tagging device, hence the remainder of this section will focus on the specifics of time tagging. Please note that the time tagger in the kit has four active channels, which allows you to extend your range of experiments beyond the ones in the kit. If you need even more active channels, please contact Swabian Instruments.

### 4.2.2 Jitter and Coincidence Window

The time tagger assigns timestamps to both the rising and falling edges of the input pulses (only the rising edges are used in this kit). This association of the timestamps to events is never perfect. The deviation of the timestamp values of two channels relative to each other can be tested by applying a very stable periodic signal to both channels, measuring many events, and plotting the differences between the measured times of the two channels. Typically, the time differences will show a Gaussian distribution with a standard deviation of  $\sigma$ . The jitter is then defined as  $\sqrt{\frac{1}{2}}\sigma$ . For the educational version of the time tagger used in this kit, the jitter is specified to be <720 ps.

As the typical coincidence window for the experiments is several nanoseconds long, this jitter is acceptable. Research grade time taggers approach jitter levels as low as 1 ps.

Assume there are two channels of the time tagger called A and B and a user-defined tagger window of  $\Delta t_t$ . Whenever an event is counted on one of the two detectors at the time  $t_1$ , the window opens. If an event on the other detector is measured at a time  $t_2$  and  $t_2 - t_1 \leq \Delta t_t$ , a coincidence event is counted. It does not matter if the event is measured first at detector A or detector B. This scheme is shown in Figure 20. Please note that the window  $\Delta t_t$  (which is a parameter to control the time tagger) and the coincidence window  $\Delta t$  used in Section 3.5 (which is the full coincidence window describing when a count on B may come to generate a coincidence with a fixed count on A) differ<sup>50</sup> by a factor of 2:

$$\Delta t = 2 \cdot \Delta t_t$$

<sup>50</sup> This difference is handled automatically by the software. The input value is  $\Delta t$ .

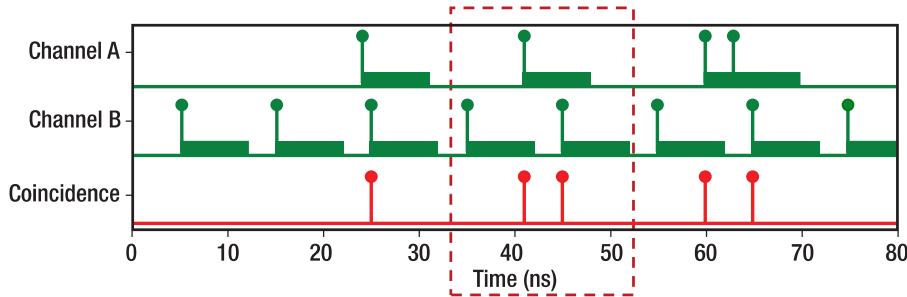


**Figure 20** Definition of a coincidence between two channels of the time tagger (bars mark the length of the coincidence window). The dashed rectangle marks an unwanted case of two coincidences created by only one event in Channel A.<sup>51</sup>

At first glance, this looks to be unsuitable for quantum optic applications, because a single detection event on one detector can cause two coincidence events, as marked with a red rectangle in Figure 20, while a single photon of a photon pair should cause a single coincidence count at maximum.

However, Figure 20 does not take the dead time of the detectors into account (see Section 4.1). This dead time is much larger than the coincidence window of a typical experiment, so the events on channel B in Figure 20 can never be close enough to cause the critical case marked with the red rectangle. Given this, the definition of coincidences as used by the time tagger is suitable for the experiments laid out in this manual.

In the quantum optics experiments in this kit, we often require triple coincidences between three channels T, A, and B, with T being the trigger detector indicating the presence of a single photon in the arm that includes detectors A and B. In this special case, triple coincidences are defined by a coincidence between the two-channel-coincidences T&A and T&B. Any two-channel coincidence event gets the time stamp of the earlier of its two counts, as seen in Figure 21.

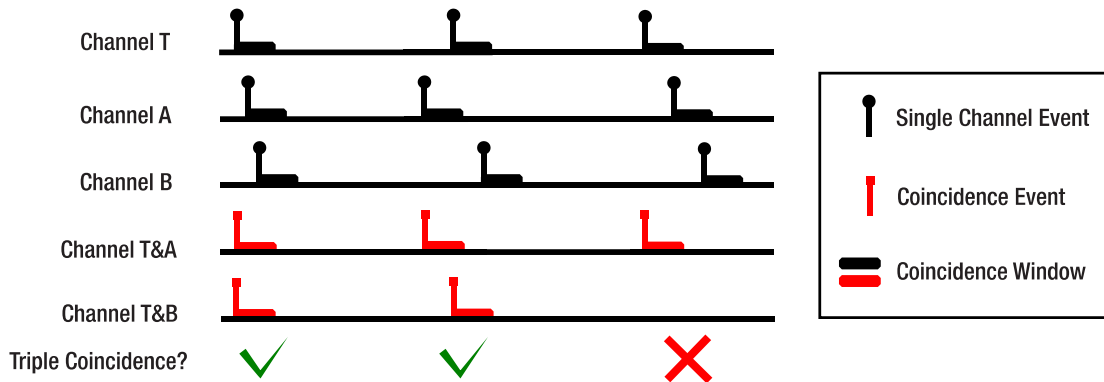


**Figure 21** Triple coincidence detection scheme. Between the second and third case, only the timing of the counts at T and A was exchanged, but the third case does not result in a triple coincidence as no two-channel coincidence between T&B is registered. This exemplifies the special role of the trigger detector in this scheme.

While triple coincidences can be defined in other ways and different detection schemes are possible, the method and definition here are the best fit for the experiments in this kit. More details are given in Section 12.1.

#### 4.2.3 Delay Compensation

If two or more detectors are connected to different channels of the time tagger, their signal will arrive at different times even if the events that caused the signals happened simultaneously. There are two causes for this:

<sup>51</sup> Figure copied from documentation of Time Tagger 20 by Swabian Instruments

- 1.) Arbitrary delays caused by jitter in the detectors and timing electronics.
- 2.) Systematic delays caused by different cable lengths, slight differences in detector circuits, differences in the path lengths to the detectors ( $30\text{ cm} \approx 1\text{ ns}$  for light in air), etc.

The systematic delays are often much larger than the arbitrary ones (on the order of several ns) but can be compensated for by just adding or subtracting a constant time from every timestamp on a given channel before calculating coincidences.

To determine the systematic delay offsets in this kit, we use the following method:

- Use a large coincidence window (20 ns or more) to find coincidences of photon pairs even with the systematic delays.
- Go back to a small coincidence window (5 ns), vary the delay of detectors A and B (compared to detector T) stepwise (0.5 ns step width) and record the number of coincidences between detectors T&A and T&B for every step. Figure 22 shows an example for such a measurement.
- The maximum number of coincidences for T&A (T&B) occurs at the delay of channel A (B) which offers the best compensation for the systematic delay differences. These delays are then used for all further measurements.

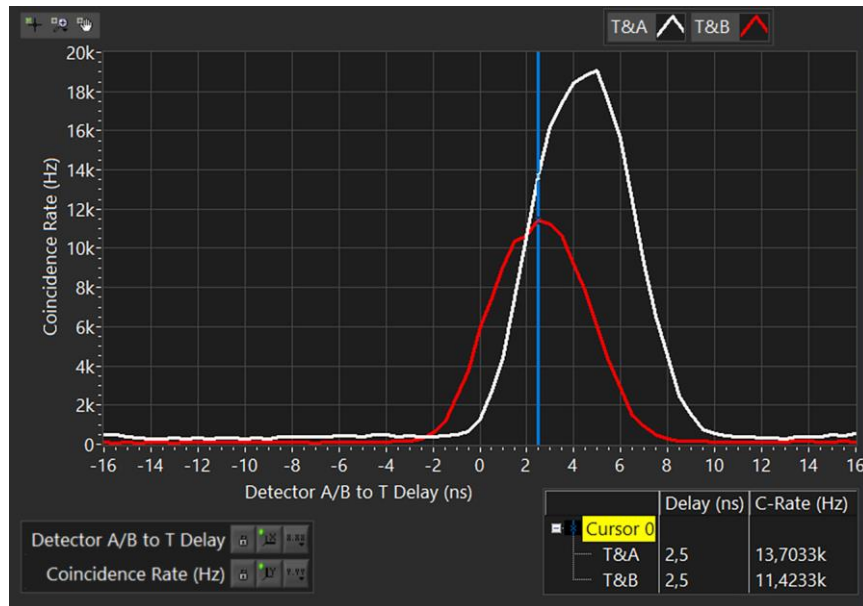


**Figure 22**      *Example measurement of detector delay. In this case, detector B has a delay of +2.5 ns compared to detector T.*

## Chapter 5 Kit Components

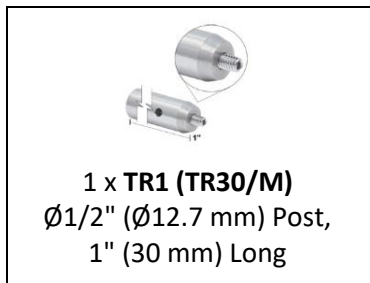
In cases where the metric and imperial kits contain parts with different item numbers, metric part numbers and measurements are indicated by parentheses unless otherwise noted.

### 5.1 Pump and Alignment Laser

			
<b>1 x LDM9T(/M)</b> Laser Diode Mount with Integrated Temperature Controller	<b>1 x L405P20<sup>52</sup></b> Laser Diode 405 nm, 20 mW	<b>1 x KLD101</b> K-Cube® Laser Diode Controller	<b>1 x C230TMD-A</b> Aspheric Lens, Mounted $f = 4.51$ mm, NA = 0.55
			
<b>1 x S1TM09</b> Lens Adapter SM1 to M9 x 0.5	<b>1 x TPS002</b> 15 V Power Supply for up to Two K-Cubes	<b>1 x CAB400</b> Cable, 9-Pin D-Sub 1.5 m Long	<b>1 x PL202</b> USB Laser Module 635 nm, 0.9 mW
			
<b>1 x AD11NT</b> Adapter without Threads for Ø11 mm Components	<b>1 x KM100CP(/M)</b> Kinematic Mirror Mount with Centering Plate for Ø1" Optics	<b>1 x DS5</b> USB Power Supply, 5 VDC	<b>1 x RS2P8E (RS2P4M)</b> Ø1" (Ø25.0 mm) Pedestal Post, 8-32 (M4) Tap, 2" (50 mm) Long
			
<b>1 x RS1.5P8E (RS1.5P4M)</b> Ø1" (Ø25.0 mm) Pedestal Post, 8-32 (M4) Tap, 1.5" (38 mm) Long	<b>1 x KB1X1 (KB25/M)</b> Magnetic Base, 1" x 1" (25 mm x 25 mm)	<b>1 x KBB1X1 (KBB25/M)</b> Magnetic Bottom Plate, 1" x 1" (25 mm x 25 mm)	<b>1 x PH1E<sup>53</sup></b> Ø1/2" (Ø12.7 mm) Pedestal Post Holder, Magnetic, 1.19" (30.1 mm) Long

<sup>52</sup> Pre-selected to be within ±1 nm. This laser diode comes with a spec sheet that includes the LIV curve.

<sup>53</sup> The EDU-QOP1/M kit comes with a 30.1 mm tall post holder. For a replacement, please contact Tech Support ([techsupport@thorlabs.com](mailto:techsupport@thorlabs.com)).



## 5.2 Crystal and Adjustment Aids

<p>1 x <b>NLCQ3</b> Ø1" Mounted β-BBO Crystal, 3.00 mm Thick, <math>\theta = 29.2^\circ</math></p>	<p>1 x <b>FGL515</b> Ø25 mm Colored Glass Filter, 515 nm Long Pass</p>	<p>2 x <b>KM100CP(M)</b> Kinematic Mirror Mount with Centering Plate for Ø1" Optics</p>	<p>1 x <b>Marked Mirror Mount<sup>54</sup></b> Kinematic Mirror Mount with Centering Plate with Extra Markings</p>
<p>1 x <b>KB1X1 (KB25/M)</b> Magnetic Base, 1" x 1" (25 mm x 25 mm)</p>	<p>2 x <b>KBT1X1 (KBT25/M)</b> Magnetic Top Plate, 1" x 1" (25 mm x 25 mm)</p>	<p>1 x <b>Axicon</b> Ø1/2", 3° Half Opening Angle of Light Cone for 635 nm</p>	<p>1 x <b>SM05L10</b> SM05 Lens Tube, 1" Thread Depth</p>
<p>1 x <b>SM05S5M</b> Ø1/2" Brass Optic Spacer, 5 mm in Length</p>	<p>1 x <b>SM05S10M</b> Ø1/2" Brass Optic Spacer, 10 mm in Length</p>	<p>1 x <b>AD1T</b> Ø1" OD Adapter for Ø1/2" Optics, Internally SM05 Threaded</p>	<p>1 x <b>PH1E<sup>55</sup></b> Ø1/2" (Ø12.7 mm) Pedestal Post Holder, Magnetic, 1.19" (30.1 mm) Long</p>
<p>1 x <b>TR1 (TR30/M)</b> Ø1/2" (Ø12.7 mm) Post, 1" (30 mm) Long</p>			

<sup>54</sup> This is a KM100CP(M) mount with extra engravings. For a replacement, please contact Tech Support ([techsupport@thorlabs.com](mailto:techsupport@thorlabs.com)).

<sup>55</sup> The EDU-QOP1/M kit comes with a 30.1 mm tall post holder. For a replacement, please contact Tech Support.

### 5.3 Optics

			
<b>4 x PF10-03-F01</b> Ø1" UV-Enhanced Aluminum Mirror	<b>4 x KM100</b> Kinematic Mirror Mount for Ø1" Optics	<b>4 x KCP1(/M)</b> Centering Plate for Ø1" Mirror Mounts	<b>5 x RS2P8E (RS2P4M)</b> Ø1" (Ø25.0 mm) Pedestal Post, 8-32 (M4) Tap, 2" (50 mm) Long
			
<b>1 x RS1.5P8E (RS1.5P4M)</b> Ø1" (Ø25.0 mm) Pedestal Post, 8-32 (M4) Tap, 1.5" (38 mm) Long	<b>1 x KB1X1 (KB25/M)</b> Magnetic Base 1" x 1" (25 mm x 25 mm)	<b>1 x CCM5-BS017(/M)</b> Mounted Beamsplitter, Non-Polarizing, Anti-Reflection Coated: 700 nm - 1100 nm	<b>1 x RS2.5P(/M)</b> Ø1" (Ø25.0 mm) Pedestal Post, 1/4"-20 (M6) Tap, 2.5" (65 mm) Long
			
<b>1 x Unmounted Iris<sup>56</sup></b> Ø15.0 mm Max Aperture, with 8-32 (M4) Stud	<b>1 x Unmounted Iris<sup>57</sup></b> Ø25.0 mm Max Aperture, with 3/4" (20 mm) Long 8-32 (M4) Setscrew	<b>1 x RSP1D(/M)</b> Rotation Mount for Ø1" Optics	<b>1 x WPH10ME-405</b> Ø1" Mounted Polymer Zero- Order Half-Wave Plate, SM1- Threaded Mount, 405 nm
			
<b>1 x LMR1(/M)</b> Ø1" Lens Holder	<b>1 x VRC4D1</b> Ø1" Visible and IR Alignment Disk	<b>1 x EDU-VS1(/M)</b> Polysterene Viewing Screen, 5.91" x 5.91"	<b>1 x SMR1(/M)</b> Ø1" Lens Mount with SM1 Internal Threads and No Retaining Lip

<sup>56</sup> This is a modified ID15(/M) iris where the TR3 (TR75/M) post is not included. For a replacement, please see the ID15(/M) iris on the website.

<sup>57</sup> This is a modified ID25(/M) iris where the TR3 (TR75/M) post is not included and a longer 8-32 (M4) setscrew is utilized. For a replacement, please contact Tech Support ([techsupport@thorlabs.com](mailto:techsupport@thorlabs.com)).

			
2 x <b>SM1D12D</b> SM1 Iris, Ring Actuated, Ø12 mm Max Aperture	1x <b>SM1CP2</b> Externally SM1-Threaded End Cap	1 x <b>SM05CP2</b> Externally SM05- Threaded End Cap	1 x <b>PH2E (PH50E/M)</b> Ø1/2" (Ø12.7 mm) Pedestal Post Holder, Magnetic, 2.19" (54.7 mm) Long
			
1 x <b>TR2 (TR50/M)</b> Ø1/2" (Ø12.7 mm) Post, 2" (50 mm) Long	1 x <b>PH1.5E (PH40E/M)</b> Ø1/2" (Ø12.7 mm) Pedestal Post Holder, Magnetic, 1.69" (44.7 mm) Long	2 x <b>TR1.5 (TR40/M)</b> Ø1/2" (Ø12.7 mm) Post, 1.5" (40 mm) Long	1 x <b>PH1E (PH30E/M)</b> Ø1/2" (Ø12.7 mm) Pedestal Post Holder, Magnetic, 1.19" (34.7 mm) Long
			
1 x <b>PH082E (PH20E/M)</b> Ø1/2" (Ø12.7 mm) Pedestal Post Holder, Magnetic, 1" (25 mm) Long	1 x <b>TR075 (TR20/M)</b> Ø1/2" (Ø12.7 mm) Post, 0.75" (20 mm) Long	1 x <b>RS4M (RS5M)</b> Spacer for Ø25 mm Posts, 4 mm (5 mm) Thick	2 x <b>RS10M</b> Spacer for Ø25 mm Posts, 10 mm Thick
			
1 x <b>RS3M (RS1M)</b> Spacer for Ø25 mm Posts, 3 mm (1 mm) Thick	1 x <b>RS06M</b> Spacer for Ø25 mm Posts, 0.6 mm Thick	1x <b>AP8E25E (AP6M4M)</b> Adapter with External 8-32 (M4 x 0.7) Threads and External 1/4"-20 (M6 x 1.0) Threads	1 x <b>SM1L03</b> SM1 Lens Tube, 0.3" Thread Depth
			
1 x <b>EBP1</b> Ø1" 30:70 Beamsplitter, AOI: 45°	1 x <b>NE30A</b> Ø25 mm Absorptive ND Filter, SM1-Threaded Mount, Optical Density: 3.0	1 x <b>SM1A1</b> Adapter with External SM05 Threads and Internal SM1 Threads	

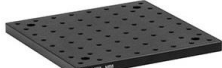
## 5.4 Detectors

			
<b>3 x SPDMA</b> Single Photon Detector 350 nm - 1100 nm $\varnothing 500 \mu\text{m}$ Detector Area	<b>3 x CXY1A</b> XY Translation Mount for $\varnothing 1"$ Optics	<b>3 x SM1NR05</b> SM1 Zoom Housing for $\varnothing 1/2"$ Optics	<b>3 x AC127-050-B</b> $\varnothing 1/2"$ Achromatic Doublet, f = 50 mm, Anti-Reflection Coated, 650 nm - 1050 nm
			
<b>3 x <math>\varnothing 1"</math> Bandpass Filter<sup>58</sup></b> CWL = $810 \pm 2$ nm, FWHM = $10 \pm 1$ nm	<b>3 x Graduated Iris<sup>59</sup></b> SM1 Ring-Actuated Iris, $\varnothing 12$ mm Max Aperture	<b>3 x SM1L05</b> SM1 Lens Tube, 0.5" Thread Depth	<b>3 x Dovetail Adapter</b>
			
<b>3 x DTSM1</b> External SM1 Threads to Female D4T Dovetail Adapter	<b>3 x SM1NT1</b> SM1 (1.035"-40) Locking Ring, 1.25" Outer Diameter, Slots for Spanner Wrench	<b>3 x PH2E (PH50E/M)</b> $\varnothing 1/2"$ ( $\varnothing 12.7$ mm) Pedestal Post Holder, Magnetic, 2.19" (54.7 mm) Long	<b>3 x TR2 (TR50/M)</b> $\varnothing 1/2"$ ( $\varnothing 12.7$ mm) Post, 2" (50 mm) Long
			
<b>3 x AP8E4M (Metric Kit Only)</b> Adapter with External 8-32 Threads and External M4 x 0.7 Threads			

<sup>58</sup> This bandpass filter is pre-selected to provide tighter specification of the bandpass window than our catalog products. If you need replacements, please contact Tech Support ([techsupport@thorlabs.com](mailto:techsupport@thorlabs.com)).

<sup>59</sup> This is a SM1D12C iris with extra engravings. For a replacement, please contact Tech Support.

## 5.5 Michelson Interferometer

			
<b>1 x MB8 (MB2020/M)</b> Aluminum Breadboard 8" x 8" (200 mm x 200 mm)	<b>1 x NFL5DP20S(/M)</b> 5 mm Travel Translation Stage with Differential Drive and 20 $\mu\text{m}$ Closed-Loop Piezo Driver	<b>1 x NFL5P1(/M)</b> Adapter Plate for Translation Stage	<b>1 x KPC101</b> K-Cube° Piezo Controller and Strain Gauge Reader
			
<b>2 x PF10-03-M01</b> $\varnothing 1"$ Protected Gold Mirror	<b>1 x KPS201</b> 15 V, 2.66 A Power Supply Unit with 3.5 mm Jack Connector for One K- or T-Cube	<b>2 x KM100</b> Kinematic Mirror Mount for $\varnothing 1"$ Optics	<b>1 x TR1.5 (TR40/M)</b> $\varnothing 1/2"$ ( $\varnothing 12.7$ mm) Post, 1.5" (40 mm) Long
			
<b>1 x KCP05(/M)</b> Centering Plate	<b>1 x RS1.5P8E (RS1.5P4M)</b> $\varnothing 1"$ ( $\varnothing 25.0$ mm) Pedestal Post, 8-32 (M4) Tap, 1.5" (38 mm) Long	<b>1 x RS6M</b> Spacer for $\varnothing 25$ mm Posts, 6 mm Thick	<b>1 x CCM5-BS017(/M)</b> Mounted Beamsplitter, Non-Polarizing, Anti-Reflection Coated: 700 nm - 1100 nm
			
<b>1 x RS2P(/M)</b> $\varnothing 1"$ ( $\varnothing 25.0$ mm) Pedestal Post, 1/4"-20 (M6) Tap, 2" (50 mm) Long	<b>1 x AP8E25E (AP6M4M)</b> Adapter with External 8-32 (M4 x 0.7) Threads and External 1/4"-20 (M6 x 1.0) Threads	<b>1 x RS3M</b> Spacer for $\varnothing 25$ mm Posts, 3 mm Thick	<b>1 x LEDMT1F</b> USB Powered LED Mount, 62 $\Omega$ Resistance, USB to Micro-B USB Cable Included
			
<b>2 x LED660L</b> LED, 660 nm, 13 mW, 18° Half Opening Angle FWHM: 14 nm	<b>1 x SMR05(/M)</b> Lens Mount without Retaining Lip for $\varnothing 1/2"$ Optics	<b>1 x SM05L10</b> SM05 Lens Tube, 1" Thread Depth	<b>1 x USB-C-72</b> 72" USB 2.0 Type-A Extension Cable

			
<b>1 x LMR1(/M)</b> Ø1" Lens Mount	<b>1 x LB1471</b> Ø1" Lens Biconvex $f = 50$ mm, Uncoated	<b>1 x Unmounted Iris<sup>60</sup></b> Ø8.0 mm Max Aperture, with 8-32 (M4) Stud	<b>2 x PH2E (PH50E/M)</b> Ø1/2" (Ø12.7 mm) Pedestal Post Holder, Magnetic, 2.19" (54.7 mm) Long

## 5.6 Time Tagger and Software

		
--	--	--

## 5.7 Quantum Eraser

			
<b>2 x LPNIRB050</b> Ø1/2" Unmounted Linear Polarizer, 650 - 1100 nm	<b>1 x LPNIRe100-B</b> Ø1" Unmounted Linear Polarizer, 600 nm - 1100 nm	<b>1 x WPH10ME-808</b> Ø1" Mounted Polymer Zero-Order Half-Wave Plate, SM1-Threaded Mount, 808 nm	<b>4 x RSP1D(/M)</b> Rotation Mount for Ø1" Optics

<sup>60</sup> This is a modified ID8(/M) iris for which the TR3 (TR75/M) post is not included. For a replacement, please see the ID8(/M) iris on the website.

			
<b>2 x SM1A6T</b> Adapter with External SM1 Threads and Internal SM05 Threads	<b>2 x RS1.5P8E (RS1.5P4M)</b> $\varnothing 1"$ ( $\varnothing 25.0$ mm) Pedestal Post, 8-32 (M4) Tap, 1.5" (38 mm) Long	<b>2 x RS2P8E (RS2P4M)</b> $\varnothing 1"$ ( $\varnothing 25.0$ mm) Pedestal Post, 8-32 (M4) Tap, 2" (50 mm) Long	<b>2 x RS4M (RS5M)</b> Spacer for $\varnothing 25$ mm Posts, 4 mm (5 mm) Thick
			
<b>2 x RS4M</b> Spacer for $\varnothing 25$ mm Posts, 4 mm Thick	<b>1 x PS3</b> 1/2" Tall Mounting Post Spacer		

## 5.8 Mounting and Tools

			
<b>5 x CF125-P5</b> Clamping Fork, 1.24" Counterbored Slot, Universal, 5 Pack	<b>2 x Clamping Fork</b> 0.40" Counterbored Slot, Universal	<b>2 x CL2(/M)</b> Heavy-Duty Variable Height Clamp, 1/4"-20 (M6) Tapped	<b>2 x CL5A</b> Table Clamp, L-Shape, Rounded Lip
			
<b>1 x SPW606</b> Spanner Wrench for SM1-Threaded Retaining Rings, Length = 1"	<b>1 x SPW909</b> Spanner Wrench for SM1-Threaded Adapters, Length = 1"	<b>1 x SPW603</b> Spanner Wrench for SM05-Threaded Retaining Rings, Length = 1"	<b>1 x SPW301</b> Spanner Wrench for Aspheric Lenses
			
<b>1 x SPW502</b> Spanner Wrench for Slotted SM05, SM1, and C-Mount Locking Rings	<b>1 x CS1</b> Screw-On Cable Straps (Qty. 15)	<b>1 x LG3</b> Laser Safety Glasses	<b>1 x Label Sheet</b>

## 5.9 Included Hardware

### 5.9.1 Imperial Kit

To Combine Components		To Mount Assemblies to Breadboard	
Type	Qty.	Type	Qty.
8-32, 1/4" Long Cap Screw	14	1/4"-20, 1/4" Long Cap Screw	14
8-32, 5/8" Long Cap Screw	1	1/4"-20, 3/8" Long Cap Screw	37
8-32, 1/2" Long Setscrew	2	1/4"-20, 1" Long Cap Screw	2
8-32, 5/8" Long Setscrew	1	1/4"-20, 2" Long Cap Screw	2
8-32, 3/4" Long Setscrew	5	1/4"-20, 2.5" Long Cap Screw	2
8-32, 1" Long Setscrew	1	1/4" Washer	100
<b>Hex Keys: 0.05", 1/16"</b>			
Ball Drivers			Slit Screwdriver
			
1 x <b>BD-5/64</b> 5/64" Ball Driver	1 x <b>BD-9/64</b> Ball Driver for 8-32 Cap Screws	1 x <b>BD-3/16</b> Ball Driver for 1/4"-20 Cap Screws	1 x <b>Screwdriver</b> 1.8 mm x 0.5 mm
			
1 x <b>1/4"-80 Removable Gold Knob</b>			

### 5.9.2 Metric Kit

To Combine Components		To Mount Assemblies to Breadboard	
Type	Qty.	Type	Qty.
M4 x 0.7, 6 mm Long Cap Screw	14	M6 x 1.0, 6 mm Long Cap Screw	14
M4 x 0.7, 16 mm Long Cap Screw	1	M6 x 1.0, 10 mm Long Cap Screw	37
M4 x 0.7, 12 mm Long Setscrew	2	M6 x 1.0, 25 mm Long Cap Screw	2
M4 x 0.7, 16 mm Long Setscrew	1	M6 x 1.0, 50 mm Long Cap Screw	2
M4 x 0.7, 20 mm Long Setscrew	5	M6 x 1.0, 65 mm Long Cap Screw	2
M4 x 0.7, 25 mm Long Setscrew	1	M6 Washer	100
<b>Hex Keys: 1.3 mm, 1.5 mm</b>			

Ball Drivers			Slit Screwdriver
			
<b>1 x BD-2M</b> 2 mm Ball Driver	<b>1 x BD-3M</b> Ball Driver for M4 Cap Screws	<b>1 x BD-5M</b> Ball Driver for M6 Cap Screws	<b>1 x Screwdriver</b> 1.8 mm x 0.5 mm
			<b>1 x 1/4"-80 Removable Gold Knob</b>

## Chapter 6 Quick Setup

This chapter provides a summary of the setup procedure for experienced users or as a reminder when rebuilding the setup several times. The assembly of the components is explained in Section 7.1 and a detailed guide to building the setup is provided in the remainder of Chapter 7.

### Preliminary Alignments (Section 7.2)

- Make sure that the pump laser is collimated.
- Make sure that the scales of all three polarizer elements are correctly calibrated (the scale should match the actual polarizer orientation). The process is described in Section 7.2.3.

### HBT Experiment with Alignment Laser (Section 7.3)

- Position the components as shown in Figure 23.

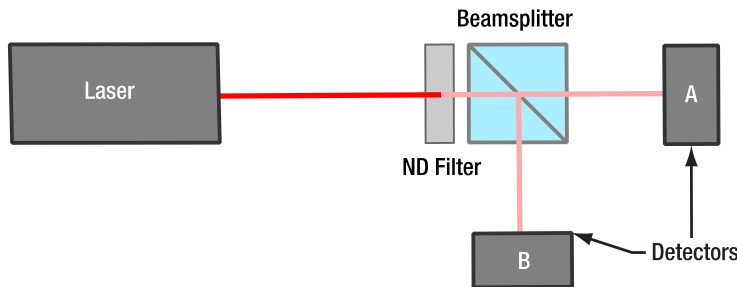


**Figure 23**      *HBT Experiment with Alignment Laser*

### Pair Source (Section 7.4)

- Position the components as shown in Figure 24.
- Make sure that the pump and alignment beam paths are identical (via a beam walk through the two iris apertures). Set the half-wave plate's fast axis to 45°.
- Use the axicon with the alignment laser to position the detectors in the light cone.
- Use the fluorescent filter to adjust the detector optics for maximum count rate.
- Use the BBO crystal and adjust the tilt (golden kinematic screw) for maximum coincidence count rate. If required, use a larger coincidence window (20 ns).
- Set the detector delay in the software.

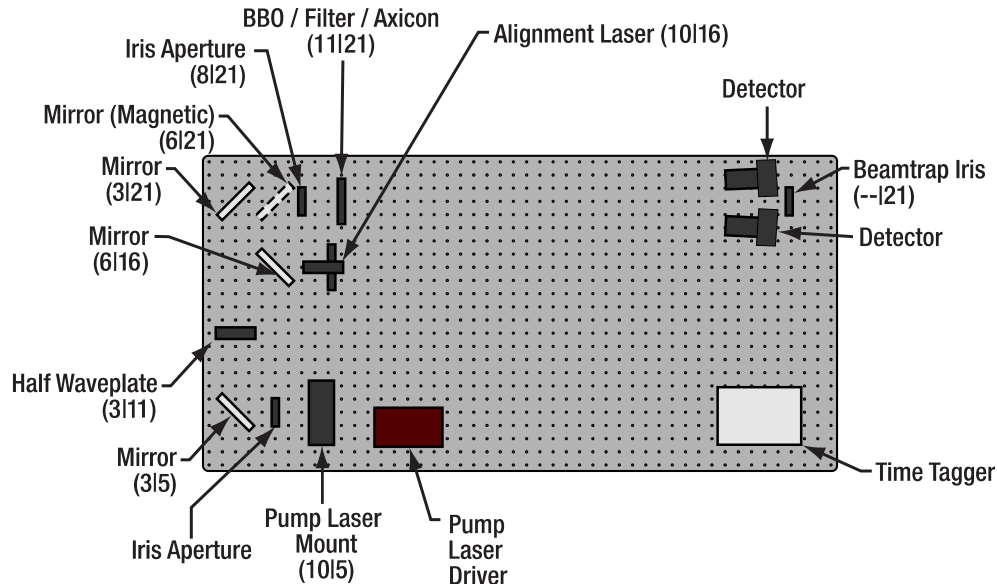


**Figure 24** Pair source setup. The numbers in parentheses are breadboard hole numbers (from left / from bottom).

### GRA Experiment (Section 7.5)

- Align a beamsplitter in the path to detector A and position detector B in the path of the other output of the beamsplitter.
- Position detector B analogously to detectors T and A (axicon → filter → BBO).
- Set the delay of detector B in the software.

### Michelson Interferometer (Section 7.6)

- Set up an additional alignment path between the BBO crystal and the beamsplitter with one additional iris aperture.
- Replace detector B with the Michelson interferometer on the small breadboard (see Figure 25)
- Adjust the interferometer with the alignment laser and red LED.
- Position detector B in the output of the interferometer. Align and set delay as before.
- Connect the stage to the KPC101<sup>61</sup> controller.

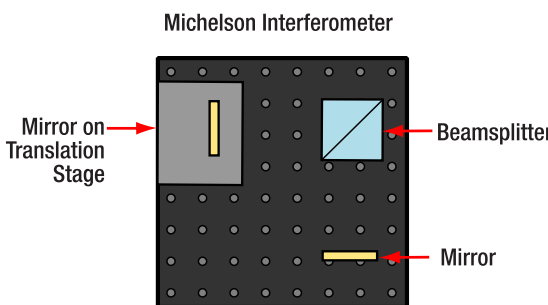


**Figure 25** Michelson Interferometer Board

### Quantum Eraser (Section 7.7)

- Insert a half-wave plate between the two beamsplitters and set it to 22.5°.
- Place the two 1/2" diameter polarizers in the arms of the interferometer and set them to 0°.
- Use the red LED to realign the interferometer.
- Figure 26 shows the complete setup.

<sup>61</sup> In previous versions of the kit, the stage is controlled via a combination of the now obsolete KPZ101 and KSG101 controllers. These controllers are still supported by the kit software.

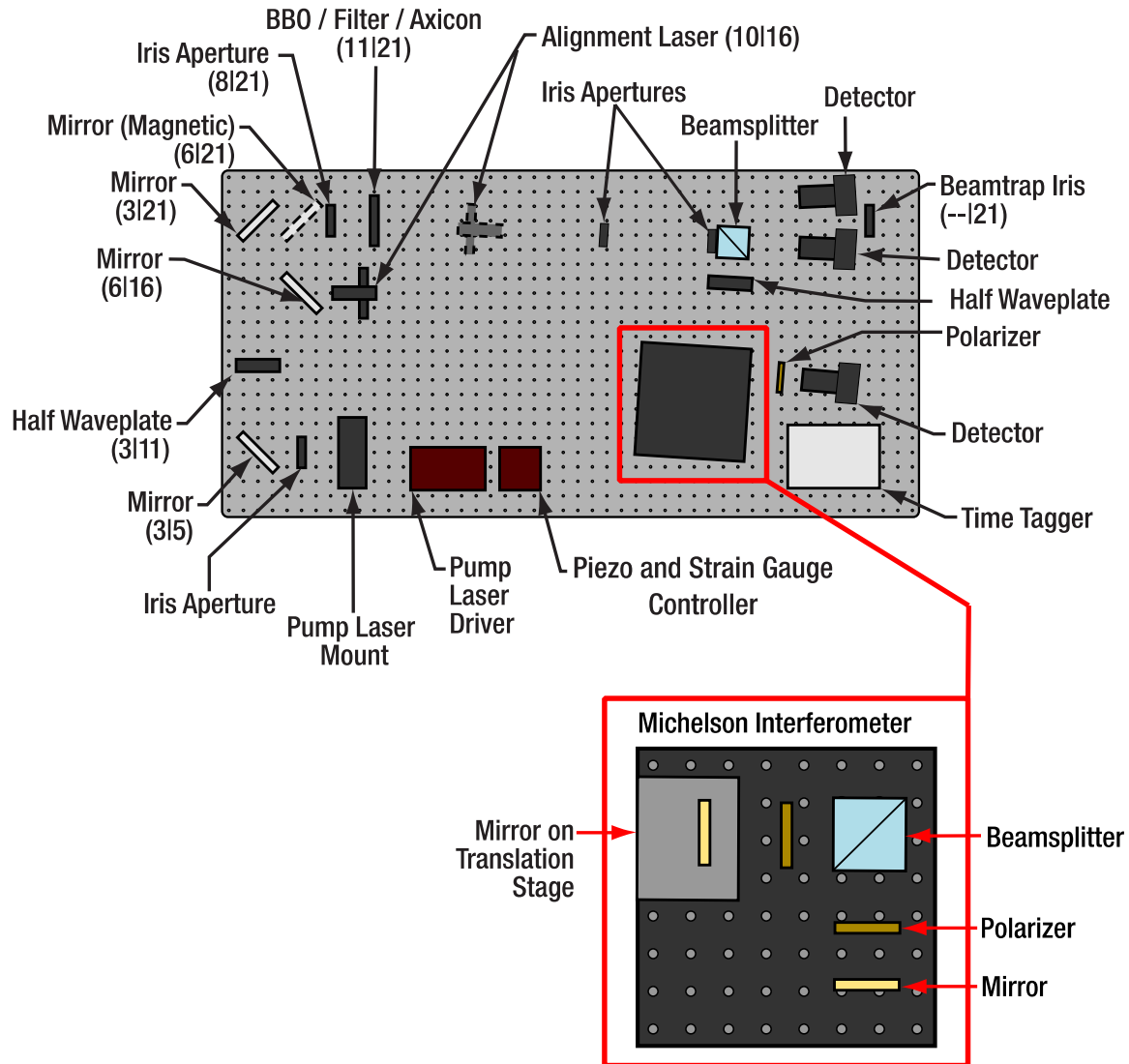


**Figure 26** Complete setup overview. The numbers in parentheses are breadboard hole numbers (from left / from bottom).

## Chapter 7 Setup and Adjustment

This chapter gives detailed and thorough instructions for setting up all the components and experiments in the kit. Chapter 6 offers a very brief summary for experienced users or repeated rebuilds.

### 7.1 Assembly of Components

#### 7.1.1 Pump Laser

- It is recommended that the user wears ESD protection equipment while assembling the pump laser to avoid damage to the laser diode via electric discharge.
- Take the LDM9T(/M) Laser Diode Mount and lay it on a table with the front plate pointing upwards. Remove the four screws in the corners of the front plate and take it off. On the inside of the diode mount are two switches for LD (Laser Diode) and PD (Photodiode). Both should be set to CG (Cathode Grounded) and the J2 jumper should not be connected, as shown in Figure 27.

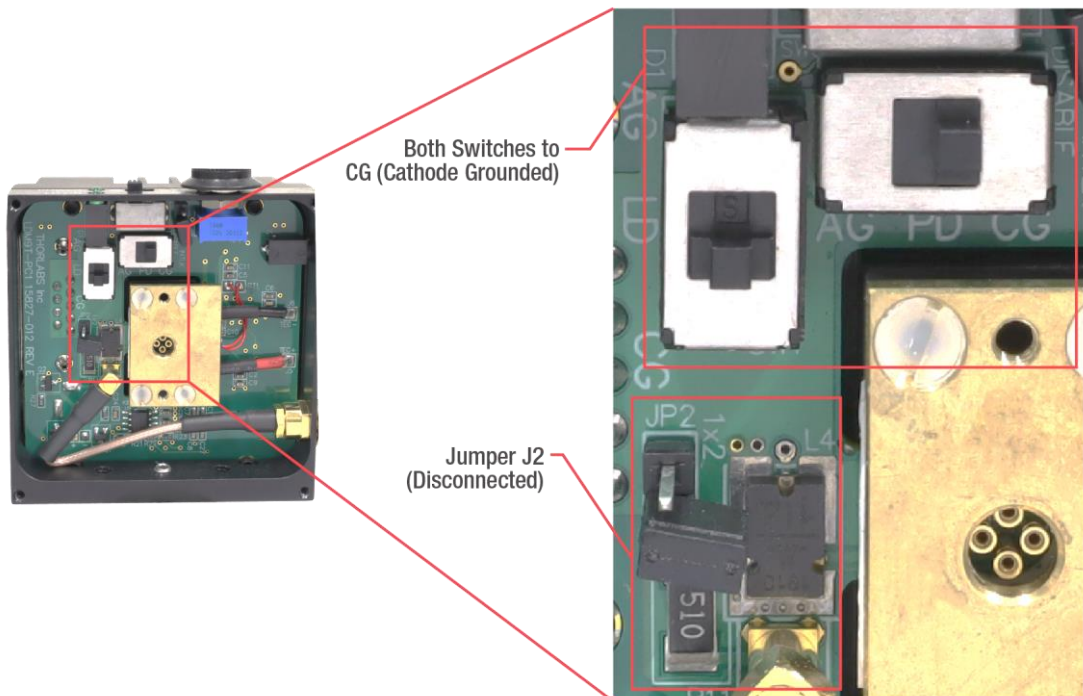


**Figure 27      Correct Switch Position of LDM9T(/M) Laser Diode Mount**

- Remove the mounting flange (if pre-installed) and assemble the pump laser as shown in Figure 28.
- Please note:
  - For steps 1-5, keep the LDM9T(/M) mount on a flat surface with the front face pointing upwards.
  - In step 1, fit the diode legs to the holes of the laser mount as shown in Figure 29.
  - The LDM9T(/M) mount comes with two different flanges. Use the smaller one in step 2.
  - During step 3, make sure that the front plate is centered on the mount.
  - Use the SPW301 spanner wrench for step 4 and the SPW909 spanner wrench for step 5.
  - During step 5, screw the S1TM09 adapter into the front plate until you notice an increased resistance due to the rubber lip of the S1TM09 adapter engaging the SM1 threading.

- During step 6, use a 5/64" (2 mm) hex key to screw the setscrew as far into the post as possible.
- In step 7, use the torque hole of the post to tighten the connection between LDM9T(/M) mount and the post.
- After completion, set the temperature of the controller to 25°C.
- The correct grounding option must also be selected for the KLD101 controller, see Section 7.2.2.

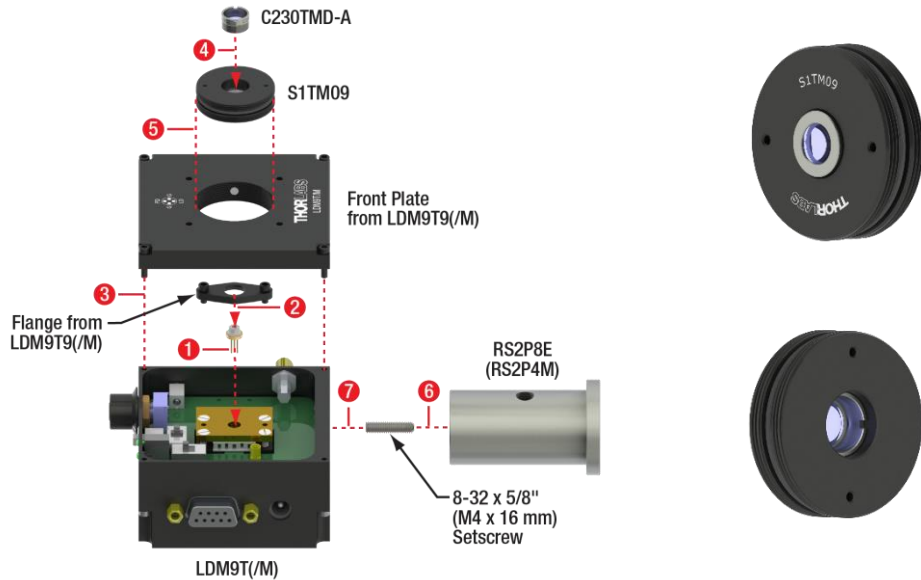


**Figure 28** Assembly of Pump Laser (Left) and Correct Orientation of the Lens (Right)

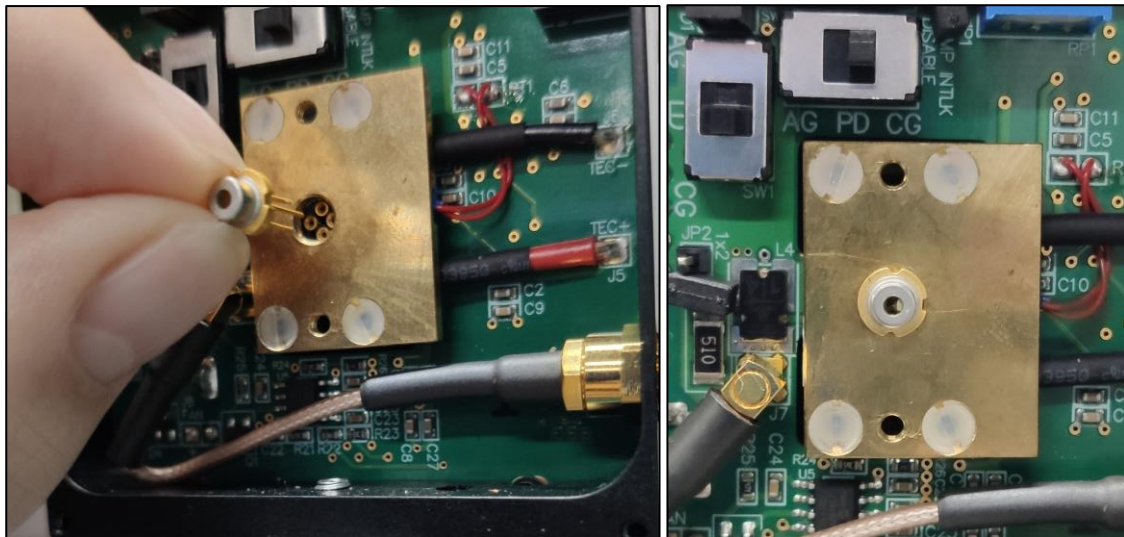


**Figure 29** Correct Mounting of L405P20 Laser Diode into LDM9T(/M) Mount

### 7.1.2 Alignment Laser

- Assemble the alignment laser and the second alignment base as shown in Figure 30.
- Please note:
  - The KM100CP(/M) mirror mount has two threaded bases. Attach the one labeled "Thorlabs" to the magnetic plate (as shown as step 2 in Figure 30). This allows better access to the adjusters when placed in the setup.
  - In step 3, use a 1/16" (1.5 mm) hex key to lock the PL202 laser in the AD11NT adapter.
  - The AD11NT adapter should be positioned approximately at the center of the PL202 laser.

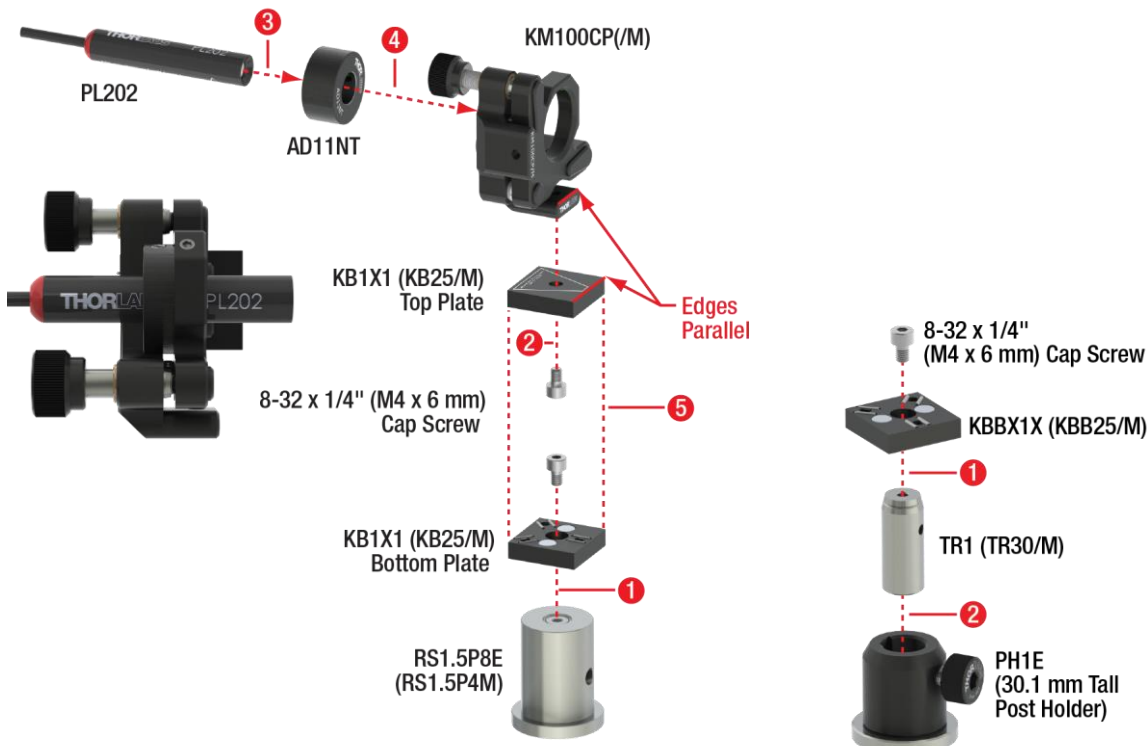


**Figure 30**      **Assembly of Alignment Laser (Left) and Finished Component (Left Inset) and Assembly of Second Alignment Base (Right)**

### 7.1.3 Mirrors

- Assemble two mirror setups as shown in Figure 31, one as shown in Figure 32, and one as shown in Figure 33.
- Please note:
  - The cap screws that connect the KM100 mount to the KCP1(/M) plate are included with the KM100 mount. The metric screws are colored black for easier distinction.
  - Take care to align the edges marked in the figures as parallel as possible.
  - Only touch the circumference of the mirrors, do not touch the mirror surface.
  - Use the nylon-tipped screw of the KM100 mount to hold the mirror in place.

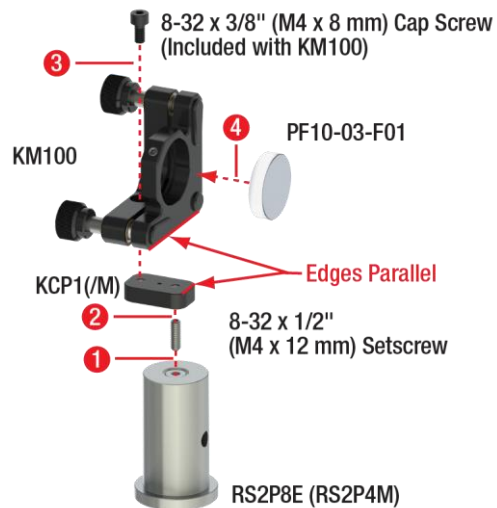


**Figure 31      First Mirror Assembly (Build Two)**

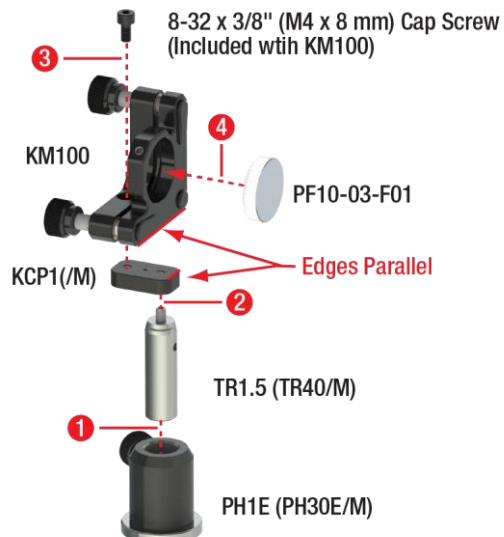


**Figure 32      Second Mirror Assembly (Build One)**

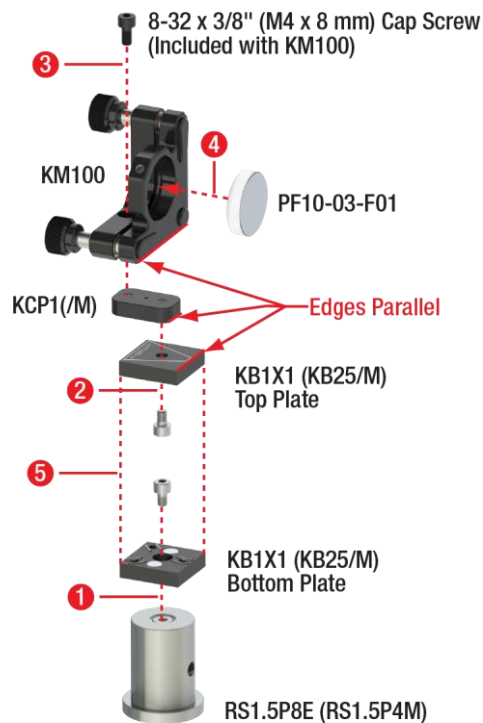


**Figure 33**      **Third Mirror Assembly (Build One)**

#### 7.1.4 Iris Apertures

- Assemble three iris aperture assemblies as shown in Figure 34.



**Figure 34**      **Iris Aperture Components**

#### 7.1.5 Half-Wave Plates

- Assemble the wave plates as shown in Figure 35.
- Please note:
  - During step 1, use the 5/64" (2 mm) balldriver to screw the setscrew as far into the RSP1D(/M) rotation mount as possible.
  - After completion, use the 5/64" (2 mm) balldriver to loosen the two locking screws on the front of the RSP1D(/M) mount, move the scale until the 0° setting is aligned with the fast axis marker on the wave plate, and re-tighten the locking screws. Do this for both wave plates.

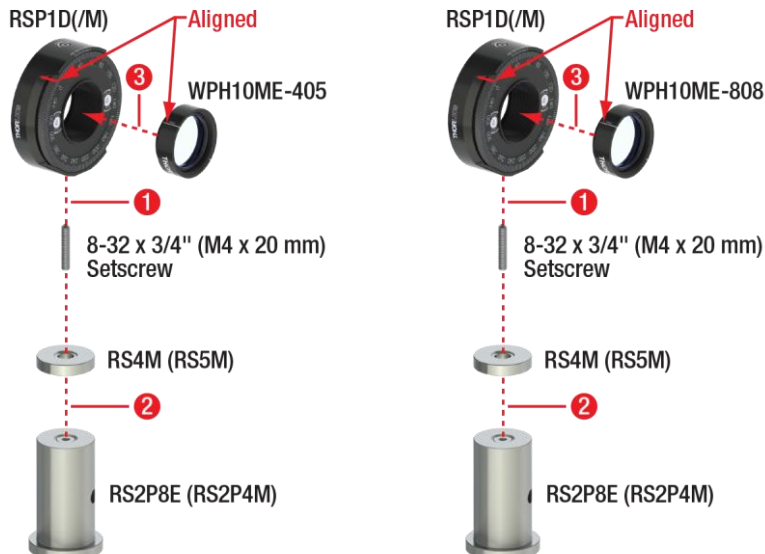


**Figure 35**      **Half-Wave Plate Components**

### 7.1.6 Crystal, Axicon, and Filter

- Remove the retaining ring from an SM05L10 lens tube and assemble the axicon as shown in Figure 36.
- Please note:
  - In step 1, the conical side of the axicon should face the bronze spacers (see Figure 37). Only touch the circumference of the axicon. Do not touch the axicon surface.
  - For step 2, use an SPW603 spanner wrench.
  - During step 5, take care to align the marked edges.

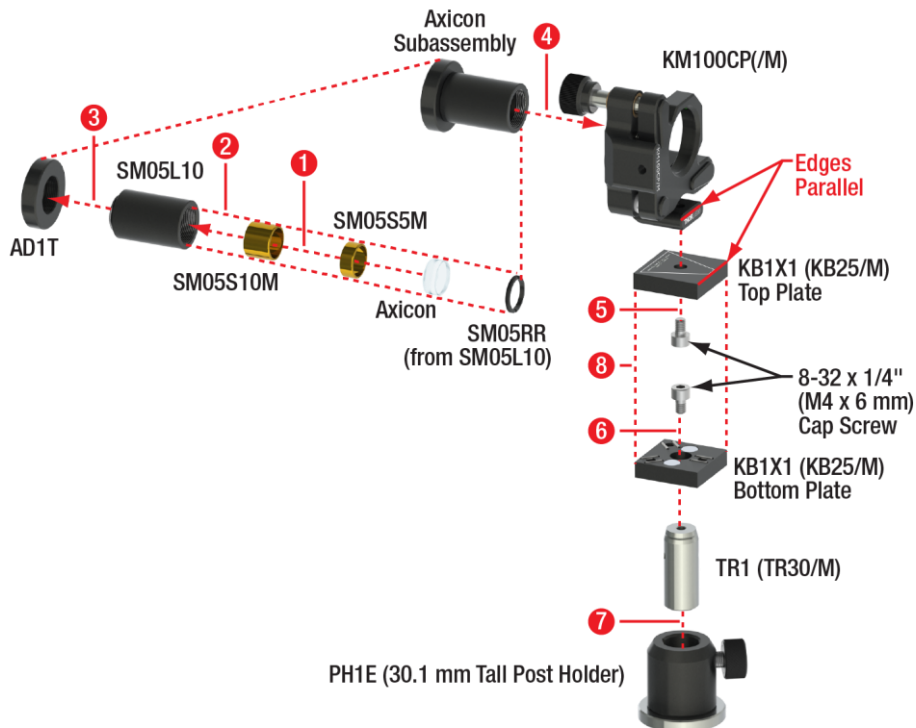


**Figure 36      Axicon Assembly**

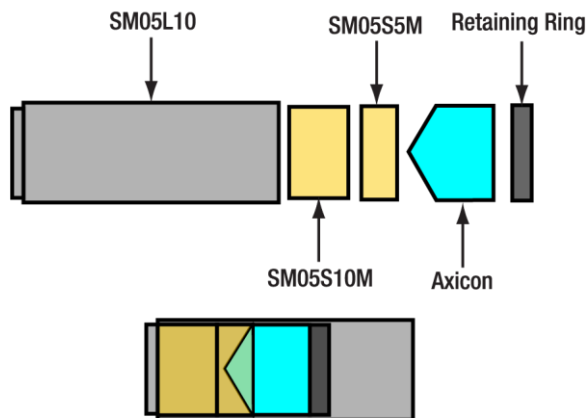


**Figure 37      Sketch of the elements of the axicon component before (upper image) and after (lower image) assembly. The axicon angle is strongly exaggerated.**

- Assemble the BBO Crystal as shown on the left side of Figure 38.
- Please note:
  - During step 1, make sure to align the marked edges as parallel as possible.
  - Make sure to align the crystal with respect to the markings on the KM100CP(M) mount as shown on the right side of Figure 38. Use the nylon-tipped screw of the KM100CP(M) mount to hold the crystal in place.
  - After completion, replace the black knob on the lower adjustment screw with a golden knob (see right side of Figure 38). Use the 5/64" (2 mm) balldriver to hold the lower adjustment screw in place while unscrewing or screwing the knobs.

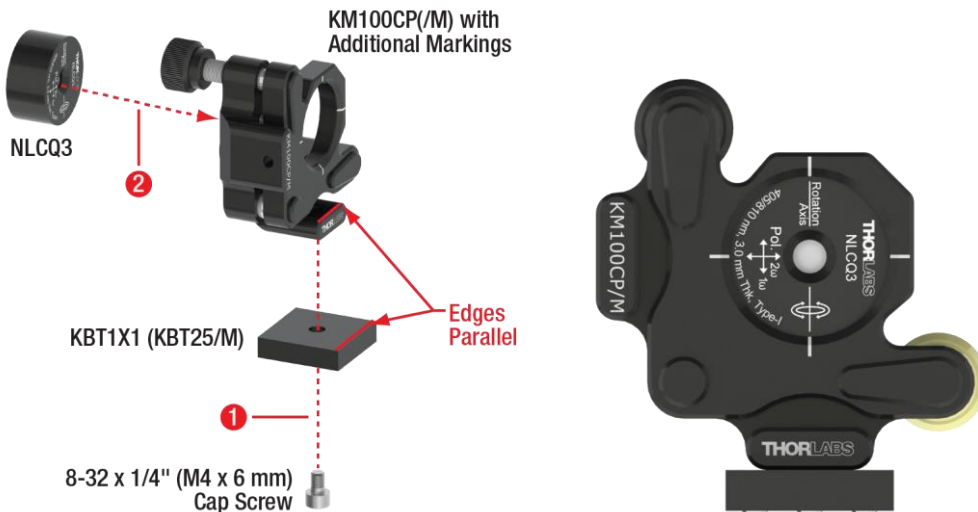


**Figure 38      BBO Crystal Assembly**

- Assemble the colored glass filter as shown in Figure 39.
- Please note:
  - During step 1, align the marked edges as parallel as possible.
  - During step 2, only touch the circumference of the glass filter; do not touch the filter surface. Use the nylon-tipped screw of the KM100CP(M) mount to hold the filter in place.



**Figure 39      Glass Filter Assembly**

### 7.1.7 Beamsplitter

- Assemble the beamsplitters as shown in Figure 40.
- Please note:
  - Before step 4 on the left side of Figure 40, use a 0.05" (1.3 mm) hex key to tighten the locking screw of the SM1D12 iris. This avoids damaging the iris blades during step 4. Loosen the locking screw after completing the assembly.

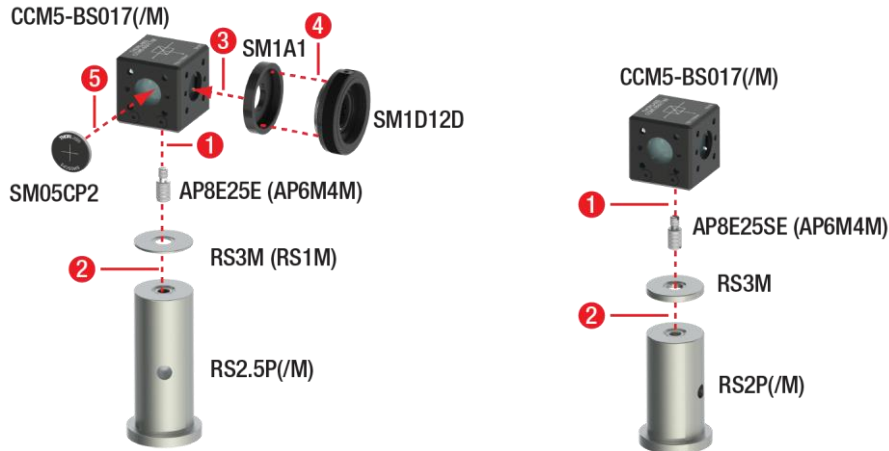


Figure 40 Beamsplitter Components

### 7.1.8 Detectors

- Remove the lens tubes from the three SPDMA detectors and assemble three detectors as shown on the left side of Figure 41.
- Please note:
  - After step 2, put a 5/64" (2 mm) ball driver through the hole in the TR2 (TR50/M) post and use it as a lever to strongly tighten the post against the SPDMA detector.
  - Use the flat head screwdriver to turn the gain screw of all three detector clockwise until a hard stop is reached (gain set to maximum), as seen on the right side of Figure 41.

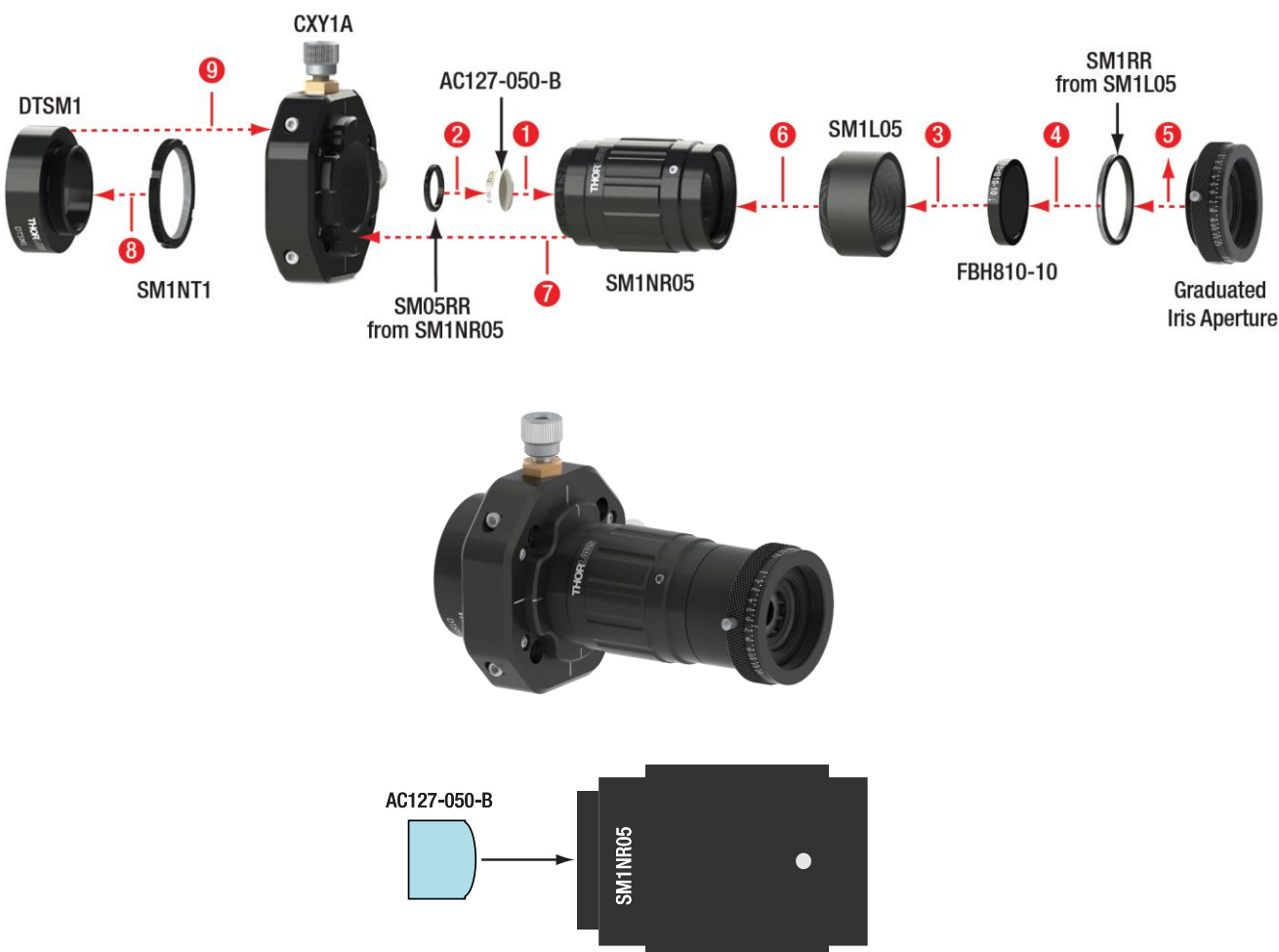


Figure 41 Detector Component (Build Three)

### 7.1.9 Detector Optics

- Assemble three detector optics as shown in Figure 42.
- Please note:
  - Before beginning the assembly, remove the SM05RR retaining ring from the SM1NR05 zoom housing and the SM1RR retaining ring from the SM1L05 lens tube.

- During step 1, the convex side of the lens should face the SM1NR05 zoom housing (see Figure 42). Only touch the circumference of the lens, do not touch the lens surface. Move the lens cell of the SM1NR05 zoom housing all the way outwards to facilitate the insertion of the lens.
- For step 2, use an SPW603 spanner wrench.
- During step 3, the arrow on the filter mount should point towards the lens tube. Only touch the circumference of the filter, do not touch the filter surface.
- For step 4, use an SPW606 spanner wrench.
- Before step 5, tighten the locking screw of the graduated iris<sup>62</sup> with a 0.05" (1.3 mm) hex key. This avoids accidentally damaging the iris blades. Loosen the locking screw after step 6.
- During steps 8 and 9, rotate the DTSM1 dovetail adapter such that its locking screw is located between both kinematic screws of the CXY1A mount, as seen in the bottom figure of Figure 42. Use the SPW502 spanner wrench to lock the rotation by screwing the SM1NT1 towards the CXY1A mount.



**Figure 42**      Exploded view (top) and assembled (middle) detector optics component (build three). The correct orientation of AC127-050-B lens in SM1NR05 zoom housing is shown on the bottom.

<sup>62</sup>This iris is a modified version of SM1D12C with additional engravings. If you need a replacement, please contact [techsupport@thorlabs.com](mailto:techsupport@thorlabs.com).

### 7.1.10 Beam Trap

- Assemble the beam trap as shown in Figure 43.
- Please note:
  - In step 1, screw the setscrew all the way into the SMR1(/M) mount. Use a 9/64" (3 mm) hex key.
  - Before step 3, use a 0.05" (1.3 mm) hex key to tighten the locking screw of the SM1D12 iris. This avoids damaging the iris blades during step 3. Loosen the locking screw after completing the assembly.



**Figure 43**      **Beam Trap Component**

### 7.1.11 Alignment Target

- Unscrew the retaining ring from an LMR1(/M) lens mount and assemble the alignment target as shown in Figure 44.
- For step 4, use an SPW606 spanner wrench.

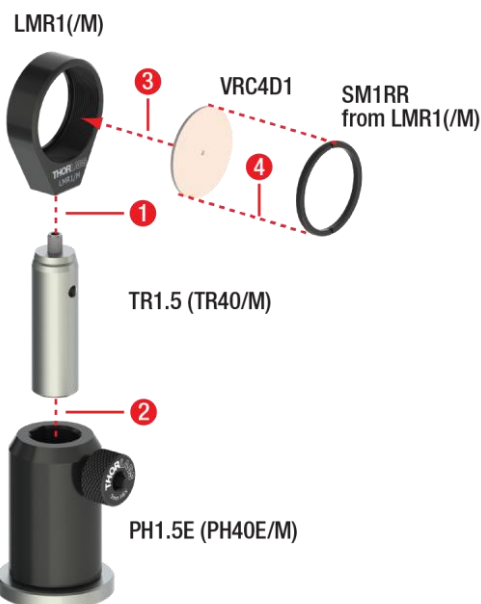


**Figure 44**      **Alignment Target Component**

### 7.1.12 Economy Beamsplitter

- Remove the retaining ring from an SM1L03 lens tube and assemble the economy beamsplitter as shown in Figure 45.
- Please note:
  - Only touch the circumference of the beamsplitter. Do not touch the beamsplitter surface.
  - For step 2, use an SPW606 spanner wrench.



**Figure 45** Economy Beamsplitter Component

### 7.1.13 Screen

- Assemble the screen as shown in Figure 46.

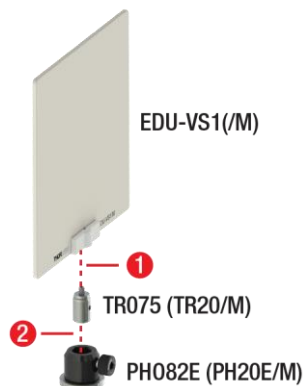


**Figure 46** Screen Component

### 7.1.14 Mirrors for Michelson Interferometer

- Assemble the mirror on the stage as shown in Figure 47.
- Please note:
  - During step 2, make sure that you are using the correct screw length. Longer screws may damage the stage!
  - During steps 2 and 3, make sure that the edges marked in Figure 47 are aligned as parallel as possible.
  - During step 4, only touch the circumference of the mirror, do not touch the mirror surface. Use the nylon-tipped screw of the KM100 to hold the mirror in place.

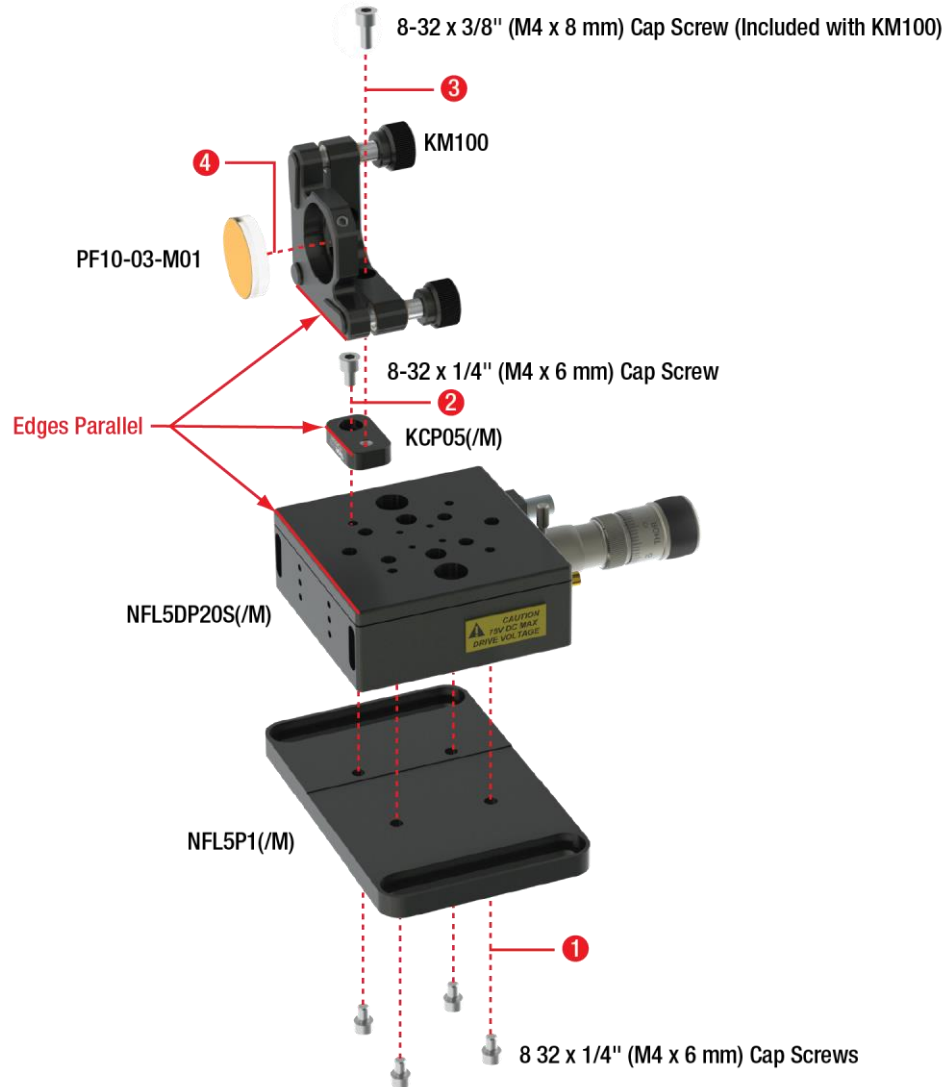


**Figure 47      First Mirror for Michelson Interferometer**

- Assemble the second mirror for the Michelson interferometer as shown in Figure 48.
- Please note:
  - During step 2, only touch the circumference of the mirror, do not touch the mirror surface. Use the nylon-tipped screw of the KM100 mount to hold the mirror in place.

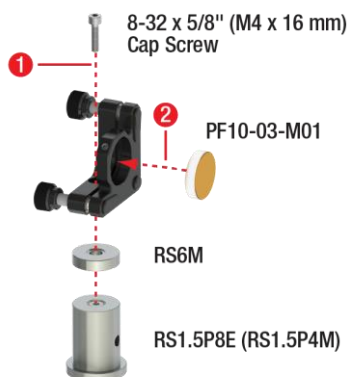


**Figure 48      Second Mirror for Michelson Interferometer**

### 7.1.15 Lens

- Unscrew the retaining ring from an LMR1(/M) lens mount and assemble the alignment lens as shown in Figure 49.
- Please note:
  - During step 3, make sure to touch the lens only on the outer circumference. Do not touch the lens surface.
  - For step 4, use an SPW606 spanner wrench.



**Figure 49**      **Lens Component**

### 7.1.16 Mounting the LED

- Assemble the LED as shown in Figure 50.
- Please note:
  - During step 3, take care of the polarity of LED and mount. The correct orientation is shown in Figure 51.

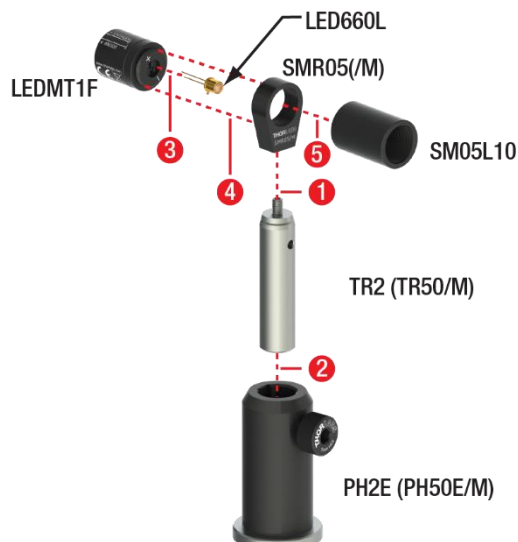


**Figure 50**      **LED Assembly**



**Figure 51**      **Polarity of LED**

### 7.1.17 Polarizers for Quantum Eraser

- Remove the retaining ring from an RSP1D(M) mount and assemble a polarizer component as shown in Figure 52.
- Please note:
  - During step 1, use a 5/64" (2 mm) hex key to screw the setscrew as far into the RSP1D(/M) mount as possible.
  - During step 3, make sure to touch the polarizer only on the outer circumference. Do not touch the polarizer surface.
  - During step 4, use an SPW606 spanner wrench.



**Figure 52**      **Large Polarizer Assembly**

- Remove the retaining rings from two RSP1D(/M) mounts and assemble two polarizer components as shown in Figure 53.
- Please note:
  - During step 1, use a 5/64" (2 mm) hex key to screw the setscrew as far into the RSP1D(/M) mount as possible.
  - The SM1A6T adapter contains two retaining rings. Instead of removing them both and then do step 3, just remove only one.
  - During step 4, make sure to touch the polarizer only on the outer circumference. Do not touch the polarizer surface.
  - During step 5, use an SPW603 spanner wrench.
  - During step 6, use an SPW909 spanner wrench.

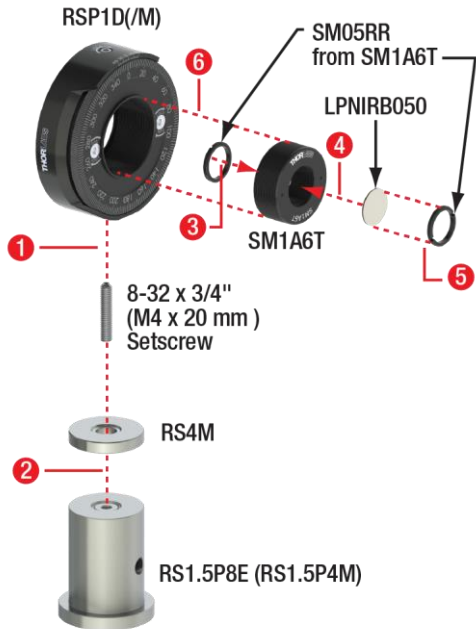


**Figure 53      Small Polarizer Assembly**

#### 7.1.18 Labelling the Time Tagger

- Use the label sheet to label the first three channels of the Time Tagger as shown in Figure 54.
  - Channel 1 → T
  - Channel 2 → A
  - Channel 3 → B



**Figure 54      Time Tagger Labels**

- Label the three detectors with labels T, A, and B, respectively as shown for detector B in Figure 55. Labeling is optional, however in the remainder of this manual we will refer to the detectors as "detector T," etc.



**Figure 55      Detector Labeling**

## 7.2 Preliminary Alignment

### 7.2.1 Software Installation

- Install the software of the kit as described in Section 11.1.

### 7.2.2 Collimating the Pump Laser

- Place the pump laser on the left side of the breadboard pointing to the right and secure its position with a CF125 clamp and a 1/4"-20 x 3/8" (M6 x 10 mm) cap screw plus washer. Connect the power supply provided with Item # LDM9T/(M) to the laser mount.
- Remove the KLD101 laser controller from its baseplate by opening the clamps. Mount the baseplate to the breadboard on the position marked in Figure 56 via two 1/4"-20 x 3/8" (M6 x 10 mm) cap screws plus washers. Connect the KLD101 controller to the baseplate and close the clamps.

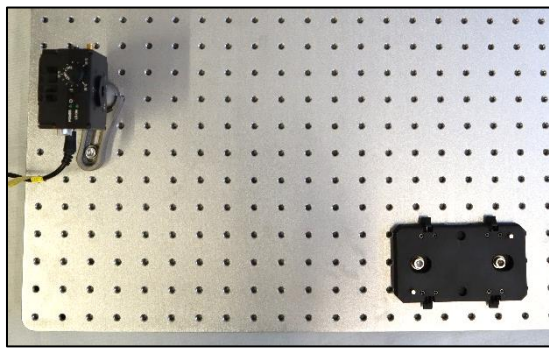


**Figure 56      Position of KLD101 Baseplate**

- Connect the KLD101 laser controller to the power grid via the TPS002 power supply and to the LDM9T/(M) mount via the CAB400 cable. Switch on both the laser mount and driver.
- Use the wheel menu of the KLD101 controller to select **2: Polarity** and make sure that the setting is **Cathode Grounded**.
- Use the wheel menu of the KLD101 controller to select **3: Max Current** and set the maximum current to 50 mA, as seen in Figure 57.



**Figure 57 Maximum Current Setting for the KLD101 Controller**

- Turn the key on the KLD101 controller and set the laser current to 15 mA by turning the wheel on the controller.
- In the next step, the laser will be switched on. **You should always wear laser safety glasses when the pump laser is turned on!** Hold a sheet of white paper in front of the laser and press the *Enable* button on the KLD101 controller. If the pump laser hits white paper, the paper will show green fluorescence that can be seen through the glasses.
- You will see some super-luminescent light, but not yet lasing. Carefully increase the laser current until the intensity jumps to a higher level, indicating you have crossed the laser's threshold. Use this setting for beam alignment. You can use the datasheet that ships with your laser diode as a reference for the threshold current.
- Fix one of the alignment cards that are included with the controllers to the front of the screen component and position it about 20 cm to the right of the laser, as seen in Figure 58. The laser should now hit the screen, as seen in Figure 59. If you do not see any light on the screen, the laser is too divergent. In this case, move the screen closer until you see the laser.

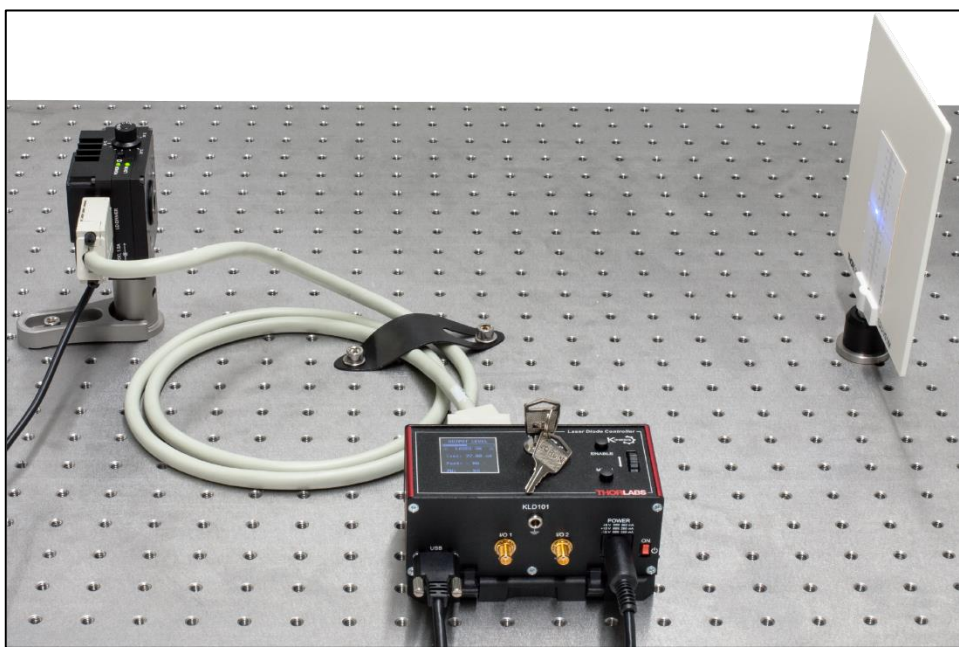


**Figure 58 Basic Collimation Setup**

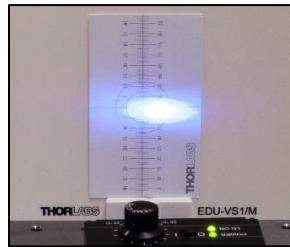


**Figure 59**      **Laser on Screen Before Collimation**

- Use the SPW909 spanner to rotate the lens adapter in front of the pump laser clockwise to change the lens position, decreasing the laser divergence until the laser on the screen looks like the one in Figure 60.

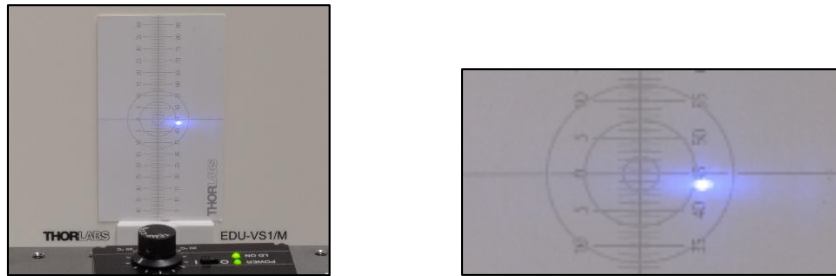


**Figure 60**      **Laser Spot on Screen After Collimation (Left) and Zoomed View (Right)<sup>63</sup>**

- Increase the distance between the screen and the laser by about 30 cm and check if the size of the spot on the screen changes in the process. Adjust the lens position to achieve a uniform beam profile over the whole distance from laser to screen, i.e., a collimated beam. Make sure that there is no focus between the laser and the screen. If there is one, you did not move the lens close enough to the diode. In that case, turn the adapter clockwise a bit more.
- Sometimes, the laser diode emits at a small angle. In this case you might not be able to hit the screen at larger distances because the beam height becomes too high or low. If that happens, turn the laser so that it emits in direction of the far breadboard edge and use a mirror angled at 45° to reflect the laser towards the screen<sup>64</sup>. You can now correct the beam deviation with the kinematic screws of the mirror so that the beam has a constant height after the mirror and is visible on the screen, as seen in Figure 61.



**Figure 61**      **Collimation Setup for Compensation of Deviating Emission Angle**

<sup>63</sup> This photo was taken with a camera. If you wear the laser safety goggles (as you should at this point!) the laser spot will look slightly different in color and brightness.

<sup>64</sup> Alternatively, you can slightly offset the front plate of the laser diode mount by loosening (not unscrewing) the 4 screws that hold it. This slightly moves the collimating lens in relation to the diode and may improve the angle deviation as well as the beam profile (more symmetric). Retighten the screws after you have found a suitable front plate position.

- Once you achieve a similar spot size on the screen directly after the laser and in 30 cm distance, move the screen all the way across the breadboard. Fine-tune the lens adapter on the laser mount until you see a laser spot like the one in Figure 60 over the whole path<sup>65</sup>.
- Switch off the laser driver and laser mount.
- Move the pump laser (in the LDM9T(/M) laser mount) to the 10<sup>th</sup> breadboard hole from the left and the 5<sup>th</sup> breadboard hole from the front, pointing towards the left edge of the breadboard as shown in Figure 71. Secure it with a CF125 clamp and a 1/4"-20 x 3/8" (M6 x 10 mm) cap screw plus washer. Use a CS1 cable straps and 1/4"-20 x 1/4" (M6 x 6 mm) cap screws plus washers to secure the power cable and the CAB400 to the breadboard as shown in Figure 71.

### 7.2.3 Calibrating the Polarizer

The goal of this procedure is to ensure that the scale of the Ø1" polarizer is calibrated<sup>66</sup>. We use the fact that the light of the alignment laser is linearly polarized (with unknown axis).

- Position the alignment laser on the left side of the breadboard, pointing to the right. Secure its position with a CF125 clamp and a 1/4"-20 x 3/8" (M6 x 10 mm) cap screw plus washer. Connect the USB cable of the alignment laser to a PC or to the power grid via the DS5 power adapter. Switch on the alignment laser.
- Position the polarizer with the 1" diameter in the alignment laser beam path and put the screen component behind the polarizer, as seen in Figure 62.

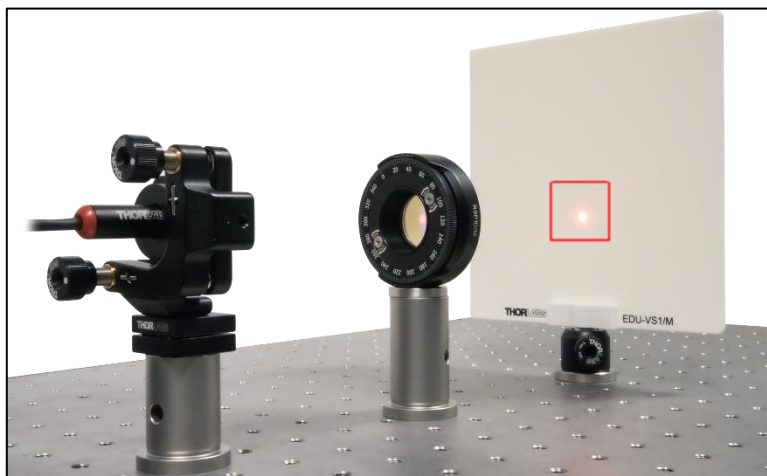
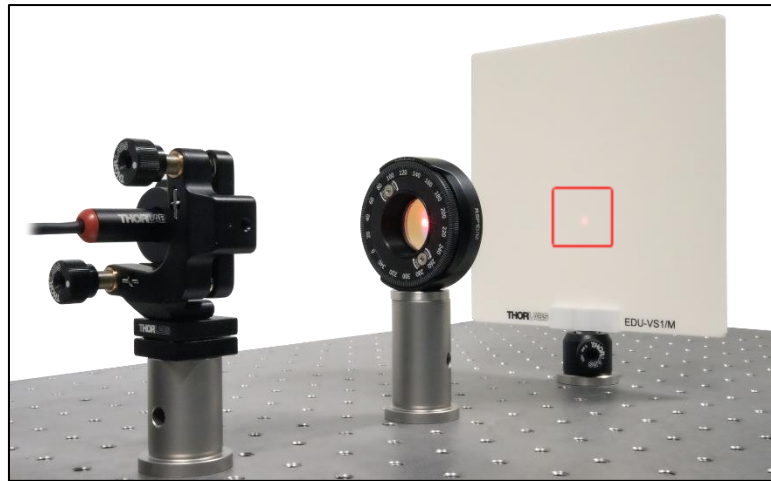


**Figure 62      Initial Position for Polarizer Calibration**

- Rotate the polarizer until the intensity on the screen is minimized and note the value on the polarizer scale (122° in the example in Figure 63).

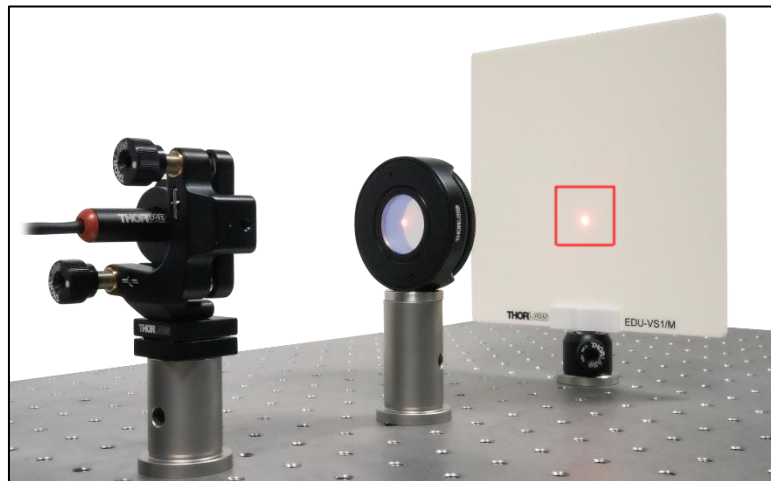
<sup>65</sup> The position of the LDM9T(/M) front plate has significant influence on the collimation. If the spot is very asymmetric or you feel that you cannot obtain good collimation, try to loosen the 4 screws of the front plate and move the plate around until the profile is more symmetric. Re-Tighten the front plate screws in this position and continue with the collimating procedure.

<sup>66</sup> A video detailing the process is available at: [https://www.thorlabs.com/newgroupage9.cfm?objectgroup\\_id=14062#VideoPolarizerHVAlign](https://www.thorlabs.com/newgroupage9.cfm?objectgroup_id=14062#VideoPolarizerHVAlign)



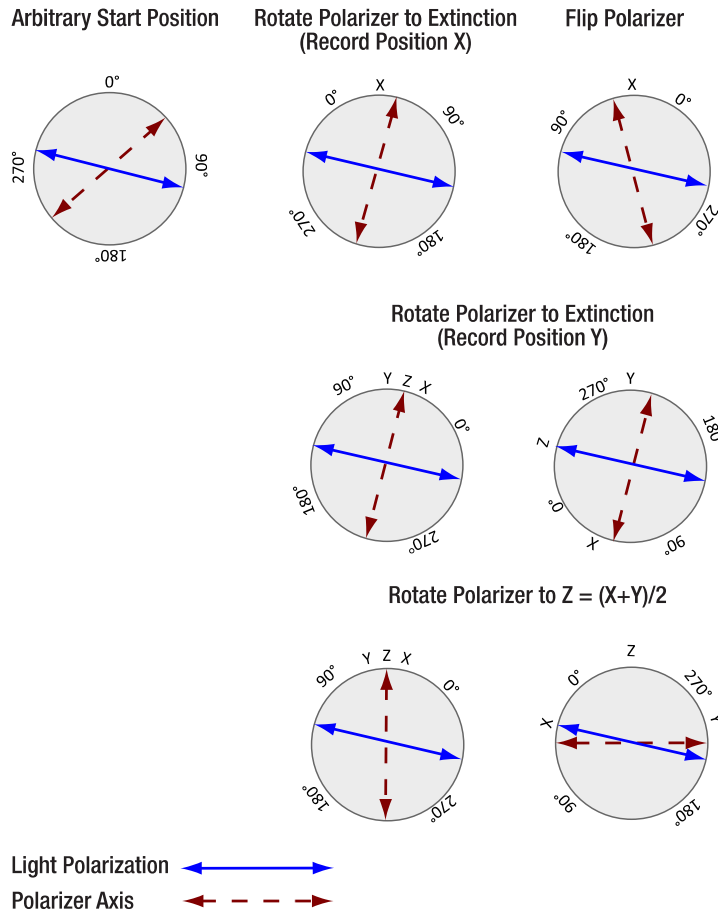
**Figure 63      Polarizer after Minimizing Transmission**

- Switch the front and back sides of the polarizer component, as seen in Figure 64.



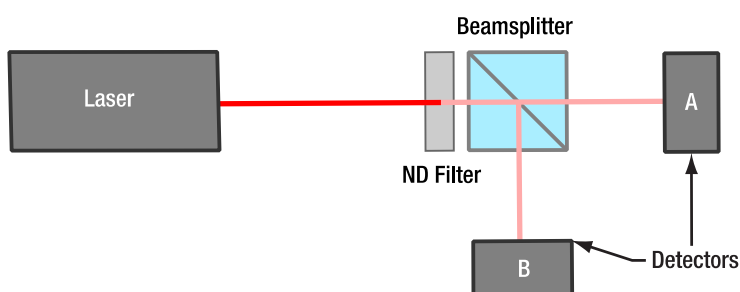
**Figure 64      Polarizer after Rotation**

- Rotate the polarizer until the intensity on the screen is minimized and note the value on the scale.
- Rotate the polarizer to the position exactly in the middle of the two scale values you noted, then tighten the locking screw of the rotation mount.
- Loosen the two screws on the front face of the rotation mount and rotate the scale until the current position is  $0^\circ$ . Retighten the two screws.
- You have now aligned this polarizer to be oriented either perpendicular or parallel to the table plane in the  $0^\circ$  setting. You will later determine which of the two directions it is.
- Figure 65 shows a schematic of this method and why it ensures that the polarizer is s- or p-polarized.

**Figure 65** Schematic of the Polarizer Calibration Procedure

### 7.3 Setting Up the HBT Experiment with the Alignment Laser

As a first experiment, it is recommended to show that an attenuated laser is not suitable as a single photon source. The experimental setup is shown schematically in Figure 66.

**Figure 66** Schematic of the HBT Experiment with the Alignment Laser

Set this experiment up as follows:

- Place the alignment laser component on the left side of the breadboard, pointing towards the right side. Secure it with a CF125 clamp and a 1/4"-20 x 3/8" (M6 x 10 mm) cap screw plus washer.
- Place the beamsplitter component with the attached iris aperture in the beam path of the alignment laser, about 20 cm away (iris facing the laser).
- Position the alignment target halfway between the alignment laser and the beamsplitter.

- Switch on the alignment laser and move the alignment target until the hole is hit by the laser.
- Move and rotate the beamsplitter until the laser passes the center of the iris **and** the reflection from the beamsplitter passes back through the hole in the target<sup>67</sup>. Secure the beamsplitter with a CF125 clamp and a 1/4"-20 x 3/8" (M6 x 10 mm) cap screw plus washer.
- Connect the lens tube with the economy beamsplitter (see Figure 45) to the detector labeled "A." Position the detector in the transmission path of the beamsplitter, about 20 cm away.
- Place the alignment target about 10 cm in front of the detector so that the laser passes through the hole. Now adjust the height, position, and angle of the detector in such a way, that **both**:
  - The reflection from the economy beamsplitter passes back through the hole of the target.
  - The light passing the hole of the target is centered on the detector chip, as seen in Figure 67.



**Figure 67**      *Laser Spot Centered on Detector Chip (Shown without Economy Beamsplitter, see Figure 82 for an Image with the Economy Beamsplitter)*

- Figure 68 shows the back side of the target before alignment. The clear red spot is the reflection from the beamsplitter. There can also be a diffuse red spot, which is the reflection from the detector chip that can be ignored.

<sup>67</sup> In case the alignment laser does not emit a beam parallel to the table plane, the reflection of the beamsplitter may always be above or below the hole in the target. In this case, use the upper adjuster of the laser mount to roughly align the laser parallel to the table plane.

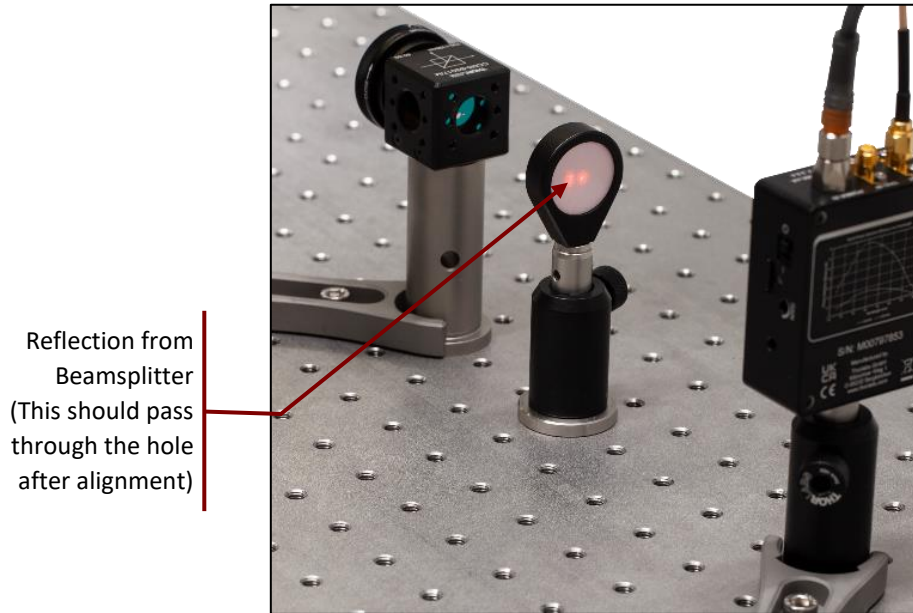


**Figure 68 Back Side of the Alignment Tool Prior To Detector Alignment**

- Secure the position of the detector with a CF125 clamp and a 1/4"-20 x 3/8" (M6 x 10 mm) cap screw plus washer. Then remove the lens tube with the beamsplitter from the detector.
- Repeat the same procedure with the detector labeled "B" in the reflection path of the beamsplitter.
- Screw the NE30A neutral density filter on the iris aperture.
- Take one of the prepared detector optics and loosen the locking screw of the DTSM1 dovetail adapter almost completely. Slide it over the dovetail adapter on the front of the detector labeled "A." Rotate the optics until one of the adjusters is pointing straight upwards and the other one is pointing away from you. Then tighten the locking screw of the DTSM1 coupler to securely connect the optics to the detector.
- Repeat this step for the detector labeled "B."
- Connect the detectors to the power grid via the included power supplies.
- Place the Time Tagger on the breadboard and connect **detector A to channel 2 and detector B to channel 3 of the tagger** via SMA-to-SMA cables.
- Connect the Time Tagger to your PC via the included USB cable and start the software.
- You might see very high count rates of both detectors in the software because of the ambient light. It may also be that you see no count rates at all because the Time Tagger is saturated.
- Darken the room as much as possible (switch off all lights, shutter any windows, and turn other light sources, such as computer screens, away from the setup). The count rates should now be significantly below 50 kHz<sup>68</sup>. If they are higher, the room needs to be darkened further<sup>69</sup>.
- Rotate the zoom housing of detector A (left detector when looking from the perspective of the filter) to about the middle of its range (test how far it can be turned in both directions and then try to turn it halfway from one endpoint). Now turn one of the differential screws of the CXY1A mount in both directions until you observe a significant increase in the count rate of detector A in the software. If you see such a signal

<sup>68</sup> The count rates of the two detectors may be different, e.g., because some stray light source, such as a computer screen, illuminates one more than the other. This is not a problem if both count rates are below the 50 kHz threshold.

<sup>69</sup> If further darkening is not possible, take note of the tips at the end of Section 13.4 for dealing with large background signals.

increase, then maximize the signal. If you do not see a signal increase, return the screw to the center position (align the marks on the front side of the CXY1A mount) and try the other differential screw<sup>70</sup>.

- Once you found the maximum in one axis, optimize further with the other differential screw.
- Once you have maximized the count rate via the differential screws, carefully turn the zoom housing again to further increase the count rate. Afterwards, you may be able to increase the count rate further via slight changes of the differential screws. Iteratively turn the zoom housing and the screws until you have reached a stable maximum count rate. This should be at least 150 kHz with alignment iris and detector apertures completely open.
- Repeat the prior two steps for the second detector, this time maximizing the count rate for detector B in the software. You should reach a similar count rate as for detector A<sup>71</sup>.
- The setup is now complete and should look like Figure 69. You can now perform the HBT experiment for the alignment laser; see Section 9.1 for more details.

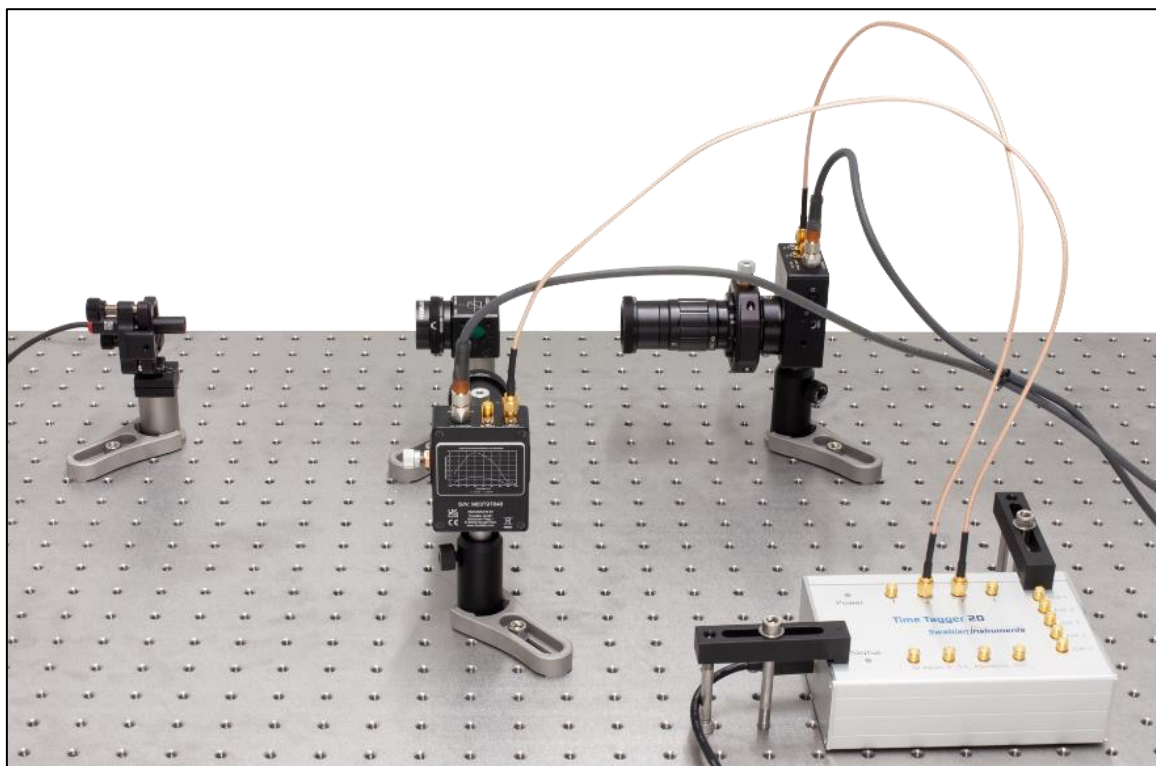


**Figure 69      HBT Setup after Detector Placement**

<sup>70</sup> Sometimes, it seems like the count rate keeps increasing in one turning direction of the screw until the end of travel is reached, because more stray light is reaching the detector from that direction. This is not the goal of the adjustment process. You can check this by turning the laser off. If the signal does not decrease significantly then you have optimized only for stray light. In this case, turn the screw back to the center position and try to find the actual signal (resulting in a much stronger and steeper count rate increase) via adjusting the other screw or the zoom housing.

<sup>71</sup> Again, slightly different count rates are not problematic, one detector might be slightly more efficient than the other or capture more stray light, resulting in an offset. Larger differences (like a factor of 2) point to one detector alignment being not fully optimized.

## 7.4 Setting Up the Photon Pair Source

In this section, the photon pair source is set up. This source forms the basis of all quantum optics experiments in this kit. In Figure 70, an overview of the photon pair setup is given. The following subsections include detailed instructions for the placement and adjustment of the components.

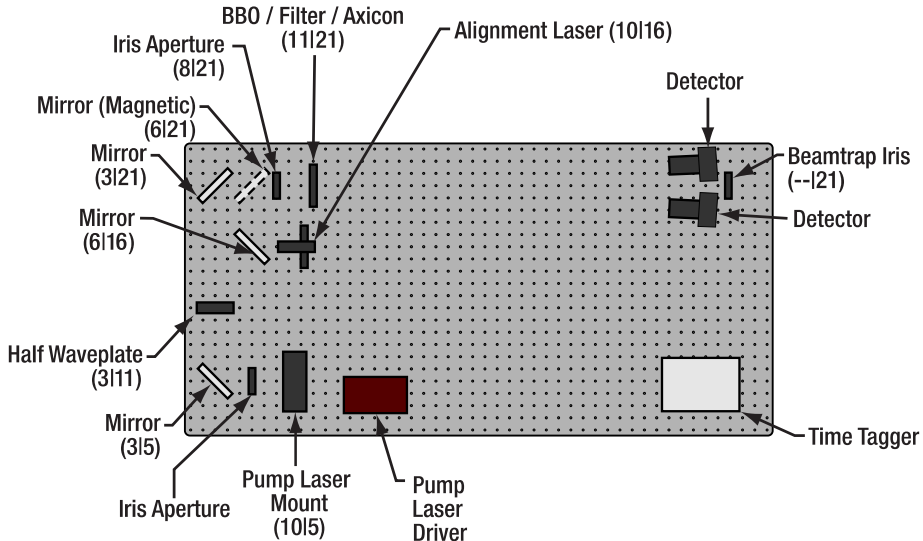


**Figure 70** Overview of the pair source setup. The numbers in parentheses are breadboard hole numbers (from left / from bottom). Components are not to scale and exact positions may deviate slightly from those given in text.

### 7.4.1 Setting up the Pump Laser Beam Path

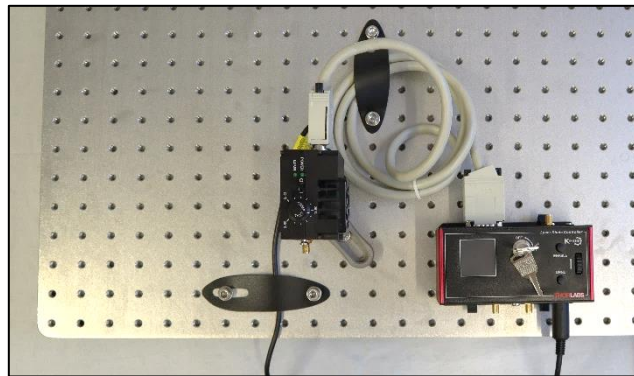


**Figure 71** Positioning of Pump Laser and Driver

- If you followed the procedure in Section 7.2.2, the pump laser is already at the correct position on the breadboard. If your laser was already collimated for you and you skipped Section 7.2.2, then position it according to the last bullet point there (10<sup>th</sup> breadboard hole from the left, 5<sup>th</sup> hole from the front, laser pointing to the left).
- Position the mirror component in the PH1E (PH30E/M) post holder to the left of the pump laser (3<sup>rd</sup> breadboard hole from the left, 5<sup>th</sup> from the front). The mirror should be angled at about 45°, so that the laser will be reflected towards the far edge of the breadboard. Secure the mirror with a CF125 clamp and a 1/4"-20 x 3/8" (M6 x 10 mm) cap screw plus washer. Place the screen in the expected beam path of the laser after the mirror, as seen in Figure 72.

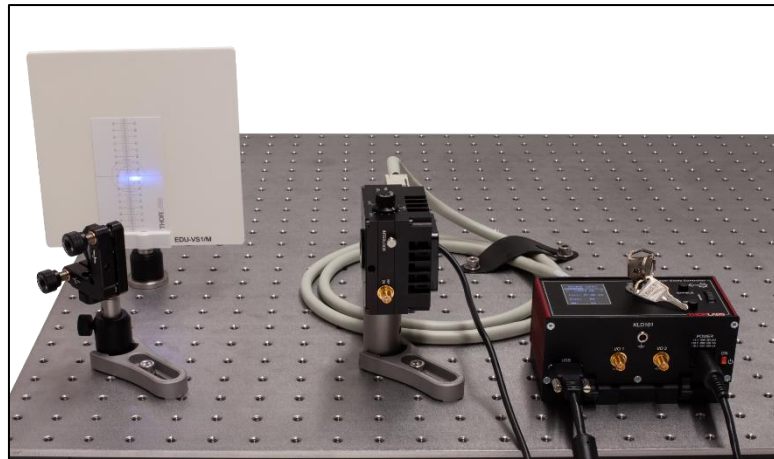


**Figure 72      Setup after Placement of First Pump Laser Mirror**

- Switch on the LDM9T(/M) mount. Set the temperature knob to 25°C.
- Switch on the KLD101 driver and set the laser current to 15 mA. Switch on the pump laser via the button on the KLD101 driver. **Be sure to always wear laser safety glasses when working with the pump laser!** Follow the beam path of the laser with a sheet of white paper and increase the laser current until the laser threshold is surpassed (brightness of the spot increases sharply).
- Loosen the clamp of the laser mount and rotate it carefully to horizontally center the beam on the mirror, then secure the clamp again.
- Adjust the height of the mirror to vertically center the laser on the mirror.
- Switch off the pump laser and position the Ø15.0 mm iris between the laser and the first mirror. Switch on the laser and adjust the position and height of the iris until the laser is centered on the iris. Here, it can be helpful to close the iris and hold a sheet of paper behind it. Adjust the iris aperture so that only the center of the laser profile is passing, and divergent stray radiation is blocked, as seen in Figure 73. This aperture will be used for all following adjustment steps and experiments. It should never be changed from now on, so that stray light from the laser diode cannot inadvertently influence experiments.

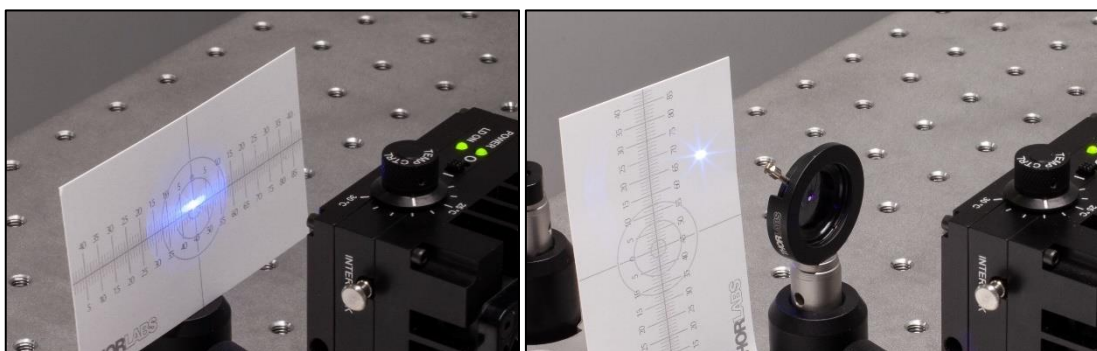


**Figure 73      Beam Profile of the Pump Laser in Front of (Left) and Behind (Right) the Beam Cleaning Iris**

- Switch off the pump laser. Place a second mirror component (with a KCP1(/M) centering plate but without a magnetic mount) on the 21<sup>st</sup> breadboard hole from the front and the 3<sup>rd</sup> from the left. It should be angled 45° to reflect the laser towards the right edge of the breadboard. Secure the mirror with a CF125 clamp and a 1/4"-20 x 3/8" (M6 x 10 mm) cap screw plus washer. Move the screen to block the expected beam path of the laser after the second mirror, as seen in Figure 75.
- Switch on the pump laser again and follow the beam with a sheet of paper. The beam should hit the center of the second mirror. Correct deviations to the left or right by either turning the lower kinematic screw of the first mirror (small deviations) or by loosening the CF125 clamp of the first mirror and turning the whole

mirror component before securing it again (larger deviations). Correct deviations in the vertical axis via the upper kinematic screw of the first mirror.

- The cards included in the K-Cube° controller packages can be used to see the laser spot while centering the beam on the mirror, as shown in Figure 74.

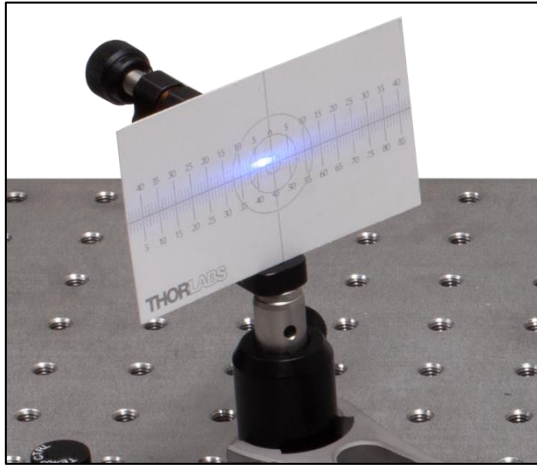


**Figure 74**      *Alignment on The Mirror*

- Place the WPH10ME-405 half-wave plate between the two mirrors on the 11<sup>th</sup> breadboard row from the front, as shown on the left side of Figure 75, so that the laser hits the wave plate in the center and under normal incidence, which can be set by rotating the mount until the beam reflected from the waveplate is aligned with the input beam. Secure the wave plate position with a CF125 clamp and a 1/4"-20 x 3/8" (M6 x 10 mm) cap screw plus washer. Set the wave plate to 45° as shown on the right side of Figure 75.



**Figure 75**      *Setup During Coarse Alignment of Pump Laser (Left) and Correct Setting of Half-Wave Plate (Right)*

- Switch off the pump laser. It is now roughly aligned. It will be aligned more precisely in a later step.

#### 7.4.2 Aligning Both Pump and Alignment Laser on the Same Path

- Place the Alignment Laser on the 10<sup>th</sup> breadboard hole from the left and 13<sup>th</sup> from the front, pointing towards the left edge of the breadboard as shown in Figure 76. Secure its position with a CF125 clamp and a 1/4"-20 x 3/8" (M6 x 10 mm) cap screw plus washer.
- Connect the USB plug of the alignment laser to either a PC/laptop or to the power grid via the DS5 power supply. To switch on the laser, press the small button on the red USB plug.
- Place a mirror (with a KCP1/(M) mount, without a magnetic base) on the 6<sup>th</sup> breadboard hole from the left and 13<sup>th</sup> from the front. It should be angled by 45°, so that the alignment laser is reflected towards the far edge of the breadboard. Fix its position with a CF125 clamp via a 1/4"-20 x 3/8" (M6 x 10 mm) cap screw plus washer.
- The alignment laser beam should be centered on the newly placed mirror. If that is not the case, use the lower kinematic screw of the alignment laser to adjust the beam position.
- Place the mirror with the magnetic base on the 6<sup>th</sup> breadboard hole from the left and the 21<sup>st</sup> from the front. Angle it by 45°, so that the alignment laser is reflected towards the right edge of the breadboard. Fix its position with a CF125 clamp via a 1/4"-20 x 3/8" (M6 x 10 mm) cap screw plus washer (the long end of the clamp should point towards the first alignment laser mirror). The setup should now look like Figure 76.

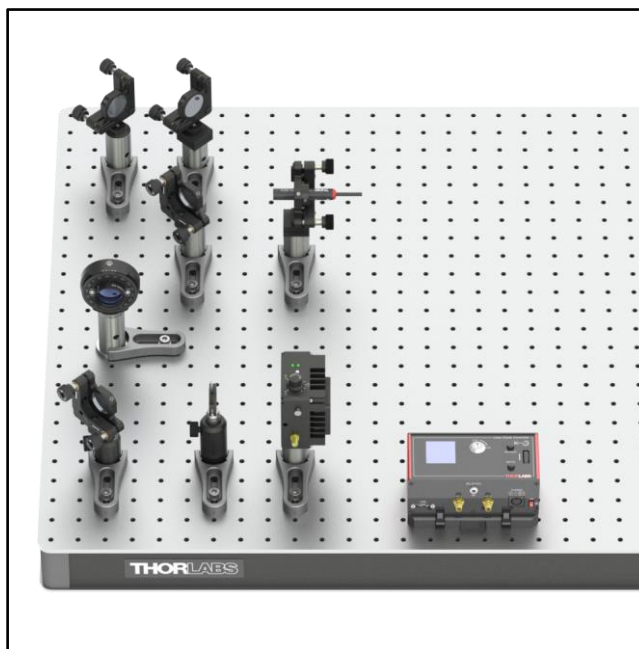


**Figure 76**      **Setup with Alignment Laser**

- The alignment laser beam should be centered on the newly placed mirror. If that is not the case, use the kinematic screws of the first mirror in the alignment laser beam path to adjust the beam position. In case of large deviations in the horizontal axis, you might need to loosen the CF125 clamp of the first mirror temporarily to rotate the whole mirror component (do not move it laterally).
- Place the beam trap iris on the 21<sup>st</sup> breadboard hole row from the front and on the 4<sup>th</sup> hole from the right edge of the breadboard. The iris should point towards the second mirror. The precise centering on the hole row is especially important for this element. Secure the iris position with a CF125 clamp and a 1/4"-20 x 3/8" (M6 x 10 mm) cap screw plus washer.
- The alignment laser should be centered on the beam trap iris. Use the kinematic screws of the second mirror in the alignment laser beam path to adjust. In case of large deviations in the horizontal axis, you might need to loosen the CF125 clamp of the second mirror temporarily to rotate the whole mirror component (do not move it laterally).

- Place the ID25/(M) iris on the 21<sup>st</sup> breadboard hole row from the front and the 8<sup>th</sup> hole from the left. The precise centering on the hole row is especially important for this element. Secure the iris position with a CF125 clamp and a 1/4"-20 x 3/8" (M6 x 10 mm) cap screw plus washer (long end of the clamp should point towards the front edge of the breadboard). This iris will be called “alignment iris” in the following. The setup should now look like Figure 77.

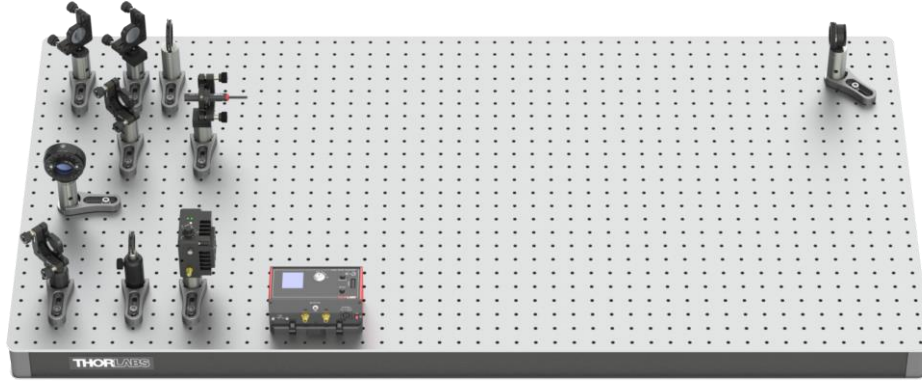


**Figure 77      Setup for Beam Alignment**

- The next step is to align the alignment laser through both irises on the 21<sup>st</sup> hole row. This can be achieved by a so called beamwalk<sup>72</sup> which is described in the following:
  - Close the alignment iris nearly completely.
  - Use the kinematic screws of the first mirror in the alignment laser beam path to center the beam on this iris. Then open it.
  - Close the beam trap iris nearly completely.
  - Use the kinematic screws of the second mirror in the alignment laser beam path to center the beam on the beam trap iris.
  - Repeat all the above steps iteratively until the alignment laser is centered on both iris apertures as shown in Figure 78.

<sup>72</sup> For more details and a video, see [https://www.thorlabs.com/newgroupage9.cfm?objectgroup\\_id=14221](https://www.thorlabs.com/newgroupage9.cfm?objectgroup_id=14221)

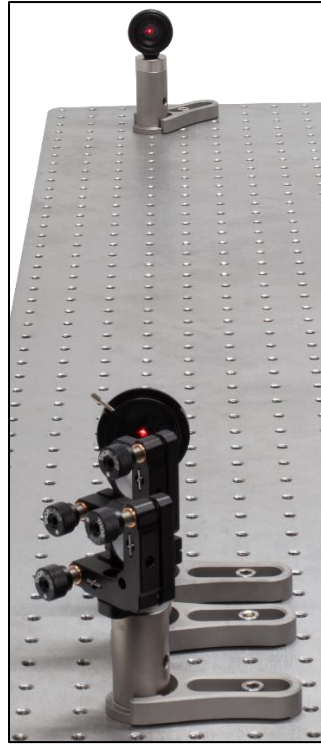


**Figure 78      Beam Path after Successful Beamwalk**

- Switch off the alignment laser and remove the mirror from the magnetic base.
- The next step is to align the pump laser on the exact same beam path as the alignment laser, as defined by the two iris apertures. **Remember to wear laser safety glasses when working with the pump laser!**
- Switch on the pump laser and repeat the beamwalk as described above. Again, use the first mirror to center on the alignment iris and the second mirror to center on the beam trap iris. As the pump laser is not easily visible on the iris apertures, use a sheet of paper to help. It can also be helpful to watch the beam behind the iris apertures to better see if it is centered. Remove the end cap of the beam trap for this step (as seen in Figure 79) but return it afterwards.

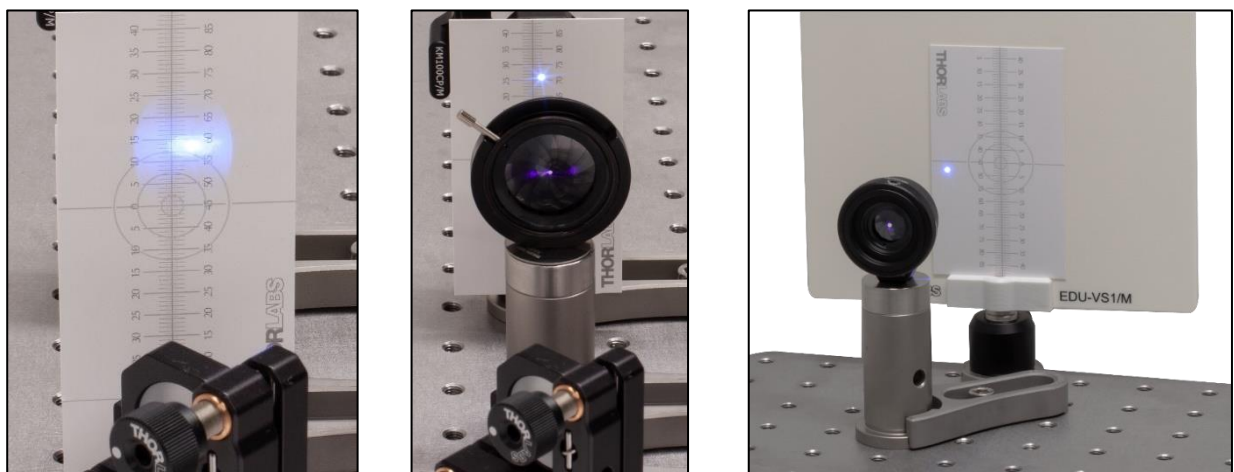


**Figure 79      Beamwalk for the pump beam path. From left to right: rough alignment with card in front of iris, test fine alignment with card behind iris, and beam trap with end cap removed and EDU-VS1(M) viewing screen behind it.**

- Switch off the pump laser. You have now aligned the beams of the pump laser and the alignment laser to the exact same beam path. This is immensely helpful as you can adjust all remaining optical elements with

the alignment laser instead of the pump laser, which is both easier and safer. You can switch between the two lasers via the mirror on the magnetic base (Mirror in = Alignment, Mirror out = Pump).

### 7.4.3 Detector Positioning

- Put the mirror on the magnetic base back into the setup and open the alignment iris completely.
- Place the fluorescent alignment target between the alignment iris and the beam trap and adjust its height so that the beam is centered on the hole in the target. Remove the target.
- Place the screen about halfway between the alignment iris and the beam trap.
- Place the post holder with the magnetic plate and the axicon on the 21<sup>st</sup> breadboard hole from the front and the 11<sup>th</sup> from the left. The lens tube should point towards the mirror, as seen in Figure 81.
- Switch on the alignment laser. You should see parts of a circle on the screen as shown on the left side of Figure 80.
- Now adjust the height and position of the axicon until the circle on the screen shows evenly distributed intensity around the entire circle, as shown on the right side of Figure 80. Secure the position of the axicon with a CF125 clamp and a 1/4"-20 x 3/8" (M6 x 10 mm) cap screw plus washer.

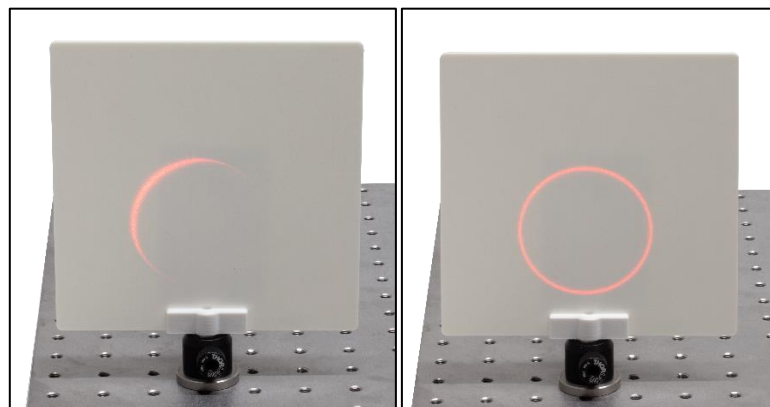


**Figure 80 Axicon Pattern Before (left) and After (right) Alignment**

- It is important that the alignment laser hits the axicon under normal incidence. To ensure this, close the iris in front of the axicon almost completely and watch the reflection of the axicon on the back side of the iris as shown in Figure 81. Use the adjusters of the axicon holder to center the reflection on the iris. This may change the pattern on the screen. Iteratively, adjust the position, angle, and height of the axicon until you achieve **both** a centered reflection on the iris **and** a homogeneous circular pattern on the screen.

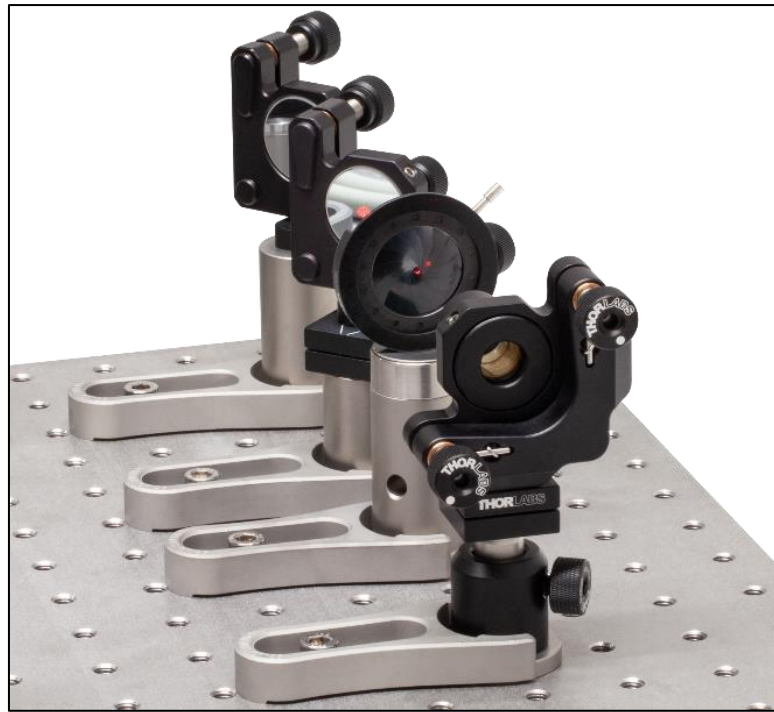


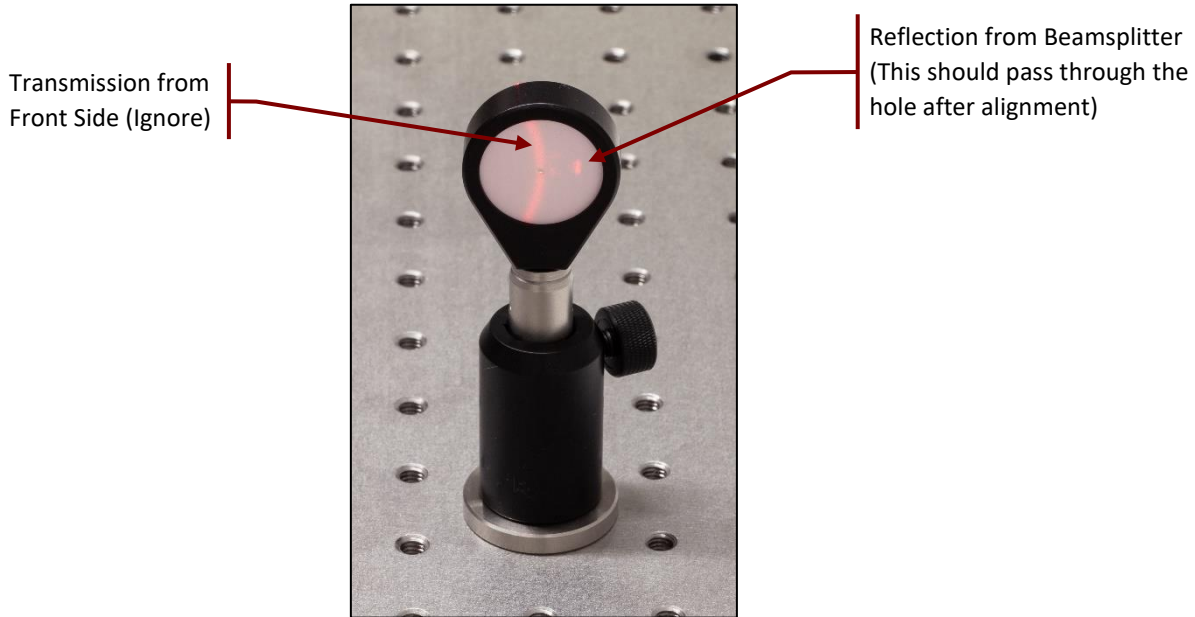
**Figure 81 Axicon Reflection on the Back Side of the Iris (Should Pass Back Through Iris After Alignment)**

- The axicon is designed to generate a cone of light with a half opening angle of  $3^\circ$  when illuminated with the wavelength of the alignment laser (635 nm). This opening angle is the same as the angle expected for the photon pairs generated by the BBO crystal. Thus, the alignment laser cone can be used to correctly position the detectors.
- Connect the lens tube with the economy beamsplitter to the detector that is labeled with “T.” Open the alignment iris completely and position the detector close to the right edge of the breadboard (about 5 cm closer to the axicon than the beam trap), so that the left part of the ring generated by the axicon hits the detector. Rotate the detector so that it points towards the axicon.
- Place the fluorescent alignment target about 10 cm in front of the detector so that the left part of the light ring passes through the hole in the target. Now adjust the height, position, and angle of the detector in such a way, that **both of the following conditions are met**:
  - The reflection from the beamsplitter passes back through the hole of the target.
  - The light passing the hole of the target is centered on the detector chip, as seen in Figure 82.



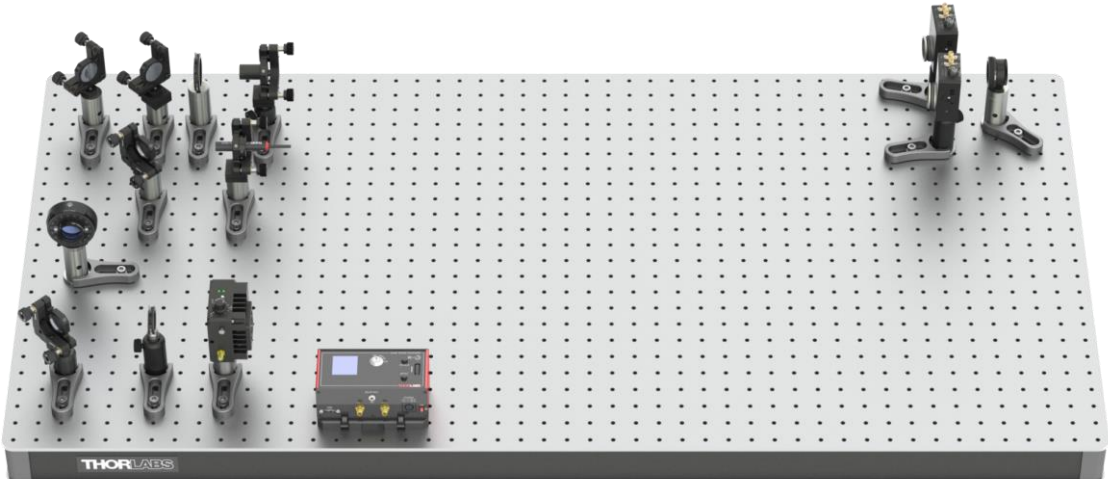
**Figure 82 Laser Spot Centered on Detector Chip**

Figure 83 shows the back side of the target before alignment. The curved line is part of the axicon cone (transmitted through the target), and the red spot to the right is the reflection from the beamsplitter. There may be a diffusive red spot which is the reflection from the detector chip and can be ignored.



**Figure 83      Back Side of the Alignment Tool Prior To Detector Alignment**

- Secure the position of the detector with a CF125 clamp and a 1/4"-20 x 3/8" (M6 x 10 mm) cap screw plus washer. Then remove the lens tube with the beamsplitter from the detector.
- Repeat the same procedure with the detector labeled "A" for the right part of the light cone. After completion, the setup should look like Figure 84.



**Figure 84      Setup after Detector Placement**

- Take one of the prepared detector optics and loosen the locking screw of the DTSM1 dovetail adapter almost completely (be careful to not completely unscrew it as it is easy to lose once dropped). Slide it over the dovetail adapter on the front of the detector labeled "T" (closer to the far breadboard edge). Rotate the optics until one of the adjusters is pointing straight upwards and the other one is pointing away from you. Then tighten the locking screw of the DTSM1 coupler to securely connect the optics to the detector<sup>73</sup>.
- Repeat this step for the second detector. This time, the two differential screws should point straight up and towards you, respectively.

<sup>73</sup> You can adjust the position of the locking screw to point upwards by repositioning the SM1NT1 locking ring.

- The two detectors are now aligned to the expected path of the photon pairs generated by the BBO crystal, as simulated by the axicon and the alignment laser. A view from the front should look like Figure 85, with the outermost parts of the light ring passing through the iris openings of the detectors.

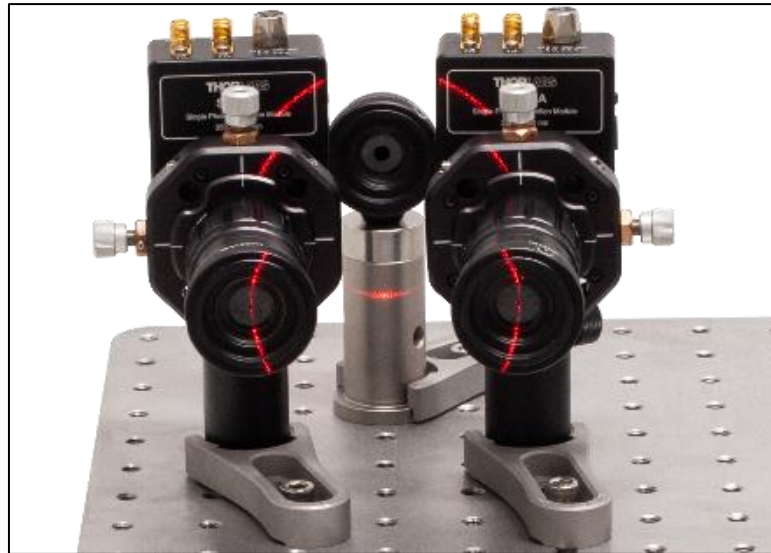


**Figure 85**      **Detectors T (left) and A (right) After Alignment**

#### 7.4.4 Detector Fine Adjustment (Colored Glass Filter)

- Replace the axicon with the colored glass filter.
- Close the alignment iris and adjust the alignment screws of the filter holder until the reflection from the filter passes back through the iris. Then open the iris completely. Switch off the alignment laser and remove the magnetically mounted mirror from the setup.
- Position the Time Tagger on the front right corner of the breadboard (see Figure 86) and fix its position with one or two CL2 clamps. For each clamp use a 1/4"-20 x 2" (M6 x 50 mm) cap screw and a 1/4"-20 x 2.5" (M6 x 65 mm) cap screw plus washer.



**Figure 86**      **Time Tagger Position**

- Connect both detectors to the power grid via the included power supplies. You can use CS1 cable strips and 1/4"-20 x 1/4" (M6 x 6 mm) cap screws plus washers for cable management. Use CA2924 cables to connect the outer SMA port of both detectors to the input channels 1 and 2 of the Time Tagger, respectively (labeled T and A, respectively). The detector and channel labeling should match.
- Connect the KLD101 driver and Time Tagger to your PC via the included USB cables. Start the EDU-QOP1 Software. Switch on both detectors and wait for their Signal LEDs to turn green. **Open the iris apertures of both detector optics completely.** They will remain that way for all of the following adjustment steps.

- You might see very high count rates of both detectors in the software because of the ambient light. It may also be that you see no count rates at all because the Time Tagger is saturated.
- Darken the room as much as possible (switch off all lights, block any windows, turn other light sources, such as computer screens, away from the setup). The count rates should now be significantly below 50 kHz<sup>74</sup>. If they are higher, the room needs to be darkened further<sup>75</sup>.
- Set the laser current in the software or at the KLD101 controller to about **5 mA below the lasing threshold** (the threshold can be determined from the spec sheet of the laser diode; see Figure 87) and switch on the pump laser. **Remember to always wear laser safety glasses when working with the pump laser!**
- The laser hits the colored glass filter in the same spot it will later hit the BBO crystal. The filter emits fluorescent light in all directions, part of which will be captured by the detectors. Thus, the detector optic can be fine-tuned to point exactly towards the future source of the photon pairs.
- Rotate the zoom housing of the T-detector to about the middle of its range (just test how far it can be turned in both directions and then try to turn it half of that from one endpoint). Now turn one of adjusters of the CXY1A mount in both directions until you observe a significant increase in the count rate of detector T (Trigger) in the software. If you see such a signal increase, then maximize the signal. If you do not see a signal increase, return the screw to the center position (align the marks on the front side of the CXY1A mount) and try the other differential screw<sup>76</sup>.
- Once you have found the maximum in one axis, optimize further with the other differential screw.
- Once you have maximized the count rate via the differential screws, carefully turn the zoom housing again to further increase the count rate. Afterwards, you may be able to increase the count rate further via slight changes of the differential screws. Iteratively turn the zoom housing and the screws until you have reached a stable maximum count rate. This should be at least 300 kHz (alignment iris and detector apertures completely open).
- Repeat the prior two steps for the A-detector, this time maximizing the count rate for detector A in the software. You should reach a similar count rate as the one you have for detector T<sup>77</sup>.

#### 7.4.5 Crystal Angle Adjustment

- Switch off the pump laser and replace the colored glass filter with the BBO crystal. Place the magnetically mounted mirror in the setup and switch on the alignment laser.
- Close the alignment iris and adjust the kinematic screws of the crystal holder until the reflection from the crystal passes back through the iris. Open the alignment iris completely, switch off the alignment laser and remove the magnetically mounted mirror.
- Set the laser current to a value that corresponds to about 13 mW output power. The current-power (LIV) curve is given on the spec sheet that comes with your laser diode, as seen in the blue curve in Figure 87 (The figure is an example, check your individual spec sheet!). Switch on the pump laser. You may already see an increase in the count rates from the detectors. Go to the Configuration tab and set the Coincidence Window to 20 ns (this helps with the alignment, as delay offsets between the detectors are not yet calibrated).

<sup>74</sup> The count rates of the two detectors may be different, e.g., because some stray light source, such as a computer screen, illuminates one more than the other. This is not a problem if both count rates are below the 50 kHz threshold.

<sup>75</sup> If further darkening is not possible, take note of the tips at the end of Section 13.4 for dealing with large background signals.

<sup>76</sup> Sometimes, it seems like the count rate keeps increasing in one turning direction of the screw until the end of travel is reached, because more stray light is reaching the detector from that direction. This is not the goal of the adjustment process. You can check this by turning the laser off. If the signal does not decrease significantly then you have optimized only for stray light. In this case, turn the screw back to the center position and try to find the actual signal (resulting in a much stronger and steeper count rate increase) via adjusting the other screw or the zoom housing.

<sup>77</sup> Slightly different count rates are not problematic, one detector might be slightly more efficient than the other (differences can be as high as 20%) or capture more stray light, resulting in an offset. Larger differences (like a factor of 2) indicate that one of the detector's alignment is not fully optimized.

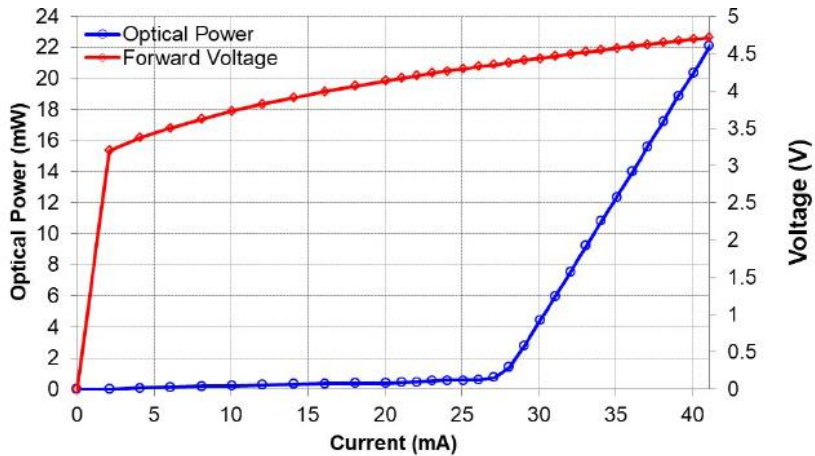


**Figure 87** Current-power dependence (blue curve, circles) in the laser diode spec sheet. In this example the lasing threshold is at about 28 mA; 13 mW of optical output power is reached with a current of 35.5 mA.

- Go back to the Alignment tab and turn the **golden** kinematic screw of the crystal mount carefully in both directions. This changes the opening angle of the generated photon pairs and in turn the count rates of the detectors. Maximize the count rates of both detectors. As the detectors are placed symmetrically to the center axis, there should be a screw position that maximizes both the count rates of detectors T and A. You should observe count rates over 100 kHz for both detectors. At the same time, you should also observe an increase in the coincidence count rate of detectors T&A in the lower graph.
- If the count rates show maxima at significantly different screw positions (and no significant increase of the coincidence count rates is observed), the detectors are not symmetrically placed, and you need to remove both detectors and repeat the positioning process.
- After maximizing the count rates of the individual detectors, switch to the Delay Adjust tab of the software and set the Coincidence Window back to 5 ns. Use the standard settings of the software and start a measurement.
- The finished measurement should look like Figure 88. There should be a sharp peak with a FWHM of about 5 ns. Drag the cursor (blue vertical line) to find the delay value at the peak maximum (4.5 ns in Figure 88).
- Enter this value (4.5 ns in the example case of Figure 88) into the **Delay A to T** field.

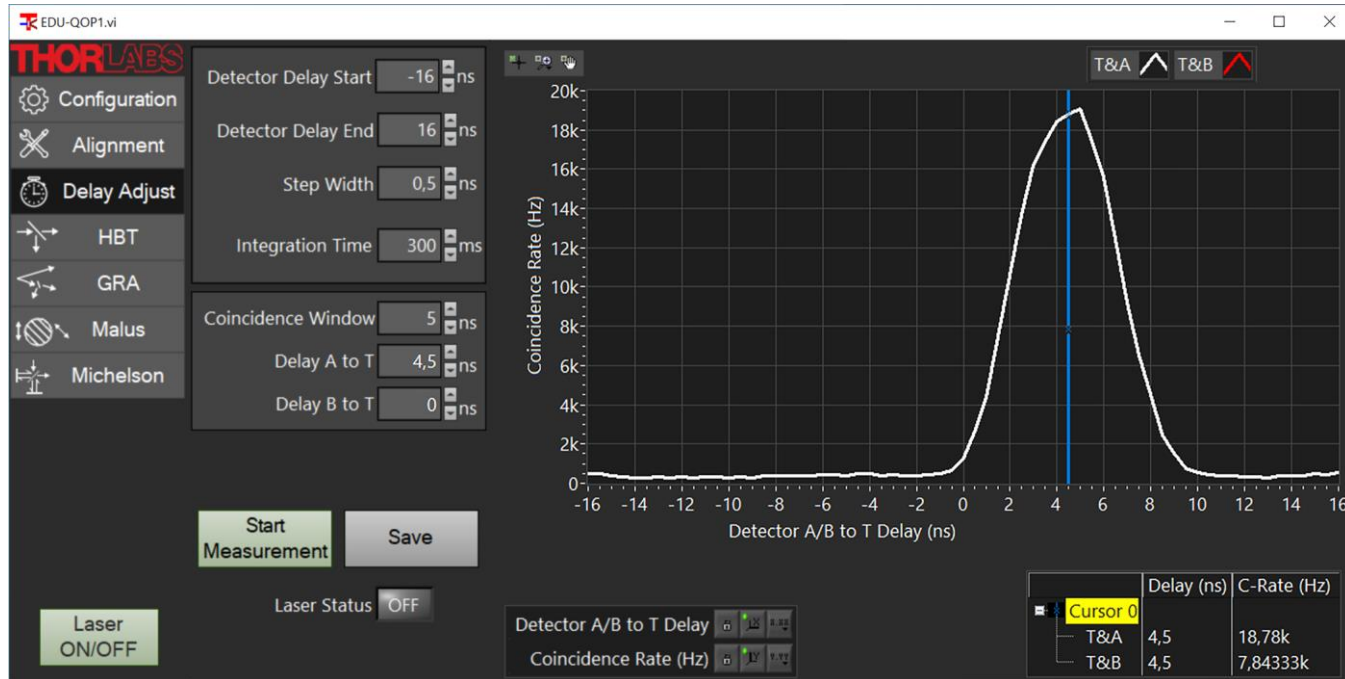


**Figure 88      Example Delay Measurement**

- Go back to the Alignment Tab. You should see the same count rates as before. The coincidence count rate should be above 10 kHz.
- Carefully rotate the WPH10ME-405 half-wave plate (between the first two mirrors in the pump beam) and watch the coincidence count rate. Optimize the wave plate angle for maximum count rate (this aligns the polarization of the pump beam with the crystal orientation for optimal phase matching, see Section 3.9 for details)<sup>78</sup>.
- Slowly close the alignment iris in front of the BBO crystal and watch the count rates as well as the coincidence count rate. At first, only the single detector count rates will decrease while the coincidence count rate remains stable. Stop closing the iris once the coincidence rate starts to drop as well. You have now found the optimal opening diameter of the alignment iris which should be somewhere between 1 mm and 3 mm. This ensures that as much stray light as possible is blocked without affecting the photon pairs. Keep the alignment iris at this diameter for all future experiments.
- Select the **g2(0)** radio button on the left side of the software. The lower graph now displays the  $g^{(2)}(0)$  values that are calculated live from the single detector and coincidence count rates. You should observe values significantly larger than 30.
- You have now set up and adjusted a photon pair source. This light source is the basis of all of the remaining experiments in this kit.

## 7.5 Setting Up the Grangier-Roger-Aspect Experiment

With a working photon pair source, you can now build the setup for the Grangier-Roger-Aspect experiment as explained in Section 3.5.3. Figure 89 shows an overview of the setup with the rectangle marking the newly placed components. The following subsections give detailed instructions for the placement and adjustment of those components.

<sup>78</sup> This step requires very careful rotation of the RSP1D(/M) rotation mount. An alternative mounting option, that allows for a bit more comfortable rotation, would be the CRM1PT(/M) precision rotation mount. Please note that a different combination of post and spacers is required in that case in order to keep the center of the waveplate at the same height.

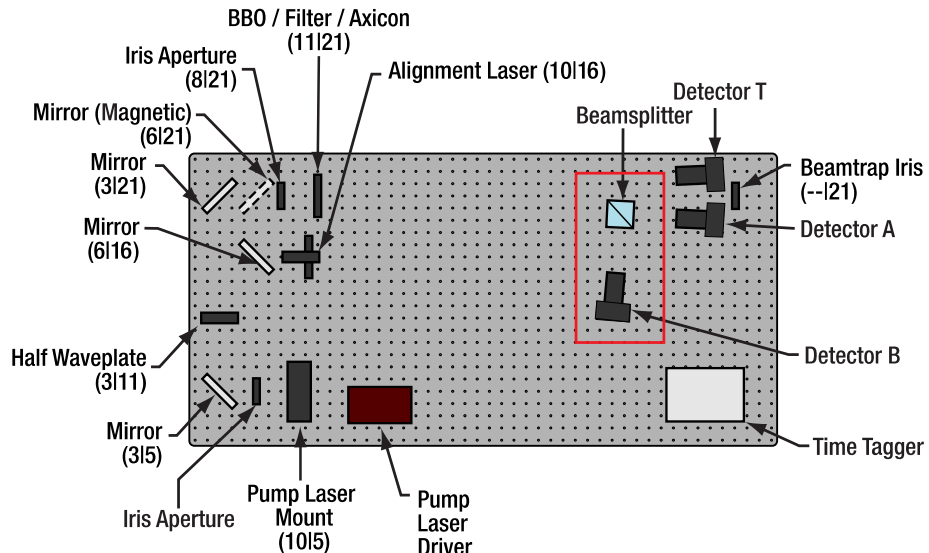


**Figure 89** Setup for the GRA Experiment. Added components are marked with a rectangle. The numbers in parentheses are breadboard hole numbers (from left / from bottom). Components are not to scale and exact positions may deviate slightly from those given in text.

### 7.5.1 Beamsplitter Positioning

- Switch off the pump laser.
- Replace the crystal with the axicon and return the magnetically mounted mirror to the setup. Switch on the alignment laser.
- Place the alignment target in the rightmost part of the light cone (viewed from the direction of the axicon).
- Place the beamsplitter with the attached iris aperture about 10 breadboard holes to the left of the detectors (iris facing the alignment target). The light passing through the target should be centered on the iris of the beamsplitter.

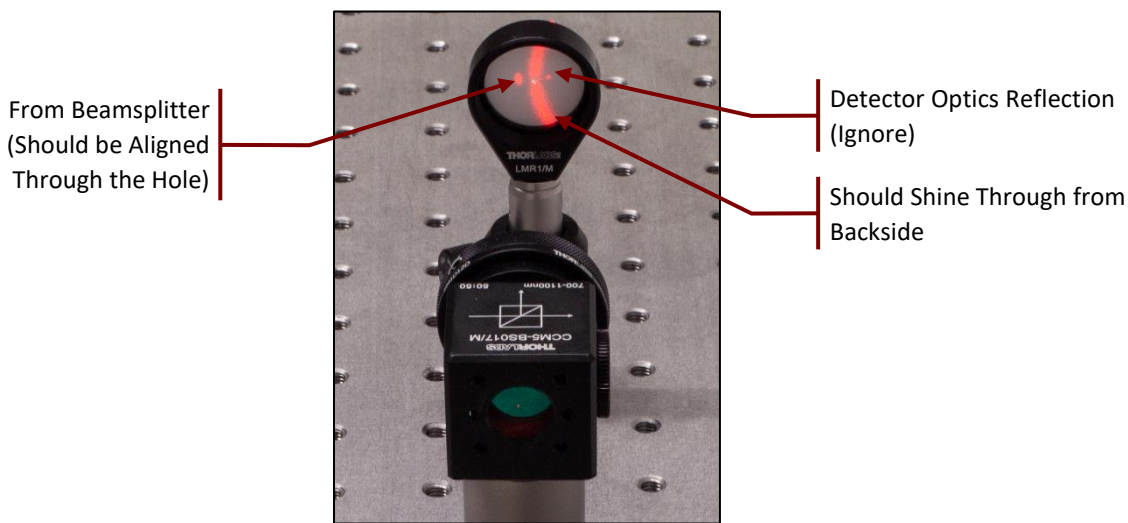


**Figure 90** Beamsplitter Positioning and Orientation (Before Alignment)

- Watch the back side of the target and carefully rotate the beamsplitter until the reflection from the beamsplitter passes back through the hole in the target.
- Check that the laser is still aligned to the center of the beamsplitter iris, then secure the position of the beamsplitter with a CF125 clamp and a 1/4"-20 x 3/8" (M6 x 10 mm) cap screw plus washer.

### 7.5.2 Third Detector Positioning

- Take the remaining detector (labeled “B”) and screw the lens tube with the economy beamsplitter on its front.
- Place the alignment target in the beam path of the light that is reflected by the beamsplitter (close to the beamsplitter) so that the light passes through the hole of the target.
- Position the detector at least 10 cm away from the target. Adjust height, position, and rotation of the detector in such a way that:
  - The light passing through the hole in the target is centered on the detector chip.
  - The reflection from the beamsplitter in front of the detector is passing back through the hole in the target.

Then secure the detector position with a CF125 clamp and a 1/4"-20 x 3/8" (M6 x 10 mm) cap screw plus washer. Remove the lens tube with the beamsplitter from the detector.

- Take the remaining detector optic and loosen the locking screw of the DTSM1 dovetail adapter almost completely. Slide it over the dovetail adapter on the front of the detector. Rotate the optics until one of the adjusters is pointing straight upwards. Then tighten the locking screw of the DTSM1 coupler to securely connect the optics to the detector. At this point, the setup should look like Figure 91.

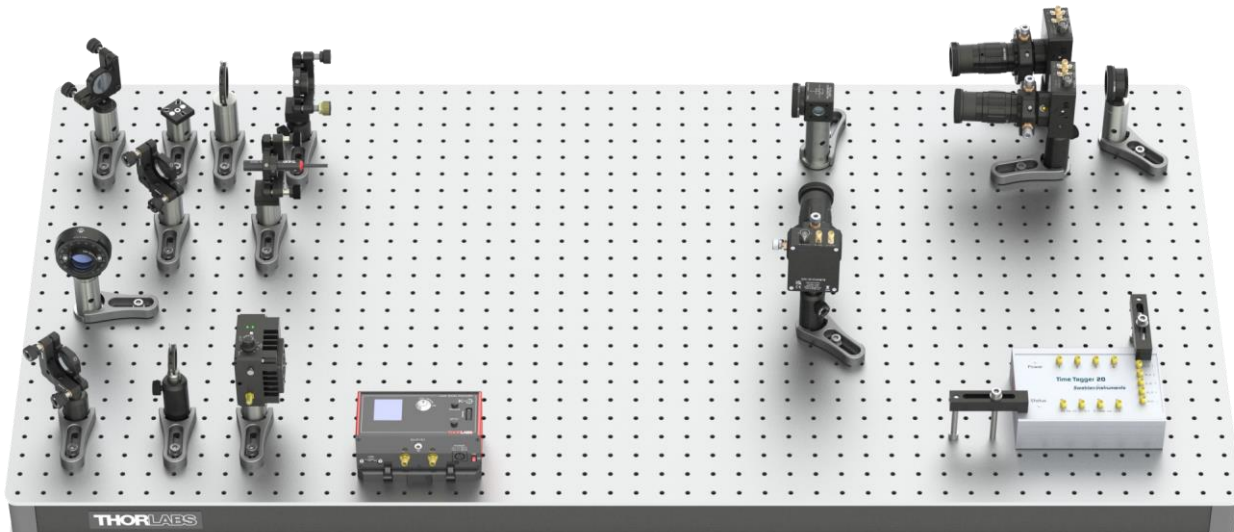


**Figure 91**      **Setup After Placement of Third Detector**

### 7.5.3 Third Detector Fine Adjustment

- Connect the detector to the power grid via the included power supply and connect the outer SMA port to Channel 3 of the Time Tagger (labeled “B”) via a CA2924 cable. Optionally, use CS1 cable strips and 1/4"-20 x 1/4" (M6 x 6 mm) cap screws plus washers for cable management. Switch on the detector.
- Switch off the alignment laser, remove the target and the magnetically mounted mirror from the setup, and replace the axicon with the colored glass filter.
- Set the current of the pump laser to about 5 mA below the lasing threshold (check the spec sheet of your laser diode) and switch on the pump laser. **Always wear laser safety glasses when working with the pump laser!** Darken the room to similar conditions as before.

- Rotate the zoom housing of the detector to about the middle of its range (just test how far it can be turned in both directions and then try to turn it half of that from one endpoint). Now turn one of the adjustment screws of the CXY1A mount in both directions until you observe a significant increase in the count rate of detector B in the software. If you see such a signal increase, then maximize the signal. If you do not see a signal increase, return the screw to the center position (align the marks on the front side of the CXY1A mount) and try the other adjustment screw.
- Once you found the maximum in one axis, optimize further with the other differential screw.
- Once you have maximized the count rate via the adjustment screws, carefully turn the zoom housing again to further increase the count rate. Afterwards, you may be able to increase the count rate further via slight changes of the adjustment screws. Iteratively turn the zoom housing and the screws until you have reached a stable maximum count rate. This should be at least 150 kHz.
- Switch off the pump laser and replace the colored glass filter with the BBO crystal.
- Set the laser current to the value that corresponds to about 13 mW (check the spec sheet of your laser diode). Set the coincidence window to 20 ns in the Configuration tab. Go back to the Alignment tab, then switch on the pump laser. You should see a sharp increase in the count rate of detector B in the software. The count rate should be similar to that of detector A and about half of that of detector T. The coincidence count rate between detectors T&B in the lower graph should also increase significantly.
- Slightly rotate the golden kinematic screw of the crystal holder back and forth to make sure that the maximum count rate of detector B is at a similar screw position compared to the other two detectors. If the screw positions of the maxima are significantly different (and no coincidences are observed), repeat the positioning of the third detector.
- Switch to the Delay Adjust tab of the software and set the coincidence window back to 5 ns. Use the standard settings of the software and start a measurement. In addition to the peak for detector A, you should now see an additional peak for detector B which has a similar height but may be shifted on the delay axis. Record the delay value for the center of the peak for detector B and write this value into the **Delay B to T** field. You should now see a similar coincidence count rate for T&A and T&B in the Alignment Tab.

#### 7.5.4 Test Measurement

- Select the GRA tab of the software, choose a measurement time (20 s is recommended) and start the measurement. This will display the count rates, the absolute counts, and the calculated  $g^{(2)}(0)$  values. The first value is the quality of the pair photon source as measured before and the second value is the Grangier-Roger-Aspect experiment. This value should be below 0.1 (everything below 1 is proof of a non-classical light source), as explained in detail in Section 3.5.3.
- The GRA experiment can be extended to measure Malus' Law by simply putting the polarizer component (1" diameter) between the beamsplitter and detector B, as shown in Figure 92. See Sections 3.7 and 9.6 for a detailed explanation of the Malus' Law experiment.

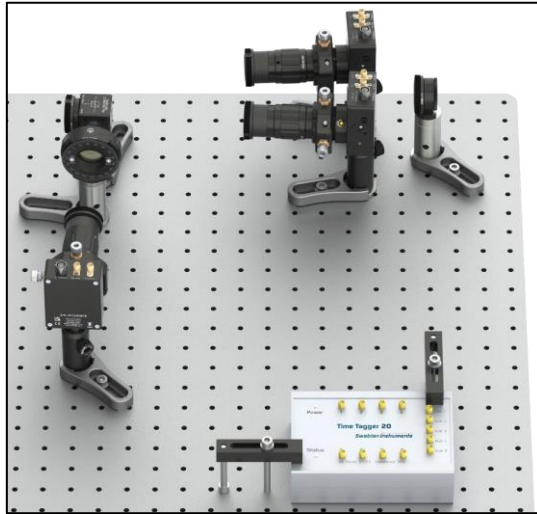


**Figure 92**      *Setup for Malus' Law Experiment*

## 7.6 Setting Up the Michelson Interferometer

In this Section, a Michelson interferometer for single photons (see Section 3.6) is constructed. In Figure 93, an overview over the setup is given, with the red rectangles marking the newly added or moved components.

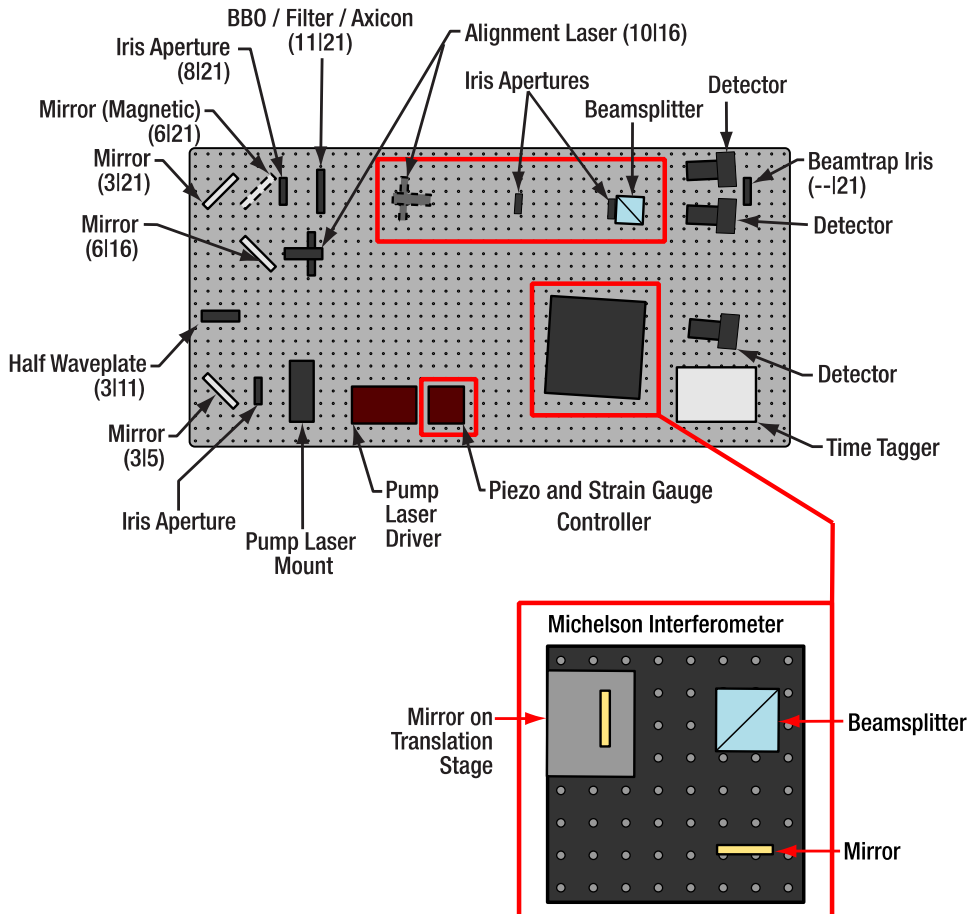


**Figure 93**      *Overview of the Michelson interferometer setup. Newly added or moved parts are marked with red rectangles. The numbers in parentheses are breadboard hole numbers (from left / from bottom). Components are not to scale and exact positions may deviate slightly from those given in text.*

### 7.6.1 Additional Alignment Path

Before setting up the interferometer, it is helpful to set up a second alignment path for the alignment laser, following the way the photons take from the crystal to the beamsplitter. Do this as follows:

- Switch off the pump laser, place the mirror on the magnetic mount in the beam path, and replace the BBO crystal with the axicon.
- Switch on the alignment laser. Place the alignment target behind the axicon in the rightmost part of the light cone.
- Place the Ø8.0 mm iris component 35 cm behind the axicon so that it does not block the pump beam path and adjust its height and position until the light that passes the target is centered on the iris. Secure the iris position with a CF125 clamp via a 1/4"-20 x 3/8" (M6 x 10 mm) cap screw plus washer. Remove the alignment target.

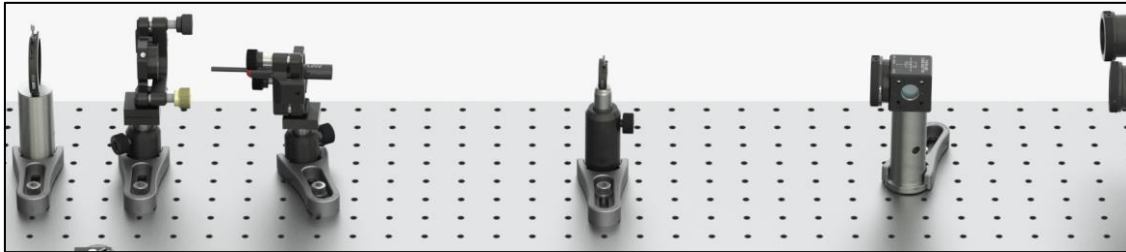


**Figure 94      Additional Alignment Path**

- Switch off the alignment laser and transfer it to the magnetic plate in the PH1E (30.1 mm tall) post holder.
- Place the alignment laser between the axicon and the Ø8.0 mm iris, as seen in Figure 94.
- Switch on the alignment laser and adjust its position until it is centered on both iris apertures. Do the following:
  - Open the Ø8.0 mm iris completely and roughly aim the alignment laser on the beamsplitter iris by positioning the component and changing the post height. Do not use the adjusters of the laser holder in this step.
  - Close the Ø8.0 mm iris and aim the laser on the face of the iris by using the adjusters of the laser mount without changing the position of the laser.
  - Once the beam is centered on the Ø8.0 mm iris, watch the beamsplitter iris. If the spot is to the left (right) of its center, move the whole alignment laser assembly a bit to the left (right) and rotate it until it is again centered on the Ø8.0 mm iris. If the spot is above (below) the center of the beamsplitter iris, adjust the post height of the alignment laser slightly up (down) and then use the adjusters of the laser mount to center the spot on the Ø8.0 mm iris again.
  - Repeat the last step iteratively until the beam is centered on both iris apertures. Figure 95 shows a completed alignment.
- Secure the position of the alignment laser with a CF125 clamp via a 1/4"-20 x 3/8" (M6 x 10 mm) cap screw plus washer. Open both iris apertures completely.

You have now completed the second alignment path. As you might have changed the laser position in its mount during the process, it is necessary to readjust the alignment of the original alignment path. Do this as follows:

- Switch off the alignment laser and move it to its original position.
- Remove the axicon and switch on the alignment laser.
- Repeat the beamwalk procedure explained in Section 7.4.2 (use only the adjusters of the mirrors, not of the alignment laser!)

You have now realigned everything. Move the alignment laser back to its position in the second alignment path and continue.



**Figure 95      Additional Alignment Path After Completed Alignment (Beam Centered on Both Apertures)**

### 7.6.2 Interferometer Adjustment

In the following steps we are going to set up the Michelson interferometer breadboard. Figure 96 shows how the board will look like after setting up the interferometer completely.

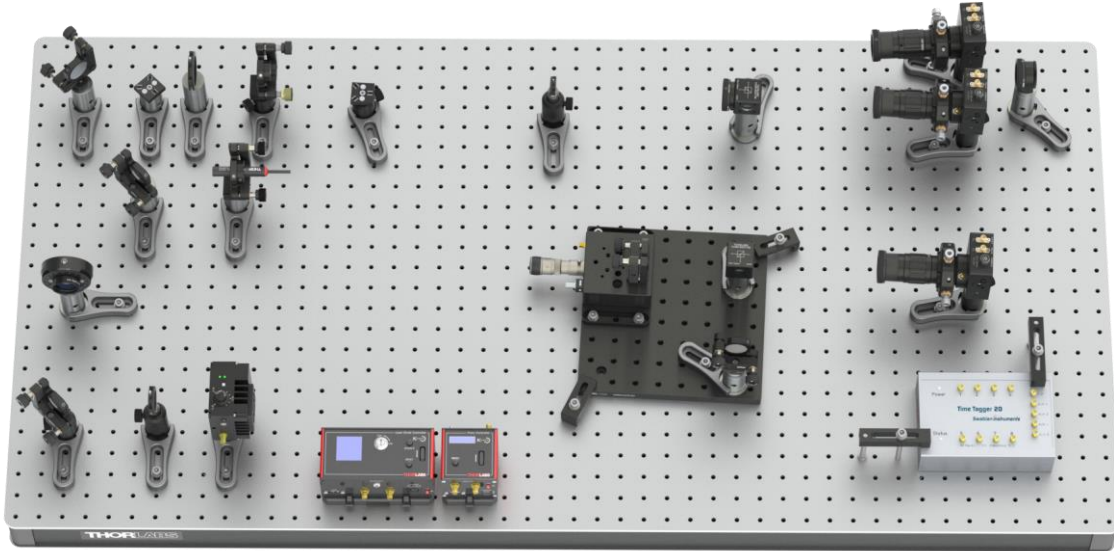


**Figure 96      Setup with Fully Aligned Michelson Interferometer**

- Place the alignment target in between the beamsplitter and detector B. Remove detector B from the breadboard and remove the optics from the detector (by loosening the locking screw on the dovetail coupler).
- Place the small breadboard on the free space to the right of the KLD101 laser driver.

- Place the stage with the gold mirror in the far-left corner of the small breadboard, so that the long edge of the stage and the edge of the small breadboard overlap, as seen in Figure 96. Secure its position with two 1/4"-20 x 3/8" (M6 x 10 mm) cap screws plus washers.
- Rotate the board such that the mirror on the stage faces the target. Switch on the alignment laser and adjust the board position such that the beam hits the center of the mirror, **and** the reflection passes back through the hole in the alignment target. Secure the breadboard position with two CL5A clamps, 1/4"-20 x 1" (M6 x 25 mm) cap screws, and washers. Adjust the height of the reflection with the upper adjuster of the mirror mount.
- Position the remaining beamsplitter component on the small breadboard about 10 cm in front of the mirror. For the correct orientation, see Figure 97.
- Position and rotate the beamsplitter component until the alignment laser hits it in the center **and** its back-reflection (as well as the reflection of the mirror behind) is directly above or below the hole in the target (due to slight upwards or downwards beam deviation at the beamsplitter the reflection usually does not fall back through the hole). It may be helpful to cover the mirror to reduce the number of reflections on the target. Secure the beamsplitter position with a CF028 clamp via a 1/4"-20 x 3/8" (M6 x 10 mm) cap screw plus washer.

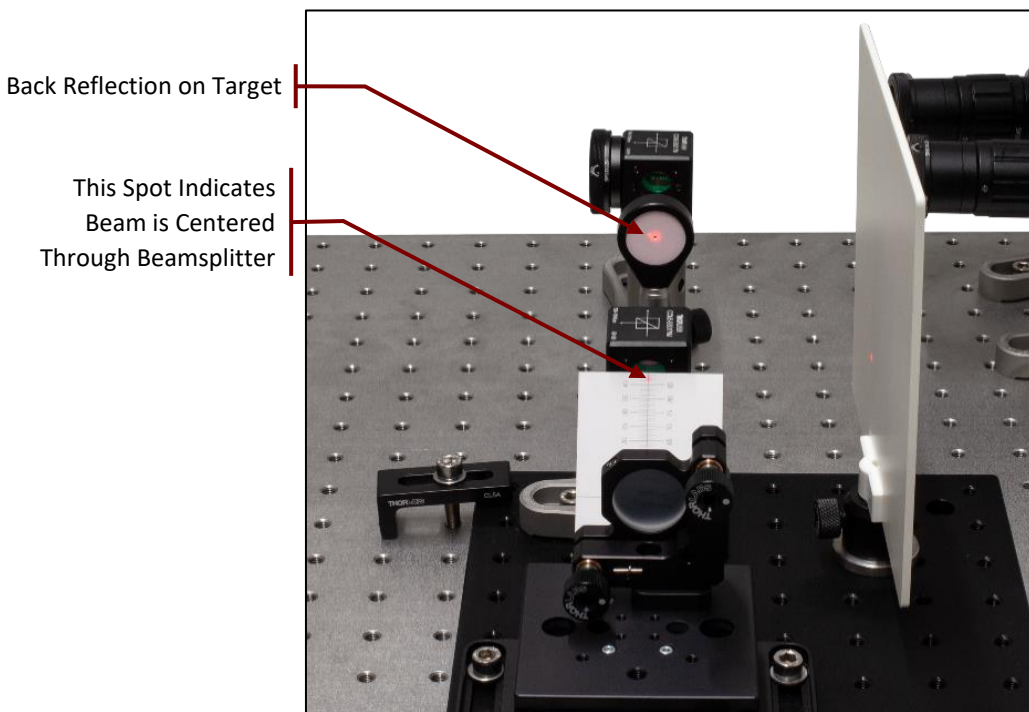


**Figure 97      Alignment of the Second Beamsplitter**

- Remove the clamps holding the small breadboard, then rotate it back into its original position (stage at the left edge). The distance between both beamsplitters should be about 20 cm. Align the board such that the laser hits the center of the beamsplitter **and** the reflection of the beamsplitter passes the hole in the alignment target. Then clamp the breadboard again in its final position.
- Now place the screen to block the mirror on the stage and position the gold mirror on the post in the path of the alignment laser that is transmitted by the beamsplitter. The distance between this mirror and the beamsplitter should be the same as between the mirror on the stage and the beamsplitter.
- Rotate and move the mirror until the alignment laser is centered on the mirror **and** you see its reflection on the back side of the alignment target. Then secure the mirror position with a CF125 clamp via a 1/4"-20 x 3/8" (M6 x 10 mm) cap screw plus washer, as seen in Figure 98.

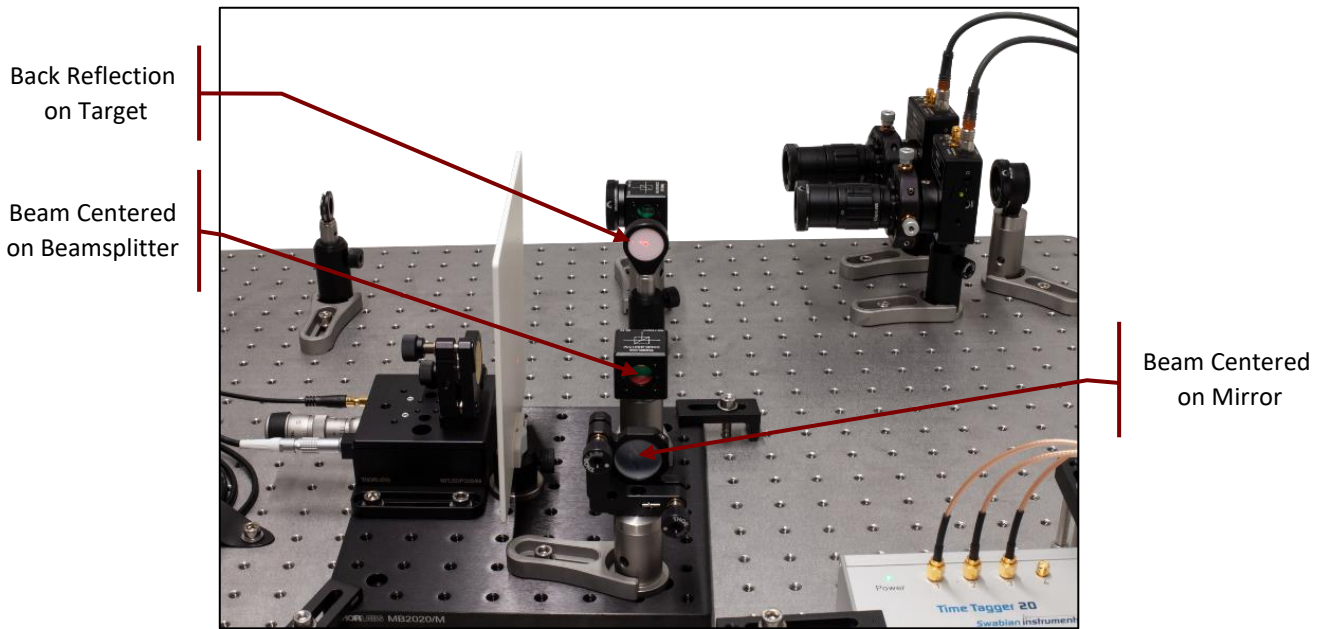


**Figure 98      Alignment of the Second Interferometer Mirror**

- Use the adjusters of the mirror mount to make the reflection pass back through the hole of the alignment target.
- Place the screen in the output arm of the interferometer (towards the right edge of the breadboard, as shown in Figure 99). You will see at least three red spots, as shown on the left side of Figure 100. If your alignment in the previous steps was very accurate, these spots already overlap. Two spots are the light coming back from the two mirrors in the interferometer (see Figure 99 b and c), the third spot (that is less intense) is a result of internal reflection in the beamsplitter (see Figure 99 a). Although this is an artifact of the beamsplitter coating not being at the same wavelength of the alignment laser, it helps with alignment. Please note that this artifact will not be present for the single photons later, as their wavelength matches the anti-reflection coating of the beamsplitter.

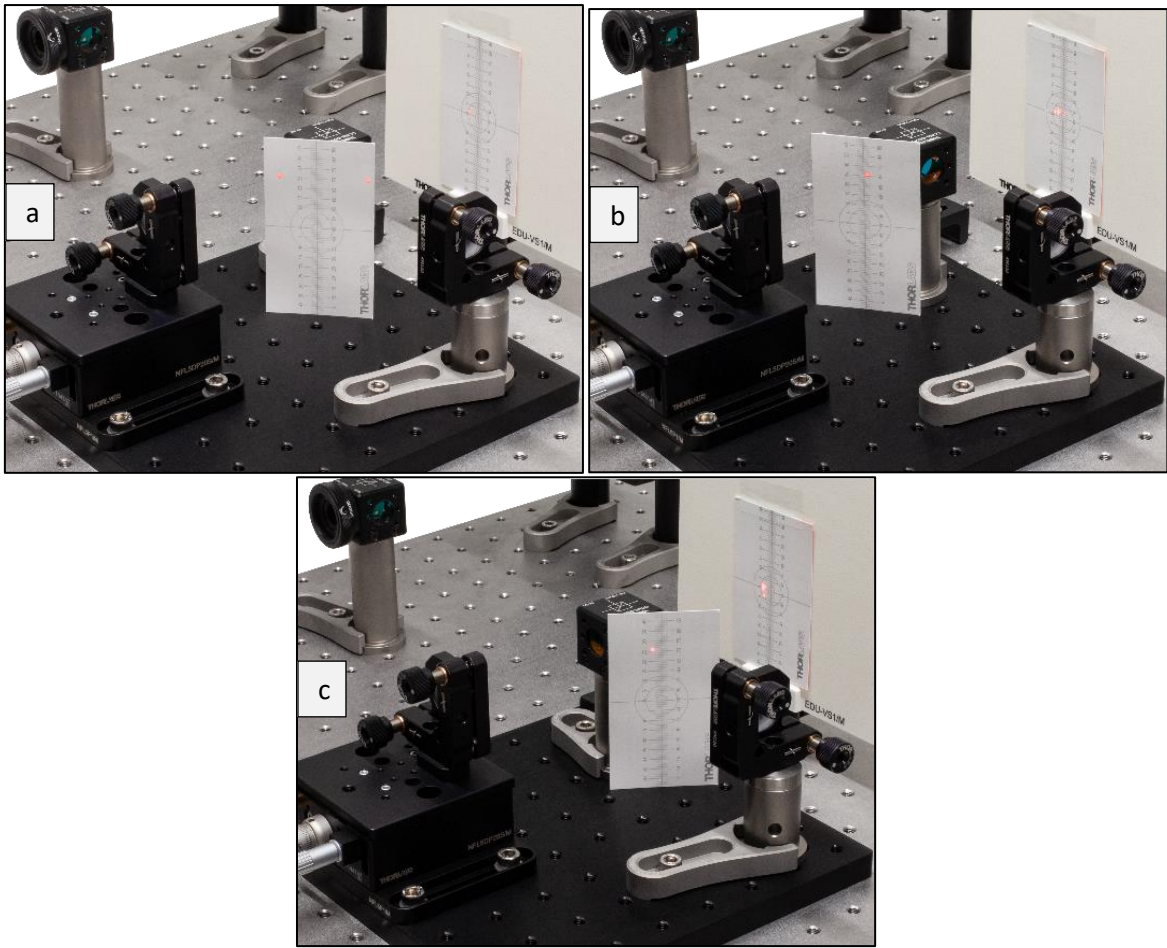


**Figure 99      Alignment of the Interferometer Arms**

- Adjust the kinematic screws of one of the mirrors in the interferometer. You will see one of the bright spots moving. Adjust the mirror until the moving spot overlaps with the internal reflection spot. Then repeat this for the other interferometer mirror until you see only one bright spot on the screen, as shown on the right side of Figure 100. There may be a few other bright spots on the screen. Those are the result of multiple reflections and can be ignored.

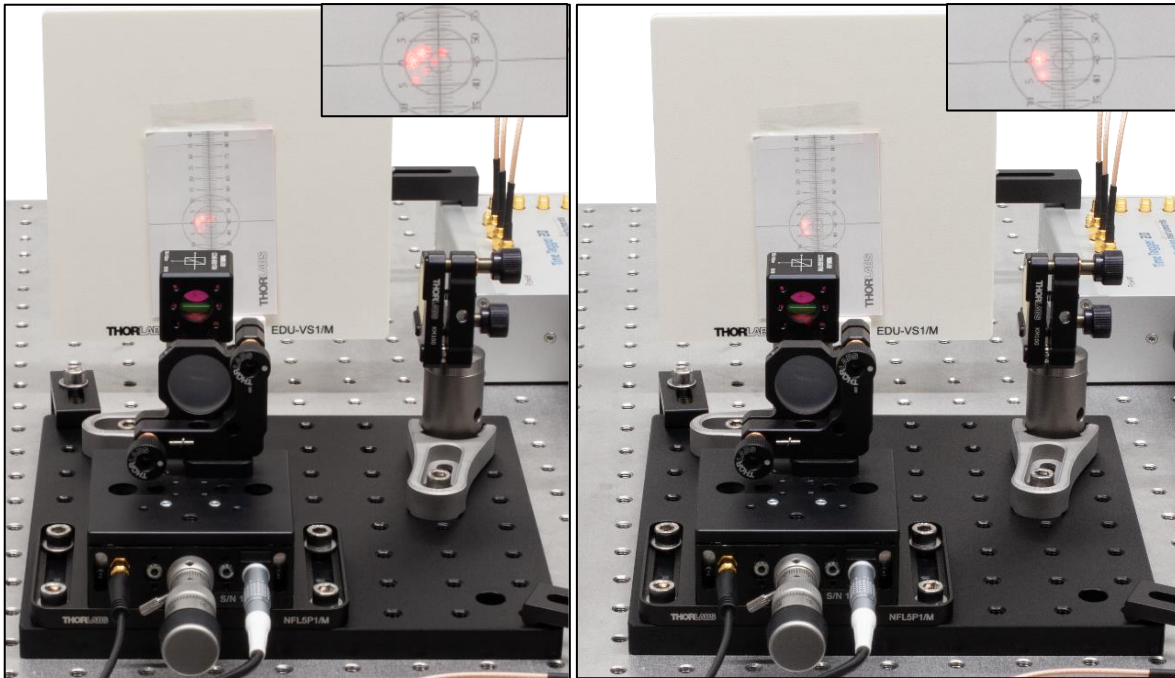


**Figure 100      Spots on the Screen Before (Left) and After (Right) Adjustment of the Interferometer Mirrors**

- Place the Ø1" lens assembly between the alignment laser and the interferometer as seen in Figure 101. Adjust the lens height and position so that the alignment laser is centered on the lens. If you block both arms of the interferometer, you will see a pattern from the internal reflections of the beamsplitter, which may be ignored.

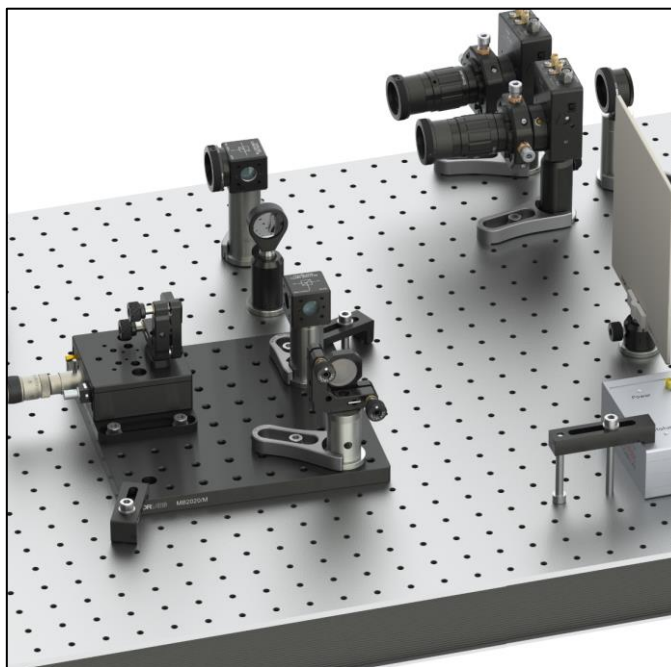


**Figure 101      Position of the Lens in Front of the Michelson Interferometer**

- Unblock both interferometer arms. At this point you may already see an interference pattern on the screen. If that is not the case, carefully turn the kinematic screws of the mirror not on the stage back and forth until an interference pattern appears. At first, this pattern will consist of stripes, as shown on the right image in Figure 102. Use the mirror adjusters to center the pattern. If the stripes are getting broader

you are turning into the right direction. If the stripes are more horizontal, use the upper adjuster, if they are more vertical, use the lower adjuster.

- You will probably see multiple interference rings (similar to the left side of Figure 102). This means that there is a significant difference between the arm lengths of the interferometer. Loosen the CF125 clamp of the mirror not on the stage and move the mirror slightly further away from the beamsplitter, then secure the clamp again. As long as there are **more than ten rings within the beam on the screen you are multiple millimeters away from the target position.**
- Adjust the kinematic screws until the interference pattern reappears, then check if the central maximum is larger or smaller than before. If it is larger, you moved the mirror in the right direction. Repeat the process until the central maximum is so large that you only see one or two interference rings on the screen (as shown on the center image of Figure 102). If the central maximum became smaller after moving the mirror, then move the mirror in the opposite direction.

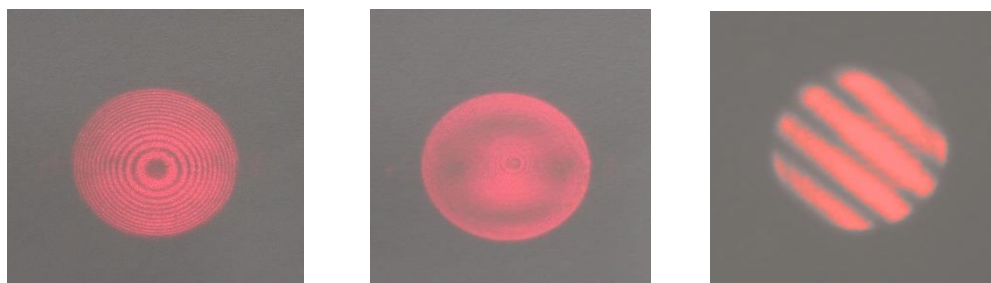


**Figure 102      Centered Interference Pattern for Large (Left) and Small (Center) Path Length Differences of the Interferometer Arms and a Non-Centered Pattern (Right)**

- Once you have found a mirror position that results in only one or two interference rings, move the coarse adjuster of the differential screw of the stage (see Figure 104) slowly in one direction and check whether the central maximum (or minimum) of the interference pattern becomes bigger or smaller. You may have to slightly adjust the kinematic screws of one mirror from time to time to move the central maximum (or minimum) back into view. The goal is to find a position of the stage at which the whole spot is either completely dark or uniformly red. This corresponds to a nearly equal distance between the two mirrors to the beamsplitter.
- Once you found this position, remove the lens, and switch off the alignment laser. Place the LED in front of the beamsplitter as seen in Figure 103. Connect the LED to the power grid via the DS5 power supply.

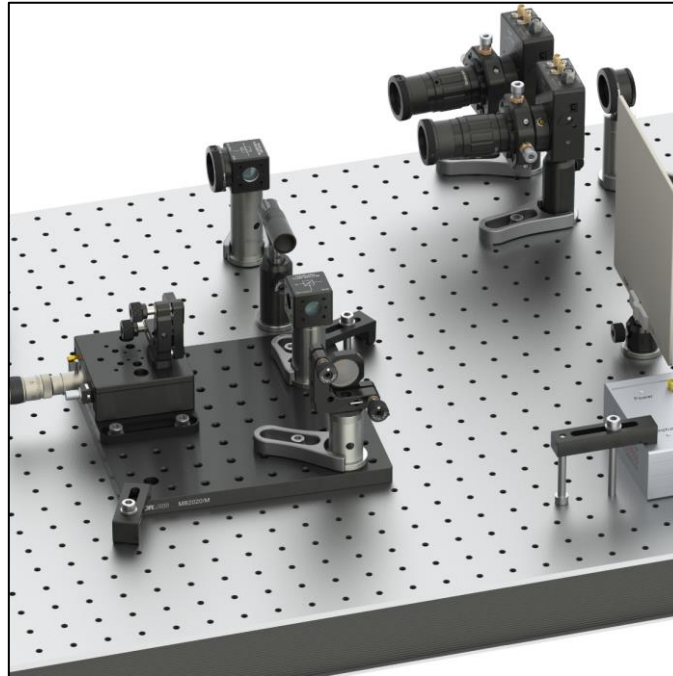


**Figure 103 Position of the LED in Front of the Michelson Interferometer**

- Probably, you will not yet see an interference pattern on the screen. Move the fine adjuster of the differential screw of the stage (see Figure 104) very slowly (about 2 small scale markers per second) in one direction, until an interference pattern appears<sup>79</sup>. If you reach the end of the travel range without seeing a pattern, turn the screw the other way until you see the pattern<sup>80</sup>.



**Figure 104 Coarse and Fine Adjuster of the NFL5DP20S/(M) Stage**

- If you see no pattern over the entire range of the stage, you need to switch back to the alignment laser and lens and change the mirror position until you see an interference pattern with an even larger central maximum/minimum.
- Once you have found the interference with the LED, you have successfully adjusted the Michelson interferometer. Remove the LED. Check whether the beam of the alignment laser is still centered on both the Ø8.0 mm iris aperture and the aperture on the beamsplitter, then switch it off and open both apertures completely.

The above procedure requires experience or time to find the interference pattern on the screen. As an alternative, one may continue to place the detector as described in Section 7.6.3, place and connect the KPC101 controller as described in Section 7.6.6, and visualize the count rate on detector B in the Michelson Interferometer tab of the software. The small portion of photons from the LED which pass the bandpass filter of the detector have a longer coherence length than the full LED spectrum, which makes it easier to find the

<sup>79</sup> The LED provides less intensity than the laser and might be difficult to see on the screen in a bright room. In this case, darken the room until the LED spot is clearly visible on the screen.

<sup>80</sup> Due to the shorter coherence length of the LED in comparison to the alignment laser, you will only see an interference pattern when the arm length difference is nearly zero. Thus, the pattern will always consist of wide stripes, or a single maximum as shown in the center image of Figure 102.

correct stage position. Close the iris of the B detector completely (to avoid detector saturation) and start a measurement and let the stage move about  $2 \mu\text{m}$ . You might already see an oscillating signal with a period of  $0.4 \mu\text{m}$ . If not, carefully turn the coarse adjuster screw (in steps of 5 small scale markers) in one direction until you see the count rate oscillating. Use the adjusters to maximize the amplitude of the oscillation, as shown in Figure 105.

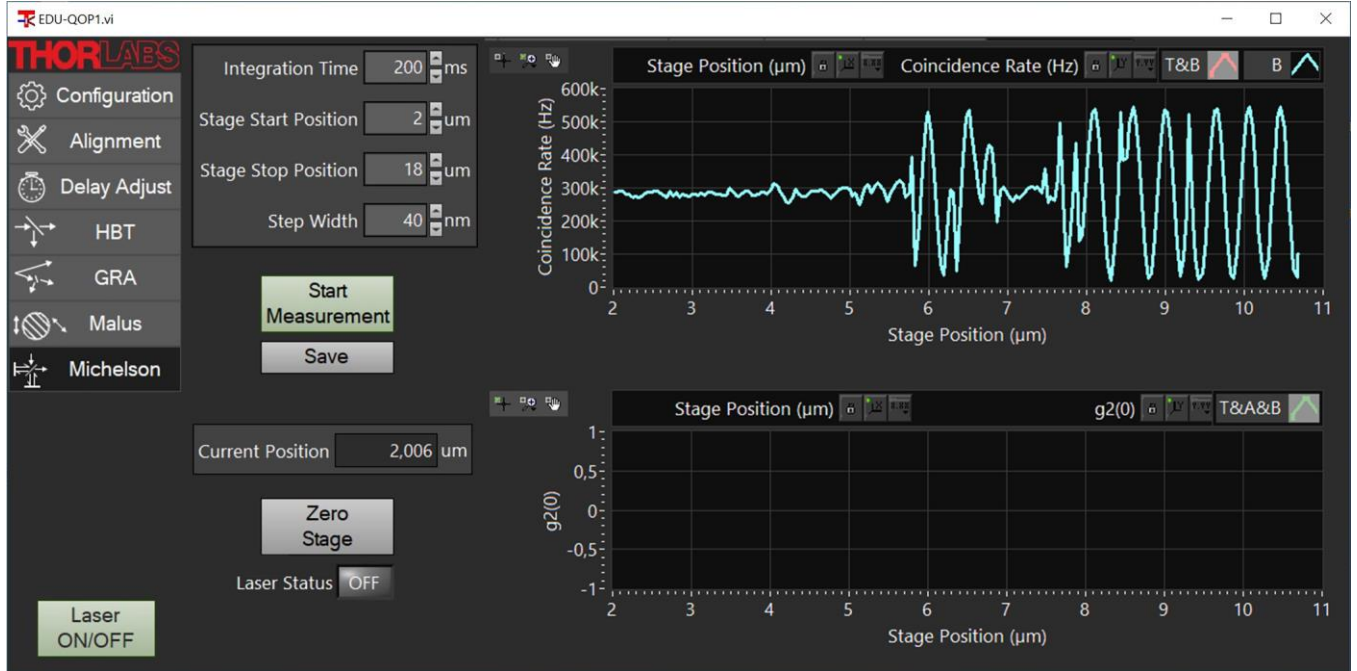


**Figure 105** Adjusting the Stage Position Using the Software

### 7.6.3 Detector Positioning

- Remove the LED and switch on the alignment laser. Remove the screen. Use the screen to block the arm of the Michelson Interferometer that leads to the mirror not on the stage, as seen in Figure 106.
- Place the alignment target in the interferometer output right next to the interferometer board so that the alignment laser passes through the hole in the target.
- Take the third detector and screw the lens tube with the economy beamsplitter on its front.
- Position the detector at least 15 cm away from the target, as seen in Figure 106.

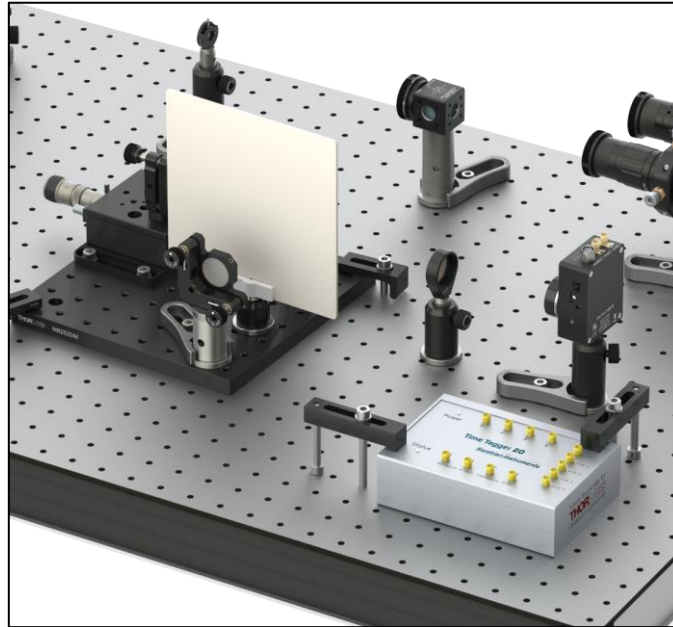


**Figure 106      Setup for Positioning the Detector in the Output of the Michelson Interferometer**

- Adjust height, position, and rotation of the detector in such a way<sup>81</sup> that:
  - The light passing through the hole in the target is centered on the detector chip.
  - The reflection from the beamsplitter in front of the detector is passing back through the hole in the target.
- Then secure the detector position with a CF125 clamp and a 1/4"-20 x 3/8" (M6 x 10 mm) cap screw plus washer. Remove the lens tube with the beamsplitter from the detector.
- Take the remaining detector optic and loosen the locking screw of the DTSM1 coupler almost completely. Slide it over the dovetail adapter on the front of the detector. Rotate the optics until one of the adjusters is pointing straight upwards. Then tighten the locking screw of the DTSM1 coupler to securely connect the optics to the detector.

#### 7.6.4    Detector Fine Adjustment

- Switch off the alignment laser and transfer it to its original position in the setup, remove the target from the interferometer output, and replace the axicon with the colored glass filter.
- Set the current of the pump laser to about 5 mA **below the lasing threshold** (check the spec sheet of your laser diode) and switch on the pump laser. **Always wear laser safety glasses when working with the pump laser!** Darken the room to similar conditions as before.
- Find the maximum count rate for detector B just like you did before by turning the two kinematic screws of the CXY1A mount and the zoom housing<sup>82</sup>. To avoid inconvenient scaling of the graphs, temporarily deactivate the curves of detectors T and A (right click on the legend and deactivate the **Plot Visible** option).
- Switch off the pump laser and replace the colored glass filter with the BBO crystal.
- Set the laser current to a value corresponding to about 13 mW output power (check the spec sheet of your laser diode) and switch on the pump laser. You should see a sharp increase in the count rate of

<sup>81</sup> The alignment laser has only an eighth of its original intensity at this point due to passing a beamsplitter three times. Thus, it can be difficult to see in a bright room. Darken the room until the alignment laser spot becomes clearly visible on the target and detector.

<sup>82</sup> If you have trouble finding the signal, you can increase the pump laser current by 5 mA to get a higher signal. Close the iris apertures in front of detectors T and A in this case to avoid saturating the Time Tagger. Remember to open them again afterwards!

detector B in the software. The count rate will be less than detector A. The coincidences T&B should also increase but will be lower (by a factor in the range of 5 to 10) than the T&A coincidence count rate.

- Slightly rotate the golden kinematic screw of the crystal holder back and forth to make sure that the maximum count rate of detector B is at a similar screw position compared to the other two detectors. If the screw positions of the maxima are significantly different, repeat the positioning of the third detector.
- Switch to the Delay Adjust tab of the software and start a measurement with standard settings. Record the delay value for the center of the peak for detector B and write this value into the **Delay B to T** field. This value might differ from the value measured earlier because the light travels a longer distance before reaching the detector, which takes about 1 ns of additional time.

### 7.6.5 Single Photon Interference Adjustment

- Remove the screen from the Michelson interferometer. Turn the fine adjuster of the differential screw of the translation stage (see Figure 104) very carefully. You should see a fluctuation of the coincidence signal between detectors T&B in the software, due to the interference. Temporarily removing the T&A curve from the lower graph (right click on the legend and deactivate the **Plot Visible** option) can help with scaling.
- In case you do not see that fluctuation:
  - Switch off the pump laser. Transfer the alignment laser to the magnetic plate behind the crystal. Place the screen in front of detector B.
  - Switch on the alignment laser and check if the light from the two interferometer arms hits the screen at the same position. If not, use the Michelson mirror that is not on the stage (**do not use the one on the stage!**)<sup>83</sup> to overlap the two spots.
  - Place the lens between alignment laser and interferometer. You should see an interference pattern on the screen. Use the Michelson mirror that is not on the stage (**do not use the one on the stage!**) to move the central maximum of the pattern to the center.
  - Switch off the alignment laser and move it to its original place in the setup. Remove the lens and place the LED in front of the interferometer. After switching on the LED, you should see an interference pattern on the screen. If not, turn the fine adjuster of the translation stage (see Figure 104) carefully in both directions until the pattern appears.
  - The pattern should still consist of a centered minimum or maximum. If not, then use the mirror that is not on the stage (**do not use the mirror on the stage!**) to move the central maximum to the center of the pattern.
  - Remove the LED and the screen.
  - Switch on the pump laser and repeat the above test for the fluctuation of the coincidences, which you should now see.

### 7.6.6 Michelson Interferometer Test Measurement

- Remove the bottom plate from the KPC101 controller and fix it to the breadboard to the right next to the KLD101 controller with a 1/4"-20 x 3/8" (M6 x 10 mm) cap screw and washer.
- Connect the controller to its bottom plate and connect it to the power grid via the KPS201 power supply. Connect the controller to your PC via the USB cable included in the controller packaging.
- Connect the HV-Output port of the KPC101 controller to the input port of the NFL5DP20S(/M) stage via the SMC-SMC cable included in the stage packaging.

<sup>83</sup> The position of the light leaving the interferometer on the detector was adjusted with the mirror on the stage. Therefore, this mirror should not be moved afterwards, and every fine alignment should be done with the other mirror.

- Connect the Strain Gauge I/P port of the KPC101 controller with the Strain Gauge port of the NFL5DP20S(/M) stage via the TypeD-to-LEMO cable included with the stage.
- It is recommended you use CS1 cable strips and 1/4"-20 x 1/4" (M6 x 6 mm) cap screws plus washers for better cable management (as seen in Figure 107). Switch on the controller. Figure 96 shows a photo of the complete Michelson Interferometer setup.

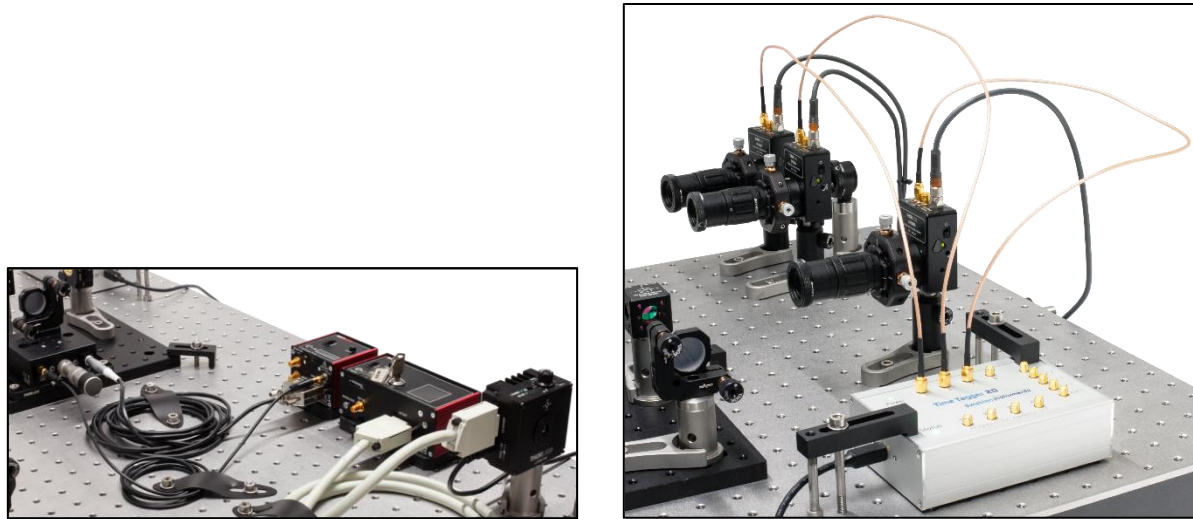


**Figure 107      Cable Management for Single Photon Michelson Interferometer Setup**

- Open the Michelson-Tab in the software and click the Zero Stage button. Wait for the calibration to finish.
- Start a measurement with the parameters that are pre-set. You should see a typical Michelson interference curve as shown in Figure 108. The maxima should be evenly spaced.

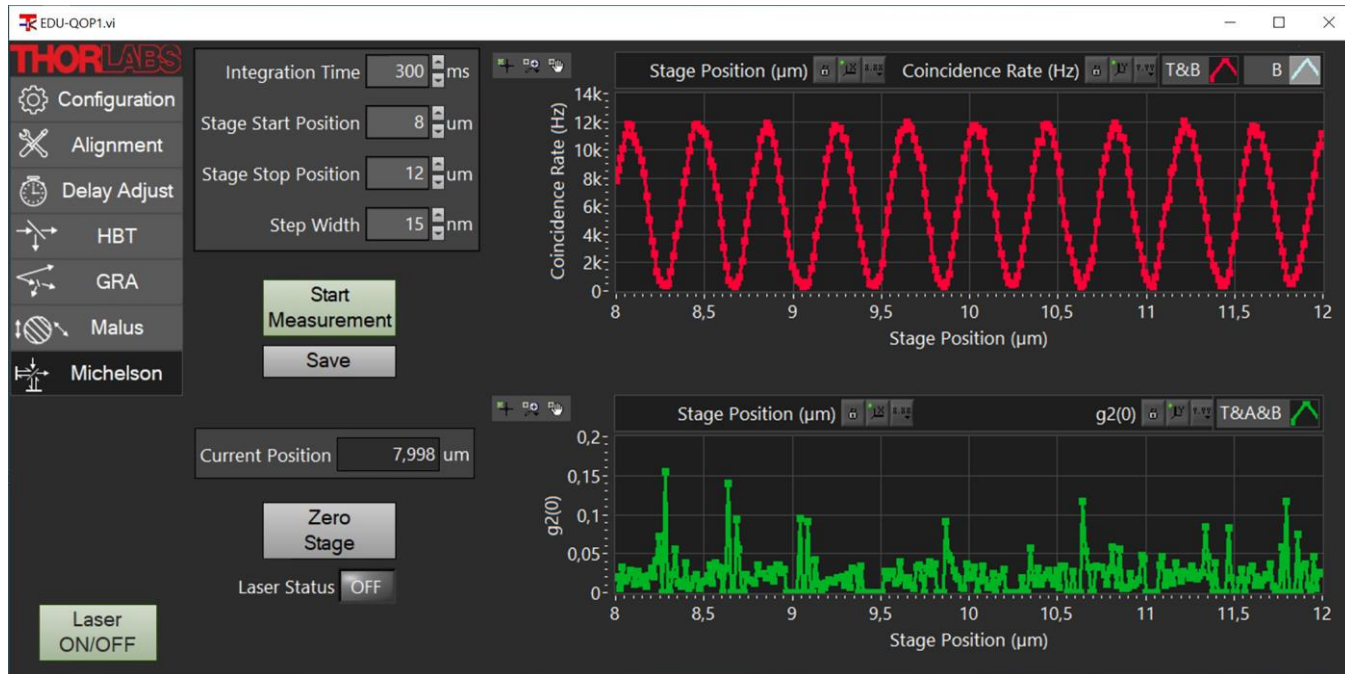


**Figure 108      Typical Result of Michelson Test Measurement**

- If you see the interference, then your Michelson Interferometer is aligned. For more details on the Michelson experiment, see Sections 3.6 and 9.7.

## 7.7 Setting Up the Quantum Eraser

As a first step, the two  $\varnothing 1/2"$  polarizers need to be calibrated as follows:

- Place the  $\varnothing 1"$  polarizer in front of the T-detector.
- Watch the count rate of the T-detector in the alignment tab of the software (deactivate the other two graphs).
- Check whether the count rate is higher for the  $0^\circ$  or  $90^\circ$  setting of the polarizer.
  - If the count rate is higher for the  $90^\circ$  setting, your polarizer axis is parallel to the table plane at the  $0^\circ$  setting, which is the desired case.
  - If the count rate is higher for the  $0^\circ$  setting, then your polarizer axis is perpendicular to the table plane at  $0^\circ$ . In this case, set the polarizer to  $90^\circ$ , lock it, and re-align the scale to show  $0^\circ$  to reach the desired case.
- Set the  $\varnothing 1"$  polarizer to  $90^\circ$  and place one of the  $\varnothing 1/2"$  polarizers behind the  $\varnothing 1"$  polarizer (You must place the  $\varnothing 1/2"$  polarizer on the PS3 spacer to make the beam heights match).
- Rotate the  $\varnothing 1/2"$  polarizer until the count rate of detector T is minimized. Then tighten the locking screw. It is now perpendicular to the  $\varnothing 1"$  polarizer. Set the scale of the  $\varnothing 1/2"$  polarizer to  $90^\circ$  (loosen two screws on the front face, set scale, and retighten screws). You have now ensured that this polarizer is calibrated exactly the same as the first one.
- Replace the  $\varnothing 1/2"$  polarizer with the other one and repeat the procedure.
- Remove the polarizers from the breadboard.

Now the polarizers are calibrated and can be inserted into the interferometer as follows:

- Switch off the pump laser and transfer the alignment laser to the magnetic plate behind the crystal.
- Place the alignment target between the small iris and the first beamsplitter, so that the alignment laser passes through the hole in the target. Set the WPH10ME-808 half-wave plate to  $22.5^\circ$  and place it between the two beamsplitters (as close as possible to the first beamsplitter), so that the scale of the rotation mount faces the interferometer. Make sure that the alignment laser is centered on the wave plate and block the beam both behind the wave plate and in front of detector A either with cards (as shown in Figure 109) or with the screen.
- Rotate the wave plate component until the reflection from it passes back through the hole in the target, as seen in Figure 109. Secure the wave plate position with a CF125 clamp via a  $1/4"-20 \times 3/8"$  (M6 x 10 mm) cap screw plus washer.

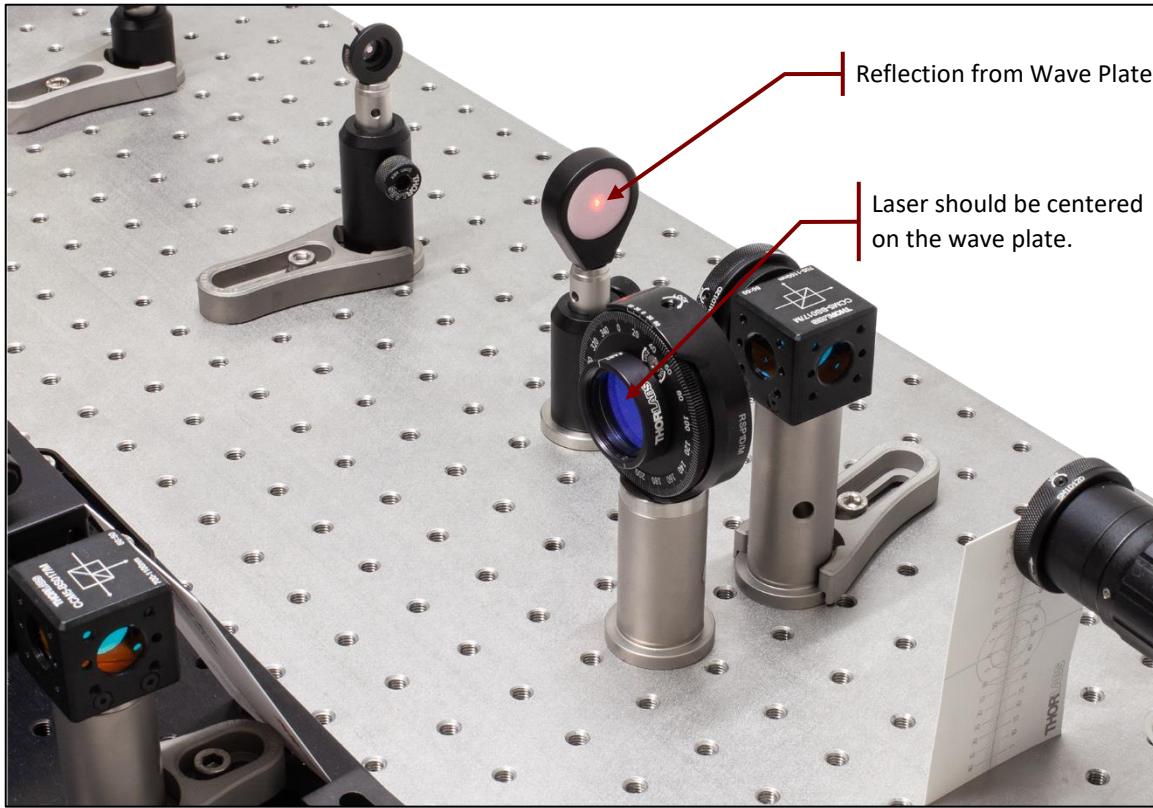


**Figure 109 Positioning of the Half-Wave Plate**

- Place the alignment target in front of the interferometer beamsplitter so that the alignment laser passes through the hole in the target.
- Place one of the polarizers with 1/2" diameter in the arm of the interferometer that leads to the mirror on the stage. Make sure the alignment laser is centered on the polarizer. Block the interferometer output with the screen, block the other arm of the interferometer with a card, and rotate the polarizer component until the reflection from the polarizer passes back through the alignment target, as shown in Figure 110. Secure the polarizer position with a CF125 clamp via a 1/4"-20 x 3/8" (M6 x 10 mm) cap screw plus washer, then set it to 0°.

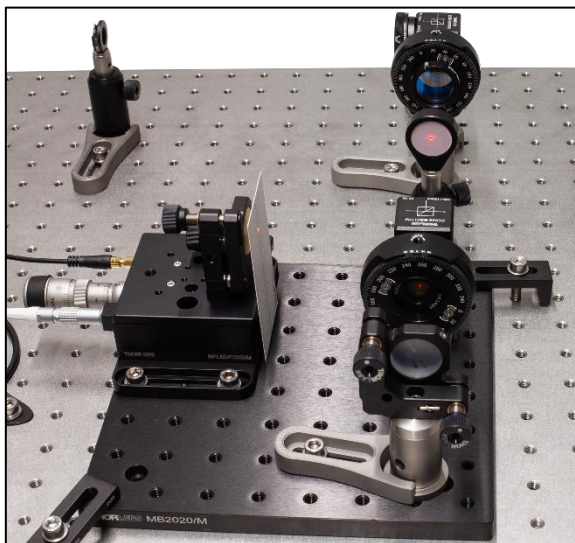


**Figure 110 Positioning of a Polarizer in the Interferometer**

- Repeat the above step for the second polarizer in the other arm of the interferometer (use a short clamp instead of a CF125 clamp). Set this polarizer to  $0^\circ$  as well. Remove the target from the breadboard, switch off the alignment laser, and transfer the laser to its original position in the setup.
- Place the LED between the two beamsplitters pointing towards the Michelson Interferometer. Place the screen in front of Detector B.
- Switch on the LED. You should see an interference pattern. If not, carefully turn the fine adjuster of the Michelson stage (see Figure 104) until you see a pattern with good contrast.
- Most likely, the pattern will consist of stripes. Use the kinematic screws of the Michelson mirror not on the stage (**do not use the one on the stage!**) to find the central maximum.
- Remove the screen and the LED from the setup. Figure 111 shows the Michelson interferometer prepared for the Quantum Eraser measurements.

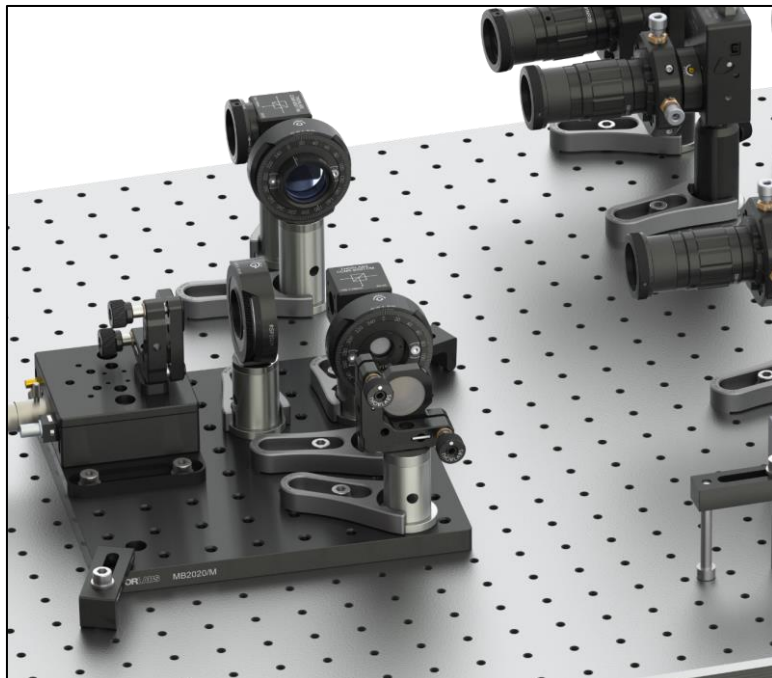


**Figure 111      Michelson Interferometer Prepared for the Quantum Eraser Measurement**

- Perform the same test measurement as described in the last step of Section 7.6.6. If you see the interference minima and maxima, you have adjusted the Quantum Eraser properly. For more details on this experiment, see Sections 3.8 and 9.8.

## Chapter 8 Learning Goals and Misconceptions

Since quantum optics is both an exciting and challenging topic, the following table summarizes the experiments and the learning goals.

Exercise	Experiment	Learning Goal	Possible Misconception
1	Attenuated Laser (Section 9.1)	Attenuated laser light is not a single photon source.	People tend to have the misconception that laser light is just a barrage of photons, visualized as little dots. In that image, attenuation leads to a reduction of photons, eventually just leaving “individually flying dots.” This image disregards the fact that photon arrival at a detector follows an underlying statistic. The attenuation of the laser light does <u>not</u> change the underlying statistic from a coherent to a non-classical source.
2	Pair Source (Section 9.2)	The BBO crystal generates photon pairs. Due to their simultaneous arrival at two detectors, the coincidence counts well exceed the expected value for a random/thermal light source.	
3	HBT in One Arm of the Pair Source (Section 9.3)	When only one arm of the pair source is considered, the light still shows classical characteristics.	The misconception here is that, once the pairs are generated, we have “two single photon sources,” namely each in one arm. This is not true. When only one arm is considered, the statistics of the light is still classical.
4	HBT with Pair Source / GRA Experiment (Section 9.4)	When both photons of the pair are considered, the light in one arm shows non-classical properties. This constitutes a photon pair source, also called a heralded single photon source (see Section 3.5.4).	
5	Fluorescent Filter (Section 9.5)	A measurement of light coming from a fluorescent filter similar to exercise 4 (i.e., with three detectors) does not yield a non-classical light source.	This exercise demonstrates to students that it is really the pair source property of the light coming from the BBO that induces the non-classical nature (and not the three-detector arrangement). If a classical light source is measured in the three-detector arrangement, the properties are still classical.
6	Malus' Law (Section 9.6)	Behavior of single photons at a polarizer	In classical wave theory, light that is incident on a polarizer can be split into parts that are parallel and perpendicular to

			<p>the polarizer's orientation. One is absorbed, the other transmitted.</p> <p>But how does this work for single photons since they cannot be split into two parts?</p> <p>In quantum optics, the photon's polarization state is expressed by a superposition of basis states. The proportionate transmission of a classical wave is replaced by the <u>probability</u> of transmitting through the polarizer. If the photon is transmitted, it retains its energy and has the polarization set by the polarizer. Otherwise, it is absorbed.</p>
7	Single Photon Michelson Interferometer (Section 9.7)	Even single photons exhibit interference.	<p>Here, the misperception of a photon as a little flying dot is revealed: similar to a double slit, a dot-like photon would only pass through either arm of the interferometer. Thus, it would not have information about the second arm and not show interference. However, interference is observable even with a heralded single photon source. The average number of photons in the setup is about 0.02 (even less in the Michelson interferometer part), so two photons interfering with each other can be ruled out.</p>
8	Quantum Eraser (Section 9.8)	Orthogonal polarizers in two interferometer arms yield the path information, thus losing interference. A suitable polarizer after the interferometer can erase that path information, thus recovering the interference.	<p>Suppose the eraser is not yet in the system. The misconception is that the photon would have to decide on one of the paths. This misconception is debunked by the fact that the polarizer after the interferometer can retrieve the interference.</p> <p>Fundamentally, the photon is in a superposition of states and is only in an individual state once it is measured. If the measurement is not designed in this regard, the photon does not have to "decide" for a path in the interferometer.</p>

## Chapter 9 Experiments

In this chapter, experiments that can be performed with the kit are described in detail. The learning goals of the experiments and common misconceptions that may be worth addressing in a lab course are summarized in Chapter 8.

If switching back and forth between experiments is intended, the Michelson board can be marked with additional clamps and moved in and out of the setup. For detailed instructions, see Section 12.13.

### 9.1 HBT-Experiment with Attenuated Laser

**Goal:** Test whether an attenuated laser is a suitable single photon source.

**Setup:** The alignment laser is attenuated by an ND filter and then hits a beamsplitter. The detectors A and B are placed in the output ports of the beamsplitter. For the adjustment of the setup, see Section 7.3.

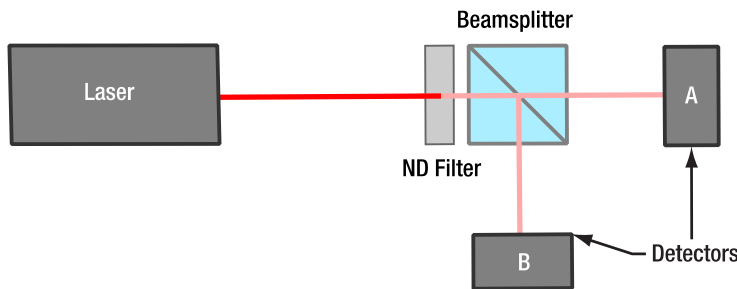


**Figure 112 Schematic Setup for the Attenuated Laser HBT Experiment**

You can also perform this experiment in the same configuration as for the experiments in Section 9.3 onwards. Simply transfer the alignment laser to the base behind the crystal or use the light cone generated by the axicon in combination with the alignment target.

**Measurement:** Darken the room, open the HBT-Tab in the software, switch on the alignment laser, and start a measurement with a measurement time of 20 s. Save the result.

**Result Analysis:** The correlation  $g_{HBT}^{(2)}(0)$  is calculated automatically via the following equation (for the derivation, see Section 3.5.2):

$$g_{HBT}^{(2)}(0) = \frac{R_{AB}}{R_A \cdot R_B \cdot \Delta t}$$

The measured  $g_{HBT}^{(2)}(0)$  will be close to 1. Less laser intensity would only increase the error bar (or increase the measurement time required to reach the same error bar), it does not change the result<sup>84</sup>. Table 1 shows the results of an example measurement.

Spec	Measured Value
$\Delta t$	5 ns
$R_A$	391118.45 Hz
$R_B$	315945.65 Hz
$R_{AB}$	619.1 Hz
$g_{HBT}^{(2)}(0)$	1.00201

**Table 1 Results of Example Measurement (HBT with Attenuated Laser)**

<sup>84</sup> If you want to show this experimentally, it is possible to use a second ND filter with higher optical density. Be aware that the measurement time to reach a meaningful statistic will be tens of minutes in this case.

**Interpretation:** Let us start with an assumption that is very compelling, **but totally wrong**: The laser emits a stream of photons with a constant time interval between them. The photon energy per time fits the laser power and when attenuating this laser by a factor  $x$ , every  $x$ th photon passes the attenuator. In this case, we could calculate the number of photons  $n$  that are in the setup at average from the length of the setup  $l$ , the speed of light  $c$  and the frequency  $f$  of photons per second as follows:

$$n = \frac{l}{c} \cdot f$$

In our case, we measure about 300 kHz of count rate at both detectors. The detection efficiency is about 0.5, so there are 600,000 photons per detector per second, resulting in an overall frequency  $f$  of 1200 kHz. The setup is about 1 m long. We get as a result:

$$n = \frac{l}{c} \cdot f = \frac{1 \text{ m}}{3 \cdot 10^8 \frac{\text{m}}{\text{s}}} \cdot 1.2 \cdot 10^6 \text{ Hz} = 0.004$$

We have only 0.004 photons in the setup on average! All photons that we measure should be single photons! Those cannot be split at the beamsplitter, so we expect no double coincidences and  $g_{HBT}^{(2)}(0) \ll 1$ .

However, this is not what we measure: We get  $g_{HBT}^{(2)}(0) = 1$ , irrespective of the attenuation. This is because the initial assumption of the “evenly spaced photons” **was totally wrong**.

In reality, laser light is quantum mechanically represented by a coherent state, as seen in Section 3.3.2. For this state, the photon statistic is a Poisson distribution (see Figure 6). Irrespective of the attenuation, the laser always emits multiple photons often enough to make  $g_{HBT}^{(2)}(0) = 1$  the expected result. Simply attenuating the laser does not change the underlying statistics of the light<sup>85</sup>.

This means that **it is not possible to perform single photon experiments with an attenuated laser**, even a strongly attenuated one!

## 9.2 Photon Pair Source

**Goal:** Test, whether the source is indeed emitting photon pairs.

**Setup:** The pump laser is generating photon pairs in the BBO crystal. One single photon detector is placed in each path, as seen in Figure 113. For the adjustment of the setup, see Section 7.3.

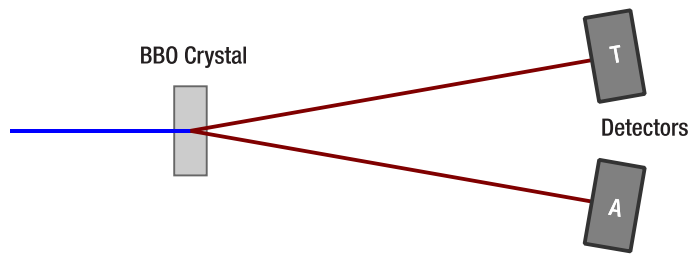


**Figure 113 Schematic Setup for the Photon Pair Source**

**Measurement:** Darken the room, open the Adjustment Tab in the software and start the laser. Record the count rates for detectors T and A in the upper graph and the coincidence count rate T&A in the lower graph. You can also use the GRA-Tab to determine the values with better accuracy.

**Result Analysis:** Calculate the correlation  $g_{PS}^{(2)}(0)$  between the two detectors via the following formula (for the derivation, see Section 3.5.2):

<sup>85</sup> In the experiment here, the laser is attenuated both before and after the beamsplitter due to the bandpass filters in front of the detectors. Ideally, the attenuation would take place only before the beamsplitter. This could be achieved by substituting the bandpass filters for ones with a central wavelength of 635 nm and using a stronger ND filter (or multiple filters). However, we do not recommend this, as it leads to significant problems with stray light. Furthermore, it will not change anything about the results of the measurement as the underlying arguments remain valid.

$$g_{PS}^{(2)}(0) = \frac{R_{TA}}{R_T \cdot R_A \cdot \Delta t}$$

Here,  $R_T$  and  $R_A$  are the single count rates of detectors T and A, respectively,  $R_{TA}$  is the coincidence count rate of the two detectors, and  $\Delta t$  is the coincidence window of the experiment.

**Interpretation:** For completely uncorrelated light, one would expect the coincidences to be completely random, resulting in a  $g_{PS}^{(2)}(0)$  value of 1. However, due to the photon pairs generated by the BBO crystal, there are many more coincidences than what would be expected in the random case. The value of  $g_{PS}^{(2)}(0)$  is the factor between the measured and expected coincidences and should be at least 30 in the measurement you have taken. Such a large  $g_{PS}^{(2)}(0)$  proves the generation of photon pairs. For a more detailed explanation, see Section 3.5.2.

### 9.3 HBT Experiment with one Arm of the Pair Source

**Goal:** Test if one arm of the photon pair source is a single photon source.

**Setup:** Take the setup from Section 9.2, place a beamsplitter in one of the detection arms and place single photon detectors at both outputs of the beamsplitter, see Figure 114. For the adjustment of the setup, see Section 7.5. Then block the arm leading to detector T with the screen.

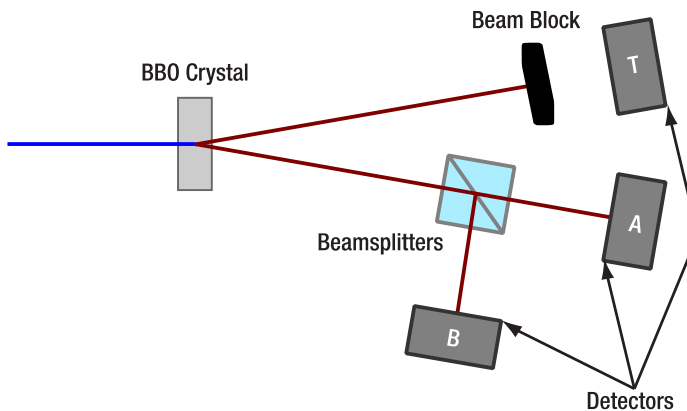


**Figure 114      Schematic Setup for the HBT Experiment with one Arm of the Pair Source**

**Measurement:** Darken the room and open the HBT tab in the software. Set the measurement time to 20 s, perform 10 measurements, and record the results of each measurement.

**Result Analysis:** The correlation  $g_{HBT}^{(2)}(0)$  is calculated automatically via the following equation (for the derivation, see Section 3.5.2):

$$g_{HBT}^{(2)}(0) = \frac{R_{AB}}{R_A \cdot R_B \cdot \Delta t}$$

The result will be  $g_{HBT}^{(2)}(0) = 1$  within the error of the measurement for every one of the 10 measurements.

**Interpretation:** A single arm of the photon pair source is not a single photon source. The photons are actually in a thermal state, so one would expect  $g_{HBT}^{(2)}(0) = 2$  with ideal detectors. However, as explained in Section 3.5.2, the time resolution of the detectors used here is far too low and integration leads to the result  $g_{HBT}^{(2)}(0) = 1$ . To perform single photon experiments with a pair source, one must use the information of the second photon of a pair to create a single photon state, which is shown in the next experiment.

### 9.4 Grangier-Roger-Aspect Experiment

**Goal:** Test whether the pair source is a single photon source when counts are measured only in coincidence with the trigger detector.

**Setup:** Take the setup from Section 9.3 and remove the screen. This setup reproduces the experiment by Grangier, Roger, and Aspect (GRA) that is explained in Section 3.5.3.

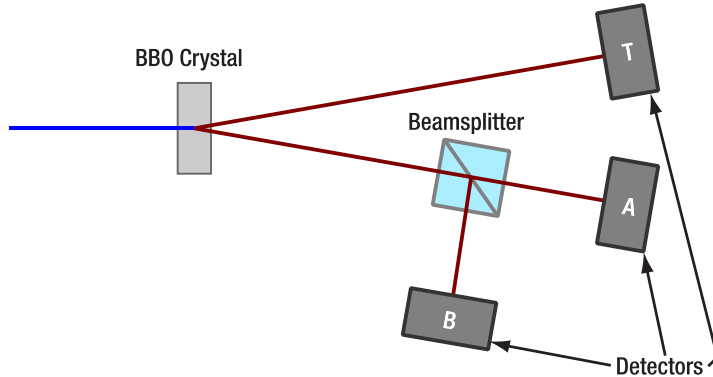


**Figure 115 Schematic Setup for the Grangier-Roger-Aspect Experiment**

**Measurement:** Darken the room and open the GRA tab in the software. Set the measurement time to 1 s, perform 10 measurements, and record the results of each measurement. Then set the measurement time to 20 s and again record ten measurements.

**Result Analysis:** The correlation  $g_{GRA}^{(2)}(0)$  is calculated automatically via the following equation (for the derivation, see Section 3.5.4):

$$g_{GRA}^{(2)}(0) = \frac{R_{TAB} \cdot R_T}{R_{TA} \cdot R_{TB}}$$

Here,  $R_T$  is the single count rate of detector T,  $R_{TA}$  and  $R_{TB}$  are the twofold coincidence count rates of detector T with detectors A and B, respectively, and  $R_{TAB}$  is the triple coincidence count rate.

Compare the measurement series with 1 s and 20 s measurement time, respectively. Calculate the expectation value as well as the standard deviation of  $g^{(2)}(0)$  for both cases.

**Interpretation:** For classical light, one would expect a certain number of triple coincidences depending on the number of trigger events, resulting in a  $g^{(2)}(0)$  value between 1 and 2. However, the experiment results in  $g^{(2)}(0)$  have values much lower than 1, proving that we are dealing with a non-classical light source. For a more detailed explanation, see Section 3.5.4.

The expectation value of  $g^{(2)}(0)$  does not depend on the measurement time. The standard deviation on the other hand can be reduced by longer measurements. Table 2 shows an example measurement<sup>86</sup>.

<sup>86</sup> This result was obtained under nearly ideal conditions. If there is a bit more of stray light in your setup or the alignment is not quite optimal, your value of  $g_{GRA}^{(2)}(0)$  might be larger, e.g., about 0.2 or similar. However, this does not impact the meaning of the result because, as described in Section 3.5.3, every value lower than 1 proves the quantum nature of light.

Spec	Measured Value
Total Measurement Time	20.000 s
Counts (Detector T)	4.638 M
Counts (Detector A)	2.905 M
Counts (Detector B)	2.925 M
Coincidence Counts (T&A)	385,865
Coincidence Counts (T&B)	324,688
Coincidence Counts (T&A&B)	513
$g^{(2)}(0)$ - Correlation T&A	114.547
$g^{(2)}(0)$ - Correlation A&B	0.0190
Triggered by T (GRA Setup)	

**Table 2 Example Measurement for the Grangier-Roger-Aspect Experiment**

## 9.5 GRA Experiment with Classical Light

**Goal:** Perform the GRA experiment with a non-pair source.

**Setup:** Use the setup of Section 9.4 and replace the BBO crystal with the fluorescent filter. The filter will emit fluorescent light in all directions, so that you can perform the GRA experiment with it. A schematic of the setup is shown in Figure 116.

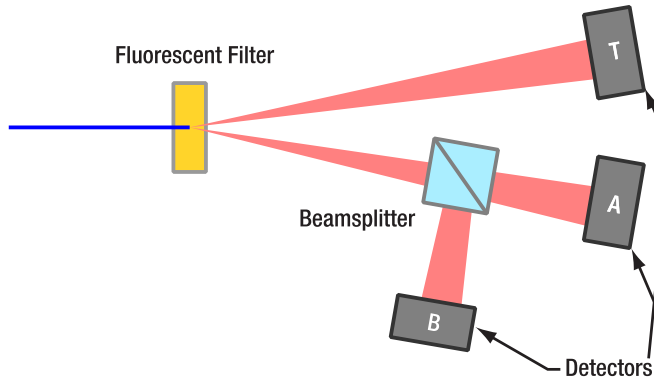


**Figure 116 Schematic Setup of the GRA Experiment with the Fluorescent Filter (Only Relevant Parts of the Fluorescent Light Cone are Shown)**

**Measurement:** Darken the room, set the laser current to about 5 mA below the lasing threshold (check the spec sheet of your laser diode), open the GRA tab of the software and perform 10 measurements with 20 s measurement time each.

**Result Analysis:** The results are generated with the same formula as in Section 9.4.

$$g_{GRA}^{(2)}(0) = g_{HBT}^{(2)}(0) = \frac{R_{TAB} \cdot R_T}{R_{TA} \cdot R_{TB}}$$

However, this time, the result will always be close to 1.

**Interpretation:** The light from the filter is in a thermal state. The fluorescent photons are not generated as pairs but randomly. Thus, there is no correlation between events on detector T and detectors A and B. In this case the triple coincidence detection scheme produces the same result as the simpler HBT experiment:  $g^{(2)}(0) = 1$ . This

proves that the result measured in Section 9.4 was not generated only by the change of the detection scheme, but that a pair photon source is required to be able to generate single photon states this way.

## 9.6 Malus' Law for Single Photons

**Goal:** Test the polarization properties of single photons.

**Setup:** Take the setup from Section 9.4 and place a rotatable linear polarizer between the beamsplitter and detector, as seen in Figure 117. For the adjustment of the setup, see Section 7.5.4.

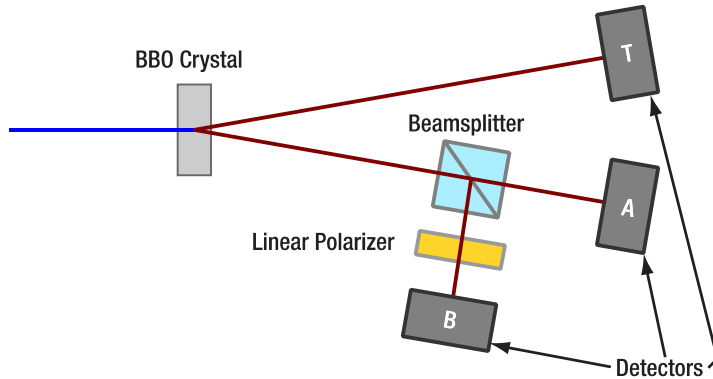


**Figure 117 Schematic Setup for the Single Photon Malus' Law Experiment**

**Measurement:** Set the polarizer to  $0^\circ$ . Darken the room and open the Malus Tab in the software. Set the measurement time to 20 s and record a measurement (the important data points are  $g_{GRA}^{(2)}(0)$  and  $R_{T\&B}$ ). Then rotate the polarizer by  $10^\circ$  and repeat the measurement. Record measurements in  $10^\circ$  steps between  $0^\circ$  and  $180^\circ$  (or  $360^\circ$  for a larger dataset).

**Result Analysis:** Plot the coincidence count rate  $R_{T\&B}$  and the correlation  $g_{GRA}^{(2)}(0)$  over the polarizer angle.

**Interpretation:** The coincidence count rate shows a  $\sin^2$ -dependence on the polarizer angle. This is known as Malus' law (for more details, see Section 3.7)<sup>87</sup>. However, the simultaneously measured correlation values  $g_{GRA}^{(2)}(0)$  are always well below 1, showing that the experiments were always in the single photon regime. The higher values for  $g_{GRA}^{(2)}(0)$  at  $0^\circ$ ,  $180^\circ$ , and  $360^\circ$  are a result of the extremely low count rates at those angles, significantly increasing the noise and the contribution of uncorrelated stray light to the signal. In summary, the experiment shows that single photons can pass through a linear polarizer (see Section 3.7) and that their probability to do so shows the same behavior as the intensity of a classical electromagnetic wave. An example measurement is shown in Figure 118.

<sup>87</sup> In Section 3.7.1, the dependence is  $\cos^2$  instead of  $\sin^2$ . This is because the polarizer is calibrated to  $0^\circ$  being the horizontal axis and the photons being vertically polarized. Be aware that if the setup is used for the first time, the polarizer might not be calibrated completely at this point, and a  $\cos^2$  dependence could be measured. See Section 7.7 on how to complete the polarizer calibration.

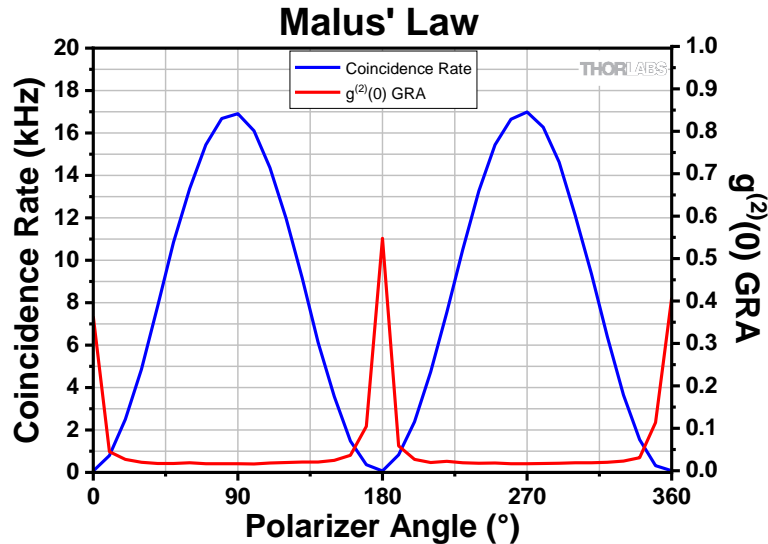


Figure 118 Example Measurement of Malus' Law for Single Photons

## 9.7 Single Photon Michelson Interferometer

**Goal:** Test the interference properties of single photons and determine their wavelength.

**Setup:** Take the setup from Section 9.4 and place a Michelson interferometer in one of the beamsplitter outputs. Place detector B in the output of the interferometer, as seen in Figure 119. For the adjustment of the setup, see Section 7.6.

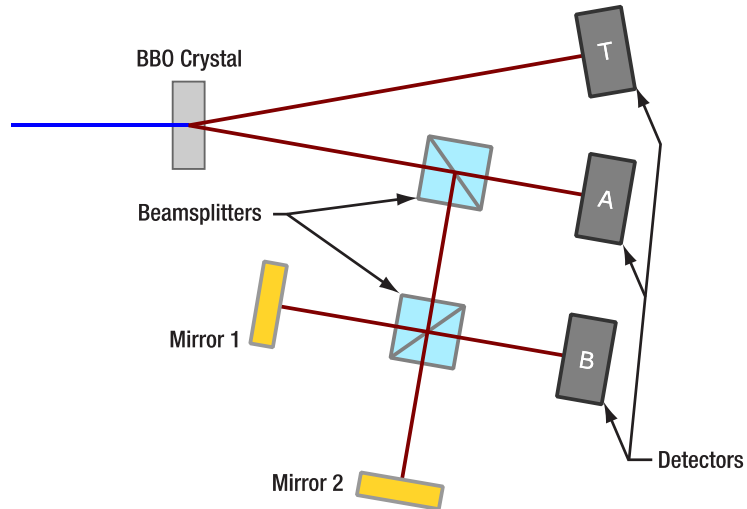


Figure 119 Schematic Setup of the Single Photon Michelson Interferometer

**Measurement:** Darken the room and open the Michelson Tab in the software. Start a measurement with a long range of stage positions (for example 2  $\mu\text{m}$  - 18  $\mu\text{m}$ ), a short integration time (such as 300 ms) and a medium step width (such as 25 nm). After the measurement is completed, save the data (see Section 11.3).

Record a second measurement, this time with a reduced measurement range (for example 9 µm Start Position and 11 µm End Position), a longer integration time (such as 1200 ms)<sup>88</sup>, and a smaller step width (such as 10 nm). Again, save the results after completion of the measurement.

**Result Analysis:** Open the .csv file of the first measurement with a spreadsheet software and plot the data for the coincidence count rate and the  $g_{GRA}^{(2)}(0)$  in one graph (use two different y-axes). Determine the average spacing of the maxima and calculate the wavelength of the single photons (see Section 3.6).

Open the spreadsheet of the second measurement and plot it in the same way. Compare the  $g_{GRA}^{(2)}(0)$  curves of both measurements.

#### Interpretation:

The first measurement shows the interferogram over nearly the entire range of the interferometer. An example measurement is shown in Figure 120. The interferogram resembles a sine curve. The maxima are evenly spaced, and the wavelength calculation should result in a value close to 810 nm (twice the pump laser wavelength; see Section 3.9), with an error of up to 3% due to the accuracy of the stage position control<sup>89</sup>. The amplitude of the interference is not changing significantly over the whole measurement range, pointing to a coherence length of the photons larger than 20 µm. Quantitatively determining the coherence length requires additional measurements (see Section 10.1).

<sup>88</sup> You could also reduce the step width below 15 nm to improve spatial resolution. However, there are small oscillations in the interferometer signal due to air currents that become more apparent at smaller step widths, negating most of the resolution gain. If you want to reduce these oscillations, we recommend placing a closed box over the interferometer (with openings for entry and exit of the beam; see Section 12.4).

<sup>89</sup> If higher precision is required, you can use the PL202 laser to do an interferometric calibration measurement of the stage. Compare the measured wavelength to the actual wavelength of the PL202 laser (given in the datasheet included with the laser) to determine a correction factor. Apply this factor to all future measurements to obtain more precise wavelength results.

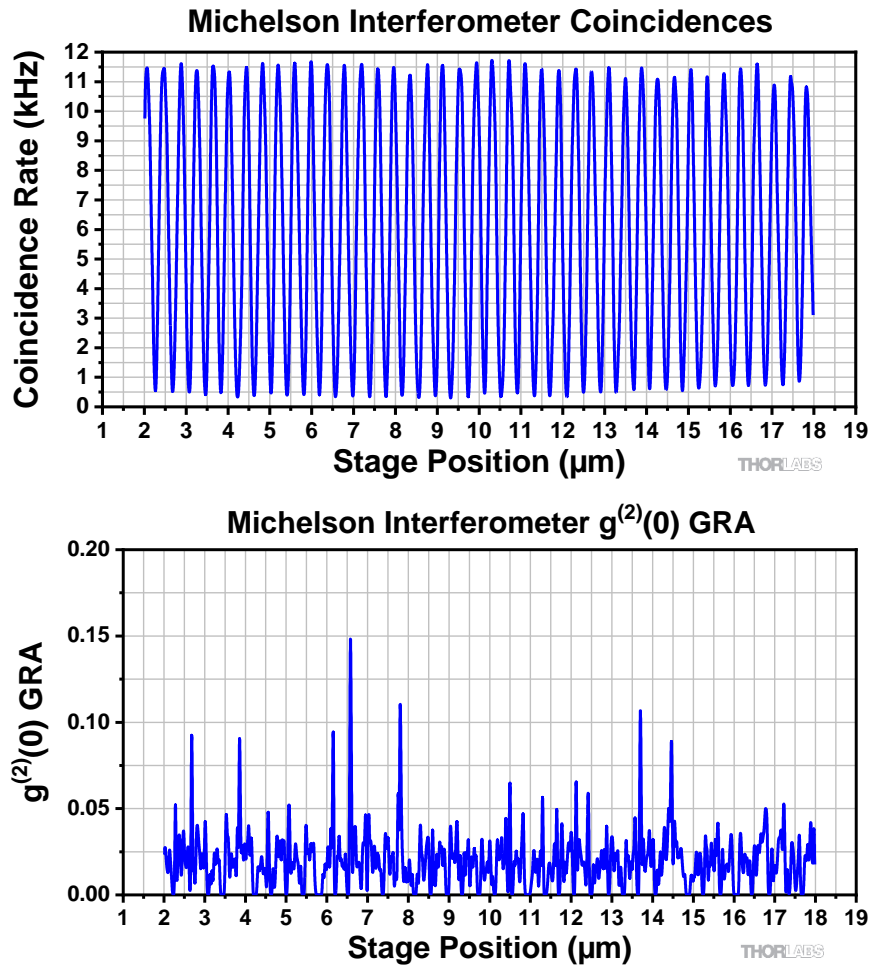


**Figure 120**    *Michelson Interferometer Measurement (Range: 2 μm - 18 μm; Step Size: 25 nm; Time per Data Point: 300 ms)*

The  $g_{GRA}^{(2)}(0)$  graph of the first measurement shows significant noise, as seen in Figure 120. For some data points  $g^{(2)}(0)$  is measured as 0 but can reach up to 0.15 at some points. The reason for this behavior is the short measurement time per data point. As the calculation of  $g_{GRA}^{(2)}(0)$  is highly sensitive to the number of triple coincidences (see Section 3.5.4), and those occur at a much lower rate than two-detector coincidences, more time is required to get meaningful values. However, the average  $g_{GRA}^{(2)}(0)$  is still well below 1, pointing to the single-photon regime.

For the second measurement, a larger time per data point and a smaller measurement range were used. An example measurement is shown in Figure 121. As a result of the increased time per data point, the noise of the  $g_{GRA}^{(2)}(0)$  curve is significantly lower than for the first measurement. The value of the function is always below 0.1, clearly proving that the whole measurement was performed with non-classical light. Around the minima of the interferogram, all coincidence count rates are much lower. This results in higher noise and a higher relative contribution of uncorrelated stray light to the signal for the  $g_{GRA}^{(2)}(0)$  values of these data points.

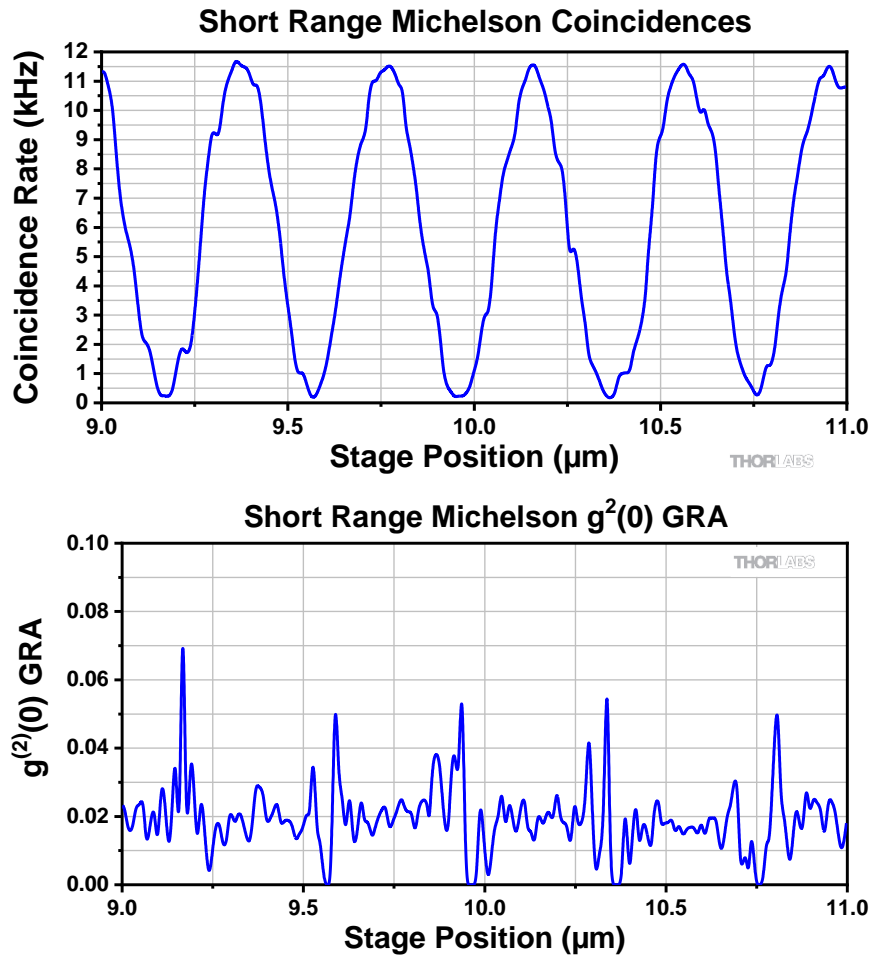


**Figure 121**    **Michelson Measurement (Range: 9  $\mu\text{m}$  - 11  $\mu\text{m}$ , Step Size: 10 nm, Time per Data Point: 1200 ms)**

## 9.8 Quantum Eraser

**Goal:** Show the quantum eraser effect for single photons.

**Setup:** Take the setup from Section 9.7 and place one 1/2" diameter polarizer in each arm of the Michelson Interferometer, as seen in Figure 122. For the adjustment of the setup, see Section 7.7.

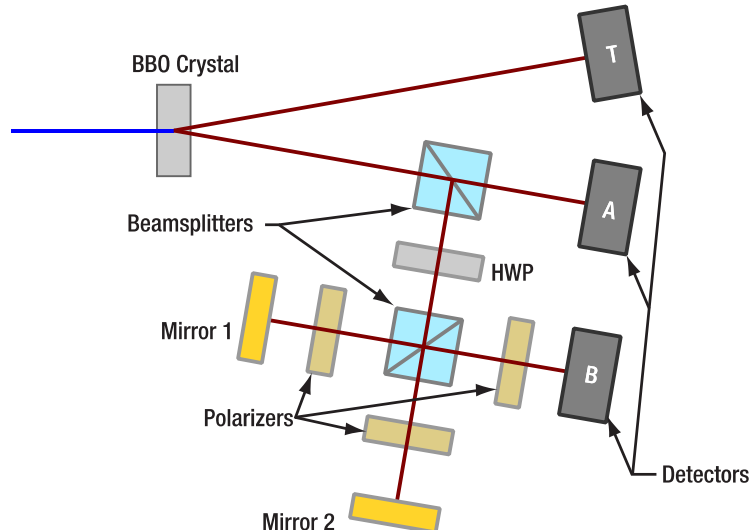


**Figure 122**    **Schematic Setup of the Quantum Eraser Experiment**

**Measurement:** Set both polarizers in the Michelson Interferometer to  $0^\circ$ , darken the room, and open the Michelson Tab in the software. Set the start and end positions of the stage at about  $1 \mu\text{m}$  apart. Record a measurement. Rotate one of the polarizers to  $90^\circ$  and record a measurement with the same parameters as before. Now place a linear polarizer set to  $45^\circ$  directly in front of detector B and repeat the measurement a third time.

**Result Analysis:** Plot the  $R_{TB}$  coincidence count rate with respect to the stage position for all three measurements in one plot. Create a second plot with the values of the  $g_2$ -function as a function of the stage position.

**Interpretation:** An example measurement is shown in Figure 123 and Figure 124. The first measurement (both polarizers at  $0^\circ$ ) shows a typical interferogram (blue curve) as the polarizations in both arms are parallel.

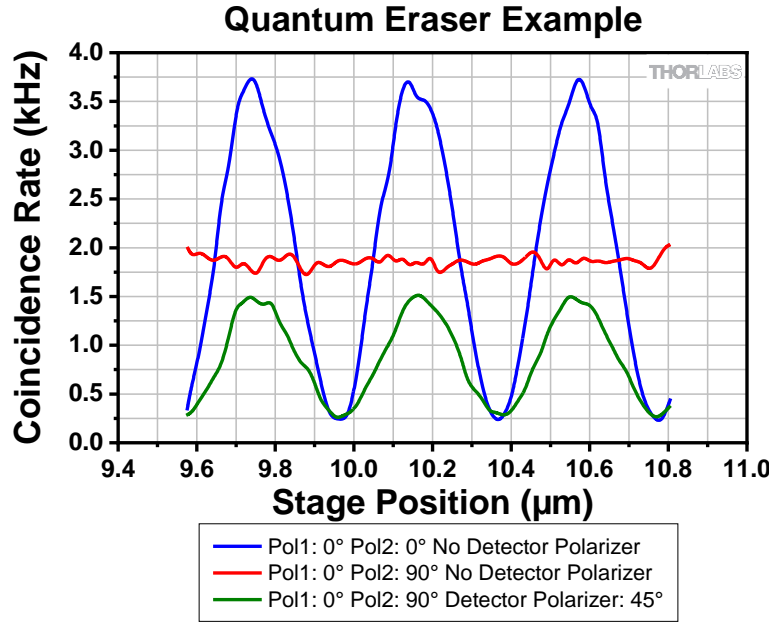


Figure 123     Coincidence Rates of Quantum Eraser Example Measurement

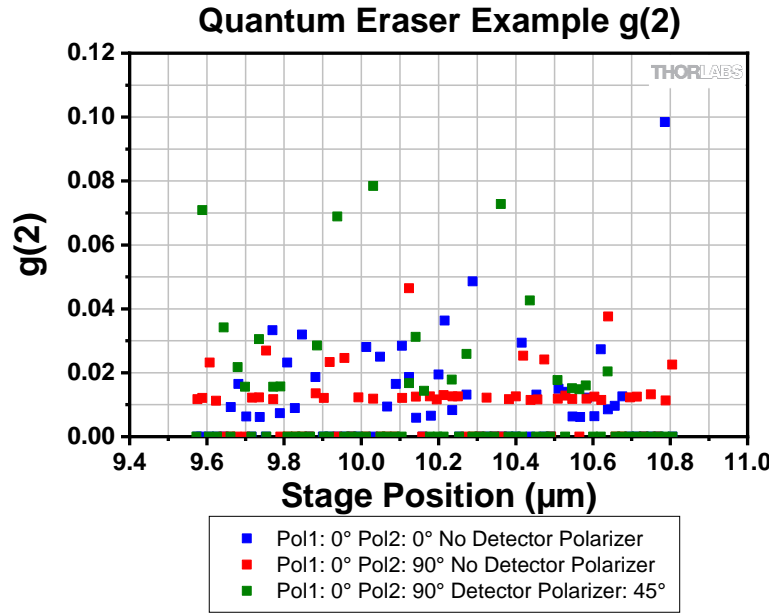


Figure 124     Values of the  $g_2$  Function of Quantum Eraser Example Measurement

In the second measurement (the red curve in Figure 123), the polarization in the arms is set to be perpendicular to each other. Because it would now be possible to determine which arm the photon took at the position of

detector B (via a simple polarization measurement), no interference is observed anymore. The constant coincidence count rate is about half of the maximum rate of the first measurement.

The information about the path can be “erased” by the  $45^\circ$  polarizer in the third measurement (the green curve in Figure 123). The probability of a photon reaching the detector is now again the same for both arms, hence an interference curve is observed in the third measurement. The third polarizer is absorbing half of the remaining photons, so the amplitude of the curve in the third measurement is much lower than the first measurement. For more details, see Section 3.8.

As Figure 124 shows, the  $g_2$  function is below 0.1 for all data points, verifying that the whole measurement is in the single photon regime.

## Chapter 10 Additional Experiments

The experiments in this chapter are suggestions for additional experiments that are not a core part of the kit. They may require parts that are not included in the kit.

### 10.1 Coherence Length

The coherence length  $l_c$  of a light source can be determined by evaluating the envelope of the interferogram taken with the source, as seen in Figure 125.

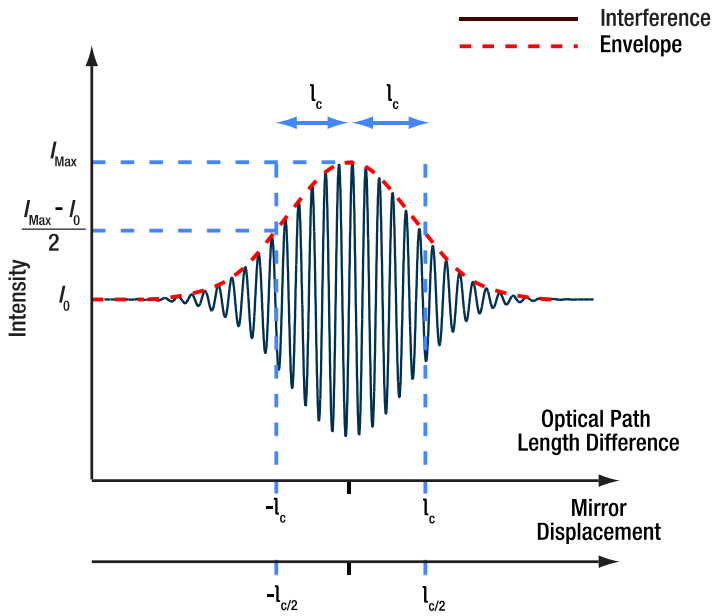


**Figure 125** How to Determine the Coherence Length  $l_c$  From an Interferogram

It can also be approximated by:

$$l_c = \frac{\lambda^2}{\Delta\lambda}$$

With  $\lambda$  being the center wavelength of the spectrum of the source and  $\Delta\lambda$  being the FWHM of the spectral distribution. The photons generated by the SPDC process in the BBO crystal have  $\lambda = 810 \text{ nm}$ . The spectral width of the photon wavelength distribution is larger than the window of the bandpass filters in front of the detectors. Hence,  $\Delta\lambda = 10 \text{ nm}$  is given by the filter window size. This yields:

$$l_c = \frac{\lambda^2}{\Delta\lambda} = \frac{810^2}{10} \text{ nm} = 65.6 \mu\text{m}$$

As the piezo moving the stage in the Michelson interferometer of the kit has a maximum range of  $20 \mu\text{m}$ , a single interferogram does not include the whole envelope. Therefore, the following method must be applied to measure the coherence length.

1. Make sure that the fine adjuster is close to the center of its travel range (6 full turns or  $300 \mu\text{m}$ ) for the maximum contrast with the red LED. If needed, use the coarse adjuster to ensure the fine adjuster has the full travel range.
2. Then use the fine adjuster to move the stage about two revolutions ( $50 \mu\text{m}$  per revolution) away from the point of maximum contrast with the red LED.

3. Set the piezo travel range such that about 2 periods of the interferogram are covered. The exact position is not important, but it must be kept the same for all following measurements.
4. Take an interferogram measurement with the above settings and read out the amplitude. Note the value together with the current fine adjuster position.
5. Use the fine adjuster screw to move the stage by 5  $\mu\text{m}$  in the opposite direction compared to step 2.
6. Repeat steps 4 and 5 until enough points have been taken for a good visualization or fit of the envelope (about 40 points).

The coherence length is equal to the full width half maximum (FWHM) of the envelope when the stage position is plotted on the x-axis (see Figure 125). An example measurement is shown in Figure 126. The FWHM of the example measurement is about 55  $\mu\text{m}$ , which is in good agreement with the approximation made above. The small side maxima are caused by the spectral function not being a Gaussian but closer to a rectangle (due to the bandpass filters). For a rectangular spectrum, the envelope is expected to resemble the shape of a  $|\text{sinc}(x)| = \left| \frac{\sin(x)}{x} \right|$  function.

Please note that the position of the differential screw can lead to an error of about 10% in the position readings due to the non-linearity of the stage. The least deviation occurs in the center of the travel range of the differential screw.

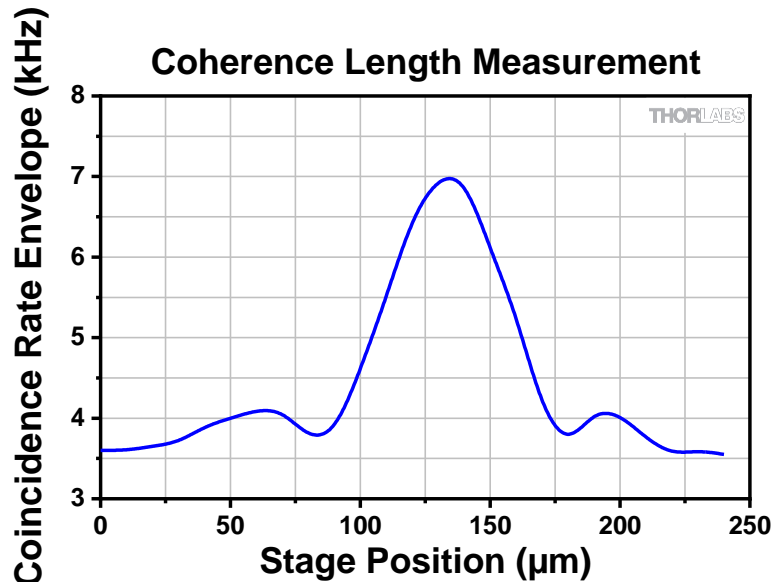


**Figure 126** Example Measurement of the Coherence Length of the SPDC Source with Bandpass Filters

An additional experiment could be to exchange the bandpass filters in front of all three detectors with filters with a broader window, such as Thorlabs' FBH800-40 filter. This way, the coherence lengths would decrease, so that the “true” spectrum of the SPDC source could be measured even with a single interferogram over the whole piezo range. Additionally, the side maxima should disappear due to the spectrum being closer to a Gaussian than to a rectangle. Figure 127 and Figure 128 show two measurements with the FBH800-40 filters, with different positions of the envelope maximum.

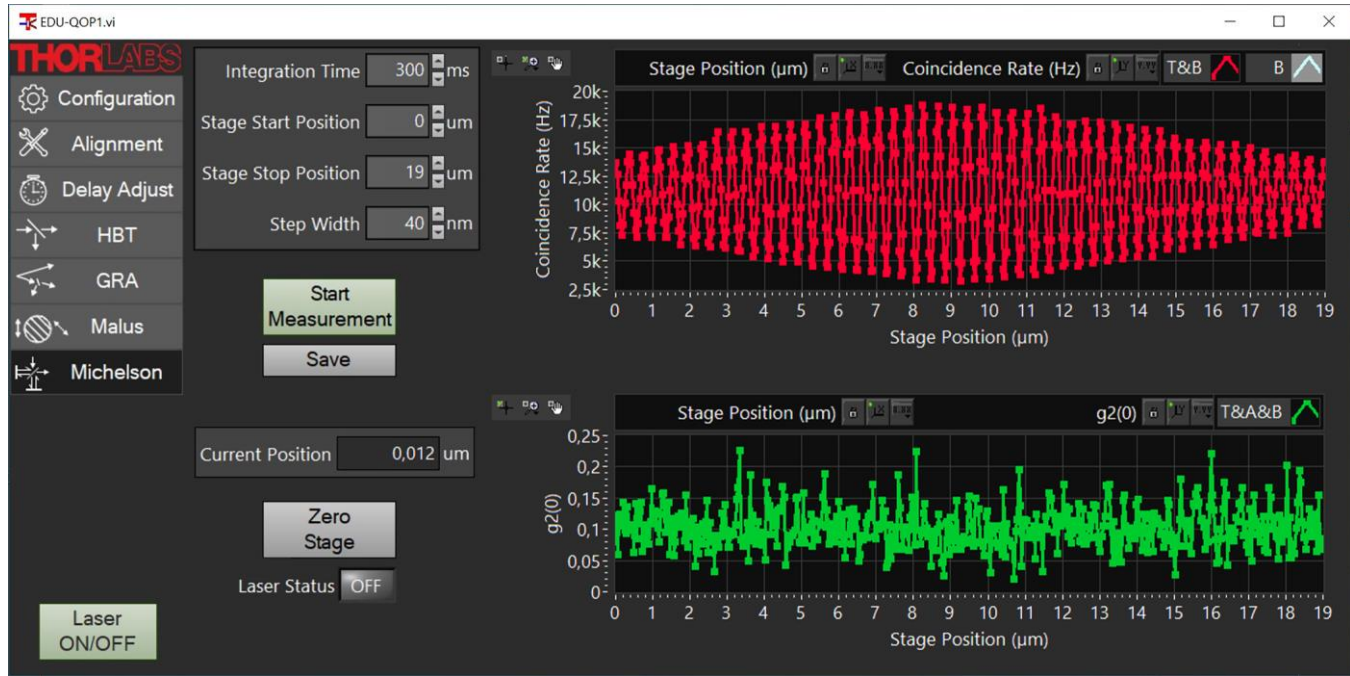


**Figure 127** Michelson Measurement with FBH800-40 Filters, Envelope Maximum Centered

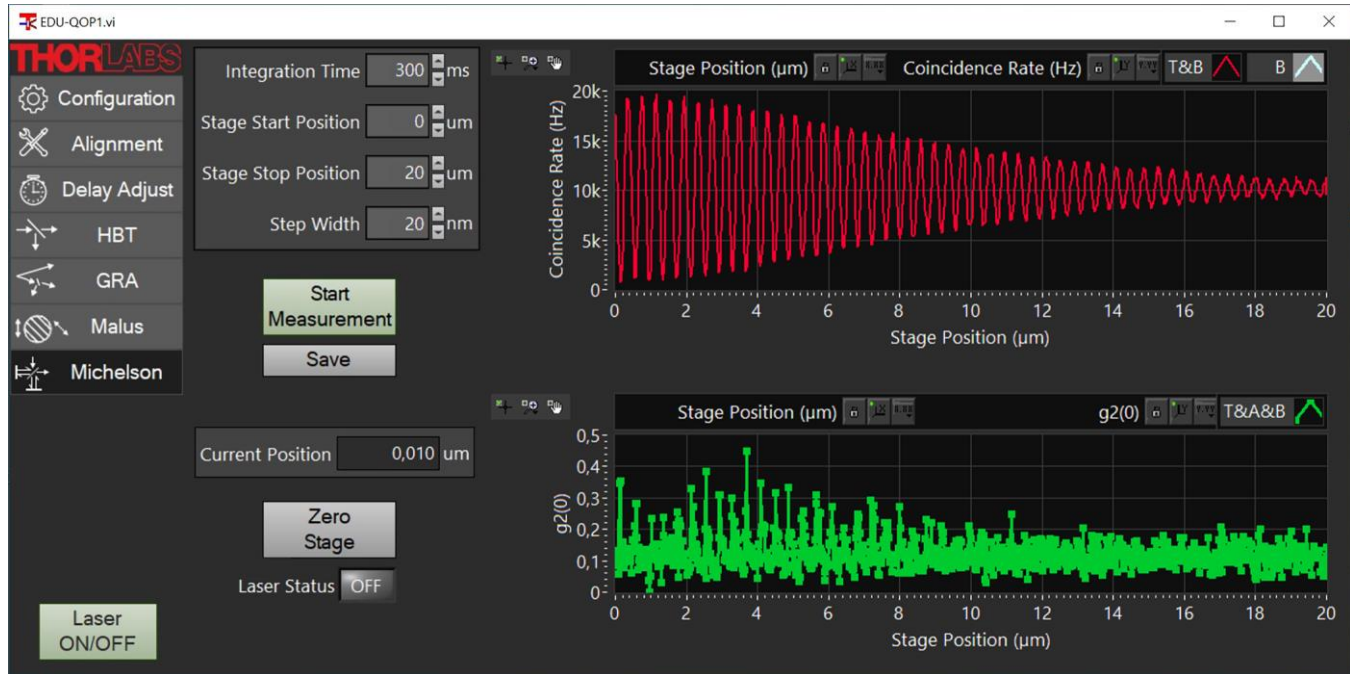


**Figure 128** Michelson Measurement with FBH800-40 Filters, Envelope Maximum at 1 μm

## 10.2 Single Photon Double Slit Experiment

### 10.2.1 Overview

Apart from Michelson Interferometry, there is a second well-known experiment used to demonstrate how single photons can “interfere with themselves”, the double slit experiment. In its classical configuration light is sent through a narrow double slit and the light that is diffracted at the individual slits results in an interference pattern on a screen at some distance from the double slit. In the case of single photons, one could naively assume that the photons either go through one slit or the other, rendering interference impossible. However, similar to the Michelson interferometer, the state of the photon after the double slit is superposition of both slits, and tracking

the position of a large number of single photons on the screen (in this case a detector) again reveals an interference pattern. This holds as long as the slits are indistinguishable. The interference can be destroyed by, for example, introducing polarizers in front of the two single slits that are perpendicular to each other. This is equivalent to the quantum eraser experiment in the Michelson interferometer. Introducing a 45° oriented polarizer behind the double slit would again erase the path information and retrieve the interference pattern<sup>90</sup>.

### 10.2.2 Theory

The double slit interference pattern for classical light is well described by classical light wave theory. However, employing a quantum mechanical formulation for single photons yields the same result<sup>90</sup>. The pattern consists of a sinusoidal interference with a period depending on the distance between the two slits, and a sinc-shaped envelope with a period depending on the width of the individual slits. The period of both the interference and the envelope additionally depends on the distance between the double slit and the screen. This can be mathematically expressed in the following way:

$$R(x) = R_m \cdot \left( \frac{\sin(C_{ss} \cdot x)}{C_{ss} \cdot x} \right)^2 \cdot \frac{1}{2} \cdot (1 + \cos(C_{ds} \cdot x)) \quad (140)$$

Here,  $R$  is the rate of photons on a specific screen position,  $R_m$  is the maximum rate (comparing all screen positions),  $x$  is the position on the screen, and  $C_{ss}$ ,  $C_{ds}$  are constants depending on the parameters of the individual slits and the double slit as follows:

$$C_{ss} = \frac{\pi \cdot W}{\lambda \cdot L} \quad (141)$$

$$C_{ds} = \frac{2 \cdot \pi \cdot D}{\lambda \cdot L} \quad (142)$$

Here,  $W$  is the width of an individual slit,  $D$  is the separation of the slits (center-to-center),  $\lambda$  is the wavelength of the light, and  $L$  is the distance between double slit and screen. See Figure 129 for a schematic drawing of these dimensions.

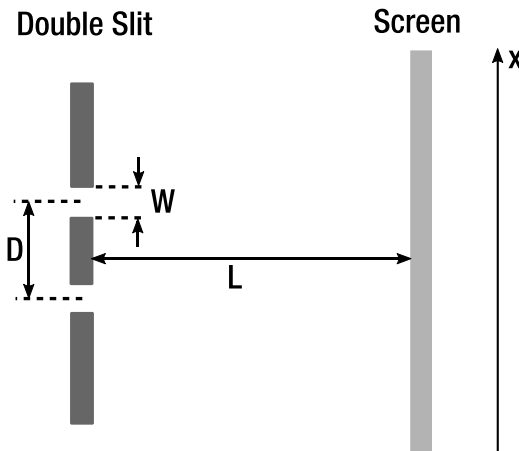


**Figure 129 Schematic Drawing of Double Slit Dimensions**

If the light has a spectral distribution instead of a single wavelength,  $\lambda$  can be approximated by the center wavelength of the distribution. This approximation works best for narrow spectral distributions while significant deviations occur for broader spectral distributions. Figure 130 shows the calculated pattern for the following parameters:

$$R_m = 100 \text{ Hz}, W = 100 \mu\text{m}, D = 300 \mu\text{m}, \lambda = 810 \text{ nm}, L = 30 \text{ cm}$$

<sup>90</sup> B. J. Luo et al., American Journal of Physics, 92(4), 308-316 (2024).

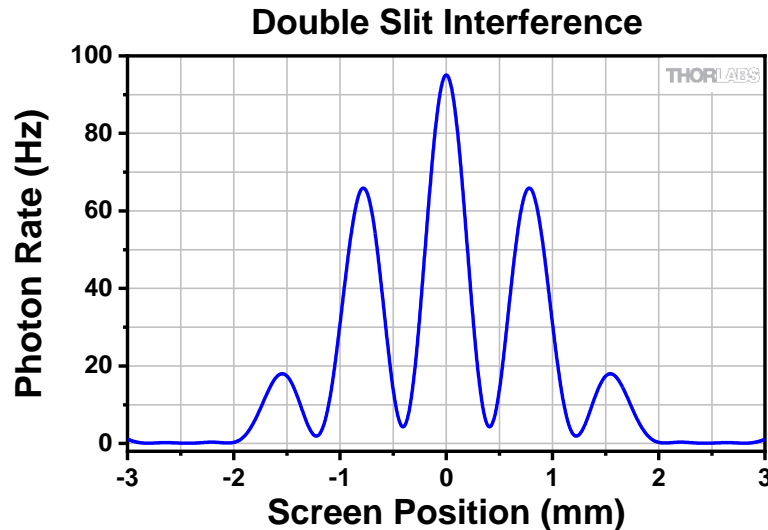


**Figure 130** Calculated Double Slit Interference Pattern for  $R_m = 100 \text{ Hz}$ ,  $W = 100 \mu\text{m}$ ,  $D = 300 \mu\text{m}$ ,  $\lambda = 810 \text{ nm}$ ,  $L = 30 \text{ cm}$

Please note that this approach is based on the assumption that the light incident on the double slit is spatially coherent, such as light coming from an ideal point source. This will not be the case in real-life experiments. In a simplified argument, a finite light source will result in different angles of incidence on the double slit depending on the source position. Each of those angles creates its own pattern on the screen, with the individual patterns being shifted in relation to each other, which will wash out the interference pattern. Assuming a finite light source with a Gaussian profile (a good approximation for the pump laser on the BBO crystal), one can use the von-Cittert-Zernicke theorem to calculate the so-called degree of spatial coherence  $\gamma$  as follows<sup>90</sup>:

$$\gamma = \exp\left(\frac{(\pi \cdot D \cdot S)^2}{(\lambda \cdot Z)^2}\right) \quad (143)$$

Here,  $S$  is the beam waist of the Gaussian light source and  $Z$  is the distance between the source and the double slit. This degree of coherence manifests itself as a visibility of the sinusoidal part of the double slit pattern, so the equation for the expected count rates changes to:

$$R(x) = \frac{2 \cdot R_m}{1 + \gamma} \cdot \left( \frac{\sin(C_{ss} \cdot x)}{C_{ss} \cdot x} \right)^2 \cdot \frac{1}{2} \cdot (1 + \gamma \cdot \cos(C_{ds} \cdot x)) \quad (144)$$

In the extreme case of completely destroyed coherence ( $\gamma = 0$ ), only the envelope term remains, while for ideal coherence ( $\gamma = 1$ ), Equation (144) reduces to Equation (140). In between these extremes, a lower degree of coherence (smaller value of  $\gamma$ ) results in a smaller amplitude of the interference term. The envelope term is also affected by the coherence, but by a much smaller degree than the interference term. Figure 131 shows a plot using the same parameters as for Figure 130, but for different degrees of coherence. Measurement results with the setup described in the next section will fall somewhere in between the curves shown here, depending on the actual experimental parameters.

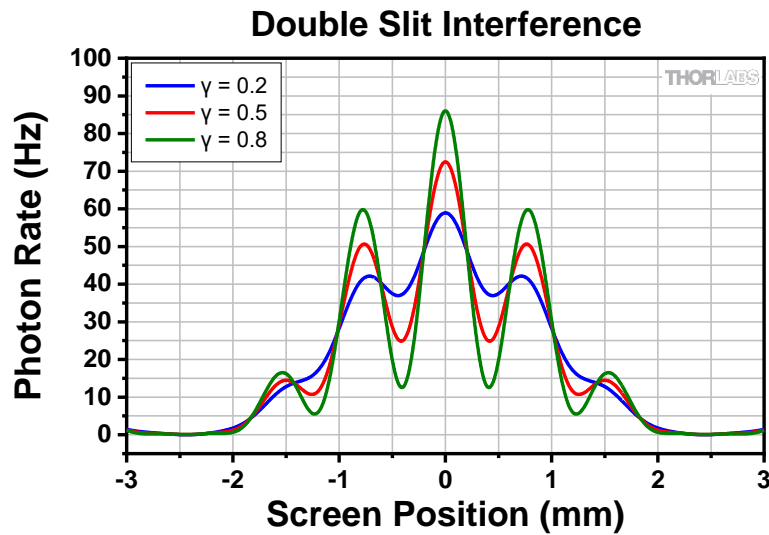


Figure 131 Calculated Double Slit Interference Pattern for Different Degrees of Coherence

### 10.2.3 Setup

The following subsection describes a possible configuration of the single photon double slit experiment as an addition to the EDU-QOP1/(M) kit. This specific configuration has been successfully tested but other configurations, e.g., based on different dimensions of the double slit, are certainly possible. Figure 132 displays a schematic of the setup.

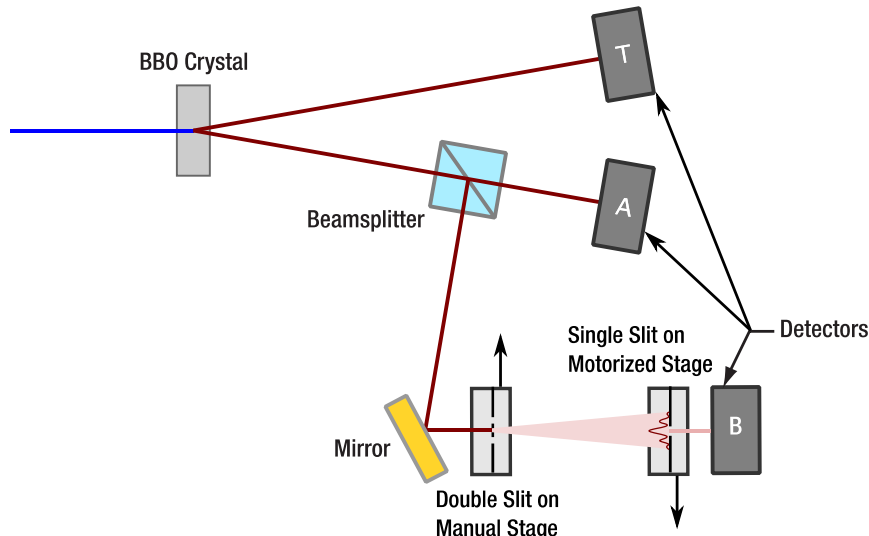


Figure 132 Schematic of the Double Slit Setup

The fundamental setup is that of the GRA experiment (see Section 7.5). A mirror is introduced into the path from the beamsplitter to detector B, deflecting the beam towards the right breadboard edge. The light then falls on a double slit, generating the pattern described above. The mirror allows a longer distance between crystal and double slit, improving spatial coherence as described above. The double slit is placed on a manual translation stage to allow fine positioning.

As the detector has limited spatial resolution, the pattern cannot be recorded in a single measurement and has instead to be scanned. This is realized by introducing a single slit in the light path behind the double slit, which is mounted on a motorized translation stage and can thus be moved perpendicular along the pattern in small precise steps. The single slit plane corresponds to the screen plane in the equations above. The light that falls through the single slit is analyzed by detector B. As the optics of the detector are optimized to focus all incident light on the detector chip, the detector does not have to be moved along with the single slit but can remain at a static position. Furthermore, due to the very small distance between single slit and focusing lens of the detector,

the diffraction effects of the single slit itself can be neglected, as all light that passes through the slit ends up on the detector chip.

Our test configuration includes the following parts that are not part of the kit:

- 1x Double slit<sup>91</sup> (100 µm single slit width, 300 µm center-to-center spacing, 10 mm long)
- 1x S100LK single slit (100 µm width)
- 2x KB1P(/M)
- 2x LRM1
- 1x PH2E (PH50E/M)
- 2x PH1 (PH20/M)
- 1x TR2 (TR50/M)
- 2x TR1 (TR20/M)
- 4x CL5
- 1x MT1(/M)-Z9 translation stage
- 1x MT1B(/M) translation stage
- 2x MT401(/M)
- 1x KDC101 controller
- 1x KPS201 power supply
- 1x KM100
- 1x PF10-03-M03
- 4x 1/4"-20 x 1/2" (M6 x 12 mm) Cap Screw
- 2x 1/4"-20 x 1/2" (M6 x 12 mm) Setscrew
- 4x 1/4"-20 x 1" (M6 x 25 mm) Cap Screw

In order to set up the experiment, first assemble the components as shown in Figure 133 and Figure 134.

---

<sup>91</sup> Thorlabs offers the SD100K3 double slit as a catalog item. This has the same slit widths and distances as the one mentioned here, but is only 3 mm long, which would result in decreased count rates (about half). If you are interested in the version with longer slits, please contact Tech Support.

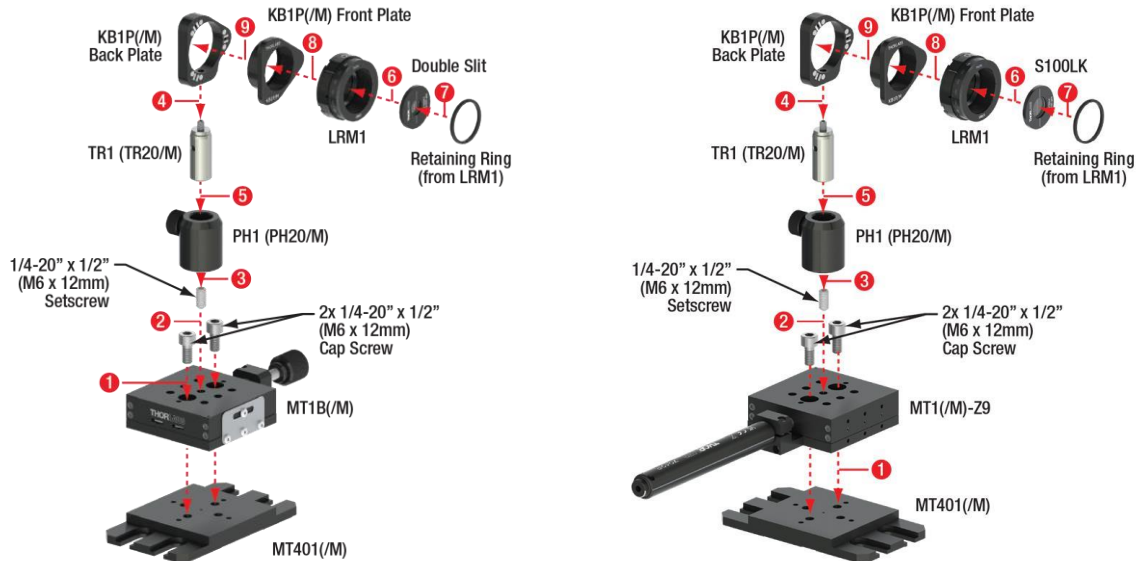


**Figure 133** Assembly of Double Slit (Left) and Single Slit (Right) Components

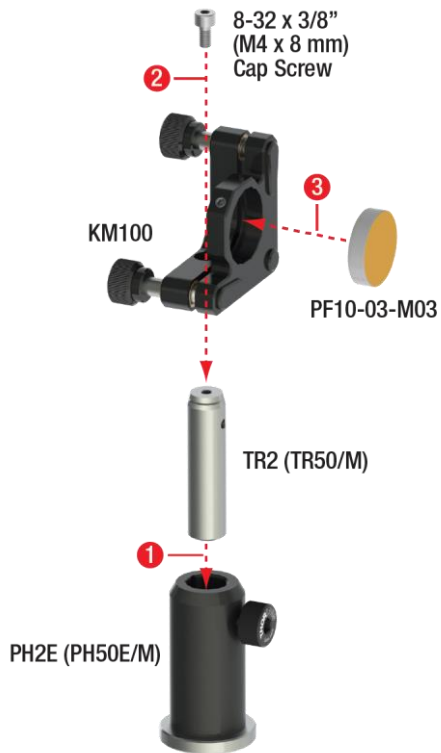


**Figure 134** Assembly of Additional Mirror Component

The setup for the double slit experiment will look like Figure 135.

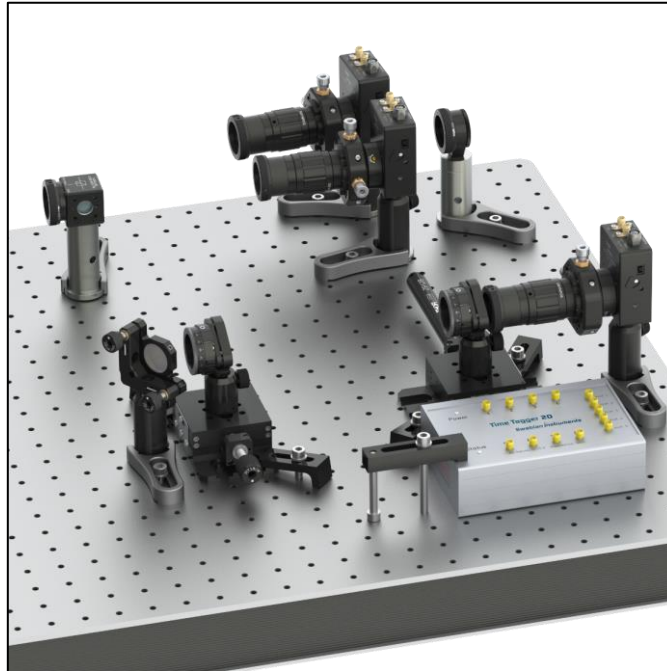


**Figure 135      Setup for the Single Photon Double Slit Experiment**

Start with the GRA configuration (see Figure 115) and do the following:

- Set up the second alignment path as described in Section 7.6.1. Position the alignment laser in the second alignment path (base after the crystal) and switch it on.
- Remove detector B and position the mirror about 25 cm behind the beamsplitter. The alignment laser should fall on the center of the mirror and the beam should be deflected towards the right breadboard edge approximately parallel to a row of breadboard holes.
- Use the alignment target to ensure a constant beam height after the mirror:
  - Position the alignment target as close as possible to the right of the mirror.
  - Set the height of the alignment target so that the alignment laser passes through the hole.
  - Position the alignment target as far away from the mirror as possible.
  - Use the upper kinematic screw of the mirror to make the alignment laser pass through the hole of the target.
  - Repeat all above steps iteratively until the laser passes through the target hole regardless of the alignment target position.
- Remove the optics from detector B and screw the economy beamsplitter on the detector. Place the detector about 40 cm to the right of the mirror. Adjust the height of the detector post to center the alignment laser spot on the detector chip.
- Place the alignment target between mirror and detector so that the alignment laser passes through the hole. Move and tilt the detector until the detector chip is centered in the alignment laser spot and the reflection passes back through the alignment target hole. Fix the detector to the breadboard, remove the economy beamsplitter and re-connect the optics to the detector.
- Screw the economy beamsplitter to the LRM1 with the single slit on the motorized stage. Connect the stage to the KDC101 controller and connect the controller to the power grid with the KPS201 power supply and to your PC via the USB cable that comes with the controller. Start Thorlabs' Kinesis software and home the controller before setting the position to 6 mm (central position).

- Position the stage with the single slit on the breadboard between the mirror and the detector. Adjust the post height of the single slit until the alignment laser spot is centered on the slit. Make sure that the front face of the LRM1 remains parallel with the edge of the stage. Position the alignment target between mirror and single slit (closer to the mirror).
- Move and tilt the stage (do not rotate the post itself) until:
  - The distance between the detector and the single slit is small.
  - The single slit is in the center of the alignment laser spot.
  - The reflection passes back through the hole in the alignment target.
- Once these conditions are met, fix the stage to the breadboard by clamping the baseplate with one CL5 clamp each on two diagonally opposed corners, using 1/4"-20 x 1" (M6 x 25 mm) cap screws and washers. Remove the magnetic front plate with the single slit and remove the economy beamsplitter from the single slit.
- Screw the economy beamsplitter on the LRM1 with the double slit. Position the manual stage with double slit directly to the right of the mirror. Position the alignment target between the beamsplitter and the additional mirror. Adjust the height of the target so that the alignment laser passes through the hole.
- Adjust the post height of the double slit until the spot is centered on the slits. Make sure that the front face of the LRM1 remains parallel with the edge of the stage.
- Move and tilt the stage with the double slit until the alignment laser is centered on the slit and the reflection passes back through the hole in the alignment target. Fix the stage position with one CL5 clamp each on diagonally opposing corners of the baseplate, using 1/4"-20 x 1" (M6 x 25 mm) cap screws and washers.
- Remove the magnetic plate with the double slit, switch off the alignment laser and put the alignment laser back to its original position.
- Start the EDU-QOP1 software. In the connection window, make sure to connect at least the laser controller and the KDC controller (by choosing the corresponding serial numbers from the dropdown menus). If the KDC controller is recognized correctly, you should see an additional tab named "KDC".
- Maximize the count rate on detector B by adjusting the detector optics as described in Section 7.5.3. If this has already been adjusted, e.g., for the GRA experiment, you can directly maximize the signal with the BBO crystal. If not, replace the crystal with the colored glass filter, then switch to the crystal once the signal is found.
- Calibrate the delay of detector B as described in Section 7.5.3.
- Re-insert the double slit front plate. Use the differential screw of the manual stage to move the double slit and maximize the T&B coincidence rate this way. As the coincidence rate will be quite low, we recommend setting the pump laser to the maximum current of 50 mA from here on. In our tests, we achieved a maximum of 2 kHz coincidence rate in this step.
- Once the signal is maximized, re-insert the single slit front plate. This is the final setup, as shown in Figure 135.
- Open the KDC tab in the software. Set the Start position to 0 mm and the end position to 12 mm. Set the integration time to 1000 ms and the step size to 0.1 mm. Start the measurement. This should give you a rough overview scan of where the pattern is found. An example is shown in Figure 136.
- For a higher resolution measurement, set the start and end position according to the overview measurement, reduce the step size to 0.05 mm, and increase the integration time to 10 000 ms (10 s).

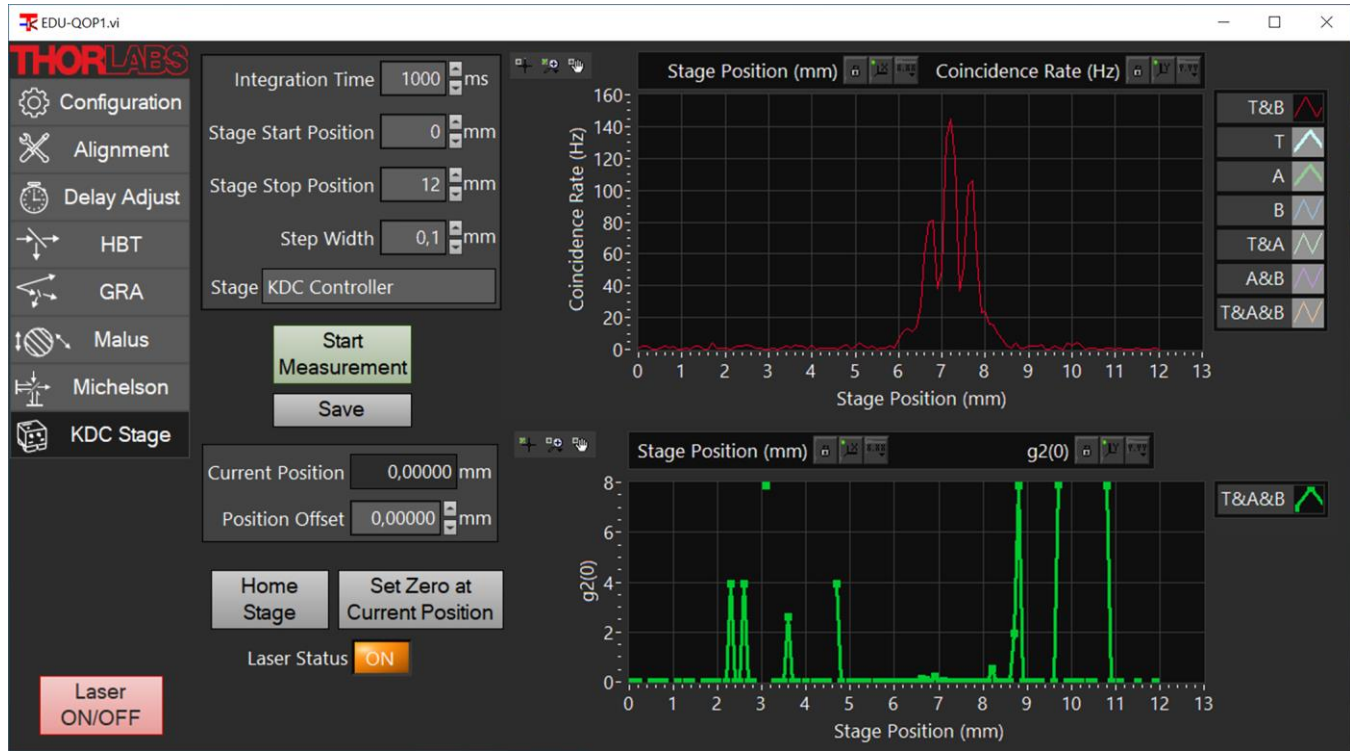


Figure 136 Example of an Overview Measurement of the Double Slit Pattern

#### 10.2.4 Measurement

The result of a measurement should look similar to Figure 137. You can see the typical double slit pattern with an interference and an envelope. Please note that the y-axis scale of the lower graph has been changed to show that the  $g_2$  value is clearly below 1 in the region of the pattern, indicating single photon character for all significant data points. The exact amount of side maxima and their spacing depends on the double slit that is used as well as on the setup geometry (see Section 10.2.2). The parameters used for the calculated patterns in Figure 131 correspond to the setup as described here.



**Figure 137** Expected Result of the Double Slit Measurement in the Setup Configuration Described Above

The degree of coherence depends mainly on the diameter of the pump laser spot on the BBO crystal (light source size) and the distance between the crystal and the double slit. Increasing the latter is cumbersome in the confines of the current setup and comes with the disadvantage of even lower count rates due to divergence of the light. In our tests, closing the iris in front of the BBO crystal (and thus reducing the size of the light source) proved to be the better way of increasing the coherence, even though it also results in a decrease of the final count rates (less pump power on the crystal). Figure 138 shows the test results for two different iris diameters. For the smaller iris diameter, the overall coincidence count rates decrease while the visibility<sup>92</sup> of the pattern improves.

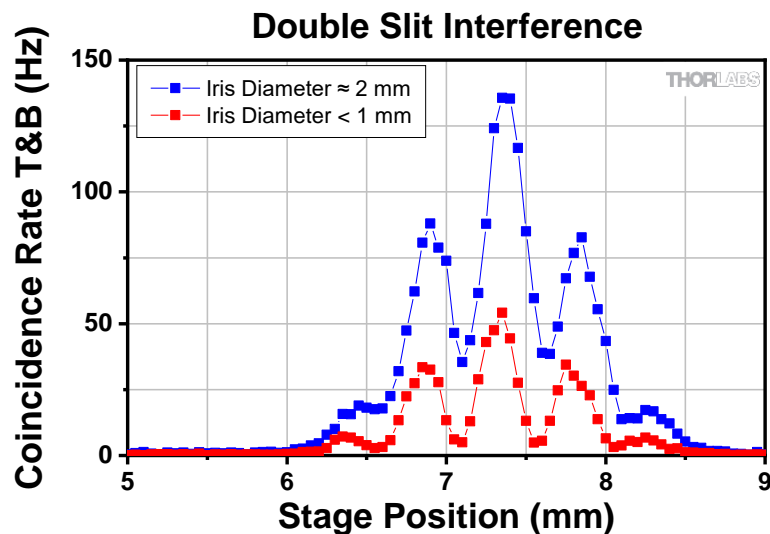


**Figure 138** Result of Test Measurements for Different Iris Diameters (Light Source Sizes)

Please note the following optimization possibilities:

<sup>92</sup> In this context visibility can be defined as  $V = \frac{C_0 - C_{min1}}{C_0 + C_{min1}}$ , where  $C_0$  and  $C_{min1}$  are the coincidence rates of the central maximum and the first minimum, respectively.

- Changing the position of the double slit via the manual translation stage has no influence on the shape of the pattern but increases/decreases the overall count rates. The optimal slit position can be obtained via a measurement series of different slit positions. We recommend steps of 450 µm (three full rotations of the differential screw).
- Sometimes the pattern is asymmetric. This is caused by the light hitting the double slit at a small angle. To achieve a symmetric pattern, rotate the lower kinematic screw of the mirror in front of the double slit with care. Clockwise rotation increases the right side-lobe and decreases the left one, while counterclockwise rotation of the screw has the opposite effect. For reference, Figure 139 shows the measured pattern after a quarter of a full clockwise screw rotation starting from the position for the symmetric pattern.

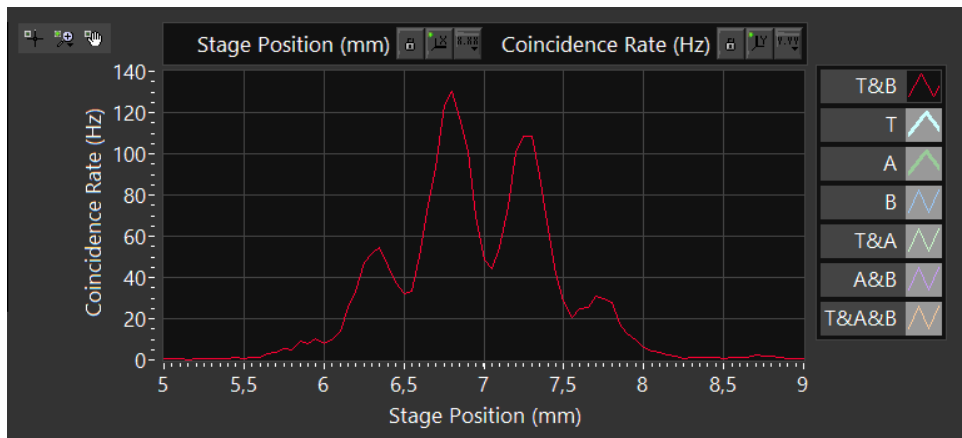


**Figure 139 Example Measurement for an Asymmetric Pattern (1/4 Clockwise Rotation of Mirror Screw)**

### 10.3 The Three-Polarizer-Paradox

The three-polarizer-paradox describes a situation where the transmission through two crossed polarizers is zero. Upon adding a third polarizer at 45° rotation (with respect to the polarization axis of the other two polarizers) in between, the intensity increases again. This may be counterintuitive when thinking about single photons. From a quantum mechanics perspective, there is a chance that a photon gets either absorbed or transmitted at each polarizer (according to Malus' law, see Section 3.7).

If there were nothing more to it, the increase of the transmitted signal could not be explained, as adding a third polarizer should only decrease the chance of transmission through all polarizers.

But in terms of quantum mechanics, each polarizer must be viewed as a measurement device. As such, the measurement does not just give a reading of the probability to end up in this polarization state, but also projects the incoming state onto the state of the measurement result (see Section 3.2.9).

Therefore, in the case of two crossed polarizers, the first polarizer projects the state onto its own axis and the second polarizer has zero probability for photons to transmit in this state. But once the third polarizer is introduced in between, the state projected by the first polarizer is measured and projected by the intermediate polarizer again. According to Malus' law, the probability to measure a transmitted photon after the 45° rotated polarizer is  $\frac{1}{2}$ . The last polarizer again measures the probability for the photons projected to the 45° rotated polarization to pass the 90° oriented polarizer, which also is  $\frac{1}{2}$ . Multiplying the probabilities at each polarizer yields  $\frac{1}{4}$  for the transmission through both polarizers after the first one.

This experiment can be set up with the components in this kit. All three polarizers can be placed in front of detector B (setup similar to Section 9.6) and the alignment laser can be used to properly line up the components. To achieve the same height for all three polarizers, you may use the Michelson interferometer breadboard or one PS3 spacer for each 1/2" polarizer (one is included in the kit).

A more detailed analysis of this topic and its implications for teaching can be found in the literature<sup>93</sup>, including the optical analogue of the Stern-Gerlach experiment.

#### 10.4 Imaging the SPDC Cone with a Camera

By placing a camera, such as CS165MU, right behind the BBO crystal, it is possible to obtain direct images of the photons generated by the SPDC process. In order to eliminate the pump light from the images, one of the bandpass filters in the detector optics should be inserted between the crystal and camera<sup>94</sup>. As the camera needs to be very close to the crystal to view the full cone without additional optics, we recommend turning the crystal mount by 180° for this exercise (so that the kinematic screws are not blocking the camera). The image quality can be increased by setting the pump laser to the maximum current of the diode (50 mA). In this configuration, one can directly examine the influence of the phase matching conditions on the SPDC cone. Rotating the crystal around its vertical axis will increase or decrease the opening angle of the cone and hence the radius of the circle in the camera image, see Figure 140.

By increasing the gain of the camera, the required integration time can be reduced to the point of a low-framerate video, imaging the above-mentioned changes in real-time.

The following parts are required to reproduce this experiment (alternatively, the LED can be unscrewed from its post allowing the post and its holder to be used temporarily for the camera, in which case only the camera is required):

- 1x CS165MU(/M)
- 1x PH2E (PH50E/M)
- 1x TR2 (TR50/M)



**Figure 140** SPDC Cone Imaged with CS165MU Camera for Phase Matching Conditions of the Experiments in the Kit (Left), and for Tilted Crystal Resulting in Larger Opening Angles (Center) or Collinear Emission (Right). These images are shown here with a false color scale to increase visibility in the (printed) manual.

#### 10.5 Spatial Correlation of the Photon Pairs

A simple experiment can highlight the spatial correlation of the photon pairs. The two photons of a pair are located at opposite sides of a cone surface originating at the BBO crystal. Thus, if one photon of a pair arrives on the lower half of the aperture of detector T, the other photon is expected to arrive at the upper half of the aperture on detector A, as sketched in Figure 141.

<sup>93</sup> J. M. Brom and F. Rioux, *The Chemical Educator*, **7**, 200 (2002).

<sup>94</sup> The bandpass filters in the kit have FWHM of 10 nm which results in some of the SPDC photons being blocked. Brighter images can be obtained by using a bandpass filter with a larger window such as FBH800-40 or a longpass filter such as FELH0750.

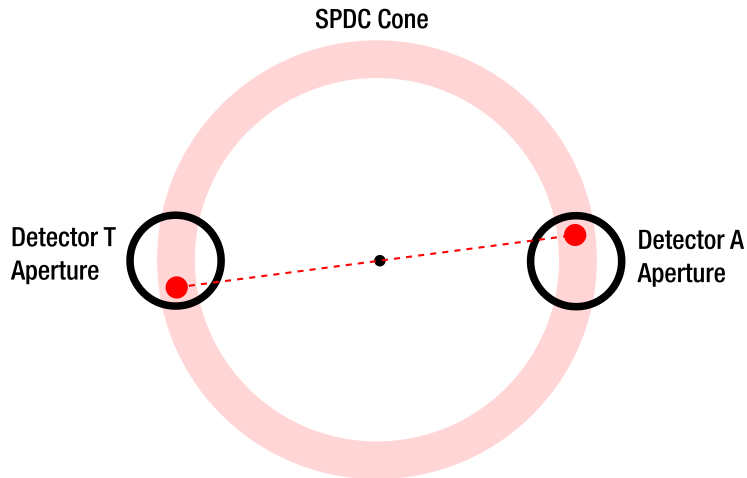


**Figure 141** This is a sketch of the spatial correlation of photon pairs. The red dots mark photons of one pair.

This can be tested by blocking the upper/lower half of the detector apertures<sup>95</sup> of T and A and recording the single detector count rates as well as the T&A coincidence count rate for all four combinations. The result of such a measurement is shown in the table below. As expected, the coincidence rate is much higher for the up/down and down/up combinations (photons of a pair are either both blocked or both pass) than for up/up and down/down (for every pair, only one photon can pass), while the single detector count rates remain stable.

	Reference (nothing blocked)	Blocked: T - upper half A - upper half	Blocked: T - upper half A - lower half	Blocked: T - lower half A - lower half	Blocked: T - lower half A - upper half
Count Rate T (kHz)	245.9	127.9	127.6	112.2	109.8
Count Rate A (kHz)	271.7	120.5	126.9	127.1	120.6
Coincidence Count Rate T&A (kHz)	57.4	0.3	26.0	1.81	21.7

## 10.6 Experiments with Different Crystal Thicknesses

The thickness of the pair generation crystal influences the count rates. For a constant pump intensity, the single detector count rates are expected to scale approximately with the square of the crystal thickness. Furthermore, the spectral distribution of the photon pairs will vary depending on the thickness. Both effects can be tested experimentally by using the NLCQ1 or NLCQ2<sup>96</sup> crystals.

<sup>95</sup> Thorlabs offers KEMK half apertures that can be mounted in a short lens tube and screwed onto the front of the detector optics. To qualitatively demonstrate the effect described here, self-made half apertures, such as half circles made of aluminum foil mounted in a lens tube, easily suffice.

<sup>96</sup> Available for purchase at: [https://www.thorlabs.com/newgroupage9.cfm?objectgroup\\_id=16384&pn=NLCQ1#16433](https://www.thorlabs.com/newgroupage9.cfm?objectgroup_id=16384&pn=NLCQ1#16433)

## 10.7 Bomb Tester - Interaction Free Measurement

The EDU-BT1(/M) kit describes the so-called bomb tester experiment. While the EDU-BT1(/M) provides an analogy experiment, the “real” bomb tester experiment can be performed with the EDU-QOP1(/M) kit. For reference, see the manual of the EDU-BT1(/M)<sup>97</sup>. For this experiment, the stability of the interferometer is important, see Section 12.4.

## 10.8 Quantum Computing

Since the experiments in this kit already show that we are dealing with (heralded) single photons, we can use these photons to demonstrate photonic quantum computing (QC). A detailed introduction to quantum computing would be out of scope of this kit. Please refer to the cited literature within this section for more context.

In the following, we give a short description of basic quantum computing algorithms with a strong focus on the general concept and the concrete technical implementation based on this kit. It is important to note that these algorithms can only deliver answers to highly specialized problems and are by no means suitable for general purpose calculations we are used to from using modern PCs.

The goal is not to provide a complete understanding of QC algorithms in general. The teaching value of this experimental realization lies in an actual implementation of a qubit system and demonstrating the actions of QC operations in an environment that can also be understood from a purely optical perspective. It further serves to demonstrate challenges, like phase-noise, in real-world implementations and how they influence the outcome of quantum computations.

This section is structured in the following way: We start by briefly introducing the concept of qubits and gate operations. Then, we present an algorithm that can be implemented based on this educational kit, the Deutsch-Jozsa algorithm (DJA). Next, we explain how the DJA is implemented in a purely optical fashion, followed by the actual experimental realization and sample measurements.

### 10.8.1 Qubits and Gates

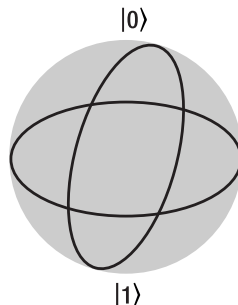
Generally, the power of QC stems from the superpositions of states: While a classical bit can only be in one state (off/on; 0/1), in QC a so-called qubit can be in any superposition of both states.

$$(a|0\rangle + b|1\rangle) \quad a, b \in \mathbb{C}$$

Since in quantum mechanics, the total amplitude must fulfill a norm condition and the global phase does not influence a measurement outcome, the two complex coefficients can be reduced to two real valued angles and any superposition state can be written as:

$$\left(\cos\frac{\theta}{2}|0\rangle + e^{i\varphi} \sin\frac{\theta}{2}|1\rangle\right)$$

Using this representation, any single qubit superposition state can be graphically represented on the surface of the so-called Bloch sphere.



<sup>97</sup> Downloadable here: [https://www.thorlabs.com/newgroupage9.cfm?objectgroup\\_id=6635&pn=EDU-BT1](https://www.thorlabs.com/newgroupage9.cfm?objectgroup_id=6635&pn=EDU-BT1)

In the following we will not only discuss a single qubit state, but also the combination of two qubits, labeled x and y. To make it clearer which state belongs to which qubit, we use  $|x\rangle$  and  $|y\rangle$  to label the state of each qubit and x,y indices to indicate which qubit the basis state belongs to. For example, the combined state  $|x\rangle|y\rangle = \frac{1}{\sqrt{2}}(|0\rangle + |1\rangle)_x \cdot |1\rangle_y$  means that qubit x is in an equal superposition state of 0 and 1, while the other qubit y is only in the 1 basis state.

Operations that change the state of one or more qubits are called gates, in resemblance of their classical bit counterparts.

One example would be the Hadamard gate, which transforms the single qubit input states:

$$|0\rangle \leftrightarrow \frac{1}{\sqrt{2}}(|0\rangle + |1\rangle) \quad \text{and} \quad |1\rangle \leftrightarrow \frac{1}{\sqrt{2}}(|0\rangle - |1\rangle)$$

and thus, can be used to transform back and forth between a qubit basis state and a superposition state.

Another often used quantum gate involving two qubits is the controlled-not (CNOT) gate. It inverts the state of one qubit y based on the state of the other (control) qubit x:

$|0\rangle_x: |y\rangle$  is left unchanged

$|1\rangle_x: |0\rangle_y \leftrightarrow |1\rangle_y$

Such multi-qubit operations can create system states that cannot be written as simple products of the single qubit states (separable states). Such states can be mixed or entangled qubit states.

In photonic QC, various properties of a single photon<sup>98</sup> can be used to represent orthogonal bases for qubits.

For example, one qubit basis could be defined by the orthogonal polarization basis  $|V\rangle$  &  $|H\rangle$ , i.e., the vertical and horizontal linear polarizations, that span the space of all polarization states. Here, the Bloch sphere is in a one-to-one correspondence to the Poincaré sphere. A halfwave plate (HWP) can be used to define a range of different gates, for example:

- If the HWP is oriented with an optic axis at  $45^\circ$  to the vertical axis, it flips a photon with vertical polarization to horizontal polarization upon transmission,  $|V\rangle \leftrightarrow |H\rangle$ . This is a NOT gate, also known as an X-gate.
- If the HWP is oriented with an optic axis at  $22.5^\circ$  to the vertical axis, the photon is projected onto the polarization states  $|V\rangle \rightarrow \frac{1}{\sqrt{2}}(|V\rangle + |H\rangle)$  and  $|H\rangle \rightarrow \frac{1}{\sqrt{2}}(|V\rangle - |H\rangle)$  which corresponds to the definition of the Hadamard gate above.
- If the HWP is oriented with its slow axis vertical, it introduces a  $180^\circ$  phase shift to the  $|V\rangle$  basis. This is a phase gate (P-gate).

Another representation of a qubit makes use of the path state of a single photon in an interferometer. Here we label the two arms of the interferometer with states  $|A\rangle$  &  $|B\rangle$ . As the experiments in this kit show, the photon will be in a superposition state of both arms. The coefficients for both states are described by the relative probability amplitudes (in the examples of this kit both arms always have the same amplitude) and the phase difference. In this representation of a qubit, beamsplitters serve as a close analog to a Hadamard gate<sup>99</sup>.

Combining the polarization state with the path state of a single photon yields a two-qubit system. Both qubit states can be manipulated independently by either changing the polarization (e.g. rotation) or the path state (e.g. a phase shift in one arm). Also, a two-qubit operation like the CNOT gate would for example flip the polarization state between horizontal and vertical polarization depending only on one arm of the interferometer.

In principle, further qubit states can be added to a single photon state, e.g., by creating more path states when nesting interferometers within each other<sup>100</sup>, or making use of the photons' orbital angular momentum<sup>101</sup>. Both

<sup>98</sup> While it is possible to use additional photons to increase the number of qubits, it is not easy to let the states of these photons interact in a controlled way.

<sup>99</sup> Strictly speaking, beamsplitters introduce different phase shifts than Hadamard gates, but this can be compensated by other optical elements or adjusting the interferometer path lengths accordingly.

<sup>100</sup> P. G. Kwiat et al., Journal of Modern Optics, **47**(2-3), 257-266 (2000).

<sup>101</sup> J. Leach et al., Optics Express, **17**(10), 8287 (2009).

notably increase the complexity of the optical setup, so we do not recommend this for introductory student setups.

### 10.8.2 Deutsch-Jozsa Algorithm

The Deutsch-Jozsa algorithm<sup>102</sup> (DJA) is one of the first proof-of-principle algorithms to run on any quantum computation platform. In the Qiskit textbook<sup>103</sup>, DJA is the first quantum algorithm presented to new learners.

Given an  $n$ -bit binary function  $f: \{0,1\}^n \mapsto \{0,1\}$ , the DJA is designed to determine whether the function is constant (same output for any input) or balanced (half of the inputs are mapped to 0 and the other half to 1). In the following we only consider the case for  $n = 1$  (also known as the Deutsch algorithm), which can be solved by a two-qubit quantum computer in one run, while a classical computer would need to evaluate both  $f(0)$  and  $f(1)$  using two function calls<sup>104</sup>.

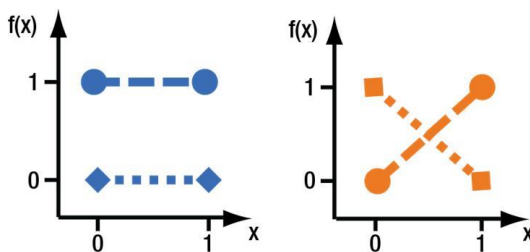


**Figure 142** The four possible functions for the Deutsch algorithm: constant (left) or balanced (right) output. The markers represent the values of each function, while the different dashed lines serve as guide to the eye to connect the markers of each function.

One possible two-qubit quantum circuit which solves the Deutsch problem is shown in Figure 143. The two rows show the operations done on each qubit from left to right.

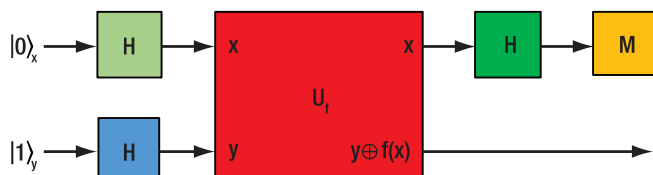


**Figure 143** Quantum circuit to solve the Deutsch problem, based on two qubits labeled  $x$  and  $y$ . It uses three Hadamard gates ( $H$ ) and a two-qubit gate ( $U_f$ ) described in the text. The result is obtained from measuring the state of qubit  $x$  ( $M$ ).

The Hadamard gates are used to prepare a separable superposition input state for both qubits ( $x$  and  $y$ ), i.e.,

$$|x\rangle|y\rangle = \frac{1}{\sqrt{2}}(|0\rangle + |1\rangle)_x \cdot \frac{1}{\sqrt{2}}(|0\rangle - |1\rangle)_y$$

The two-qubit gate  $U_f: |x\rangle|y\rangle \rightarrow |x\rangle|y \oplus f(x)\rangle$  flips the state of the second qubit based on the defined function value for the first qubit's states and can be simply realized by (controlled) NOT gates. After this operation the qubit state is:

$$|x\rangle|y\rangle = \frac{1}{2}\left((-1)^{f(0)}|0\rangle + (-1)^{f(1)}|1\rangle\right)_x \cdot (|0\rangle - |1\rangle)_y$$

<sup>102</sup> D. Deutsch and R. Jozsa, *Proceedings of the Royal Society of London. Series A: Mathematical and Physical Sciences*, **439**(1907), 553 (1992).

<sup>103</sup> <https://learn.qiskit.org/course/ch-algorithms/quantum-circuits>

<sup>104</sup> A didactical metaphor that can be used to describe the benefits of the Deutsch algorithm (even though it does not help to understand how the algorithm works) is that of a coin test: If you want to know if your friend is using a standard coin (one side heads and one side tails) or a fake coin (both sides heads or both sides tails) for your game of coin flips, you need two measurements in the classic case: Look at one side and then look at the other side to see if it is the same or different. With the Deutsch algorithm, you only need to look at the coin once to know if it is standard or fake.

Note that due to the properties of the chosen input superposition state, the resulting  $y$ -qubit state remains identical to the input, while the information about the solution is imprinted onto the  $x$ -qubit via a process called phase-kickback<sup>105</sup>.

Thus, depending on whether the function is constant or balanced, the  $x$ -qubit will be in one of two superposition states  $|x\rangle \propto (|0\rangle \pm |1\rangle)$ . After the last Hadamard gate the  $x$ -qubit ends up in a clean  $|0\rangle$  or  $|1\rangle$  basis state which, theoretically, can be measured without uncertainty. If the measurement returns the  $|0\rangle$  state, the function is constant. If the  $|1\rangle$  state is measured, the function is balanced.

### 10.8.3 Optical Implementation

The above quantum circuitry can be mapped onto an optical interferometry setup<sup>106</sup> with a 1:1 correspondence between quantum gates and optical elements, as can be seen in Figure 144.

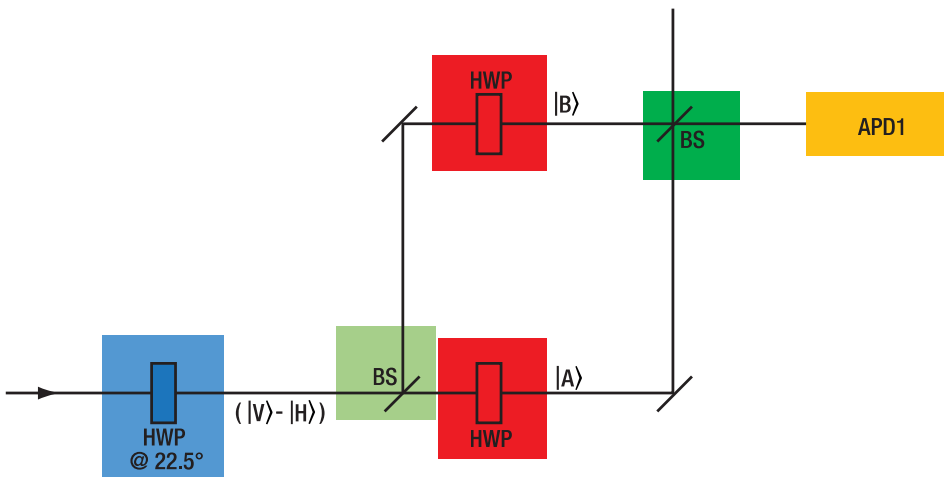


**Figure 144** Scheme for the optical implementation of the Deutsch algorithm in a Mach-Zehnder interferometer configuration. The color-highlighted elements correspond to elements of the quantum circuit in Figure 143.

Here, the first qubit state  $|x\rangle$  is represented by the two path states of the single photon in an interferometer and the qubit  $|y\rangle$  is given by its polarization state.

State initialization is performed by setting the polarization to  $|y\rangle \propto |V\rangle - |H\rangle$ , i.e., linear polarization is rotated by  $45^\circ$  against the vertical axis. This can be done using a polarizer or a half-wave plate. The  $|x\rangle \propto |A\rangle + |B\rangle$  state is generated by a 50:50 beamsplitter and the relative phase is adjusted via the path lengths of the interferometer.

Depending on which kind of function is used to demonstrate the Deutsch algorithm (constant or balanced function), the polarization states  $|V\rangle \leftrightarrow |H\rangle$  must be flipped if  $f(x) = 1$ . This is done by introducing HWP(s) set to  $45^\circ$  with respect to the vertical into one of the interferometer arms for a balanced function or to none or both arms for a constant function.

The last Hadamard gate is again represented by combining both arms at a beamsplitter, where due to interference between states  $|A\rangle$  &  $|B\rangle$  photons exit through only one of the outputs, depending on the type of the function.

A second way to interpret what is happening in the interferometer does not require any knowledge of quantum mechanics and just considers the effects of the optical elements on the photons:

An interferometer is set up in a way, that all photons are linearly polarized and exit through one output of the recombining beamsplitter (constructive interference). Now if a HWP is introduced to one of the arms, such that

<sup>105</sup> <https://learn.qiskit.org/course/ch-gates/phase-kickback>

<sup>106</sup> M. Scholz et al., Physical Review Letters, 96(18), 180501 (2006).

the slow axis is aligned with the polarization axis, the relative phase difference between the arms is shifted by  $\pi$ , which makes all photons exit at the other output port of the beamsplitter. Introducing HWPs in both arms keeps the phase difference and output port unchanged compared to the initial situation. When the photon's polarization is aligned with the slow axis of the HWP, its polarization state also remains unchanged, fully in line with the conclusions that can be drawn from the quantum circuitry analysis.

In the kit we use an interferometer in Michelson configuration instead of the above discussed Mach-Zehnder configuration. The latter one is beneficial for theoretical discussion, as each gate operation corresponds to a single optical element. The Michelson interferometer is more practical for experimental realizations, as it is easier to align and control the phase difference between both arms. The analogy with the quantum circuitry is left unchanged, but we require only one beamsplitter element for both Hadamard operations on the path qubit. In the Michelson configuration, the elements in the interferometer arms are passed in both directions; therefore, the phase shifts are doubled. To achieve the same phase shifts as in the Mach-Zehnder configuration, we use quarter-wave plates (QWP) instead of HWPs.

#### 10.8.4 Experimental Realization

For experimental realization, the following extra components which are not included in this kit are required:

- 2 x LCC1511-B
- 2 x KLC101
- 1 x TPS002
- 2 x Mounting kit, each:
  - RS1.5P8E (RS1.5P4M)
  - RS4M
  - 8-32 (M4) setscrew, 3/4" (20 mm) long<sup>107</sup>
  - RSP1D(/M)

We recommend using a 20 x 20 cm stainless steel board instead of the MB8 (MB2020/M) aluminum breadboard as the basis for the Michelson interferometer to reduce thermal drift effects. This can be ordered from Thorlabs as a special, comparable to the MB6S (MB15S/M) breadboard.



The phase difference between the arms of the interferometer plays a crucial role for the quantum computation. Since manual alignment attempts, such as moving a wave plate, strongly disturb this phase relation, we use a pair of liquid crystal cells (LCC) to control the phases in both arms and switch the effective presence of a wave plate in each arm without moving mechanical parts. This way, the setup needs to be aligned only once, analog to the quantum eraser experiment (Section 7.7), to correct for beam deviations introduced by the cells. As the glass walls of the cells add a considerable amount of dispersion, a cell must be used in each arm or a suitable compensation plate must be placed in the arm without a liquid crystal cell.

The KLC101 controllers are used to apply the correct alternating voltage signals for long life-time operation of the LCCs. The controllers can be operated manually using their front panel controls or with the Kinesis software (recommended)<sup>108</sup>. Their operation is not integrated in the software for this kit. Please refer to the KLC101 controller manual for operation details.

<sup>107</sup> These screws can be ordered as packs of 50 under Item # SS8S075 (SS4MS20).

<sup>108</sup> When using the Kinesis software, do not connect to the KLD101, and KPC101 controllers, otherwise the EDU-QOP1 software cannot connect to them. We recommend starting the EDU-QOP1 software first; then only the KLC101 controllers will be listed in Kinesis.

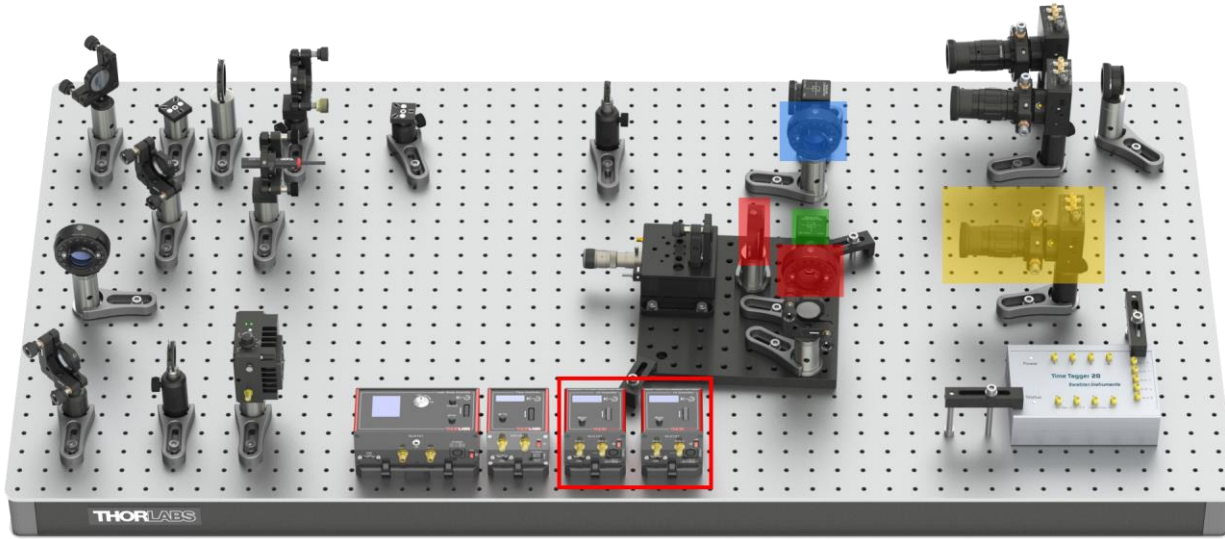


**Figure 145** Fully set up Deutsch algorithm. The color-highlighted elements correspond to elements of the quantum circuit in Figure 143 and Figure 144. Details are given in the text. Additional KLC101 controllers are placed in the red rectangle.

Figure 145 shows the implementation of the DJA based on this kit, using two LCC1511-B liquid crystal retarders and KLC101 liquid crystal controllers. The HWP between the two beamsplitters and the rest of the setup stay in the same orientation in the quantum eraser experiment. When viewed from the Michelson board towards the first beamsplitter, the fast axis of the HWP should be oriented at  $22.5^\circ$  counterclockwise.

1. Assemble the LCC components in their mounts as shown in the explosion rendering and insert them into the Michelson interferometer in the same way as the polarizers in the Quantum Eraser experiment (see Section 7.7). The orientations of the slow axis of the LCCs can be seen in Figure 146.
  - a. When looking from the **fixed mirror** towards the beamsplitter, the slow axis of the wave plate in this arm should be oriented at  **$45^\circ$  counterclockwise** from the 12 o'clock (vertical) position.
  - b. When looking from the **stage mirror** towards the beamsplitter, the slow axis of the wave plate in this arm should be oriented at  **$45^\circ$  clockwise** from the 12 o'clock (vertical) position.



**Figure 146      Orientation of the LCCs in the Michelson Interferometer**

2. Set both KLC101 controllers to  $V_{\text{HIGH}} = 20 \text{ V}$ , where the LCC acts like there is no wave plate in the system. This voltage can be saved as “Preset 1” in the KLC101 controller. On the front panel of the KLC101 controller, use the menu button and scroll wheel to navigate to “LC config” → “Set Preset 1” → “Set Volt 1: 20V” and confirm to save the preset. To actually select a preset navigate to “LC output” → “Preset1 V1 enabled” → “Preset V1 20V”. In the Kinesis software you only need to click on the Preset indicators to select them (will light up green) and set the voltage of the preset with the blue “set” arrow.
3. Align the interferometer, analog to the description for the Quantum Eraser (see Section 7.7), such that you see an interference pattern from the LED.
4. Use the Michelson tab in the software to record a single photon interference pattern. Look for a stage position with a minimum in the interference signal (see Figure 147). Enter this value as the start position in the Michelson tab. The stage will be kept at this position as long as no scan is started.

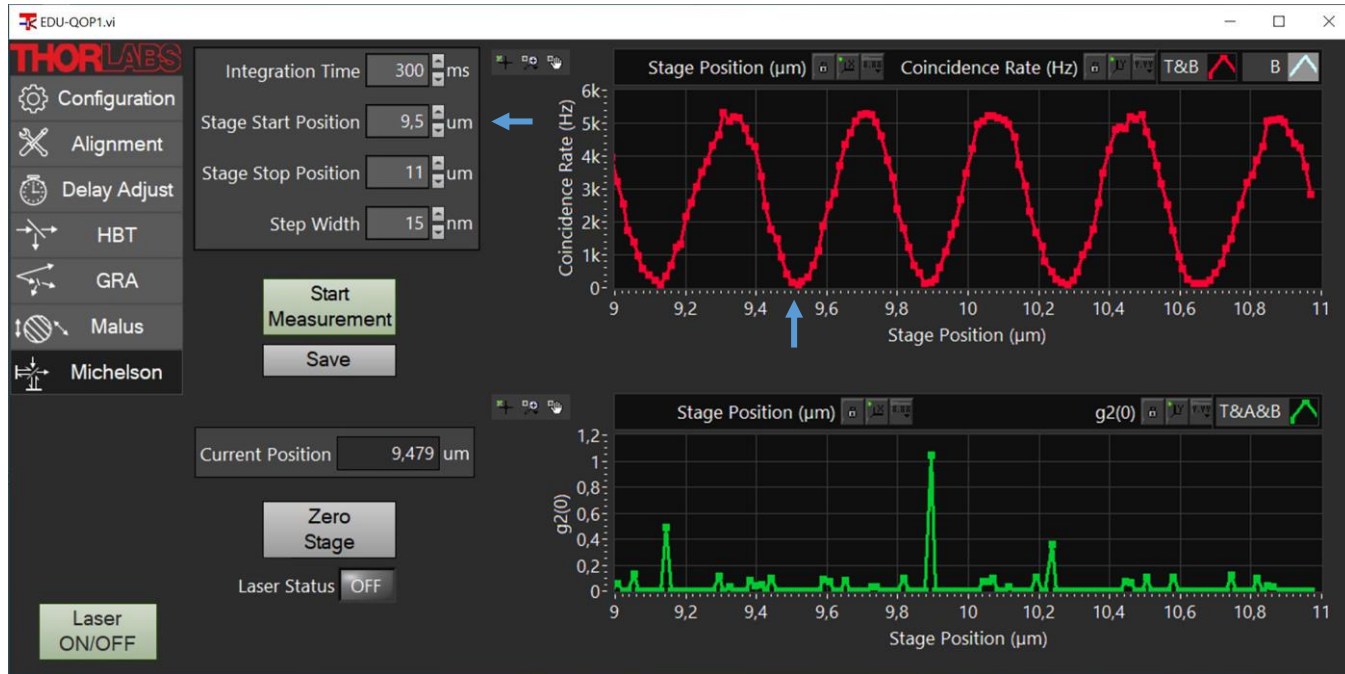


**Figure 147** Choosing a working point in the interference signal. Here  $9.5\text{ }\mu\text{m}$  is selected.

5. This will be the working point for calibration of the LCCs and later measurements. If the Michelson breadboard changes temperature and expands or contracts, this affects the phase of the interferogram at the working position. During calibration of the LCCs the phase must be stable. Should you observe notable phase drift during calibration, you need to start again with a new working point.
6. Move to the Alignment tab of the software and monitor the T&B coincidence count rate while adjusting the voltage  $V_{\text{LOW}}$  ("Preset 2") of one of the KLC101 controllers between 2.4 and 3.6 V<sup>109</sup>. Once a maximum in the rate is reached, you have calibrated the correct voltage setting for the desired (relative) quarter-wave retardance. The interference patterns in the Michelson tab should exhibit a half-wave phase shift, when changing between the two defined high and low voltage settings at the controller, as shown in Figure 148.
7. Reset both KLC101 controllers to  $V_{\text{HIGH}} = 20\text{ V}$  and repeat the process to calibrate the second liquid crystal cell as well.
8. Changing environmental conditions, such as temperature and humidity, shift the phase of the interference pattern over time. In order to get correct results from the Deutsch algorithm, you have to readjust the stage position as explained in the fourth step to update the working point from time to time. See also Section 10.8.6.

<sup>109</sup> From the factory test sheet of the liquid crystal cell, it is possible to calculate a narrower voltage range where quarter-wave retardance can be found.

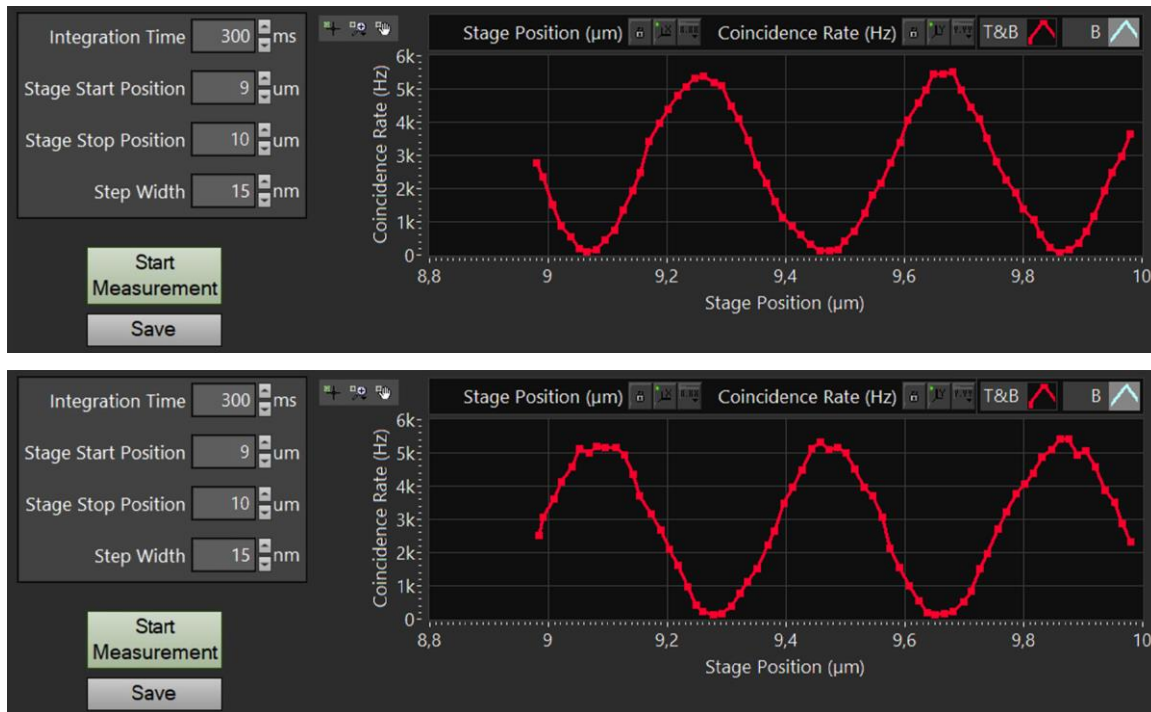


**Figure 148** Michelson Signal with Both LCC Voltages at 20 V (Top) and one LCC Voltage at Calibrated Low Voltage (Bottom).

### 10.8.5 Sample Measurements

The Deutsch algorithm can now be tested for any of the four possible function inputs:

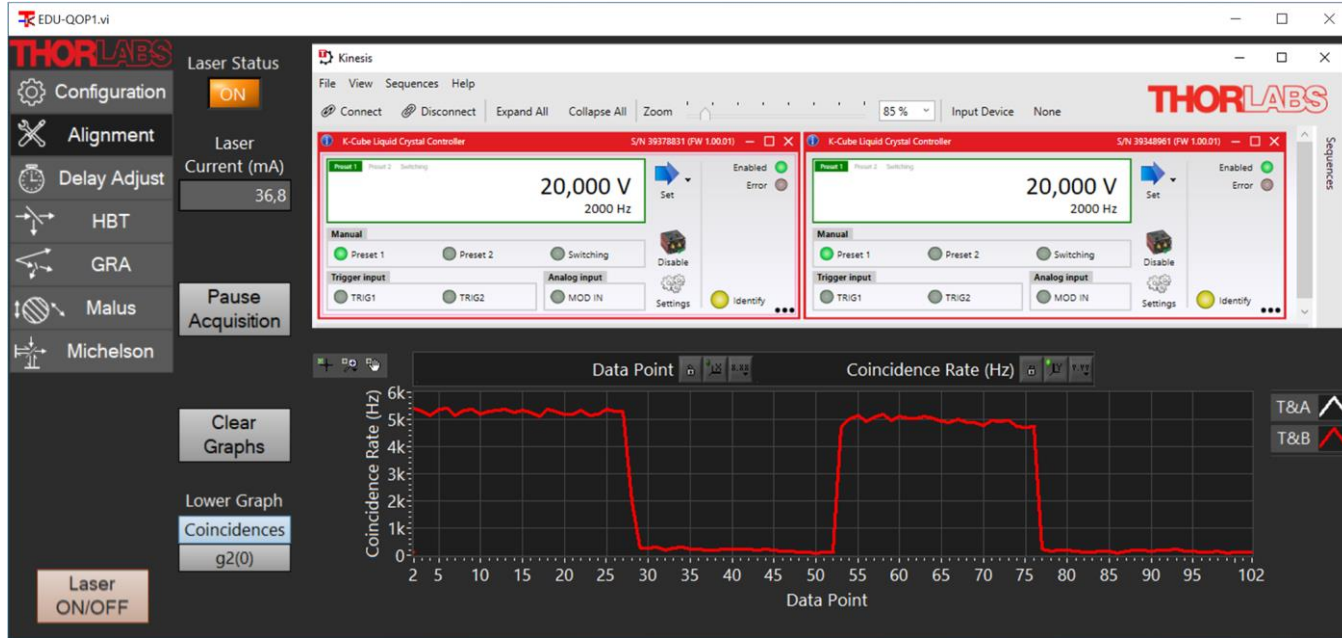
- Two constant functions – Minimum T&B coincidence count rate:
  - Both LCC voltages are set to  $V_{HIGH}$ . Effectively, no arm contains a wave plate.
  - Both LCC voltages are set to  $V_{LOW}$ . Effectively, both arms contain a wave plate.
- Two balanced functions – Maximum T&B coincidence count rate:
  - Only one LCC voltage is set to  $V_{HIGH}$ , the other is at  $V_{LOW}$ . Only the arm set at  $V_{LOW}$  voltage effectively contains a wave plate.

Figure 149 shows the output state of the Deutsch algorithm for all four possible functions. All single photons exit the Michelson interferometer either at the output with the detector in case of balanced functions (maximum count rate) or leave through the input in case of constant functions (minimum count rate). This way, we may differentiate both types of functions from our detector signal.

While the results can be fully interpreted by the quantum-mechanical formalism introduced above, there is another explanation which requires no quantum mechanics at all:

- The linear input polarization of our single photons is aligned exactly with the slow axes of the LCCs. Therefore, there is no net change of the polarization state, but only additional retardance by a quarter wavelength with each pass through the cell, if the voltage is set at  $V_{LOW}$ .
- With both LCCs at minimum retardance (set at  $V_{HIGH}$ ), the working point for the interferometer has been chosen such, that destructive interference is obtained at the detector output and all photons leave through the input.
- Switching one of the LCCs to low voltage ( $V_{LOW}$ ) introduces a half-wavelength phase shift in the respective interferometer arm. This inverts the interference conditions for the output ports and all photons now leave at the detector port.

- Switching both LCCs to low voltage ( $V_{LOW}$ ) introduces the same phase shift in both arms and the interference conditions are analog to the first condition.



**Figure 149** T&B coincidence signal for all four functions of the Deutsch algorithm with voltage combinations  $V_{HIGH}V_{LOW} \rightarrow V_{LOW}V_{LOW} \rightarrow V_{LOW}V_{HIGH} \rightarrow V_{HIGH}V_{HIGH}$ . The inset shows the Kinesis settings for the last combination.

#### 10.8.6 Discussion of Error Sources

Unless the setup is perfectly in thermal equilibrium with its environment, the Michelson breadboard's temperature changes over time and contracts or expands. This may lead to a drift of the relative phase between both interferometer arms, which decreases the count rate contrast between both output states and eventually may even invert the meaning of minimum and maximum rate states. This visualizes the immense importance that phase stability and phase noise play in quantum circuitry and is a good opportunity to discuss this challenge in modern research. In this example, the noise affects the phase difference between  $|A\rangle\&|B\rangle$  of the  $|x\rangle$  qubit state. The noise can be lowered by:

- Replacing the aluminum breadboard with a stainless-steel counterpart reduces thermal drift effects.
- Air currents also introduce phase noise and can be suppressed by housing the interferometer in a box (see Section 12.4).

Furthermore, we can demonstrate the importance of clean qubit state initialization: It is possible to rotate the HWP between both beamsplitters, which defines the input polarization state, i.e., the initial qubit state  $|y\rangle$ . This changes the results for the balanced function configuration. As soon as the HWP is rotated out of the optimal position, the coincidence count rate of the balanced functions state decreases. If we only use a single photon to detect the state, our calculation would not be reliable anymore, as there is a chance that the photon does not reach the detector but leaves at the input port of the Michelson interferometer. Finally, identical count rates are obtained for all functions if the input polarization is rotated by  $90^\circ$  onto  $|y\rangle \propto |V\rangle + |H\rangle$ . Using the quantum-mechanical formalism, one can show that the DJA does not work with this input state. From the optical perspective, it can be understood like this: The input polarization is now perpendicular to the slow axes of the LCCs. Therefore, switching the retardance of the LCC does not have any effect for the transmitted photons.

### 10.8.7 Further Algorithm Ideas

Other optical implementations of QC algorithms, such as Grover's<sup>110</sup> and Shor's<sup>111,112</sup> algorithm, can be found in literature. If you have concrete implementations that could usefully extend the scope of this kit, please do not hesitate to contact us.

## 10.9 Direct Event Pulse Observation

For educational purposes one may want to view the TTL pulses generated by the three detectors directly. Observing the incoming pulses can be helpful to establishing an understanding of the different temporal distribution for the pair source compared to a classical light source. Based on these observations the statistical quantities described in the theory section can be motivated further.

Viewing the pulses directly also helps when discussing technical aspects of the detectors, like pulse length, jitter, or afterpulsing (see Chapter 4).

To view the detector pulses, you can use any kind of oscilloscope or logic level analyzer with a timing resolution on the order of nanoseconds, i.e., a minimum bandwidth of about 1 Gigahertz. The Time Tagger included in the kit also has a logic level scope integrated as a software module, which will be described at the end of this section.

Recommended general settings for any kind of scope are:

- A displayed time window of 200 - 500 nanoseconds
- A maximum voltage level of 5 V
- A trigger level at 0.5 - 2 V
- A negative trigger delay of a few 10s of nanoseconds, to show what happens before the trigger pulse arrives
- Trigger input on pulses of detector T

You may choose to trigger on detectors A or B instead as well. However, triggering on detector T will show similar relative frequencies of coincidence events as in the experiments described above. As the detection rates on detector T are highest (while A or B have at maximum half the rate due to the beamsplitter), many trigger events will only show a trigger pulse without coincidence. Even without the beamsplitter, as stated in Section 4.1, the chances of coincidences are relatively low, as the detection efficiency of the SPDMA detectors is below 50% meaning that often only one photon of a pair will be detected.

To use the scope module of the time tagger, start the Time Tagger Lab software that comes with the installation of the drivers required for the kit. Choose the Time Tagger that is connected to detectors, as seen in Figure 150.

<sup>110</sup> P. G. Kwiat et al., *Journal of Modern Optics*, **47**(2-3), 257-266 (2000).

<sup>111</sup> C. Y. Lu et al., *Physical review Letters*, **99**(25), 250504 (2007).

<sup>112</sup> B. P. Lanyon et al., *Physical Review Letters*, **99**(25), 250505 (2007).

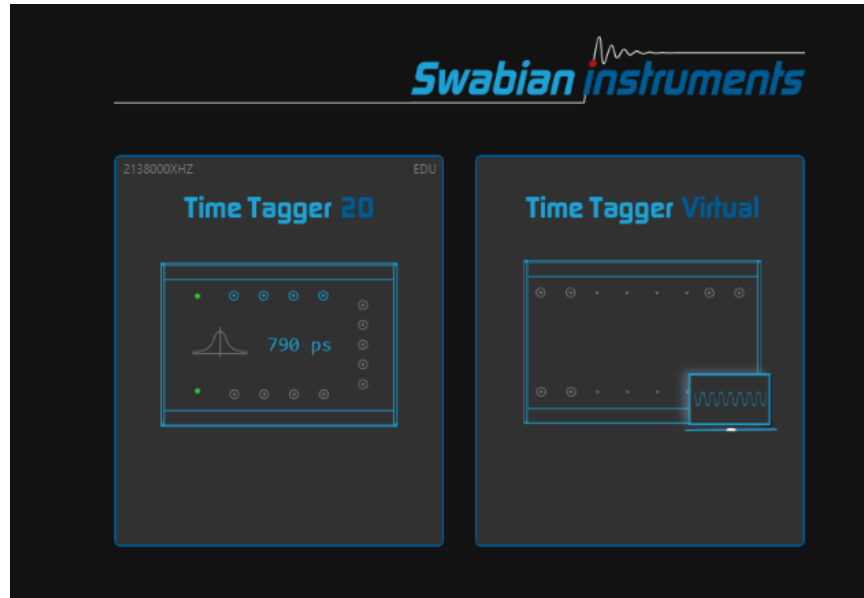


**Figure 150      Startup Page of the Time Tagger Software**

After connecting to your Time Tagger, you will see the “Home” tab with a visual representation of the device and a live view of incoming count rates at the three connected detector inputs. Use the switch above to change to the detailed view, where you can set the input delays (see Figure 151). Note that you must set the same delay values for rising and falling flanks for the scope module to show the true input signals. You may use zero delay for channel T (1) and the same input delay values for channels A (2) and B (3) as calibrated using the delay tab of this kit’s software. It is also possible to assign names to the channels here, which will be shown throughout the software.

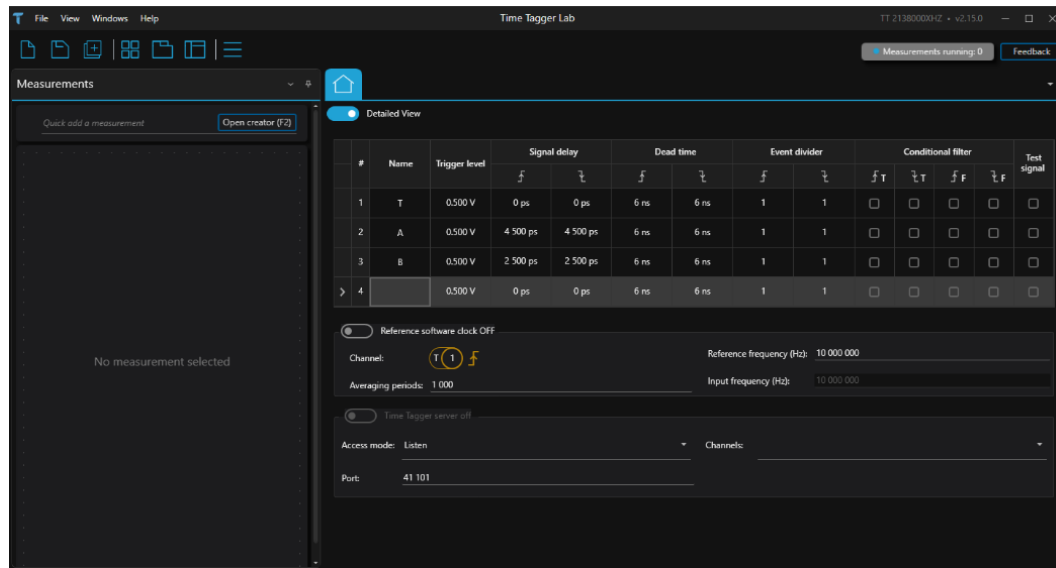


**Figure 151      Detailed View of the Home Screen in the Time Tagger Software**

In the left “Measurements” side panel click “Open creator” (or press the F2 key) and choose “Logic level time trace – Scope” in the new window. Here you may already adjust the scope settings as given below (see Figure 152). After clicking on the “Add measurement” button in the lower left corner, the scope tab opens.

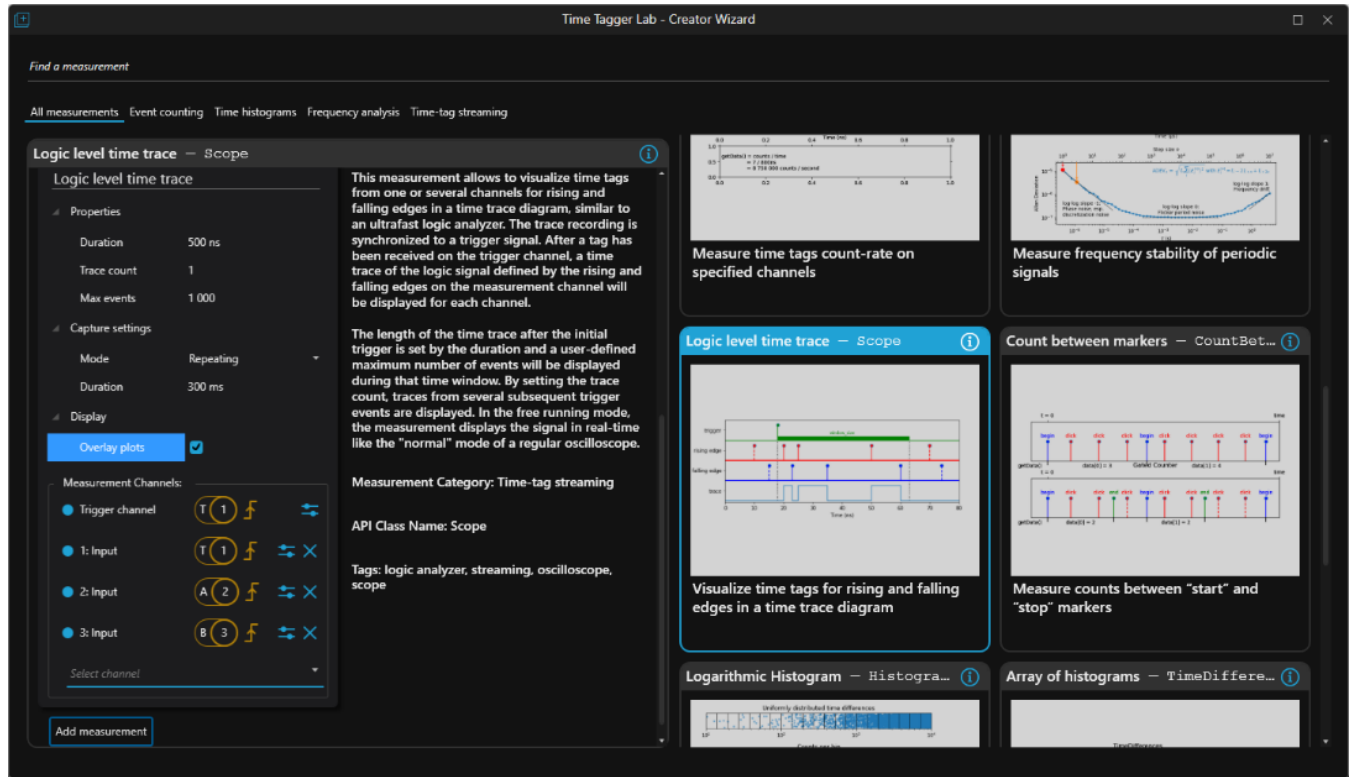


**Figure 152** Setting Up the Scope in the Time Tagger Software

In the “Logic level time trace” tab (see Figure 153), the top graph displays the time trace, as set in the properties panel on the left. You may need to start the measurement using the play button to the left of the top graph. The bottom graph shows a visualization of the count rates at the input ports from the start of the measurement. The measurement of these rates is not restricted to the duration set for the time trace display.

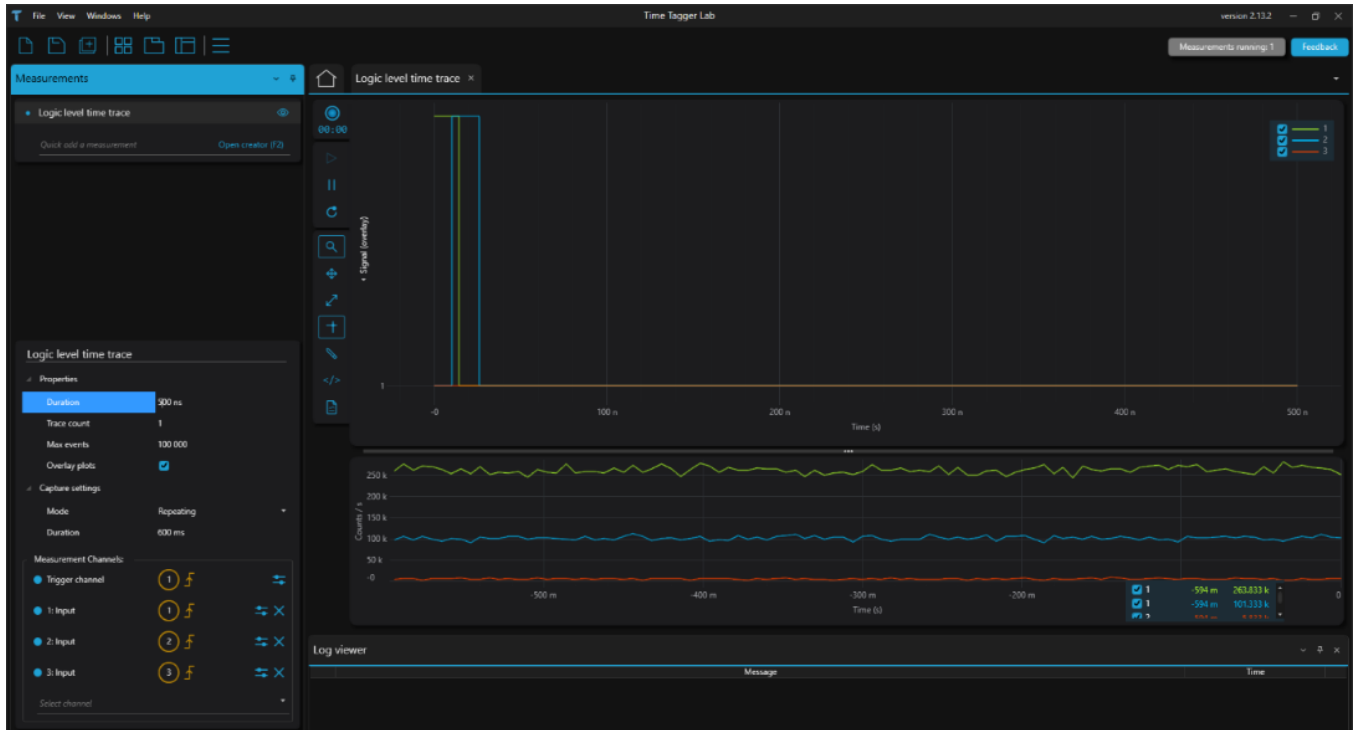


**Figure 153** Logic Level Time Trace Tab in the Time Tagger Software

Note that the Time Tagger hardware can only be used by one software application at a time. To use the software for the kit, you need to close the Time Tagger Lab (and the other way round).

## Chapter 11 Software

### 11.1 Software Installation

- Connect the USB-Stick that is included in the kit to your PC.
- The folder on the stick contains four installers (EDU-QOP1 software, Thorlabs Kinesis, Swabian Instruments Time Tagger software, and dotnet-runtime). Install all four elements (the dotnet-runtime file has to be installed before the Time Tagger software).
- Alternatively, you can visit the Thorlabs, Swabian Instruments, and Microsoft webpages<sup>113</sup> to install the most recent version of the respective software.

### 11.2 General Remarks

- Upon starting the software, a connection check for the Time Tagger is performed. If the device is not connected to the PC, an error message will be displayed. The software will still start but will not have any functionality. In this case, close the software, connect the time tagger to the PC and start the software again.
- The software is optimized to run with the KLD101 laser driver included in the kit but can in principle be used with any laser. In case a different laser driver is used, functions like the on/off button or setting the laser power will not be functional in the software and must be controlled manually.
- With the standard settings, the software will not control the laser switch (except for the On/Off button at the bottom of the tab bar). It is possible to automatize the laser (see Section 11.10) so that it is switched on when a measurement starts and switched off when it ends as well as when the tab is changed, or the software is closed.
- The second order autocorrelation function  $g^{(2)}(0)$  is displayed as **g2(0)** in the software UI.
- You can change the displayed curves in all graphs by right-clicking on the line symbols in the legend (top right of the graph) and checking/unchecking the “Plot Visible” option. You can also turn the automatic scaling of the axes on and off and zoom in and out with the standard LabVIEW options on top of every graph.
- The standard values for most of the control elements in the software are loaded from a config file named **Settings.xml**. This file will automatically be created upon the first start of the software and is located in your documents folder under **\Thorlabs\EDU-QOP1**. If you wish to have different standard values than the ones supplied, you can either use the respective button in the Configuration tab, see Section 11.10, or change the values in the config file directly. The first option is preferred as it ensures that only valid parameters are set. You can always revert to the original values by deleting the config file. It will then be created again upon the next software start.

### 11.3 Saving Results

- After clicking a **Save** button in any tab, a dialog window to select the path and filename appears. It is sufficient to just enter the name without the data type suffix as the file will automatically be saved as a .csv file. If activated (see Section 11.10), a screenshot of the current tab will also be saved in the same folder.
- If the dialog is cancelled, the measurement will not be saved. If you choose a file that already exists, you will be asked whether to overwrite or not. If you choose not to overwrite, the measurement will not be saved. If you choose to overwrite and the file is currently opened, an error message will be displayed.

<sup>113</sup> For Kinesis, the link is: [https://www.thorlabs.com/software\\_pages/ViewSoftwarePage.cfm?Code=Motion\\_Control](https://www.thorlabs.com/software_pages/ViewSoftwarePage.cfm?Code=Motion_Control)

- After selecting the path, you have the option to write a comment that will be saved above the data file header.
- Along with the measurement data, the current values of all settings will be saved to a separate .xml file. This file has the same name as the measurement file with an added “\_Settings” at the end.
- If a new measurement is started before the current one is saved, the current data is lost. The same is true for exiting the software without saving first. Changing the tab, however, does not result in a data loss. It is possible to go back and save the last measurement if you do not start a new one beforehand.
- It is also possible to directly export data from any graph by right-clicking in the graph and choosing **Export → Copy to Clipboard**. Then it can be pasted into any spreadsheet software.

## 11.4 Connection Window

Upon starting of the software, the Connection window, as shown in Figure 154, is displayed first. It consists of several drop-down menus in which the serial numbers of the connected controllers can be selected by left-clicking into the respective fields.

- Make sure that all controllers you want to connect are switched on and connected to your PC via USB. If you already started the software and connected or switched on your controller afterwards, a click on the **Refresh** button will add its serial numbers to the respective drop-down menu.
- A KLD101 **Laser Controller** has to be connected to allow control of the pump laser via the software. It is possible to not connect a controller and manually control the laser.
- To use the Michelson tab (see Section 11.9), either a KPC101 controller or both a KPZ101 and a KSG101 controller have to be connected. The **Strain Gauge Reader** menu will automatically become active if the serial number selected in the **Piezo Controller** field is recognized as belonging to a KPZ101 controller.
- Multiple KDC Controllers can be connected for additional experiments that are not part of the core kit, such as the single photon double slit (see Section 10.2) or automatized rotation stages (see Section 27.3). In case of multiple KDC101, we recommend giving them identifiable names, by changing the entries in the **Name** column.
- At the bottom of the connection window is the checkbox **Show Tabs for EDU-QOPA1 Polarization Entanglement Addon**. This box should be left unchecked if you don't own the addon kit or only want to do the experiments of the main EDU-QOP1(/M) kit.
- Once you have finished the device selection, click the **Connect** button to start the main software.
- Your selection will be saved, so that the serial numbers are pre-selected the next time you start the software. If you do not change the controllers, you can just directly click **Connect** on subsequent starts.

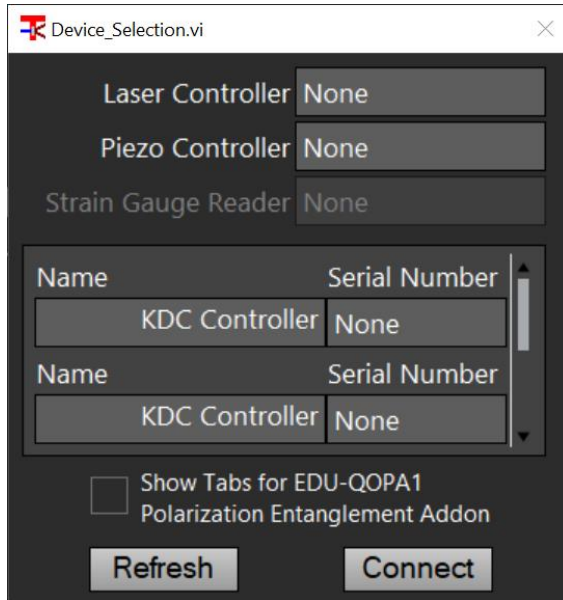


Figure 154 Connection Window

## 11.5 Alignment Tab

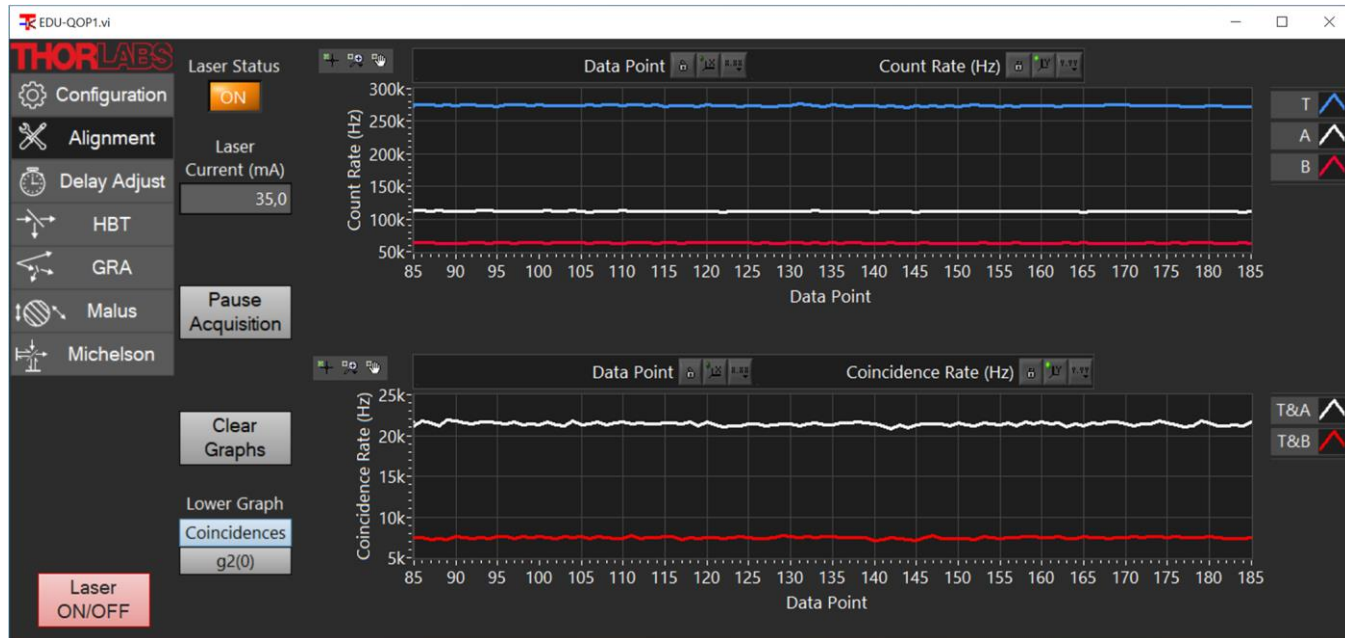


Figure 155 Alignment Tab

This tab, as shown in Figure 155, is used to align the setup before taking measurements. The count rates of the three detectors T, A, and B are shown in the upper graph, while the lower graph can be selected to either show the coincidence count rates between T&A and T&B, respectively or the second order autocorrelation  $g^{(2)}(0)$  for these detector pairs (for details on the calculation of these values, see Section 3.5.2). Count rates are measured over intervals of 0.5 s and both graphs are updated at the corresponding rate (twice per second).

On the left side of the graphs are the following control elements:

- The **Laser Status** LED displays the current laser status.

- **Laser Current (mA):** Here, you can set the laser current for the pump laser to adjust the pump power. The maximum is 100 mA, but the current will be limited by the maximum current setting of the KLD101 controller (see Section 7.2.2).
- The **Pause Acquisition** button pauses/unpauses the acquisition of data in the window. This can be helpful if the user wants to compare values for different adjustments of the setup.
- The **Clear Graphs** button deletes all data from both graphs.
- The **Lower Graph** radio buttons switch this graph between showing the coincidence count rates or the  $g^{(2)}(0)$  values calculated from the coincidences and single channel count rates (see Section 3.5.2).

## 11.6 Delay Adjust Tab

In this tab, as shown in Figure 156, the delay compensation measurement is performed, as described in Sections 4.2.3, 7.4.5, and 7.5.3. The graph displays the coincidence count rates between detectors T&A and T&B, respectively, in dependence of the delay offset between the detectors.

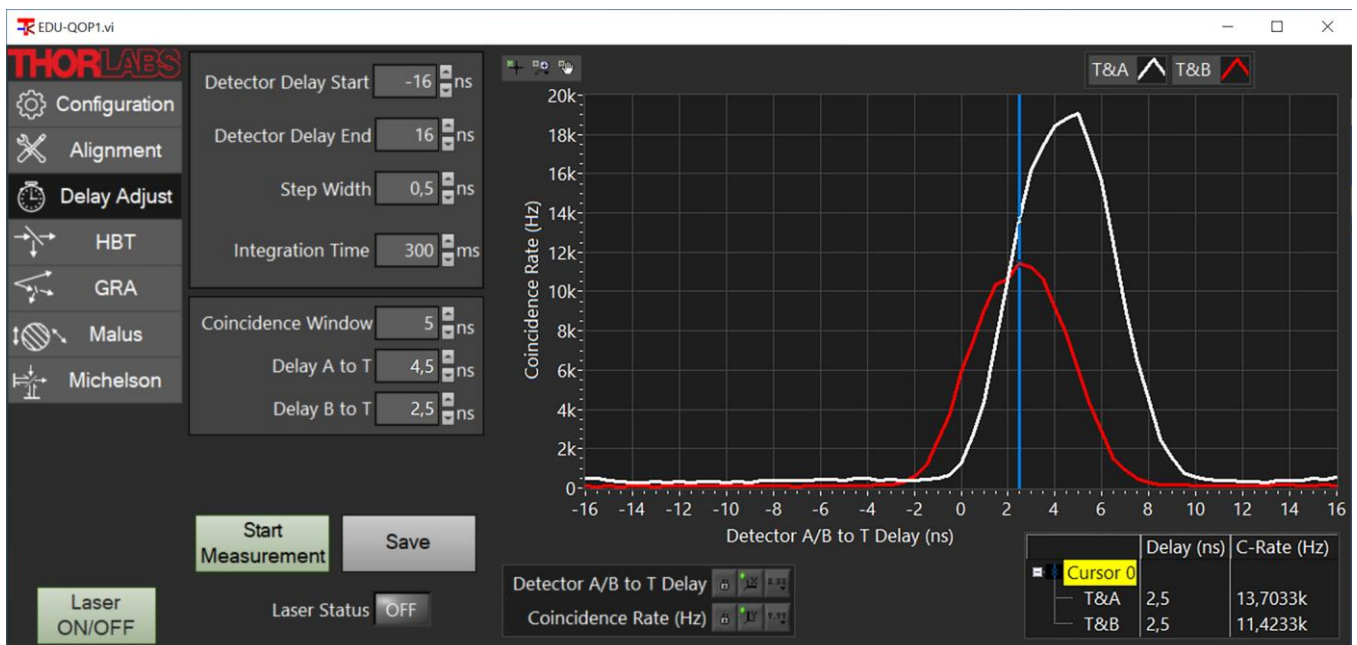


**Figure 156      Delay Adjust Tab**

To the left of the graph are the following control elements:

- **Detector Delay Start / Detector Delay End:** Here, the start and end points of the delay offset are set. Detectors A and B are delayed by the specified amount in relation to detector T. The minimum value is -100 ns, and the maximum value is 100 ns. The standard range from -16 ns to 16 ns should cover most experimental cases. Smaller ranges can be chosen to speed up the measurement.
- **Step Width:** Here, the step width of the measurement is set. The minimum is 0.001 ns. The standard value of 0.5 ns offers a good compromise between measurement time and precision. Larger step widths can be chosen to speed up the measurement.
- **Integration Time:** Here, the time over which counts are collected for a single data point is set. The minimum is 10 ms. Longer times lead to less noise but increase the measurement time. The standard value of 300 ms offers a good compromise.
- **Coincidence Window:** Set the time window for when two events are counted as a coincidence, as defined in Section 4.2.2.

- **Delay A/B to T:** Set the time delay compensation for each channel as read out from the measurement. These values will be used for all other measurements in the software and compensate the delay caused by electronics and optical path length differences.
- **Start Measurement:** Clicking this button will trigger a measurement. If the automatic laser control is turned off (standard setting) and the software detects that the laser is not activated, a reminder to switch on the laser will be displayed. During a running measurement, the button changes to **Stop Measurement** and can be used to end the measurement.
- **Save:** This button saves the last measurement in this tab as a delimited text file (.csv) that can easily be imported in spreadsheet programs. Additionally, the current software settings are saved to a separate .xml file at the same directory. A screenshot of the software is also saved if the respective setting is activated, see Section 11.10.

There is one control element within the graph window:

- **Cursor:** The blue vertical line in the graph window is the cursor. After a completed measurement, it is located at the far left of the graph and can be moved by dragging and dropping. The table in the lower right corner of the tab shows the cursor position.

The laser status is displayed below the buttons.

Once a measurement is finished, the values of the curves can be read out by dragging the cursor left and right and monitoring the values in the cursor table.

## 11.7 HBT and GRA Tabs

In these tabs, as shown in Figure 157 and Figure 158, the Hanbury-Brown-Twiss experiment and the Grangier-Roger-Aspect experiment, as explained in Sections 3.5.1 and 3.5.3, respectively, can be performed. Both tabs have a similar structure, only differing in the shown quantities.

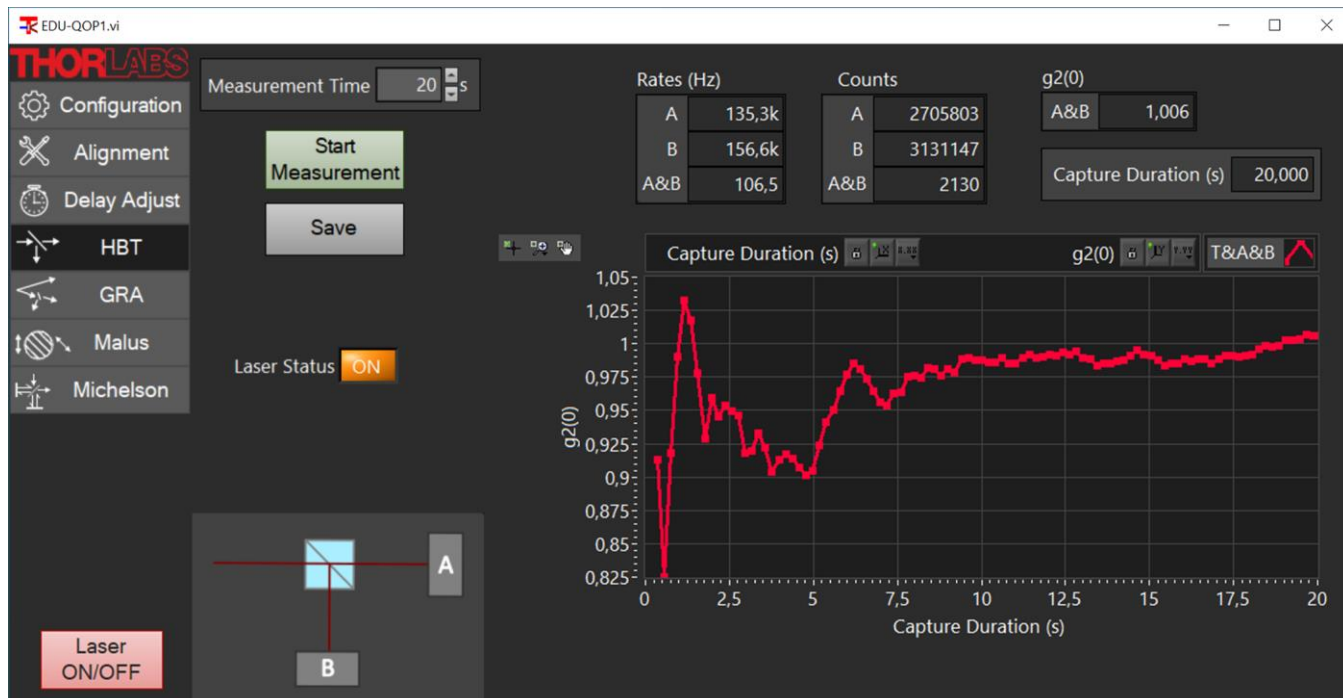


Figure 157      HBT Tab

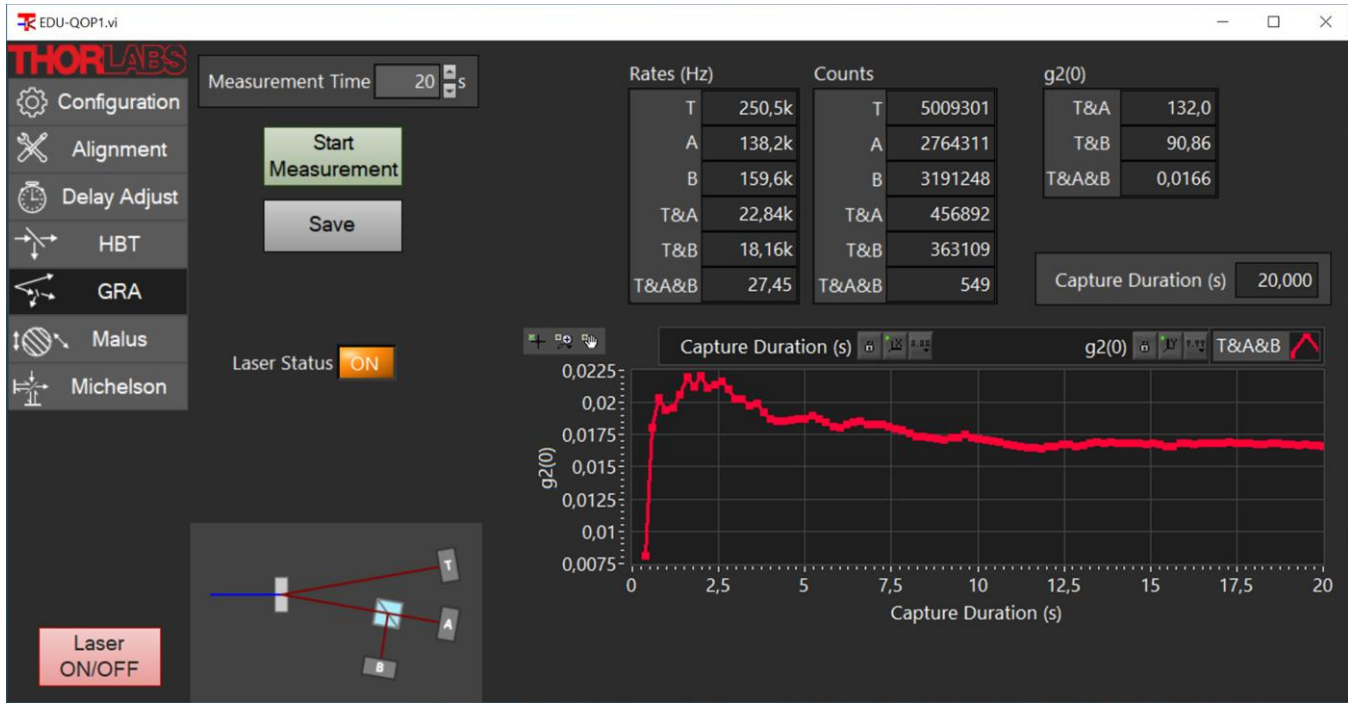


Figure 158     GRA Tab

On the left side of the tabs, the following control elements are located:

- **Measurement Time:** This value sets the overall time of the measurement. Longer times lead to higher count totals and in turn decrease the statistical uncertainty of the calculated autocorrelation functions.
- **Start Measurement:** Clicking this button will trigger a measurement. If the automatic laser control is turned off (standard setting) and the software detects that the laser is not activated, a reminder to switch on the laser will be displayed. During a running measurement, the button changes to **Stop Measurement** and can be used to end the measurement.
- **Save:** This button saves the last measurement in this tab as a delimited text file (.csv) that can easily be imported in spreadsheet programs. Additionally, the current software settings are saved to a separate .xml file at the same directory. A screenshot of the software is also saved if the respective setting is activated, see Section 11.10 for details.

The laser status is displayed below the buttons.

The boxes in the right part of the tab contain the measurement results:

- The count rates
- The absolute count numbers
- The  $g^{(2)}(0)$  value calculated by the software. In the GRA tab, three different  $g^{(2)}(0)$  functions for different detector correlations are acquired. For details on those values and their calculation, see Section 3.5.4.
- Below the result boxes, the  $g^{(2)}(0)$  values are plotted over time, making it possible to see how the correlation function stabilizes with increasing measurement duration.

## 11.8 Malus' Law Tab

This tab, as shown in Figure 159, is used for the measurement of Malus' law for single photons, as described in Sections 3.7 and 9.6.

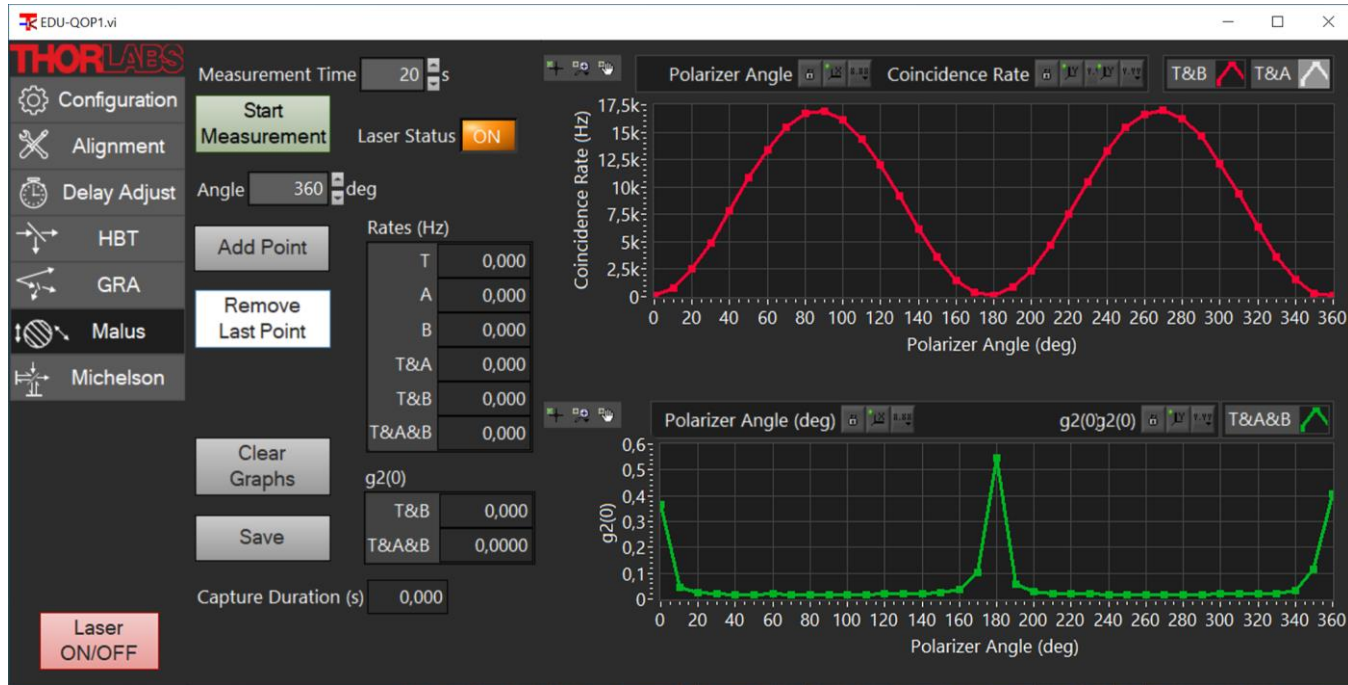


**Figure 159      Malus' Law Tab**

In this tab, you can perform several Grangier-Roger-Aspect-like measurements for different polarizer angles and add those data points to two plots. The collected results can then be saved in a single file.

On the left side of the tab are the following elements from top to bottom:

- **Measurement Time:** This value sets the overall time of the measurement. Longer times lead to higher count totals and in turn decrease the statistical uncertainty of the calculated autocorrelation functions.
- **Start Measurement:** Clicking this button will trigger a measurement for a single data point (polarizer angle). If the automatic laser control is turned off (standard setting) and the software detects that the laser is not activated, a reminder to switch on the laser will be displayed. During a running measurement, the button changes to **Stop Measurement** and can be used to end the measurement.
- **Results Box:** Here, the results of the current measurement are displayed, similar to the result of the GRA tab, as seen in Section 11.7.
- **Angle:** Here, you can set the angle of your polarizer for the current measurement. This value will be taken as the x-coordinate of the data point in the plot, when using the **Add Point** button.
- **Add Point:** This button adds the last completed measurement to the plots. The x-coordinate is read from the **Angle** field.
- **Remove Last Point:** This button removes the last data point from the plots (e.g., if you accidentally used the wrong angle value). It can be used multiple times to remove more than one point. Please note that removed data points are lost and cannot be restored.
- **Save:** This button saves the current plots as a delimited text file (.csv) that can easily be imported in spreadsheet programs. Additionally, the current software settings are saved to a separate .xml file at the same directory. A screenshot of the software is also saved if the respective setting is activated, see Section 11.10 for details.
- **Clear Graphs:** This button clears all data points from both graphs. Please note that the data is lost if not saved prior to clearing.

On the right side of the tab are the data plots:

- The upper plot shows the T&B coincidence count rates as a function of the polarizer angles.
- The lower plot shows the  $g^{(2)}(0)$  values calculated from the count rates as a function of the polarizer angle.

The laser status is displayed to the right of the Start Measurement button.

### 11.9 Michelson Interferometer Tab

In this tab, as shown in Figure 160, the single photon interference experiments (see Sections 3.6 and 9.7) as well as the quantum eraser experiment (see Sections 3.8 and 9.8) can be performed.

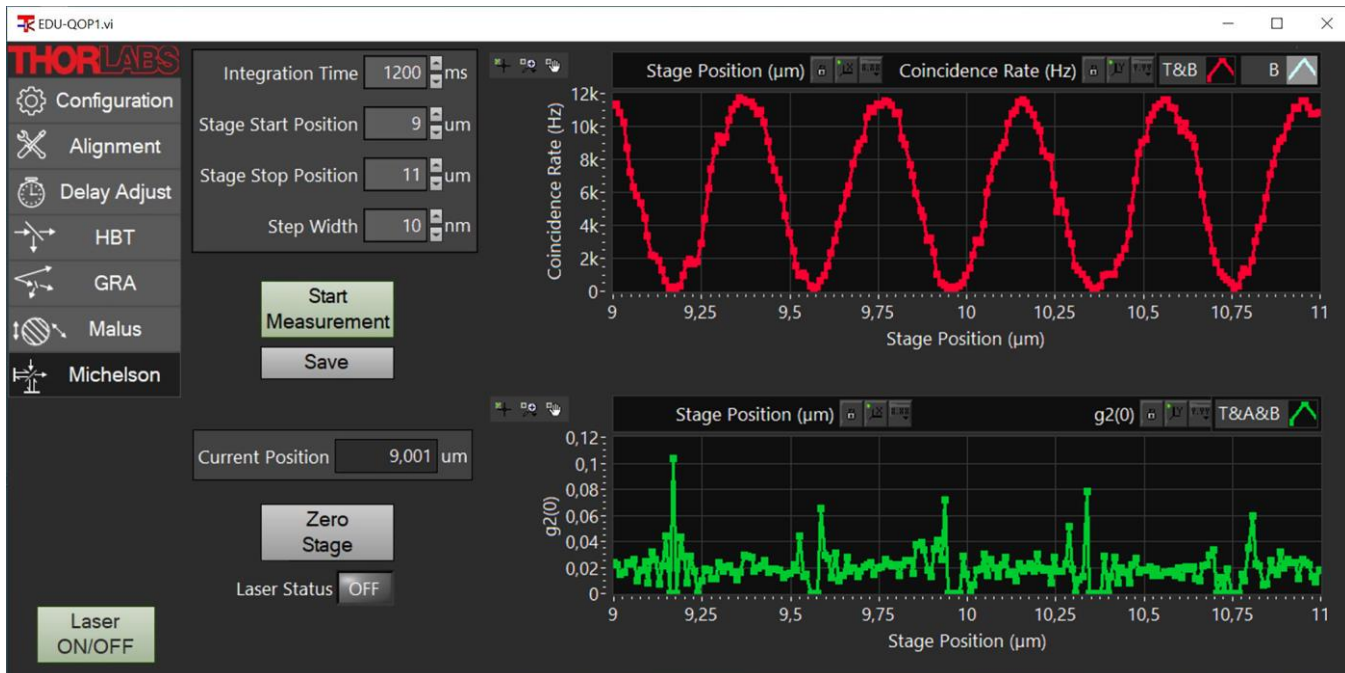


**Figure 160      Michelson Interferometer Tab**

This software tab utilizes the KPC101 controller<sup>114</sup>. The connection for the controller has to be established upon start of the software (see Section 11.4). If no connection can be found (controller disconnected or switched off), an error message will be displayed. You can still view the tab, but the measurement will not move the stage. The stage should be calibrated before first use, as described below.

The graphs show the coincidence count rate of detectors T&B (upper graph) and the autocorrelation  $g^{(2)}(0)$  (lower graph) as a function of the stage position of the Michelson interferometer. For details on the calculation of  $g^{(2)}(0)$ , see Section 3.6.

On the left side of the tab are the following control elements:

- **Integration Time:** Here, the time over which counts are collected for a single data point is set. The minimum is 100 ms. Longer times lead to less noise (especially in the  $g^{(2)}(0)$  calculation) but increase the measurement time. For measurements where only the upper graph is of importance and for large measurement ranges, we recommend the minimum setting of 300 ms. For smaller ranges and if the  $g^{(2)}(0)$  value is of interest, significantly longer times (e.g. 5000 ms) are advantageous.
- **Stage Start Position / Stage End Position:** Here, the start and end point of the measurement are set.
- **Step Width:** Here, the step width of the measurement is set. The minimum value is 1 nm, and the maximum is 20000 nm. Larger step widths speed up the measurement at the cost of spatial resolution. The typical period of the interferogram is about 400 nm.

<sup>114</sup> Revision A of the kit includes the KPZ101 and KSG101 controllers instead of the KPC101 controller. The software is compatible with these controllers as well.

- **Start Measurement:** Clicking this button will trigger a measurement. If the automatic laser control is turned off (standard setting) and the software detects that the laser is not activated, a reminder to switch on the laser will be displayed. During a running measurement, the button changes to **Stop Measurement** and can be used to end the measurement.
- **Save:** This button saves the last measurement in this tab as a delimited text file (.csv) that can easily be imported in spreadsheet programs. Additionally, the current software settings are saved to a separate .xml file at the same directory. A screenshot of the software is also saved if the respective setting is activated, see Section 11.10.
- **Zero Stage / Calibrate Stage:** The Zero Stage button starts the Zeroing process for the KPC101 controller. Zeroing is required every time the KPC101 has been switched off and on, or if a different stage is connected to the controller.

If the software is used for an older revision of the kit with KPZ101 and KSG101 controllers, the name of the button changes to Calibrate Stage, and starts a calibration routine for the controllers, which is required to obtain precise position readings. It is highly recommended to calibrate the stage at the first start of the software, else the software loads an emergency calibration which may lead to deviations in the position reading. If optimal accuracy is required, re-calibrating the stage at each start of the software or after alterations to the setup/environment is recommended. The calibration process takes about 30 seconds. During the process, all software controls are deactivated.

- The current position and the laser status are displayed below the Zero Stage button.

## 11.10 Configuration Tab

This tab (shown in Figure 161) displays all the settings made in the other tabs as well as additional global settings. Those are:

- **Laser Current (mA):** Here, you can set the laser current for the pump laser to adjust the pump power. The maximum is 100 mA, but the current will be limited by the maximum current setting of the KLD101 controller (see Section 7.2.2).
- **Lock KLD Front Panel:** If this checkbox is activated, the front panel of the KLD101 controller is locked and the laser power can only be set via the software. The standard setting is an unlocked front panel.
- **Switch Laser On/Off Automatically:** If this checkbox is activated, the software is allowed to control the laser. It will turn on the laser with the beginning of every measurement and turn it off at the end of a measurement, when a different tab is chosen, or when the software is closed. The standard setting is no automatic control.
- **Save Settings on Exit:** If this checkbox is activated (standard setting), the software will write all values displayed in the configuration tab in a config file and load them upon the next start of the software. If the setting is deactivated, the config file will not be overwritten when closing the software.
- **Save Screenshot with Data:** If this checkbox is activated (standard setting), a screenshot of the current tab will be saved every time a **Save** button is clicked in any tab.
- **Save Current Settings:** With this button, you can write the current settings in the config file to be loaded after the next software start. Make sure to deactivate the **Save Settings on Exit** checkbox in this case or the config file will be overwritten again upon closing the software.
- **Restore Default Settings:** With this button, you can restore the settings to the state that is set when opening the software for the first time (default state).
- **Check for Latest Version Online:** With this button, you can check whether there is a newer version of the software available for download. If that is the case, the new version number is displayed and you may

choose to open a direct download link via your browser, open the software information web page, or do nothing at all.

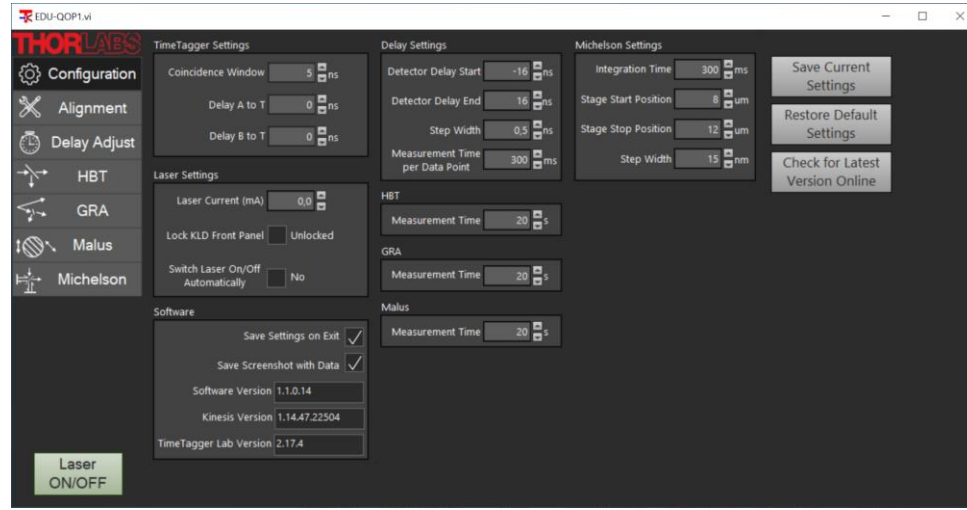


**Figure 161 Configuration Tab**

### 11.11 KDC Stage Tab

While the KDC101 controller is not part of the kit, it is required for some additional experiments such as the single photon double slit described in Section 10.2. If one or more KDC101 controllers are connected to the PC and have been selected in the connection window, the KDC Stage tab will appear at the bottom of the tab list, as displayed in Figure 162.

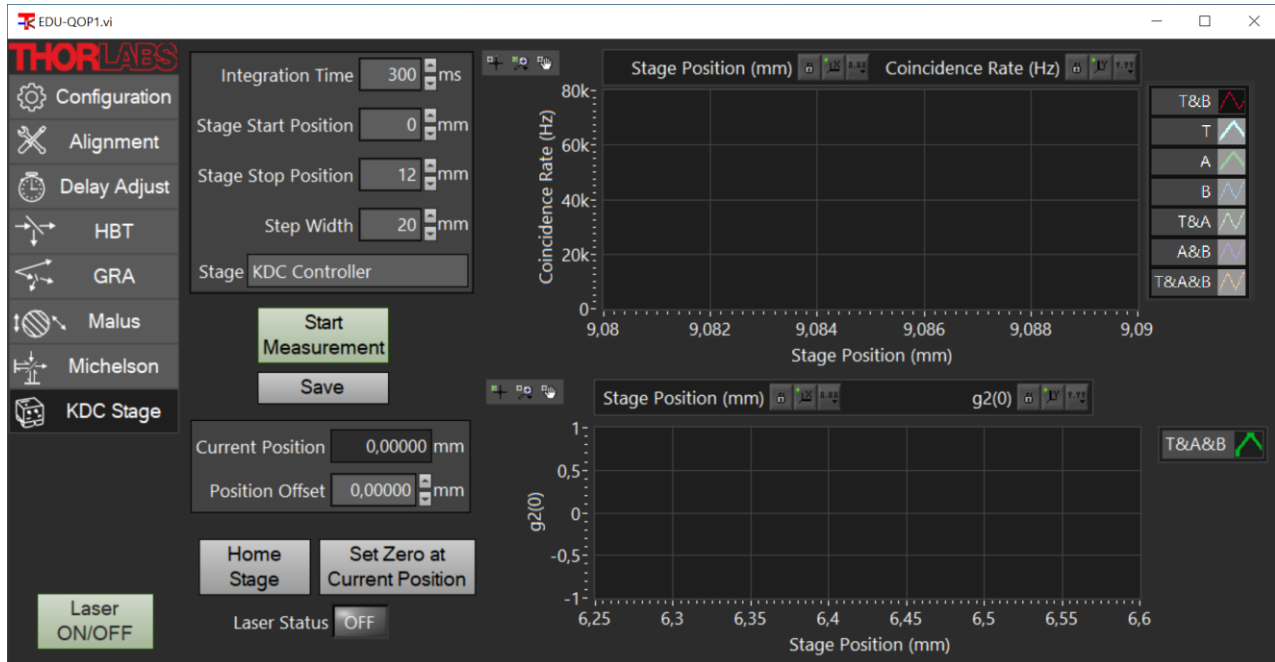


**Figure 162 KDC Stage Tab**

The tab is similar to the Michelson tab with the difference that a translation stage with several mm of range is moved via the KDC101 controller instead of a piezo stage via the KPC101 controller. On the right side, two graphs display the count rates of choice (upper graph) and the  $g_2$  correlation function (lower graph) as a function of the stage position. The stage can be a linear stage or a rotation stage. The software will automatically detect which stage is used and display the correct units (mm or  $^\circ$ , respectively). The measurement settings to the left of the graph work identically to those of the Michelson tab (Section 11.9) as do the **Start Measurement** and **Save** buttons.

Below the **Save** button, the **Current Position** is displayed. Sometimes, it can be desirable to add an offset to the stage position. This can be done by changing the value of the **Position Offset** field. A quick way to do this is to move the stage to the desired zero position (by changing the value of the **Stage Start Position** field) and then click the **Set Zero at Current Position** button, which will add the current position as a negative offset.

The **Home Stage** button starts the homing process of the stage, which is required to give correct position readings. Homing has to be repeated every time the KDC101 controller has been switched off or if a different stage has been connected.

## 11.12 Hidden Settings

There are two settings that make more complex changes and are therefore not controllable via the software. Those settings can be changed directly via the config file, which is located in your documents folder under \Thorlabs\EDU-QOP1. The hidden settings are:

- **Coincidence Mode:** In Section 12.1, we describe three different ways to define coincidences and their advantages and disadvantages. The software can use all three modes. The mode can be changed via the lines in the config file that are shown in Figure 163. A value of 2 (standard setting) is the Coincidence of Coincidence mode, a value of 1 is the Gated Counting mode and a value of 0 is the standard definition of triple coincidences (see Section 12.1).

```
<EW>
<Name>Coincidence mode</Name>
<Choice>Triple Coincidences</Choice>
<Choice>Gated Counting</Choice>
<Choice>Coincidences of Coincidences</Choice>
<Val>2</Val>
</EW>
```

**Figure 163** Settings file code for changing the coincidence mode. The red circle marks the important value.

- **Laser Operation Mode:** The laser can be operated in the Constant Current mode (standard setting) or in the Constant Power mode. If you want to use the latter, search for the lines displayed in Figure 164 in the config file and change the value from 0 to 1. To use the Constant Power Mode, the slope of the current-power curve needs to be set. Please refer to the KLD101 driver manual for details.

```
<EW>
<Name>Laser Operation mode</Name>
<Choice>Constant Current (mA)</Choice>
<Choice>Constant Power (mW)</Choice>
<Val>0</Val>
</EW>
```

**Figure 164** Settings file code for changing the laser mode. The red circle marks the important value.

## 11.13 Operating Labview Graphs

As the software is written in LabView™, the graphs come with the native LabView control elements. In this chapter, we will explain how these work:

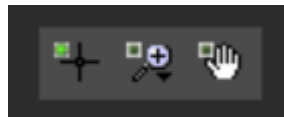


**Figure 165** The Zoom/Move Bar

- In the top left corner of each graph, the zoom/move bar is located, see Figure 165. It consists of three elements from left to right:
  - Cursor Mode: By clicking this element, the cursor will be reset to normal. If a zoom mode was selected prior to this, it will be deactivated. Only with a normal cursor can cursor elements in graphs be moved.

- The zoom menu: Clicking this element opens the zoom dropdown menu, which is explained in detail shortly.
- Move Graph: By clicking on this element the user can activate/deactivate the Move Graph mode. When activated, the cursor changes to a hand and clicking plus dragging with the left mouse button inside the graph area moves the graph inside the window.

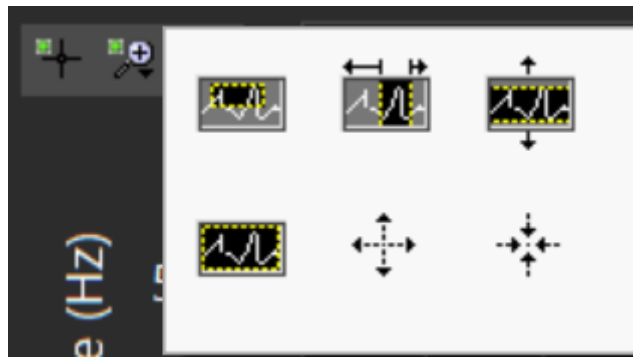


**Figure 166      The Zoom Menu**

- The zoom menu (see Figure 166) consists of six elements, from left to right and top to bottom:
  - Zoom Window: By clicking this element and then drawing a rectangle inside the graph area by clicking plus dragging with the left mouse button, the user can select an area to zoom in on. The area inside the rectangle will then fill the graph window.
  - X-Axis zoom: Works similar to the zoom window element above with the difference that the y-axis will remain unchanged and the user selects a section of the x-axis to zoom in on
  - Y-Axis zoom: Same as X-Axis zoom but for the y-axis
  - Auto-Zoom: By clicking this element, both axes are automatically scaled to include all data points of the present graph.
  - Zoom In: By clicking this element, the cursor will change to the zoom in symbol. Clicking with the left mouse button will zoom into the graph with the point directly under the cursor staying constant and the axes rescaled to spread other points apart.
  - Zoom Out: Opposite to zoom in.



**Figure 167      The Axis Bar**

- On top of each graph there are the axis bars (as displayed in Figure 167). The x-axis is left and the y-axis is right. Each axis bar consists of four elements, from left to right:
  - Axis Label: The axis label is an editable text box. Clicking inside allows the user to modify the axis label by just changing the text.
  - Axis Lock: If activated and new data-points are added to the plot, this axis automatically rescales to show all data points of currently visible plots.
  - Auto-Scaling: Manually trigger the automatic axis rescaling once as described above.
  - Axis Format Menu: Clicking on this element opens a dropdown menu consisting of several options to modify the axis format, such as changing or the number format or switching between

linear and logarithmic scaling. They are mostly self-explanatory and will not be introduced in detail here.



**Figure 168      The Plot Legend**

- On the top right or to the right of the graphs is the plot legend (see Figure 168), it consists of one or more plots with a label to the left and a preview of the plot style to the right.
  - Clicking on the label allows to rename the graph by changing the text
  - Clicking on the plot preview opens the plot dropdown menu. This menu includes many self-explanatory options to format the plot style. The topmost option can be used to make the plot visible/invisible. This can be helpful as invisible plots do not contribute to auto-scaling.

## Chapter 12 Technical Notes

### 12.1 Matrix Notation of Quantum States and Operators

It is possible to use a matrix notation instead of the quantum-mechanical bra-ket notation. While the bra-ket notation is more general and does not depend on a specific basis, some operations can be easier or more intuitive when noted as matrix operations. Here, we will give a short introduction with two examples, a more detailed explanation can be found in textbooks<sup>115</sup>.

To write a quantum mechanical state  $|\psi\rangle$  in matrix notation, one needs to choose a set of orthonormal basis vectors  $|u_1\rangle, |u_2\rangle, \dots, |u_n\rangle$  with  $n$  being the dimension of the Hilbert space<sup>116</sup>. The state  $|\psi\rangle$  can then be expressed as a vector with the components being the projections onto the basis vectors, i.e.:

$$|\psi\rangle \equiv \begin{pmatrix} \psi_1 \\ \psi_2 \\ \vdots \\ \psi_n \end{pmatrix} \text{ with } \psi_i = \langle u_i | \psi \rangle \quad (145)$$

Any operator  $\hat{A}$  can be expressed as a  $n \times n$  matrix as follows:

$$\hat{A} \equiv \begin{pmatrix} A_{11} & \dots & \dots & A_{1n} \\ \dots & \dots & \dots & \dots \\ \dots & \dots & \dots & \dots \\ A_{n1} & \dots & \dots & A_{nn} \end{pmatrix} \text{ with } A_{ij} = \langle u_i | \hat{A} | u_j \rangle \quad (146)$$

Both the vector components  $\psi_i$  and the matrix components  $A_{ij}$  are complex numbers in general.

If the operator  $\hat{A}$  acts on the state  $|\psi\rangle$ , the resulting state can be determined by a matrix multiplication, e.g.:

$$\hat{A}|\psi\rangle \equiv \begin{pmatrix} A_{11} & \dots & \dots & A_{1n} \\ \dots & \dots & \dots & \dots \\ \dots & \dots & \dots & \dots \\ A_{n1} & \dots & \dots & A_{nn} \end{pmatrix} \begin{pmatrix} \psi_1 \\ \psi_2 \\ \vdots \\ \psi_n \end{pmatrix} = \begin{pmatrix} A_{11}\psi_1 + \dots + A_{1n}\psi_n \\ \vdots \\ A_{n1}\psi_1 + \dots + A_{nn}\psi_n \end{pmatrix} \quad (147)$$

Using this notation, it is very important to make sure that all state vectors and operators are expressed in the same basis, only then will the result be correct!

As an example, the way of a photon through a Michelson interferometer, as calculated in Dirac notation in Section 3.6.1 can be described neatly with the matrix notation. Consider the Michelson interferometer as displayed in Figure 169 with a single photon incident from the left. We call the state with the photon in the paths on the lower left side of the beamsplitter  $|\alpha\rangle$  and the state with the photon being in one of the paths on the top right side  $|\beta\rangle$ .

<sup>115</sup> F. J. Duarte and T. S. Taylor, *Quantum Entanglement Engineering and Applications*. (IOP Publishing, Bristol, 2021).

<sup>116</sup> The matrix notation does work for infinitely dimensioned Hilbert spaces as well, but we will limit ourselves to finite dimensions here.

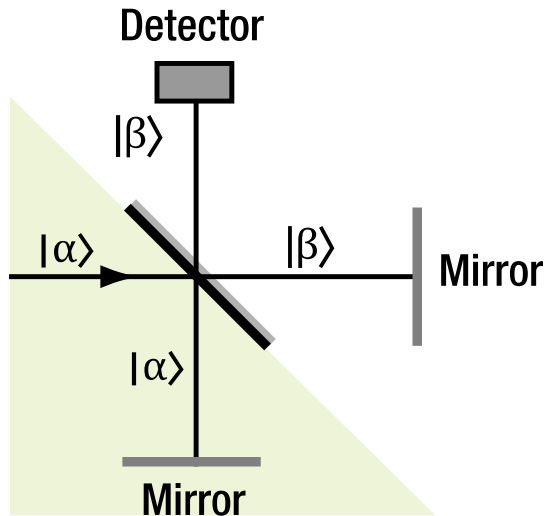


**Figure 169 State definition for the matrix notation of the Michelson interferometer. The photon being on the greenly shaded side of the beamsplitter is defined as state  $|\alpha\rangle$  and it being on the other side is defined as state  $|\beta\rangle$ .**

$|\alpha\rangle$  and  $|\beta\rangle$  are then the orthonormal basis of the system and we can describe all states as column elements in that basis.

The initial state is thus  $\begin{pmatrix} 1 \\ 0 \end{pmatrix}$ . A beamsplitter with two inputs and two outputs, with equal transmission and reflection coefficients and an  $180^\circ$  phase shift occurring only upon reflection on one side of the beamsplitter, is (for this specific basis and state definition) represented by the so-called Hadamard gate  $H_G$ :

$$H_G \equiv \frac{1}{\sqrt{2}} \cdot \begin{pmatrix} 1 & 1 \\ 1 & -1 \end{pmatrix} \quad (148)$$

The photon is first incident on the beamsplitter, then picks up some phase difference between the  $|\alpha\rangle$  and the  $|\beta\rangle$  paths, which is (in our chosen basis) represented by the following matrix  $A(\varphi)$ :

$$A(\varphi) \equiv \begin{pmatrix} 1 & 0 \\ 0 & e^{i\varphi} \end{pmatrix} \quad (149)$$

Afterwards, the light passes the beamsplitter for a second time. The final state  $|x(\varphi)\rangle$  is therefore:

$$|x(\varphi)\rangle = H_G A(\varphi) H_G \begin{pmatrix} 1 \\ 0 \end{pmatrix} = \frac{1}{\sqrt{2}} H_G A(\varphi) \begin{pmatrix} 1 \\ 1 \end{pmatrix} = \frac{1}{\sqrt{2}} H_G \begin{pmatrix} 1 \\ e^{i\varphi} \end{pmatrix} = \frac{1}{2} \begin{pmatrix} 1 + e^{i\varphi} \\ 1 - e^{i\varphi} \end{pmatrix} \quad (150)$$

The probability to detect the photon is the probability  $P_\beta$  to find it in path  $|\beta\rangle$  after exiting the interferometer, which is:

$$\begin{aligned} P_\beta(\varphi) &= |\langle \beta | x(\varphi) \rangle|^2 = \left| (0 \quad 1) \cdot \frac{1}{2} \cdot \begin{pmatrix} 1 + e^{i\varphi} \\ 1 - e^{i\varphi} \end{pmatrix} \right|^2 = \left| \frac{1}{2} (1 - e^{i\varphi}) \right|^2 = \frac{1}{4} (1 - e^{i\varphi})(1 - e^{-i\varphi}) \\ &= \frac{1}{4} (1 + 1 - e^{i\varphi} - e^{-i\varphi}) = \frac{1}{2} (1 - \cos \varphi) \end{aligned} \quad (151)$$

For the final equality, we used the relation  $\cos(\varphi) = \frac{e^{i\varphi} + e^{-i\varphi}}{2}$ . This is the same result that we obtained in the classical case (Section 3.1.2) and via calculation in the Dirac notation (Section 3.6.1).

## 12.2 Different Detection Schemes

### 12.2.1 Standard Triple Coincidences

When looking at the Time Tagger in this kit and many coincidence electronics in the literature, the standard way to define triple coincidences deviates from the definition used in Section 3.5.4. (from here on called “coincidence of coincidences” (CC)).

In the standard definition, a triple coincidence works like double coincidences, i.e., a triple coincidence is counted whenever **both** other detectors fire within the tagger window after an event on any detector. This definition is stricter than the CC definition, meaning that there are count sequences that are counted as a triple coincidence in the CC definition but not in the standard definition. Such a sequence is shown in Figure 170. It is not a triple coincidence by the standard definition, as the count on detector B is not in the window after the first count of the sequence (detector A). It is a triple coincidence by the CC definition because the counts at detectors A and B are both in coincidence with the count on detector T.

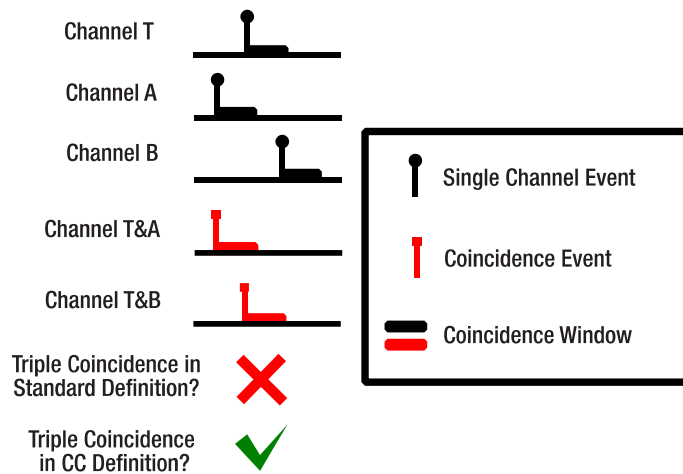


**Figure 170** An Event Sequence That is Counted as a Triple Coincidence in CC Definition but not in the Standard Definition (Since There is no Overlap Between all Three Windows)

When deciding which definition to use for the quantum optics experiments, the decisive factor is whether Equation (101) results in the correct values for the second order correlation function. Performing an experiment with completely uncorrelated light (such as explained in Section 9.5), one expects  $g_{GRA}^{(2)}(0) = 1$ .

In the uncorrelated case, all coincidences are purely accidental. The expected rate of accidental counts for double coincidences of two detectors T and A is given in the literature<sup>117</sup> as:

$$R_{TA}^{(acc)} = 2 \cdot R_T \cdot R_A \cdot \Delta t \quad (152)$$

The rate of accidental triple coincidences between three detectors T, A, and B in the **standard definition** is:

$$R_{TAB,st}^{(acc)} = 3 \cdot R_T \cdot R_A \cdot R_B \cdot \Delta t^2 \quad (153)$$

In the uncorrelated case, the rates in Equation (101) are given by the purely accidental rates which yields:

$$g_{GRA,st}^{(2)}(0) = \frac{R_{TAB,st}^{(acc)} \cdot R_T}{R_{TA}^{(acc)} \cdot R_{TB}^{(acc)}} = \frac{3 \cdot R_T^2 \cdot R_A \cdot R_B \cdot \Delta t^2}{4 \cdot R_T^2 \cdot R_A \cdot R_B \cdot \Delta t^2} = \frac{3}{4} \quad (154)$$

This deviates from the expectation  $g_{GRA}^{(2)}(0) = 1$  for uncorrelated light and shows that the standard definition of triple coincidence is not perfectly suited for the GRA experiment.

<sup>117</sup> C. Eckart and F. R. Shonka, *Physical Review*, 53(9), 752 (1938)

A stochastic view helps to calculate  $g_{GRA}^{(2)}(0)$  for the CC definition of triple coincidences. The probability for an event on detector T to be coincident both with events on detector A and B is  $P(TA \cap TB)$ . As we are dealing with completely uncorrelated events, TA and TB are stochastically independent and the joint probability becomes:

$$P(TA \cap TB) = P(TA) \cdot P(TB) \quad (155)$$

The probabilities of the double coincidences are simply:

$$P(TA) = \frac{R_{TA}^{(acc)}}{R_T} \quad \text{and} \quad P(TB) = \frac{R_{TB}^{(acc)}}{R_T} \quad (156)$$

Hence, the rate  $R_{TAB\_CC}^{(acc)}$  of trigger events that occur in coincidence with events **both** on detector A and detector B (the CC definition of triple coincidences) is:

$$R_{TAB\_CC}^{(acc)} = R_T \cdot P(TA \cap TB) = R_T \cdot P(TA) \cdot P(TB) = R_T \cdot \frac{R_{TA}^{(acc)}}{R_T} \cdot \frac{R_{TB}^{(acc)}}{R_T} = \frac{R_{TA}^{(acc)} \cdot R_{TB}^{(acc)}}{R_T} \quad (157)$$

Substituting this in Equation (101) for the uncorrelated case yields:

$$g_{GRA\_CC}^{(2)}(0) = \frac{R_{TAB\_CC}^{(acc)} \cdot R_T}{R_{TA}^{(acc)} \cdot R_{TB}^{(acc)}} = \frac{R_{TA}^{(acc)} \cdot R_{TB}^{(acc)} \cdot R_T}{R_{TA}^{(acc)} \cdot R_{TB}^{(acc)} \cdot R_T} = 1 \quad (158)$$

This result is reproduced when using the CC definition for triple coincidences. However, as fewer triple coincidences are counted with the standard definition, but the number of twofold coincidences stays the same, using the standard definition results in  $g_{GRA}^{(2)}(0) < 1$  (the experiments in this kit show  $g_{GRA}^{(2)}(0) = 0.75$ ) for uncorrelated light, which is counterintuitive. For this reason, the CC definition for triple coincidences is used in this kit.

### 12.2.2 Gated Detection Scheme

In this scheme (which was used in the original GRA experiment), gated counts are registered instead of coincidences. In this case one of the detectors (in our case: T) is specified as the gate detector. A count on this detector opens a gate window of length  $\Delta t_g$ . Counts at the other detectors are only registered when they occur during an open gate window. All other events are discarded. For example, instead of the coincidence rate  $R_{TA}$  one registers the gated count rate  $R_A^{(g)}$ . The main difference between the two is that in the gated case, the event at the gate detector T must come first, while the order of the events is irrelevant in the coincidence case.

In the gated scheme, gated coincidences are counted instead of triple coincidences. A gated coincidence between channels A and B occurs when both detectors A and B register an event during the **same** gate window after a count on detector T, as seen in Figure 171. The gated coincidence rate is denoted  $R_{AB}^{(g)}$ .

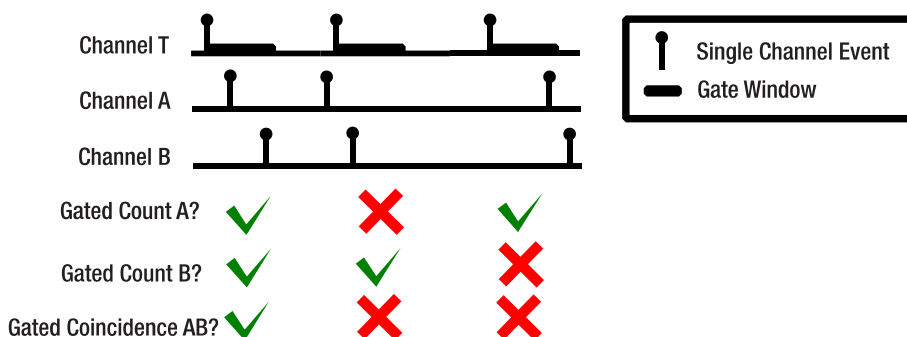


**Figure 171      Gated Detection Scheme, Definition of Gated Counts and Gated Coincidences**

The equations for the second order correlation function in the GRA experiment become:

$$g_{GRA}^{(2)}(0) = \frac{R_{AB}^{(g)} \cdot R_T}{R_A^{(g)} \cdot R_B^{(g)}}$$

The time window used for gating  $\Delta t_g$  is the same as the coincidence window  $\Delta t$  used in Equation (98) amongst others, i.e.,  $\Delta t_g = \Delta t$ .

The photon pairs produced by the SPDC process induce a correlation to the events at the detector. We expect counts at detector T to occur at the same time as counts on detector A. Here, we see a disadvantage of the gated scheme. Half of those simultaneous events will not be detected as gated counts because statistically, the event on A will be registered slightly before the event on T half of the time and thus will be discarded. In the triple coincidence scheme, the order of the events is irrelevant, and all simultaneous events will be counted as twofold coincidences.

This can be avoided by introducing an artificial delay to the counts on detectors A and B. If this delay is not larger than the gate window, all events that occur simultaneously will be counted as gated counts, because the count on A (B) is ensured to be registered after the one on T. In fact, if the artificial delay is chosen to be exactly half the size of the gate window, the gated scheme becomes identical to the triple coincidence scheme (with the CC definition of triple coincidences) for all count sequences, whether correlated or uncorrelated, which is shown in Figure 172.

For any count on T (black marker) there is a gate window (black bar) and a tagger coincidence window of half the size of the gate window (red bar). In the triple coincidence scheme any count on A or B must be in a time window that is symmetric around T with a width of twice the tagger window to be counted as a coincidence. This window is the grey rectangle on the second line. In the gated scheme, counts on A or B must simply lie in the gate window to be counted as a gated count, as marked by the grey rectangle in the third line. It becomes apparent that the windows have the same size but are shifted by half the size of the gate window to each other. Hence, shifting all counts on A and B by this amount relative to T results in the same position of the counts relative to the grey rectangle as in the triple coincidence scheme, making them identical.

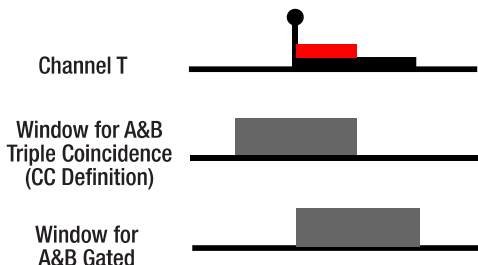


**Figure 172 Comparison for triple coincidence and gated scheme. The window in which counts on A and B must lie to be counted as coincidences is marked by the grey rectangles. The black bar in the upper line marks the gate window and the red bar marks the tagger coincidence window.**

It is important to stress that the gated scheme produces the same results for the second order correlation function  $g_{GRA}^{(2)}(0)$  with or without the artificial delay, as the rates for gated counts and gated coincidences are both affected by the ordering issue described above. However, the overall count rates will be lower without the artificial delay, making the experiments less efficient.

To avoid the complication of setting up the artificial delay and the risk of missing all coincidence counts when setting the delay wrong, this kit uses the triple coincidence scheme (with the CC definition of triple coincidences) instead of the gated scheme.

### 12.2.3 Changing the Detection Scheme in the Software

While we recommend sticking with the triple coincidence scheme with the CC definition, the software is prepared to operate with the gated scheme or the standard definition of triple coincidences. To change the scheme, open

the Settings.xml file in the software folder, search for the code shown in Figure 173 and change the value in the second to last line to “0” to use the triple coincidence scheme with the standard definition or to “1” to use the gated detection scheme. The changed detection mode is loaded with the next start of the software (make sure not to overwrite your changes to the settings file automatically when closing the software). Delay times and coincidence window definition set in the Time Tagger are updated automatically to match the changed mode.

```
<EW>
  <Name>Coincidence mode</Name>
  <Choice>Triple Coincidences</Choice>
  <Choice>Gated Counting</Choice>
  <Choice>Coincidences of Coincidences</Choice>
  <Val>0</Val>
</EW>
```

**Figure 173** Part of the settings.xml file that allows choosing the detection scheme. The important value is highlighted by the circle.

### 12.3 Environmental Conditions

We recommend using the setup in rooms that can be completely darkened (no windows, or shutters) since the best performance is reached in darkness. Sunlight is especially problematic as its spectrum includes the transmission range of the bandpass filter in front of the detectors and thus results in large background count rates.

If you want to use the setup but do not have the possibility to block sunlight from entering the room, you can use a box with transparent wavelength-filtering walls, like the one depicted in Figure 174.



**Figure 174** Setup with Wavelength Filtering Enclosure

Please contact [Techsupport@thorlabs.com](mailto:Techsupport@thorlabs.com) for a part list recommendation and a construction manual for such a box.

BBO is a hygroscopic crystal, and its properties can degrade due to the crystal taking on water. Fortunately, this problem is substantially mitigated by the anti-reflection coating of the crystals in the kit. In environments with reasonable humidity, the crystals will not degrade significantly over the course of several years.

### 12.4 Avoiding Fluctuations in the Michelson Interferometer

The Michelson Interferometer is an extremely sensitive instrument. Slight changes in the parameters can have significant influence on the measured signal. For example, the minuscule changes in the refractive index of air at

different temperatures can introduce visible fluctuations in the interferogram, when temperature gradients or air currents are present. An example measurement is shown in Figure 175.

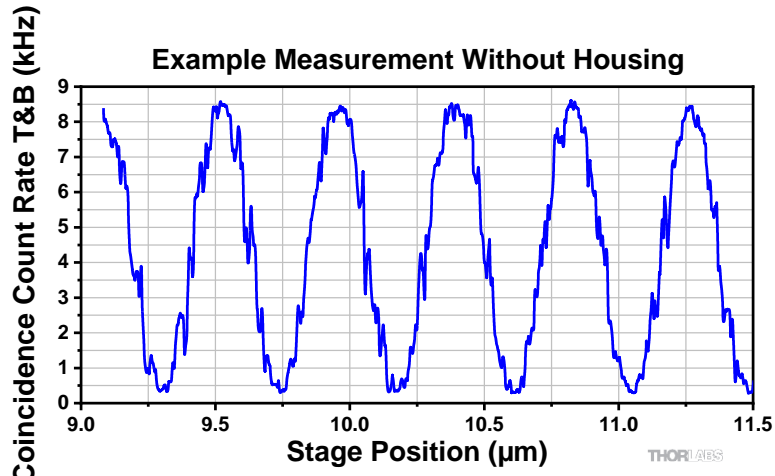


**Figure 175      Example Interferogram with Air Current in the Michelson Interferometer**

This problem can be alleviated by housing the interferometer in a box that prevents air currents from entering the interferometer. An example of such a housing is shown in Figure 176. This is made of acrylic glass with custom recesses for entry and exit of the light and for the clamps to fix the board. A measurement with the same parameters as Figure 175 but with the housing is displayed in Figure 177, clearly showing the noise-reducing effect of the housing.

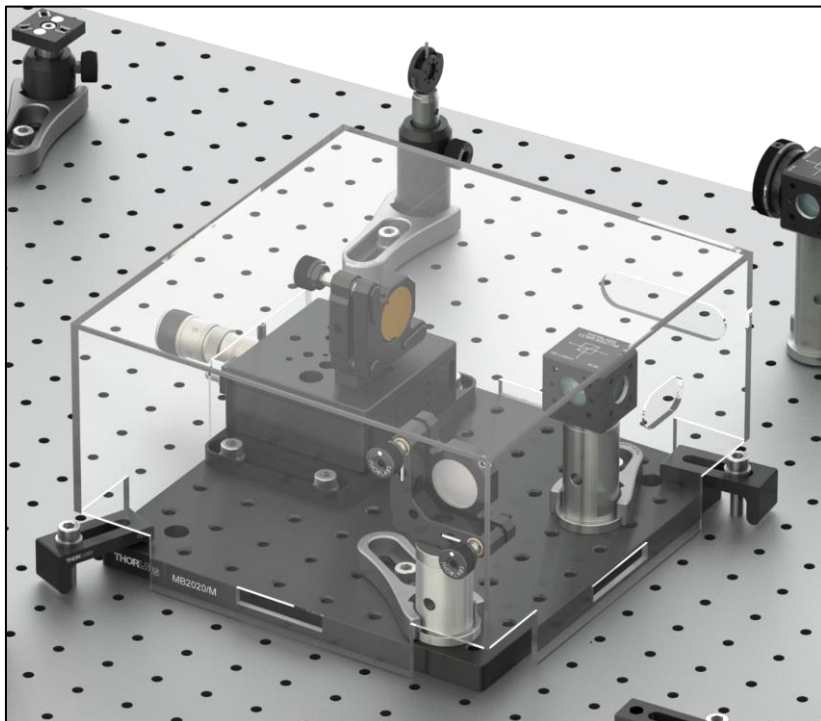


**Figure 176      Acrylic Housing for Michelson Interferometer**

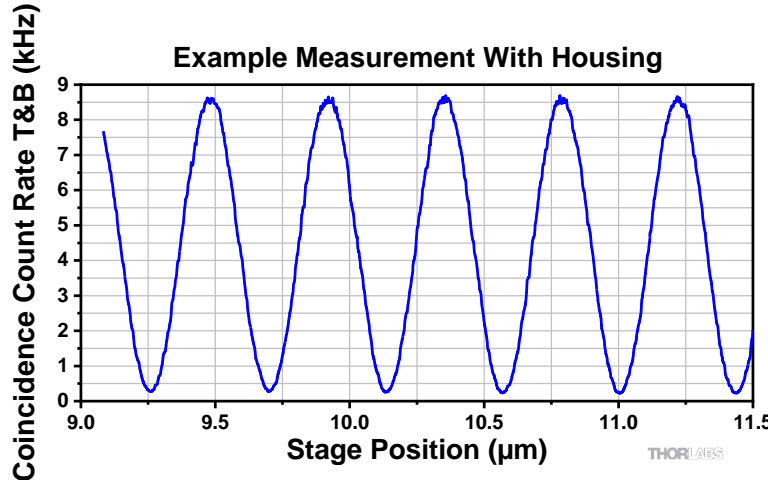


**Figure 177      Example Measurement with Interferometer Housing**

## 12.5 Accidental Coincidences

In Section 3.5.7, we discussed the influence of the count rate and the coincidence window on the rate of accidental coincidences and the measurement results of  $g_{GRA}^{(2)}(0)$ . In this section, we lay out a simplified example calculation to quantify and visualize the effect.

The following assumptions are made:

- The count rates caused by background (detector dark counts and stray light) are small against the signal count rates and can be ignored.
- The overall detection efficiency for photons incident on a detector is  $\eta = 0.5$
- The splitting ratio of the beamsplitter is perfectly 50:50.

Under these assumptions, the trigger count rate  $R_T$  is:

$$R_T = \eta \cdot R_{pp} = \frac{R_{pp}}{2}$$

Here,  $R_{pp}$  is the rate of photon pairs emitted in the direction of the detectors. The count rates on detectors A and B are then (due to the beamsplitter ratio):

$$R_A = R_B = 0.5 \cdot \eta \cdot R_{pp} = \frac{R_{pp}}{4}$$

The rate of double coincidences  $R_{TA}$  ( $R_{TB}$ ) can be determined stochastically. The coincidence is registered only if both chances come true, so:

$$R_{TA} = R_{TB} = 0.5 \cdot 0.25 \cdot R_{pp} = \frac{R_{pp}}{8}$$

The rate of accidental triple coincidences is then (see Section 3.5.7):

$$R_{acc}^{2+1} = (R_{TA} \cdot R_B + R_{TB} \cdot R_A) \cdot \Delta t = \left( \frac{R_{pp}^2}{32} + \frac{R_{pp}^2}{32} \right) \cdot \Delta t = \frac{R_{pp}^2}{16} \cdot \Delta t$$

The correlation function  $g_{GRA}^{(2)}(0)$  is then:

$$g_{GRA}^{(2)}(0) = \frac{R_{acc}^{2+1} \cdot R_T}{R_{TA} \cdot R_{TB}} = \frac{R_{pp}^2 \cdot \Delta t \cdot 8 \cdot 8 \cdot R_T}{R_{pp}^2 \cdot 16} = 4 \cdot R_T \cdot \Delta t = 4 \cdot \frac{N_T}{T} \cdot \Delta t$$

with  $N_T$  being the absolute number of measured counts at the trigger detector and  $T$  being the measurement duration.

For the calculation of the  $g_{GRA}^{(2)}(0)$  measurement's statistical error, we assume that the error is dominated by the event counting measurements. In turn, the errors of the coincidence window width  $\Delta t$  and the measurement duration  $T$  are neglected. The distribution of the measured counts is Poissonian, so for example the error  $\Delta(N_T)$  is:

$$\Delta(N_T) = \sqrt{N_T}$$

As the error of the measurement duration is neglected, the relative error of a count rate is the same as that of the corresponding absolute count number (at the example of  $R_T$ ):

$$\frac{\Delta(R_T)}{R_T} = \frac{\Delta(N_T)}{N_T} = \frac{1}{\sqrt{N_T}} = \frac{1}{\sqrt{R_T \cdot T}}$$

The statistical errors of different count measurements are independent. The relative error for  $g_{GRA}^{(2)}(0)$  is then:

$$\begin{aligned} \frac{\Delta(g_{GRA}^{(2)}(0))}{g_{GRA}^{(2)}(0)} &= \sqrt{\left(\frac{\Delta(R_{acc}^{2+1})}{R_{acc}^{2+1}}\right)^2 + \left(\frac{\Delta(R_T)}{R_T}\right)^2 + \left(\frac{\Delta(R_{TA})}{R_{TA}}\right)^2 + \left(\frac{\Delta(R_{TB})}{R_{TB}}\right)^2} \\ &= \sqrt{\frac{1}{R_{acc}^{2+1} \cdot T} + \frac{1}{R_T \cdot T} + \frac{1}{R_{TA} \cdot T} + \frac{1}{R_{TB} \cdot T}} \approx \frac{1}{\sqrt{R_{acc}^{2+1}}} \cdot \frac{1}{\sqrt{T}} \end{aligned}$$

In the last step, we neglected all terms under the square root but the first as the accidental count rate is much smaller than all other count rates. It becomes apparent that a lower rate of accidental count rates results in an increase of the relative error of  $g_{GRA}^{(2)}(0)$ .

The complete calculation is visualized in Figure 178 (constant coincidence window, varying trigger count rate) and Figure 179 (vice versa).

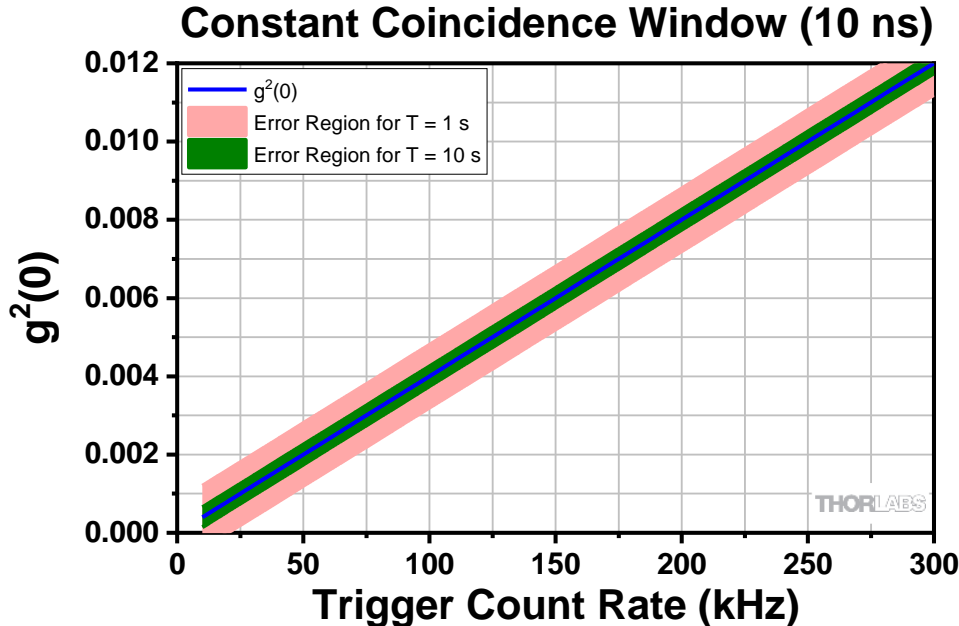


**Figure 178**    *Expected Measurement Results as a Function of the Trigger Count Rate for a Constant Coincidence Window of 10 ns*

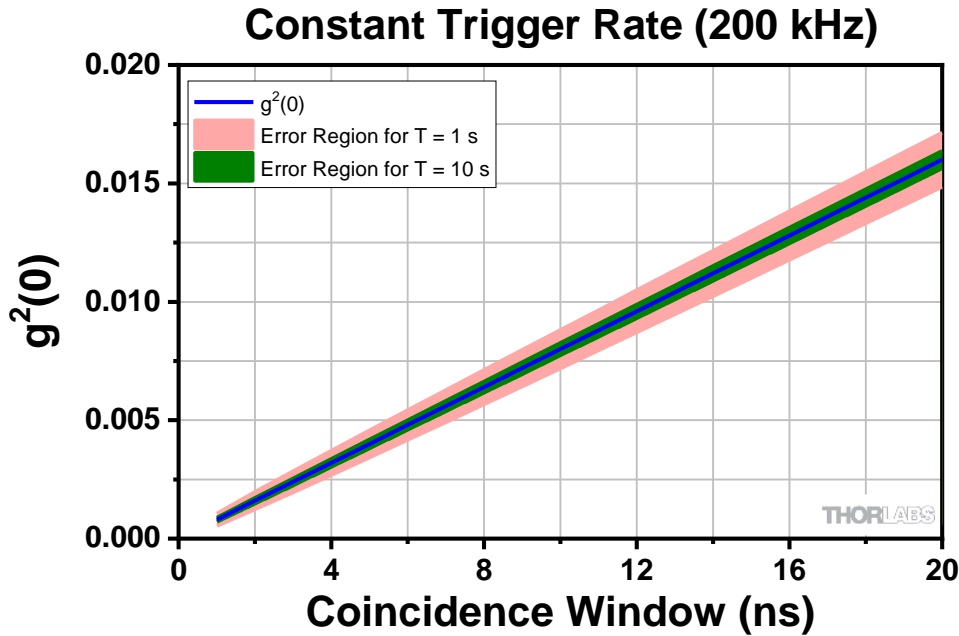


**Figure 179      Expected Measurement Results as a Function of the Coincidence Window Width for a Constant Trigger Count Rate of 200 kHz**

The following conclusions can be drawn from the calculation results:

- When aiming to measure values of  $g_{GRA}^{(2)}(0)$  as close to the ideal result of 0 as possible, it is best to first reduce the coincidence window, as this does not influence the relative error of the measurement. However, the coincidence window cannot be reduced infinitely, as the jitter of the electronics and detectors act as a lower limit.
- Reducing the trigger count rate (via lowering the pump laser power) results in a lower expectation value of  $g_{GRA}^{(2)}(0)$ , i.e., one closer to the ideal result but at the same time the relative uncertainty of the measurement increases.
- The increased uncertainty can of course be compensated for by increasing the measurement duration.

In the end, the user must formulate the degree of uncertainty and deviation from the ideal result they are willing to accept and choose the parameters accordingly. The standard values recommended throughout this manual provide a good balance between the competing goals.

It is important to note that the assumptions made here break down for very low trigger count rates, as background signal and dark counts cannot be neglected any more in this case. These effects will increase the measured value of  $g_{GRA}^{(2)}(0)$ .

## 12.6 Time-Dependent Second-Order Correlation Function

Similar to the explanation given at the end of Section 3.5.2, the width of a dip or peak in a  $g^{(2)}(\tau)$  function can theoretically be related to properties of the light source, e.g. the coherence time (classic HBT experiment) or the photon emission rate of a single photon source (like a Nitrogen-Vacancy center in diamond).

In our case of a spontaneous parametric down-conversion source (see Section 3.9), the related property would be the coherence time of the heralded single photons (inversely proportional to their spectral bandwidth). Due to

the rather broad spectrum of our source, the coherence time is on the order of 0.2 ps<sup>118</sup>. Ideally, this narrow time window would define the time window for coincidence detection.

However, due to the timing uncertainty of the detection system (i.e. jitter; see Section 4.2.2), real double coincidence events are also detected by the system as long as the time differences are within the timing uncertainty window. In our system, this uncertainty window is on the order of 1 ns wide and thus orders of magnitude larger than the coherence time of the source. Thus,  $g_{GRA}^{(2)}(\tau)$  would not indicate any source property, but would instead be limited by the timing uncertainty of the measurement system<sup>119</sup>. As there are easier methods to quantify the system jitter, there is no use in trying to set up a measurement for  $g_{GRA}^{(2)}(\tau)$ .

## 12.7 Maximizing the Count Rate

If you want higher count rates, there are several ways to do that:

- Increase pump laser power. Make sure not to exceed the maximum current/power for the laser diode. You can see the characteristics of your individual laser diode in its spec sheet.
- Reduce the distance between detectors and BBO crystal (more photons of the cone pass the detector aperture).
- Rotate the BBO crystal and the polarization of the pump beam (by rotating the HWP in the pump beam path) by 90°. In our tests, this configuration increased the coincidence count rate by about 20%. However, be aware that in this configuration, the polarization of the photons in the two arms is not parallel anymore but shifted by about 6° in relation to each other due to an effect first described by Alan Migdall<sup>120</sup>.

Please be aware that higher count rates are not always beneficial. For a fixed coincidence window, higher count rates result in more accidental coincidences, thus moving the  $g^{(2)}(0)$  closer towards 1, as explained in Section 12.5.

## 12.8 Choice of Polarizers

We use two distinct types of linear polarizers in this kit, one LPNIRE100-B polarizer and two LPNIRB050 polarizers.

The LPNIRE100-B polarizer is the more cost-efficient solution and its extinction ratio of >1000:1 is good enough for all experiments in this kit. However, its parallelism is only about 20 arcmin, which leads to a significant deviation of the beam path when rotating the polarizer. This makes the LPNIRE100-B polarizer unsuitable for usage inside the Michelson interferometer during the Quantum Eraser experiment, as even small angular deviations in the interferometer can lead to a significant loss of contrast in the measurement. Thus, we include the more expensive LPNIRB050<sup>121</sup> polarizers, which have a parallelism of <0.5 arcmin.

The LPNIRE100-B polarizer can still be used whenever the angular deviation is of no consequence, such as directly in front of the detectors in the Malus' Law experiment or as the "eraser-polarizer" in the Quantum Eraser experiment.

## 12.9 Polarizers vs. Quarter-Wave Plates

Changing the polarization of the photons in the interferometer arms is possible by either using polarizers as in this kit or by inserting a quarter-wave plate (QWP) in one arm of the interferometer. In the Michelson interferometer, the beam passes through the QWP twice, effectively acting as a half-wave plate (HWP), i.e., rotating the linear

<sup>118</sup> Calculated from using the spectral bandwidth, which is limited by the 10 nm bandpass filters in front of the detectors. With a broader filter, the coherence length and coherence time are even lower (compare to Section 10.1).

<sup>119</sup> S. Bettelli, Physical Review A, **81**, 037801 (2010).

<sup>120</sup> A. Migdall, Optical Society of America B, **14**(5), 1093-1098 (1997).

<sup>121</sup> The LPNIRB050 polarizers are based on nanoparticles. Thus, their polarization axis can change when operated outside their specified wavelength range. For example, if used with the 405 nm pump laser, the axis will be tilted by about 90°.

polarization of the incoming photon by twice the angle difference between photon polarization and fast axis orientation.

### Advantage of QWP

A QWP has the advantage of being nearly absorption-free, so using one will result in reaching higher count rates in the experiment.

### Disadvantage of QWP

The function of the QWP is highly wavelength-sensitive, and optimal functionality is only guaranteed at exactly the design wavelength of the QWP. As the wavelength of the photons generated by the SPDC process varies by up to several nanometers, the QWP induces ellipticity to the polarization of the photons instead of just turning the linear polarization. This in turn makes a complete suppression of the interference pattern in the quantum eraser experiment impossible. Even when the polarizations are theoretically crossed and no interference pattern should appear, there will be a residual interference pattern due to the elliptical polarization component.

Due to this reason, polarizers are used in the kit. They are achromatic and do not suffer from the same problems as the QWPs. A complete suppression of the interference can be reached, which is important for a didactic experiment. The count rates in this kit are high, so a loss of half the counts is not critical.

### Important Parameters

If you want to use QWPs in your kit instead of polarizers, be aware of the following points:

- The QWP should be achromatic, i.e., offer a retardation of very close to 0.25 for a range of at least 800 - 820 nm.
- The QWP must have a low beam deviation. Deviations below 1 arcmin are recommended. Higher deviations will result in a significant loss of interference contrast when turning the QWP due to misalignment of the beam paths from the interferometer arms.

### 12.10 Axicon Design

The axicon is designed to emulate the cone of photon pairs generated in the BBO crystal. A schematic is shown in Figure 180.

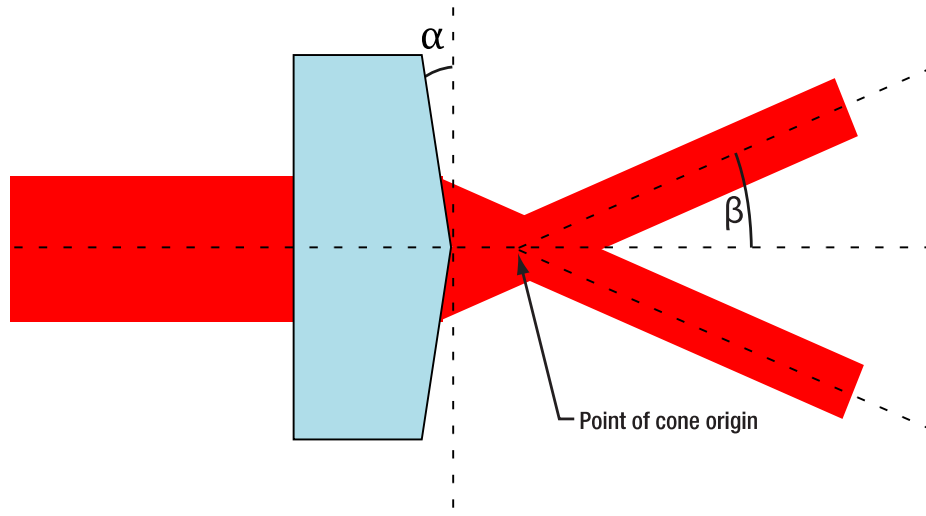


**Figure 180      Schematic of the Axicon**

As the BBO is designed for a half opening angle of  $3^\circ$ , the axicon parameters are chosen to produce a cone with an opening angle of  $3^\circ$  when illuminated with the alignment laser (635 nm wavelength). The following equation was used to determine the required axicon angle  $\alpha$ :

$$\alpha = \tan^{-1} \left( \frac{\sin \beta}{n(\lambda) - \cos \beta} \right)$$

Here,  $\beta$  is the desired half-opening angle of the cone ( $3^\circ$  in our case) and  $n(\lambda)$  is the spectrally dependent index of refraction for the axicon material.

The glass used for our axicon has  $n(635 \text{ nm}) = 1.4584$  leading to  $\alpha = 6.49$ .

The equation above can be used to design axicons for different alignment laser wavelengths or cone-angles.

In Figure 179, one can see that the origin of the output cone is not exactly on the axicon tip, but some distance after it. The exact distance depends on the beam diameter of the alignment laser. To ensure that the origin of the cone is the same for the axicon and the BBO crystal, we offset the axicon by 15 mm via the lens tube spacers.

## 12.11 Temperature Dependence of Pump Laser Wavelength

The center wavelength of the L405P20 laser diode depends on the temperature. The wavelength increases linearly with temperature and the coefficient is about  $0.05 \frac{\text{nm}}{\text{K}}$ . This means that the wavelength can be tuned by 0.5 nm over the full temperature range of the LDM9T/(M) diode mount. Please note that the diode temperature is influenced not only by the setpoint of the controller, but also by the laser current. A higher current increases the temperature and therefore leads to slightly longer wavelength at the same controller setpoint. Vice versa, a change in temperature can change the output power at the same current.

## 12.12 Adjustable Count Rate Ratio

In some of the experiments, it can be desirable to adjust the ratio of photons that go to detector A and B. This can be achieved by a combination of a half-wave plate and a polarizing beamsplitter in the arrangement displayed in Figure 181.

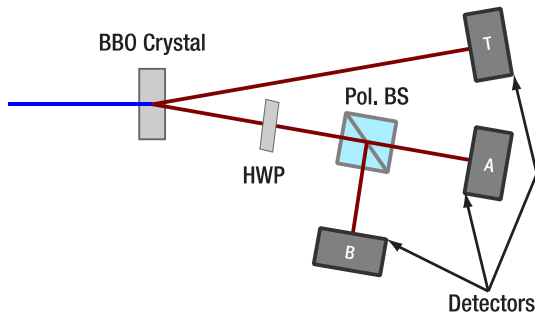


**Figure 181 Using a Polarizing Beamsplitter to Adjust the Count Rate Ratio Between Detectors A and B**

By turning the HWP, the polarization of the photons incident on the polarizing beamsplitter is changed, so that different ratios of photons are transmitted/reflected. Thus, the count rate ratio can be continuously varied. Exercise caution when using this arrangement for polarization sensitive experiments. A suitable wave plate (Item # WPH10ME-808) is part of the kit and Thorlabs offers other suitable beamsplitters such as the CCM5-PBS202/(M) beamsplitter.

## 12.13 Movable Michelson Interferometer

Our standard setup procedure involves clamping the Michelson interferometer board to the table at its final position, such that it cannot move in any direction during operation. The fine alignment of the Michelson depends on the force and position of clamping. If you want to be able to move the interferometer in and out of the beam path, e.g. for switching between the GRA configuration and the Michelson experiment, there is another option to define a repeatable position for the Interferometer board, as shown in Figure 182. Additional clamps and screws are not included in the kit.

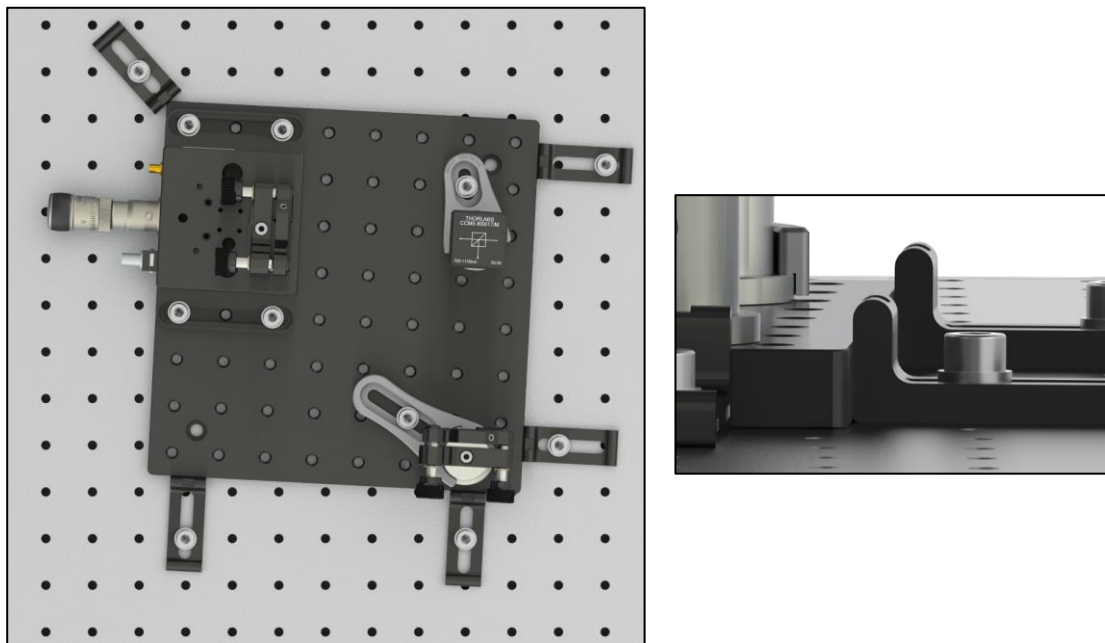


**Figure 182      Repeatable positioning of the Michelson interferometer board, using five additional CL5A clamps (not included). The inset shows a side view.**

- Set up the Interferometer in its final position (see Section 7.6) and use at least one clamp to fix the position temporarily. Fine alignment using the LED is not yet required.
- Press four CL5A clamps (or similar) flat against two neighboring sides of the breadboard and fix their position using 1/4"-20 x 1/2" (M6 x 12 mm) cap screws plus washers (not included). Larger spacing between clamps on the same side improves positioning accuracy.
- Remove the temporary clamps from the first step. Now the Michelson board can be moved in and out of the measurement position.
- In the measurement position, the board should be secured against lateral movement by a fifth clamp which is pressed against the board diagonally to the axes defined by the other clamps.
- With the board fixed in this position, you can do the fine alignment procedure of the Michelson. Moving the board carefully around the table usually does not affect the alignment of the Michelson much, such that comparable amplitudes of the interferometer signal can be achieved between multiple repositions.

## 12.14      Polarization In the SPDC Process

Since the light in this setup has various orientations of linear polarization, we shortly follow the light path from pump laser to detector:

- The pump laser polarization is perpendicular to the plane of the optical table.
- The first half-wave plate (at 45°) rotates the pump beam polarization parallel to the table plane.
- The BBO crystal is oriented such that its optical axis lies parallel to the table plane. The marking on the housing shows the axis of rotation which is used to tune the phase matching and should be perpendicular to the table, as well as the polarizations of the pump, signal, and idler photons, see Figure 183. The text on the crystal mount also denotes the wavelength range of the anti-reflection coating (400 nm - 500 nm) and the thickness of the crystal (3 mm).
- The photon pair polarization is perpendicular to the table plane and remains unaffected by the beamsplitter in the arm of detector A.

- The HWP (at 22.5°) rotates the single photon polarization by 45° counterclockwise, when viewed against the beam direction from the HWP towards the first beamsplitter.
- This way, the polarization axis is aligned exactly with the slow axis of the liquid crystal cell in the interferometer arm with the fixed mirror, in case of the additional experiments for Quantum Computing (see Section 10.8 for details).
- In the interferometer arm with the moving mirror, the polarization axis is rotated 45° clockwise, when viewed from the moving mirror towards the interferometer beamsplitter. This is due to the reflection in the beamsplitter.

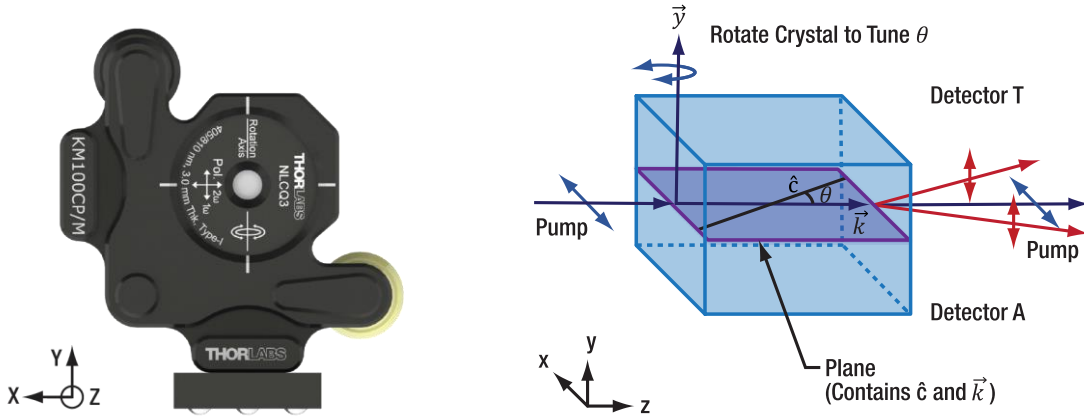


**Figure 183** *Polarization vectors and crystal axes of the setup ( $\hat{c}$  is the optic axis of the crystal and  $\vec{k}$  is the propagation vector of the light). The red arrows for detectors T and A are in the same plane as  $\hat{c}$  and  $\vec{k}$ .*

## 12.15 Improving Laser Safety

In principle, it is possible to perform all experiments in this kit with a class 2 pump laser, such as the PL205 pointer laser. This laser is based on the exact same laser diode as the one used in the kit, only operated at a low current to limit output power. However, the main drawback to such an approach is significantly reduced count rates.

When using the PL205, coincidence count rates can be expected to be lower by a factor of 20 to 30. Using a GBE05-A beam expander in reverse to shrink the beam profile of the PL205 helps, but the best-case scenario is still a 10-fold reduction. This means, that one would have to measure 10 times as long to obtain results that are similar to what is shown in this manual. This can be done for the HBT and GRA measurements (see Sections 9.1 through 9.5) but is not recommended for the Malus experiment and the interferometer based experiments (Sections 9.6 through 9.8) because the overall measurement times would be several hours. Furthermore, at such low count rates and with longer measurement times, stray light and phase drift become much more pronounced and need to be addressed accordingly, see Section 12.4.

A special version of the kit is available with the PL205 laser, if you are interested please contact Tech Support. One of the things to consider is that the standard PL205 is not wavelength-pre-selected like the laser diodes in this kit. Instead, the PL205's specified wavelength window is 400 nm to 410 nm, which poses the danger that the down-converted photons have a wavelength outside of the detector filter's transmission window.

An alternative approach to reach class 2 laser safety is to use a custom housing with walls that completely block the pump laser and a dichroic mirror window behind the BBO crystal. The 405 nm pump beam is reflected by the dichroic mirror and can be trapped with a suitable component, such as the one described in Section 7.1.10, while the 810 nm photon pairs are transmitted by the mirror and leave the housing (see Figure 184). This way, the right part of the setup is still open for adjustment, but only the photon pairs leave the housing, making the setup class 1.

We successfully tested the feasibility of this approach with a DMLP490 dichroic mirror. The right wall of the box should have a small angle, so that the reflected pump laser can go past the BBO crystal, but the beam offset for

the photon pairs remains small (see Figure 184). In our feasibility test, no re-adjustment of the setup was required after introducing the dichroic mirror at such a small angle.

These are only suggestions. Please always discuss the details of your implementation with your local laser safety officer.

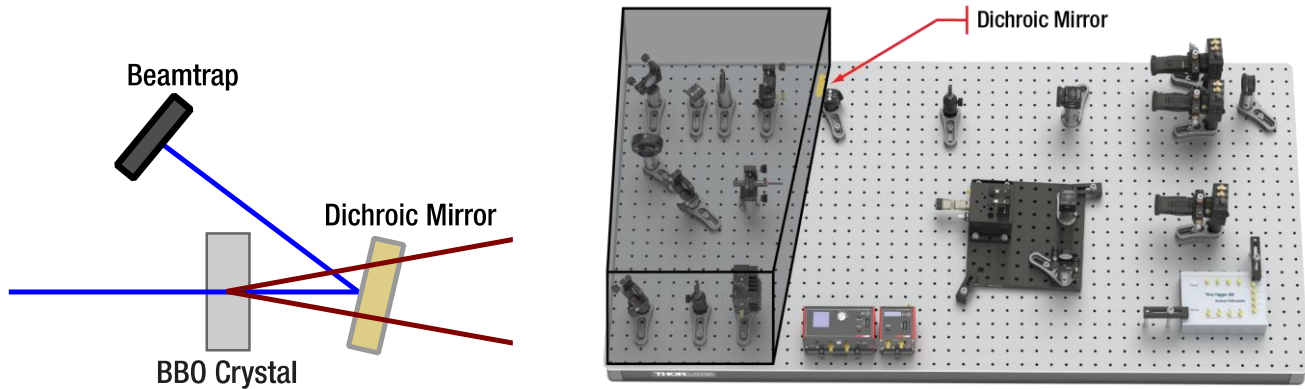


**Figure 184** *Blocking the pump beam directly after the crystal with a dichroic mirror. A sketch is shown on the left and an example setup on the right.*

## Chapter 13 Troubleshooting

### 13.1 Pump Laser not Working

Problem: The pump laser is not lasing.

Solution:

- Make sure that the KLD101 driver and LDM9T(/M) mount are securely connected via the CAB400 cable.
- Make sure that the LDM9T(/M) mount is connected to the power grid and switched on.
- Make sure that the KLD101 driver is set to “Cathode Grounded” and that you have set a laser current between 25 and 40 mA (compare to the spec sheet of the laser diode).
- Make sure that the internal switches and jumpers of the LDM9T(/M) mount are set exactly as described in Section 7.1.
- Make sure that the connection of the laser diode to the LDM9T(/M) mount is exactly as described in Section 7.1.

In rare cases, the laser diode might have burned out. If you have checked all the above points and the pump laser is not working, please contact [techsupport@thorlabs.com](mailto:techsupport@thorlabs.com).

### 13.2 Collimation of Pump Laser not Working

Problem: The beam profile of the pump laser is strange and/or the beam deviation of the pump laser is too large.

Solution:

- Both problems can be caused by the collimating lens not being centered in front of the laser diode. Often, this is caused by the front plate of the LDM9T(/M) not being centered on the mount.
- Please make sure to assemble the pump laser while it is lying on a table to facilitate centering of the front plate
- You can also loosen the front plate screws during the collimation process and try to find the optimal front plate position, as shown in Figure 185.



**Figure 185      Adjusting the Front Plate of the Pump Laser Mount**

### 13.3 Detectors not Working

Problem: The detectors are switched on, but you see no signal at all.

Solution:

- Switch the detector off and on (wait about 20 s after switching on).
- Verify that the detector is connected to the channel of the TimeTagger that you are observing.
- Try switching the power supply with that of another detector. If this solves the problem, the original power supply was defective. In that case, contact [techsupport@thorlabs.com](mailto:techsupport@thorlabs.com) for a replacement.

### 13.4 Low Count Rates with Filter

Problem: In Section 7.4.4, the count rates are much smaller than 300 kHz.

- If the count rates are 0, the detectors might still be switched off or the detectors are connected to the wrong channel of the Time Tagger.
- Make sure that the pump laser is switched on and that the laser current is about 5 mA below the lasing threshold of your diode (check the spec sheet).
- Make sure that all iris apertures in front of the detectors are opened as far as possible.
- Check all other iris apertures in the setup. None of them should be completely closed.
- Make sure that the gain of the detectors is set to maximum (rotate gain screw clockwise until you reach hard stop).

If the above points do not solve the problem, recenter the CXY1A mount (turn adjusters until markings on the front align) and repeat the detector positioning process, as explained in Section 7.4.3. An experimental environment with significant stray light leads to large background signals. This complicates the adjustment process, but satisfactory results can still be reached by applying the following methods:

- When adjusting the detector optics to maximize for count rate (either with the alignment laser in Section 7.3 or with the colored glass filter), switch the laser off and on again. If the count rate in the alignment tab changes, you are optimizing on actual signal, keep going. If it does not change, you are seeing only signal from stray light and are far away from the target adjustment.
- Use higher pump laser power to more clearly separate actual signal from stray light. When adjusting the third detector, you might need to temporarily close the iris apertures in front of the other detectors to avoid saturation of the Time Tagger. Lower the pump laser power once you are sure that you are optimizing on actual signal rather than stray light (see prior point).

### 13.5 Low Count Rates with BBO crystal

Problem: In Section 7.4.4, the count rates are correct, but after inserting the BBO crystal in Section 7.4.5., the count rates are too low.

- Make sure that the laser current is set to a value that corresponds to about 13 mW of output power (compare the spec sheet of your individual laser diode).
- Make sure that the crystal is oriented correctly (see Figure 38)
- Make sure that the 405 nm half-wave plate is positioned between the two mirrors of the pump beam path and is set to 45°. Turn the HWP to see if there is a significant increase in the count rates.
- Check, whether the pump laser is still centered on both the alignment iris and the beam trap iris. If that is not the case, use the two mirrors in the pump beam to re-center the pump laser on both iris apertures (see Section 7.4.2).

- Make sure that the BBO crystal is perpendicular to the pump beam (back reflection with target and alignment laser) before trying to tilt it to maximize the count rate.

If the above points do not solve the problem, repeat the detector positioning process, as described in Section 7.4.3.

### 13.6 Low Coincidence Count Rates

Problem: In Section 7.4.5, you see high single detector count rates ( $>100$  kHz), but low coincidence count rates ( $<1$  kHz).

- Make sure you have calibrated the detector delay offset as described in Section 7.4.5
- Check that the maximum single detector count rates are at the same crystal tilt angle. If the maxima are at significantly different angles, you must repeat the positioning process (Sections 7.4.3 and 7.4.4)

### 13.7 Malus' Law Measurement is Asymmetric

Problem: The measurements for Malus' law (Section 9.6) show an asymmetric signal rate. An example is shown in Figure 186.

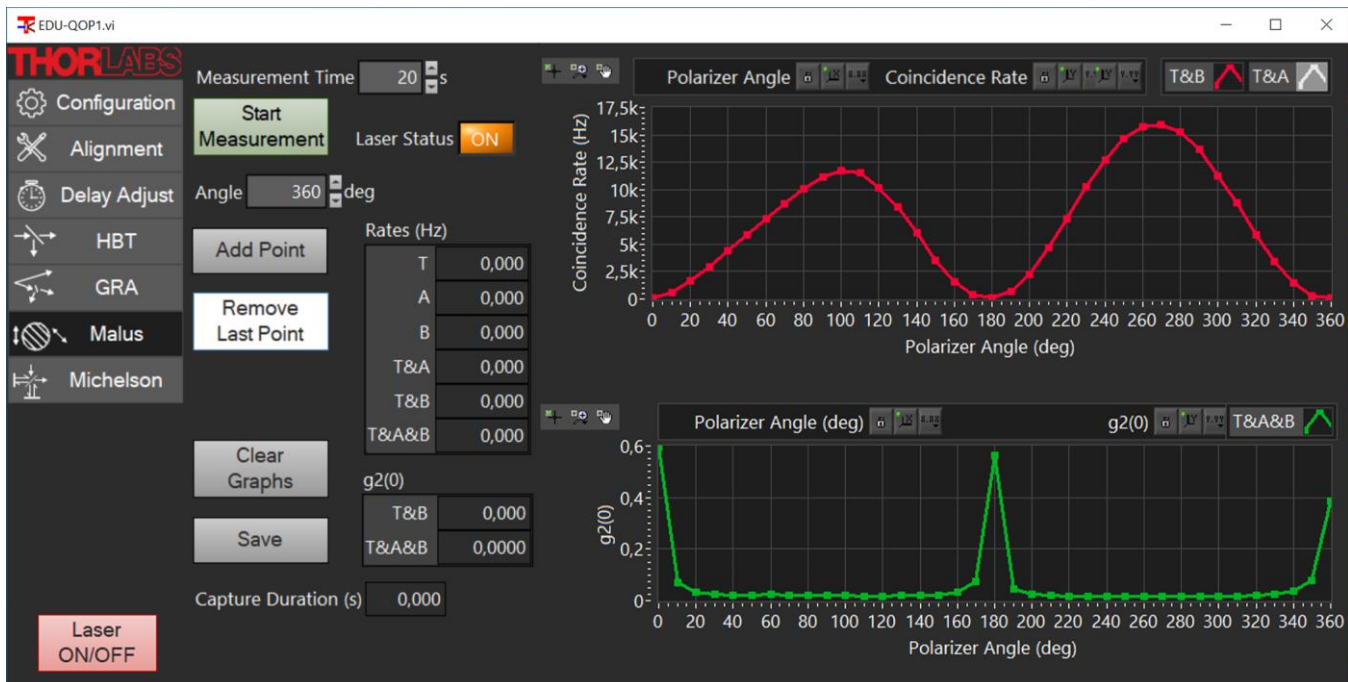


**Figure 186 Example Measurement with Asymmetric Signal for Malus' Experiment**

- Make sure the polarizer is centered with respect to the alignment laser and that its reflection goes back through the alignment target (similar to the alignment of the half-wave plate in Section 7.7)
- The  $\varnothing 1"$  economy polarizer can give rise to a beam deviation, which walks the spot out of the active detector area if it is close to the edge. In the Alignment tab, optimize the T&B coincidence signal for the smaller maximum (in the above example with the polarizer at  $90^\circ - 100^\circ$ ) by turning the two kinematic screws of the CXY1A mount and the zoom housing.

### 13.8 Michelson Interferometer Problems

If in Section 7.6.6, you see a very low count rate on detector B and/or a very low coincidence count rate T&B:

- Move the alignment laser to the magnetic post behind the crystal and use it to check whether all iris apertures and optical elements are correctly positioned (the beam should pass through the center). If an iris is not hit correctly, repeat the beamwalk as described in Section 7.6.1. If an element is not positioned

correctly, move the element (or the whole Michelson board until the positioning is correct; check back reflections with the target to ensure normal incidence).

In Section 7.6.6, you see coincidence count rates, but no interference pattern when moving the stage.

Softly press against the holder of the Michelson mirror that is not on the stage. If you do not see any variation of the coincidence count rate:

- Test your interferometer adjustment: Put the LED in front of the interferometer and check whether you see an interference pattern at the output.
- Make sure that the interference pattern is centered on detector B.

If you see a variation with the above test, but not when moving it via the software:

- Make sure that both the voltage input and the strain gauge output of the stage are connected to the KPC101 controller.
- Make sure that the KPC101 controllers is connected to power and switched on. Sometimes the power supply cable is not fully connected to the controller. This will result in its display to work, but not any other functionality.
- Click the Zero Stage / Calibrate Stage button in the Michelson tab in the software.

If you see an interference pattern in the software, but the contrast is low:

- Slightly move the differential screw of the stage and check whether the contrast improves.
- Very carefully turn the kinematic screws of the interferometer mirror not on the stage. Use a hex key to be able to turn as slow as possible. Check whether this improves the contrast.
- Alternatively, use the LED for the alignment process, as described in Section 7.6.2.

### 13.9 Quantum Eraser Problems

In Section 7.7, if you see the interference pattern with both polarizers at 0°, but you also still see a pattern with crossed polarizers, this is a sign for a non-optimal calibration of the polarizers or polarization changes induced by a slight inclination of the beamsplitter. In this case, try the following:

- Put the Ø1" polarizer in front of detector B and set it to 0°
- Block one arm of the interferometer, turn the Ø1/2" polarizer in the other arm until the coincidence count rate T&B is minimized.
- Block the other arm of the interferometer, turn the Ø1" polarizer to 90°, and then turn the Ø1/2" polarizer in the open arm until the coincidence count rate T&B is minimized.
- Now, you have ensured that the light coming from the arms of the interferometer is perpendicularly polarized. Remove the Ø1" polarizer, unblock both arms, and test whether the interference pattern is indeed fully suppressed (and whether it can be recovered when inserting the Ø1" polarizer set to 45°)

### 13.10 Software not Working

If the software does not start up to show the Device Connection window (see Section 11.4), there is most likely an issue with the software installation.

- In case LabView runtime engine prompts you to specify the path to the Swabian Instruments Time Tagger Library (.dll file), please download and (re)install the latest version of the Swabian Instruments Software.
- If any other file is reported as missing or not executable, the files installed on your hard drive, or the installer file may have been corrupted. Please download the latest version of the EDU-QOP1 software installer from our website.

If there are no controllers available in the drop-down menus in the Device Connection window, even though they are connected to the PC with their USB 3.0 cables and powered on, please check the following:

- Thorlabs Kinesis motion control software must be installed. This also installs the proper USB drivers for the controllers.
- Controllers should show up in Kinesis. If this is not the case, please contact our Tech Support team to troubleshoot the Kinesis connection.
- The controllers can only be recognized by one program at the same time. Thus, the Kinesis software, the EDU-QOP1 software or any other (third-party) software connecting to the K-Cube° controllers cannot be used simultaneously. Please close the Kinesis software before starting the EDU-QOP1 software.

## Chapter 14 Laser Safety Calculation

### 14.1 Laser System

In this EDU-Kit we are using the **L405P20** laser diode. Each institution that uses this educational kit should have a laser safety officer to determine the safety requirements. However, here we give one approach to calculate the risk assessment based on the laser used in this kit.

This laser has a maximum output power of 20 mW and emits in the wavelength range of  $405 \text{ nm} \pm 5 \text{ nm}$ . There is a lens on the laser, which provides a collimated beam. The beam divergence is not known but will be in the range of a few mrad. The laser beam is not circular, it has an elliptical shape with widths of 3 mm x 1 mm.

During normal operation, the laser beam is guided by optics and directed to a working area. As the laser beam is not shielded, there is direct access to this laser radiation. As a result, a reflection (single fault case) of the complete laser radiation could leave the working area.

### 14.2 Laser Class Calculation

For the classification of laser devices, the accessible emission limits (AEL) must be considered. The AEL for the respective protection classes are defined according to the possible hazards that can be caused by the light radiation for the human body and especially for the human eye.

The limit values depend on several factors defined in the EN60825-1 standard to cover different parameters influencing the hazard.

To determine the laser class of the system, the maximum emitted laser power in the case of a fault must be considered. According to the measuring conditions described in the DIN EN60825-1 Norm, the measurement is performed according to condition 3 at a distance of 100 mm from the source with a measuring aperture diameter of 7 mm. Only the laser radiation detected with this measuring aperture is relevant for the evaluation.

The laser radiation has a maximum output power of  $P = 20 \text{ mW}$ , a wavelength range of  $405 \text{ nm} \pm 5 \text{ nm}$ , and is not pulsed. Due to the beam widths of 3 mm x 1 mm, the complete power of the laser radiation is relevant for the classification. The following table shows the laser classes and their power limits for operating the laser in CW mode.

Laser class	Accessible Emission Limits for CW Mode	
1	$AEL_{LC1}$	0.39 mW
2	$AEL_{LC2}$	1 mW
3R	$AEL_{LC3R}$	5 mW
3B	$AEL_{LC3B}$	500 mW

**Table 3 Accessible Emission Limits for CW Mode**

The table shows that the L40P20 laser exceeds the limits of laser classes 1, 2, and 3R and is thus classified in **class 3B**.

For class 3B laser systems, looking into the direct beam is normally dangerous, including short-time accidental irradiation.

### 14.3 Laser Safety Glasses Calculation

Using personal safety equipment (such as laser safety glasses), ensures that the user will not encounter emission that exceeds laser class 1. The standard DIN EN 207:2017 provides a guideline for the selection and application of laser safety eyewear. The following calculations are based on the specification of this standard.

With a laser power of 20 mW and a limit value of 0.39 mW, a maximum transmittance of  $10^{-2}$  is relevant for laser safety eyewear.

In addition to the transmittance, the resistance of the safety googles to the laser radiation is also relevant. For this purpose, the maximum irradiance of the laser beam must be determined. The beam as a 3 mm x 1 mm beam profile, but as a worst case, it was assumed that the beam is circular with a diameter of 1 mm. With the laser power of 20 mW, the irradiance is:

$$E = \frac{P}{A} = \frac{P}{\pi \cdot r_{beam}^2} = \frac{20 \text{ mW}}{\pi * (0.5 \cdot 10^{-3} \text{ m})^2} \cdot 2 = 50.93 \cdot 10^3 \frac{\text{W}}{\text{m}^2}$$

The additional factor of 2 in the formula describes the maximum irradiance in the center of the Gaussian beam. This irradiance must be used for the selection of the laser safety eyewear.

Both the transmittance and the maximum irradiance must be complied with by the used safety eyewear. For an Irradiance  $< 100 \cdot 10^3 \frac{\text{W}}{\text{m}^2}$ , safety goggles with scale number of D LB4 are required according to the EN207:2017 norm (see green field in Figure 187).

From the Thorlabs portfolio, the **LG3** glasses are therefore a viable choice, as it has a protection level of **D LB4** in the relevant wavelength range.

Max. Power Density (E, W/m <sup>2</sup> ) & Energy Density (H, J/m <sup>2</sup> ) in Specified Wavelength Range											
Wave-length Range		180 - 315 nm			>315 - 1400 nm				>1400 nm - 1000 μm		
		For Pulse Duration (seconds)									
Scale Number	T	D $> 3 \cdot 10^{-4}$	I, R $10^{-9}$ to $3 \cdot 10^{-4}$	M $< 10^{-9}$	D $> 5 \cdot 10^{-4}$	I, R $10^{-9}$ to $5 \cdot 10^{-4}$	M $< 10^{-9}$	D $> 0.1$	I, R $10^{-9}$ to 0.1	M $< 10^{-9}$	
LB1	$10^{-1}$	0.01	$3 \cdot 10^2$	$3 \cdot 10^{11}$	$10^2$	0.05	$1.5 \cdot 10^{-3}$	$10^4$	$10^3$	$10^{12}$	
LB2	$10^{-2}$	0.1	$3 \cdot 10^3$	$3 \cdot 10^{12}$	$10^3$	0.5	$1.5 \cdot 10^{-2}$	$10^5$	$10^4$	$10^{13}$	
LB3	$10^{-3}$	1	$3 \cdot 10^4$	$3 \cdot 10^{13}$	$10^4$	5	0.15	$10^6$	$10^5$	$10^{14}$	
LB4	$10^{-4}$	10	$3 \cdot 10^5$	$3 \cdot 10^{14}$	$10^5$	50	1.5	$10^7$	$10^6$	$10^{15}$	
LB5	$10^{-5}$	$10^2$	$3 \cdot 10^6$	$3 \cdot 10^{15}$	$10^6$	$5 \cdot 10^2$	15	$10^8$	$10^7$	$10^{16}$	
LB6	$10^{-6}$	$10^3$	$3 \cdot 10^7$	$3 \cdot 10^{16}$	$10^7$	$5 \cdot 10^3$	$1.5 \cdot 10^2$	$10^9$	$10^8$	$10^{17}$	
LB7	$10^{-7}$	$10^4$	$3 \cdot 10^8$	$3 \cdot 10^{17}$	$10^8$	$5 \cdot 10^4$	$1.5 \cdot 10^3$	$10^{10}$	$10^9$	$10^{18}$	
LB8	$10^{-8}$	$10^5$	$3 \cdot 10^9$	$3 \cdot 10^{18}$	$10^9$	$5 \cdot 10^5$	$1.5 \cdot 10^4$	$10^{11}$	$10^{10}$	$10^{19}$	
LB9	$10^{-9}$	$10^6$	$3 \cdot 10^{10}$	$3 \cdot 10^{19}$	$10^{10}$	$5 \cdot 10^6$	$1.5 \cdot 10^5$	$10^{12}$	$10^{11}$	$10^{20}$	
LB10	$10^{-10}$	$10^7$	$3 \cdot 10^{11}$	$3 \cdot 10^{20}$	$10^{11}$	$5 \cdot 10^7$	$1.5 \cdot 10^6$	$10^{13}$	$10^{12}$	$10^{21}$	

**Figure 187** Table 1 of the EN207:2017 Norm. The important value for this kit is marked in green.

## Chapter 15 Acknowledgements

We are grateful for the various insights we have collected over the years from numerous committed educators who have taken on the challenge of experimentally teaching quantum optics to students.

The experimental realization in this kit was heavily influenced by our collaborators from the Leibniz University Hannover. We cordially thank Dr. Kim-Alessandro Weber and Dr. Rüdiger Scholz for their outstanding contributions to this kit. Between them, they have more than 40 years of experience in designing quantum optics and photon statistics experiments. This kit's design borrows many ideas from the experiments they set up to teach both college students as well as teachers and students from high schools. We are grateful for their enthusiasm to share this experience with the rest of the teaching community by means of this kit. Moreover, they have been invaluable partners to discuss matters of quantum optics in general and didactics in particular. Finally, we thank them for testing and providing extensive feedback on the SPDMA single-photon detector incorporated into this kit during its development.

We cordially thank Paul Schlummer, Adrian Abazi, Carsten Schuck, and Wolfram Pernice from the University of Münster for supporting the development of this educational quantum optics setup. We acknowledge countless fruitful discussions, both on the physical as well as the teaching aspects of quantum systems. In particular, we are grateful for the thorough comparison to a type-II BBO system and their detailed feedback on our SPDMA single photon detector.

We also gratefully acknowledge the contributions of Prof. Dr. Jan-Peter Meyn who was one of the early adopters of real quantum optics experiments in the German teaching community (e.g., P. Bronner *et al* 2009 *Eur. J. Phys.* **30** 1189). His expertise and the optical design of his setups helped spread knowledge among educators and was also an inspiration to certain design elements in the setups from Dr. Kim-Alessandro Weber and Dr. Rüdiger Scholz.

## Chapter 16 Disposal, Warranty, and RMA Information

Thorlabs verifies our compliance with the WEEE (Waste Electrical and Electronic Equipment) directive of the European Community and the corresponding national laws. Accordingly, all end users in the EC may return "end of life" Annex I category electrical and electronic equipment sold after August 13, 2005 to Thorlabs, without incurring disposal charges. Eligible units are marked with the crossed out "wheelie bin" logo (see right), were sold to and are currently owned by a company or institute within the EC and are not dissembled or contaminated. Contact Thorlabs for more information. Waste treatment is your own responsibility. "End of life" units must be returned to Thorlabs or handed to a company specializing in waste recovery. Do not dispose of the unit in a litter bin or at a public waste disposal site. It is the user's responsibility to delete all private data stored on the device prior to disposal.



Annex I

### 16.1 Return of Devices

This precision device is only serviceable if returned and properly packed into the complete original packaging including the complete shipment plus the cardboard insert that holds the enclosed devices. If necessary, ask for replacement packaging. Refer servicing to qualified personnel.

## Chapter 17 Thorlabs Worldwide Contacts

For technical support or sales inquiries, please visit us at [www.thorlabs.com/contact](http://www.thorlabs.com/contact) for our most up-to-date contact information.



### Corporate Headquarters

Thorlabs, Inc.  
43 Sparta Ave  
Newton, New Jersey 07860  
United States  
[sales@thorlabs.com](mailto:sales@thorlabs.com)  
[techsupport@thorlabs.com](mailto:techsupport@thorlabs.com)

### EU Importer

Thorlabs GmbH  
Münchner Weg 1  
D-85232 Bergkirchen  
Germany  
[sales.de@thorlabs.com](mailto:sales.de@thorlabs.com)  
[europe@thorlabs.com](mailto:europe@thorlabs.com)

### Product Manufacturer

Thorlabs GmbH  
Münchner Weg 1  
D-85232 Bergkirchen  
Germany  
[sales.de@thorlabs.com](mailto:sales.de@thorlabs.com)  
[europe@thorlabs.com](mailto:europe@thorlabs.com)

### UK Importer

Thorlabs Ltd.  
204 Lancaster Way Business Park  
Ely CB6 3NX  
United Kingdom  
[sales.uk@thorlabs.com](mailto:sales.uk@thorlabs.com)  
[techsupport.uk@thorlabs.com](mailto:techsupport.uk@thorlabs.com)



**THORLABS**

[www.thorlabs.com](http://www.thorlabs.com)

---





# EDU-QOPA1(/M) Polarization-Entanglement Extension Kit

## User Guide





# Table of Contents

<b>Chapter 18</b>	<b>Introduction .....</b>	<b>1</b>
18.1	Intended Use .....	1
18.2	Explanation of Safety Warnings .....	1
18.3	Laser Radiation Warning .....	1
<b>Chapter 19</b>	<b>Product Description .....</b>	<b>2</b>
<b>Chapter 20</b>	<b>Theory.....</b>	<b>4</b>
20.1	Entanglement .....	4
20.2	Two-Photon Polarization States .....	5
20.2.1	Preparation of Entangled States.....	5
20.2.2	Entangled State Versus Mixed State .....	5
20.2.3	Expected Experimental Results .....	6
20.2.4	General Entangled State.....	11
20.2.5	Interferometer Analogy.....	13
20.2.6	Mixed Phase .....	13
20.3	Bell-Test .....	14
20.3.1	The Einstein-Podolsky-Rosen Paradox .....	14
20.3.2	Hidden Variable Theories and Bell Test.....	15
20.3.3	CHSH Inequality.....	16
20.3.4	Bell States.....	18
20.4	Generating and Controlling Entangled States.....	18
20.4.1	Generation of Pairs of Polarization-Entangled Photons.....	19
20.4.2	Walk-Off Effects .....	22
20.4.3	Entangled State Phase Adjustment .....	25
<b>Chapter 21</b>	<b>Addon Components .....</b>	<b>28</b>
21.1	Crystals.....	28
21.2	Polarization Optics.....	29
21.3	Mounting, Tools, and Software .....	29
21.4	Included Hardware .....	29
21.4.1	Imperial Kit .....	29
21.4.2	Metric Kit.....	29
<b>Chapter 22</b>	<b>Setup.....</b>	<b>30</b>
22.1	Assembly of Components.....	30
22.1.1	Crystals .....	30
22.1.2	Polarizers.....	33
22.2	Setting up the Entangled Pair Source .....	34
<b>Chapter 23</b>	<b>Learning Goals and Misconceptions .....</b>	<b>41</b>
<b>Chapter 24</b>	<b>Experiments .....</b>	<b>43</b>
24.1	Coincidence Rates at Polarizers - Mixed State .....	43
24.2	Coincidence Rates at Polarizers - Entangled State .....	44
24.3	Bell Test with Entangled Source.....	45

---

<b>24.4</b>	<b>Changing the Phase of the Entangled State.....</b>	<b>47</b>
24.4.1	Adjusting the Phase .....	47
24.4.2	Coincidence Rates at Polarizers .....	48
24.4.3	Bell test .....	49
<b>24.5</b>	<b>Changing the Detector Iris Apertures.....</b>	<b>50</b>
<b>24.6</b>	<b>Spatial Compensators .....</b>	<b>51</b>
<b>24.7</b>	<b>Changing the Temporal Walk-Off Compensation .....</b>	<b>53</b>
<b>24.8</b>	<b>Grangier-Roger-Aspect Experiment for the Entangled Source (No Polarizers) .....</b>	<b>54</b>
<b>24.9</b>	<b>Order of Experiments.....</b>	<b>55</b>
<b>Chapter 25</b>	<b>Software .....</b>	<b>57</b>
25.1	Bell-Test Tab.....	57
<b>Chapter 26</b>	<b>Extended Theory .....</b>	<b>59</b>
26.1	Entanglement Proof.....	59
26.2	Partial Measurements.....	60
26.3	Collapse of the Entangled State.....	60
26.4	Different Experimental Results for Mixed and Entangled States .....	61
26.5	EPR Argument .....	64
26.6	Proving the CHSH Inequality.....	65
26.7	Experimental Test of the CHSH Inequality.....	70
26.8	Toy Model for a Local Causal Hidden Variable Theory .....	70
26.9	Possible Interpretations of the Bell Test Result.....	72
26.10	Loopholes in Bell Test Setups .....	73
26.11	Spatial Walk-Off .....	74
26.12	Temporal/Chromatic Walk-Off.....	78
26.13	Imbalanced Pair Generation.....	81
<b>Chapter 27</b>	<b>Technical Notes.....</b>	<b>82</b>
27.1	Polarization In the SPDC Process .....	82
27.1.1	Polarization Distorting Effects.....	82
27.2	Comparison Between Crossed Type-I and Type-II SPDC.....	85
27.3	Crystal Thickness Choice .....	86
27.4	Automized Rotation Stages for Detector Polarizers.....	87
<b>Chapter 28</b>	<b>Troubleshooting.....</b>	<b>90</b>
28.1	No Oscillations When Tilting Temporal Compensation Crystal.....	90
28.2	Bell Test Results in S < 2 .....	90
28.3	Steep Slope of S-Value Versus Detector Iris Aperture.....	90
28.4	Breakdown of Coincidence Rates at Small Iris Aperture Diameters.....	91

---

<b>Chapter 29</b>	<b>Disposal, Warranty, and RMA Information .....</b>	<b>92</b>
29.1	Return of Devices.....	92
<b>Chapter 30</b>	<b>Thorlabs Worldwide Contacts .....</b>	<b>93</b>



Scan Here For  
More Information

---



## Chapter 18 Introduction

### 18.1 Intended Use

This kit is intended to be used as teaching aid for the set of experiments outlined in Chapter 24 and similar concepts for physics and optics courses at high-school to university level.

### 18.2 Explanation of Safety Warnings

Below is a list of warning symbols you may encounter in this manual or on your device



Warning: Laser Radiation



General Warning

### 18.3 Laser Radiation Warning



#### Warning

The class 3B laser diode used in this kit can emit more than 35 mW of optical power, which can cause damage to the eyes if viewed directly. The laser driver is equipped with a key switch and safety interlock, which should be used appropriately to avoid injury. Additionally, we recommend wearing appropriate laser safety glasses when using this kit.



## Chapter 19 Product Description

In our EDU-QOP1(/M) Quantum Optics Kit, pairs of photons are generated. The kit introduces fundamental principles of quantum optics, such as the second-order correlation measurement, which verifies the quantum nature of the light source, single photon interferometry and the well-known quantum eraser experiment.

The EDU-QOPA1(/M) Polarization-Entanglement Extension Kit goes one step further and introduces students to the peculiar world of entanglement. To do so, the type-I BBO from the Quantum Optics Kit is replaced with a pair of type-I BBOs, mutually rotated by 90°. This crystal combination can generate pairs of polarization-entangled photons.

However, generating a truly entangled state with significant count rates on the detectors is not so easy. Firstly, a temporal compensation crystal is needed in front of the type-I BBO pair. The temporal compensation crystal's purpose is to set the correct phase relation between the pairs generated in the first type-I BBO and the pairs generated in the second type-I BBO.

Furthermore, there is a second walk-off effect that needs to be considered. Pairs generated in the first crystal travel through the second crystal, experiencing a walk-off with respect to the pairs generated in the second crystal due to the birefringent nature of the BBO crystal. To compensate for that effect, we introduce spatial compensation crystals behind the type-I BBO pair.

In the kit, the different walk-off effects are experimentally verified, and it is demonstrated how their compensation increases the quality of the measured results significantly.

The highlight of the kit is the measurement of Bell's inequality, one of the most fundamental measurements of quantum mechanics. It addresses the Einstein-Podolsky-Rosen (EPR) paradox and tests whether local hidden variables can explain quantum correlations. It shows that the predictions of quantum mechanics cannot be replicated by any classical theory based on local realism, which assumes that information cannot travel faster than light and that particles have pre-existing properties before measurement. Violations of Bell's inequality, observed in experiments, demonstrate that quantum entanglement allows for stronger correlations between particles than allowed by classical physics. This has profound implications, suggesting that nature defies our classical intuitions about separability and locality. Bell's inequality thus plays a critical role in understanding the non-local nature of quantum reality.

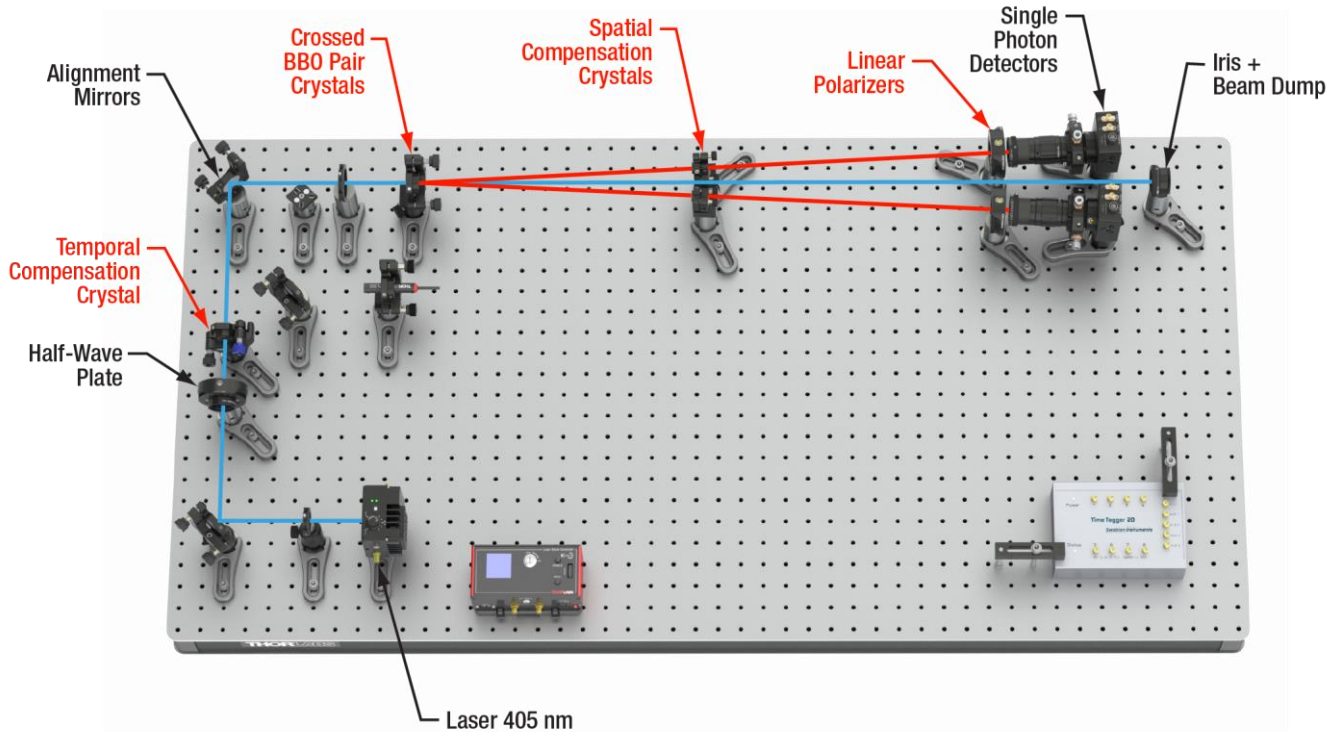


**Figure 188      The Parts of the Entanglement Add-on Kit That are Used to Measure Bell's Inequality**

Experimentally, we continue to use the reliable methods from the EDU-QOP1(/M) Quantum Optics Kit. Even with the more complex crystal arrangement, the alignment procedure with the axicon and colored glass filter proves to be a straightforward and student-friendly procedure.

## Chapter 20 Theory

In this chapter, the theoretical basis for the understanding of the terms “entanglement” and “Bell test” is provided. The quantum mechanical formalism used here is described in Section 3.2 and the remainder of Chapter 3 introduces the theoretical framework for quantum optics. We focus on the most important parts here to allow for an uninterrupted buildup of information. Whenever more lengthy calculations and explanations are required for complete understanding, these are provided in later sections and referred to here.

### 20.1 Entanglement

In classical physics, when the state of a system consisting of several subsystems is completely known, each subsystem is also completely described. For example, complete knowledge about the state of the solar system automatically includes complete knowledge about the state (mass, position, velocity) of every planet in it. The reverse is also true, i.e., the state of the whole system can be completely described by giving the state of each subsystem. Such systems are called separable, and all classical system states are separable.

However, not all the states of a quantum system are separable. Quantum states of a system that cannot be expressed as the tensor product of pure states of the subsystems are called entangled states. Recall from section 3.2.11 that a pure state is a state that can be represented with a single ket vector, whereas, a mixed state is an statistical ensemble of pure states, which is very different from an entangled state, as we will learn in the experiments in this kit.

As an example, consider a quantum system consisting of two subsystems, A and B, with some property that can be expressed as a linear combination of two orthonormal state vectors  $|0\rangle$  and  $|1\rangle$ . First, consider the system to be in the following state  $|S\rangle$ , using the notation for combined quantum states explained in Section 3.2.12:

$$|S\rangle = \frac{1}{\sqrt{2}}(|0\rangle_A \otimes |0\rangle_B + |0\rangle_A \otimes |1\rangle_B) \quad (159)$$

This is a separable (non-entangled) state, as we can write:

$$|S\rangle = \frac{1}{\sqrt{2}}(|0\rangle_A \otimes |0\rangle_B + |0\rangle_A \otimes |1\rangle_B) = \frac{1}{\sqrt{2}} \cdot |0\rangle_A \otimes (|0\rangle_B + |1\rangle_B) \quad (160)$$

Here, we use the fact that the tensor product  $\otimes$  is distributive. The result is a single tensor product between the states  $|0\rangle_A$  and  $\frac{1}{\sqrt{2}}(|0\rangle_B + |1\rangle_B)$ , both of which are pure states for subsystem A and B, respectively (any linear combination of pure states is itself a pure state). Now consider a different state called  $|N\rangle$

$$|N\rangle = \frac{1}{\sqrt{2}}(|0\rangle_A \otimes |0\rangle_B + |1\rangle_A \otimes |1\rangle_B) \quad (161)$$

The state  $|N\rangle$  cannot be written as a tensor product of pure states of the subsystems A and B, it is non-separable and thus entangled (for the proof, see Section 26.1).

If a system is in such an entangled state, the subsystems viewed in isolation have no defined pure state but exist in a superposition of states until measured. For a more detailed description on how to handle subsystems of entangled states, see Section 26.2.

If a measurement is performed on one subsystem of an entangled state, the whole system state changes. In case of a system with exactly two subsystems, a measurement on one subsystem also fixes the state for the second subsystem. Afterwards, both subsystems are in pure states, i.e., the system state is not entangled anymore. This is often called a collapse of the entangled state. For details, see Section 26.3.

The existence of entangled states is one of the most important differences between quantum mechanics and classical physics. Generally, entanglement is not limited to the description of two “real” objects. The subsystems may also refer to abstract objects like qubits (see Section 10.8), represented by different properties and states of the same “real” object (e.g. a single photon).

In this extension kit, experiments are performed with pairs of photons that are polarization entangled. The theory for this case is described in the following section.

## 20.2 Two-Photon Polarization States

When characterizing the state of a photon pair, the existence of entangled states makes it important to not just describe the polarization state of the individual photons that make up the pair, but to describe the combined state of the photon pair.

We use short-hand notations for the combined Hilbert space of the polarization states of both photons (see Section 3.2.12):

$$|A\rangle_1 \otimes |B\rangle_2 \equiv |AB\rangle \equiv |A\rangle_1 |B\rangle_2 \quad (162)$$

Here,  $A$  and  $B$  denote the individual polarization states of photon 1 and 2. For example,  $|HH\rangle$  denotes a two-photon state where both photons are horizontally polarized, while  $|HV\rangle$  describes a state where photon 1 is polarized horizontally and photon 2 vertically.

### 20.2.1 Preparation of Entangled States

The preparation process of the photon pair states is described in depth in Section 20.4, but we introduce the general outline of the process here, because it will help us to tackle common misconceptions right at the beginning. In Section 3.9, a description of the SPDC process in a type-1 non-linear crystal is provided. If a pair is created by this process, both photons of the pair have the same polarization axis, which is perpendicular to the plane containing the pump propagation direction and the optical axis of the crystal.

Consider taking two identical type-1 crystals, rotating the second one by  $90^\circ$  around the pump propagation axis, and combining them to a pair crystal, as displayed in Figure 189. In such a combined crystal, both horizontally polarized photon pairs (the state  $|HH\rangle$ ) and vertically polarized photon pairs (the state  $|VV\rangle$ ) can be generated with the same efficiency, if the polarization of the pump beam is oriented at  $45^\circ$  towards the planes of the optical axes of both crystals.

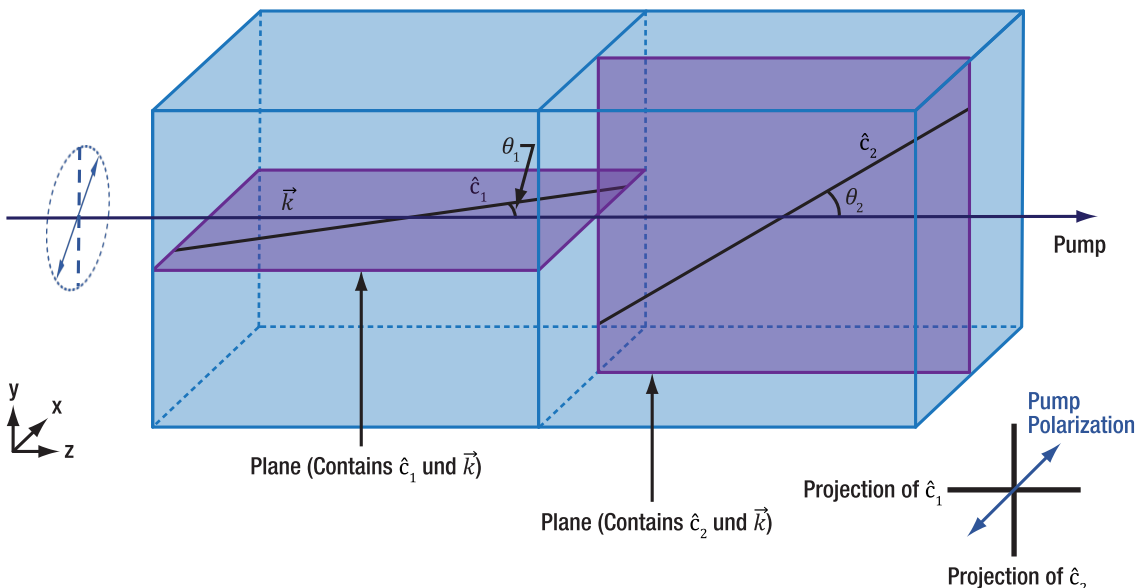


**Figure 189** The left figure is a side view of a crossed BBO Pair. The dark blue arrow indicates the pump beam direction. Black lines indicate the orientations of the optical axes of both crystals while the purple planes are a visual aid for identifying the planes the optical axes are in. The pump beam polarization (blue double arrow) includes an angle of  $45^\circ$  with both purple planes. The bottom right figure shows the projection of the pump beam polarization and the crystals' optical axes looking towards the pump laser (z-axis).

### 20.2.2 Entangled State Versus Mixed State

Which state is generated by such a pair crystal? It is tempting to assume that the states  $|HH\rangle$  and  $|VV\rangle$  are created with equal probability and that the system state is either  $|HH\rangle$  or  $|VV\rangle$ . The resulting state would then be a mixed state with the density matrix  $\hat{\rho}_M$ :

$$\hat{\rho}_M = \frac{1}{2}(|HH\rangle\langle HH| + |VV\rangle\langle VV|) \quad (163)$$

However, **this is not the case**. Instead, the pair crystal generates the entangled state  $|\psi_{E,\phi}\rangle$ :

$$|\psi_{E,\phi}\rangle = \frac{1}{\sqrt{2}}(|HH\rangle + e^{-i\phi}|VV\rangle) \quad (164)$$

The indices M and E indicate (here and in the remainder of the chapter) a mixed state and an entangled state, respectively. The exact state depends on the difference of the optical paths between a photon pair generated in the  $|HH\rangle$  state and one generated in the  $|VV\rangle$  state, represented by the phase  $\Phi$ . The whole beam path from the pump laser to the detectors determines the phase, making the state very sensitive to small changes of the experimental setup. In order to perform reliable experiments, it is crucial to control the phase (in Section 20.2.4 the influence of the phase is presented and Section 20.4.3 discusses how to control it in this kit). For the calculations here, we assume that the experimental settings are actively chosen to yield  $\Phi = 0$ . Then, the state becomes:

$$|\psi_E\rangle = \frac{1}{\sqrt{2}}(|HH\rangle + |VV\rangle) \quad (165)$$

Why is an entangled state generated and not a statistical mixture? It can help to envision the case of the Michelson interferometer described in Section 3.6. When a photon is incident on a beamsplitter, the state after the beamsplitter is also **not a statistical mixture** of the photon being in one of the two paths in the interferometer. That would mean that, excuse our language here, some photons would travel through path 1 of the interferometer while some travel through path 2. However, as demonstrated in Section 3.6, the single photon interferometer experiment can only be understood by picturing the photon state **as a superposition** of both paths.

For the pair crystal considered here, the situation is similar. The generation of both horizontally and vertically polarized photon pairs is possible. Thus, if the generation processes in both parts of the pair crystal are otherwise indistinguishable (for more details, see Section 20.4.1), and no measurement takes place, the generated photon pair state is **a superposition rather than a statistical mixture** and this superposition defines the entangled state.

One could even create entanglement via a literal interferometer. Sending the pump laser through a Mach-Zehnder interferometer and placing a crystal creating only  $|HH\rangle$  pairs in one arm and a crystal creating only  $|VV\rangle$  pairs in the other arm, can also generate entangled states at the output ports of the interferometer. Details are given in Section 20.4.1.

### 20.2.3 Expected Experimental Results

**The calculations in this section apply to the experiments in Sections 24.1 and 24.2.**

Entangled states lead to experimental results that cannot be explained by classical physics. In this section, we demonstrate this fact by considering a simple experiment and comparing the expected results for the states  $\hat{\rho}_M$  (mixed) and  $|\psi_E\rangle$  (entangled) introduced in the prior section. An analysis of a more general entangled state is given in Section 20.2.4, but here we will use the specific state  $|\psi_E\rangle$  in equation (165) to illustrate the most important features of entangled states.

Consider an experimental setup in which a linear polarizer is introduced in each path of the two photons that make up the pair, after which ideal detectors are placed (see Figure 190). We are interested in the probability that both photons of a pair pass their respective polarizers, i.e., both detectors register coincident events, for various settings of the polarizer orientations.

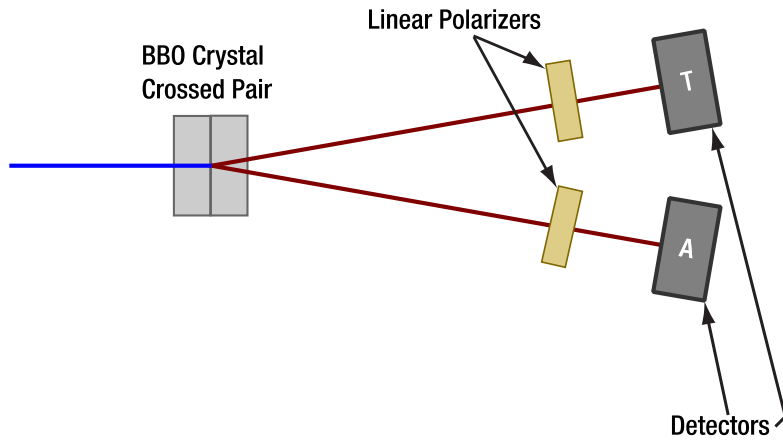


**Figure 190 Schematic Drawing of a Setup to Test Entanglement**

We start with both polarizers in horizontal orientation and calculate the probability of a coincidence for both the mixed and entangled state. The probability  $P_{HH}$  of both photons passing their H-oriented polarizers is the expectation value of the photon pair state to be measured as  $|HH\rangle$  (see Sections 3.2.9 and 3.2.10):

$$P_{HH,M} = \langle HH | \hat{\rho}_M | HH \rangle = \frac{1}{2} \cdot (\langle HH | HH \rangle \langle HH | HH \rangle + \langle HH | VV \rangle \langle VV | HH \rangle) = \frac{1}{2} \quad (166)$$

$$\begin{aligned} P_{HH,E} &= \langle HH | \hat{P}_{\psi_E} | HH \rangle = \langle HH | \psi_E \rangle \cdot \langle \psi_E | HH \rangle \\ &= \frac{1}{2} \cdot (\langle HH | HH \rangle + \langle HH | VV \rangle) (\langle HH | HH \rangle + \langle VV | HH \rangle) = \frac{1}{2} \end{aligned} \quad (167)$$

Here<sup>122</sup>,  $\hat{P}_{\psi_E} = |\psi_E\rangle\langle\psi_E|$  is the projection operator<sup>123</sup> onto the entangled state  $|\psi_E\rangle$ . In this case, the same probability to measure the system in the state  $|HH\rangle$  is obtained for both the entangled state and the mixed state. The same result would also be obtained when using two vertically oriented polarizers, i.e., calculating the probability of measuring the state  $|VV\rangle$ .

It appears that when measuring only along the H and V axes, the expectations for the mixed and entangled state are identical. But what happens if we set both our polarizers to 45°? A linear polarization along the 45° axis generates a photon state that can be expressed as  $|D\rangle = \frac{1}{\sqrt{2}}(|H\rangle + |V\rangle)$ . Note that:

$$|DD\rangle = |D\rangle_1 |D\rangle_2 = \frac{1}{\sqrt{2}} \cdot (|H\rangle + |V\rangle)_1 \frac{1}{\sqrt{2}} \cdot (|H\rangle + |V\rangle)_2 = \frac{1}{2}(|HH\rangle + |HV\rangle + |VH\rangle + |VV\rangle) \quad (168)$$

The indices 1 and 2 mark the two photons of a pair. Let's compare the expected results for this case. We start with the mixed state:

$$\begin{aligned} P_{DD,M} &= \langle DD | \hat{\rho}_M | DD \rangle \\ &= \frac{1}{2} \cdot (\langle HH \rangle + \langle HV \rangle + \langle VH \rangle + \langle VV \rangle) \frac{1}{2} \cdot (\langle HH \rangle \langle HH \rangle + \langle VV \rangle \langle VV \rangle) \frac{1}{2} \\ &\quad \cdot (\langle HH \rangle + \langle HV \rangle + \langle VH \rangle + \langle VV \rangle) \\ &= \frac{1}{8} \cdot (\langle HH | HH \rangle \langle HH | HH \rangle + \langle VV | VV \rangle \langle VV | VV \rangle) = \frac{1}{4} \end{aligned} \quad (169)$$

Followed by the entangled state:

$$\begin{aligned} P_{DD,E} &= \langle DD | \hat{P}_{\psi_E} | DD \rangle \\ &= \langle DD | \psi_E \rangle \cdot \langle \psi_E | DD \rangle \\ &= \frac{1}{2\sqrt{2}} \cdot (\langle HH | HH \rangle + \langle VV | VV \rangle) \cdot \frac{1}{2\sqrt{2}} \cdot (\langle HH | HH \rangle + \langle VV | VV \rangle) = \frac{1}{2} \end{aligned} \quad (170)$$

Here, we see different expectations for the coincidence probability. While only one quarter of photon pairs pass both polarizers in the mixed case, half of them do in the entangled case.

The following table summarized the expected results:

<sup>122</sup> As described in Chapter 3, the scalar product for identical vectors (such as  $\langle HH | HH \rangle$ ) is 1, while it is 0 for orthogonal vectors (such as  $\langle HH | VV \rangle$ ).

<sup>123</sup> The projection operator is used for pure states instead of the density operator for mixed states. The projection operator could be viewed as a density operator with only one element (that of the pure state) in the sum.

Polarizer Setting	Expected Coincidence Probability	
	Entangled State $ \psi_E\rangle$	Mixed State $\hat{\rho}_M$
HH (0° / 0°)	0.5	0.5
VV (90° / 90°)	0.5	0.5
DD (45° / 45°)	0.5	0.25

These specific examples already hint at a fundamental difference between the expected results of the mixed and entangled state. In fact, it can be shown that the specific mixed state  $\hat{\rho}_M$  used here is the only one for which the probabilities are the same as those of the entangled state for the first two polarizer settings (see Section 26.4). As it differs from the entangled state for the third setting, no mixed state can reproduce the expected results of the entangled state for all three of the experiments above.

More generally, the coincidence probability for the entangled state is always 0.5, as long as the polarizers have the same setting, regardless of which setting that is. This can be shown by applying the state for an arbitrary linear polarization angle  $|\varphi\rangle$  to the calculations above:

$$|\varphi\rangle = \cos \varphi \cdot |H\rangle + \sin \varphi \cdot |V\rangle \quad (171)$$

$$\begin{aligned} |\varphi\varphi\rangle &= |\varphi\rangle_1 |\varphi\rangle_2 = (\cos \varphi \cdot |H\rangle + \sin \varphi \cdot |V\rangle) \cdot (\cos \varphi \cdot |H\rangle + \sin \varphi \cdot |V\rangle) \\ &= \cos^2 \varphi \cdot |HH\rangle + \sin^2 \varphi \cdot |VV\rangle + \cos \varphi \sin \varphi \cdot |HV\rangle + \sin \varphi \cos \varphi \cdot |VH\rangle \end{aligned} \quad (172)$$

$$\begin{aligned} P_{\varphi\varphi,E} &= \langle \varphi\varphi | \hat{\rho}_{\psi_E} | \varphi\varphi \rangle = \langle \varphi\varphi | \psi_E \rangle \cdot \langle \psi_E | \varphi\varphi \rangle \\ &= \frac{1}{\sqrt{2}} (\cos^2 \varphi \cdot \langle HH | HH \rangle + \sin^2 \varphi \cdot \langle VV | VV \rangle) \cdot \frac{1}{\sqrt{2}} \cdot (\cos^2 \varphi \cdot \langle HH | HH \rangle + \sin^2 \varphi \cdot \langle VV | VV \rangle) \\ &= \frac{1}{2} \end{aligned} \quad (173)$$

This coincidence probability of 50% irrespective of the angle setting of the identical polarizers cannot be explained with conventional classical physics. One would either have to introduce new hidden variables that affect the polarization measurements (we will see in Section 20.3 that even this approach fails when more setting combinations are taken into account) or propose that the measurement result of one photon affects the state of the other. For example, the result of Equation (173) could be explained as follows: whatever polarization the first photon is measured to have, the second photon will instantly change its state to exactly this polarization. Or in other words: the two photons have individually undefined polarization, but they will always be measured to be in the same<sup>124</sup> polarization state. The situation is visualized in Figure 191.

While this sounds hard to believe at first, a closer look at the quantum mechanical calculations shows that this is exactly what quantum mechanics predicts for entangled states, see Section 26.3.

<sup>124</sup> This only holds true for the specific entangled state  $|\psi_E\rangle = \frac{1}{\sqrt{2}}(|HH\rangle + |VV\rangle)$  state and not for entangled states in general. However, knowledge of the entangled state and polarization state of one photon always allows for calculation of the polarization state of the other photon, see Section 26.3. Examples for other entangled states are given in Section 20.2.4.

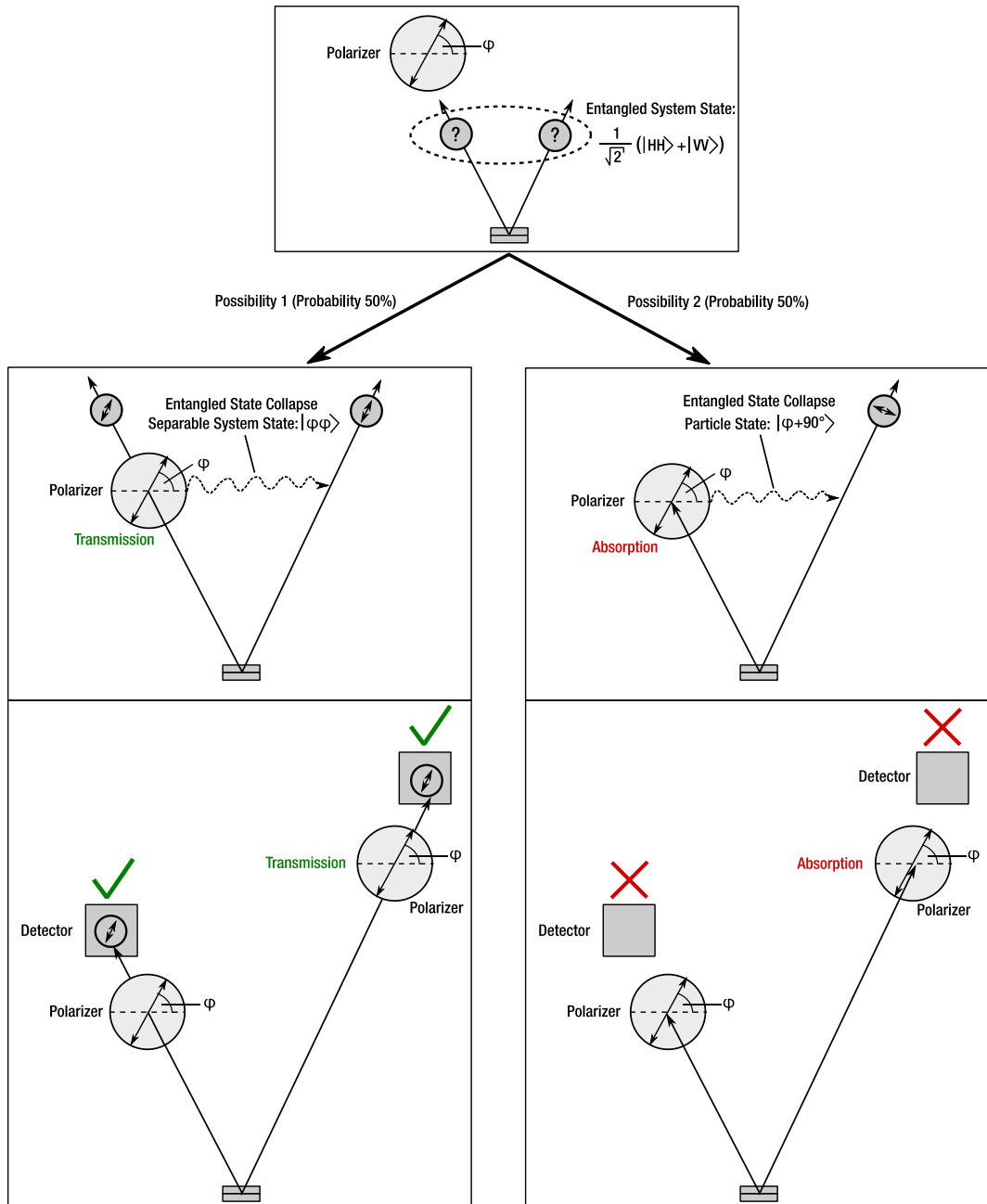


**Figure 191** This figure provides a visualization of entanglement and how a measurement on the left photon affects the system state. Because the polarization state of the right photon is changed according to the measurement result of the left photon, either both or none of the two photons are detected. Please be aware, that the situation is symmetrical, i.e., the same result would occur when measuring the right photon first (or both at the same time). The state after measurement remains a two-subsystem state ( $|\varphi\varphi\rangle$ ) on the left side but becomes a one subsystem state ( $|\varphi + 90^\circ\rangle$ ) on the right side because one of the photons was absorbed.

This behavior was the basis of a major debate in physics because it is contrary to the principle of locality (a measurement at one system cannot instantaneously influence properties of another system which is separated in space), which is fundamental in classical physics. This was first pointed out by Einstein, see Section 20.3.1.

We already see from equations (166) and (168) that this effect does not occur for the mixed state. The general result is:

$$\begin{aligned}
 P_{DD,M} &= \langle \varphi\varphi | \hat{\rho}_M | \varphi\varphi \rangle \\
 &= \frac{1}{2} \cdot (\cos^4 \varphi \cdot \langle HH | HH \rangle \langle HH | HH \rangle + \sin^4 \varphi \cdot \langle VV | VV \rangle \langle VV | VV \rangle) \\
 &= \frac{1}{2} \cdot (\cos^4 \varphi + \sin^4 \varphi) = \frac{1}{2} \cdot ((\cos^2 \varphi + \sin^2 \varphi)^2 - 2 \cdot \cos^2 \varphi \sin^2 \varphi) \\
 &= \frac{1}{2} - \cos^2 \varphi \sin^2 \varphi
 \end{aligned} \tag{174}$$

In contrast to the entangled state, the coincidence probability for the mixed state depends on the specific angle of the identical polarizers. In Figure 192, the expected coincidence probabilities for the entangled and mixed state are plotted as a function of the polarizer angle (same angle for both polarizers). This kit allows one to experimentally verify this plot, see Sections 24.1 and 24.2.

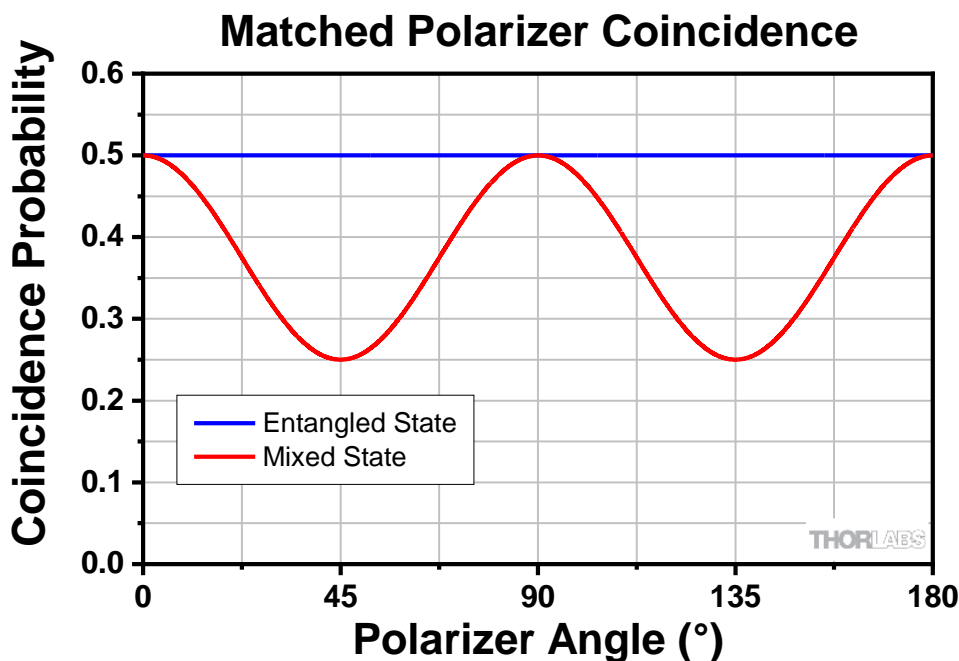


Figure 192      *Coincidence Probability Plotted as a Function of Polarizer Angle (Same Angle for Both Polarizers) for the Entangled and the Mixed State*

If we are not considering identical polarizer angles, but crossed polarizers, i.e., combinations such as  $0^\circ/90^\circ$  or  $45^\circ/135^\circ$ , we see a similar behavior. Again, the expected probabilities for the entangled state  $|\psi_E\rangle$  and the mixed state  $\hat{\rho}_M$  are the same for polarizers in the HV basis but differ for the  $45^\circ$  basis. These expectations are summarized in the following table<sup>125</sup>. They can be understood intuitively as follows:

- For the first two table rows the polarizers are crossed in the HV basis and neither entangled nor mixed state result in any coincidences.
  - In the entangled state, whenever one of the photons of a pair passes its polarizer, the other one is changed to the polarization of the passed polarizer and therefore absorbed at its own (crossed) polarizer, making coincidences impossible.
  - For the mixed state, neither the HH nor the VV state can contribute coincidences as one of the photons of a pair is always absorbed at the polarizer which is orthogonal to the pair polarization.
- The third table row still has crossed polarizers, this time in the  $45^\circ/-45^\circ$  basis.
  - For the entangled state, nothing changes from the description given in the first two table rows.
  - For the mixed state, both the HH and the VV state behave the same: both photons of a pair pass their individual polarizer with a probability of 50%. As this is a classical state, the probabilities of the individual photons have to be statistically independent, which means that the coincidence probability is  $50\%^2 = 25\%$ .

Polarizer Setting	Expected Coincidence Probability	
	Entangled State $ \psi_E\rangle$	Mixed State $\hat{\rho}_M$
HV ( $0^\circ / 90^\circ$ )	0	0
VH ( $90^\circ / 0^\circ$ )	0	0
D/D <sup>-</sup> ( $45^\circ / -45^\circ$ ) <sup>126</sup>	0	0.25
Generalized: $\varphi / \varphi + 90^\circ$	0	$\cos^2 \varphi \sin^2 \varphi$

## 20.2.4 General Entangled State

The calculations in this section apply to the experiments in Sections 24.4.1 and 24.4.2.

In the prior sections we looked at the specific entangled state with a phase of  $0^\circ$  (here, and in the remainder of the manual, we will use degrees as the unit for the phase instead of radians, as this makes some situations more intuitive). In this section, we will investigate how the expected experimental results change if we use different entangled states (different phases).

In general, the state generated by the pair crystal mentioned in Section 20.2.1 is the following:

$$|\psi\rangle = (c_{HH}|HH\rangle + c_{VV}|VV\rangle) \quad (175)$$

where the complex coefficients  $c_{HH}$  and  $c_{VV}$  describe the amplitude (or probability of generating this pair) and phase of both polarization states. As long as neither of the coefficients is zero, this is an entangled state because it is not possible to write it as a product of single photon states of photons 1 and 2.

Let's assume we have adjusted the setup to equal probabilities for both polarizations and a stable phase difference  $\Phi$  between the two polarization states. Then the entangled state can be written as

$$|\psi_{E,\Phi}\rangle = \frac{1}{\sqrt{2}}(|HH\rangle + e^{-i\Phi}|VV\rangle), \quad (176)$$

Now imagine an ensemble of many photon pairs generated this way. As the phase difference  $\Phi$  is constant, this ensemble is in the pure state  $|\psi_{E,\Phi}\rangle$ .

<sup>125</sup> While these specific cases are insightful, a full understanding of the entanglement phenomena requires understanding of the underlying mathematics. We therefore recommend to look at the more general formulas in Sections 26.2 and 26.3.

<sup>126</sup> The state  $|D^-\rangle$  is defined as  $|D^-\rangle = \frac{1}{\sqrt{2}}(|H\rangle - |V\rangle)$

In Section 20.2.3, we saw that the special entangled state with  $\Phi = 0$  leads to the same results as the mixed state when the polarizers were both set horizontally (or both vertically) and different expected results than the mixed state when the polarizers were both set to  $45^\circ$ . Now we calculate the expected coincidence probabilities for the general entangled state in these cases:

$$\begin{aligned} P_{HH,E,\Phi} &= \langle HH | \hat{P}_{\psi_{E,\Phi}} | HH \rangle \\ &= \frac{1}{\sqrt{2}} (\langle HH | HH \rangle + e^{-i\Phi} \cdot \langle HH | VV \rangle) \frac{1}{\sqrt{2}} \cdot (\langle HH | HH \rangle + e^{i\Phi} \cdot \langle VV | HH \rangle) = \frac{1}{2} \end{aligned} \quad (177)$$

$$\begin{aligned} P_{DD,E,\Phi} &= \langle DD | \hat{P}_{\psi_{E,\Phi}} | DD \rangle = \frac{1}{2\sqrt{2}} \cdot (\langle HH | HH \rangle + e^{i\Phi} \langle VV | VV \rangle) \cdot \frac{1}{2\sqrt{2}} \cdot (\langle HH | HH \rangle + e^{-i\Phi} \langle VV | VV \rangle) \\ &= \frac{1}{8} \cdot (\langle HH | HH \rangle \langle HH | HH \rangle + e^{-i\Phi} \langle VV | VV \rangle \langle HH | HH \rangle + e^{i\Phi} \langle HH | HH \rangle \langle VV | VV \rangle \\ &\quad + \langle VV | VV \rangle \langle VV | VV \rangle) \\ &= \frac{1}{8} \cdot (2 + e^{-i\Phi} + e^{i\Phi}) = \frac{1 + \cos(\Phi)}{4} \end{aligned} \quad (178)$$

From equation (177), we see that if measuring along the H and V axes, the result remains the same irrespective of the phase difference  $\Phi$ . However, when both polarizers are oriented along the  $45^\circ$  axis, as in equation (178), the phase difference of the entangled state determines the expected result of the experiment. The probability of both photons passing the polarizers can be as high as 0.5 (in the  $\Phi = 0^\circ$  case considered above) and as low as 0 (for  $\Phi = 180^\circ$ ). It is thus important to know the phase difference when determining the expectations for this kind of experiment. The two special cases calculated in equations (177) and (178) are plotted in Figure 193. This plot can be experimentally verified with this kit. The measurement for the red curve is described in Section 24.4.1., while the blue curve can be measured the same way by just setting both polarizers to  $0^\circ$ .

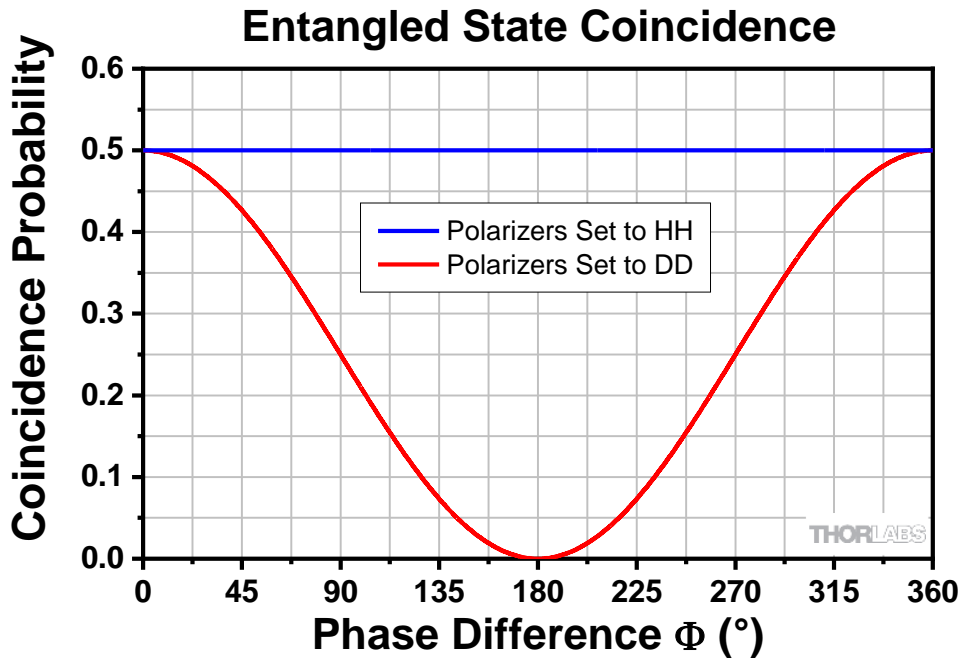


**Figure 193**    *Coincidence Probability for HH and DD Polarizer Settings for Different Entangled States  
(Characterized by the Phase Difference  $\Phi$  in  $|\psi_{E,\Phi}\rangle = \frac{1}{\sqrt{2}}(|HH\rangle + e^{-i\Phi}|VV\rangle)$ )*

Changing the phase leads to different expected results for all experiments. In Section 20.2.3, we calculated the expected results for the state  $|\psi_{E,0^\circ}\rangle = \frac{1}{\sqrt{2}}(|HH\rangle + |VV\rangle)$  with a phase difference of  $0^\circ$ . If we set the phase difference to  $180^\circ$  instead, we arrive at the different state  $|\psi_{E,180^\circ}\rangle = \frac{1}{\sqrt{2}}(|HH\rangle - |VV\rangle)$ . The following table summarizes the expected results for selected polarizer settings (we recommend doing the calculations for some or all of the table entries to further understanding of the underlying mechanism):

Polarizer Setting	Expected Coincidence Probability	
	$ \psi_{E,0^\circ}\rangle$	$ \psi_{E,180^\circ}\rangle$
HH (0° / 0°)	0.5	0.5
HV (0° / 90°)	0	0
D/D (45° / 45°)	0.5	0
D/D (45° / -45°)	0	0.5
Generalized: $\varphi / \varphi$	0.5	$0.5 \cdot \cos^2(2\varphi)$
Generalized: $\varphi / \varphi + 90^\circ$	0	$0.5 \cdot \sin^2(2\varphi)$
Generalized: $\varphi / -\varphi$	$0.5 \cdot \cos^2(2\varphi)$	0.5

**Table 4 Collection of Expected Coincidence Probabilities for Polarizer Settings that are Used in this Kit.** The second to last row represents rotating two orthogonal polarizers in the same direction while the last row represents rotating the two polarizers in opposite directions (beginning with both at 0°).

While the results of specific experiments change, the state  $|\psi_{E,180^\circ}\rangle$  (and all states of the form given in equation (176)) is an entangled state and its expected results cannot be reproduced by any mixed state.

### 20.2.5 Interferometer Analogy

The  $1 + \cos(\Phi)$  term in equation (178) looks remarkably like the interference term when detecting single photons after passing through a Michelson interferometer, see Section 3.6. In fact, multiple analogies can be drawn between the concept of polarization entanglement and single photon interference:

In the interferometer case, the state after the interferometer is a superposition of the states that describe the photon having taken one path or another, as long as the paths are indistinguishable. This superposition cannot be expressed as a product state of the “single path” states. Due to this, the phase difference between the two paths determines the final state and hence the probability in which interferometer output port the photon will be found (constructive interference, destructive interference, or something in between). If there is a way to obtain the path information, such as in the quantum eraser experiment (see Section 3.8), there is no superposition and hence no influence of the phase difference on the final state and the output probabilities.

In the entanglement case, if the two pair states are indistinguishable, the final state will also be a superposition of the two possible pair states that cannot be expressed as product of these states. Thus, the final state is non-separable (entangled) and the phase difference between the two possible pair states influences the result of the experiment, in this case the coincidence probability. If the information about which pair was created can be obtained, the final state becomes a mixed state instead of a superposition, and no entanglement can be observed. This situation arises for example, if effects inside the pair crystal introduced in Section 20.2.1 lead to a significant difference in the arrival time of the  $|VV\rangle$  pairs created in the first crystal of the pair compared to the  $|HH\rangle$  pairs created in the second crystal. In that case, the pairs become distinguishable via a time measurement and no superposition (entanglement) is observed. This and other effects can be a problem in real-life experiments and have to be accounted for, see Section 20.4.2.

### 20.2.6 Mixed Phase

**The calculations in this section apply to the experiments in Sections 24.5, 24.6, and 24.7.**

In Section 20.2.4, we considered an ensemble of photon pairs in an entangled state with an arbitrary, but constant, phase difference. However, in real-life experiments the state will never be perfect<sup>127</sup> and instead a mixture of states with different phases will be measured. In the extreme case, every phase between 0° and 360° is possible and all phases have the same probability. In this case, the resulting state is called a completely mixed state and is described by the following density operator (see Section 3.2.11):

<sup>127</sup> The reasons for this are manifold, examples include: the emission spectrum of the pump laser not being a perfectly sharp line, the detector chip not being a single point in space, noise (such as thermal or electric noise) in all experimental parameters, and the impossibility of perfect alignment.

$$\begin{aligned}
 \hat{\rho}_{M,comp} &= \frac{1}{2\pi} \int_0^{360^\circ} \frac{1}{2} (|HH\rangle + e^{-i\Phi}|VV\rangle)(\langle HH| + e^{i\Phi}\langle VV|) d\Phi \\
 &= \frac{1}{4\pi} \int_0^{360^\circ} (|HH\rangle\langle HH| + e^{i\Phi}|VV\rangle\langle HH| + e^{-i\Phi}|HH\rangle\langle VV| + |VV\rangle\langle VV|) d\Phi \\
 &= \frac{1}{2} \cdot (|HH\rangle\langle HH| + |VV\rangle\langle VV|)
 \end{aligned} \tag{179}$$

The second and third term in the integral vanish when integrating because of the Euler identity  $e^{i\Phi} = \cos\Phi + i\sin\Phi$  and the fact that the integral of both sine and cosine function over a whole period is zero.

This is the same result that we obtained for an equal statistical mixture of  $|HH\rangle$  and  $|VV\rangle$  pairs, but this time we arrived there via an equal statistical mixture of entangled states with all possible phase differences. This shows that even when every state that makes up a mixed state is an entangled state, the mixed state itself can behave like a separable (non-entangled) state. This means that if the range of possible phases in an experiment is too large, the entanglement cannot be observed even though only entangled states are generated. As a result, a source of entangled states can still behave like a classical source if states with too many different phases are emitted (and detected).

In any experiment aiming to show entanglement effects, it is thus crucial to keep the phase-range of measured states much lower than  $360^\circ$ .

In this kit, we use additional birefringent crystals (see Section 20.4.2) in order to minimize the phase-range. The effects of omitting these components or of not adjusting them optimally can be observed experimentally, see Sections 24.6 and 24.7.

## 20.3 Bell-Test

This section is about one of the most important experiments regarding the interpretation of quantum mechanics, the Bell test (which can be performed with this kit, see Section 24.3). The underlying theorem was first proposed by J.S. Bell in 1964<sup>128</sup> and states that a group of theories (local hidden variable theories, explained later in this section) can never match the predictions of quantum mechanics. Over the years, both the theorem and its experimental tests have seen numerous variations and implementations, consistently validating the quantum-mechanical predictions.

### 20.3.1 The Einstein-Podolsky-Rosen Paradox

To understand the implications and importance of the Bell test, it is helpful to consider the historical background of the origin of quantum mechanics and its interpretations.

In the year 1935, the initial philosophical debate around the new field of quantum mechanics had somewhat settled, with the so-called Copenhagen interpretation<sup>129</sup> becoming generally accepted. Einstein, however, had serious concerns about some aspects of quantum mechanics. He did not like the fact that quantum mechanics (in the Copenhagen interpretation) only treated the outcomes of measurements and provided no answers to what is true in the absence of observations. Furthermore, he was worried about the way that probabilities (as formulated in the Born rule<sup>130</sup>) were a fundamental part of the theory (as opposed to statistical mechanics where they only arise from not knowing the finer details)<sup>131</sup>. Einstein concluded that quantum mechanics was incomplete (i.e., the quantum state did not reveal all knowable truths about a system). To this effect, he, together with two of his assistants, Boris Podolsky and Nathan Rosen, published an article intending to prove the incompleteness of

<sup>128</sup> J. S. Bell, *Physics*, 1(3), 195-200 (1964).

<sup>129</sup> J. Faye, "Copenhagen Interpretation of Quantum Mechanics", *The Stanford Encyclopedia of Philosophy* (Summer 2024 Edition), Edward N. Zalta & Uri Nodelman (eds.), URL = <<https://plato.stanford.edu/archives/sum2024/entries/qm-copenhagen/>>.

<sup>130</sup> Simplified Born Rule: "The probability density is proportional to the absolute square of the wavefunction."

<sup>131</sup> A. Fine and T. A. Ryckman, "The Einstein-Podolsky-Rosen Argument in Quantum Theory", *The Stanford Encyclopedia of Philosophy* (Summer 2020 Edition), Edward N. Zalta (ed.), URL = <<https://plato.stanford.edu/archives/sum2020/entries/qt-epr/>>.

quantum mechanics<sup>132</sup>. This article had a large impact on discussions over the interpretation of quantum mechanics, with debates continuing even today.

Very abbreviated, the authors make two assumptions that they maintain should hold in general:

- a) Separability: All physical quantities have defined values at all times.
- b) Locality: If systems are spatially separate, a measurement on one of the systems does not directly (i.e., faster-than-light) affect anything about the other system.

They then introduce a system of two entangled particles and prove that, under the two assumptions above, the entangled quantum state does not include all knowable information about the particles, i.e., that quantum mechanics is incomplete. A critical role is played by what Einstein called “spooky action at a distance”, namely that if one particle of an entangled pair is measured, the state of the other changes instantaneously, as depicted in Figure 194. For a more detailed description of the Einstein-Podolsky-Rosen (EPR) argument, see Section 26.5.

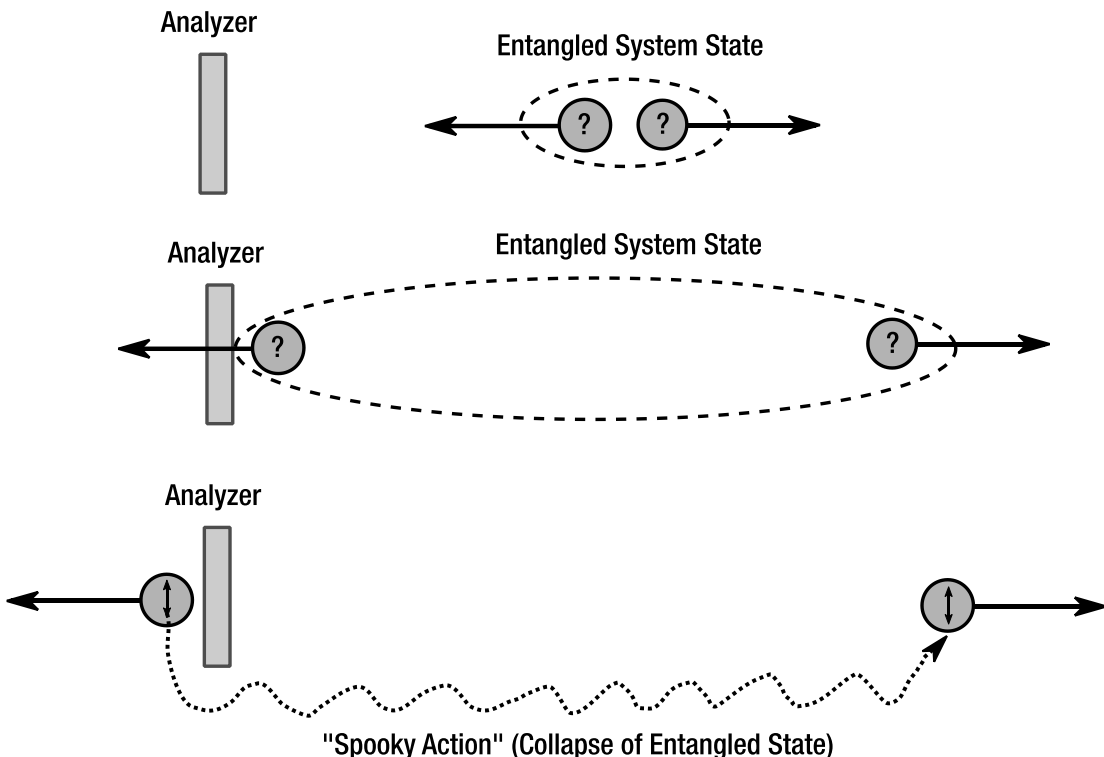


**Figure 194** Drawing of “Spooky Action at a Distance”. In the entangled state, no polarization can be attributed to the individual particles (symbolized by the question marks). The entanglement persists even for large distances in space. Once a polarization measurement on the left particle occurs, the state of the right particle is instantaneously fixed as well.

However, quantum mechanics does not have to be incomplete because the EPR paradox can also be resolved by abandoning either the separability or locality assumption.

Einstein wanted to preserve both separability and locality, so he thought quantum mechanics to be incomplete. However, in contrast to what is often purported, he did not believe that it was promising to attempt to supplement the quantum mechanical wave function with additional parameters (see the next section). Instead, he advocated to look for new concepts<sup>133</sup>.

### 20.3.2 Hidden Variable Theories and Bell Test

In the light of the problem described by the EPR paradox, an intuitive idea is to regard quantum mechanics as incomplete and to try to introduce additional so-called hidden variables to the theory in order to “rescue”

<sup>132</sup> A. Einstein, B. Podolsky, and N. Rosen, Physical Review, **47**, 777-780 (1935).

<sup>133</sup> A. Einstein, B. Podolsky, and N. Rosen, Physical Review, **47**, 777-780 (1935).

separability and locality. The aim would be to find a theory that assigns real values to all properties of any system and does not require measurements on one system to instantaneously influence the state of other spatially separated systems, but at the same time reproduces the predictions of quantum mechanics (because they are verified by experimental reality). A simple example for such a theory (related to polarization) is given in Section 26.8.

The possibility of such hidden variable theories was the subject of investigations by J. S. Bell, who in his famous article from 1964<sup>134</sup> proposed an experimental setting for which the predictions of quantum mechanics and a subgroup of hidden variable theories (those that include a principle he called “Local Causality”), can never be the same for all possible measurement settings (an example of a local hidden variable theory is given in Section 26.8). This local causality principle is closely related to Einstein’s conditions of separability and locality, although not fully identical.

In this article, Bell first formulates his assumptions for this local causality and then introduces a framework of two spin-1/2 particles that are perfectly anti-correlated. He presents an experiment (measuring the spin of the particles) with a specific set of experimental parameters and derives boundaries to the predictions of hidden variable theories that follow his local causality assumptions in this situation. The quantum mechanical predictions lie outside these boundaries, i.e., no hidden variable theory that includes these local causality assumptions can match the quantum mechanical predictions, which have been verified by real-life experiments. His conclusion (cited directly from the 1964 article) is the following:

In a theory in which parameters are added to quantum mechanics to determine the results of individual measurements, without changing the statistical predictions, there must be a mechanism whereby the setting of one measuring device can influence the reading of another instrument, however remote.

This is Bell’s theorem. In the original version, the proof does not lend itself well to experimental testing, as some of its assumptions are difficult to realize experimentally. Over the years following this groundbreaking work, Bell himself as well as others (most notably Clauser, Horne, Shimony, and Holt (CHSH)) managed to prove similar theorems that are more easily testable in real world experiments. These theorems are summarized under the term Bell-type theorems and the corresponding experiments are called Bell tests. They are characterized by providing some kind of inequality (called Bell-type inequalities) that must hold for all local causal hidden variable theories but is violated by quantum mechanical predictions.

All experimental data gathered so far agrees with the predictions of quantum mechanics, so if one believes in the validity of this data, one must rule out all causal local hidden variable theories as a description for reality<sup>135</sup>.

It is important to note that the Bell test does not rule out **all** hidden variable theories, only those that contain local causality. If one abandons this assumption, it is possible to construct hidden variable theories providing the exact same predictions as orthodox quantum mechanics. One example is the De-Broglie-Bohm theory which adds definite positions of particles to the theory (these are the hidden variables) and explicitly abandons the locality assumption by assuming a single wavefunction that describes all the particles. Therefore, if one particle changes, the whole all-particle wavefunction changes, which is inherently non-local<sup>136</sup>.

### 20.3.3 CHSH Inequality

**The calculations in this section apply to the experiments in Sections 24.3 through 24.7.**

The specific Bell test performed in this kit employs an inequality first shown by Clauser, Horne, Shimony, and Holt (CHSH). It is very briefly described here for the specific case of the setup used in the kit. A more general and detailed proof is given in Section 26.6.

<sup>134</sup> J. Faye, "Copenhagen Interpretation of Quantum Mechanics", *The Stanford Encyclopedia of Philosophy* (Summer 2024 Edition), Edward N. Zalta & Uri Nodelman (eds.), forthcoming URL = <<https://plato.stanford.edu/archives/sum2024/entries/qm-copenhagen/>>.

<sup>135</sup> W. Myrvold, M. Genovese, and A. Shimony, "Bell's Theorem", *The Stanford Encyclopedia of Philosophy* (Spring 2024 Edition), Edward N. Zalta & Uri Nodelman (eds.), URL = <<https://plato.stanford.edu/archives/spr2024/entries/bell-theorem/>>.

<sup>136</sup> S. Goldstein, "Bohmian Mechanics", *The Stanford Encyclopedia of Philosophy* (Fall 2021 Edition), Edward N. Zalta (ed.), URL = <<https://plato.stanford.edu/archives/fall2021/entries/qm-bohm/>>.

The version of the CHSH inequality we use in this kit is based on the experimental setup shown in Figure 195. A source is emitting pairs of entangled photons with the photons being sent in different directions. In each arm, there is a linear polarizer, either transmitting or absorbing incident photons depending on the photon's polarization and the polarizer angle setting. One detector in each arm registers transmitted photons.

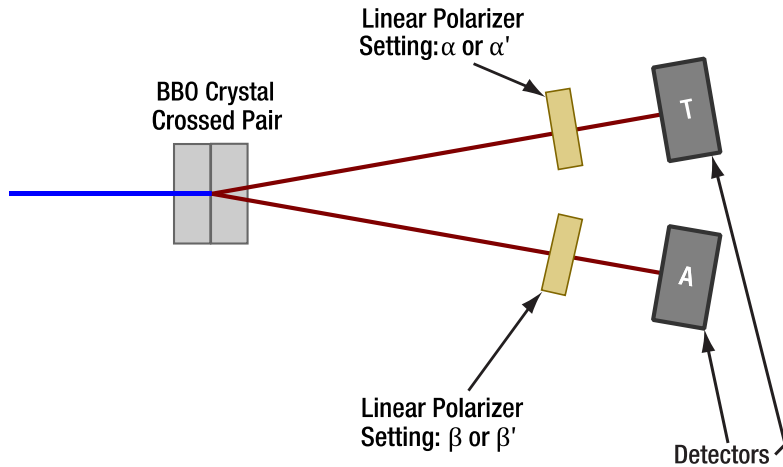


**Figure 195 Schematic Drawing of the Experiment Envisioned in the proof of a Bell-type theorem**

In Section 20.2, we presented multiple cases of entangled states resulting in expected experimental results that show a strong correlation between the polarizations of the entangled photons. The idea behind all Bell inequalities is to show that these correlations are in fact stronger than what can be explained by any hidden variable theory based on local causality. One way to infer the expected correlations experimentally is by observing the probabilities of both photons of a pair to be transmitted as a function of the polarizer settings. These probabilities can be measured in the above experiment via the coincidence rates of the detectors. CHSH defines specific relations (called the  $E$ -parameter) of these coincidence rates as follows:

$$E(\alpha, \beta) \equiv \frac{R(\alpha, \beta) - R(\alpha, \beta + 90^\circ) - R(\alpha + 90^\circ, \beta) + R(\alpha + 90^\circ, \beta + 90^\circ)}{R(\alpha, \beta) + R(\alpha, \beta + 90^\circ) + R(\alpha + 90^\circ, \beta) + R(\alpha + 90^\circ, \beta + 90^\circ)} \quad (180)$$

Here, the  $R$  are coincidence count rates. The values  $\alpha, \beta$  in parentheses are the analyzer angles for a specific  $E$ -parameter.

Using four  $E$ -parameters for four different experiment settings (analyzer angles), the following quantity is defined:

$$S(\alpha, \alpha', \beta, \beta') \equiv E(\alpha, \beta) - E(\alpha, \beta') + E(\alpha', \beta) + E(\alpha', \beta') \quad (181)$$

CHSH proved that, under the assumptions of locality and causality (defined in a strict and abstract way in the proof), all hidden variable theories must obey the CHSH inequality:

$$S(\alpha, \alpha', \beta, \beta') \leq 2 \quad (182)$$

At the same time, one can find sets of specific entangled states and the four analyzer angles  $\alpha, \alpha', \beta, \beta'$ , for which quantum mechanics predicts  $S(\alpha, \alpha', \beta, \beta') > 2$ . One such set (the one used in this kit) is:

$$\begin{aligned} |\Phi\rangle &= \frac{1}{\sqrt{2}}(|H\rangle_1|H\rangle_2 + |V\rangle_1|V\rangle_2) \\ \alpha &= 0^\circ \\ \beta &= 22.5^\circ \\ \alpha' &= 45^\circ \\ \beta' &= 67.5^\circ \end{aligned} \quad (183)$$

For this set, the quantum mechanical prediction is  $S(\alpha, \alpha', \beta, \beta') = 2 \cdot \sqrt{2}$ . This is also the maximum value that can be reached with any state-settings combination, a rule that is known as Tsirelson's bound<sup>137</sup>.

An important takeaway from the CHSH inequality and the Bell test is the following: When talking about quantum entanglement, it is often highlighted how the polarizations of the two photons are in perfect correlation<sup>138</sup> when the analyzers are set parallelly or perpendicularly. The example calculations in Section 20.2.3 are such a case. These cases are easy to calculate, and the results are different from what would intuitively be expected (when thinking in classical terms). However, this behavior can be explained with a local hidden variable theory. What Bell discovered, was that quantum mechanics predicts stronger correlations than allowed by local hidden variable theories at those analyzer orientations that deviate from perfectly parallel or perpendicular (that is why 22.5° steps provide the maximum violation of the CHSH inequality, see Section 20.3.3).

Bell's theorem means that, since experiments (Bell tests) confirm the quantum mechanical predictions, local causal hidden variable theories must be ruled out as a description of reality. The generally accepted conclusion is that our reality is non-local.

It is also important to note that, while non-locality allows the state of an un-measured subsystem of an entangled system to change instantaneously with the measurement of a different subsystem, this fact cannot be used to transmit any information faster than light because the results of the measurement are still probabilistic; forcing specific results to encode information (by changing the state of one of the subsystems) will lead to a collapse of the entanglement, making the transfer of the encoded information impossible.

#### 20.3.4 Bell States

In quantum information theory, any subsystem of a larger system that can have two distinct states is called a qubit, see also Section 10.8.2. A maximally entangled state for a system of two qubits A and B is called a Bell state. There are 4 Bell states that form a basis in the space of two-qubit states:

$$\begin{aligned} \circ \quad |\Phi^+\rangle &= \frac{1}{\sqrt{2}}(|0\rangle_A|0\rangle_B + |1\rangle_A|1\rangle_B) \\ \circ \quad |\Phi^-\rangle &= \frac{1}{\sqrt{2}}(|0\rangle_A|0\rangle_B - |1\rangle_A|1\rangle_B) \\ \circ \quad |\Psi^+\rangle &= \frac{1}{\sqrt{2}}(|0\rangle_A|1\rangle_B + |1\rangle_A|0\rangle_B) \\ \circ \quad |\Psi^-\rangle &= \frac{1}{\sqrt{2}}(|0\rangle_A|1\rangle_B - |1\rangle_A|0\rangle_B) \end{aligned} \tag{184}$$

The state of Equation (242) that we used to prove the Bell-type theorem, is the Bell state  $|\Phi^+\rangle$  with the qubits being represented by the photons and the basis states being represented by polarization along the x-axis (bit 0) and along the y-axis (bit 1). In the experimental context of the qubits in this kit,  $|0\rangle$  and  $|1\rangle$  correspond to  $|H\rangle$  and  $|V\rangle$  polarizations (see also Section 20.2). We could also violate the CHSH inequality with any of the other Bell states, although we would have to choose different analyzer angles to do so.

Our suggested alignment and experiment settings aim for a generation of the Bell state  $|\Phi^+\rangle = \frac{1}{\sqrt{2}}(|HH\rangle + |VV\rangle)$ , but by adjusting the phase of the entangled state, the state  $|\Phi^-\rangle$  can be generated instead. For the generation of  $|\Psi^\pm\rangle$  Bell states, the polarization of one of the photons in the pair can be rotated by 90° using a half-waveplate (set to 45°).

### 20.4 Generating and Controlling Entangled States

There is a range of variations of SPDC processes for the generation of pairs of polarization-entangled photons. Here, we will discuss the implementation used in the kit addon.

<sup>137</sup> B. S. Cirel'son, *Letters in Mathematical Physics*, 4(2), 93-100 (1980).

<sup>138</sup> Corresponding to maximal (or zero) coincidence count rates in the context of the measured quantities.

### 20.4.1 Generation of Pairs of Polarization-Entangled Photons

A basic prerequisite for pairs of polarization-entangled photons is the presence of two orthogonally polarized states in both arms of the pair source. We are looking for a physical system that generates the Bell state  $\frac{1}{\sqrt{2}}(|HH\rangle + |VV\rangle)$  (compare to Section 20.2.1). However, the single-crystal type-I SPDC process, as introduced in Section 3.9, only generates photon pairs in a single polarization state, which is  $|VV\rangle$ . The simplest solution<sup>139</sup> to generate additional photon-pairs with an orthogonal polarization is using two identical crystals, rotated by 90° against each other along the pump beam direction. For both crystals, photon pairs are then emitted on a cone (as shown in Figure 196) and by adjusting the phase matching conditions (tilting the crystal pair) the two cones can be made to overlap.

---

<sup>139</sup> Another (more) famous solution is to use crystals cut for Type-II SPDC (e.g., Item # NLCQ5), where a single photon-pair state has orthogonal polarization states in signal vs. idler arms. Please refer to Section 27.2 for a comparison between Type-II and Type-I processes.

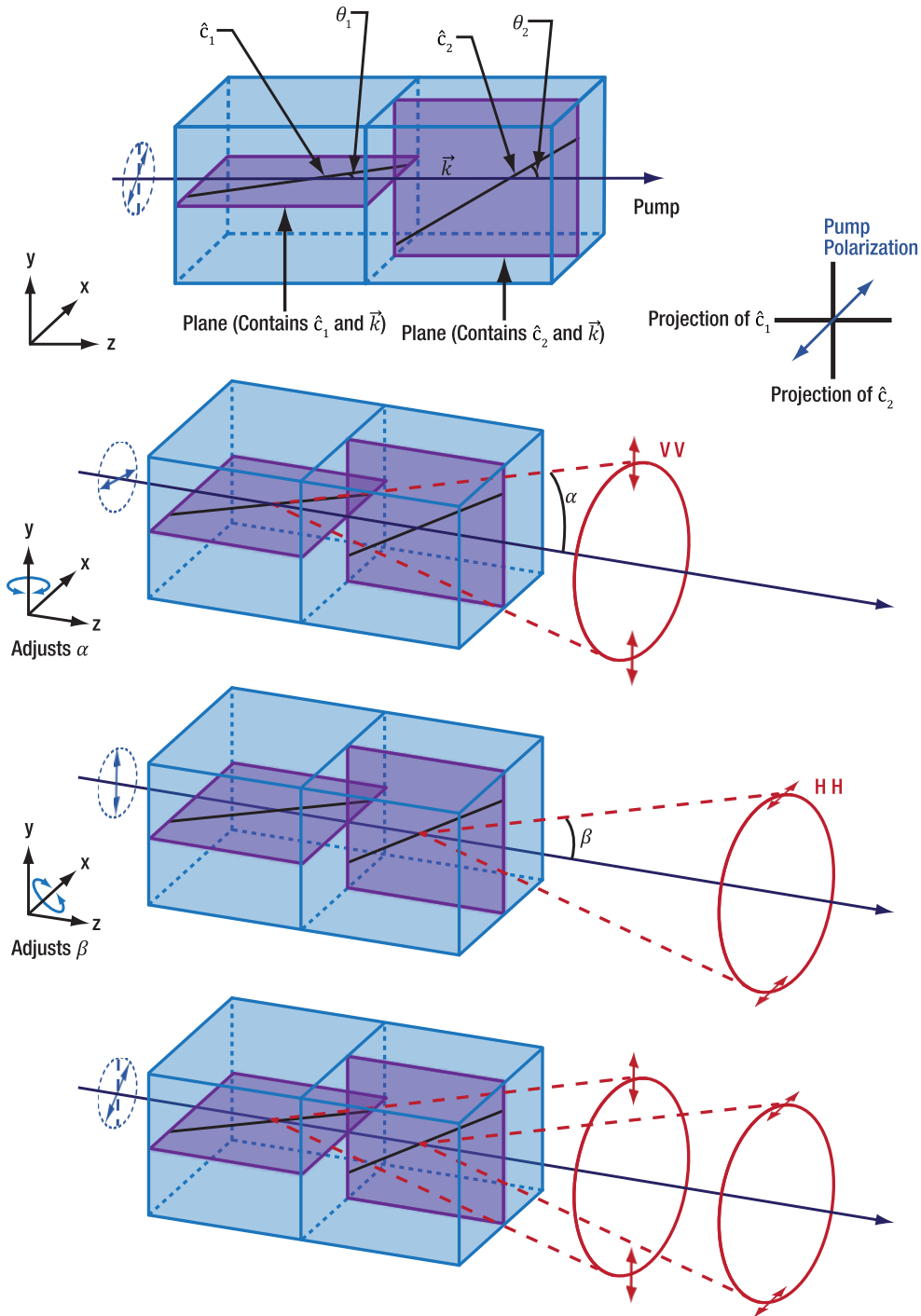


**Figure 196** Top Row: Side View of Crossed BBO Pair. The dark blue arrow indicates the pump beam direction. Black lines indicate the orientations of the optical axes of both crystals, with the purple planes acting as markers of the planes the optical axes are in. The pump beam polarization (dark blue double arrow) includes an angle of 45° with both purple planes. The bottom right figure in the top row shows the projection of the pump beam polarization and the crystals' optical axes looking towards the pump laser (z-axis). Rows 2 and 3: Overview of a crossed Type-I SPDC process using two BBO crystals. Each BBO crystal generates a photon pair cone. Due to the 90° rotation of the crystals against each other, the photon pair polarizations of each cone are orthogonal to each other. Both cones' opening angles can be adjusted separately by tuning the orientation of the crystal stack perpendicular to the respective optical axis (OA) as depicted in the respective coordinate systems. Row 4: Both crystals emit photon pairs on the cones shown in rows 2 ad 3 when the pump polarization is 45° to both optical axes. If these cones are tuned to overlap, the resulting state is polarization entangled.

In order to generate photon pairs in both crystals at equal rates, the pump beam polarization must contribute to the extraordinary polarization components in each crystal with the same amplitude, which means that the pump polarization must be oriented at a 45° angle with respect to the planes containing the optical axis and the pump beam in each crystal, as shown in Figure 196.

As described in Section 3.9, the polarization of photon pairs created by type-I SPDC is always perpendicular to the optical axis in the generating crystal. Figure 196 shows the generation processes for both polarization states in the respective crystal that fulfills the phase-matching conditions for the orthogonal pump polarization. Since polarization entanglement requires both the VV and HH polarized photon pairs to be otherwise indistinguishable from each other, detectors should be placed much further away from the crossed BBO pair than the thickness of the crystals in the pair. In such an arrangement, the emission/detection angle for both crystals are virtually identical.

A very important detail to note is that it is extremely unlikely to generate one photon pair in each crystal at the same time, which can easily be verified by a GRA experiment as described in Section 24.8. Polarization-entanglement does not require the simultaneous creation of two photon pairs with horizontal and vertical polarization. Neither can the crossed BBO pair crystal be viewed as a cannon that is shooting pairs randomly polarized in either the horizontal or vertical direction (which would be the mixed state described in Section 20.2.2). Instead, the two-photon polarization state created by the crossed BBO pair is a superposition of a photon pair with horizontal polarization and vertical polarization, simply because there is no way of telling which of the two crystals created the pair and thus which of the polarizations it must be. Again, this is analogous to the single photon interferometer, where nature tends to realize both pathways at the same time, as long as one cannot tell which path the photon took.

There is also no strict requirement to have the two crystals of the crossed pair stuck together face to face, it just allows the experiment to be set up with the rather simple geometry used in this kit. It may be helpful to consider both crystals<sup>140</sup> being placed into different arms of a Mach-Zehnder interferometer. Next, imagine a pump photon entering the interferometer and being cast into a superposition state of both interferometer arms, equal to  $(\frac{1}{\sqrt{2}}(|1\rangle_{\alpha}|0\rangle_{\beta} + e^{-i\phi}|0\rangle_{\alpha}|1\rangle_{\beta}))$  (compare to Section 3.6). Now, if depending on which arm the photon takes, there is a chance to produce either a horizontally or vertically polarized photon pair in the respective arm, such that the superposition state becomes  $\frac{1}{\sqrt{2}}(|HH\rangle_{\alpha}|0\rangle_{\beta} + e^{-i\phi}|0\rangle_{\alpha}|VV\rangle_{\beta})$ . After recombination at the second beamsplitter, the probability wavefunction at one of the output ports is then proportional to  $\frac{1}{\sqrt{2}}(|HH\rangle + e^{-i\phi}|VV\rangle)$ . Theoretically, the two pair generation processes could be arbitrarily far apart and still, one would be able to produce an entangled state. In practice however, such a setup is difficult to stabilize to a constant phase relationship for both interferometer arms and the colinear geometry of the pair production does not automatically separate the two photons of a pair.

Thus, bonding both crystals together does not cause any kind of interaction that magically creates entanglement. Instead, this is an easy way to guarantee well-defined and stable phase differences between horizontal and vertical polarizations. We even may keep the above interferometer analogy in the sense that the diagonally polarized pump photon is split into a superposition state of horizontal and vertical polarization, instead of being split by a beamsplitter into a superposition state of two pathways.

---

<sup>140</sup> For this example, one would need to cut the crystals slightly differently, such that the produced pair are emitted colinearly with the pump beam.

### 20.4.2 Walk-Off Effects

The content of this section applies to the experiments in Sections 24.5, 24.6, and 24.7.

As described in Section 20.2.6, mixing entangled states with a wide range of phases can mask their entanglement properties. This is generally unwanted in experiments but cannot be completely avoided, as will be explained in the following.

In every experiment, an ensemble of photon pairs is measured. If there are parameters in the setup that influence the phase of the pair state and vary from pair to pair, the ensemble state will be an integral over different pair states.

In the experiments in this kit, there are parameters that affect the phase, the detection angle  $\alpha$  and the pump wavelength  $\lambda$ . The entangled state of a single pair can then be written as:

$$|\psi_E(\alpha, \lambda)\rangle = \frac{1}{\sqrt{2}}(|HH\rangle + e^{-i\Phi(\alpha, \lambda)}|VV\rangle) \quad (185)$$

As shown in Section 20.2.6, the observability of entanglement is completely lost when the range of possible phases (maximum possible phase minus minimum possible phase) is  $360^\circ$  and every phase has the same probability. To ensure a good observability of entanglement, it is thus important to ensure that the probability distribution is concentrated on a narrow phase range, see Figure 197.

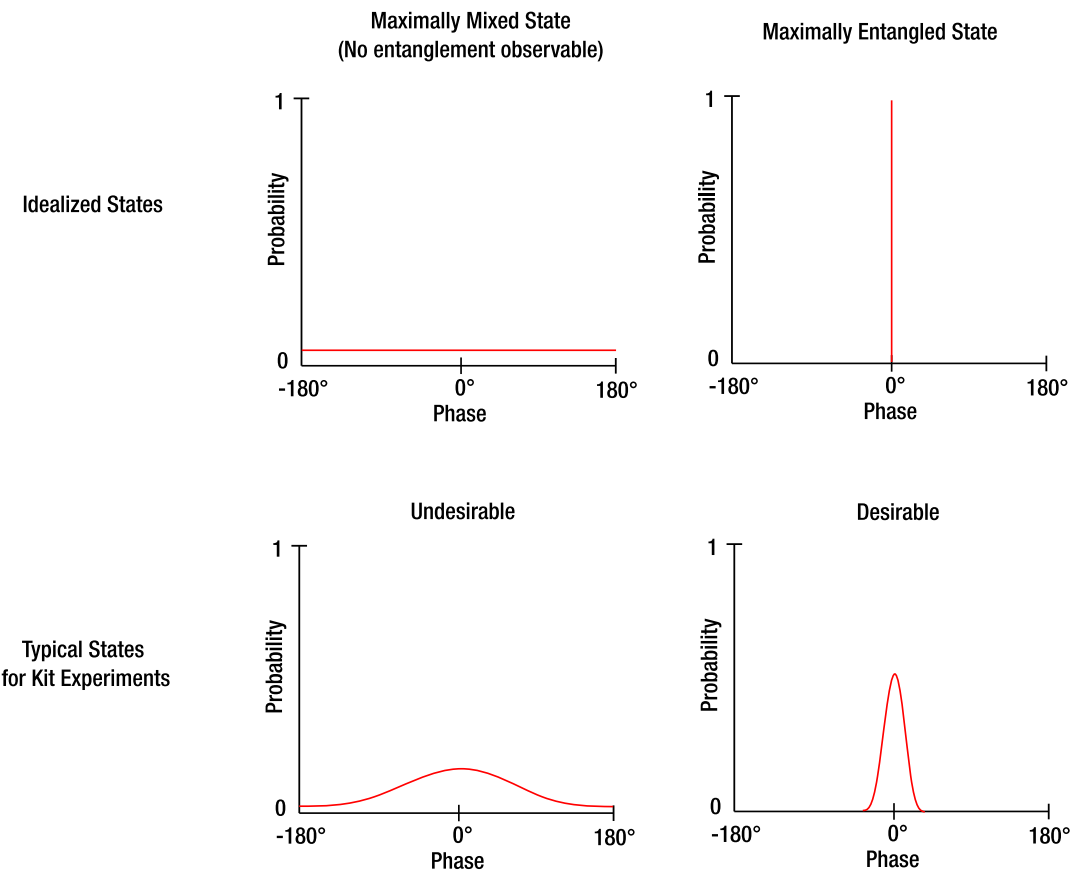


**Figure 197 Selected Probability Distributions of Phases in the Measured Photon Ensemble**

In the following, we take a closer look at why the detection angle and pump wavelength influence the entangled state and what can be done to keep the phase distribution narrow enough to observe entanglement in the measurements.

### Why does the detection angle vary between different detected photon pairs?

Not all photon pairs leave the crossed BBO pair under the same angle because the phase matching conditions of the SPDC process allow for different wavelength (and thus angle) combinations. In our experiment, we collect the photons in a certain angle range  $\alpha_{\min}$  to  $\alpha_{\max}$  (determined by the iris diameter in front of the detector optics) and focus them onto the detector chip<sup>141</sup>, as schematically shown in Figure 198.

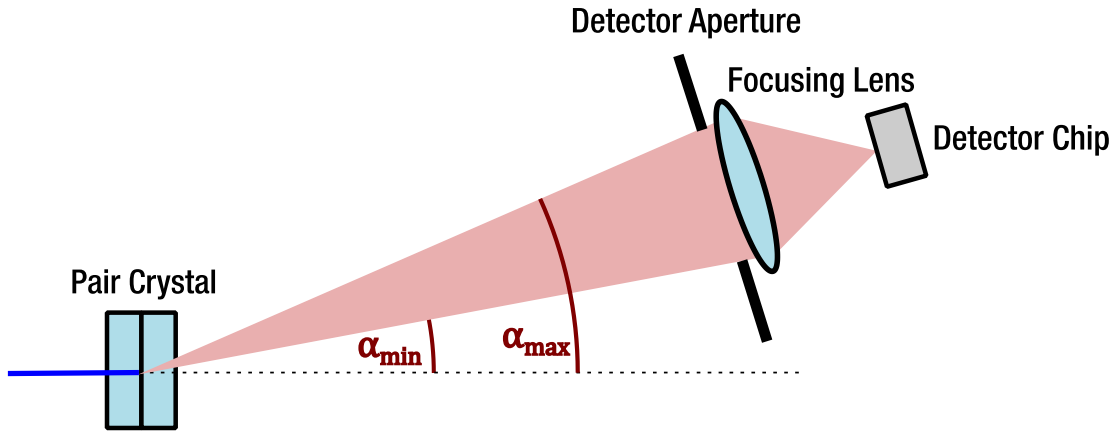


**Figure 198** Schematic Drawing of the Emission Angle Range Collected by the Detector Optic (Angles are Exaggerated)

### Why does the phase of the photon pair state depend on the detection angle $\alpha$ ?

The phase of the state of an entangled photon pair is determined by the optical path length difference (from pump laser to detector) between the VV-polarized pairs (generated in the first crystal of the crossed BBO pair) and the HH-polarized pairs (generated in the second crystal). Here we assume the pair is emitted symmetrically, so the path lengths of each of the photons of the pair from the crystal to the detectors are identical in length. Therefore, when determining the path difference contributing to the phase of the entangled state (the  $\Phi$  in equation (185)), we can just take twice the path difference of one of the photons in the pair.

Figure 199 shows the paths for two different detection angles in the schematic on the top left side, labelled 1 and 2. The bottom of the figure shows the paths of HH-polarized and VV-polarized pairs generated in the first or second crystal, with the paths shown in one plane. The blue paths contribute to the phase difference between the HH- and VV-polarized pairs (the red paths cancel out). The length of the blue paths is different when comparing the left and right sides. As established above, the path difference directly translates to the phase of the entangled state. Therefore, the entangled states detected under the angles 1 and 2 in Figure 199 have a different phase. More generally the phase will change along with the emission angle, as shown in the top right part of Figure 199. This effect is called spatial walk-off. A more quantitative explanation of the beam paths is given in Section 26.11.

<sup>141</sup> The detectors are very far away from the crystal compared to the diameter of the pump laser beam. It is therefore a reasonable approximation to treat the crystal as a point source so that the spot of a photon on the detector plane is determined solely by its emission angle.

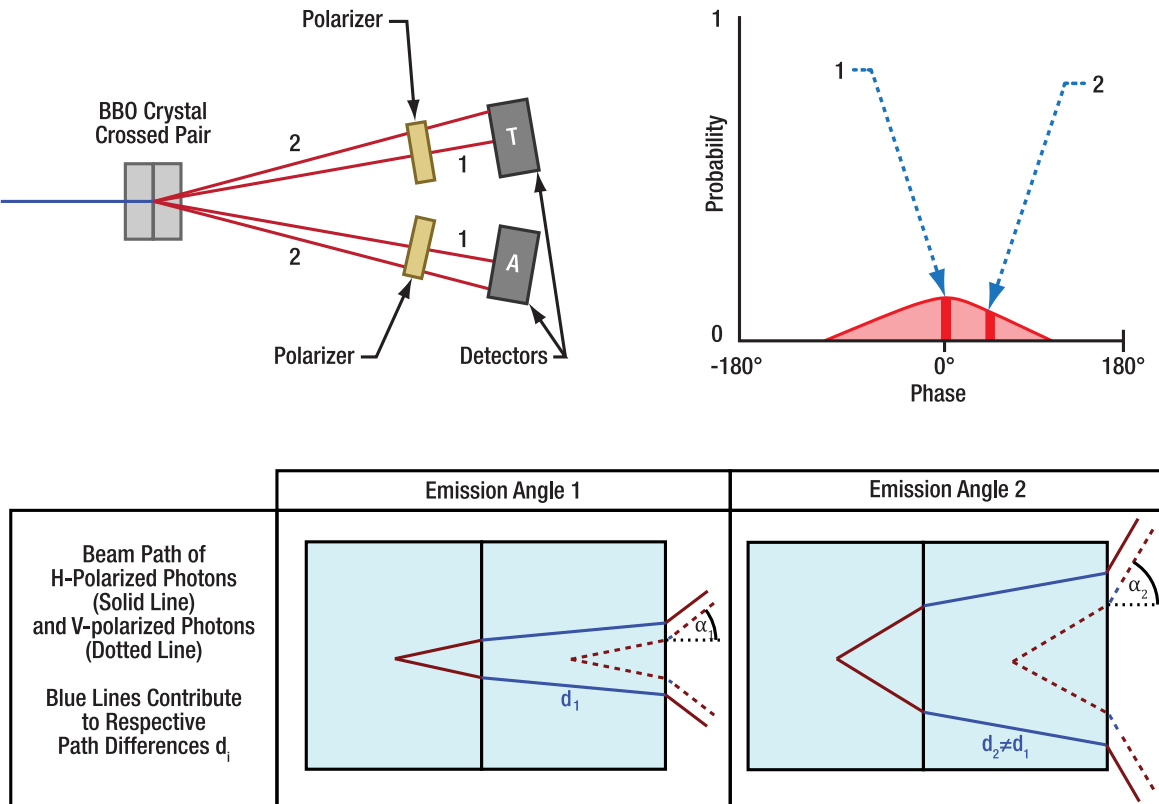


**Figure 199 The Effect of Emission Angle on the Entangled State Phase.** The top left image shows the Bell test measurement setup for two different emission angles, labeled 1 and 2. The top right shows the phase probability distribution function, with labels indicating the entangled state phase of angle 1 and 2. The bottom image shows a comparison of beam paths for HH-polarized pairs (solid lines) and VV-polarized pairs (dotted lines) through the crossed BBO pair crystal for two different emission angles (exaggerated angles for better visibility). The pump beam is omitted as its path is not dependent on the emission angle. Paths that contribute to the path difference between HH- and VV-pairs pairs, and therefore to the phase of the entangled state, are colored blue (red parts cancel out). The overall length of the blue paths is different for the two emission angles, hence the entangled state generated on the right side has a different phase than the one generated on the left.

### How can spatial walk-off be reduced?

The most straightforward way is to reduce the detector aperture. This allows a smaller range of detection angles and thus a smaller spread of phases in the detected ensemble. However, it also reduces the number of detected photons and therefore reduces the signal-to-noise ratio.

One could also choose a thinner pair crystal, which would lower the phase difference for the same angle difference. But this would reduce the rate of photon pair generations, causing the same signal-to-noise problem.

The best solution is to introduce additional birefringent crystals (Spatial Compensation Crystals or SCCs) into the path of the pair photons and design them so that they have the reverse walk-off effect of the pair crystal. Compensation of spatial walk-off with SCCs lowers the range over which the phase varies across all points in the detectors by about an order of magnitude compared to without compensation, leading to a narrower range of phases and thus more easily observable entanglement at higher signal-to-noise levels at a constant detector iris aperture size. For details, see Section 26.11. The experiments in Sections 24.5 and 24.6 explore the influence of the detector aperture size and SCCs on the results of the Bell test measurements.

### Why does the pump wavelength vary between different detected photon pairs?

No laser is perfectly monochromatic; hence the pump laser has some spectral distribution around its center wavelength. In our kit, a common laser diode is employed which has a relatively broad distribution, with about 0.5 nm full width at half maximum<sup>142</sup>.

### Why does the phase of the photon pair state depend on the pump wavelength?

Let's assume a fixed detection angle. Then, there is a fixed geometrical path difference between the V- and H-polarized photons inside the pair crystal. Furthermore, the pump itself must travel a different optical path inside the pair crystal to generate H- compared to V-polarized photons, thus picking up a different phase. Additionally, due to dispersion and birefringence, different pump wavelengths (and the resulting pair photon wavelengths) "see" different optical indices inside the crystals.

As a result, the optical path difference (and hence the phase of the pair state) varies with the pump wavelength even for identical geometrical paths. This effect is called spectral or temporal walk-off and is explained in more detail in Section 26.12.

### How can temporal walk-off be reduced?

Thinner pair crystals will lead to lower phase variations for the same variation of the pump wavelengths, but as explained above, this also reduces the number of generated photon pairs and thus negatively affects the signal-to-noise ratio.

A better approach is to use a laser with an especially narrow spectral distribution (so-called single frequency lasers) to pump the crystal, which is, however, quite expensive.

Analogous to spatial walk-off, temporal walk-off can be compensated by an additional birefringent crystal. Here, the compensation crystal, placed in front of the pair crystal, delays one polarization component of the pump against the other, pre-compensating the temporal walk-off of the crossed BBO pair. A more quantitative description is given in Section 26.12.

### Summary

- The phase of the entangled state of a single photon pair depends on its detection angle (spatial walk-off) and the pump wavelength generating it (temporal walk-off).
- An experiment is always an integration over many photon pairs, with a varying phase depending on the factors above.
- If the range of possible phases at the detector is too large, entanglement effects cannot be observed anymore due to the mixing of different entangled states.
- In our kit, additional birefringent crystals are used to reverse the walk-off effects and keep the phase range small (in the range of 10° to 50°), ensuring good entanglement observability.

#### 20.4.3 Entangled State Phase Adjustment

---

##### The content of this section applies to the experiments in Section 24.4.1

After having ensured that the phase spread of the entangled state is low enough for a good observability of entanglement in measurements, one can approximate the mixed state by the pure entangled state with a fixed phase (center of the phase distribution). However, one still requires a way to properly set this center phase (the  $\Phi$  in  $\frac{1}{\sqrt{2}}(|HH\rangle + e^{-i\Phi}|VV\rangle)$ , referred to simply as "phase" in the following) of the entangled state to a certain value.

---

<sup>142</sup> The spectral distribution is non-gaussian and depends on the distribution of lasing modes in the diode. These in turn vary depending on the operating conditions of the laser diode (i.e., diode current and temperature) and due to production variances.

All experiments in the kit make use of linearly polarized Bell states to show entanglement properties. Thus, according to Section 20.3.4, we must adjust the phase to  $\Phi = N \cdot \pi$ ,  $N \in \mathbb{N}$ , where even or odd  $N$  correspond to the  $|\Phi^+\rangle$  or  $|\Phi^-\rangle$  Bell State. The default software parameters for the Bell test are chosen for the  $|\Phi^+\rangle$  Bell state.

As discussed in previous sections, the phase of the entangled state depends on all the birefringent elements between the pump laser source and the polarizers. **This means that any change to one of those elements affects the state phase to some extent. Therefore, adjusting the state phase should always be the last step when the setup is realigned.** The required changes to the phase (or equivalently: birefringent path lengths) are less than one wavelength to switch between the states of interest and on a similar order of magnitude as the spatial phase compensation in the SCCs, but orders of magnitude smaller than the phase differences in the crossed BBO pair or TCC.

In this kit, adjusting the state phase by tilting the SCC does not work well in practice, as it affects the spatial compensation in addition to the state phase. Tilting the crossed BBO pair has a rather strong effect on the state phase, but it also affects the phase matching and efficiency of the pair creation processes (see Section 3.9). Tilting the pump half-wave plate<sup>143</sup> is not sensitive enough and also affects the polarization state negatively. However, the TCC introduces a sufficiently large phase shift between both polarizations (together with group delay), such that tilting it causes sufficiently large changes in the phase shift, without worsening the group delay notably. Furthermore, tilting the TCC perpendicular to the optical axis does not affect the pump polarization state<sup>144</sup>, the pair generation efficiency, or spatial walk-off.

The change of the entangled state phase is then equal to the change of the phase shift between the horizontal and vertical polarization components of the blue pump beam when adjusting the TCC tilt angle perpendicular to its optical axis. The calculation of this phase shift is identical to the calculation of  $\Phi_{\text{tot,comp}}$  as described in Section 26.11, only that one has to consider the blue pump beam and the TCC instead of the infrared pair photons and the SCC. The change is then the difference between two settings of the tilt-angle  $\alpha$ :

$$\Delta\Phi = \Phi_{\text{tot,comp}}(\alpha_{\text{tilt},1}) - \Phi_{\text{tot,comp}}(\alpha_{\text{tilt},2}) \quad (186)$$

Whether entanglement is observable (i.e., walk-offs compensated well enough) and the phase is set correctly can be verified by the same measurement that was introduced in Section 20.2.4: if the coincidence rate is measured with polarizers introduced at a 45° angle in front of the detectors, there will be oscillations in the coincidence count rate, proportional to the phase of the entangled state (see Equation (178)). The amplitude of those oscillations depends on the spread of the phase distribution<sup>145</sup> introduced by walk-off effects as discussed above.

Figure 200 shows a calculated oscillation curve when the TCC is tilted. Using the calculation methods laid out in Section 26.12, we determined an approximately linear dependence between the TCC tilt angle and the induced change in the phase difference  $\Delta\Phi$ , requiring a tilt angle of 1.2° for one oscillation period (360° phase change for  $\Delta\Phi$ ).

<sup>143</sup> The polymer waveplate used for rotation of the pump beam polarization has a rather flat retardance vs. angle-of-incidence curve. For phase adjustments with a separate waveplate, it is advisable to use a quartz plate like the WPMH05M-405 waveplate instead, with the fast axis oriented horizontally. The phase may then be adjusted by rotating the plate around the post axis.

<sup>144</sup> Strictly speaking, this changes the ellipticity of the polarization state, since the phase between H and V polarizations is changed. However, the amplitudes remain unchanged - which is the important polarization characteristic in this case.

<sup>145</sup> Assuming identical pair detection rates for both "individual" pair generation processes in both crystals. If more vertically or horizontally polarized photons are generated/detected, this also lowers the oscillation amplitude.

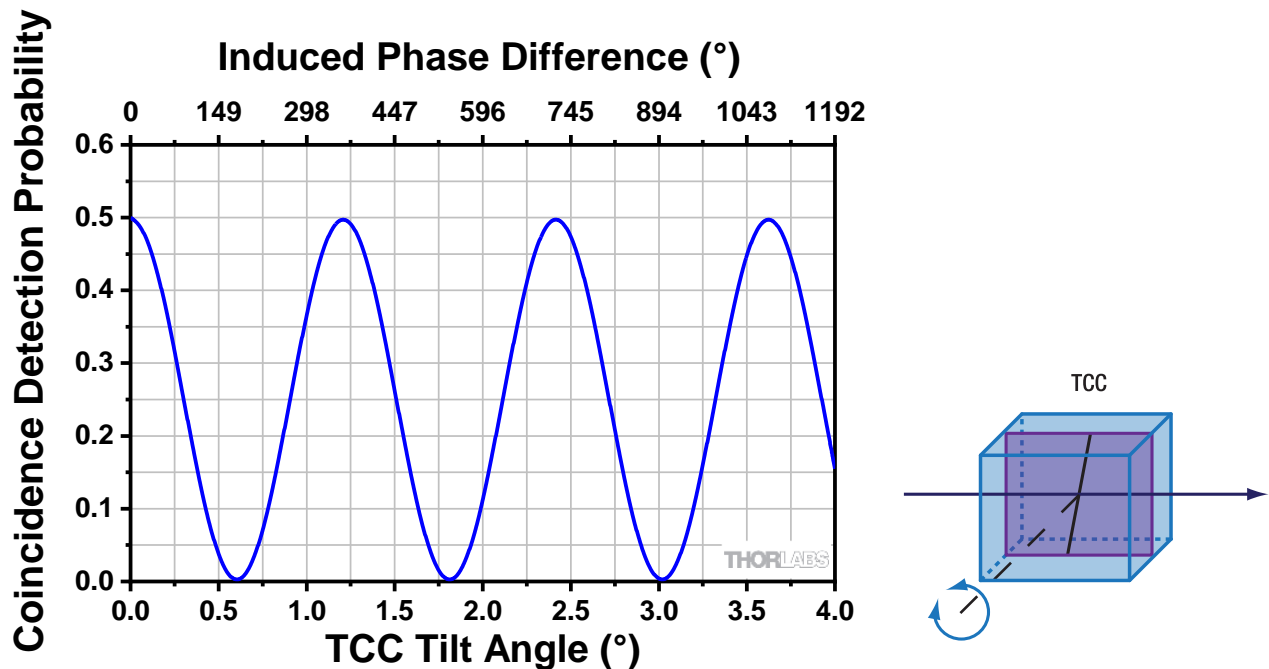


Figure 200     Change of the Phase Difference When the TCC is Tilted, Leading to Oscillations in the Coincidence Detection Probability When Both Polarizers in Front of the Detectors are set to 45°.

## Chapter 21 Addon Components

In cases where the metric and imperial kits contain parts with different item numbers, metric part numbers and measurements are indicated by parentheses unless otherwise noted.

### 21.1 Crystals

			
<b>1 x Crossed BBO-Crystal Type 1</b> 2x 1.2 mm Thick, Cutting Angle: 29.2°	<b>1 x Temporal Compensation BBO-Crystal</b> 0.85 mm Thick, Cutting Angle: 80.0°	<b>2 x Spatial Compensation BBO-Crystal</b> 1.2 mm Thick, Cutting Angle: 12.7°	<b>2 x 1" Marked Mirror Mount<sup>146</sup></b> Kinematic Mirror Mount with Centering Plate with Extra Markings
			
<b>3 x KB1X1 (KB25/M)</b> Magnetic Base, 1" x 1" (25 mm x 25 mm)	<b>1 x KBT1X1 (KBT25/M)</b> Magnetic Top Plate, 1" x 1" (25 mm x 25 mm)	<b>2 x 1/2" Marked Mirror Mount<sup>147</sup></b> Kinematic Mirror Mount with Centering Plate with Extra Markings	<b>1 x 1/4"-80 Removable Knob, Blue<sup>148</sup></b>
			
<b>2 x Ø1/2" Post Spacer, 4 (5) mm Thick<sup>149</sup></b>	<b>2 x RS2P8E (RS2P4M)</b> Ø1" (Ø25.0 mm) Pedestal Post, 8-32 (M4) Tap, 2" (50 mm) Long	<b>1 x TR2 (TR30/M)</b> Ø1/2" Optical Post, 2" (30 mm) Long	<b>1 x PH1E<sup>150</sup></b> Ø1/2" (Ø12.7 mm) Pedestal Post Holder, Magnetic, 1.19" (30.1 mm) Long

<sup>146</sup> This is a KM100CP(/M) mount with extra engravings. For a replacement, please contact Tech Support ([techsupport@thorlabs.com](mailto:techsupport@thorlabs.com)).

<sup>147</sup> This is a KM05(/M) mount with extra engravings and custom thumbscrews. For a replacement, please contact Tech Support.

<sup>148</sup> Replacements can be ordered in packs of 10 as item # F25SSK1-BLUE.

<sup>149</sup> Replacements can be ordered in packs of five as item # TR4M (TR5M).

<sup>150</sup> The EDU-QOPA1/M kit comes with a 30.1 mm tall post holder. For a replacement, please contact Tech Support.

## 21.2 Polarization Optics

			
<b>2 x LPNIRB050-MP2</b> Ø1/2" SM05-Mounted Linear Polarizer, 650 - 1100 nm	<b>2 x SM1A6</b> Adapter with External SM1 Threads and Internal SM05 Threads	<b>2 x RSP1X225(/M)</b> Rotation Mount for Ø1" (Ø25.4 mm) Optics, 360° Continuous or 22.5° Indexed Rotation	<b>2 x RS2P8E (RS2P4M)</b> Ø1" (Ø25.0 mm) Pedestal Post, 8-32 (M4) Tap, 2" (50 mm) Long

## 21.3 Mounting, Tools, and Software

		
<b>1 x CF125-P5</b> Clamping Fork, 1.24" Counterbored Slot, Universal, 5 Pack	<b>1 x Label Sheet</b>	<b>1 x USB Stick</b> EDU-QOP1 Software

## 21.4 Included Hardware

### 21.4.1 Imperial Kit

Type	Qty.
8-32, 1/4" Long Cap Screw	5
8-32, 1/2" Long Cap Screw	2
8-32, 1/2" Long Setscrew	2
1/4"-20, 3/8" Long Cap Screw	5

### 21.4.2 Metric Kit

Type	Qty.
M4 x 0.7, 6 mm Long Cap Screw	5
M4 x 0.7, 12 mm Long Cap Screw	2
M4 x 0.7, 12 mm Long Setscrew	2
M6 x 1.0, 10 mm Long Cap Screw	5

## Chapter 22 Setup

### 22.1 Assembly of Components

#### 22.1.1 Crystals

- Assemble the crossed BBO Crystal Pair as shown on the left side of Figure 201.
- Please note:
  - During step 1, make sure to align the marked edges as parallel as possible.
  - Make sure to align the crystal with respect to the markings on the KM100CP(/M) mount as shown on the right side of Figure 201. Use the nylon-tipped screw of the KM100CP(/M) mount to hold the crystal in place. Firmly hold the crystal in place while engaging the nylon-tipped screw and check afterwards for proper alignment. Rotation of the crystal in the mount can negatively impact the quality of the experimental results later on.

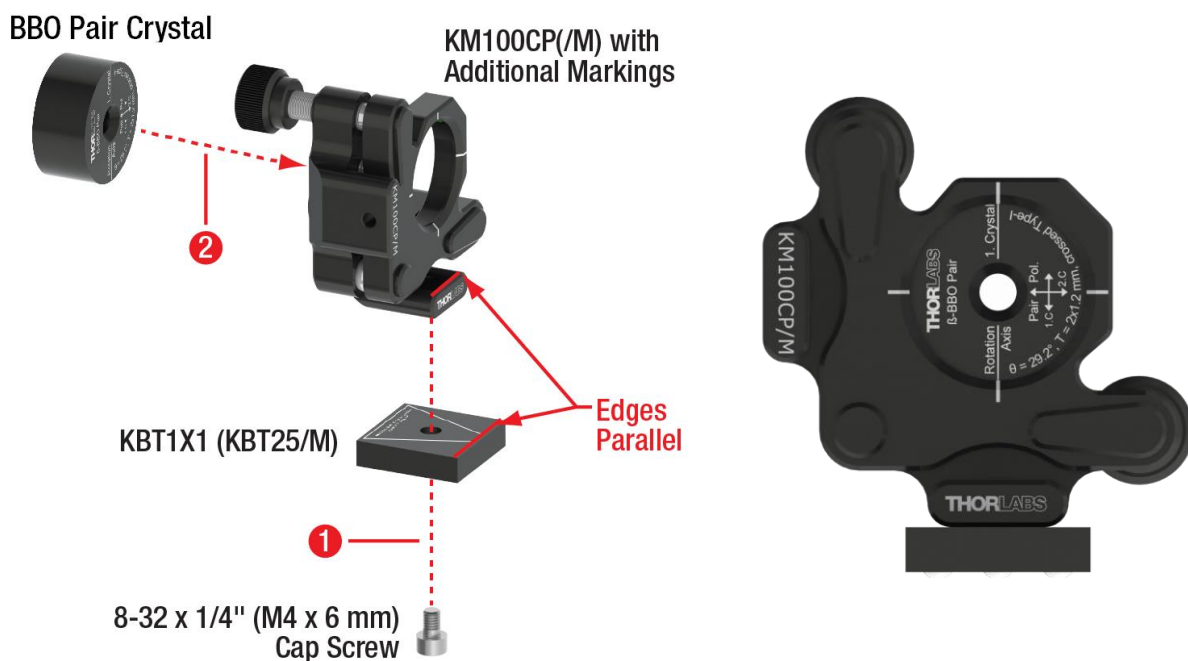


**Figure 201**      **Assembly (Left) and Orientation (Right) of the Crossed BBO Pair Crystal**

- Assemble the BBO Crystal for temporal compensation ( $80^\circ$  cut-angle, 0.85 mm thickness, see right side of Figure 202) as shown on the left side of Figure 202.
- Please note:
  - During step 1, make sure to align the marked edges as parallel as possible.
  - Make sure to align the crystal with respect to the markings on the KM100CP(/M) mount as shown on the right side of Figure 202. Use the nylon-tipped screw of the KM100CP(/M) mount to hold the crystal in place. Firmly hold the crystal in place while engaging the nylon-tipped screw and check afterwards for proper alignment. Rotation of the crystal in the mount can negatively impact the quality of the experimental results later on.
  - After completion, replace the black knob on the upper adjustment screw with a blue knob (see right side of Figure 202). Use the 5/64" (2 mm) balldriver to hold the upper adjustment screw in place while unscrewing or screwing the knobs.

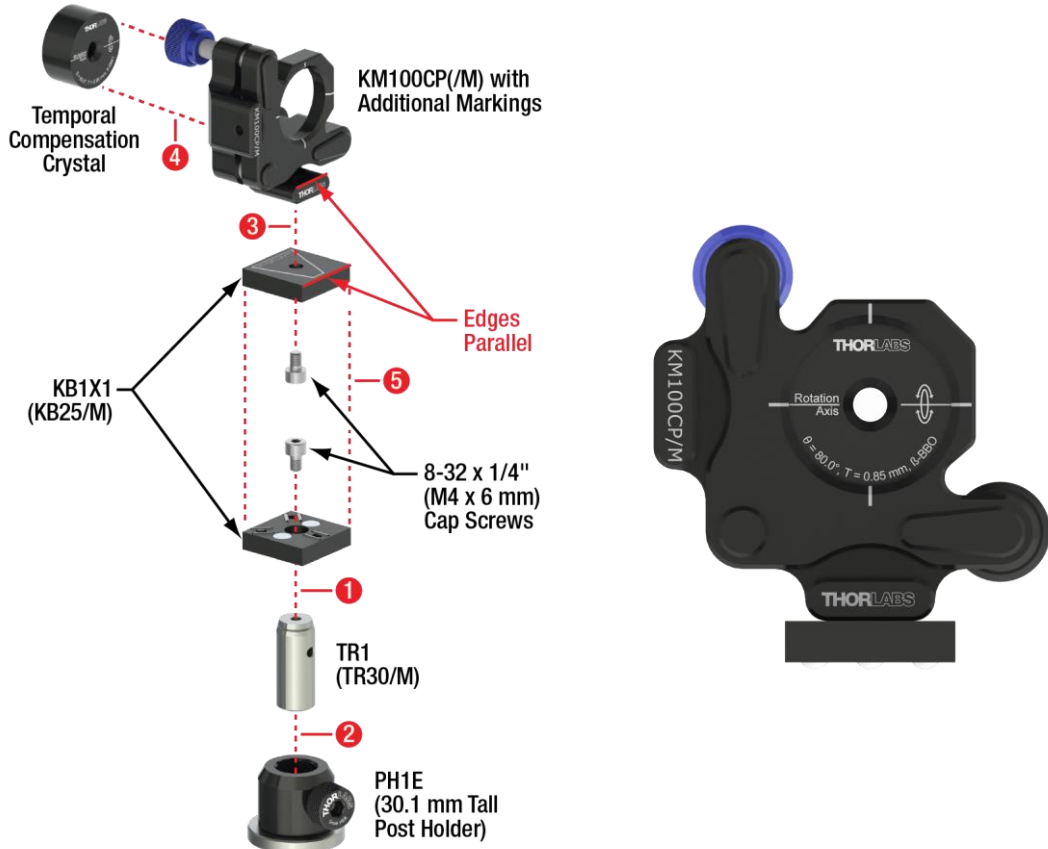


**Figure 202      Assembly (Left) and Orientation (Right) of the Temporal Compensation Crystal**

- Assemble one of the BBO Crystals for spatial compensation (crystals in 0.5" mounts) as shown on the left side of Figure 203.
- Please note:
  - During step 1, make sure to align the marked edges as parallel as possible.
  - Make sure to align the crystal with respect to the markings on the KM05(/M) mount as shown on the left side of Figure 204. Use the nylon-tipped screw of the KM05(/M) mount to hold the crystal in place. Firmly hold the crystal in place while engaging the nylon-tipped screw and check afterwards for proper alignment. Rotation of the crystal in the mount can negatively impact the quality of the experimental results later on.
- Assemble the second BBO Crystal for spatial compensation in the same way, but with the vertical arm of the KM05(/M) mount on the opposite side and with the crystal housing rotated by 180° in the mount (see right sides of Figure 203 and Figure 204).

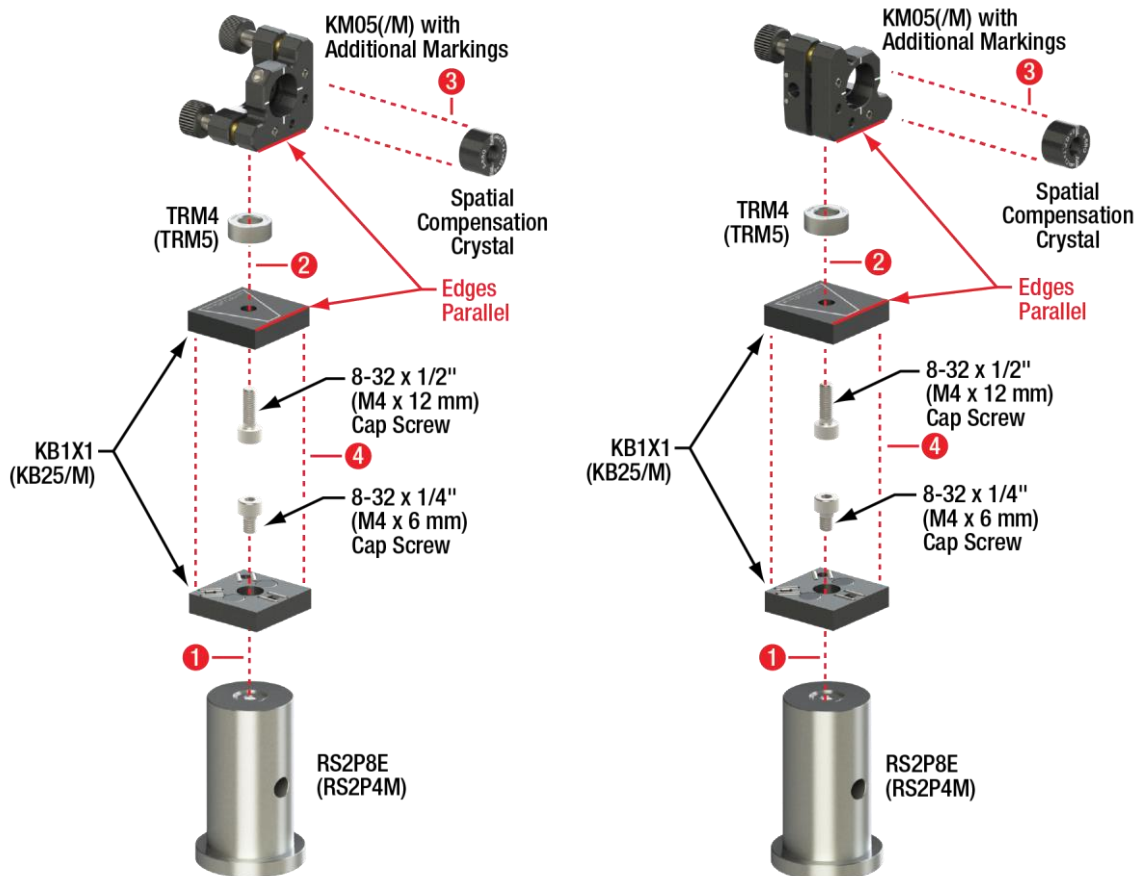


**Figure 203      Assembly of the Spatial Compensation Crystals**



**Figure 204      Orientation of the Spatial Compensation Crystals**

### 22.1.2 Polarizers

- Remove the retaining rings from the two RSP1X225(/M) mounts and assemble two polarizer components as shown on the left side of Figure 205.
- Please note:
  - During step 4, screw the SM1A6 adapter with the polarizer into the RSP1X225(/M) mount until about 3 mm of the SM1 thread is free on the front side of the mount, such that the SM1RR retaining ring can fit in completely.
  - During step 5, use an SPW909 spanner wrench from the backside and an SPW606 from the frontside to counter the SM1A6 adapter and the SM1RR retaining ring against each other.
  - Tighten the locking screw on top of the RSP1X225(/M) rotation mount. Then loosen the two screws on the front of the mount and rotate the scale until the 90° marker is parallel to the transmission axis of the polarizer (as marked on the LPNIRB050-MP2 housing). Re-tighten the screws to fix the scale. The correct orientation is shown on the right side of Figure 205.
  - For precise alignment of the polarizer axis, it is necessary to calibrate the scale in the setup. If you already have a calibrated polarizer (e.g. from the Quantum Eraser experiment, then you can use this to calibrate the new ones, as described in Section 7.7. Otherwise, you can calibrate the polarizer as described in Section 7.2.3.

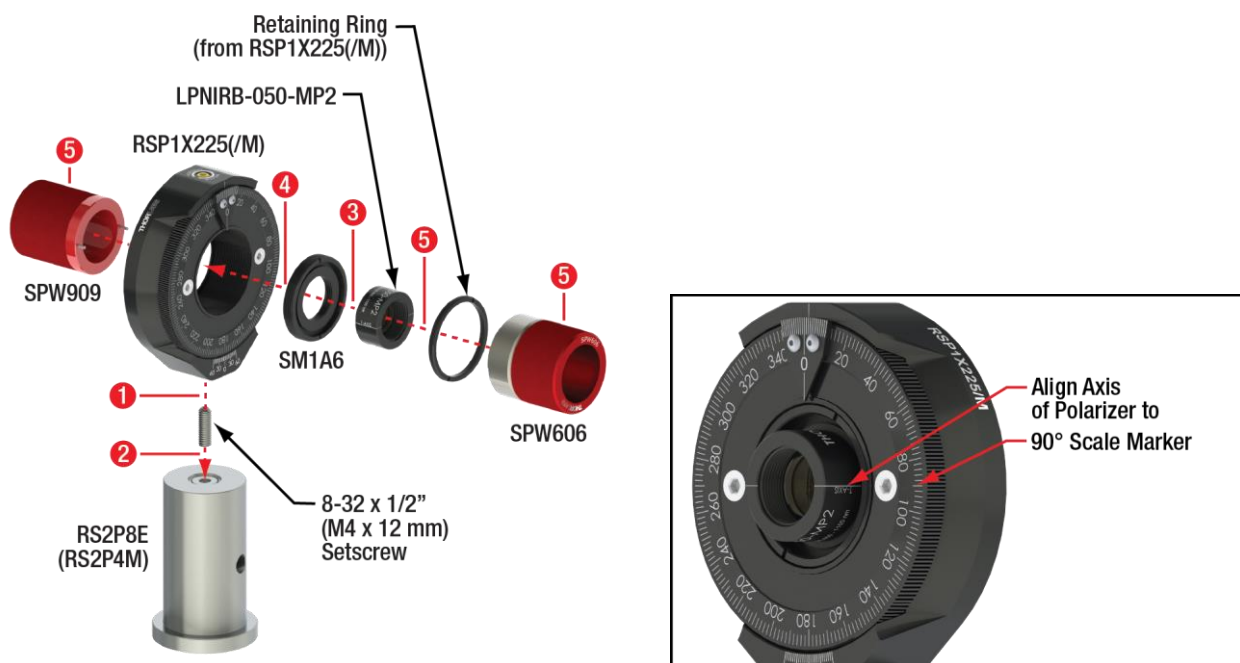


**Figure 205** The left image shows the assembly of a polarizer (assemble two of these). The right image shows the correct orientation of the scale. The transmission axis of the polarizer should line up with the 90° marker of the scale.

## 22.2 Setting up the Entangled Pair Source

This chapter describes the setup procedure based upon the pair source setup of the base kit EDU-QOP1(/M) (up to and including Section 7.4.4). You should have already aligned the following parts:

- Red alignment laser and blue pump laser aligned to both irises of the main beam path.
- Detectors placed and aligned to the Axicon cone.
- Detectors optics aligned to the signal of the colored glass filter.

We assume that the detector delay is already properly calibrated – it is not affected by exchanging the SPDC crystals. It is not necessary to align the pair source with the base kit crystal NLCQ3 first; the crossed BBO pair can be used directly after alignment with the colored glass filter. If the detector delay is not yet calibrated, use a coincidence window of 20 ns up to step 5 below and adjust the detector delay according to Section 7.4.5 afterwards. The completely aligned setup is shown in Figure 206 with the numbers marking the component to be adjusted in the respective step of the alignment procedure.

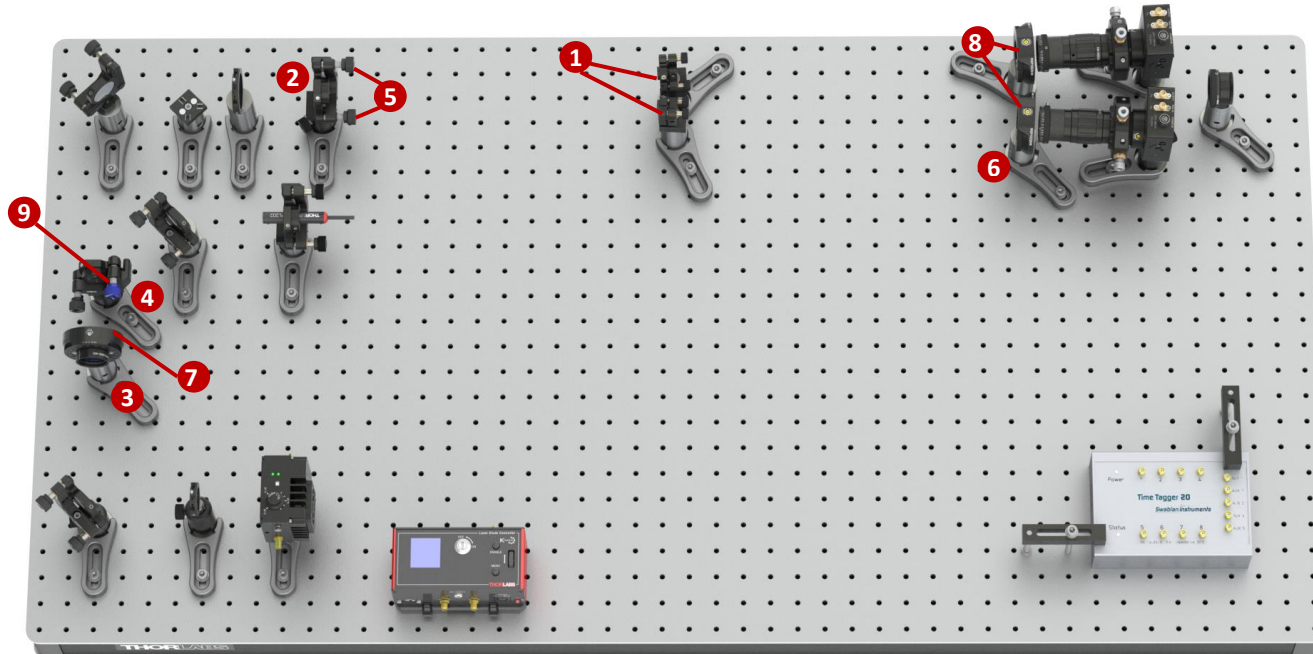


**Figure 206** Complete setup for Bell test. The numbers indicate which component should be adjusted for the respective step number in the alignment procedure.

1. Put the axicon and the alignment laser mirror in the beam path and use the red laser cone to place the spatial compensation crystals in both arms of the cone.
  - Place one of the spatial compensation crystal components between the axicon and one of the detectors at 30 cm distance between the front plates of the KM100CP(/M) axicon mount and the KM05(/M) crystal mount. If you already have placed the Ø8.0 mm iris component from the base kit, you can place the crystal closely in front of it.
  - The crystal must be oriented such that the beta-BBO labels on the front are rotated by 90° towards the inside of the cone (see Figure 207).
  - Place the alignment target halfway between the axicon and the crystal, about 15 cm in front of the crystal.

- Ensure that the cone hits the center of the crystal at normal incidence by observing the back-reflection on the alignment target (see right side of Figure 207), then fix the position of the crystal with a CF125 clamp and a 1/4" 20 x 3/8" (M6 x 10 mm) cap screw plus washer. You can use the kinematic screws of the crystal mount to fine-adjust the orientation (center the back-reflection on the target hole). Use an alignment card to check that the light from the laser is well centered on the crystal.
- Repeat the above procedure with the second crystal in the other arm.
- Optional: In case you want to start out conducting experiments without spatial compensation (as discussed in Section 24.9), remove the spatial compensation crystals from their magnetic mounting bases now and continue the remaining steps. The compensation crystals may be inserted later and are already aligned. After adding or removing the spatial compensation crystals one has to repeat the alignment from step 7 onwards.

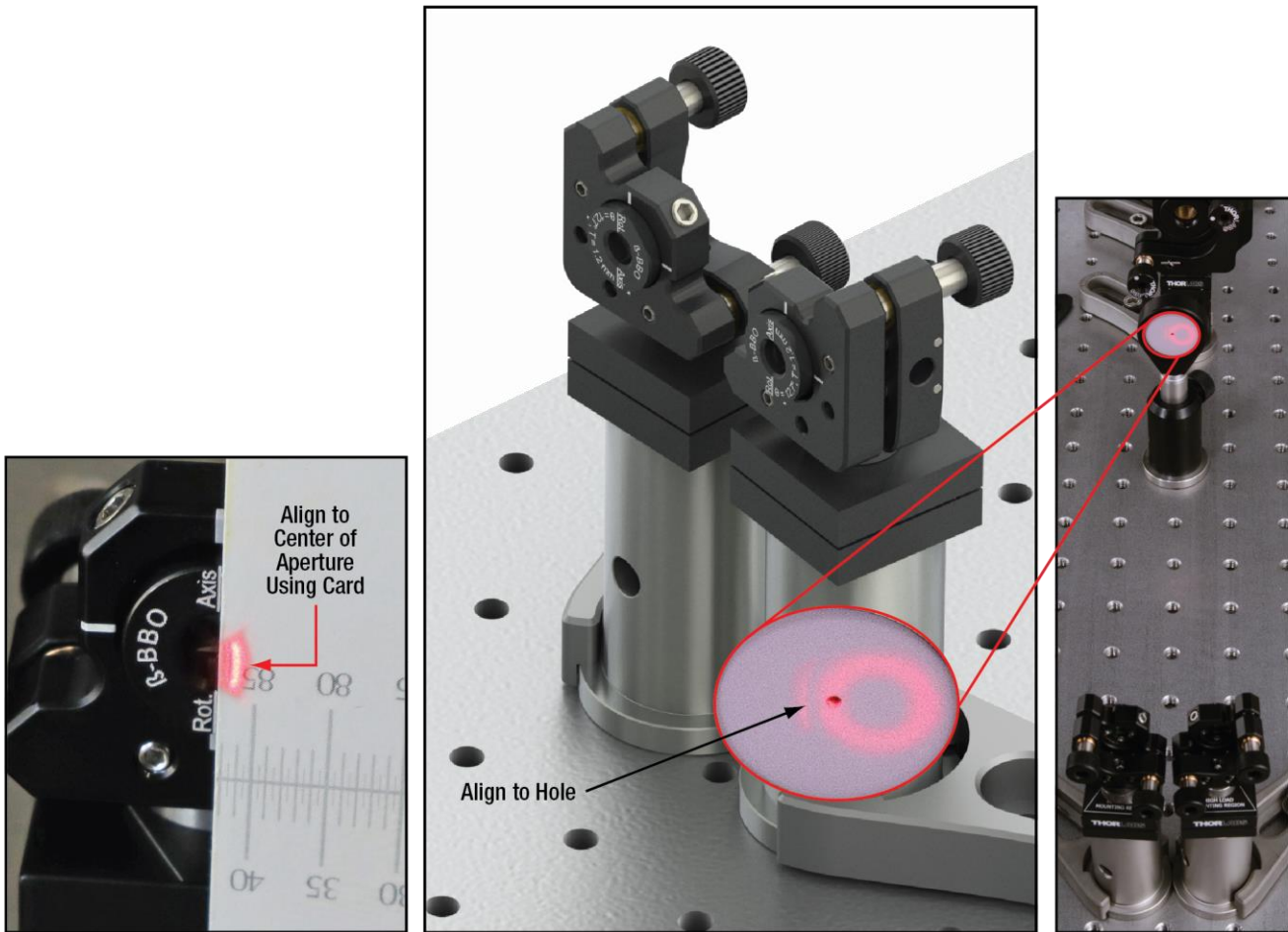


**Figure 207 Alignment and Positioning of the Spatial Compensation Crystals (Left and Center) and Adjusting Their Orientation via the Back Reflection (Right)**

2. Take the new crossed BBO pair and mount it in place of the axicon. Use the kinematic screws of the mount to align the orientation of the crossed BBO pair such that its back-reflection falls back through the hole in the iris in front of the crystal. Switch off the alignment laser and remove the mirror on the magnetic mount.
3. Turn the pump half-waveplate (HWP) to the 22.5° setting, ensuring that the polarization incident onto the BBO is oriented along the 45° axis.
4. For phase adjustment of the entangled state and temporal walk-off compensation, insert the temporal compensation BBO crystal after the pump HWP:

- Place the temporal compensation crystal ( $\theta = 80^\circ, T = 0.85$  mm) mounted onto the magnetic post holder between the HWP and the second pump mirror (hole 3|14, see Figure 208), with the adjustment screws of the crystal mount pointing towards the HWP.
- Reduce the diode current for the blue pump laser just below lasing threshold and switch on the laser.
- Adjust the position and post height of the crystal until the pump beam passes the center of the crystal.
- Fix the position using a CF125 clamp and a 1/4" 20 x 3/8" (M6 x 10 mm) cap screw plus washer.
- Place the alignment target between the pump HWP and the crystal, such that the pump beam passes through the hole in the target. If necessary, adjust the height of the alignment target for the blue pump laser to pass through, but set it back to the original main beam height afterwards.<sup>151</sup>
- Align the temporal compensation crystal via the kinematic screws of the crystal mount such that the back reflection is aligned with the hole of the alignment target. The laser diode current may be increased above the lasing threshold to increase the visibility of the spot on the target through the laser safety goggles.

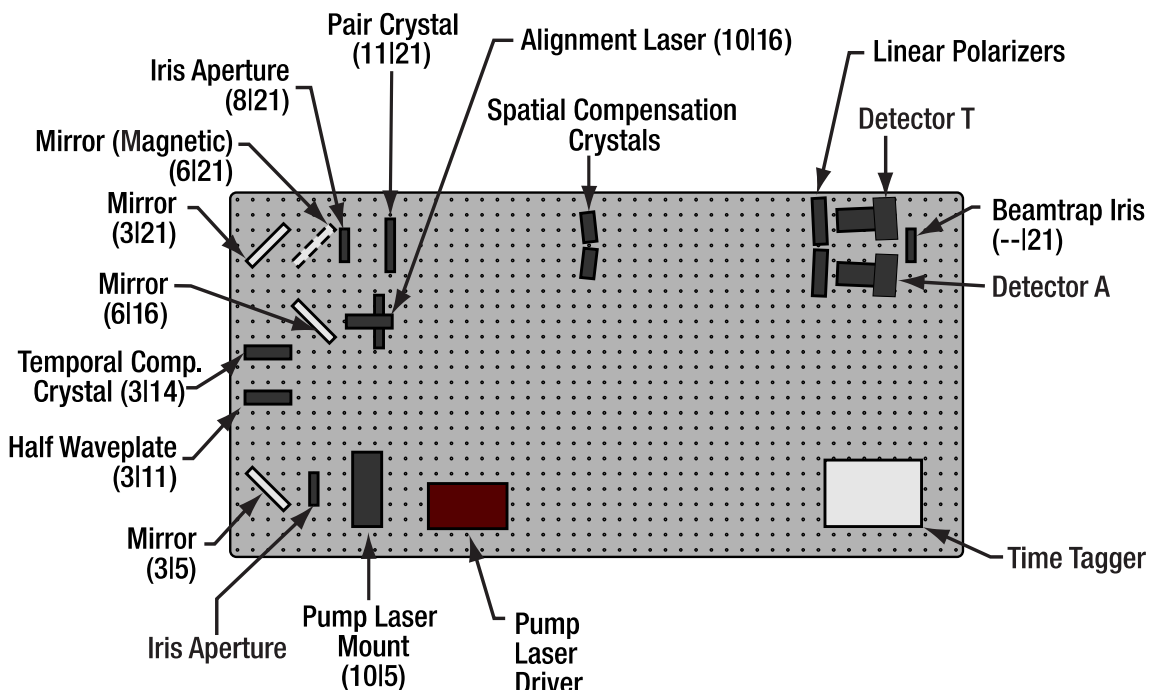


**Figure 208      Overview of component positions. The numbers in parentheses are breadboard hole numbers (from left / from bottom). Components are not to scale and exact positions may deviate slightly from those given in text.**

<sup>151</sup> Depending on the emission angle of the pump laser assembly, the beam may pass the half-waveplate under a small angle. This is not an issue for the experiments in the kit, as the retardance of the polymer waveplate is rather insensitive to the angle of incidence. See also Section 13.2 on how to correct the pump-laser emission angle.

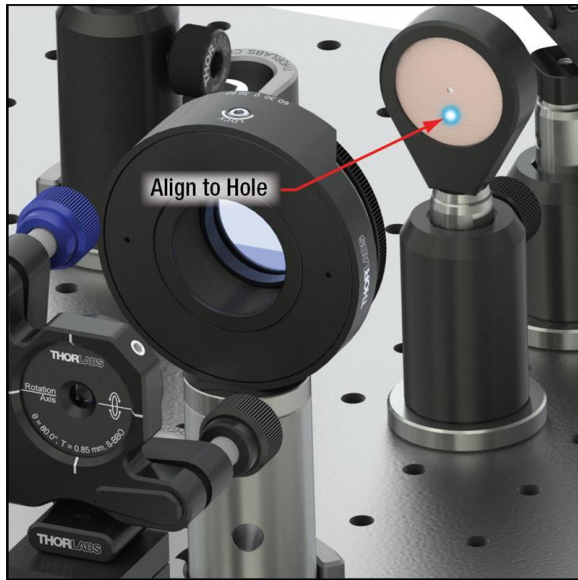


**Figure 209 Positioning of the Temporal Compensation Crystal and Adjustment via Back Reflection**

5. Increase the laser current, such that the optical output power is 20 mW, based on your diode's data sheet (compare to Figure 87). Ensure that the irises in front of both detectors are fully open. Adjust both axes of the crossed BBO pair mount to maximize the coincidence rate at the detectors, by using both **kinematic** screws of the KM100CP(/M) mount. In contrast to the crystal used in the base kit, it is important to find the maximum position for both axes. If you detune one axis away from the optimal setting, there should still be some coincidence count rate left. With both axes optimized, you should see at least 15 kHz for the coincidence count rate. Usually, one axis contributes more to the count rate than the other, which is not a problem (this will be corrected in a later step).

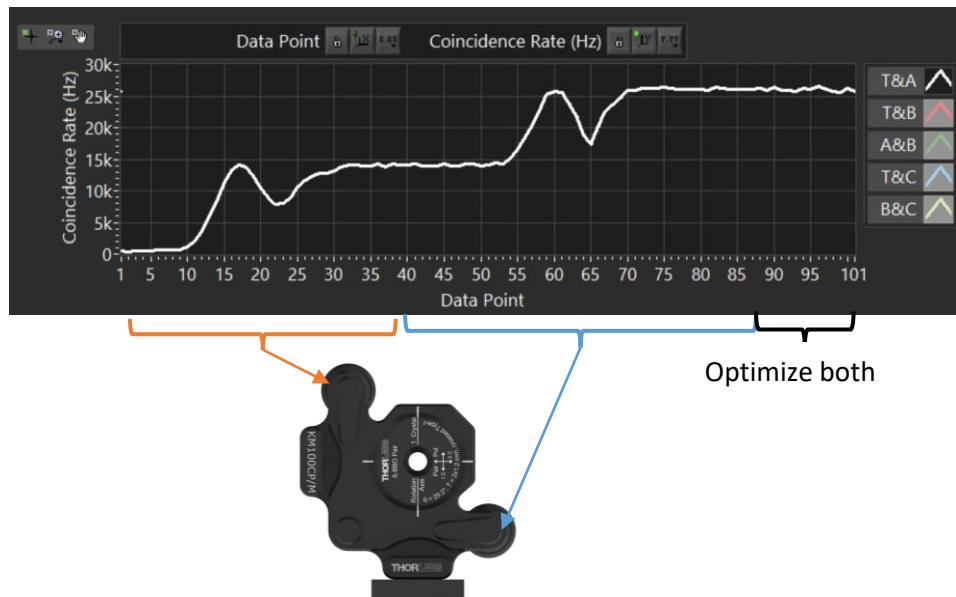


**Figure 210 Alignment Process for Both Axes of the Crossed BBO Pair: One of the axes is adjusted first, passing fully over the signal peak to clearly identify the maximum (at data point 17). The adjuster is then turned back to the maximum coincidence rate (at data point 32). Afterwards, the same procedure is repeated with the other axis. Finally, both adjusters are slowly turned iteratively to verify both axes are fully optimized (no further increase of coincidence rate).**

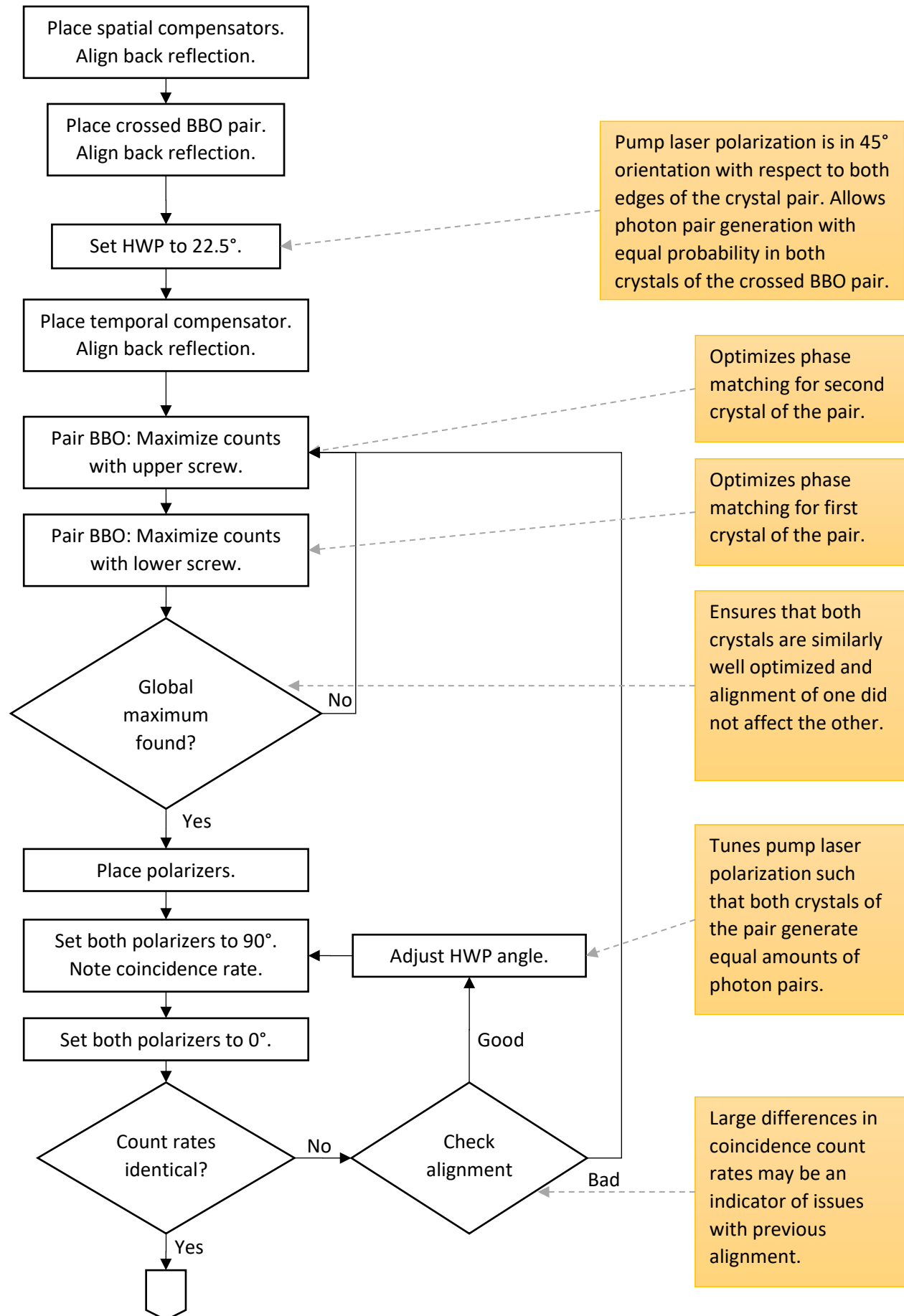
- In case you already have polarizers mounted in front of the detectors from previous experiments, it is not necessary to remove those. You can set both polarizers to 90°, such that vertical polarization is transmitted, and adjust the lower kinematic screw to tune the phase-matching for the first crystal of the pair. Alternate with setting both polarizers to 0° (horizontal polarization) and adjusting the upper kinematic screw for the second crystal in the pair. Switch between both configurations to ensure both axes are optimized. Since only the matching half of the generated pairs passes the polarizers and there is a small fraction of additional reflection, absorption and beam clipping, the expected minimal coincidence rates are reduced to about 4 kHz for the mean value of both settings.
6. Switch off the pump laser and switch to the axicon and the alignment laser. Put the two 1/2" polarizers centered in front of the detectors, such that their surfaces are parallel<sup>152</sup> to the irises of the detectors. Use an alignment card to check that the axicon cone passes through the center of the polarizers. Fix the positions using a CF125 clamp and a 1/4" 20 x 3/8" (M6 x 10 mm) cap screw plus washer, each.
  7. Switch off the alignment laser and replace the axicon with the crossed BBO pair. Switch on the pump laser. Set both polarizers to 90° (vertical polarization), then compare the coincidence count rate to the setting with both polarizers set to 0°. Both coincidence rates need to have equal values. To ensure this, carefully adjust the pump HWP rotation setting, until the coincidence count rate is identical to within the noise level (about 0.5 kHz) in both polarizer settings (at least 4 kHz). This may require a few iterations between 0° and 90° polarizer settings. If you encounter issues, ensure that the crossed BBO pair is optimally aligned (step 5) and the “single photon spot” is centered on the detectors, not just hitting them at the edge<sup>153</sup>.
  8. Set the polarizer in front of detector T to +45° and the one in front of detector A to -45°.
  9. Adjust the angle of the temporal compensation crystal carefully from the previous setting, using the blue upper kinematic screw. You should see oscillations in the coincidence rate. The amplitude of these oscillations should be in the regime of 80% to 90% of the coincidence count rate you get when both polarizers are set to 0°. Adjust to the minimum closest to the setting you started from, which should lie within one full revolution of the kinematic screw.
  10. Repeat step 7 with 0° and 90° settings to ensure there still are equal coincidence rates for both settings.

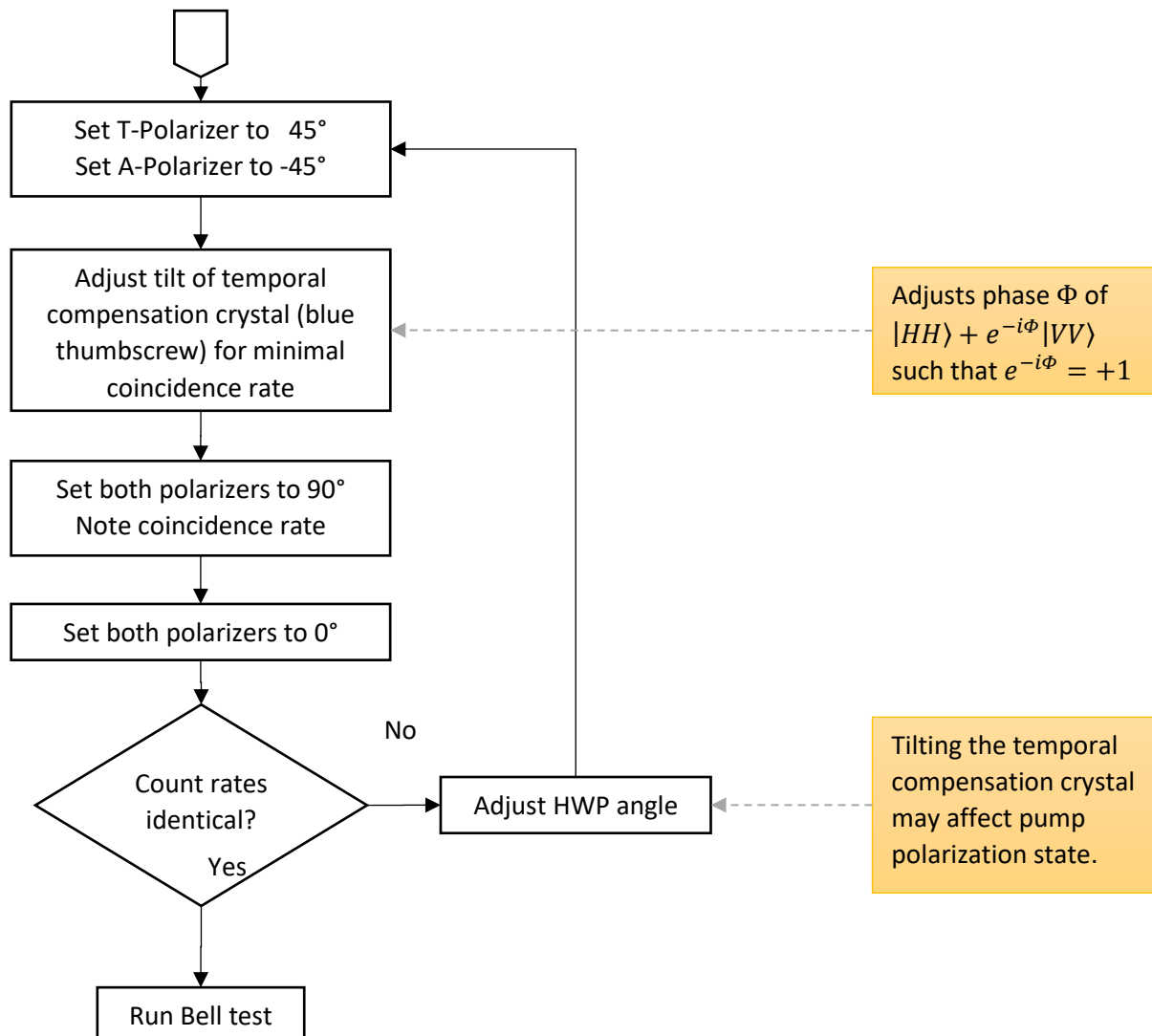
With these settings you should be able to reach an S-value of about 2.4 or higher in the Bell test (see Section 24.3).

---

<sup>152</sup> Looking from atop allows this to be seen more clearly. One may also use the back reflection onto the alignment target, but this level of accuracy is not required here. There is no need to have the polarizer mounts touching the irises. There may be some centimeters of free space in between.

<sup>153</sup> In the polarizer setting with lower count rates, use the XY adjuster screws on the detector optics to test whether the count rates can be improved significantly. If this is the case, the spot has been close to the edge of the detector. Turn the adjuster a bit further and check the alignment again with both polarizer settings, then continue.





## Chapter 23 Learning Goals and Misconceptions

The following table summarizes the experiments and the learning goals.

Exercise	Experiment	Learning Goal	Possible Misconception
1	Polarization Correlation - Mixed State (Section 24.1)	The coincidence probability of the mixed state for different polarizer settings follows the expectations of classical light statistics.	
2	Polarization Correlation - Entangled State (Section 24.2)	The entangled state results in stronger correlations between the polarizations of the two photons than the mixed state.	<p>It is tempting to think that the entangled state:</p> $\frac{1}{\sqrt{2}}( HH\rangle +  VV\rangle)$ <p>is a statistical mixture of HH and VV states. But the different results of experiments 1 and 2 show that this is wrong.</p>
3	Bell Test (Section 24.3)	Local Hidden-Variable theories can be ruled out as a description of reality.	
4	Changing the Phase (Section 24.4)	There is more than one entangled state. The exact correlations and parameters required for the Bell test depend on the entangled state, but the correlations (or anti-correlations) between the photon polarizations are always stronger than can be explained by classical means.	<p>One could think that entanglement means that both photons have the same polarization. This experiment shows that other entangled states exist as well.</p>
5	Influence of the Iris Apertures (Section 24.5)	A larger aperture size reduces the S-value because of spatial walk-off. The dependence is weak with the spatial compensation crystals, where a violation of the CHSH inequality can be measured even with fully open apertures.	
6	Influence of the Spatial Compensation Crystals (Section 24.6)	Without the spatial compensation crystals, the spatial walk-off for larger aperture sizes is stronger, causing the S-value to fall below the classical limit of 2 for larger apertures. Smaller iris diameters keep the entanglement observable even without spatial compensation.	
7	Influence of the Temporal Compensation Crystals (Section 24.7)	Without the temporal compensation crystal, the S-value will be significantly lower because of temporal walk-off than with temporal compensation. When increasing the walk-off further with negative compensation, the S-value lowers even more. Thus, temporal walk-off reduces the observability of entanglement.	

<b>8</b>	GRA-Experiment - Entangled State (Section 24.8)	The $g_2(0)$ -value is still significantly below 1, proving the single-photon character of the prior experiments.	One could think that two photon pairs (H H and V V) are generated at the same time and that this creates the entanglement. This experiment shows that we are generating one photon pair at a time.
----------	---	---	--

## Chapter 24 Experiments

In this chapter, experiments that can be performed with the kit are described in detail. The order in which these experiments are presented here start out with analyzing the difference between entangled and mixed states with respect to polarization-dependent coincidence count rates (compare to Section 20.2).

To ease alignment, the following experiments start out with the best preparation of the Bell state possible, which shows clearest signs of entanglement used for alignment, and also yields the highest violation of CHSH inequality.

Afterwards, the experiments demonstrate the influence of the entangled state phase and walk-off effects onto the Bell test. Note, that from a purely didactical perspective, the order of experiments could be changed to run these experiments earlier and have students work their way up to larger violations of the CHSH inequality. Refer to Section 24.9 for a detailed discussion.

All experiments in this chapter share a common setup, as shown in Figure 211, with minor changes in the configuration. The pump laser power should be set to 20 mW (refer to the spec sheet of the laser to infer the corresponding laser current).

The time estimates given for each exercise are given to provide a guideline for the **minimal time** required to run the experiments with the suggested parameters and number of data points. Much more time is required for data analysis and discussion.

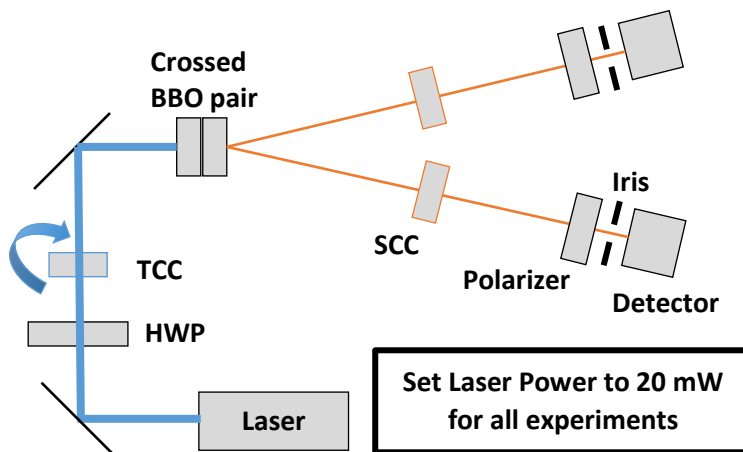


**Figure 211** Setup Schematic (TCC/SCC: Temporal/Spatial Compensation Crystals, HWP: Half-Wave Plate)

### 24.1 Coincidence Rates at Polarizers - Mixed State

**Exercise:** Measure the average coincidence count rates of each of the states of a mixed state ensemble of photon pairs in order to simulate a mixed state. The individual states of the mixed state can be produced by alternatingly pumping the SPDC process in only one of the crystals of the pair at a time. Observe how the coincidence count rates are influenced by the polarizers in front of the detectors, when both are turned from 0° to 90° in parallel. The Malus tab in the EDU-QOP software may be used to record the count rate diagrams.

**Time Estimate:** 20 minutes

**Goal:** Classical example: Observe the behavior of photon pairs at a pair of polarizers for a mixed state. Here, both horizontally and vertically polarized pair contributions follow Malus law.

**Setup:** The setup procedure for the entangled source is described in Chapter 22. As we only pump one of the crystals in the crossed BBO pair to generate one of the photon pair polarizations at a time, the birefringent compensation crystals have no effect. This means that this experiment may be conducted already during step 7 of the setup procedure in Section 22.2, before the pump beam half-waveplate is adjusted.

**Measurement:** For the ensemble result we will sum up the counts from both pair polarizations for each of the polarizer settings that contribute to the mixed state, so it does not matter in which order we generate and measure the HH-states and VV-states. To speed up the process, it is advisable to set the pump half-waveplate to

$0^\circ$  first (vertically polarized pump beam; horizontal photon pair polarization) and measure the coincidence count rate at about eight different settings of the detector polarizers between  $-20^\circ$  and  $100^\circ$  (both polarizers should show the same rotation angles). Afterwards, repeat the measurements with the pump half-waveplate set to  $45^\circ$  (horizontally polarized pump beam; vertical photon pair polarization) with identical polarizer angles as before. An example measurement is given in the figure below.

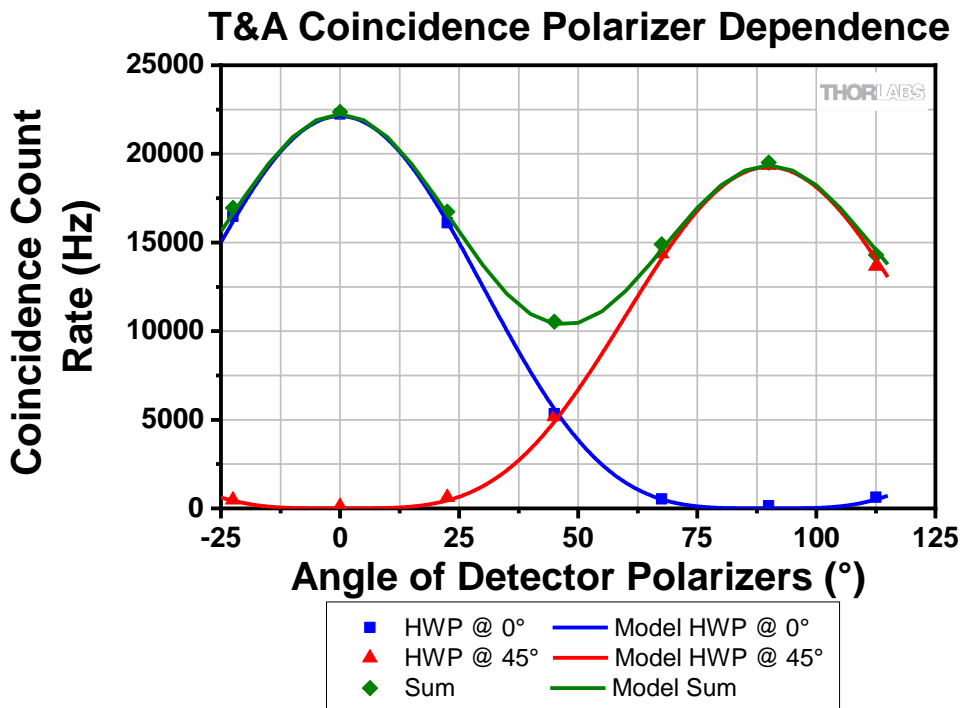


Figure 212 Example Measurement for Mixed State Experiment with Identical Polarizers

**Interpretation:** This mixed state is an example of an ensemble of states that contains similar large amounts of photon pairs polarized along the horizontal **or** vertical axis. As per the design of our experiment, we only generate one of the two polarizations at a time, and we know which one is generated. Therefore, there is neither superposition of states nor entanglement present in the density operator used to describe the ensemble of states we produced. The sums of the coincidence count rates for each of the polarizer settings that generate the HH-state and VV-state, thus, follows Equation (174). To fit the model to the measured data, the horizontal and vertical polarization contributions should be weighted by the measured coincidence count rates at  $0^\circ$  and  $90^\circ$ . At  $45^\circ$  detector polarizer orientations we observe a minimum of the curve at half the maximum coincidence count rate, as, according to Malus law, the probability for both a horizontally or vertically polarized photon to pass through each individual polarizer in each arm is equal to  $\frac{1}{2}$  and the probability for the pair to pass in coincidence is the product thereof ( $\frac{1}{4}$ ). In contrast, at the maximum points of the curve at  $0^\circ$  and  $90^\circ$  the chance for either the horizontal or vertical polarizations to pass in each arm is equal to 1, but the respective other half of the photons (vertical or horizontal polarization) is blocked completely, such that we only detect half of the generated photons pair - but still twice as many as at the minimum.

## 24.2 Coincidence Rates at Polarizers - Entangled State

**Exercise:** Repeat the previous experiment with the entangled Bell state and compare your results.

**Time Estimate:** 8 minutes

**Goal:** Observe the different behavior of states generated by the entangled pair source.

**Setup:** The setup procedure for the entangled source is described in Chapter 22. Follow the instructions given there to optimally set up the polarization-entangled pair source.

**Measurement:** Unlike in Section 24.1, only one measurement is required for each polarizer angle, as the entangled pair source produces photon pairs with both polarization components. Apart from that, the measurement process is the same: Use the Malus law tab to record the coincidence count rates for about eight different detector polarizers settings between  $-20^\circ$  and  $100^\circ$  (both polarizers always show the same rotation angle).

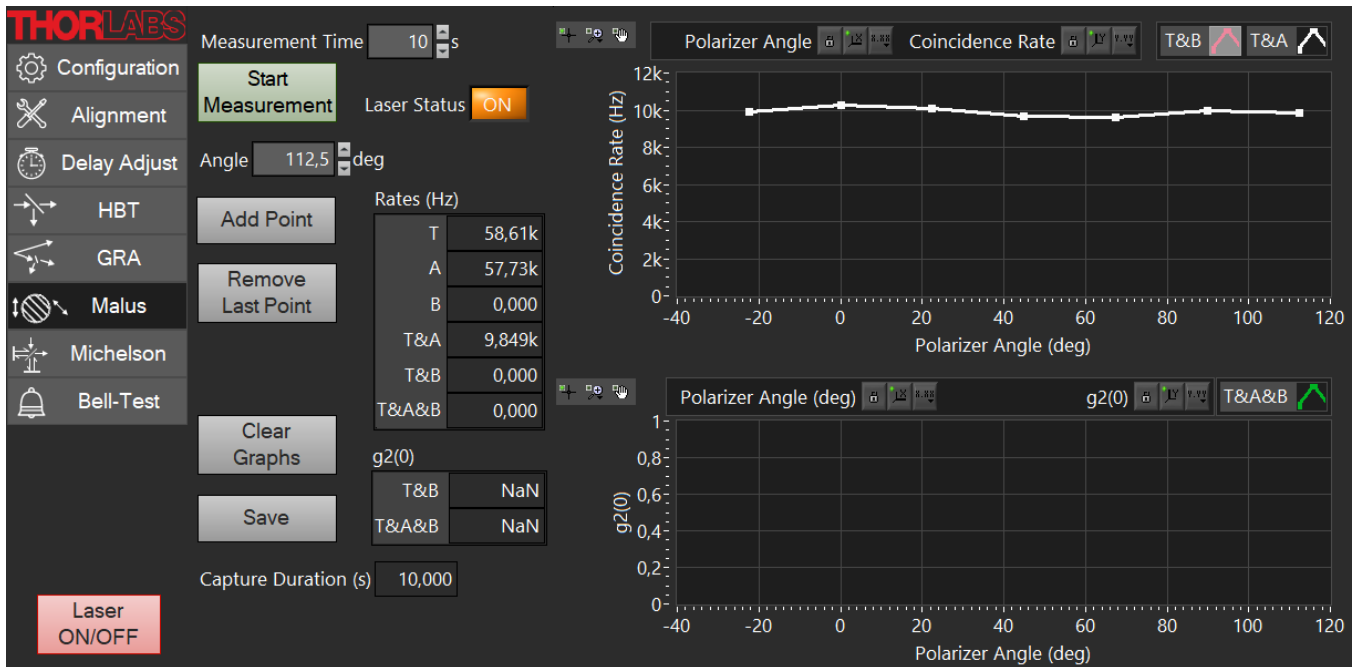


**Figure 213** Example Measurement for Entangled State Experiment with Identical Polarizers

**Interpretation:** In contrast to the minima in the curve for the mixed state, the polarization-dependent coincidence count rates from the entangled state constantly are at a similar level as the maxima in the mixed state curve and, thus, follow Equation (173). For the cases of  $0^\circ$  and  $90^\circ$  orientation of the polarizers, we may use the same explanation as before: Only half of the generated photon pairs will pass through the polarizers, which are the ones with matching horizontal or vertical polarization. For any other polarizer setting, however, the above arguments do not hold up anymore and we observe higher coincidence rates than for the mixed state.

Outside of the  $0^\circ$  and  $90^\circ$  polarizer settings, we cannot tell the origin of the photon pair with certainty. Therefore, the polarization states of the single photons are not definable (however, the two-photon state is well defined). The moment one of the photons is “measured” by the polarizer (i.e., pass or block – both have the same probability of  $\frac{1}{2}$ ), the state of the other photon in the pair is determined by the result of the measurement (see Section 20.2.3). The  $|\Phi^+\rangle$  Bell state in this example leads to both photons being polarized along the same direction, thus they either both pass through or both get blocked by the polarizers in both arms equally.

Furthermore, this result also explains the alignment process used to set up the entangled pair source. During the step that adjusts the entangled state phase, the polarizers in front of both detectors are oriented in a crossed configuration. If the entangled state phase is adjusted for the  $|\Phi^+\rangle$  Bell state, both photons of a pair will have the same polarization orientation, but can only pass through one of the polarizers, while being blocked at the other one, resulting in a coincidence rate of zero (in the idealized case).

### 24.3 Bell Test with Entangled Source

**Exercise:** Run the Bell test using the Bell-Tab in the EDU-QOP software. Interpret the result of the CHSH inequality.

**Time Estimate:** 7 minutes

**Goal:** Test, whether local-realistic Hidden Variable theories can explain the results of the Bell test.

**Setup:** The setup procedure for the entangled source is described in Chapter 22. Follow the instructions given there to optimally set up the polarization-entangled pair source.

**Measurement:** Open the Bell-Tab in the software. The table in the upper right corner of the software tab shows the settings for the polarizers A & T for each row and column. For all 16 table entries, rotate the polarizers in front of detectors A and T to the given values for the respective row and column and then click on the table element to start a measurement for this configuration. After the measurement ends, the table entry shows the coincidence count rate for this polarizer setting. With 10 seconds measurement time for each table entry, it takes about 5 minutes to run the full Bell test.

In case you are using two KDC101 controllers with PRM1/(M)-Z8 rotation stages (not included in the kit) for automated rotation of polarizers, you can start the measurement with the Start Measurement button to the left and the program will run through all 16 configurations automatically (similar total measurement time).

An example measurement is shown in Figure 214.

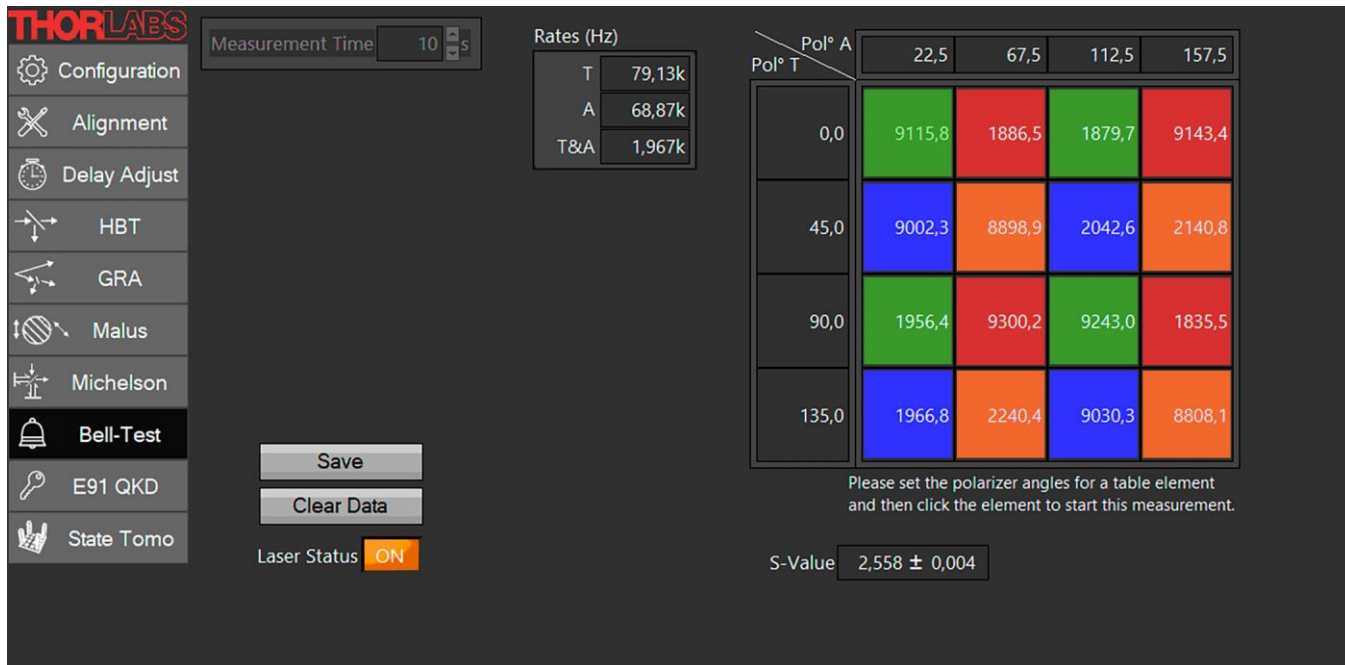


**Figure 214      Example Measurement of the Bell Test**

**Result Analysis:** Calculate the S-value according to Equations (229) and (243). In the screenshot of the example measurement above, the value groups that go into the calculation of each parameter E are highlighted with the same colors. For example, values highlighted in green go into the calculation of

$$E(\alpha = 0^\circ, \beta = 22.5^\circ) = \frac{R(0^\circ, 22.5^\circ) - R(0^\circ, 112.5^\circ) - R(90^\circ, 22.5^\circ) + R(90^\circ, 112.5^\circ)}{R(0^\circ, 22.5^\circ) + R(0^\circ, 112.5^\circ) + R(90^\circ, 22.5^\circ) + R(90^\circ, 112.5^\circ)}$$

where R are the coincidence rates measured in each configuration<sup>154</sup> (see Section 20.3.3). For the S-value, the  $E(\alpha = 0^\circ, \beta = 67.5^\circ)$  value of the red terms is subtracted from the other three E values:

$$S(0^\circ, 22.5^\circ, 45^\circ, 67.5^\circ) = E(0^\circ, 22.5^\circ) - E(0^\circ, 67.5^\circ) + E(45^\circ, 22.5^\circ) + E(45^\circ, 67.5^\circ)$$

**Interpretation:** The measurement above yields a value of  $S = 2.610 \pm 0.003$ . The S-value we measured is thus more than 200 standard deviations above the limit of  $S \leq 2$  for local-realistic Hidden Variable Theories. Due to the very high number of standard deviations, it is practically impossible to end up with such a result due to statistical fluctuations in the measurement values. This indicates that the non-local nature of quantum mechanics may be a suitable description of physics and any Hidden Variables theory based on local realism can be ruled out. Note however, that we cannot rule out loopholes, as discussed in Section 26.10, due to the general design of this educational setup.

<sup>154</sup> Note that the probabilities used in the theoretical derivation of Equation (243) can be calculated by dividing the individual rates through the sum of all four coincidence rates for this E value, assuming a constant pair creation rate and neglecting the fair sampling loophole. In the original setup discussed in the theory section, all four of these rates are measured simultaneously by four detectors.

## 24.4 Changing the Phase of the Entangled State

**Exercise:** In this exercise the phase of the entangled state is changed by tilting the temporal compensation crystal and the previous experiments are run again with the new state. This exercise is split into three subsections.

**Time Estimate:** 30 minutes

**Goal:** Understand the importance of the entangled state's phase for the Bell test and learn how to adjust it.

**Setup:** Start out from the previous experiment settings and set the polarizers in front of detectors T & A to +/- 45°. Carefully tilt the temporal compensation crystal to change the phase delay between horizontal and vertical polarization. This effect can be observed in the coincidence count rate plot of the Alignment tab in the software. For a quantitative analysis, one should use the Malus tab instead (as shown in the measurement below).

### 24.4.1 Adjusting the Phase

**Exercise:** Tilt the temporal compensation crystal using the upper adjuster knob to change the phase of the entangled state and record coincidence count rate measurements with polarizers in front of detectors T & A set to +/- 45°. Use the upper kinematic adjuster of the crystal mount and turn it ¼ revolution per step (at least 10 steps).

**Interpret the Results:** How does the coincidence count rate change and why (compare to Sections 20.2.4 and 20.4.3)?

**Measurement:**

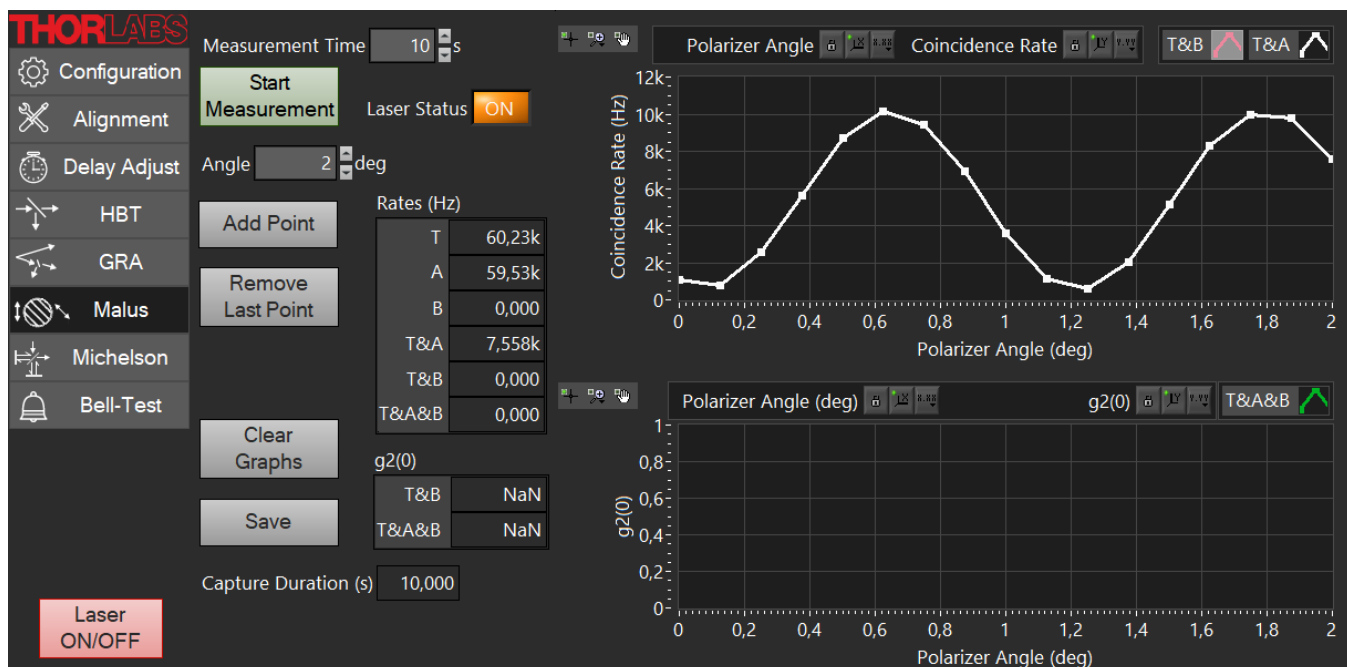


Figure 215 Example Measurement for Varying Phase of the Entangled State

The screenshot above shows a measurement of the coincidence rates for a range of tilt settings of the temporal compensation crystal (TCC) between 0° and 3° angle of incidence for the blue pump beam. The upper adjuster knob on the KM100CP crystal mount has been turned by ¼ revolution for each measurement along the same direction. The tilt angle is estimated from the specified 0.5° tilt angle per revolution for this mount<sup>155</sup>.

### Result Analysis:

The observed rates resemble the shape of a (shifted) sine function with respect to the tilt angle. Comparing to Equation (178), we can explain the minima and maxima in our measurement result, which occur at  $\Phi = 0$  and

<sup>155</sup> Rotating the adjuster knob causes a linear motion of the adjuster tip, which tilts the KM100CP front plate due to a lever action. Thus, the dependence between tilt angle and knob rotation is actually the tangent function. Due to the small angle within the adjuster range, it can be approximated linearly.

$\Phi = \pi$  respectively (both modulo  $2\pi$ ). As discussed in Section 20.4.3, the absolute phase  $\Phi$  between both polarizations depends on the exact thicknesses and orientations of all birefringent elements in the beam paths and varies between every new alignment of the setup. The phase shift  $\Delta\Phi$  is generally not a linear function with respect to the tilt angle of the birefringent element used to tune the phase. The temporal compensation crystal used in the kit is designed to allow for multiple periods in the phase shift  $\Delta\Phi$  within the tilt range of a kinematic mount. In this small angular range, a linear approximation can be justified for this crystal.

The period of the oscillations is  $1.2^\circ$  of TCC tilt angle change, in line with the theoretical calculations in Section 20.4.3 (compare to Figure 200).

#### 24.4.2 Coincidence Rates at Polarizers

##### Exercise:

Turn the blue thumbscrew of the temporal compensation crystal in order to adjust the phase for a maximum coincidence rate at  $\pm 45^\circ$  polarizer settings (this sets the state to  $\frac{1}{\sqrt{2}} \cdot (|HH\rangle - |VV\rangle)$ ). Compare the coincidence count rates for both polarizers at  $0^\circ$  and both polarizers at  $90^\circ$  and adjust the HWP until both values are about the same.

Do the same measurement as in Section 24.4.1 (use the Malus tab again), but this time leave the TCC untouched and instead change both polarizer angles simultaneously (steps of  $22.5^\circ$ ). How does the coincidence rate depend on the polarizer settings when both polarizer angles are rotated with the same orientation (as in Section 24.2) or when the polarizer in front of detector A is always rotated in the opposite direction to the negative angle of the polarizer in front of detector T?

##### Measurement:

After selecting the smallest TCC tilt angle with maximum coincidence count rate ( $0.2^\circ$ ) from the measurement above, the following dependences of the coincidence count rates with respect to the polarizer angles is measured. Note that there is a small imbalance between the horizontal and vertical pair production rate, as the fine alignment of the pump half-waveplate has not been adjusted after changing the angle of the birefringent TCC.

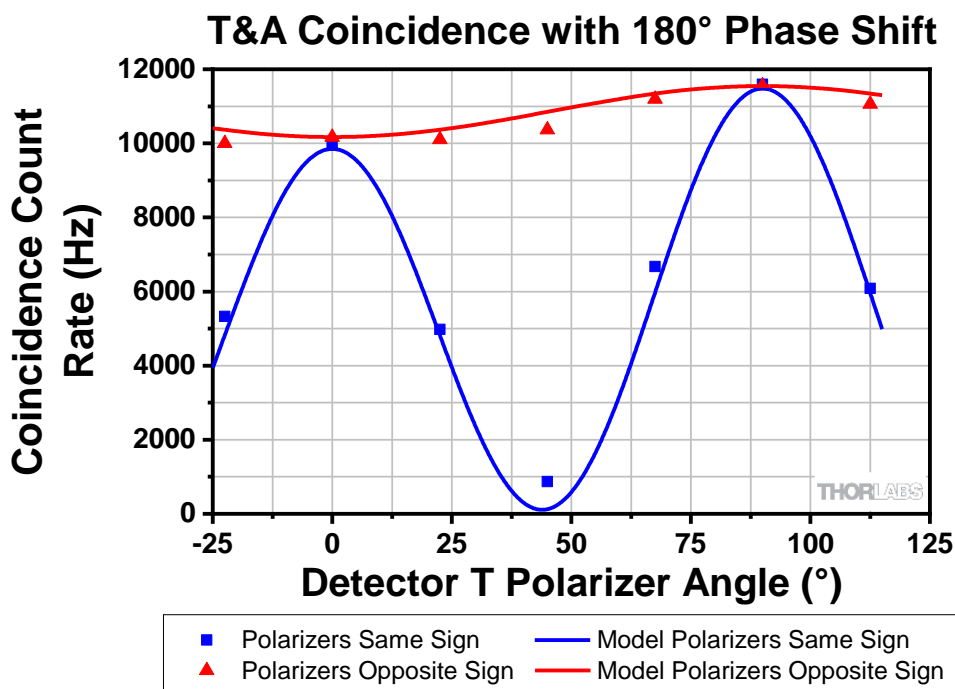


Figure 216 Example Measurement of the Entangled State with  $180^\circ$  Phase Shift

## Result Analysis:

The result when rotating both detector polarizers in parallel may be surprising at first, as the curve is more similar to the one of the mixed state (Section 24.1), instead of the entangled state measured in Section 24.2. However, note that in this case the curve approaches zero in the 45° polarizer setting, which is not possible for the mixed state. With the changed phase of the entangled state, the polarizations measurable in both arms are now not parallel anymore - instead the second measurement confirms that the polarizations in both arms are now mirror-symmetric with respect to the center plane between the two detectors (see calculations in Section 20.2.4). With the polarizers at 45° orientations, the two arms' polarizations are orthogonal to each other.

These results can be compared to Equation (173), where the changed phase leads to “-” signs instead of “+” in the equation, which yields the model curve plotted above. To fit the models to our data, we weighted the unbalanced contributions of horizontal and vertical state generation by the coincidence count rates measured at 0° and 90° (see Section 26.13 for a derivation of the formula):

$$R(\varphi) = (\sqrt{R(0^\circ)} \cdot \cos^2 \varphi \pm \sqrt{R(90^\circ)} \cdot \sin^2 \varphi)^2 \quad (187)$$

The version with “-” is used to fit the measurement with parallel polarizer orientations, whereas the “+” is used for measurements with mirror symmetric polarizer orientations. This is because, when one of the polarizer angles has flipped sign, then the “-” signs in Equation (173) cancel and the result is P = 0.5 for all angles again (in the idealized case of equal contribution of horizontal and vertical states).

### 24.4.3 Bell test

#### Exercise:

Repeat the Bell test at the current phase setting with maximal coincidence count rate at  $\pm 45^\circ$  polarizer orientations. How can the result of the test be interpreted? Can the test itself or the evaluation equations be changed to adapt the test to the changed input state?

#### Measurement:

Running the Bell test shows a “failed” result with S close to zero. Comparing to the result in Section 24.3, the order of results with high and low count rates is the same in the 0° and 90° rows (first and third) but changed in the 45° and 135° rows.

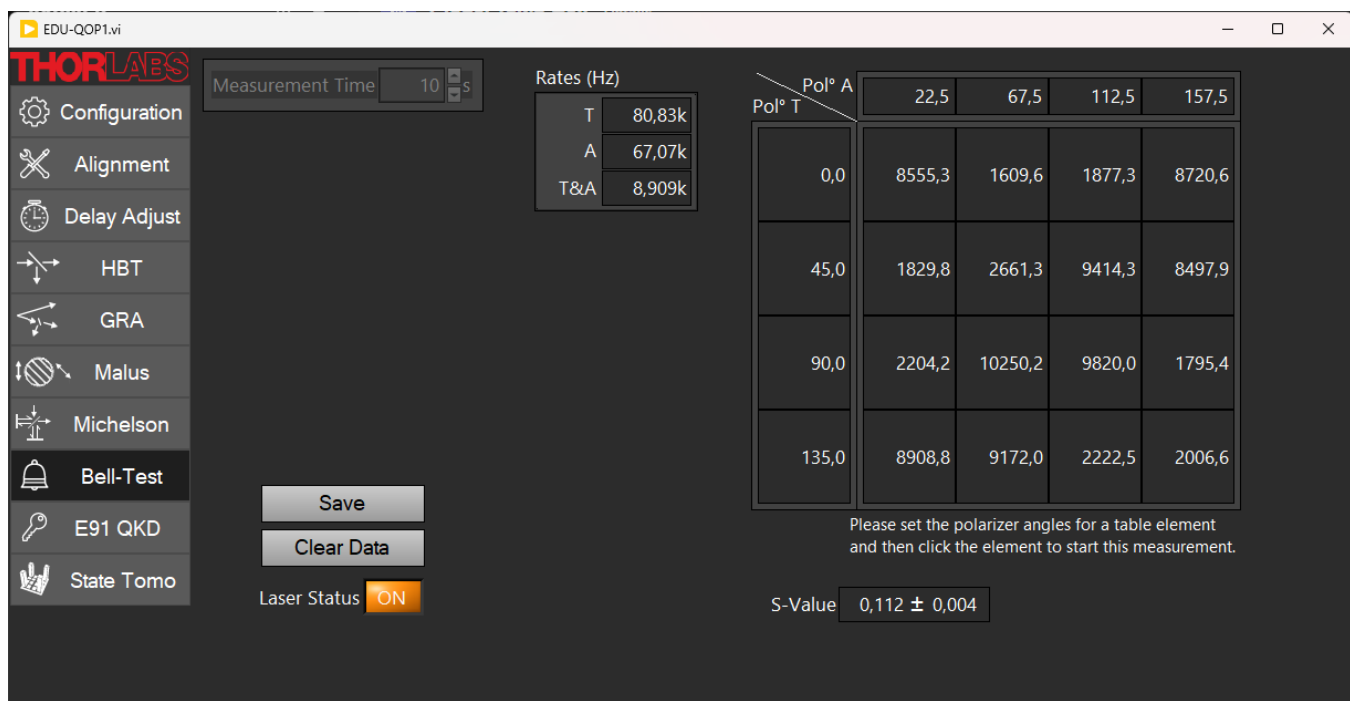


**Figure 217      Example Measurement of Bell Test with 180° Phase Shift of the Entangled State**

### Result Analysis:

The S-value obtained with the default settings (as shown in the screenshot) for the Bell test is rather close to zero instead of breaking the limit of 2. The explanation of this result can be found by evaluating Equation (245) for a  $|x\rangle_1|x\rangle_2 - |y\rangle_1|y\rangle_2$  state and following the derivation, resulting solely in a change from the difference  $\alpha - \beta$  in the arguments of the (co)sine functions towards  $\alpha + \beta$  (and the variants with primed letters) in Equation (248). However, the values we used for  $\alpha, \alpha', \beta, \beta'$  now result in different values for the four  $E$  terms when evaluating Equation (255):

$$\begin{aligned} S_\phi(a, a', b, b') &= \cos(2\alpha + 2\beta) - \cos(2\alpha + 2\beta') + \cos(2\alpha' + 2\beta) + \cos(2\alpha' + 2\beta') \\ &= \cos(2 \cdot 22.5^\circ) - \cos(2 \cdot 67.5^\circ) + \cos(2 \cdot 67.5^\circ) + \cos(2 \cdot 112.5^\circ) \\ &= \frac{1}{\sqrt{2}} - \left(-\frac{1}{\sqrt{2}}\right) + \left(-\frac{1}{\sqrt{2}}\right) + \left(-\frac{1}{\sqrt{2}}\right) = 0 \end{aligned} \quad (188)$$

Thus, this setting is not suitable to violate the CHSH inequality and other parameters are required. Considering that we changed the sign of the angle of one of the polarizers during alignment to set this Bell state, it is easy to motivate just changing the sign for all the angles in the Bell test of one of the polarizers. This assumption can be further justified, as we look at the mathematical derivation again. We noticed earlier that, with the  $|x\rangle_1|x\rangle_2 - |y\rangle_1|y\rangle_2$  state, we get  $\alpha + \beta$  for all the effective angles involved for the evaluation of  $S$  and we need to find a new set of angles to obtain a maximum value of  $S$ . On the other hand, we already know that our previous set of angles with the term  $\alpha - \beta$  is a desired solution. Therefore, inverting the sign of all our angles  $\beta, \beta'$  must then also yield a desired solution for this Bell state. The same holds true for inverting only the  $\alpha, \alpha'$  angles, as  $\cos(2\theta)$  is symmetric under inversion of sign.

Alternatively, we may change the definition of  $S$  in Equation (229): By shifting the minus sign in the equation from the  $a, b'$  term to the  $a, b$  term, we end up with another asymmetric equation, yielding the same type of inequality as before. However, when still using the default angles with positive sign, this changes the first two signs in the evaluation of  $S$  above:

$$S = \left| -\left(\frac{1}{\sqrt{2}}\right) + \left(-\frac{1}{\sqrt{2}}\right) + \left(-\frac{1}{\sqrt{2}}\right) + \left(-\frac{1}{\sqrt{2}}\right) \right| = 2\sqrt{2} \quad (189)$$

Plugging in our measured values above into this changed equation, we now obtain  $S = 2.552 \pm 0.004$ , well above the limit of 2 and fully in line with the result obtained in Section 24.3.

**Interpretation:** It is possible to reformulate the CHSH inequality also with other Bell states than shown in the theory section. However, a single formulation of the Bell test together with a certain choice of test angles is always directly linked to a certain Bell state, i.e., Bell tests are generally not universal. Thus, the result of the Bell test is also an indicator of how well the matching Bell state has been generated.

## 24.5 Changing the Detector Iris Apertures

**Exercise:** Compare the results of the Bell test when the aperture diameter of the irises in front of the detectors are reduced equally. Interpret the resulting curve.

**Time Estimate:** 20 minutes

**Goal:** Observe, how the detector iris apertures affect the measurement result.

**Setup:** Set up the experiment as in Section 24.3. Repeat the Bell test for 2-3 different iris aperture diameters between 3 to 10 mm in front of the detector pair<sup>156</sup>. To reduce errors in the iris aperture diameter measurement due to backlash, it is advisable to close the irises to 1 mm and only monotonously increase the opening diameter from 3 to 10 mm during the measurement series.

<sup>156</sup> Note that at large iris aperture diameters around and above 10 mm, this aperture won't be the single limiting factor of the effective detector aperture. Clipping at apertures of other optical elements (polarizers, focusing lenses) in the beam path become relevant as well. The exact value depends on the alignment of the beam path. With more precise alignment of the optical components' centers to the axicon beam this upper limit increases. Above that limit, the differences in the measured S-value become negligible, as the effective detector aperture barely changes size.

**Measurement:** The figure below shows the results of four Bell test measurements between 3 and 9 mm iris aperture diameter with respect to the classical limit and Tsirelson's bound.

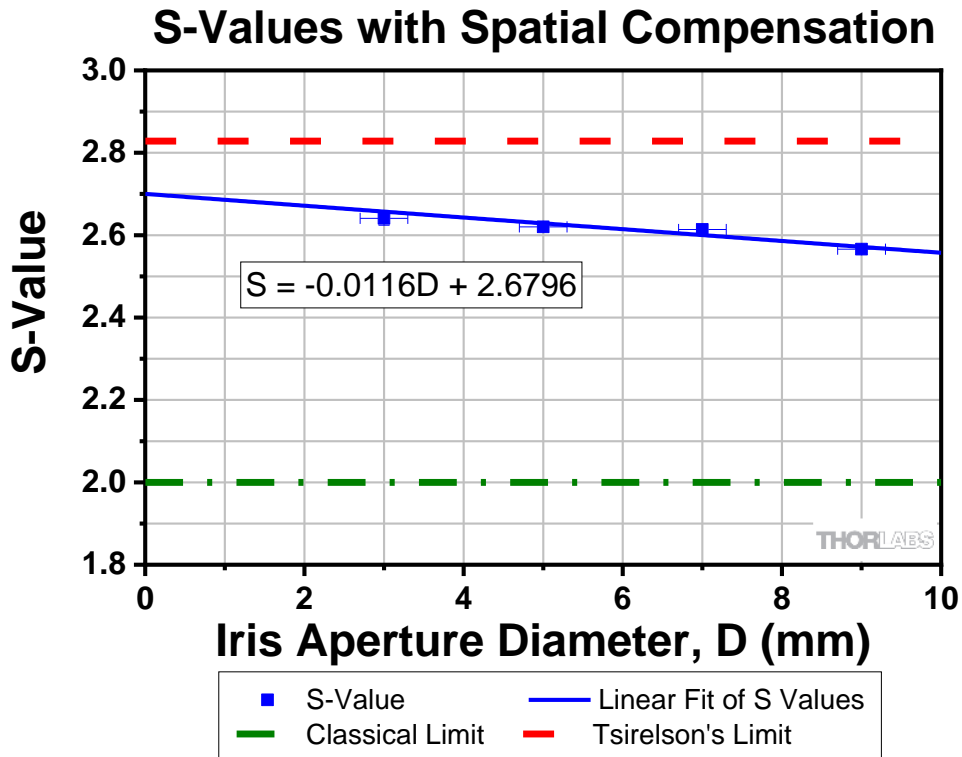


**Figure 218 Example Measurement for Different Iris Diameters with Spatial Compensation**

Here, the S-value of the Bell test is similarly high for all measurements, but slightly increases with smaller iris diameters. It violates the CHSH inequality for all iris diameters. The blue dotted line indicates a linear fit to the data, which may be used to extrapolate the S-value for zero diameter.

**Interpretation:** The S-value of the Bell test only reaches Tsirelson's bound of  $2\sqrt{2}$  for optimally prepared Bell states and is one indicator of how well the Bell state has been prepared. As discussed in Sections 20.4.2 and 26.12, the generation of photon pairs is subject to walk-off, which needs to be compensated. The measurements above indicate that our walk-off compensation is not perfect: Because we average over a smaller collection area, the phase range due to spatial walk-off decreases with smaller iris diameters, thus improving the quality of the detected Bell states. Extrapolating to zero diameter, i.e., simulating the collection at a single point in space without negative effects of spatial walk-off, shows that the optimal S-value still cannot be reached. This may be an indicator that there still is temporal walk-off or other effects that reduce the Bell state quality (e.g., see Section 27.1.1). Note however, that the extrapolation is to be taken with care, as a linear approximation of the curve cannot be justified in all cases. Compare this result to the result from Section 26.11 (especially Figure 230): the broadening of the entangled state phase distribution is generally not a linear function with respect to the iris aperture diameter. Instead, the phase maps are curved surfaces.

## 24.6 Spatial Compensators

**Exercise:** Remove the spatial compensation crystals from the setup. Now again, compare the results of the Bell test when the aperture diameter of the irises in front of the detectors are changed equally. Interpret the change of the slope of the curve in comparison to the previous experiment.

**Time Estimate:** 20 minutes

**Goal:** Understand the importance of spatial compensation and the interplay with detector iris aperture.

**Setup:** Set up the experiment as in Section 24.3, but remove the spatial compensation crystals from the beam path before aligning the phase of the entangled state (higher count rates at the minima than before are expected).

This is equivalent to skipping the first step in Section 22.2. Now run the experiment described in Section 24.4.1 again and compare the results.

Note: It is further possible to remove just one of the spatial compensation crystals. Again, adjust the phase properly before the measurement. In this case, the obtained result will then be about half-way between the full compensated and uncompensated result.

**Measurement:** The figure below shows the results of four Bell test measurements between 3 and 9 mm iris aperture diameter<sup>156</sup> with respect to the classical limit and Tsirelson's bound, when no spatial compensation is used.

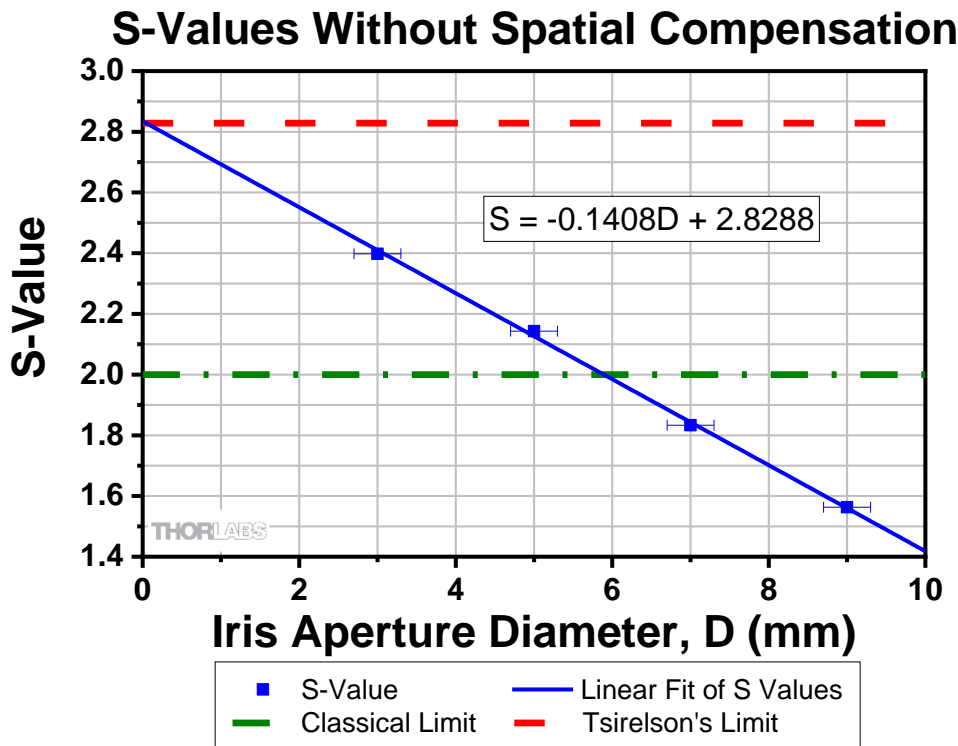


**Figure 219 Example Measurement for Different Iris Diameters Without Spatial Compensation**

Here, the S-value of the Bell test significantly decreases with larger iris diameters. The violation of the CHSH inequality cannot be shown for all iris diameters. The blue dotted line indicates a linear fit to the data, which may be used to extrapolate the S-value for zero diameter.

**Interpretation:** Without the spatial compensation crystals, the S-value and thus the quality of the Bell state drop off much faster with increasing iris diameter than for a properly compensated source. Due to the large spatial walk-off present in the crossed BBO crystal pair, the phase distribution for the pairs of entangled photons is so broad, when collected over large iris diameters, that the measured two-photon state is closer to a separable state instead of a Bell state. The effect is strong enough to cause the S-value to drop below the limit of 2 for large iris diameters and the test then fails to violate the CHSH inequality. It does not mean that now Hidden Variable theories involving local realism would suddenly be allowed. Instead, we just failed to set up the Bell test under proper conditions.

The S-value significantly improves with smaller iris diameters, as we filter out a smaller subset of photon pairs with a narrower phase distribution, closer to the ideal Bell state. Seemingly, the S-value may always be improved by more restrictive spatial filtering. However, note that the coincidence count rates decrease rapidly with smaller iris diameters, which in turn increases the uncertainty of the measurement.

Comparing with the fully spatially compensated result of Section 24.4.1, we conclude that using spatial compensation allows the measurement of high S-values together with significantly higher count rates at large iris diameters. This compensation allows for lower uncertainties and/or shorter measurement times for the Bell test, easier alignment of the system and leaves enough room for loss of count rate due to alignment issues or additional

optical elements for additional experiments. The S-value extrapolated towards zero iris aperture diameter is larger here without spatial compensation due to the polarization distorting effects (see Section 27.1.1) being reinforced by the birefringent spatial compensation crystals; if the input polarization is not matching to the optical axes plane of the crystal, it can further enhance the distortion, as it acts similar to a waveplate as well. These kinds of effects vary from setup to setup. Also remember the note on the validity of the extrapolation from the previous section.

## 24.7 Changing the Temporal Walk-Off Compensation

**Exercise:** Compare the results of the Bell test without temporal walk-off compensation and with increased walk-off. Interpret the results.

Can the detector irises be used to mitigate effects of temporal walk-off, as before? Are there other measures to reduce temporal walk-off?

**Time Estimate:** 25 minutes

**Goal:** Understand the importance of temporal compensation.

**Setup:** Two configurations for the temporal compensation can be compared to the experiment in Section 24.3. Both require the spatial compensation crystals to be aligned in the beam path. Remember to adjust the half-waveplate for equal coincidence count rates in horizontal and vertical polarizer settings for both configurations.

1. Negative compensation: Rotate the temporal compensation crystal in its mount by 90° (see Figure 220). Set up the experiment as in Section 24.3. To align the phase of the entangled state, use the lower (black) kinematic screw of the temporal compensation crystal mount instead of the upper (blue) one. Remember to rotate the temporal compensation crystal back after this experiment section and realign its mount using the pump beam back reflection (see Section 22.2).

Bonus: Run the experiment again with the detector irises closed down to 4 mm.



**Figure 220 Orientation of the Temporal Compensation Crystal After 90° Rotation**

2. No compensation: Set up the experiment as in Section 24.3, but remove the temporal compensation crystal from the beam path. To align the phase of the entangled state, use the lower kinematic screw of one of the spatial compensation crystal mounts<sup>157</sup>. This is an exception for this configuration only! Remember to realign the spatial compensation crystal using the axicon after the experiment (see Section 22.2).

**Measurement:** Running the Bell test in the two configurations as described should yield the following results:

- Negative Compensation should result in an S-value significantly lower than measured before with the correct compensation. This value can even be below 2.

<sup>157</sup> Be careful not to block the beam path towards the detectors. A 5/64" (2 mm) ball driver or hex key can be used to turn the adjuster from a position below the beam path.

- No compensation results in an S-value about halfway in between the values measured for correct compensation and negative compensation.
- The Bonus measurement (negative compensation, 4 mm iris apertures) should result in an S-value similar to the negative compensation result.
- Below are the results of an example measurement:

$$\begin{array}{ll} 1. \quad S = 2.143 \pm 0.004 & (\text{Bonus}): S = 2.246 \pm 0.012 \\ 2. \quad S = 2.317 \pm 0.004 & \end{array}$$

**Interpretation:** Without the temporal compensation crystal, the S-value and thus the quality of the Bell state drop in comparison to the properly compensated configuration used in Section 24.3. Due to the finite spectral bandwidth of the pump laser, a range of different pump wavelengths may cause a photon pair generation in the SPDC process. As the birefringent refractive indices of the BBO crystals are dispersive, the photon pairs generated by different pump wavelengths acquire different phases on their way to the detector, which adds to the width of the phase distribution of the ensemble of entangled states and reduces the observability of entanglement effects.

In the usual orientation, the temporal compensation crystal pre-compensates this wavelength-dependent phase walk-off between both polarizations. Inserting the temporal compensation crystal in the “wrong” 90° rotated orientation flips the fast and slow axes of the birefringent crystal, which inverts the sign of the phase compensation and thus doubles the walk-off, instead of compensating it.

When reducing the detector iris aperture, there is no significant improvement of the S-value (compare to Section 24.6). The measured increase of the S-value is similar to what can be observed in Section 24.5 and is due to the residual spatial walk-off still present in the system. This means that the temporal walk-off cannot be mitigated by smaller iris apertures, as it is not depending on the detection angle (i.e., spatial walk-off). The only alternative to reduce the effect of temporal walk-off is the reduction of the pump laser’s spectral bandwidth<sup>158</sup>, e.g. by using a single-frequency laser.

## 24.8 Grangier-Roger-Aspect Experiment for the Entangled Source (No Polarizers)

**Exercise:** Perform the Grangier-Roger-Aspect experiment for the entangled pair source. Does this source emit single photon pairs?

**Time Estimate:** 10 minutes

**Goal:** Understand that entanglement is NOT caused by two pairs (HH and VV) emitted at the same time, but by superposition of states of a single pair.

**Setup:** Remove the polarizers from the Bell test setup and add a beamsplitter and the third detector as described in Section 7.5.

**Measurement:** Go to the GRA tab of the software, choose a measurement time and start the measurement. The result of an example measurement is shown in Figure 221.

---

<sup>158</sup> One could alternatively limit the bandwidth by using much narrower bandpass filters in front of the detectors instead. But this causes very low system efficiency, as most of the pairs generated by a comparably broad pump bandwidth won’t be detected and pump beam power is wasted.

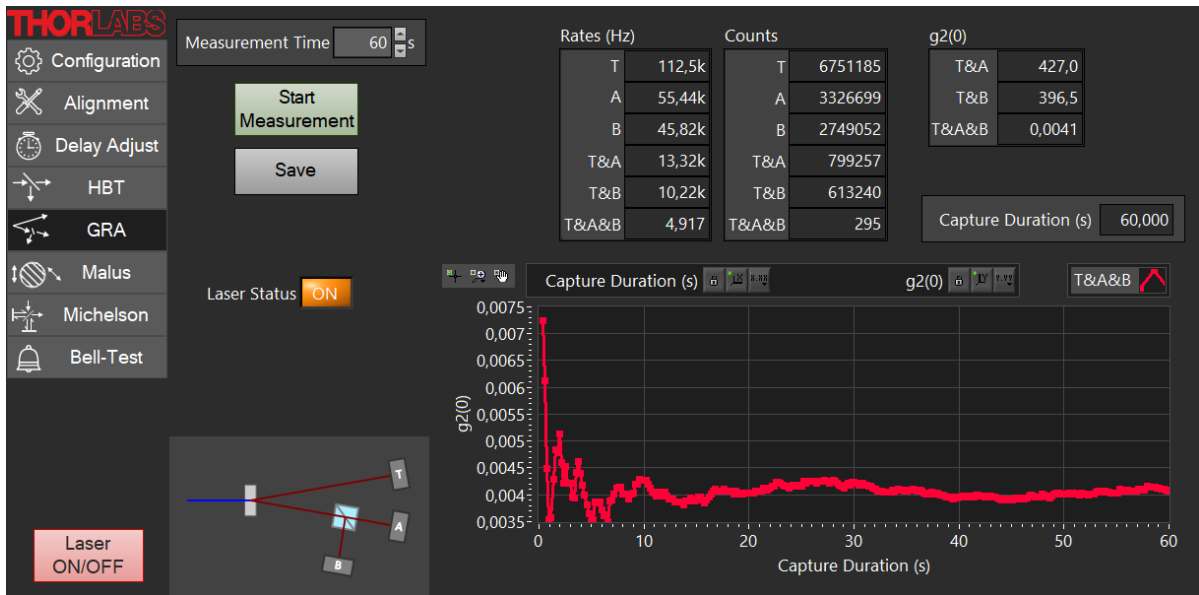


**Figure 221** Example Measurement for GRA experiment with the Entangled Pair Source

**Interpretation:** The result is a value of  $g_{GRA}^{(2)}(0)$  of 0.1 or lower. This proves that the entangled pair source emits single photon pairs, just as the source of the base kit (see Section 3.5.3 for the theory). It thus becomes clear that the entanglement cannot be caused by HH and VV pairs being emitted simultaneously but that a single pair of photons is in a superposition of the HH and VV states. In this experiment, the polarizers were removed. Re-introducing them can only absorb photons, not create any new ones, so the single-pair character of the source remains intact and does not depend on the polarizer settings in any way.

## 24.9 Order of Experiments

The order of experiments as listed above is designed to teach students about the behavior of entangled photon pair states at a pair of polarizers and then directly introduces the Bell test with the setup fully optimized for a large violation of the CHSH inequality.

The proper preparation of Bell states suitable for the Bell test is a complex topic and comes with some pitfalls. To help students to focus on the physics and the substantial implications for the interpretation of quantum mechanics, we recommend starting out with a configuration of the setup that shows the clearest signatures of entanglement. E.g. the oscillations of the coincidence count rate with changing entangled state phase (see Equation (178)) are used during alignment to set the proper phase for the Bell state. Thus, we want to provide a clear signal to optimize the settings for, when one runs this kind of experiment for the first time. The interpretation of the first measurement of the Bell test is suitable for a detailed discussion about its interpretation in terms of quantum mechanics.

After developing an understanding of the Bell test and getting to know how the entanglement signatures look and behave during alignment, we take on the more technical aspects of the Bell test and analyze the requirements to successfully show the inequality violation. Specifically, students should learn about the meaning of the entangled state's phase and how broadening of the phase distribution of an ensemble of entangled states gradually hides the observability of entanglement, making it look more and more like a separable state.

One could argue that this order may not be satisfying or didactical for students, while conducting the experiments, as one starts out with a lot more crystals in the setup as required for the basic understanding of the Bell test. The "highlight", a maximum violation of the CHSH inequality, is also presented rather early in the list of suggested experiments and from there on, one may take a lot of additional measurements that "only" show that we made our results worse.

The following list, thus, gives a suggestion, how the experiments can be reordered for a bottom-up experience that motivates students by yielding larger violations of the Bell test after each step. However, this approach may require more time for alignment and discussions in the beginning or more support from a supervisor.

1. How do entangled and mixed states behave at polarizers (experiments 24.1 and 24.2)? When set up without spatial compensators, start with iris apertures in front of the detectors reduced to 4 mm diameter. The temporal compensation crystal is required to tune the entangled states phase and may be discussed for only this purpose at first.
2. Run the first Bell test without properly adjusting the phase (see experiment 24.4). Please note that the result will be random (as the phase is not controlled), so students will get widely different results here.
3. Open up the detector irises (experiment 24.6) and observe the trade-off between count rates and entanglement quality.
4. Introduce spatial compensation crystals (experiment 24.4.1) and observe that one still gets high entanglement quality, but also much higher coincidence count rates at the same time. Strictly, this already contains the measurement for experiment 24.3.
5. Revisit the temporal compensation crystal and its purpose with experiment 24.7.
6. The Bell test and the interpretation of quantum mechanics and hidden variable theories. Use the best results of experiment 24.4.1 for the detailed analysis and discussion of experiment 24.3.

## Chapter 25 Software

The extension kit uses the same software as the base kit. By activating the respective checkbox in the connection window upon software startup (see Section 11.4), you can display an additional tab which is dedicated to the polarization entanglement experiments.

### 25.1 Bell-Test Tab

This tab (shown in Figure 222) is used to perform the Bell test experiment, which is the central part of the EDU-QOPA1(/M) extension kit.

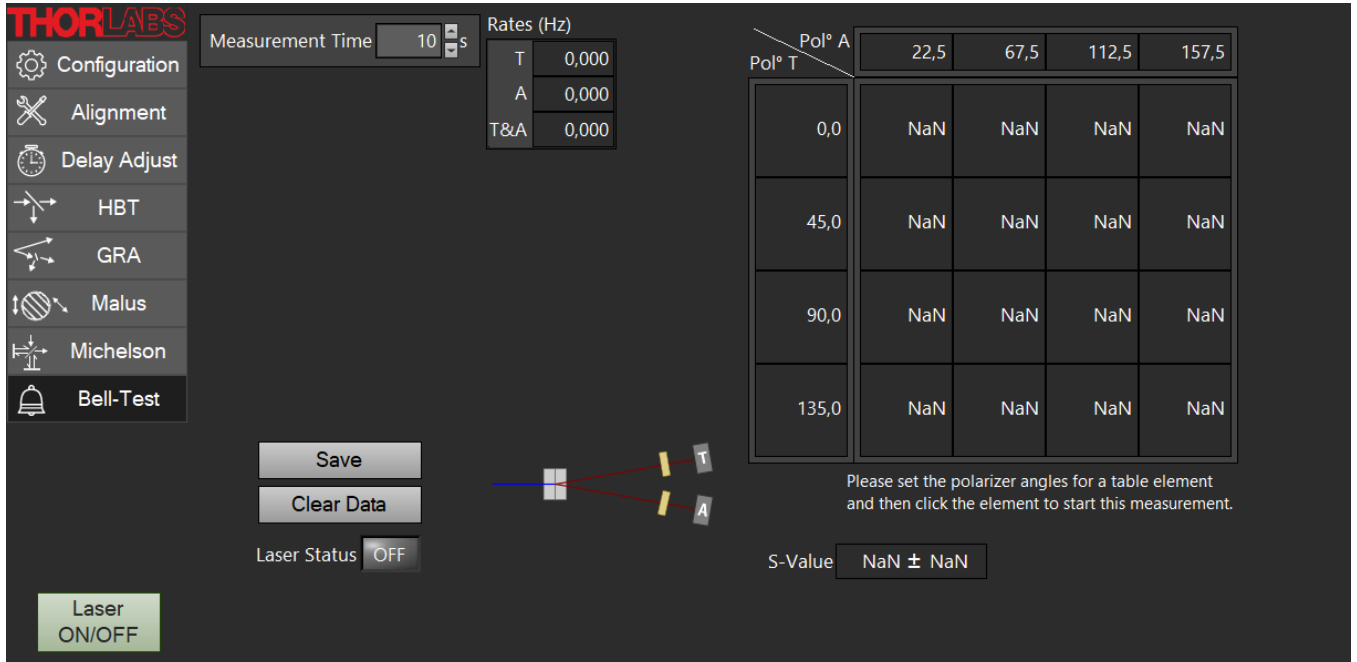


**Figure 222      Bell-Test Tab**

On the right side of the tab a 4 by 4 table displays the measurement results depending on the angle settings of the polarizers in front of detectors T and A. The standard values for the angles are recommended for the Bell test, but they are changeable in case you want to modify the Bell test, e.g. to test a different Bell state (see Section 24.3 for more details).

For the complete Bell test, 16 measurements with different polarizer settings are required. To start one of these measurements, click the table field that matches your current polarizer settings. You can adjust the **Measurement Time** via the control field in the upper left corner of the tab. During the measurement, the single detector count rates of detectors T and A as well as their coincidence count rate are updated in the **Rates (Hz)** indicator field.

Once the measurement is finished, the final coincidence rate will be displayed in the respective table field. If you want to repeat a measurement (for example because you accidentally used the wrong polarizer settings), just click the respective field again. Once all 16 fields contain a finite value, the indicator field **S-Value** in the bottom right corner of the tab will display the S-value of the Bell test as calculated by the software according to equations in Sections 20.3.3 and 24.4.3.

You can save your data at any point by clicking the **Save** button in the lower left corner of the tab (see Section 11.3 for more details). If you want to start a new set of measurements, you can set the table back to the starting point via the **Clear Data** button.

If you have connected at least two KDC101 controllers for automated rotation of the polarizers via motorized rotation stages (not included in EDU-QOP1(/M) or EDU-QOPA1(/M), see Section 27.3), a checkbox named **Use Rotation Stages** will appear below the **Measurement Time** field. If this checkbox is activated, the tab will change to the configuration shown in Figure 223.

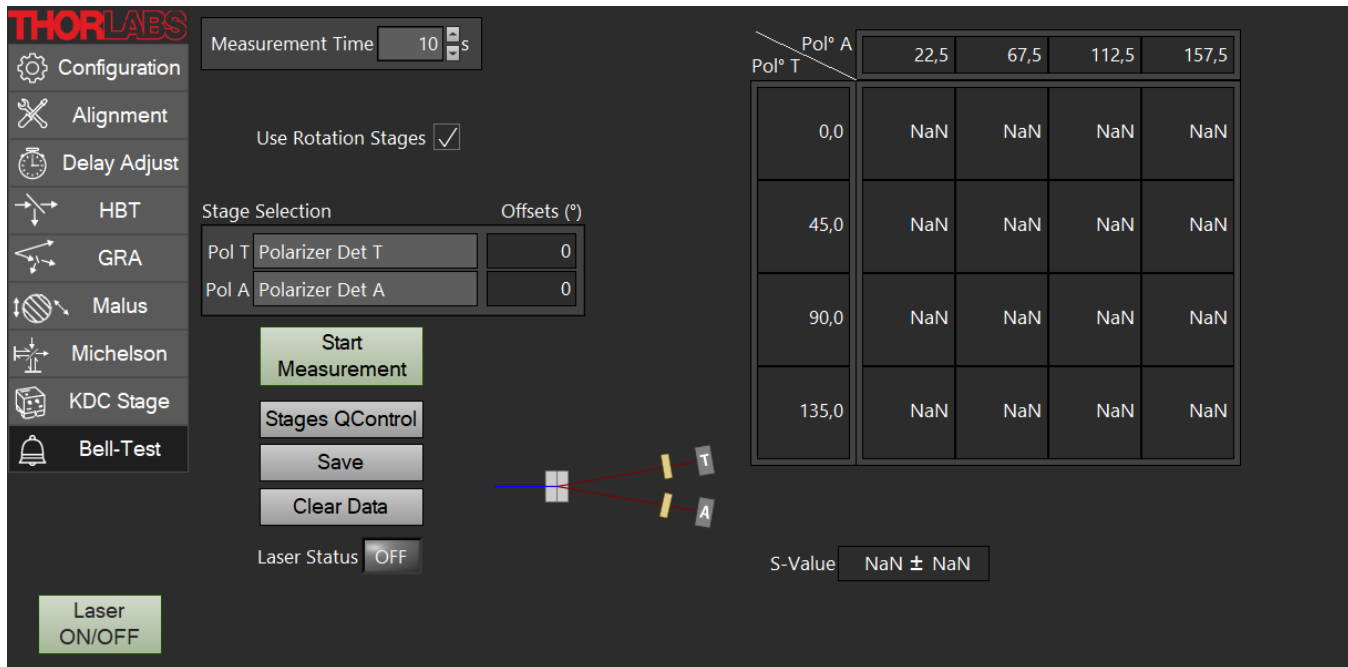


**Figure 223**      *Bell-Test Tab in the Configuration for Automatic Measurement*

On the left side, three new elements appear:

- In the **Stage Selection** table, the KDC controllers can be assigned to the detectors T and A by clicking into the name field and selecting the correct controller from the dropdown menu (the names are the one given in the connection window, see Section 11.4).
- By clicking the button named **Start Measurement**, the complete set of 16 measurements will be performed automatically. A countdown will be displayed in the field of the result table that is currently measured.
- By clicking the button **Stages QControl**, a popup window, as displayed in Figure 224, opens. This window will remain present even when changing from the Bell-Test to another tab. It can be used to quickly set the polarizer positions, e.g., for alignment of the polarizers in the KDC tab or for the experiments in Sections 24.1 and 24.2.

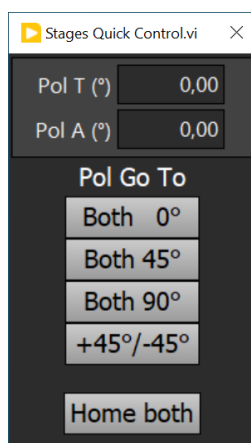


**Figure 224**      *Quick Control Window for Polarizers in the Automatic Configuration*

## Chapter 26 Extended Theory

In this chapter, we give additional information that was omitted from 0 for brevity and readability. Please be aware that the sections of this chapter are not directly connected to each other. For a coherent buildup of information, see 0 and follow the references to this chapter as they appear.

### 26.1 Entanglement Proof

For states with two subsystems (called bipartite states), there exist a number of general criteria to determine whether a given state is entangled or not. For the specific Bell state

$$|N\rangle = \frac{1}{\sqrt{2}}(|00\rangle + |11\rangle) \quad (190)$$

we can show the entanglement via the following short proof:

If  $|N\rangle$  were not entangled, it could by definition be written as a product state of two pure states for the subsystems:

$$|N\rangle = |\varphi\rangle_A \otimes |\psi\rangle_B \equiv |\varphi\psi\rangle \quad (191)$$

We will show that this leads to a contradiction by comparing the results of three specific scalar products for the expressions of  $|N\rangle$  in Equations (190) and (191). Those three scalar products are  $\langle 01|N\rangle$ ,  $\langle 00|N\rangle$ , and  $\langle 11|N\rangle$ .

According to Equation (190):

$$\langle 01|N\rangle = \frac{1}{\sqrt{2}}(\langle 01|00\rangle + \langle 01|11\rangle) = 0 \quad (192)$$

$$\langle 00|N\rangle = \frac{1}{\sqrt{2}}(\langle 00|00\rangle + \langle 00|11\rangle) = \frac{1}{\sqrt{2}} \quad (193)$$

$$\langle 11|N\rangle = \frac{1}{\sqrt{2}}(\langle 11|00\rangle + \langle 11|11\rangle) = \frac{1}{\sqrt{2}} \quad (194)$$

According to equation (191):

$$\langle 01|N\rangle = \langle 01|\varphi\psi\rangle = \langle 0|\varphi\rangle \cdot \langle 1|\psi\rangle \quad (195)$$

$$\langle 00|N\rangle = \langle 00|\varphi\psi\rangle = \langle 0|\varphi\rangle \cdot \langle 0|\psi\rangle \quad (196)$$

$$\langle 11|N\rangle = \langle 11|\varphi\psi\rangle = \langle 1|\varphi\rangle \cdot \langle 1|\psi\rangle \quad (197)$$

Now we substitute the results of the first set of equations into the second set and obtain:

$$\langle 0|\varphi\rangle \cdot \langle 1|\psi\rangle = 0 \quad (198)$$

$$\langle 0|\varphi\rangle \cdot \langle 0|\psi\rangle = \frac{1}{\sqrt{2}} \quad (199)$$

$$\langle 1|\varphi\rangle \cdot \langle 1|\psi\rangle = \frac{1}{\sqrt{2}} \quad (200)$$

This set contains a contradiction. According to Equation (198), at least one of the two terms  $\langle 0|\varphi\rangle$  and  $\langle 1|\psi\rangle$  has to be equal to 0. However, if the first term is 0, then Equation (199) cannot be true and if the second term is 0, then Equation (200) cannot be true.

From this contradiction, it follows that our assumption in Equation (191) was wrong and thus the state  $|N\rangle$  cannot be written as a product state of two pure states. This is the definition of  $|N\rangle$  being an entangled state.

## 26.2 Partial Measurements

As mentioned in Section 20.1, the subsystems of a system in an entangled state cannot be described by pure states (that is the definition of an entangled state). However, it is certainly possible to measure such a subsystem in isolation. How can we calculate the expected outcomes of such a measurement?

The states of the subsystems can be expressed as mixed states (see Section 3.2.11). Note, that there is no real statistical mixing of states going on, it is just a convenient way to calculate the expected probabilities of measurement outcomes when subsystems are measured in isolation.

As an example, we consider the following state:

$$|N\rangle = \frac{1}{\sqrt{2}}(|0\rangle_A \otimes |0\rangle_B + |1\rangle_A \otimes |1\rangle_B) \quad (201)$$

We determine the density operator  $\hat{\rho}_A$  of subsystem A when the system is in state  $|N\rangle$  by performing what is called a partial trace over B:

$$\begin{aligned} \hat{\rho}_A &= \sum_{m=0,1} {}_B\langle m|\hat{P}_N|m\rangle_B = \sum_{m=0,1} {}_B\langle m|N\rangle\langle N|m\rangle_B \\ &= \frac{1}{2} \cdot ({}_B\langle 0|0\rangle_B \cdot |0\rangle_{AA}\langle 0| \cdot {}_B\langle 0|0\rangle_B + {}_B\langle 0|1\rangle_B \cdot |1\rangle_{AA}\langle 1| \cdot {}_B\langle 1|0\rangle_B + {}_B\langle 1|0\rangle_B \cdot |0\rangle_{AA}\langle 0| \cdot {}_B\langle 0|1\rangle_B \\ &\quad + {}_B\langle 1|1\rangle_B \cdot |1\rangle_{AA}\langle 1| \cdot {}_B\langle 1|1\rangle_B) \\ &= \frac{1}{2} \cdot (|0\rangle_{AA}\langle 0| + |1\rangle_{AA}\langle 1|) \end{aligned} \quad (202)$$

Here,  $\hat{P}_N = |N\rangle\langle N|$  is the projection operator of the state  $|N\rangle$ , see Section 3.2.4. The density operator  $\hat{\rho}_A$  cannot be reduced to a pure state, showing that the state of subsystem A is not in a pure state, but in a superposition of two states. The probabilities for the results of a measurement are the same as for an ensemble of particles in the mixed state  $\hat{\rho}_A$ , even though this is not the case of a statistical mixture of particles.

The fact that the subsystems are in a mixed rather than a pure state is a defining property of an entangled system state. In general, the system state is separable (non-entangled) if, and only if, the subsystems are in pure states. In our example, the partial trace over one system yields a mixed state for the other subsystem, hence the system state  $|N\rangle$  must be entangled.

## 26.3 Collapse of the Entangled State

In the prior section we have determined the outcome probabilities for a measurement on one of the subsystems. What happens to the state of the whole system after such a measurement?

We know from Section 3.2.9, that if the measurement on some single particle quantum state  $|\psi\rangle$  results in some eigenvalue  $\lambda$  of the corresponding Hermitian operator, then the state of the particle is changed to the corresponding eigenstate  $|\lambda\rangle$ . This can be expressed as a projection onto the state  $|\lambda\rangle$ , followed by renormalization:

$$|\lambda\rangle = \frac{|\lambda\rangle\langle\lambda| |\psi\rangle}{\langle\lambda|\psi\rangle} \quad (203)$$

Here,  $|\lambda\rangle\langle\lambda|$  is the projection operator onto the state  $|\lambda\rangle$ .

How does this work for partial measurements on a multi-particle state, such as measuring the polarization of one of the two photons of the photon pair? In this case, we perform a partial projection. For example, consider a two-particle state  $|\psi_1\rangle_1 \otimes |\psi_2\rangle_2$  with particles 1 and 2, where the state of particle 1 is measured to be  $|\lambda\rangle_1$ . In this case, the partial projection operator  $|\lambda\rangle_1\langle\lambda| \otimes \hat{I}_2$  is used. Here,  $\hat{I}_2$  is the identity operator in the Hilbert space of particle 2, leaving all states with the index 2 unchanged.

Imagine we prepared the entangled two-photon state  $|\psi_E\rangle = \frac{1}{\sqrt{2}}(|HH\rangle + |VV\rangle)$  and then measured the polarization of photon 1 to be linearly polarized with an angle  $\varphi$  to the horizontal axis. Photon 1 is thus in the state  $|\varphi\rangle_1 = \cos\varphi \cdot |H\rangle_1 + \sin\varphi \cdot |V\rangle_1$  after the measurement. Via partial projection, the two-photon state changes to:

$$\begin{aligned}
|\varphi\rangle_{11}\langle\varphi| \otimes \hat{I}_2 |\psi_E\rangle &= \frac{1}{\sqrt{2}} \cdot {}_1\langle\varphi|H\rangle_1 |\varphi\rangle_1 \otimes |H\rangle_2 + \frac{1}{\sqrt{2}} \cdot {}_1\langle\varphi|V\rangle_1 |\varphi\rangle_1 \otimes |V\rangle_2 \\
&= \frac{1}{\sqrt{2}} \cdot |\varphi\rangle_1 \otimes ({}_1\langle\varphi|H\rangle_1 \cdot |H\rangle_2 + {}_1\langle\varphi|V\rangle_1 \cdot |V\rangle_2) \\
&= \frac{1}{\sqrt{2}} \cdot |\varphi\rangle_1 \otimes (\cos\varphi \cdot |H\rangle_2 + \sin\varphi \cdot |V\rangle_2) \\
&= \frac{1}{\sqrt{2}} \cdot |\varphi\rangle_1 \otimes |\varphi\rangle_2
\end{aligned} \tag{204}$$

The factor  $\frac{1}{\sqrt{2}}$  cancels out during renormalization<sup>159</sup> and the resulting two-photon state is  $|\varphi\rangle_1 \otimes |\varphi\rangle_2$ . This is a product state of pure states of the two subsystems and hence not an entangled state anymore. Photon 1 is in the state  $|\varphi\rangle_1$  (it has to be because that's what we measured), but photon 2 is now in a pure state  $|\varphi\rangle_2$  as well. This means, whatever polarization angle  $\varphi$  we measured for photon 1, we will find photon 2 with the same polarization angle afterwards. This is the explanation for the experimental results described in Section 20.2.3!

This transition from an entangled state to a separable state by measurement of one subsystem is called collapse of the entangled state. It is also what Einstein called "spooky action at a distance" because the state change occurs instantaneously, even if the subsystems are far apart in space (see Section 20.3.1 for more details about Einsteins relation to quantum mechanics).

Different entangled two-photon states can lead to different correlations of the polarization of the two photons after measurement of one of them, but they will always end up in a separable state after the measurement on photon 1, i.e., the polarization of photon 2 is well defined even though no measurement has been performed on it. Let's consider one more example. This time we start with the state  $|\psi_-\rangle = \frac{1}{\sqrt{2}}(|HH\rangle - |VV\rangle)$  and again measure photon 1 in the state  $|\varphi\rangle_1$ :

$$\begin{aligned}
|\varphi\rangle_{11}\langle\varphi| \otimes \hat{I}_2 |\psi_-\rangle &= \frac{1}{\sqrt{2}} \cdot {}_1\langle\varphi|H\rangle_1 |\varphi\rangle_1 \otimes |H\rangle_2 - \frac{1}{\sqrt{2}} \cdot {}_1\langle\varphi|V\rangle_1 |\varphi\rangle_1 \otimes |V\rangle_2 \\
&= \frac{1}{\sqrt{2}} \cdot |\varphi\rangle_1 \otimes ({}_1\langle\varphi|H\rangle_1 \cdot |H\rangle_2 - {}_1\langle\varphi|V\rangle_1 \cdot |V\rangle_2) \\
&= \frac{1}{\sqrt{2}} \cdot |\varphi\rangle_1 \otimes (\cos\varphi \cdot |H\rangle_2 - \sin\varphi \cdot |V\rangle_2) \\
&= \frac{1}{\sqrt{2}} \cdot |\varphi\rangle_1 \otimes (\cos(-\varphi) \cdot |H\rangle_2 + \sin(-\varphi) \cdot |V\rangle_2) \\
&= \frac{1}{\sqrt{2}} \cdot |\varphi\rangle_1 \otimes |-{\varphi}\rangle_2
\end{aligned} \tag{205}$$

Again, we end up with a separable two-photon state, but this time photon 2 is polarized along the axis with the angle  $-\varphi$ , i.e., its polarization axis is mirrored at the horizontal axis when compared to photon 1.

## 26.4 Different Experimental Results for Mixed and Entangled States

In Section 20.2.3, we considered the experiment shown in Figure 225, and calculated the expected results for the entangled state:

$$|\psi_E\rangle = \frac{1}{\sqrt{2}}(|HH\rangle + |VV\rangle) \tag{206}$$

We determined the following expected results:

Polarizer Setting Arm A	Polarizer Setting Arm B	Probability of Coincidence at Detectors
0°	0°	0.5
90°	90°	0.5
45°	45°	0.5

<sup>159</sup> In the general case, the renormalization works by dividing by the scalar product of the post- and pre-measurement state. For brevity, we omitted this here as one can easily see that the state can be normalized by just dropping the factor  $\frac{1}{\sqrt{2}}$ .

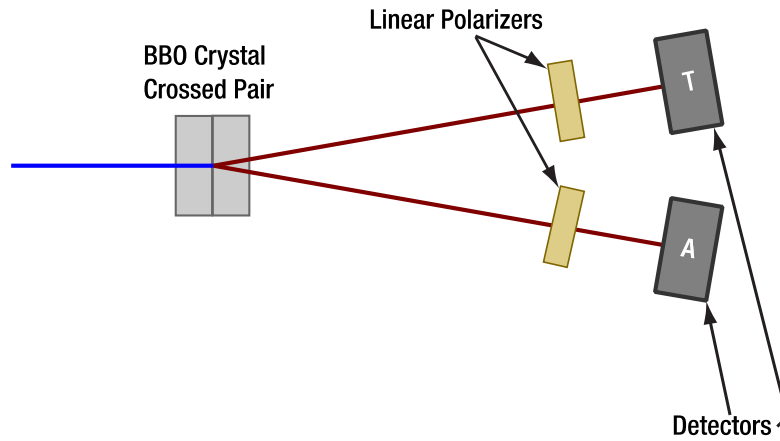


**Figure 225 Sketch of Experiment to Test Entanglement**

We claimed that no mixture of separable states can reproduce these three results. Here, we will prove that claim.

Let's assume a general mixture of two linear polarized pair states<sup>160</sup> (the proof can easily be extended to an arbitrary number of states in the mixture, but is easier to write with just two):

$$\hat{\rho} = C \cdot |\varphi\psi\rangle\langle\varphi\psi| + (1 - C) \cdot |\varphi'\psi'\rangle\langle\varphi'\psi'| \quad (207)$$

Here, the state  $|\varphi\psi\rangle$  means that the first photon of the pair is polarized with an angle  $\varphi$  from the horizontal axis, and the second photon is polarized with an angle  $\psi$  from the horizontal axis. No relation between the four angles  $\varphi, \psi, \varphi'$  and  $\psi'$  is assumed. The factors  $C$  and  $(1 - C)$  represent the probabilities of finding the individual states in the mixture.

In Section 3.7.1, we showed that the transmission probability of a photon polarized with an angle  $\varphi$  from the horizontal axis passing a polarizer with an angle setting of  $\theta$  from the horizontal axis follows Malus' law, i.e.,

$$P(\varphi \parallel \theta) = \cos^2(\varphi - \theta) \quad (208)$$

This means that the photon has the following probabilities to pass a polarizer set along the H and V directions respectively:

$$\begin{aligned} P(\varphi \parallel H) &= \cos^2(\varphi) \\ P(\varphi \parallel V) &= \cos^2(\varphi - 90^\circ) = \sin^2(\varphi) \end{aligned} \quad (209)$$

The probabilities of the photons to pass their respective polarizers are statistically independent. The probability of two photons, one of which is polarized along the  $\varphi$  axis and the other along the  $\psi$  axis, to both pass a horizontally oriented polarizer, is thus:

$$P(\varphi\psi \parallel HH) = P(\varphi \parallel H) \cdot P(\psi \parallel H) = \cos^2(\varphi) \cdot \cos^2(\psi) \quad (210)$$

The probability for both of them passing a vertically oriented polarizer is then:

$$P(\varphi\psi \parallel VV) = \sin^2(\varphi) \cdot \sin^2(\psi) \quad (211)$$

We now want to know which mixtures of states can reproduce the experimental results of the first two rows of the table above. Our mixture thus has to fulfill the following two equations:

$$P(\hat{\rho} \parallel HH) = C \cdot \cos^2(\varphi) \cdot \cos^2(\psi) + (1 - C) \cdot \cos^2(\varphi') \cdot \cos^2(\psi') = 0.5 \quad (212)$$

$$P(\hat{\rho} \parallel VV) = C \cdot \sin^2(\varphi) \cdot \sin^2(\psi) + (1 - C) \cdot \sin^2(\varphi') \cdot \sin^2(\psi') = 0.5 \quad (213)$$

Using the fact that  $\cos^2(\varphi) + \sin^2(\varphi) = 1$  for every angle, we can rewrite Equation (213):

<sup>160</sup> We restrict ourselves to linear polarization states here to keep the length of the proof manageable. However, the logic of the proof can be replicated to show that the inclusion of elliptic or circular polarization states does not change the result. This might be an insightful math exercise.

$$\begin{aligned}
0.5 &= C \cdot \sin^2(\varphi) \cdot \sin^2(\psi) + (1 - C) \cdot \sin^2(\varphi') \cdot \sin^2(\psi') \\
&= C \cdot (1 - \cos^2(\varphi)) \cdot (1 - \cos^2(\psi)) + (1 - C) \cdot (1 - \cos^2(\varphi')) \cdot (1 - \cos^2(\psi')) \\
&= C + C \cdot \cos^2(\varphi) \cdot \cos^2(\psi) - C \cdot (\cos^2(\varphi) + \cos^2(\psi)) + 1 - C + (1 - C) \cdot \cos^2(\varphi') \cdot \cos^2(\psi') \\
&\quad - (1 - C) \cdot (\cos^2(\varphi') + \cos^2(\psi')) \\
&= C \cdot \cos^2(\varphi) \cdot \cos^2(\psi) - C \cdot (\cos^2(\varphi) + \cos^2(\psi)) + 1 + (1 - C) \cdot \cos^2(\varphi') \cdot \cos^2(\psi') \\
&\quad - (1 - C) \cdot (\cos^2(\varphi') + \cos^2(\psi'))
\end{aligned} \tag{214}$$

We now reorder the terms on the right side of the equation and substitute Equation (212) for the first two terms:

$$\begin{aligned}
0.5 &= C \cdot \cos^2(\varphi) \cdot \cos^2(\psi) + (1 - C) \cdot \cos^2(\varphi') \cdot \cos^2(\psi') + 1 \\
&\quad - C \cdot (\cos^2(\varphi) + \cos^2(\psi)) - (1 - C) \cdot (\cos^2(\varphi') + \cos^2(\psi')) \\
&= 0.5 + 1 - C \cdot (\cos^2(\varphi) + \cos^2(\psi)) - (1 - C) \cdot (\cos^2(\varphi') + \cos^2(\psi'))
\end{aligned} \tag{215}$$

Summarizing the equation, we obtain:

$$C \cdot (\cos^2(\varphi) + \cos^2(\psi)) + (1 - C) \cdot (\cos^2(\varphi') + \cos^2(\psi')) = 1 \tag{216}$$

When multiplying equation (212) by 2 and comparing it to equation (216), the relation between the terms  $2 \cdot \cos^2(\varphi) \cdot \cos^2(\psi)$  and  $\cos^2(\varphi) + \cos^2(\psi)$  becomes interesting. The following table shows the possible relations:

$\cos^2(\varphi)$	$\cos^2(\psi)$	Equation
0	0	$\cos^2(\varphi) + \cos^2(\psi) = 0 = 2 \cdot \cos^2(\varphi) \cdot \cos^2(\psi)$
0	1	$\cos^2(\varphi) + \cos^2(\psi) = 1 > 0 = 2 \cdot \cos^2(\varphi) \cdot \cos^2(\psi)$
1	1	$\cos^2(\varphi) + \cos^2(\psi) = 2 = 2 \cdot \cos^2(\varphi) \cdot \cos^2(\psi)$
$\in \{0, 1\}$	0	$\cos^2(\varphi) + \cos^2(\psi) = \cos^2(\varphi) > 0 = 2 \cdot \cos^2(\varphi) \cdot \cos^2(\psi)$
$\in \{0, 1\}$	1	$\cos^2(\varphi) + \cos^2(\psi) = \cos^2(\varphi) + 1 > 2 \cdot \cos^2(\varphi) = 2 \cdot \cos^2(\varphi) \cdot \cos^2(\psi)$
$\in \{0, 1\}$	$\in (0, 1)$	$ \begin{aligned} \cos^2(\varphi) + \cos^2(\psi) &= \frac{\cos^2(\varphi) \cos^2(\psi)}{\cos^2(\psi)} + \frac{\cos^2(\psi) \cos^2(\varphi)}{\cos^2(\varphi)} \\ &= \left( \frac{1}{\cos^2(\psi)} + \frac{1}{\cos^2(\varphi)} \right) \cdot \cos^2(\psi) \cos^2(\varphi) \\ &> 2 \cdot \cos^2(\varphi) \cdot \cos^2(\psi) \end{aligned} $

We see that only for the cases where  $\cos^2(\varphi)$  and  $\cos^2(\psi)$  are both 0 or 1, the terms  $\cos^2(\varphi) + \cos^2(\psi)$  and  $2 \cdot \cos^2(\varphi) \cdot \cos^2(\psi)$  are equal. In all other cases, the first term is strictly larger. The same is true for a different pair of angles  $\varphi'$  and  $\psi'$ . We now combine Equations (212) and (216) to:

$$\begin{aligned}
C \cdot (\cos^2(\varphi) + \cos^2(\psi)) + (1 - C) \cdot (\cos^2(\varphi') + \cos^2(\psi')) &= 1 \\
&= 2 \cdot C \cdot \cos^2(\varphi) \cdot \cos^2(\psi) + (1 - C) \cdot \cos^2(\varphi') \cdot \cos^2(\psi')
\end{aligned} \tag{217}$$

From the results of our table, we can see that this equation can only be fulfilled if both  $\cos^2(\varphi)$  and  $\cos^2(\psi)$  as well as both  $\cos^2(\varphi')$  and  $\cos^2(\psi')$  are 0 or 1.

However, if all four terms are 0 or all four terms are 1, Equation (212) is violated. Hence, the only solution left is one pair of terms being 1 and the other being 0. By inserting these values into Equation (212) we can determine the factor  $C$ :

$$C \cdot \cos^2(\varphi) \cdot \cos^2(\psi) + (1 - C) \cdot \cos^2(\varphi') \cdot \cos^2(\psi') = C = 0.5 \tag{218}$$

Here, we set  $\cos^2(\varphi')$  and  $\cos^2(\psi')$  to 0 without loss of generality. The factor  $C$  has to be 0.5.

The requirement that  $\cos^2(\varphi)$  and  $\cos^2(\psi)$  are 1 is fulfilled for  $\varphi = \psi = 0^\circ$ , which is a polarization along the H-axis, and the requirement that  $\cos^2(\varphi')$  and  $\cos^2(\psi')$  are 0 is fulfilled for  $\varphi' = \psi' = 90^\circ$ , which is a polarization along the V-axis.

Thus, we have derived from the general mixture  $\hat{\rho} = C \cdot |\varphi\psi\rangle\langle\varphi\psi| + (1 - C) \cdot |\varphi'\psi'\rangle\langle\varphi'\psi'|$  the only possible solution for Equations (212) and (213) as:

$$\hat{\rho} = \frac{1}{2} \cdot |HH\rangle\langle HH| + \frac{1}{2} \cdot |VV\rangle\langle VV| \quad (219)$$

As shown in Section 20.2.3, this state does not reproduce the expected experimental result for the third row of the table at the top of the section, but yields 0.25 instead of 0.5. Hence, we have proven that no mixed state can reproduce the expected results of the entangled state for all three polarizer settings.

## 26.5 EPR Argument

The centerpiece of the original EPR article is a thought experiment including two particles that are strongly correlated in position and momentum but separated in space<sup>161</sup> (here called particle I and particle II). The authors make three fundamental assumptions:

- (1) Separability: Spatially separated systems have real physical states, which means that for each system, all physical quantities have defined values at all times.
- (2) Locality: If systems are spatially separate, the measurement of one system does not directly (i.e., faster-than-light) affect the reality (real state) of the other.
- (3) Completeness: The real state of a system includes all knowable information about the system.

They go on to prove that under these assumptions, quantum mechanics cannot be complete. The argument for this in the original paper is convoluted, but Einstein later provided clearer versions of the central statement<sup>162</sup>, one of which goes as follows:

- According to quantum mechanics, the quantum state of a system includes all knowable information about that system (i.e. it is the real state of the assumptions above).
- Quantum mechanics allows particles to be in entangled states. Consider two particles (I and II) in a position-momentum entangled state.
- When measuring either position or momentum on particle I, quantum mechanics states that the measurement always affects the state, so we can either measure position or momentum. Afterwards, system I will be in a position or momentum eigenstate, respectively. This means that the other quantity is completely undefined.
- Quantum mechanics states that if a measurement is performed on one of the entangled particles, the entangled state will collapse, and the other particle will instantly take on the corresponding state. In our example case, the state of particle II will become a position (momentum) eigenstate if the position (momentum) of particle I was measured.

Particle II has a real physical state (assumption 1) that remains constant before and after any measurement on particle I (assumption 2). However, this real state would be represented by one of two different quantum states (position or momentum eigenstate) depending on what measurement is performed on particle I. This violates assumption 3 because the real state should include all knowable information but position and momentum eigenstates include complementary information.

The main point here is the following: Not being able to know the position and momentum of a single particle is okay, because the argument is that the measurement changes the state. However, via entanglement, the position and momentum of particle II can in principle both be determined only by measurements on particle I. Therefore, as long as assuming locality and separability (assumptions 2 and 1), assumption 3 demands that the state of particle II contains complete information about both position and momentum. This, however, fundamentally disagrees with quantum mechanics.

---

<sup>161</sup> Today, we would call the particles "entangled", but the term wasn't coined yet when the article was written.

<sup>162</sup> N. Harrigan and R. W. Spekkens, *Foundations of Physics*, **40**, 125-157 (2010).

## 26.6 Proving the CHSH Inequality

In this section, a proof will be presented that leads to the Clauser, Horne, Shimony, and Holt (CHSH) inequality, a Bell-type inequality that is testable by experiments (as included in this extension kit). This proof closely follows the description given in the Stanford Encyclopedia<sup>163</sup>.

### Framework

The starting point is a system made up of two subsystems, labeled as 1 and 2. They are specified by a complete state called  $\lambda$ . No assumption about the nature of this state is made (it could be a quantum state, a quantum state with additional variables or something else entirely). The space  $\Lambda$  is the state space and includes all possible states  $\lambda$  of the systems. The probability of the system being in a specific state  $\lambda$  upon generation is given by the probability density  $\sigma(\lambda)$ . Here, we make the first two assumptions:

*A1: The probability density  $\sigma(\lambda)$  is independent of what happens to the systems after generation.*

*A2: The state  $\lambda$  determines the probabilities of the outcomes of any measurements performed on the systems.*

Now, experiments can be performed on the two systems. We call experiments on system 1 a and a' and experiments on system 2 are called b and b'. Here, we make another assumption:

*A3: The choice of which experiments are performed and the probability density  $\sigma(\lambda)$  are independent of each other.*

The result of an experiment with the setting a on system 1 is called s and takes on values from a discrete set  $S_a$  in the interval [-1,1]. For system 2, the results are called t out of the discrete set  $T_b$  in the same interval [-1,1]. The possible sets of outcomes can depend on the actual experiment (i.e.,  $S_{a'}$  can be different from  $S_a$ ). This definition is only a matter of convenience, the parameter space could be bigger or smaller than given here, or only described by probabilities of outcomes, without affecting the proof.

Because of assumption A2, the state  $\lambda$  determines probabilities for the measurement results of experiments a and b. The probability of getting both result s for experiment a and result t for experiment b when the systems are in state  $\lambda$  is expressed as the following probability function:

$$p_{a,b}(s, t | \lambda)$$

This function takes on values in the interval [0,1] and summation over all s in  $S_a$  and t in  $T_b$  yields 1. We then define marginal probabilities (the notation  $\sum_s$  meaning summation over all s in  $S_a$ ):

$$p_{a,b}^1(s | \lambda) \equiv \sum_t p_{a,b}(s, t | \lambda) \quad (220)$$

$$p_{a,b}^2(t | \lambda) \equiv \sum_s p_{a,b}(s, t | \lambda) \quad (221)$$

We then define the expectation values of the experiments a and b for a state  $\lambda$  as:

$$A_\lambda(a, b) \equiv \sum_s s \cdot p_{a,b}^1(s | \lambda) \quad (222)$$

$$B_\lambda(a, b) \equiv \sum_t t \cdot p_{a,b}^2(t | \lambda) \quad (223)$$

And we define the expectation value for the product  $s \cdot t$  as:

$$E_\lambda(a, b) \equiv \sum_{s,t} s \cdot t \cdot p_{a,b}(s, t | \lambda) \quad (224)$$

At this point, the most central assumption is invoked. As a result of Bell's definition of local causality, we assume:

*A4: For any a, b,  $\lambda$  there exist probability functions  $p_a^1(s | \lambda)$  and  $p_b^2(t | \lambda)$ , such that:*

$$p_{a,b}(s, t | \lambda) = p_a^1(s | \lambda) \cdot p_b^2(t | \lambda) \quad (225)$$

<sup>163</sup> W. Myrvold, M. Genovese, and A. Shimony, "Bell's Theorem", The Stanford Encyclopedia of Philosophy (Spring 2024 Edition), Edward N. Zalta & Uri Nodelman (eds.), URL = <<https://plato.stanford.edu/archives/spr2024/entries/bell-theorem/>>.

Here, it is helpful to think about the meaning of this equation. It says that for two experiments a and b on the spatially separated<sup>164</sup> subsystems 1 and 2 of a system in the state  $\lambda$ , the probability of getting the result s for an experiment a on system 1 only depends on the state  $\lambda$  and the experiment a, NOT on which experiment b is carried out on system 2 or what result t this experiment provides. In the same vein, the result t of the experiment b on system 2 is NOT influenced by the experiment a on system 1 or its result s.

This local causality assumption is the key point. It stems from a general idea about how a physics theory should work and seems very intuitive. However, we will see in the following proof that this assumption limits the predictions a theory can make and that the quantum mechanical predictions lie outside that limit for specific experiments, making the assumption incompatible with the observed reality.

### Proof Part 1: Deriving the CHSH Inequality

We now use this framework to derive the CHSH inequality:

Substituting Equation (225) in Equation (222) yields:

$$\begin{aligned} A_\lambda(a, b) &= \sum_s s \cdot p_{a,b}^1(s|\lambda) \\ &= \sum_s \sum_t s \cdot p_{a,b}(s,t|\lambda) = \sum_s \sum_t s \cdot p_a^1(s|\lambda) \cdot p_b^2(t|\lambda) = \sum_s s \cdot p_a^1(s|\lambda) \equiv A_\lambda(a) \end{aligned} \quad (226)$$

The second to last equality uses the fact that the sum of all probabilities must be unity:  $\sum_t p_b^2(t|\lambda) = 1$ . We see that the function  $A_\lambda(a, b)$  defined above does not depend on b, so we can use the expression  $A_\lambda(a)$  instead.

The same calculation can be used to show:

$$B_\lambda(a, b) = \sum_t t \cdot p_b^2(t|\lambda) \equiv B_\lambda(b) \quad (227)$$

Multiplying Equations (226) and (227) yields:

$$\begin{aligned} A_\lambda(a) \cdot B_\lambda(b) &= \sum_s s \cdot p_a^1(s|\lambda) \cdot \sum_t t \cdot p_b^2(t|\lambda) = \sum_{s,t} s \cdot t \cdot p_a^1(s|\lambda) \cdot p_b^2(t|\lambda) \\ &= \sum_{s,t} s \cdot t \cdot p_{a,b}(s,t|\lambda) = E_\lambda(a, b) \end{aligned} \quad (228)$$

For the last two equalities, we used Equations (225) and (224), respectively.

We define the quantities  $S_\lambda$  as follows<sup>165</sup>:

$$S_\lambda(a, a', b, b') = E_\lambda(a, b) - E_\lambda(a, b') + E_\lambda(a', b) + E_\lambda(a', b') \quad (229)$$

Now we generalize this result to the probability distribution  $\sigma$  and the expectation values of the  $E_\lambda$ s:

$$S_\sigma(a, a', b, b') \equiv \langle E_\lambda(a, b) \rangle_\sigma - \langle E_\lambda(a, b') \rangle_\sigma + \langle E_\lambda(a', b) \rangle_\sigma + \langle E_\lambda(a', b') \rangle_\sigma \quad (230)$$

We can use the same probability distribution  $\sigma$  for all four expectation values (even though they describe different experiments) because of assumption A3.

The absolute value of the average of a random variable cannot be greater than the average of its absolute value, so that follows:

$$|S_\sigma(a, a', b, b')| \leq \langle |S_\lambda(a, a', b, b')| \rangle_\sigma \quad (231)$$

Combining Equations (228) and (229) yields:

$$\begin{aligned} |S_\lambda(a, a', b, b')| &= |A_\lambda(a)(B_\lambda(b) - B_\lambda(b')) + A_\lambda(a')(B_\lambda(b) + B_\lambda(b'))| \\ &\leq |A_\lambda(a)(B_\lambda(b) - B_\lambda(b'))| + |A_\lambda(a')(B_\lambda(b) + B_\lambda(b'))| \end{aligned} \quad (232)$$

<sup>164</sup> In Bell's original article and all follow ups, spatially separated means spacelike separation in spacetime, i.e., the information of the experiment from one system cannot reach the other system before its experiment when travelling at the speed of light.

<sup>165</sup> In the literature, several distinct but similar definitions of this S-value can be found. They only differ in which exact polarizer angles are required to violate the inequality, not in any general conclusion that can be drawn.

As the experimental results  $s$  lie in the interval  $[-1,1]$ , the expectation values  $A_\lambda(a)$  and  $A_\lambda(a')$  do as well, allowing one to conclude the following inequality from Equation (232):

$$|S_\lambda(a, a', b, b')| \leq |(B_\lambda(b) - B_\lambda(b'))| + |(B_\lambda(b) + B_\lambda(b'))| \quad (233)$$

For any two numbers  $K$  and  $L$ , the following relations hold (you can check this via case distinction):

$$|K - L| = \max(|K|, |L|) - \text{sgn}(K) \cdot \text{sgn}(L) \cdot \min(|K|, |L|) \quad (234)$$

$$|K + L| = \max(|K|, |L|) + \text{sgn}(K) \cdot \text{sgn}(L) \cdot \min(|K|, |L|) \quad (235)$$

Here, the sign-function  $\text{sgn}()$  is defined as:

$$\begin{aligned} \text{sgn}(x) &= -1 \text{ for } x < 0 \\ \text{sgn}(x) &= 1 \text{ for } x \geq 0 \end{aligned} \quad (236)$$

and hence:

$$|K - L| + |K + L| = 2 \cdot \max(|K|, |L|) \quad (237)$$

Setting  $K = B_\lambda(b)$  and  $L = B_\lambda(b')$  in Equation (237) and substituting into (233) yields:

$$|S_\lambda(a, a', b, b')| \leq |(B_\lambda(b) - B_\lambda(b'))| + |(B_\lambda(b) + B_\lambda(b'))| = 2 \cdot \max(|B_\lambda(b)|, |B_\lambda(b')|) \quad (238)$$

And because the  $B_\lambda(b)$  and  $B_\lambda(b')$  lie in the interval  $[-1,1]$  (same reasoning as for the  $A_\lambda(a)$  above), we obtain:

$$|S_\lambda(a, a', b, b')| \leq 2 \cdot \max(|B_\lambda(b)|, |B_\lambda(b')|) \leq 2 \quad (239)$$

Since this is true for every value of  $\lambda$ , it must also be true for the expectation value of  $S_\lambda$ :

$$\langle |S_\lambda(a, a', b, b')| \rangle_\sigma \leq 2 \quad (240)$$

Combining Equations (240) and (231) yields:

$$|S_\sigma(a, a', b, b')| \leq 2 \quad (241)$$

This is the CHSH inequality, which holds for all theories that follow the framework and assumptions above. Now, in order to prove a Bell's type theorem, one has to find a quantum system for which the quantum mechanical predictions violate the inequality.

### Proof Part 2: Violation of the CHSH inequality by Quantum Mechanical Predictions

Consider a pair of photons propagating in opposite directions along the z-axis. The states  $|x\rangle_j$  and  $|y\rangle_j$  represent photon  $j$  ( $j = 1, 2$ ) being polarized in the x- and y-direction, respectively. Now take the following state vector:

$$|\Phi\rangle = \frac{1}{\sqrt{2}}(|x\rangle_1|x\rangle_2 + |y\rangle_1|y\rangle_2) \quad (242)$$

Now we insert a polarization analyzer (such as a birefringent crystal) into the path of each photon. The analyzer separates the photons into an ordinary and an extraordinary ray<sup>166</sup>, at the end of which a detector is placed. The axis of the analyzer is defined such that if the photon is polarized parallel to the axis, it will end up in the ordinary ray with certainty, while it will end up in the extraordinary ray with certainty if it is polarized perpendicular to the analyzer axis. The analyzer is assumed to be perfect, so that all photons end up in one of the two rays (no reflection or absorption) and the detectors are ideal in the sense that they detect every photon incident on them. The setup<sup>167</sup> is sketched in Figure 226.

<sup>166</sup> Please note that "ray" is used here because it is common language when talking about birefringent crystals. In the quantum picture, one must not imagine the photons as little balls forming a ray. The "rays" here only specify the two directions that the photons may take after the birefringent crystal.

<sup>167</sup> For the experiments in this kit, we do not use an analyzer with two detectors in each arm, but instead a linear polarizer with only one detector per arm. This is both easier to set up and saves the cost of the additional detectors. For the implications on the experiment, see Section 26.10. Here, we stick to the description with the analyzers, as this is closer to the original literature.

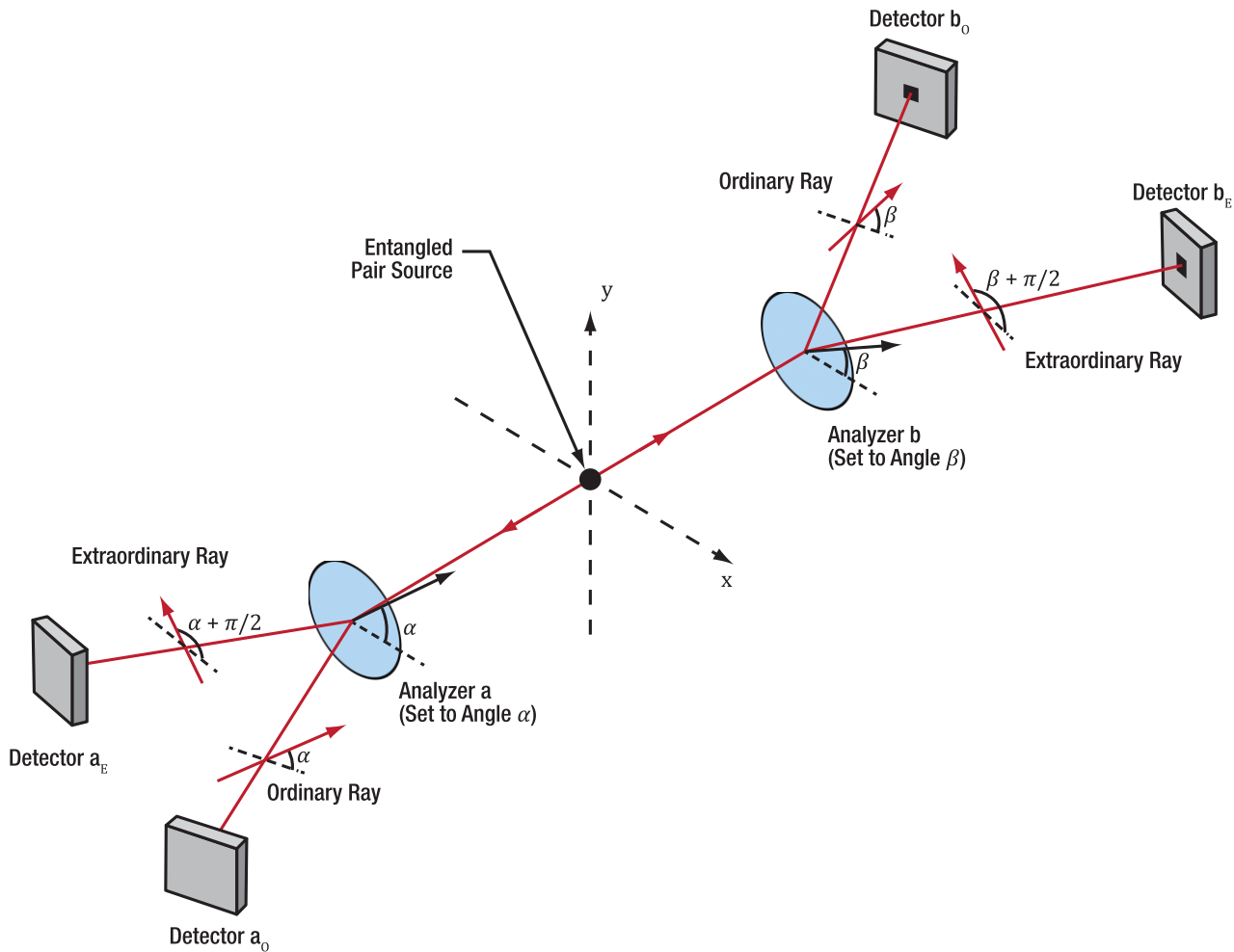


**Figure 226 Schematic Drawing of the Experiment Envisioned in the Proof of a Bell-Type Theorem**

We assign the result  $s = 1$  to the experiment a, if the photon 1 emerges in the ordinary ray (is detected at detector  $a_o$ ) and  $s = -1$  in case it emerges in the extraordinary ray (is detected at detector  $a_e$ ). The same assignments are made for the result  $t$  of experiment b in the case of photon 2. The experiments a and b are characterized by the respective analyzer angles  $\alpha$  and  $\beta$  (relative to the x-axis).

We now calculate the expectation value  $E_\Phi(a,b)$  from Equation (224) for the experimental case outlined here. As the results can only take the values 1 and -1, the sum has 4 terms:

$$\begin{aligned} E_\Phi(a,b) &= \sum_{s,t} s \cdot t \cdot p_{a,b}(s,t|\Phi) \\ &= p_{a,b}(1,1|\Phi) - p_{a,b}(1,-1|\Phi) - p_{a,b}(-1,1|\Phi) + p_{a,b}(-1,-1|\Phi) \end{aligned} \quad (243)$$

In quantum mechanics, the probabilities are given as the square of the absolute value of the projection of the system state onto the result state. For example, the result state corresponding to  $p_{a,b}(1,1|\Phi)$  is the state of both photons emerging in the ordinary ray, i.e., being polarized parallel to the respective analyzer axes, i.e.  $|\alpha\rangle_1 \cdot |\beta\rangle_2$ . In this case, detectors  $a_o$  and  $b_o$  in Figure 226 would detect a photon at the same time (coincidence). The result state corresponding to  $p_{a,b}(1,-1|\Phi)$  is the state of photon 1 emerging in the ordinary ray, i.e. being polarized parallel to the analyzer axis  $\alpha$  and photon 2 emerging in the extraordinary ray, i.e. being polarized perpendicular to the analyzer axis  $\beta$ , i.e. parallel to  $\beta + \frac{\pi}{2}$ , the state then being  $|\alpha\rangle_1 \cdot |\beta + \frac{\pi}{2}\rangle_2$  (coincidence of detection events at detectors  $a_o$  and  $b_e$ ). The remaining two result states follow the same logic. Hence, Equation (243) becomes:

$$E_\Phi(a,b) = \left| \langle \Phi | \alpha, \beta \rangle_{1,2} \right|^2 - \left| \langle \Phi | \alpha, \beta + \frac{\pi}{2} \rangle_{1,2} \right|^2 - \left| \langle \Phi | \alpha + \frac{\pi}{2}, \beta \rangle_{1,2} \right|^2 + \left| \langle \Phi | \alpha + \frac{\pi}{2}, \beta + \frac{\pi}{2} \rangle_{1,2} \right|^2 \quad (244)$$

Each of the four terms describes the probability of measuring the photons at a specific pair of detectors if the photon pair state is  $\Phi$  and the analyzer settings are  $\alpha, \beta$ . In the experiment with the setup shown in Figure 226,  $E_\Phi(a, b)$  can be determined by comparing the coincidence rates of the respective detector pairings, because the probabilities and count rates are proportional. Each of the four terms corresponds to one pairing of detectors.

Let's tackle these terms one by one by substituting the state  $|\Phi\rangle$  as given in Equation (242) starting with:

$$|\langle \Phi | \alpha, \beta \rangle_{1,2}|^2 = \left| \frac{1}{\sqrt{2}} \cdot ({}_2\langle x|_1\langle x| + {}_2\langle y|_1\langle y|) |\alpha\rangle_1 |\beta\rangle_2 \right|^2 = \frac{1}{2} \cdot |\langle x|\alpha\rangle_1 \cdot \langle x|\beta\rangle_2 + \langle y|\alpha\rangle_1 \cdot \langle y|\beta\rangle_2|^2 \quad (245)$$

Now, a state  $|\alpha\rangle$  describes the angle relative to the x-axis and can thus be written as (same applies for  $|\beta\rangle$ ):

$$|\alpha\rangle = \cos \alpha \cdot |x\rangle + \sin \alpha \cdot |y\rangle \quad (246)$$

Using this formulation and noting that  $\langle x|y\rangle = 0$  due to orthonormality of the Hilbert space basis, we obtain:

$$|\langle \Phi | \alpha, \beta \rangle_{1,2}|^2 = \frac{1}{2} \cdot |\langle x|\alpha\rangle_1 \cdot \langle x|\beta\rangle_2 + \langle y|\alpha\rangle_1 \cdot \langle y|\beta\rangle_2|^2 = \frac{1}{2} \cdot |\cos \alpha \cdot \cos \beta + \sin \alpha \cdot \sin \beta|^2 \quad (247)$$

The last term can be rewritten via a trigonometric equation, and we get:

$$|\langle \Phi | \alpha, \beta \rangle_{1,2}|^2 = \frac{1}{2} \cdot |\cos \alpha \cdot \cos \beta + \sin \alpha \cdot \sin \beta|^2 = \frac{1}{2} \cdot |\cos(\alpha - \beta)|^2 = \frac{1}{2} \cdot \cos^2(\alpha - \beta) \quad (248)$$

The second term in Equation (244) can then be written by the same logic as:

$$\begin{aligned} \left| \langle \Phi | \alpha + \frac{\pi}{2}, \beta \rangle_{1,2} \right|^2 &= \frac{1}{2} \left| \langle x|\alpha\rangle_1 \cdot \langle x|\beta + \frac{\pi}{2}\rangle_2 + \langle y|\alpha\rangle_1 \cdot \langle y|\beta + \frac{\pi}{2}\rangle_2 \right|^2 \\ &= \frac{1}{2} \cdot |- \cos \alpha \cdot \sin \beta + \sin \alpha \cdot \cos \beta|^2 \\ &= \frac{1}{2} \cdot |\sin(\alpha - \beta)|^2 = \frac{1}{2} \cdot \sin^2(\alpha - \beta) \end{aligned} \quad (249)$$

Using similar analysis, one finds that:

$$\left| \langle \Phi | \alpha + \frac{\pi}{2}, \beta + \frac{\pi}{2} \rangle_{1,2} \right|^2 = \frac{1}{2} \cdot \sin^2(\alpha - \beta) \quad (250)$$

$$\left| \langle \Phi | \alpha + \frac{\pi}{2}, \beta + \frac{\pi}{2} \rangle_{1,2} \right|^2 = \frac{1}{2} \cdot \cos^2(\alpha - \beta) \quad (251)$$

Now we substitute Equations (248) through (251) into Equation (244) and obtain:

$$\begin{aligned} E_\Phi(a, b) &= \frac{1}{2} \cdot \cos^2(\alpha - \beta) - \frac{1}{2} \cdot \sin^2(\alpha - \beta) - \frac{1}{2} \cdot \sin^2(\alpha - \beta) + \frac{1}{2} \cdot \cos^2(\alpha - \beta) \\ &= \cos^2(\alpha - \beta) - \sin^2(\alpha - \beta) = \cos(2\alpha - 2\beta) \end{aligned} \quad (252)$$

Now we substitute this result into the definition of the CHSH parameter  $S_\lambda(a, a', b, b')$  (Equation (229)):

$$\begin{aligned} S_\phi(a, a', b, b') &= E_\Phi(a, b) - E_\Phi(a, b') + E_\Phi(a', b) + E_\Phi(a', b') \\ &= \cos(2\alpha - 2\beta) - \cos(2\alpha - 2\beta') + \cos(2\alpha' - 2\beta) + \cos(2\alpha' - 2\beta') \end{aligned} \quad (253)$$

We choose a set of experiments, i.e. a set of analyzer angles such that:

$$\beta - \alpha = \alpha' - \beta = \beta' - \alpha' = \gamma \quad (254)$$

This results in  $\beta' - \alpha = 3\gamma$  and:

$$\begin{aligned} S_\phi(a, a', b, b') &= \cos(2\alpha - 2\beta) - \cos(2\alpha - 2\beta') + \cos(2\alpha' - 2\beta) + \cos(2\alpha' - 2\beta') \\ &= 3 \cdot \cos(2\gamma) - \cos(6\gamma) \end{aligned} \quad (255)$$

We can show that this violates the CHSH inequality. Taking the derivative yields that the maximal violation occurs at  $\gamma = \frac{\pi}{8} = 22.5^\circ$ :

$$S_\phi(a, a', b, b') = 3 \cdot \cos\left(\frac{\pi}{4}\right) - \cos\left(\frac{3\pi}{4}\right) = 3 \cdot \frac{1}{\sqrt{2}} - \left(-\frac{1}{\sqrt{2}}\right) = \frac{4}{\sqrt{2}} = 2\sqrt{2} \quad (256)$$

As an example, a set of experiments with  $\alpha = 0^\circ, \beta = 22.5^\circ, \alpha' = 45^\circ, \beta' = 67.5^\circ$  will lead to such a maximum violation.

## Conclusion

The above section demonstrates that the CHSH Inequality (241) holds for all theories that follow from the local causality assumption (and some auxiliary assumptions) and provides an explicit experiment for which the quantum mechanical predictions significantly violate the inequality. As a result, if the experimental results agree with the quantum mechanical predictions, all theories with the local causality assumption must be ruled out.

### 26.7 Experimental Test of the CHSH Inequality

If one wants to experimentally test the CHSH equation just proven, one can build a setup as shown in Figure 226 and perform a set of coincidence measurements with the goal to determine the four quantities  $E_\Phi(a, b)$ ,  $E_\Phi(a, b')$ ,  $E_\Phi(a', b)$ , and  $E_\Phi(a', b')$ , which in turn make up  $S_\Phi(a, a', b, b')$ . The theoretical proof only includes the probabilities of the photon pairs to end up at specific detector pairs. In the real-life experiment, the measurable quantities are coincidence count rates between specific sets of detectors.

Assuming ideal detectors and the configuration given in Figure 226, the probabilities are just the coincidence count rates of the 4 possible detector pairings, divided by the overall amount of coincidence events. As an example:

$$|\langle \Phi | \alpha, \beta \rangle_{1,2}|^2 = \frac{R_{a_0, b_0}(\alpha, \beta)}{R_{a_0, b_0}(\alpha, \beta) + R_{a_0, b_e}(\alpha, \beta) + R_{a_e, b_0}(\alpha, \beta) + R_{a_e, b_e}(\alpha, \beta)} \quad (257)$$

Substituting all the probabilities in Equation (244) results in:

$$E(a, b) = \frac{R_{a_0, b_0}(\alpha, \beta) - R_{a_0, b_e}(\alpha, \beta) - R_{a_e, b_0}(\alpha, \beta) + R_{a_e, b_e}(\alpha, \beta)}{R_{a_0, b_0}(\alpha, \beta) + R_{a_0, b_e}(\alpha, \beta) + R_{a_e, b_0}(\alpha, \beta) + R_{a_e, b_e}(\alpha, \beta)} \quad (258)$$

This relation still holds if the detectors have a detection efficiency below 100%, as long as the efficiencies are equal for all detectors. However, detection efficiencies below a certain threshold allow explanation of the results by a specific local hidden variable theory, opening a so-called loophole, see Section 26.10.

Because there are two detectors in each arm, all coincidence count rates in Equation (258) can be measured in a single measurement. Hence, to determine  $S_\Phi(a, a', b, b')$ , four measurements with different analyzer settings are required: one for each  $E_\Phi$ -quantity. If the prepared pair state is the one given in Equation (242) and the goal is to show maximum violation of the inequality, the analyzer settings should be the ones determined in the proof of the CHSH equation, i.e.,  $\alpha = 0^\circ, \beta = 22.5^\circ, \alpha' = 45^\circ$  and  $\beta' = 67.5^\circ$ .

Of course, the CHSH inequality can be violated with other entangled states, however the optimal analyzer settings to do so depend on the actual state.

When comparing the setup and the CHSH inequality used here with the setup and inequality used in the kit (Section 20.3.3), one will notice some differences. Only two instead of four detectors are used in the kit and linear polarizers are used instead of the analyzers. The setups are largely equivalent, with a photon going to the extraordinary ray for any analyzer angle of  $\varphi$  in the 4-detector setup being equivalent to a photon transmitted by a polarizer with an angle of  $\varphi + 90^\circ$  in the kit setup:

$$R_{a_0, b_e}(\alpha, \beta) \rightarrow R(\alpha, \beta + 90^\circ) \quad (259)$$

The kit setup is more economical (saving two expensive detectors) but has the disadvantage that four measurements are required for each E-quantity (16 measurements overall), while only one measurement per E-quantity (4 overall) is required with the 4-detector setup. Furthermore, the kit setup requires additional assumptions about losses in the system, see Section 26.10.

Students should be aware that an experiment with an educational setup does not constitute a perfect Bell test, as several so-called loopholes exist that allow one to explain the results with local causal hidden variable theories, if the setup is not very carefully designed. A description of the most important loopholes is given in Section 26.10.

### 26.8 Toy Model for a Local Causal Hidden Variable Theory

The Bell test rules out local causal hidden variable theories as a description of reality, but what does such a theory even look like? In this section, we present a simple local hidden variable theory that comes as close to the QM

predictions as possible for the experiment described in Section 26.7<sup>168</sup>. The following assumptions made for this theory are only made to emulate the quantum mechanical predictions for the specific experiment as well as possible, there is no physical meaning to any of the introduced quantities (hence the term “toy model”):

- Both photons of a pair have an imagined property called quasi-polarization  $\lambda$  (this is the hidden variable), which can be understood similar to a linear polarization axis.
- For each pair, this quasi-polarization takes on a different value in an unpredictable way (it does not need to be random, it could be deterministic in a way yet to be discovered), such that it homogeneously covers the whole range of possible quasi-polarizations ( $0^\circ$  to  $180^\circ$ ).
- The behavior of the hidden variable (quasi-polarization) obeys the following (hidden) law: When incident on an analyzer, the photon will always emerge in the ordinary ray if  $\lambda$  is closer to the analyzer axis (specified by the angles  $\alpha$  and  $\beta$ ) than to the axis perpendicular to the analyzer axis, and otherwise will always emerge in the extraordinary ray i.e.,

$$s = -1 \text{ for } \frac{\pi}{4} < |\alpha - \lambda| \leq \frac{3\pi}{4} \quad (260)$$

$$s = 1 \text{ otherwise}$$

$$t = -1 \text{ for } \frac{\pi}{4} < |\beta - \lambda| \leq \frac{3\pi}{4} \quad (261)$$

$$t = 1 \text{ otherwise}$$

This theory fulfills the locality assumption because the measurement result for the first photon only depends on its property  $\lambda$  and the analyzer setting  $\alpha$  and in no form on the setting or result of the experiment with particle 2 and the same is true in reverse.

It can be shown that the probability to find both photons in the ordinary beams for this toy model is:

$$p_{a,b}^{toy}(1,1) = \left| \frac{1}{2} - \frac{|\beta - \alpha|}{\pi} \right|, \quad |\beta - \alpha| \in [0^\circ, 180^\circ] \quad (262)$$

A comparison of this result with the quantum mechanical predictions derived above (Equation (248)) is displayed in Figure 227. Both curves are the calculated probabilities for both photons of a pair to end up in the ordinary rays. The orange curve is calculated assuming quantum mechanics and the blue curve is calculated assuming the toy model described above.

One can see that the toy model agrees with the QM predictions for parallel and perpendicular polarizers (angle differences  $0^\circ$ ,  $90^\circ$ , and  $180^\circ$ ) and for angle differences of  $45^\circ$  and  $135^\circ$  but shows less correlation or anti-correlation for all other analyzer pairings.

If we calculate the S-value for the angles used in the proof of the Bell theorem above, our toy model results in  $S = 2$ , i.e., for this specific experiment, it comes as close to the QM predictions as possible for a local hidden variable theory.

Of course, it is possible to think of many other causal local hidden variable theories, but none of them can come closer to the orange curve than the simple model presented here<sup>168</sup>. This means that neither the toy model introduced above, nor any other causal local hidden variable theory can correctly predict the experimental results, (which reliably follow the QM predictions) and therefore none of them describes reality.

<sup>168</sup> D. Dehlinger and M. W. Mitchell, American Journal of Physics, **70**, 903-910 (2002).

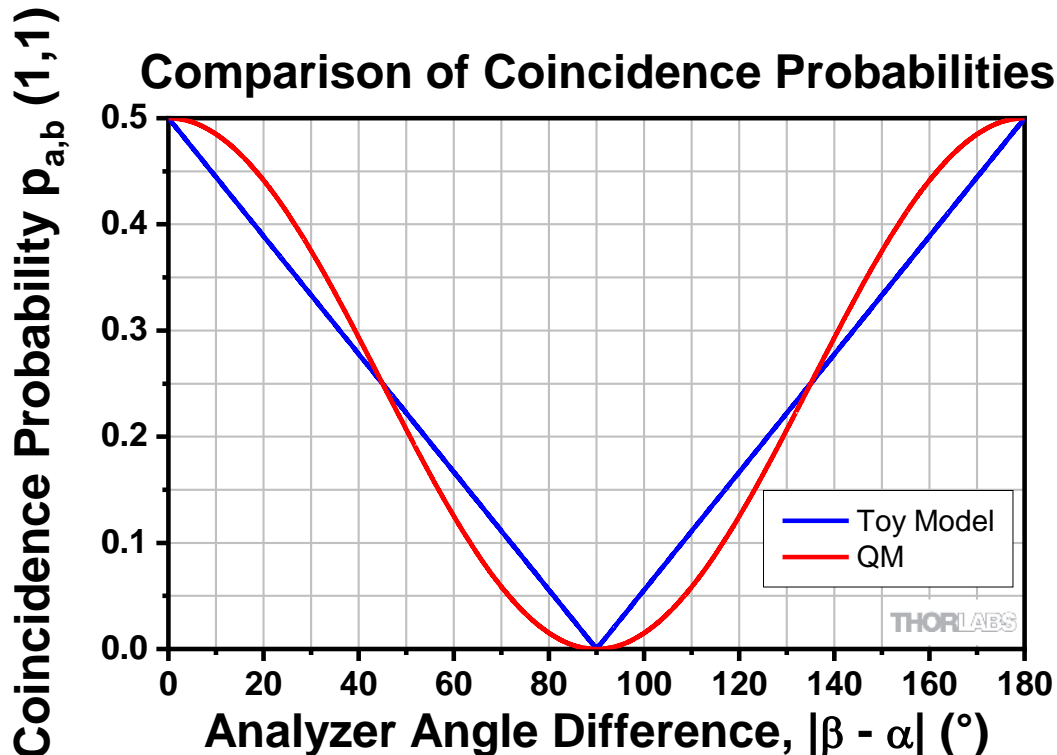


Figure 227 Comparison of a Hidden Variable Toy Model with QM Predictions

## 26.9 Possible Interpretations of the Bell Test Result

During the derivation of the Bell-type inequality in Section 26.6, the following four assumptions were made:

A1: *The probability density  $\sigma(\lambda)$  (describing the generated systems) is independent of what happens to the systems after generation.*

A2: *The system state  $\lambda$  determines the probabilities of the outcomes of any measurements performed on the systems.*

A3: *The choice of which experiments ( $a$  and  $b$ ) are performed and the probability density  $\sigma(\lambda)$  are independent of each other.*

A4: *For any  $a, b, \lambda$  there exist probability functions  $p_a^1(s|\lambda)$  and  $p_b^2(t|\lambda)$ , such that:*

$$p_{a,b}(s, t|\lambda) = p_a^1(s|\lambda) \cdot p_b^2(t|\lambda) \quad (263)$$

Assumption A4 is the local causality assumption. Its meaning is that the setting of one experiment cannot have any influence on the result probabilities of the another spatially separated experiment. Therefore, the experimental results are statistically independent, and the joint probability can be written as a product.

If one accepts the experimental evidence for quantum mechanical predictions, then one or more of these assumptions must be abandoned. The choice of which one to abandon leads to different interpretations of quantum mechanics. In the following, we present some interpretation options without aiming for completeness.

- Orthodox quantum theory abandons local causality (Assumption A4), as it includes entangled states that cannot be written as product states of pure subsystem states. This means that measurements on one of the particles influence the probabilities of a measurement on the second particle and the joint probability cannot be written as a product of subsystem probabilities as in Equation (263).
- Bohmian mechanics abandons the local causality (A4) in a different way. It is a hidden variable theory, with particle positions added as hidden variables, but the trajectories of these particles are guided by the many-particle wave function, leading to obvious non-locality.

- Some interpretations deny that measurements have unique outcomes (implicit in assumption in A2). These include the many-world interpretations where every possible result of a measurement occurs simultaneously, and every quantum measurement results in a splitting of worlds in consequence.
- One can also reject A1. One way to do this is to suppose some form of retrocausality, i.e., the possibility that an experiment in one arm influences the state of the particles at the source (in the past) and thus the result of the experiment in the other arm.
- Denying A3 is also a possibility by invoking the possibility that the experimenters are not free in their decision about the experiment settings, but rather that both the state of the particles and the setting decisions by the experimenters are caused deterministically in such a way that the results always confirm with QM predictions although they are in fact local deterministic. This approach is called super-determinism.
- One could also assume a different spacetime than a Minkowski one and try to explain the results of quantum experiments via wormholes or wrapped dimensions.

Most of these options are just interpretations of the QM results that cannot be experimentally proven one way or the other. For some of them, experimental tests might be possible at some point in the future.

## 26.10 Loopholes in Bell Test Setups

Instead of accepting the experimental results and choosing one of the interpretations above, several possible loopholes in the actual experiments could explain the results without ruling out local hidden variable theories. Again, we touch on two important ones without aiming for completeness:

- Fair sampling: In real-life experiments neither the analyzers nor the detectors will be perfect. As a result, not every photon that leaves the source will be detected: some will be absorbed, some will reach the detector but not trigger a signal. It is usually assumed that the photons that are detected form a fair sample of all photons, but it can be argued (and has been<sup>169</sup>) that this does not have to be the case. For example, one can imagine a case where the analyzer setting has an influence on the detection probability, which would distort the experimental results. It has been shown that for experiments with a maximally entangled state, the quantum efficiency of the detectors has to be at least 83% to close this loophole. Moreover, schemes employing not-maximally entangled states have been developed to lower this requirement to 66%.
  - In this kit, the detection efficiency of the SPDMA detectors is lower than 50% and most of the photons in the SPDC cone are not detected at all because they don't reach the detectors. Furthermore, by using just two detectors, we can't measure both orthogonal polarizations at the same time, since we lose all the photons which are blocked by the polarizer. Therefore, the fair sampling loophole is open.
- Communication loophole: One can envision a situation where the information of one measurement result is transferred to the other detector at the speed of light and influences the measurement there. The remedy here is to place the detectors so far apart that information of one cannot reach the other in the timescale of the experiment even at speed of light. The same has to be ensured for communication between the analyzers and the source (for example by employing automatic mechanisms that change the settings while the photons are already in flight).
  - In this kit, the detectors are separated by less than 30 cm, which corresponds to less than 1 ns travel time for light. However, the coincidence window of the measurements is 5 ns. Furthermore, decisions about the measurement settings occur at least some seconds before the experiment, so the communication loophole is also open.

<sup>169</sup> P. M. Pearle, *Physical Review D*, 2, 1418 (1970).

In 2015, two groups separately performed experiments that closed both loopholes simultaneously<sup>170,171</sup> and therefore provide very convincing experimental proof of the QM predictions.

## 26.11 Spatial Walk-Off

In this section, we provide a more detailed explanation of the spatial walk-off effect and the required calculations to design suitable compensation crystals. We will closely follow the elaborate derivation given in the literature<sup>172</sup>. Naming conventions are taken over from this reference and deviations from the original source are marked where appropriate.

Figure 228 schematically compares the two possible paths of the photon (one of the pair, the other one is symmetrical) through the crossed BBO pair crystal to the detector. In both cases, the photon must travel in the same direction  $k_\alpha$  external to the crystals in order to reach the detector. Since both photon pair generation processes create ordinarily polarized photons in each crystal, each of the photons travels in the same direction and the same distance in its generating crystal, thus picking up the same phase  $\Phi_o$ . However, if it is generated in the first crystal, it additionally travels through the second crystal as the extraordinary beam, picking up an additional phase  $\Phi_{eff}$  inside the crystal. Due to the different exit points at the back surface of the second crystal, there also is a phase difference  $\Phi_\Delta$  from propagation in air towards the detector.

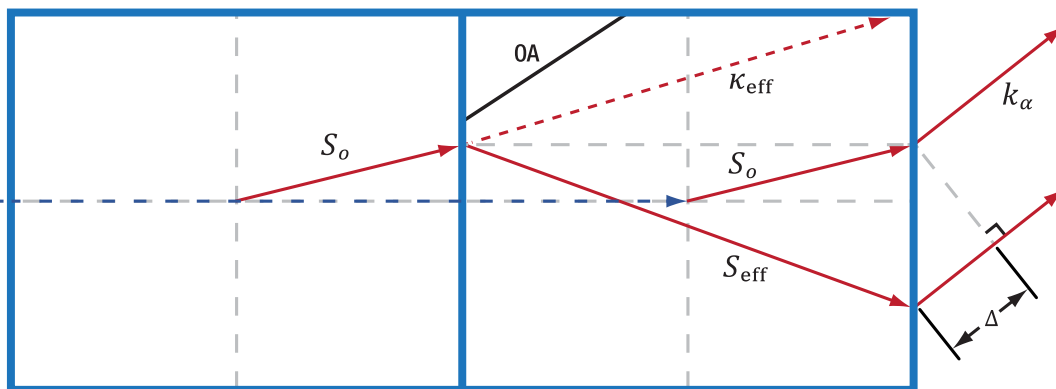


**Figure 228** Schematic of the ray paths through a BBO pair. Photons generated in a crystal ( $S_o$ ) are ordinarily polarized and experience the same refractive index, thus parallel ordinary rays inside the crystals are still parallel on their way towards the detector ( $k_\alpha$ ). Photons generated in the first crystal travel an additional distance with extraordinary polarization in the second one ( $S_{eff}$ ) and, due to different optical indices, experience additional Poynting vector walk-off (difference between  $\kappa_{eff}$  and  $S_{eff}$ ) away from the optical axis (OA). Due to the difference in exit points, there is an additional path length difference  $\Delta$  in air between both rays.

In a real setup, the detector aperture is not just a single point, but a finite area. Hence, each ray in Figure 228 and Figure 229 actually represents a bundle of rays with a small angular spread – all reaching the detector area. Here we define the detector aperture as the aperture of the iris in front of the detector optics assembly, as any ray passing through the iris opening is focused onto the detector's active area by the lens.

All of the ray paths and the phase differences depend heavily on the collection angle, thus the phase difference between the VV and HH states is not homogenous over the detector aperture, but actually varies over few 100° in typical setup geometries. This effect is known as “spatial walk-off”. Because of this, the ensemble of measured photon pair states is strongly mixed and the properties of entangled states are hidden in measurements (see Section 20.2.6).

<sup>170</sup> M. Giustina et al., Physical Review Letters, **115**, 250401 (2015).

<sup>171</sup> B. Hensen et al., Nature, **526**, 682-686 (2015).

<sup>172</sup> J. B. Altepeter, E. R. Jeffrey, and P. G. Kwiat, Optics Express **13**, 8951-8959 (2005).

One very simple countermeasure to reduce the phase variance of collected photon pairs is to reduce the detector aperture, thus reducing the spread of detection angles. However, this strongly reduces the coincidence count rates<sup>173</sup> and signal-to-noise ratio as well.

A more powerful solution is the compensation of the spatial walk-off with additional birefringent elements. These elements add to the relative walk-off with opposite sign, such that the total walk-off between both polarizations is effectively very close to zero<sup>174</sup>. In order to choose optimal compensation crystals, one has to calculate the phase of each polarized ray passing through the crystals towards the detectors, as described in the following. The notation used throughout this and following sections is given in the table below:

Variable	Definition
$k_\alpha$	Incident photon's unit momentum vector outside of the crystal.
$\kappa_o$	Unit momentum vector for ordinarily polarized light inside the crystal.
$\kappa_{\text{eff}}$	Unit momentum vector for extraordinarily polarized light inside the crystal.
$\alpha$	Angle between $N_{\text{surf}}$ and $k_\alpha$ .
$\Psi_o$	Angle between $N_{\text{surf}}$ and $\kappa_o$ .
$\Psi_{\text{eff}}$	Angle between $N_{\text{surf}}$ and $\kappa_{\text{eff}}$ .
OA	Crystal optic axis.
$S_o$	Ordinary Poynting vector inside the crystal. Always equal to $\kappa_o$ .
$S_{\text{eff}}$	Extraordinary Poynting vector inside the crystal.
$\beta$	Angle between $N_{\text{surf}}$ and $S_{\text{eff}}$ .
$\rho$	Angle between $S_{\text{eff}}$ and $\kappa_{\text{eff}}$ .
$\Delta$	Free-space distance that the extraordinary but not the ordinary beam must travel.
$n_o, n_e$	The crystal's ordinary and extraordinary indices of refraction
$n_{\text{eff}}(\theta)$	The index of refraction for a direction which is at an angle $\theta$ from the optic axis.

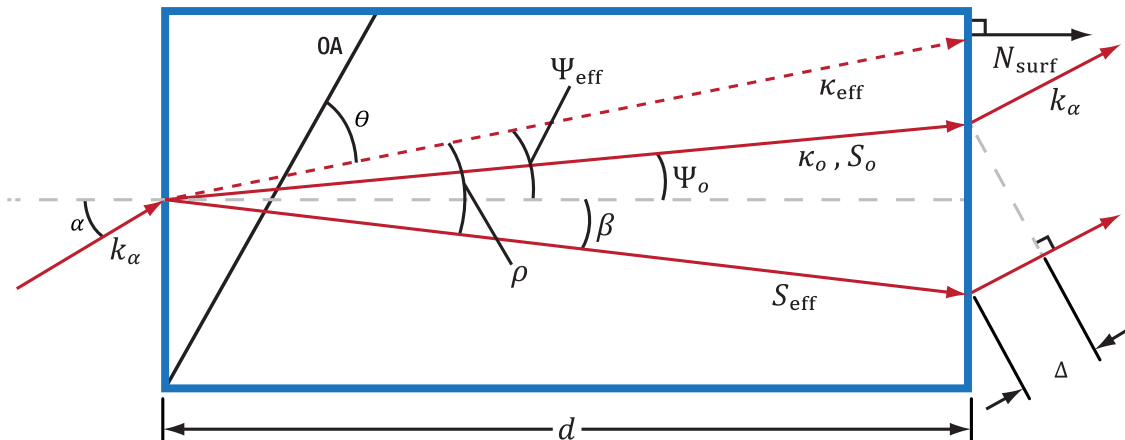


**Figure 229** Diagram illustrating all relevant vectors, angles, and variables used for calculating angle-dependent phase differences due to birefringent crystals. This shows the situation for a compensation crystal,

<sup>173</sup> Scaling with the detector aperture area, folded with the emission cone width. Reducing the detector aperture area reduces the coincidence rates. However, this scaling is non-linear, as the photon rate in the emission cone is not homogenous. As the alignment of both detectors is usually not perfectly symmetric, at very small apertures, they mostly pick up photons from different pairs and the coincidence rate drops.

<sup>174</sup> Note, that the relevant quantity is the total phase added up from both signal and idler arms. There may still be considerable walk-off with opposite signs for the phases in each arm. For the two-photon state only the sum of the phases in both arms is relevant and both contributions cancel each other out.

i.e., photons of both polarizations passing the whole crystal. Arbitrarily polarized light is incident from the left onto a negative uniaxial crystal (e.g., BBO) with its optic axis (OA) in the plane of the page.<sup>175</sup>

Figure 229 shows an overview of all angles, distances and ray vectors involved in the calculation. Note that this is a special case where all axes and angles lie in the drawing plane. This is typically not the case and the plane of incidence does not necessarily contain the optical axis as well. Thus,  $\beta$ ,  $\rho$  and  $\theta$  usually do not share the same plane with each other or the common plane of  $\alpha$ ,  $\Psi_{\text{eff}}$  and  $\Psi_o$ .

The relevant phases to be calculated are:

$$\Phi_o = \frac{d n_o}{\cos \Psi_o} S_o \cdot \kappa_o \frac{2\pi}{\lambda} = \frac{d n_o}{\cos \Psi_o} \frac{2\pi}{\lambda} \quad (264)$$

$$\Phi_{\text{eff}} = \frac{d n_{\text{eff}}}{\cos \Psi_{\text{eff}}} S_{\text{eff}} \cdot \kappa_{\text{eff}} \frac{2\pi}{\lambda} = \frac{d n_{\text{eff}}}{\cos \Psi_{\text{eff}}} \cos \rho \frac{2\pi}{\lambda} \quad (265)$$

$$\Phi_{\Delta} = \Delta \frac{2\pi}{\lambda} \quad (266)$$

The unit vector dot products in the equations for  $\Phi_o$  and  $\Phi_{\text{eff}}$  account for the possible mismatch between Poynting vector (i.e., the direction the light actually travels along) and the wavefront orientations, making the effective optical path length smaller than the traversed distance. This factor is equal to the cosine of the angle between the  $S$  and  $\kappa$  vectors, which is, per definition, unity for the ordinary beam and angle  $\rho$  for the (effective) extraordinary beam.

The Poynting vector walk-off angle  $\rho$  is given by:

$$\rho = \text{sgn}(n_o - n_e) \left( \theta - \tan^{-1} \left[ \frac{n_o^2}{n_e^2} \tan \theta \right] \right) \quad (267)$$

For negative uniaxial crystals ( $n_o > n_e$ ), like BBO, the Poynting vector is further away from the optical axis than the wavevector  $\kappa_e$ , by this angle.

The angles  $\Psi$  are calculated via Snell's law as  $\Psi = \sin^{-1} \left( \frac{\sin \alpha}{n} \right)$  using the respective index of refraction and, together with  $\alpha$ , reside in the plane of incidence, while the remaining angles are calculated from the dot product between the respective three-dimensional unit vectors.

The effective refractive index  $n_{\text{eff}}$  can be calculated from:

$$n_{\text{eff}} = \sqrt{\frac{n_e^2 n_o^2}{(n_e \cos \theta)^2 + (n_o \sin \theta)^2}} \quad (268)$$

It is important to note that the angle  $\theta$  here is not identical to the crystal's cut-angle, as the incidence angle is non-zero. Hence,  $\theta$  should be calculated for each ray individually from the angle between the ray's k-vector<sup>176</sup> with the optical axis. Since, by Snell's law, the k-vector inside the crystal depends on the refractive index itself, the resulting equations have a highly non-linear circular dependence. This can be resolved by calculating the index of refraction, internal angle and k-vector self-consistently<sup>177</sup>.

Since the ordinary Poynting vectors  $S_o$  are practically identical in both crystals of the crossed BBO pair for the two generated polarizations, the phase contributions are identical and may be omitted. Thus, the phase difference between both polarizations after the crossed BBO pair is the sum  $\Phi_{\text{tot,SPDC}} = \Phi_{\text{eff}} + \Phi_{\Delta}$ , picked up at the second crystal (compare to Figure 228).

<sup>175</sup> J. B. Altepeter, E. R. Jeffrey, and P. G. Kwiat, *Optics Express*, **13**(22), 8951-8959 (2005).

<sup>176</sup> Which already is an approximation. For a detailed calculation it is better to calculate  $\frac{\pi}{2} - \theta$  from the overlap between the ray's polarization and the optical axis.

<sup>177</sup> A self-consistent calculation iteratively improves the accuracy of an approximated solution. In this example, one may start with a rough estimate of the effective refractive index and then calculate the internal angle from Snell's law. Using this angle, one may calculate a more accurate refractive index for the ray, which in turn can be used to calculate a better approximation of the internal angle, and so on. Here, the solution quickly converges to a consistent result for the angle and refractive index within few iterations.

At this point our derivation differs from the reference<sup>172</sup> when it comes to the calculation of the distance  $\Delta$  in case of the BBO pair. The reference discusses this distance at the example of the compensation crystals, where both polarizations travel through the full crystal. But in the BBO pair, only the extraordinary beam enters the crystal at the front facet, while the ordinary beam is generated effectively half-way in the crystal. This affects the point of exit for the ordinary beam of this second crystal in the pair and, thus, the equation for the path difference  $\Delta$  must be different in both cases. For the crossed BBO pair the equation is (compare to Figure 228):

$$\Delta = d \left( N_{\text{surf}} \cdot k_\alpha - \frac{S_{\text{eff}} \cdot k_\alpha}{\cos \beta} \right) = d \left( \cos \alpha - \frac{S_{\text{eff}} \cdot k_\alpha}{\cos \beta} \right) \quad (269)$$

The path difference is calculated directly from the projections of the Poynting vector or surface normal onto the exit beam vector. Note that the Poynting vectors are unit vectors and hence the division by the cosine accounts for additional length required to reach the exit surface.

For the crystal and setup parameter combinations we tested, this change in the calculation effectively flips the sign of the total phase  $\Phi_{\text{tot,SPDC}}$  (normalized to the center ray) and a minor change of the absolute value. As can be seen from the full calculations, this change of sign is compensated by a 180° rotation of the spatial compensation crystals, which is extremely hard to note in a real setup (markers for optical axis orientations usually do not specify the difference between these orientations).

The remaining derivation is again on par with the reference<sup>172</sup>. For the compensation crystal we compare the extraordinary beam to the ordinary beam that fully traverses the crystal and thus the additional path difference after the crystal is (compare to Figure 229):

$$\Delta = d \left( \frac{S_o \cdot k_\alpha}{\cos \Psi_o} - \frac{S_{\text{eff}} \cdot k_\alpha}{\cos \beta} \right) \quad (270)$$

The total phase difference between both polarizations picked up in the spatial compensation crystal is:

$$\Phi_{\text{tot,comp}} = \Phi_o - (\Phi_{\text{eff}} + \Phi_\Delta) \quad (271)$$

Finally, the total phase after the crossed BBO pair and the spatial compensation crystal in each arm is the sum:

$$\Phi_{\text{tot,system}}(k_\alpha) = \Phi_{\text{tot,SPDC}} + \Phi_{\text{tot,comp}} \quad (272)$$

Note, that the detected photons pairs arrive at different relative locations at the detector apertures: The SPDC process is rotationally symmetric around the pump beam, thus a photon arriving a bit above the pump beam at one detector is paired with a photon that arrives a bit below the pump beam at the other detector. For degenerate (= same wavelength) photon-pair production the  $k_{\text{signal}}$  and  $k_{\text{idler}}$  vectors are also mirror symmetric for both detectors in the left/right direction<sup>178</sup>. This means that  $k_{\text{idler}} = k_{\text{signal}} \cdot \begin{pmatrix} -1 \\ -1 \\ +1 \end{pmatrix}$ .

For the complete entangled state, the directional dependence thus behaves like<sup>179</sup>:

$$\Phi_{\text{ent}} = \Phi_{\text{tot,system}}(k_{\alpha,\text{signal}}) + \Phi_{\text{tot,system}}(k_{\alpha,\text{idler}}) - \Phi_{\text{off}} \quad (273)$$

where  $\Phi_{\text{off}}$  is an arbitrary phase offset (independent of spatial directions), chosen such that the central ray has zero phase difference, when plotting the spatial walk-off phase maps, as shown Figure 230. The actual value in the experiment also depends on other birefringent elements in the setup and may be adjusted (as discussed in the next sections) to set the phase of the entangled state.

Note, that, in practice, it is not possible to flatten the phase distribution to exactly zero, but we can reduce the effect by about one order of magnitude for our crystal system in the kit.

<sup>178</sup> In a more detailed analysis, this becomes much more complex, as due to the finite sharpness of the phase-matching condition the pair partners smear out from their idealized locations. Furthermore, the finite pump bandwidth drives (symmetric) pair creation over a spread of cone half-opening angles, while the non-degenerate contributions to the SPDC process generate pairs with shorter/longer wavelengths at smaller/larger cone half-opening angles.

<sup>179</sup> Note that reference 172 gives the summed phase of signal and idler arms as twice the phase of one arm, which is not generally accurate, but only when the beam directions are symmetric to the optical axis of the second crystal and further asymmetry effects (see Section 27.1.1) are neglected.

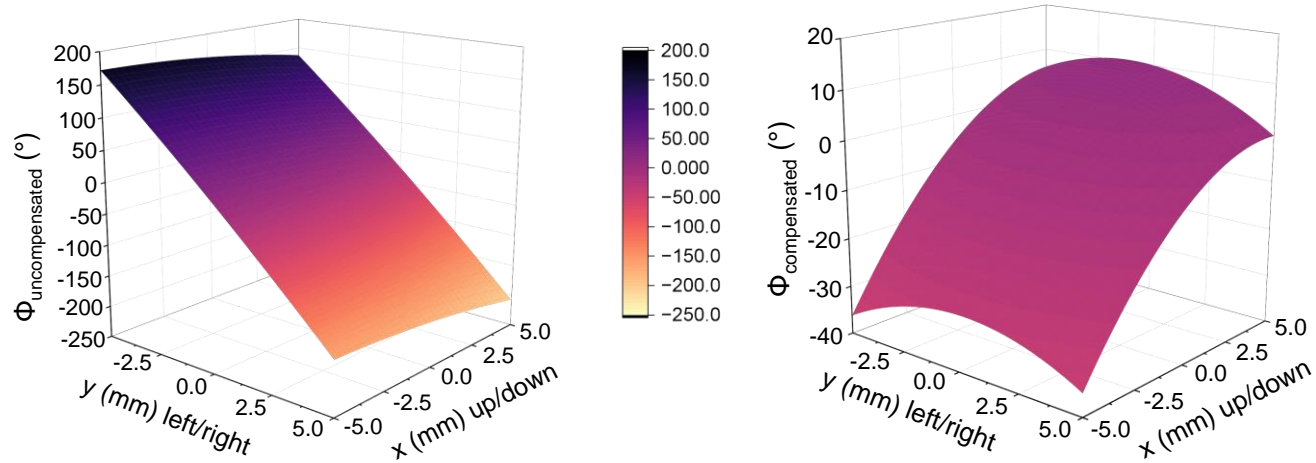


**Figure 230** Maps of the entangled state phase distribution over a  $1 \text{ cm}^2$  area at the detection plane. The left plot shows the broadly spread phase distribution acquired in the crossed BBO pair, while the right plot shows the phase distribution after inserting spatial compensation crystals. Note that the z-axis range on the right side is much narrower than on the left. The results shown here also take the Migdall effect to account (see Section 27.1.1).

Note that during these discussions, it is assumed that the photon pairs are always created in the center of their respective crystal. As will be seen, the largest part of the walk-off effects are not generated in the same crystal as the pair is being produced in. Instead, when the pair production in both crystals happens at equal distances from the front facete, the effects from both “active” crystals cancel out. Even when comparing photon pairs generated at the very front of the first crystal with another one created at the very end of the second crystal (or the other way round), these effects are generally smaller than the contributions picked up in the “passive” crystal. Also, while the probability of creating a photon pair is constant everywhere along the pump beam path through each crystal, the mean value of both extreme cases (equal to both pairs created in the center) also has the maximum likelihood. This can be understood from the fact that there are many more position combinations that result in a similar strength of an intermediate walk-off effect, than the few combinations that result in a maximum effect. An analog example would be throwing two dice: Even though there is an equal probability for each dice to show any of the numbers 1 to 6, the probability distribution of the sum of the numbers shown is highest for the mean number 7 and lowest for the extreme cases 1 and 12.

For this kit, we chose the parameters of the spatial compensation crystals in such a way that a good balance is struck between the following criteria:

- Negligible influence on temporal walk-off (small cut-angle)
- Zero angle of incidence for single photon beam paths (allowing alignment with axicon)
- Thickness optimized for small relative thickness tolerance during cutting process

## 26.12 Temporal/Chromatic Walk-Off

In this section, we provide a more detailed explanation of the temporal/chromatic walk-off effect and the required calculations to design suitable compensation crystals.

The calculation of the phases for the spatial walk-off in the previous section is only carried out for a single wavelength. However, the finite pump bandwidth and short crystal length allow for the generation of a rather broad range of degenerate photon-pair wavelengths. Due to dispersion of the refractive indices (see Figure 16), the different wavelengths pick up different phase contributions along the path through the crystals. While the spatial walk-off introduced a spread of the state phase due to different angles through the crystals, the walk-off effect discussed here further spreads the phase distribution due to the spread of wavelengths involved.

It would be possible to just repeat the previous calculations for a bunch of different wavelengths within the pump-beam bandwidth and calculate the phase-spread from those results. However, due to the rather weak correlation

between wavelength and emission angle, one may discuss and compute wavelength-dependent effects also along another elegant route (which will also explain the commonly used term “temporal” walk-off):

The bandwidth-dependent phase spread is, in first approximation, just the integral of the derivative of the phase with respect to the frequency ( $\frac{d\Phi}{d\omega}$ ) over the frequency bandwidth. Per definition, this derivative is also called the group delay ( $\tau_g = -\frac{d\Phi}{d\omega}$ ), which defines the time for a light *pulse* to travel a certain distance. Hence, minimizing the bandwidth-dependent phase spread difference between both polarizations is conceptually identical to having equal pulse travel times through the system for both polarizations – even though the actual experiment uses a continuous-wave laser, instead of a pulsed light source<sup>180</sup>.

All phase terms in the previous section explicitly contain the frequency dependence as the factor  $\frac{2\pi}{\lambda} = \frac{\omega}{c}$  and the (extra-)ordinary phases picked up inside the crystal contain the additional implicit frequency dependence in the refractive index  $n \equiv n(\omega)$ . When calculating the group delay (or “travel time”) in the crystals, one has to apply the product rule for derivatives:

$$\tau_g \sim \frac{d\Phi_{e,o}}{d\omega} \sim \frac{d n(\omega)}{d\omega} \omega + n(\omega) = g(\omega) \quad (274)$$

where  $g(\omega)$  is called the group index, which may also be expressed in terms of the wavelength as (see Figure 231):

$$g(\lambda) = n(\lambda) - \frac{d n(\lambda)}{d\lambda} \lambda \quad (275)$$

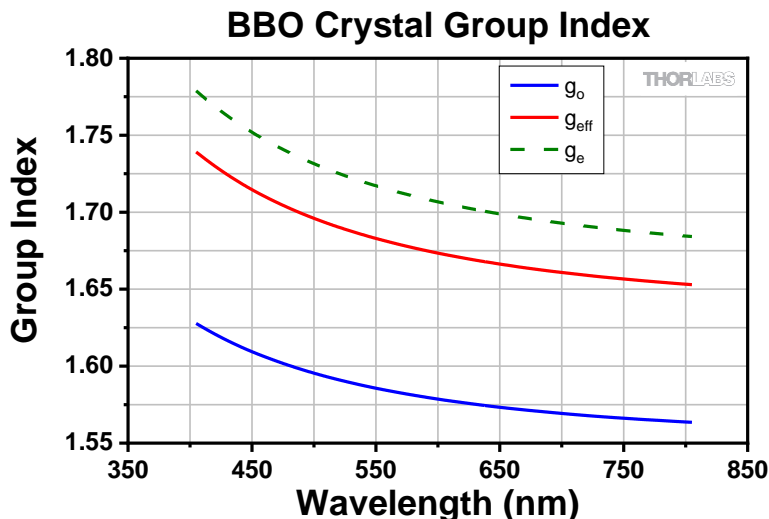


**Figure 231** Group indices in the crossed BBO pair crystal ( $\theta=29.2^\circ$ ). The blue line is ordinary polarization  $g_o$ , the green dashed line is the extraordinary polarization  $g_e$ , and the full red line is the effective extraordinary polarization for this cut  $g_{eff}$  ( $\theta=29.2^\circ$ ).

In order to calculate the group delay differences between both polarizations in the crystals, one can use the same equations as above, where the phase factor  $\frac{2\pi}{\lambda}$  is replaced by  $\frac{1}{c}$  and the refractive indices are replaced by the respective group indices.

In addition to the previous section, the contribution of the blue pump beam is now also relevant. Depending on the point of view, one can think about this either as the pump phase of each polarization being transferred to the pair photons generated from it or as the total pulse travel times from the laser diode through the birefringent crystals to the detector being equal for both generated polarizations.

<sup>180</sup> Put into historic context, early versions of SPDC experiments made use of pulsed light sources to generate coherent light in the ultra-violet to blue range via second harmonic generation.

For the discussion of temporal walk-off, we're extending Figure 196 with another birefringent crystal for temporal compensation (see Figure 232), while neglecting the spatial compensation crystal<sup>181</sup>. In the following we'll stick to the temporal (pulse travel time) point of view, as it is more convenient and commonly used in literature<sup>182</sup>.

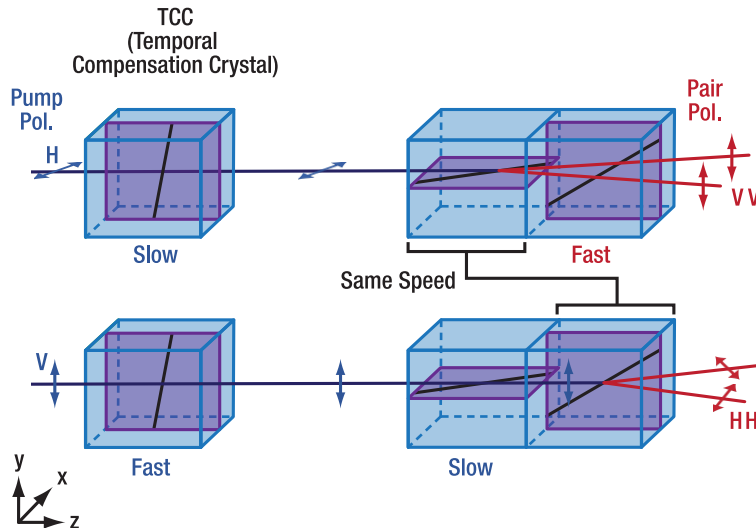


**Figure 232** Temporal walk-off between both polarizations in the crossed BBO pair (right) and its pre-compensation in another birefringent crystal (left). “Slow” and “Fast” labels denote the relative pulse propagation speed (inverse group delay).

First, let's note that two cases are virtually identical in Figure 232: In each case where a crystal generates an ordinarily polarized photon pair from an extraordinarily polarized pump polarization, the travel times for both the pump and the pair are identical. Since these contributions cancel each other out when comparing both pair polarizations, we do not need to consider those cases and can simply omit them.

The left-over comparison in the crossed BBO pair is then between the ordinarily polarized pump beam travelling fully through the first crystal and the extraordinarily polarized photon pair that passes fully through the second crystal. As can be seen in Figure 231, the ordinary blue beam has a higher group index and travels slower than the extraordinary red beam. Thus, there is a time delay being picked up between both photon-pair polarizations in the BBO pair, which is equal to<sup>183</sup>:

$$\Delta t_{\text{SPDC}} = t_{\text{eff}}(\lambda = 810 \text{ nm}) + t_{\Delta}(\lambda = 810 \text{ nm}) - t_o(\lambda = 405 \text{ nm}) \quad (276)$$

This time delay can be compensated by an additional birefringent crystal. It is placed in front of the BBO pair, such that it only affects the pump beam and not the photon pairs. This way the temporal compensation does not influence the spatial walk-off. The orientation of the crystal's optical axis is chosen such that it introduces a delay between both horizontal and vertical polarizations of the pump beam, without rotating the pump polarization<sup>184</sup>. This delay must have opposite sign to the one picked up in the crossed BBO pair and can be calculated from:

$$\Delta t_{\text{comp}} = t_o(\lambda = 405 \text{ nm}) - t_{\text{eff}}(\lambda = 405 \text{ nm}) \quad (277)$$

Another way to reduce this walk-off effect is to reduce the bandwidth of the pump beam<sup>185</sup>. Suitable laser systems for generation of light with even narrower bandwidth than the one used in this kit are commonly called “single

<sup>181</sup> This is done mainly to discuss the walk-off compensation for both effects separately and keeping the discussion streamlined. In reality, spatial compensation plates may add a considerable temporal walk-off with same or opposite sign to the one from the BBO pair. For this kit we choose the spatial compensation in such a way that its temporal walk-off is low in comparison to the BBO pair (<5%), such that it may be neglected when analyzing the experiments.

<sup>182</sup> R. Rangarajan, M. Goggin, and P. Kwiat, *Optics Express*, **17**(21), 18920-18933 (2009).

<sup>183</sup> Strictly,  $t_{\Delta}$  does only depend on geometry and not the wavelength, but we keep the dependency to denote that this contribution comes from the photon-pair part, not the pump.

<sup>184</sup> Due to the rather large and dispersive phase delay added between both polarizations, the pump polarization state is scrambled after the crystal (which may be verified by trying to extinguish the beam with a linear polarizer). The important part is that the **amplitudes** of both polarization components remain equal.

<sup>185</sup> One could alternatively limit the bandwidth by using much narrower bandpass filters in front of the detectors instead, but this causes very low system efficiency, as most of the pairs generated by a comparably broad pump bandwidth won't be detected and pump beam power is wasted.

frequency" lasers but are rather expensive. The use of temporal compensation crystals is thus more economical and also allows to add more didactical experiments about temporal walk-off.

For the kit, we chose the parameters of the temporal compensation crystals such that a good balance is struck between the following criteria:

- Minimizing the Poynting vector walk-off for the extraordinary beam (maximum at 45° cut-angle)
- High enough birefringence on thinner (=cheaper) crystals (requiring large cut-angle)
- Tunability of the entangled state phase by tilting the crystal (close to zero at cut-angle of 90°).

### 26.13 Imbalanced Pair Generation

The general entangled state is:

$$|\psi\rangle = (c_{HH}|HH\rangle + c_{VV}|VV\rangle) \quad (278)$$

with  $c_{HH}$  and  $c_{VV}$  being complex parameters. During the whole manual, we assumed that the setup is adjusted ideally, so that the weights of the HH and VV generation in the crossed BBO pair crystal are equal, resulting in the entangled state:

$$|\psi_{E,\phi}\rangle = \frac{1}{\sqrt{2}}(|HH\rangle + e^{-i\phi}|VV\rangle) \quad (279)$$

However, in a real setup there is often a small imbalance between the pair generation rates of the two parts of the crossed BBO pair crystal, leading to the following state:

$$|\psi_{E,C,\phi}\rangle = \sqrt{C} \cdot |HH\rangle + \sqrt{1-C} \cdot e^{-i\phi} \cdot |VV\rangle \quad (280)$$

The real-valued parameter  $C$  is the normalized generation rate for horizontally polarized photon pairs:

$$C = \frac{R_{HH}}{R_{HH} + R_{VV}} \quad (281)$$

Here,  $R_{HH}$  and  $R_{VV}$  are the generation rates for horizontally and vertically polarized photon pairs, respectively.

What is the effect of this imbalance on the expected experimental results? This can be calculated by substituting this state in the respective equations given in 20.2 for various settings of the polarizers. As an example, we will calculate how the coincidence rates vary with the angle of the polarizers if both polarizers are rotated in the same or opposite directions. We use a phase setting of 180° here, as this is one of the suggested experiments in the kit (see section 24.4.2). The state is thus:

$$|\psi_C^-\rangle = \sqrt{C} \cdot |HH\rangle - \sqrt{1-C} \cdot |VV\rangle \quad (282)$$

As described in section 20.2.3, the probability of the coincidence for turning the polarizers in identical directions can be calculated as:

$$\begin{aligned} P_{\varphi\varphi,\psi_C^-} &= \langle\varphi\varphi|\hat{P}_{\psi_C^-}|\varphi\varphi\rangle = \langle\varphi\varphi|\psi_C^-\rangle \cdot \langle\psi_C^-|\varphi\varphi\rangle \\ &= (\sqrt{C} \cdot \cos^2 \varphi \cdot \langle HH|HH\rangle - \sqrt{1-C} \cdot \sin^2 \varphi \cdot \langle VV|VV\rangle)^2 \\ &= (\sqrt{C} \cdot \cos^2 \varphi - \sqrt{1-C} \cdot \sin^2 \varphi)^2 \end{aligned} \quad (283)$$

The overall rate of generated pairs (in the direction of the detectors) is  $R_{HH} + R_{VV}$ , so in an experiment we would expect to measure the coincidence rates,  $R_{coin}(\varphi)$ , as:

$$\begin{aligned} R_{coin}(\varphi) &= (R_{HH} + R_{VV}) \cdot P_{\varphi\varphi,\psi_C^-} = (R_{HH} + R_{VV}) \cdot (\sqrt{C} \cdot \cos^2 \varphi - \sqrt{1-C} \cdot \sin^2 \varphi)^2 \\ &= (\sqrt{R_{HH}} \cdot \cos^2 \varphi - \sqrt{R_{VV}} \cdot \sin^2 \varphi)^2 \end{aligned} \quad (284)$$

Here, we used Equation (281) for the final step. The generation rates are usually not known, but they can be experimentally inferred by measuring the rates at 0° and 90°, as:

$$R_{coin}(0^\circ) = (\sqrt{R_{HH}} \cdot \cos^2 0^\circ - \sqrt{R_{VV}} \cdot \sin^2 0^\circ)^2 = R_{HH} \quad (285)$$

$$R_{coin}(90^\circ) = (\sqrt{R_{HH}} \cdot \cos^2 90^\circ - \sqrt{R_{VV}} \cdot \sin^2 90^\circ)^2 = R_{VV} \quad (286)$$

## Chapter 27 Technical Notes

### 27.1 Polarization In the SPDC Process

Since the light in this setup has various orientations of linear polarization, we shortly follow the light path from pump laser to detector:

- The pump laser polarization is perpendicular to the plane of the optical table.
- The first half-wave plate (at 22.5°) rotates the pump beam polarization to an angle of 45° to the table plane.
- The temporal compensation crystals do not rotate the pump polarization, but rather split the 45° orientation into equal amplitudes of parallel and perpendicular polarizations, which pick up a large delay. Due to the spectral bandwidth of the pump laser, the phase difference between both polarizations is not homogeneous and the total polarization state is rather mixed. Even for very narrow bandwidths the polarization would more likely be elliptical than linear, due to the acquired phase shift. However, the main axis of the polarization ellipsis remains at 45°.
- The crossed BBO pair crystals (first/second) are oriented such that their optical axes lie parallel/perpendicular to the table plane. The marking on the housing shows the rotation axis as a solid line and the polarization axes of the photon pairs with arrows (see Figure 233, left side).
- The photon pair polarization generated in the first/second crystal is perpendicular/parallel to the table plane and remains unaffected by the spatial compensation crystal.

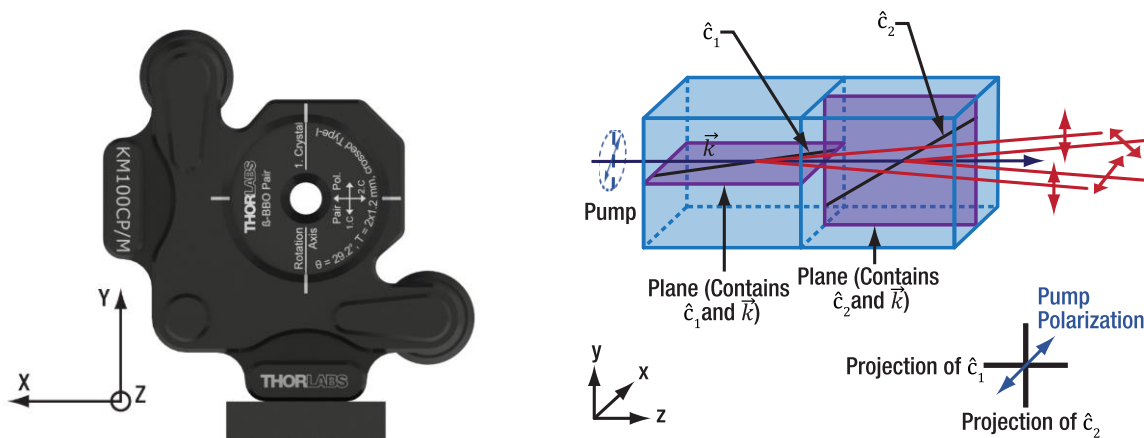


**Figure 233**    *Polarization vectors and crystal axes of the crossed BBO pair ( $\hat{c}$  is the optic axis of the crystal and  $\vec{k}$  is the propagation vector of the light). The red arrows for detectors T and A are in the same plane as  $\hat{c}_1$  and  $\vec{k}$ .*

#### 27.1.1 Polarization Distorting Effects

The polarization states generated by each individual crystal of the pair can be measured within the Bell-test setup. For this measurement, no compensation crystals should be used in the beam path before and after the crossed BBO pair and the pump-beam half-waveplate must be aligned to either 0° or 45°, such that the pump polarization only stimulates emission of photon pairs in one of the crystals. By rotating the polarizers in front of the detectors and measuring the single count rates, the rotation angle of the linear polarization state can be measured. See Section 24.1 for more details.

When performing these measurements, we observe two effects that influence the polarization of the photon pairs, causing a deviation from the idealized horizontal and vertical orientations assumed in the theoretical discussion of the experiments.

The first effect already impacts the polarization state upon generation of a photon pair in a single BBO crystal and it was discovered by A. Migdall<sup>186,187</sup>: In a Type-I SPDC process, the polarization of the generated photons is always perpendicular to the optical axis of the crystal and the propagation direction of the emitted photon, leading to the polarization distribution around the emission cone shown in Figure 234. The upper part of the figure displays an overview and the coordinate system, and the lower part depicts the polarization at different points of the emission cone for the two possible orientations of the BBO crystal viewed along the z-axis. For the crystal orientation in the lower left image, the polarizations at the detector points (left- and rightmost points of the cone) are not perfectly horizontal but slightly rotated (about 3° if our kit geometry is applied). For the orientation in the lower right image, perfectly vertical orientation of the polarization at the detector points is expected (this is why we use this configuration for the EDU-QOP1(/M) base kit).

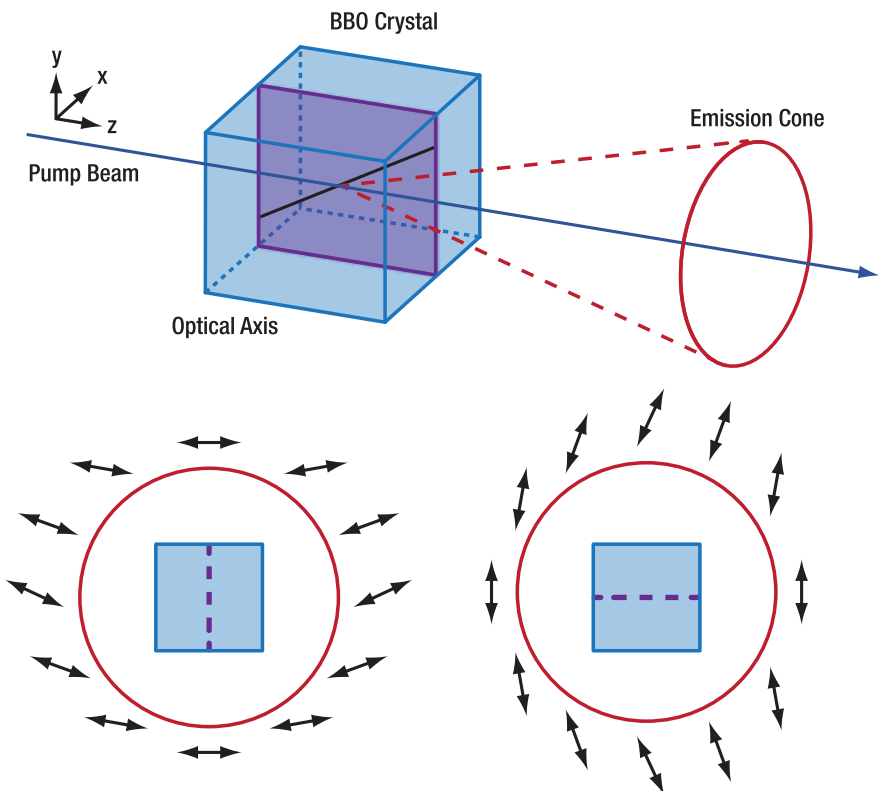


**Figure 234** Sketch of the Migdall effect. The upper image shows an overview and provides the coordinate system. The lower left image shows the polarization distribution around the emission cone for the geometry of the upper image. The lower right image shows the distribution after the BBO crystal is rotated by 90° around the z-axis. Both lower images are viewed along the z-axis. The figure was adapted from the source in footnote 187.

The second effect comes from pairing the crystals after each other. As the photons generated in the first crystal traverse the second birefringent crystal with a small cone-opening angle away from a high symmetry direction, their polarization state will be altered.

The following discussion gives more details for the orientation of the optical axes in the crossed BBO pair (assuming the usual setup geometry of this kit):

<sup>186</sup> A. Migdall, *Journal of the Optical Society of America B*, **14**(5), 1093–1098 (1997).

<sup>187</sup> R. Rangarajana, A. B. U'Ren, and P. G. Kwiat, *Journal of Modern Optics*, **58**(3-4), 312–317, (2011).

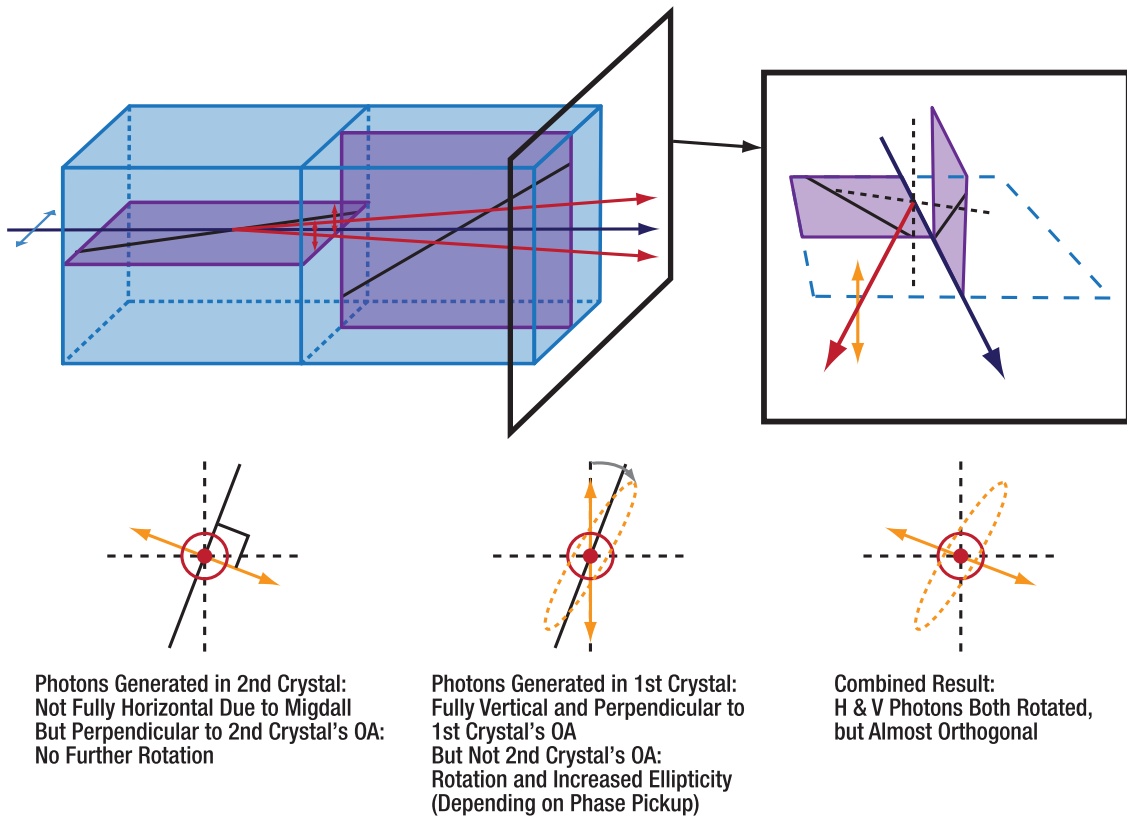


**Figure 235** 3D overview of the pump beam entering the crossed crystal pair. The dashed arrow sketches direction of a down-converted photon traversing the crystal. All angles are exaggerated (cone angle and polarization rotation effects both are about 3° in our case) and refraction at interfaces is neglected. The large gray plane contains pump beam and both down-converted beams reaching the detectors. Smaller planes contain the pump beam and the respective optical axis of the crystal. Dotted gray lines indicate the coordinate system used in the other plots to show the polarization state when viewed against the beam direction of the down-converted photon.

Vertically polarized photons are generated in the first crystal. Here, the optical axis of the second crystal in the pair lies in the mirroring plane between both detection arms. The rays of single photons generated in the first crystal, however, do not travel within this mirror plane but deviate towards the outside by few degrees. Thus, the projection of the second crystal's optical axis onto a plane perpendicular to the single photon rays is not parallel to the vertical photon polarization. This effective rotation angle between polarization and optical axis leads to increased ellipticity and rotation of the polarization main axis, as, due to its birefringence, the second crystal acts like a multi-order waveplate. The strength of the effect depends a lot on the details of the ray geometry, optical axis orientation and the thickness of the second crystal modulo the single photon wavelength. Therefore, considering tolerances of manufacturing and setup alignment, it is not possible to model this in general. In our test measurements we usually see similar orders of magnitude and the same direction of polarization rotation as the Migdall effect. Within each arm, the "vertical" polarization is usually tilted far enough to be roughly orthogonal to the "horizontal" polarization (tilted by the Migdall effect, as discussed above).

Rotating the crossed crystal pair by 90° to swap the relative orientations of the optical axes does not improve the situation. In this configuration, vertical polarization would be pure, but the horizontal polarization is distorted both by the Migdall effect and the second crystal. In our tests, both configurations yield comparable results for the experiments suggested in this manual.

In the Bell test, the small rotational offset between both arms effectively shifts the difference between  $\alpha, \alpha'$  and  $\beta, \beta'$  angles by up to 6°, thus reducing the maximum value of S from 2.83 to 2.77. However, the distorted polarization state also does not match up with the design polarizations for the spatial compensation crystals, thus

the compensation is unavoidably worsened as well, further reducing the optimal S-value achievable in the Bell test.

## 27.2 Comparison Between Crossed Type-I and Type-II SPDC

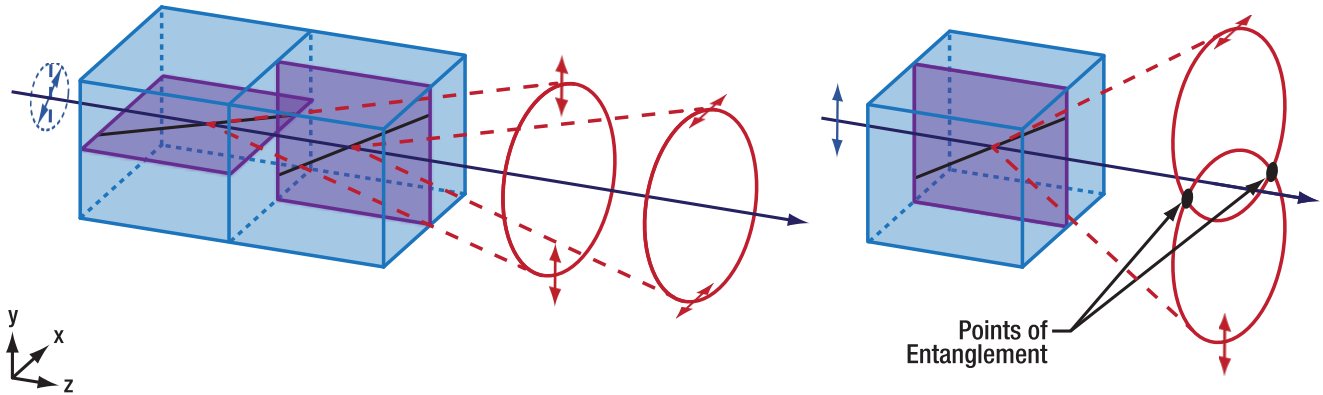


**Figure 236** Schematic view of Type-I (left) and Type-II (right) SPDC processes. Arrows and circles denote vertical and horizontal polarizations, respectively.

Another method often used for the creation of pairs of polarization-entangled photons is the use of crystals cut for the Type-II SPDC process. Here, the created pair does not have the same polarization state (in Type-I both photons are ordinarily polarized), but instead only one photon is ordinarily polarized while the other is extraordinarily polarized. See Figure 236 for an overview of the polarizations and a comparison to Type-I SPDC. Both polarizations can be found on both sides of the pump beam, therefore, only one crystal is required for the generation of photon pairs with both polarizations (prerequisite for entanglement). However, due to the crystal's birefringence, the different polarizations are emitted on two different cones which do not share a common center with each other or with the pump beam. Hence, the area where both polarizations exist at the same locations and are not distinguishable is only a small region of overlap between both cones. Any photons outside of this overlapping area that are collected by the detector are not polarization entangled and will worsen the overall entanglement observability. Thus, for polarization-entanglement based on Type-II SPDC, alignment is very critical. Only the small overlapping area may be focused on the detectors, limiting the effectively usable detector aperture and requiring a good alignment of the overlapping area onto the center of the aperture.

For Type-I SPDC, on the other hand, the cones for both polarizations are symmetric around the pump beam and can be adjusted individually to fully overlap each other over the full area of photon pair emission. Hence, larger apertures won't pick up photon pairs with just one polarization, so the useable aperture size is not limited by an overlap area. See Figure 237 for camera images of the cone cross-sections for a pair of type I crystals compared to a type-II crystal. Conceptually, the walk-off compensation is easier in case of the Type-II SPDC, as spatial and temporal walk-off between both polarizations just comes from the photon pair wavelength and not the common pump beam. This walk-off arises due to the travel of (extra-)ordinary polarized photons through half of the SPDC crystal (assuming the photon pairs are generated in the center of the crystal). The easiest way to compensate the walk-off is to flip the roles of ordinary and extraordinary polarizations in the compensation crystal, while keeping the relative orientations of the pair beams with respect to the optical axis. This can be accomplished by using a half-waveplate (HWP) in a 45° setting<sup>188</sup>, which rotates both polarizations such that H and V flip. After traversing the compensation crystal, any photon has picked up identical phases, both from H and V polarizations (extra-/ordinary). Apart from manufacturing tolerances of the crystals, the HWP is the largest limiting factor for the quality of the compensation. The retardance must be very close to a half-wave for the full measured photon-pair bandwidth and the angle of incidence range (around 3°). Deviations from optimal retardance cause slightly elliptical beam polarizations and improper polarization rotation (which is amplified by the birefringent

<sup>188</sup> When considering the Migdall effect, the generated polarizations aren't exactly orthogonal to each other, so flipping both polarizations requires slightly different settings of the HWP by few degrees.

compensation crystal). This partially scrambles the polarization states of the photon pairs and reduces the entanglement observability.

As in Type-II SPDC both pair polarizations are generated from the same pump polarization, separate temporal pre-compensation in the pump beam is not possible. Compensation can only be done after the pair-generating crystal (post-compensation) and typically affects both spatial and temporal walk-offs. The crossed Type-I system used in this kit, separates the compensation of both effects to a large extend<sup>189</sup> which offers the opportunity to investigate and discuss those effects separately.

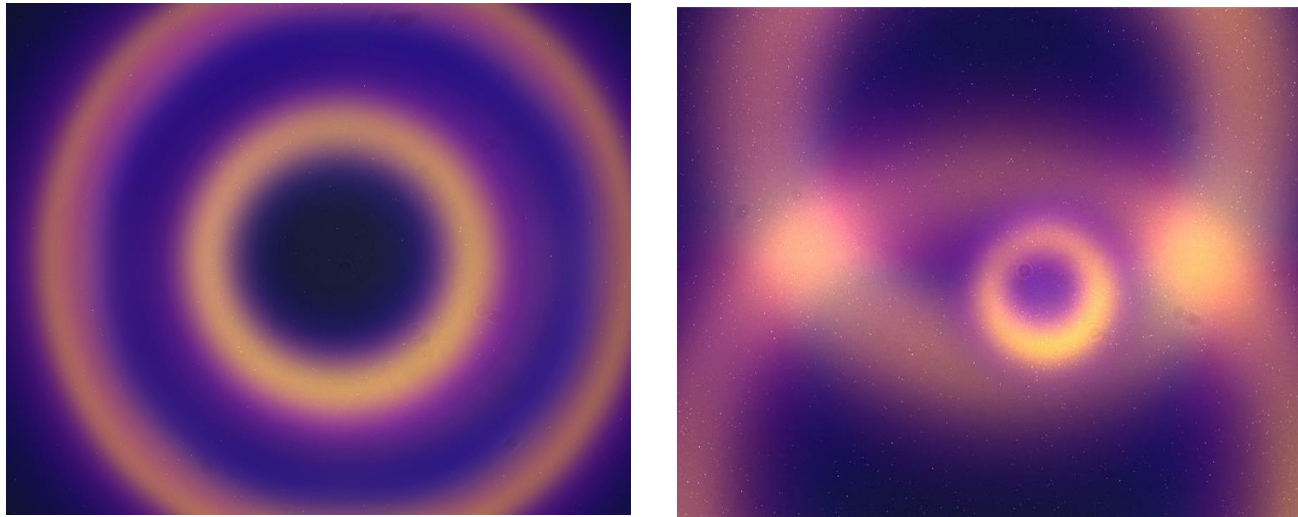


**Figure 237** Comparison of Type-I (left) and crossed Type-II (right) photon pair cones imaged on a camera (see Section 10.4). The small circle in the right image is a contribution from the pump laser. For the left image, the phase matching has been detuned for one of the crystals in the pair to separate the two cones from each other. These images are shown here with a false color scale to increase visibility in the (printed) manual.

### 27.3 Crystal Thickness Choice

The crossed BBO pair thickness of 1.2 mm per crystal has been selected as a compromise between high coincidence count rates and low enough walk-off effects. This section will summarize the important factors for this decision and discuss alternatives.

Generally, the pair photons generated in the SPDC process have a small uncertainty in the output angle, so that even for a single frequency pump input and fixed signal and idler wavelength, there is a finite spread of angles under which photons are emitted along the cone (that is why the rings in Figure 237 are blurred instead of sharp lines). This spread gets smaller with increasing crystal thickness, which leads to a narrower divergence angle of photon output along the cone. Even if the photon pair generation rate would not increase with thickness, more of the generated photons hit the detector aperture area. This causes the single detector count rate to grow approximately proportional to the square of the crystal thickness. Since the narrower divergence angle also makes coincidences more likely, the coincidence rate grows faster than with the square of the crystal thickness in our experiments, which is helpful.

The walk-off effects, as described in Section 20.4.2, scale linearly with the crystal thickness and they increase the width of the entangled state phase distribution. However, the observability of entanglement effects does not scale linearly with the width of the phase distribution, but rather falls off exponentially with crystal thickness<sup>190</sup>. While we can, in principle, compensate larger walk-off effects from thicker SPDC crystals with equally thicker compensation crystals, there are some issues to consider:

- Spatial walk-off compensation is never perfect but can reduce the walk-off significantly. The remaining walk-off still grows linearly with SPDC crystal thickness.

<sup>189</sup> Spatial compensation crystals also contribute to temporal walk-off, but typically to a small extend (scales with cut-angle).

<sup>190</sup> S. Cialdi et al., *Applied Optics*, **47**(11), 1832-1836 (2008).

- In a first order approximation, temporal walk-off depends on the first derivative of the phase with frequency/wavelength (sometimes called phase dispersion or group delay), as described in section 26.12.. But there are also higher-order derivative effects, i.e., the second derivative of phase with frequency (known as group delay dispersion). This means that the quality of our temporal walk-off compensation varies for different wavelengths. Similar to the spatial walk-off case above, there will always be a small residual walk-off that cannot easily be compensated and grows linearly with thickness.
- As mentioned shortly throughout sections 26.11 and 26.12, walk-off compensation is designed for the most likely (equivalent) case of both photon pair polarizations being created in the center of their respective crystal. Still, there are less likely cases to generate pairs with a different phase relationship (i.e., pair generation at the front face of one crystal and more towards the back facet of the other crystal), which cannot be properly compensated for. This effect also scales linearly with SPDC crystal thickness.

How much walk-off is acceptable? For this question, we refer to the central experiment in this kit – the Bell test. In our suggested setup geometry, it should be possible to measure a significant violation of the CHSH inequality with coincidence count rates of few kHz. Therefore, enough photon pairs must be generated and reach the detector lens aperture (i.e., use a thick enough crystal) and it should not be required that the detector iris apertures be closed because of spatial walk-off, such that a large fraction of the photon pairs are blocked.

With crossed BBO pair crystal thicknesses of 0.5 mm each, we are able to violate the CHSH inequality even with fully open detector iris apertures and without spatial compensation crystals. However, the coincidence count rate is only just a few hundred counts per second, leaving no room for inaccurate alignment and leading to low signal-to-noise ratios.

With the 1.2 mm thickness chosen for this kit, the coincidence rates are already much higher. However, as can be seen in the example experiment in Section 24.6, without spatial compensation, it is not possible to violate the CHSH inequality, while making use of the maximum coincidence rates at fully open iris apertures. Hence, we require the spatial compensation crystals for optimal performance.

Using even thicker crystal pairs would further increase the coincidence count rates. However, the experiments presented in this manual do not benefit much from this. In contrast, thicker crystals would negatively impact the performance, due to increased residual walk-off, and increase the cost of all crystals in the kit, as more material is required. Furthermore, it would be harder to show that violation is the CHSH inequality is possible even without spatial compensation, by closing the iris apertures in Section 24.6.

In literature, one can often see another direction taken to optimize system performance: A reduction of crystal thickness to levels of negligible walk-off effects (e.g., 0.1 mm per crystal) is compensated by much higher pump laser power (e.g., Thorlabs' L404P400M laser diode with 400 mW)<sup>191</sup>. Note however, that this significantly increases laser hazards.

## 27.4 Automated Rotation Stages for Detector Polarizers

The EDU-QOP software supports motorized stages that pair with a KDC101 controller. They can be used to automatically rotate the polarizers, e.g., for the 16 Bell test measurements.

These components are not part of the addon kit but can be purchased from our catalog. For each polarizer (and waveplate) assembly you want to automate, you require one full set of these components:

- 1x KDC101 controller
- 1x KPS201 power supply
- 1x PRM1/(M)Z8 rotation stage

The remaining mounting components are identical to the parts used for the manual rotation mounts. Assemble the rotation stage as displayed in Figure 238. Please note:

---

<sup>191</sup> Raul Lahoz Sanz, et al., EPJ Quantum Technology, **11**, 86 (2024).

- During step 4, screw the SM1A6 into the stage until the surface with the part number is at the level of the stage surface. Then fine-adjust the rotation of the adapter until the transmission axis marker on the LPNIRB050 polarizer is parallel to the 90° scale marker of the stage.
- During step 5, use the SPW606 spanner wrench to screw in the SM1RR retaining ring until it is stuck against the backside of the SM1A6 adapter. Use an SPW909 spanner wrench to keep the adapter stable (transmission axis of polarizer parallel to 90° scale marker)

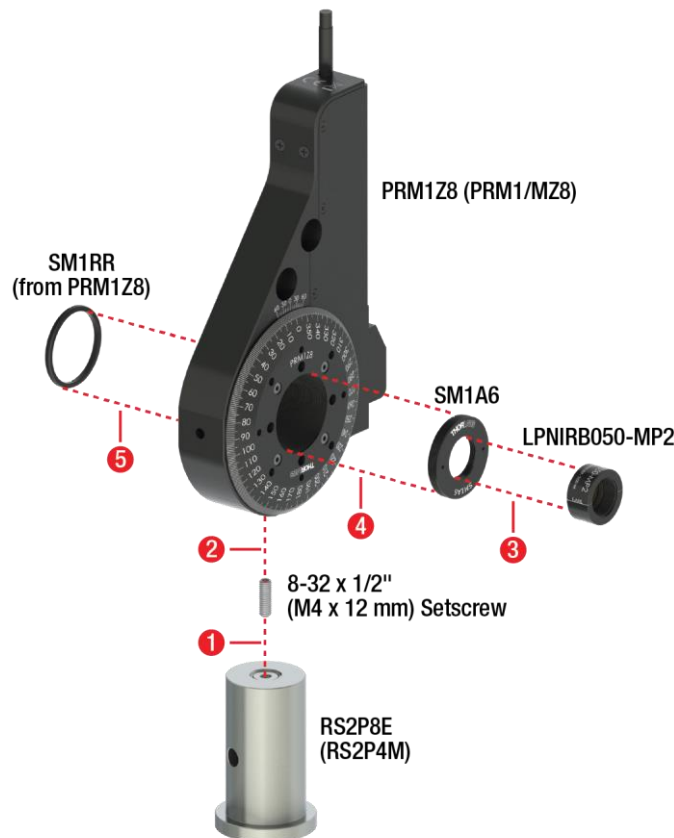


**Figure 238      Assembly of an Automated Polarizer**

The rotation stage cannot be moved by hand, you have to use the KDC101 front panel controls<sup>192</sup>, the Kinesis motion control software<sup>192</sup>, or the EDU-QOP software. In the latter, you can use either the quick control pop-up window (see Section 25.1) or the KDC-Tab (see Section 11.11).

To use the rotation stage in the EDU-QOP software, select the serial number of the KDC101 controller attached to it in the connection window (refer to Section 11.4) and enter a descriptive name, e.g. “Polarizer T”.

In the Bell-Tab (Section 25.1), you must select which KDC101 controllers control the polarizers in front of the detectors T and A, respectively. This naming is also used in the quick control pop-up window.

Always remember to run a homing sequence for any stage connected to a KDC101 controller after booting up the controller.

The calibration process for the polarizers as given in Section 7.7 can still be used as normal. However, after determining the zero position, the dial of the PRM1/(M)Z8 rotation stage cannot be adjusted manually. Instead, the position offset is only applied in the EDU-QOP software, by clicking the Set Zero at Current Position button in the KDC-Tab (refer to Section 11.11).

This offset is saved between restarts of the software, as long as the connect button is not used without the KDC101 controllers being selected. Note that the offset value is matched to the serial number of the KDC101 controller, not the actual motion stage attached to it. To prevent issues with outdated offset values, they are deleted from

<sup>192</sup> Please refer to the KDC101 manual for settings and control of the motion control unit by its front panel or with Kinesis.

memory if the software is run without the respective controller connected. It makes sense to record the correct calibration value for each rotation stage. The calibrated offset values only change if the polarizer is rotated or remounted inside the rotation stage or if the rotation stage itself is mounted in a different rotation configuration (multiple mounting holes are available on the stage).

As an alternative to finding the minimum transmission position in the crossed polarizer setting by monitoring the count rates in the alignment tab, you may also use the KDC-Tab to run a small measurement series for a range of polarizer angles and determine the minimum position by fitting the curve.

## Chapter 28 Troubleshooting

See also Chapter 13 for general issues with components and count rates.

### 28.1 No Oscillations When Tilting Temporal Compensation Crystal

**Problem:** When tilting the temporal compensation crystal (using the blue thumbscrew) to adjust the phase of the entangled state, no oscillations of the coincidence count rate are visible.

**Solution:**

- Check whether correct polarizer settings are used. The axis of the polarizer in front of the T-detector should be oriented at 45° (rotated counterclockwise) and the one in front of detector A should be rotated 45° clockwise (scale shows -45°). Also ensure that both polarizers are correctly calibrated (see Section 7.7).
- The tilt angle difference between minimal and maximal coincidence count rate is about 0.6° (1.2 revolutions of the kinematic mount adjuster). Do not turn the adjuster faster than about ¼ revolution per second.
- Make sure that the crossed BBO pair and all walk-off compensating crystals are placed and oriented correctly. Refer to the figures in Section 22.2 for the required orientations. Note that rotations by 180° around the surface normal or flipping front- and backside of the crystals can effectively flip the sign of the walk-off compensation effect and instead add to the walk-off. In these cases, one obtains mixed states with strongly suppressed oscillations (compare to Equation (179)).
- Ensure equal coincidence count rates for both horizontal and vertical pair polarizations. Check that the pump beam path is still centered on the two irises shared with the alignment laser beam path and that both axes of the kinematic mount of the crossed BBO pair are aligned for maximum pair generation rate. Then adjust the pump beam half-waveplate if necessary (refer to Section 22.2).

### 28.2 Bell Test Results in $S < 2$

**Problem:** When running the Bell test, as described in Section 24.3, it yields  $S$ -values below the classical limit of 2.

**Solution:**

- Check whether walk-offs are properly compensated. See Section 28.1.
- Ensure that the phase of the entangled state is properly adjusted. Set the polarizer axes in front of the A/T detectors to  $\pm 45^\circ$ . Slowly tilt the temporal compensation crystal, such that the coincidence count rate is at a minimum (refer to Section 22.2).
- Ensure that the chosen set of angles used for the Bell test is suitable for this Bell-state. Compare to Sections 24.3 and 24.4.
- Ensure that both polarizers are correctly calibrated (see Section 7.7). When using automatic rotation stages, also ensure that the position encoder is homed and the zero offset is calibrated correctly.

### 28.3 Steep Slope of S-Value Versus Detector Iris Aperture

**Problem:** When closing the iris apertures in front of the detectors, good  $S$ -values can be achieved in the Bell test. With the irises fully open, the  $S$ -value drops below the classical limit of 2.

**Solution:** No or wrong spatial walk-off compensation is used. Compare to Section 24.6. Check spatial compensation crystal orientations and adjust the phase of the entangled state afterwards (refer to Section 22.2).

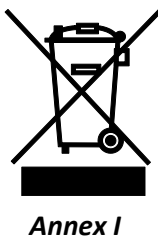
## 28.4 Breakdown of Coincidence Rates at Small Iris Aperture Diameters

**Problem:** When closing the iris apertures in front of the detectors, the (coincidence) count rates are expected to drop faster than linearly with the aperture area. However, at very small aperture diameters below about 4 mm, the coincidence count rates may rapidly approach zero. For the experiment described in Section 9.2,  $g_{PS}^{(2)}(0)$  rapidly decreases when closing the irises.

**Solution:** This is an indicator that the detector alignment is not symmetric with respect to the pump beam (along the up/down or left/right directions). The detectors predominantly see photons from different pairs, which do not cause coincident detection events. Repeat the alignment of the two detectors (refer to Section 7.4.3). Note that, for iris aperture diameters below 2 mm, it will be hard to optimize the detector alignment perfectly, but this is also not required for the experiments in this manual.

## Chapter 29 Disposal, Warranty, and RMA Information

Thorlabs verifies our compliance with the WEEE (Waste Electrical and Electronic Equipment) directive of the European Community and the corresponding national laws. Accordingly, all end users in the EC may return "end of life" Annex I category electrical and electronic equipment sold after August 13, 2005 to Thorlabs, without incurring disposal charges. Eligible units are marked with the crossed out "wheelie bin" logo (see right), were sold to and are currently owned by a company or institute within the EC and are not dissembled or contaminated. Contact Thorlabs for more information. Waste treatment is your own responsibility. "End of life" units must be returned to Thorlabs or handed to a company specializing in waste recovery. Do not dispose of the unit in a litter bin or at a public waste disposal site. It is the user's responsibility to delete all private data stored on the device prior to disposal.



Annex I

### 29.1 Return of Devices

This precision device is only serviceable if returned and properly packed into the complete original packaging including the complete shipment plus the cardboard insert that holds the enclosed devices. If necessary, ask for replacement packaging. Refer servicing to qualified personnel.

## Chapter 30 Thorlabs Worldwide Contacts

For technical support or sales inquiries, please visit us at [www.thorlabs.com/contact](http://www.thorlabs.com/contact) for our most up-to-date contact information.



### Corporate Headquarters

Thorlabs, Inc.  
43 Sparta Ave  
Newton, New Jersey 07860  
United States  
[sales@thorlabs.com](mailto:sales@thorlabs.com)  
[techsupport@thorlabs.com](mailto:techsupport@thorlabs.com)

### EU Importer

Thorlabs GmbH  
Münchner Weg 1  
D-85232 Bergkirchen  
Germany  
[sales.de@thorlabs.com](mailto:sales.de@thorlabs.com)  
[europe@thorlabs.com](mailto:europe@thorlabs.com)

### Product Manufacturer

Thorlabs GmbH  
Münchner Weg 1  
D-85232 Bergkirchen  
Germany  
[sales.de@thorlabs.com](mailto:sales.de@thorlabs.com)  
[europe@thorlabs.com](mailto:europe@thorlabs.com)

### UK Importer

Thorlabs Ltd.  
204 Lancaster Way Business Park  
Ely CB6 3NX  
United Kingdom  
[sales.uk@thorlabs.com](mailto:sales.uk@thorlabs.com)  
[techsupport.uk@thorlabs.com](mailto:techsupport.uk@thorlabs.com)



**THORLABS**

[www.thorlabs.com](http://www.thorlabs.com)